SANDIA REPORT

SAND2007-6023
Unlimited Release
August 2007

Sonar Atlas of Caverns Comprising the U.S. Strategic Petroleum Reserve Volume 2: Big Hill Site, Texas

Christopher A. Rautman and Anna Snider Lord

Prepared by
Sandia National Laboratories
Albuquerque, New Mexico 87185 and Livermore, California 94550

Sandia is a multiprogram laboratory operated by Sandia Corporation, a Lockheed Martin Company, for the United States Department of Energy under Contract DE-AC04-94AL85000.
Approved for public release; distribution is unlimited.

Issued by Sandia National Laboratories, operated for the United States Department of Energy by Sandia Corporation.

Available to DOE and DOE contractors from
U.S. Department of Energy
Office of Scientific and Technical Information
P.O. Box 62
Oak Ridge, TN 37831

Telephone:(865)576-8401
Facsimile:(865)576-5728
E-Mail:reports@adonis.osti.gov
Online ordering: http://www.doe.gov/bridge

Available to the public from
U.S. Department of Commerce
National Technical Information Service
5285 Port Royal Rd
Springfield, VA 22161

Telephone:(800)553-6847
Facsimile:(703)605-6900
E-Mail:orders@ntis.fedworld.gov
Online order: http://www.ntis.gov/help/ordermethods.asp?loc=7-4-0#online

SAND2007-6023

Unlimited Release
Draft: August 30, 2007 3:10 pm

Sonar Atlas of Caverns Comprising the U.S. Strategic Petroleum Reserve Volume 2: Big HillSite, Texas

Christopher A. Rautman and Anna Snider Lord
Geotechnology and Engineering Department
P.O. Box 5800
Sandia National Laboratories
Albuquerque, New Mexico 87185-0706

ABSTRACT

Downhole sonar surveys from the four active U.S. Strategic Petroleum Reserve sites have been modeled and used to generate a four-volume sonar atlas, showing the three-dimensional geometry of each cavern. This volume 2 focuses on the Big Hill SPR site, located in southeastern Texas. Volumes 1, 3, and 4, respectively, present images for the Bayou Choctaw SPR site, Louisiana, the Bryan Mound SPR site, Texas, and the West Hackberry SPR site, Louisiana. The atlas uses a consistent presentation format throughout.

The basic geometric measurements provided by the down-cavern surveys have also been used to generate a number of geometric attributes, the values of which have been mapped onto the geometric form of each cavern using a color-shading scheme. The intent of the various geometrical attributes is to highlight deviations of the cavern shape from the idealized cylindrical form of a carefully leached underground storage cavern in salt. The atlas format does not allow interpretation of such geometric deviations and anomalies. However, significant geometric anomalies, not directly related to the leaching history of the cavern, may provide insight into the internal structure of the relevant salt dome.

This page intentionally left blank.

CONTENTS

FIGURES

TABLES

This page intentionally left blank.

INTRODUCTION

This sonar atlas is intended to provide a comprehensive, "snapshot" view of the cavern geometry for all oil-storage caverns currently constituting the four active sites of the U.S. Strategic Petroleum Reserve (SPR). The atlas presents visual images of the most current (as of August 2007) downhole sonar surveys, which have been rendered in three-dimensional view, using three-dimensional geological computer modeling. Images are presented both for each cavern, individually, and for the cavern field, as a whole, at each SPR site. An index map showing the locations of the four active SPR sites, located along the Gulf Coast of Texas and Louisiana, is presented in figure 1. As described below, this volume 2 focuses on caverns at the Big Hill SPR facility.

The rationale underlying the compilation of this sonar atlas is two-fold. First, a single, comprehensive "view" or "picture" of all of the SPR caverns does not exist. Thus, it may be useful to have such a compendium, for broad-scale general reference across the Strategic Petroleum Reserve Project. Second, the leaching of large underground-storage caverns may be conceptualized as a large-scale geologic "test" of the enclosing salt mass at a particular location within the salt-dome structure. Although the details of cavern geometry will change with ongoing storage operations, the effects of the major geological influences present within the salt stock, will be reflected in the overall cavern geometry. Thus, it may be possible to infer a meaningful amount of information regarding the internal structure of the salt dome from examining the cavern geometry.

This report is organized as follows. We present a very brief overview of the sonar imaging technique. As downhole sonar surveys are the fundamental raw data upon which this sonar atlas is constructed, it is important that some of the physics and limitations of the sonar surveying process

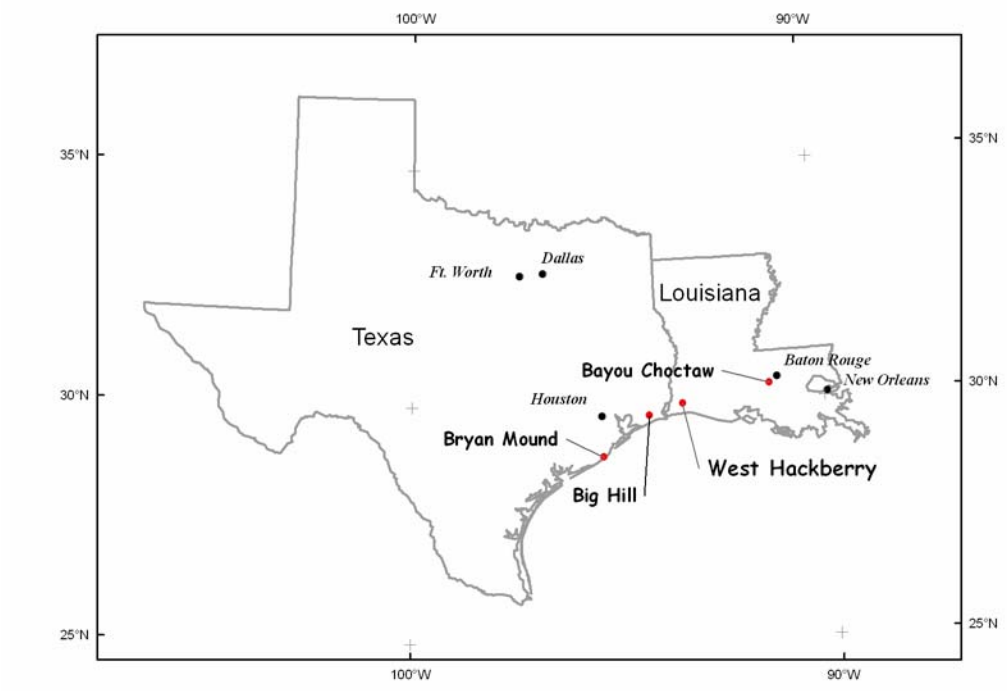

Figure 1. Index map showing the locations of the four active Strategic Petroleum Reserve sites along the Gulf Coast of Texas and Louisiana.

be understood. We then present the rationale and formulation of the various geometrical "attributes", which we compute for each sonar survey, and which are intended to enhance visualization of likely important geologic features, above and beyond the simple three-dimensional geometric form of the sonar results.

After presenting the methodology underlying the visual images that form the bulk of the atlas, we present the visualizations, themselves. For each of the four active, SPR sites — Bayou Choctaw (La.), Big Hill (Tex.), Bryan Mound (Tex.) and West Hackberry (La.) (fig. 1) — we first present results for each cavern individually. The visual presentations follow a more-or-less uniform format, in order to facilitate comparisons between caverns. We then present visualizations of the overall cavern field, for each of these sites. Again, the presentation format is intended to be consistent across the four sites.

Because of the large number of images generated for each cavern, this sonar atlas is presented in four separate physical volumes. Volume 1 contains images for sonar surveys obtained at the Bayou Choctaw SPR site, in central southern Louisiana. Volume 2 of the sonar atlas contains images for the Big Hill SPR site, which is located in extreme southeastern Texas. Volume 3 contains images from the Bryan Mound SPR site, also located in southeastern Texas, but to the west of the Big Hill site. Finally, Volume 4 presents the sonar images derived from surveys conducted at the West Hackberry SPR facility. West Hackberry is located in extreme southwestern Louisiana.

In keeping with the concept of an atlas, this multi-volume report is limited to presenting the objective sonar images, themselves. No interpretation or discussion of the cavern shapes is included.

METHODOLOGY

Sonar Surveying

The downhole sonar surveys, upon which this sonar atlas are based, make use of focused and directionally oriented acoustic signals to determine the distances from the sonar tool to the cavern wall. Knowing the velocity of sound in the particular medium within the cavern (usually oil or brine), the two-way travel time of the acoustical signal may then be post-processed to represent a distance. The apparent spatial position of the nominal reflecting point on the cavern-wall surface may then be computed using simple geometrical relationships. The survey tool is rotated through 360 degrees, obtaining radial time-distance measurements at specified angular increments. The resulting (large) collection of reflecting points, in three-dimensional space, is then modeled, using appropriate software, to display a geometric representation of the full three-dimensional cavern. A conceptual representation of the initial, in-the-field, portion of this surveying process is presented in figure 2.

As shown in the conceptual view of figure 2, the sonar tool is lowered into the cavern through a well via a wireline. The sonar signal, idealized here as a very narrow, linear beam, is transmitted from the tool, reflected from a nominal point on the wall of the cavern, and received back by a receiver, also located on the downhole tool. The uphole equipment multiplies the elapsed time from transmission to reception of the reflected signal by the velocity of the signal and divides by two, to yield the straight-line distance from the tool to the cavern wall. Figure 3 presents the basic

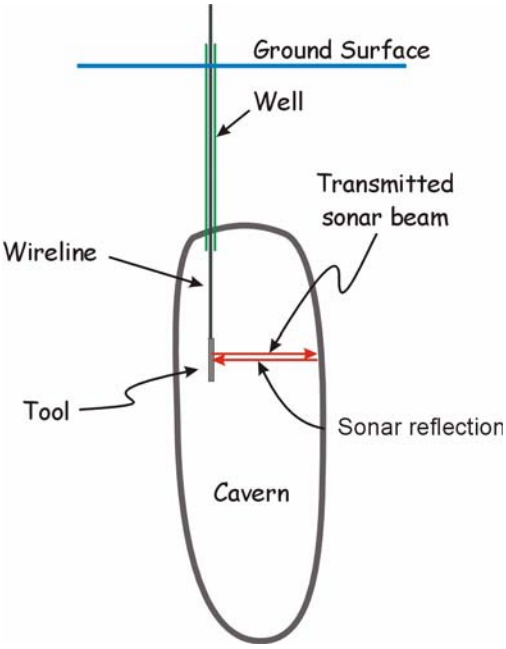

Figure 2. Highly schematic, conceptual representation of the downhole mechanics of a sonar survey. No scale.

geometric calculations that are necessary to reduce the nominal straight-line distance to an actual spatial position.

As the majority of the sonar measurements in a typical underground storage cavern are taken in the horizontal plane (transmitted and reflected beams in fig. 2), much of the computation is simple two-dimensional trigonometry. The *x*-coordinate of the nominal reflection point, with respect to the position of the sonar tool, is computed using the cosine of the angle of the direction of the sonar beam (θ), whereas the *y*-coordinate is computed, similarly, using the sine of that angle.

Adding these *x*- and *y*-coordinate increments to the *x*- and *y*-coordinates of the well through which the survey tool was lowered into the cavern, and appending the depth/elevation of the tool within the cavern, yields an *x*-*y*-*z* triplet associated with the particular direction (azimuth) of the sonar measurement.

Near the top and bottom of a cavern, the sonar measurements are typically taken with the direction of the sonar beam inclined in the vertical plane. This is done, not only to prevent possible collision between the tool and the cavern roof or floor, but also to enable the sonar beam to be incident upon the reflecting surface as close to 90 degrees as possible.

This geometric arrangement requires three-dimensional trigonometry to compensate for the angle of inclination. However, the computations are simple, and involve merely multiplying the two-dimensional result by the cosine or sine (*x* and *y*, respectively) of the angle of inclination (ϕ).

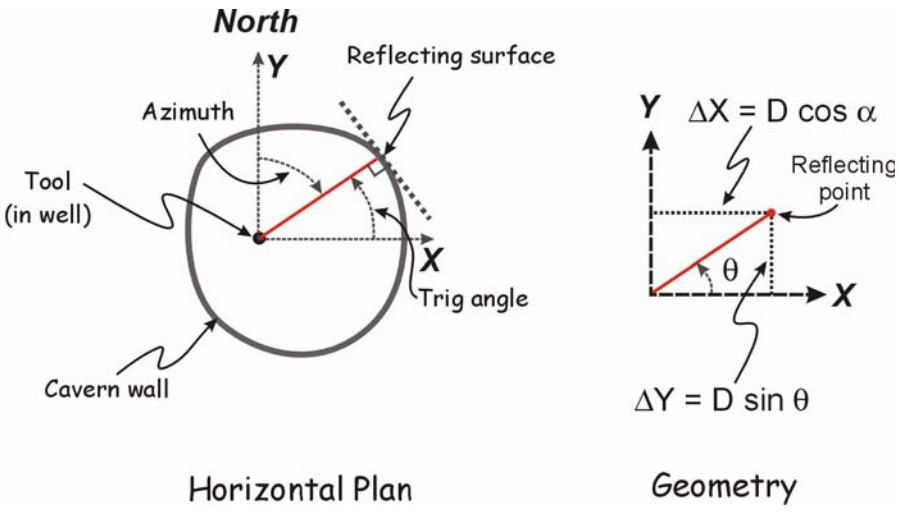

Figure 3. Geometry assumed in reducing the nominal, measured sonar distances to cavern geometry (coordinates of the reflecting point). No scale.

"Up" is taken as a positive angle, whereas "down" is taken as negative. For inclined measurements, the *z*-coordinate of the reflecting point is computed from the depth of the tool plus-or-minus the depth increment attributable to the angle of inclination. This geometry is shown schematically in figure 4.

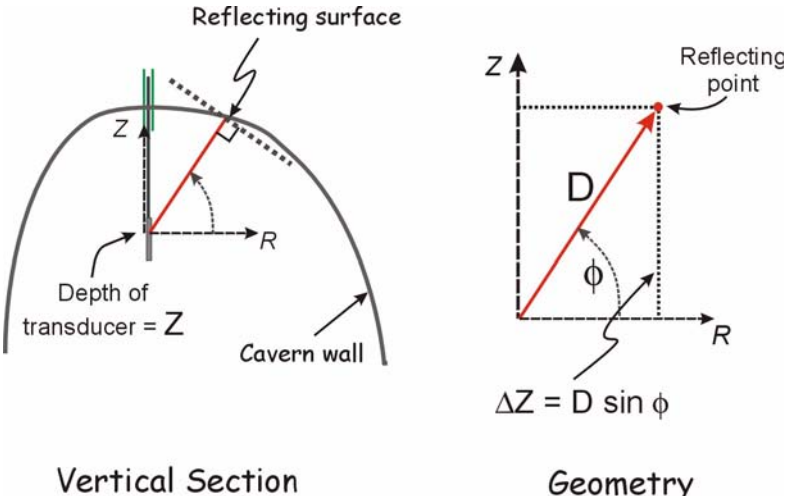

Figure 4. Geometry assumed in reducing *inclined* sonar distances to cavern geometry (coordinates of reflecting point). No scale.

Computation of the *x*-, *y*-, and *z*-coordinates, as performed in generating the cavern geometries shown in this report, are summarized as equations (1) through (3), below.

$$x_{(i,j)} = X_{collar} + D \cos\phi_{(i,j)} \cos\theta_{(i,j)} \quad (1)$$

$$y_{(i,j)} = Y_{collar} + D \cos\phi_{(i,j)} \sin\theta_{(i,j)} \quad (2)$$

$$Z_{(i,j)} = Z_{collar} - Z_{(j)} + D \sin\phi_{(i,j)} \quad (3)$$

where:

- j indicates a particular depth for a set of circumferential measurements,
- i indicates a particular azimuthal angle within that sweep of measurements,
- θ indicates the trigonometric equivalent azimuthal angle of the measurement, and
- ϕ indicates the angle of inclination of the measurement.

D is the fundamental, measured two-way transit time converted to distance.

X_{collar}, Y_{collar}, *and* Z_{collar} are the spatial and elevation coordinates of the well collar, or more properly, the *x*- and *y*-coordinates of the casing shoe. The casing shoe is the actual point from which the sonar tool hangs inside the larger cavern. However, for most SPR caverns, the absolute horizontal difference between collar and shoe locations is minimal.

In practice, the idealized conditions and mechanisms outlined above may be far from reality. The sonar "beam" is, in fact, nowhere near a zero-width linear entity, traveling in a straight line from source to wall to receiver. The beam is more properly a waveform, that expands radially outward from the sonar-tool transmitter. Neither is the cavern wall a flat surface oriented precisely at 90 degrees to the path of travel of the sonar signal.

To complicate matters further, the velocity of the acoustical signal is not necessarily well known, nor even constant along the path of travel. This latter issue of non-constant velocity is of particular concern when making inclined sonar distance measurements. Some of these real-world problems, which combine to make the two-way travel time, and subsequently the distance measurements, uncertain to varying degrees, are illustrated in figures 5 and 6.

In figure 5, the sonar signal is shown as a wavefront, expanding radially away from the source. The signal becomes both weaker (and potentially less recognizable) with distance traveled, and wider. The increase in width of the beam means that reflections may be generated from portions of the cavern wall *not* directly in the intended (nominal) path of the beam. The position of the nominal reflecting point will be estimated incorrectly, as a result.

In this illustration, the time (= distance) values, associated with the "oblique reflection path" or the "shorter travel-time reflection path", would be used in association with the azimuthal angle of the "nominal sonar beam". Thus, the computed radial distance, along that *assumed*, nominal path, will be shorter than the actual distance, in that direction, to the cavern wall. In reality, any number of off-nominal reflection geometries may be present for a given sonar survey.

Figure 6 shows yet-another confounding issue affecting sonar measurements conducted using inclined signals, particularly those made near an interface between fluids of differing composition

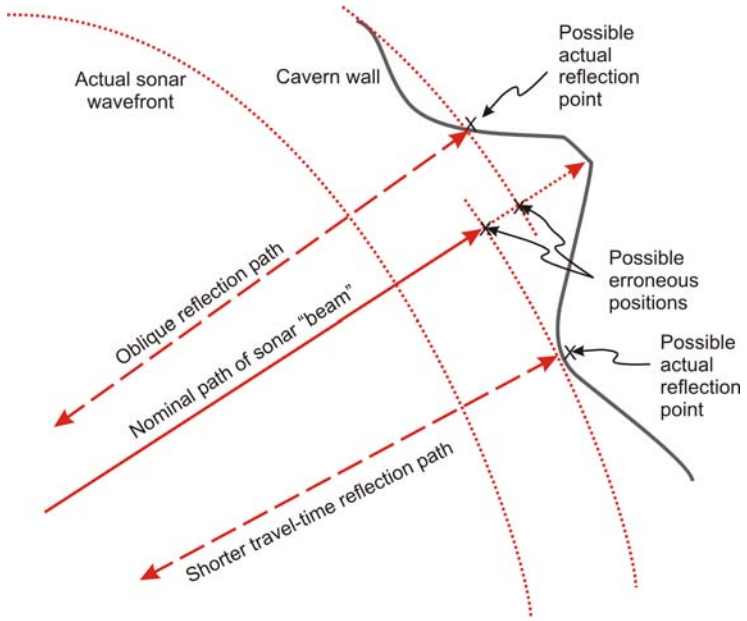

Figure 5. Conceptual illustration of possible spurious, calculated reflection positions resulting from irregular cavern-wall geometry. No scale.

— and hence of differing velocities. Here, in the figure, an upward-directed sonar pulse passes first through a layer of brine, and then through a layer of oil, on its way to being reflected and passing through the oil and brine, again, in reverse order. Because of the differing velocities of sound in these two fluids, the waveform is refracted at the interface, and thus the signal impinges on the cavern wall in a geometry not captured by the idealized computations of figure 4. Both the actual distance and the angular position of the reflecting point are affected by the differing velocities of sound in the two media.

Three-dimensional Computer Visualization

The geometric calculations, outlined above as equations (1) through (3), produce a large number of spatially distributed points in three-dimensional space. Although merely displaying the collection of computed reflecting points would convey some information, visualization of the cavern geometry is facilitated by converting the assortment of points to a surface. The visualization software used by Sandia, performs this conversion through use of a finite-element-like mesh.

Because the sonar measurements are recorded and reported in a known order, and because the number of measurements for each 360-degree sweep of the cavern at a given depth level is constant, it is a relatively simple matter to list the mesh nodes and, more importantly, to describe the connectivity among the set of nodal coordinates. The result of processing the resulting 2-D surface mesh in three-dimensions is illustrated in figure 7.

In part (a) of this illustration, each horizontal ring of line intersections (the *nodes*) represents a single *nominal* reflection point. The nodes in the illustration have been connected by lines to aid

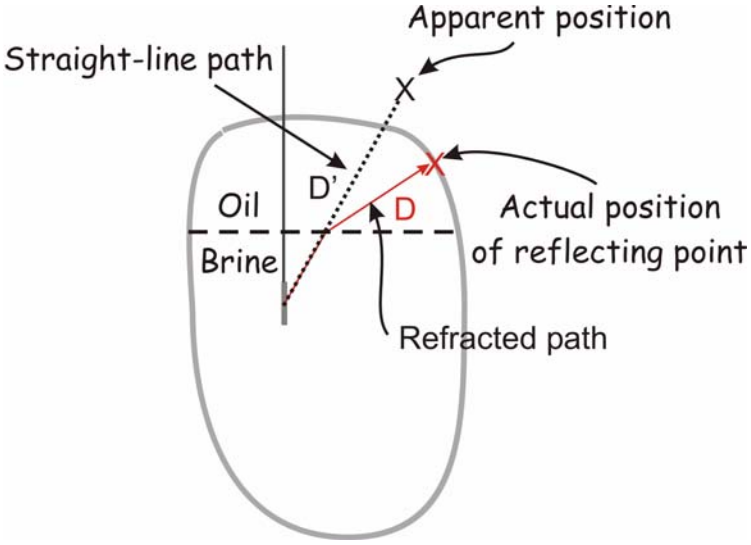

Figure 6. Calculation of an erroneous apparent reflecting point on the wall of a cavern resulting from refraction of the sonar beam at the density interface between the oil- and brine-filled portions of the cavern. No scale.

visualization of these zero-size objects. The lines also indicate the *connectivity* among the nodes, which is essential for generating an actual surface for visualization [fig. 7(b)].

Cavern Attributes

In addition to the basic geometry of a cavern, Sandia has developed a set of attributes — or computed quantities derived from the basic distance-measurement data. Using the computer, the *values* of these attributes may be mapped onto the geometric outline of the cavern using various colors. Part (b) of figure 7 repeats the same mesh from part (a). However, in this view, the quadrilateral cells, between each set of four reflecting-point nodes, have been filled in, and they are colored by their subsea elevation.

Through judicious selection of the specific attributes computed, and by manipulation of the color scale applied to mapping those attributes onto the cavern "shell", it is possible to highlight departures from the idealized cylindrical shape of a carefully constructed SPR-type cavern. Such departures may be related either to the leaching history of the cavern (including small-scale leaching associated with oil movements) or to the solubility of the salt itself. It is this latter characteristic that is believed to allow interpretation of geological features within the salt stock. Ultimately, understanding the internal structure of the SPR salt domes is one of the major justifications for this atlas.

The attributes we use are of four basic types. The first type is simply the *elevation* of the surface at each nodal location. The second type of attribute are several values directly related to the *radius* of the cavern.There are two different "radius values" (described below), as well as the min-

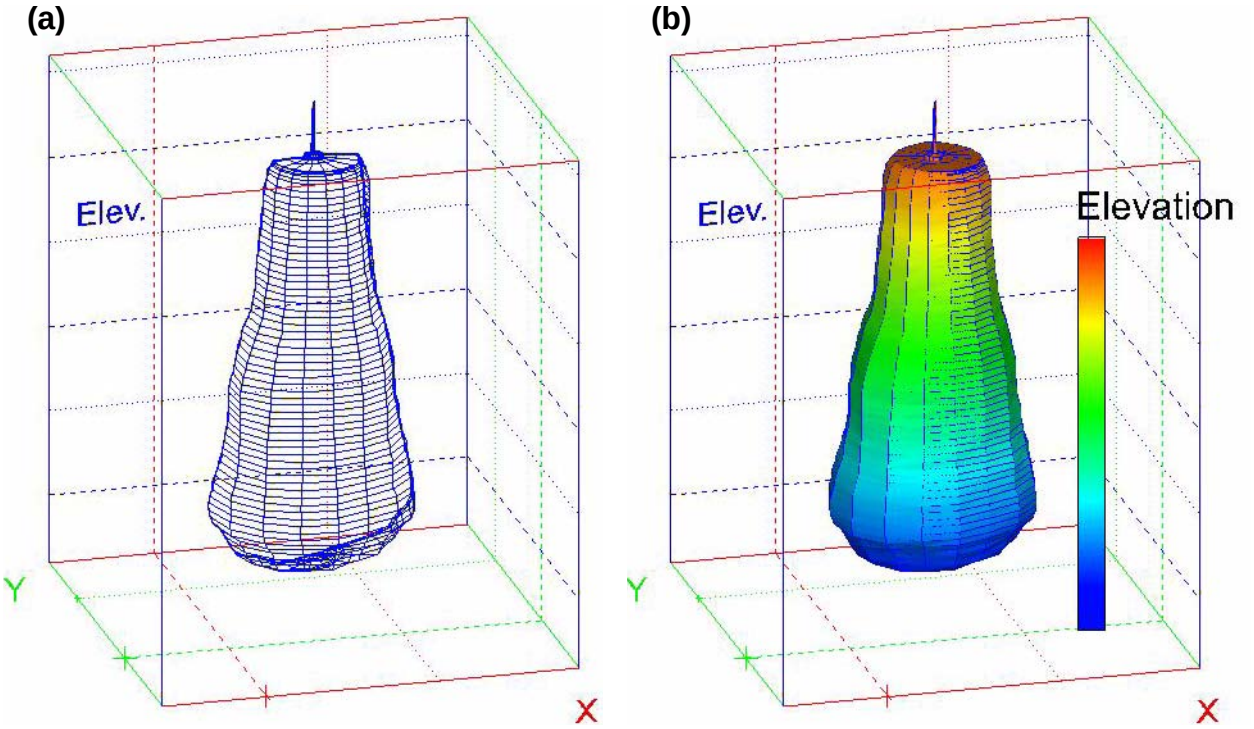

Figure 7. Visualization of a simplified sonar mesh representing the walls of an underground storage cavern. (a) Visualization of computed mesh nodes, located at intersections of lines. Only the "front" of the cavern is shown for clarity. (b) Solid mesh generated by connecting the nodes in (a) to form (mostly) quadrilateral cells (rainbow colors). No spatial scale; color bar represents elevation.

imum, average, and maximum radii observed at any given depth level. The third type of attribute values are those related explicitly to *deviations from symmetry*. The computation of these various attributes is presented below. The final type of attribute values involve the *relationship* of a base cavern to other caverns within the cavern field.

Elevation

The elevation attribute is not particularly revealing of anything specifically related to the geometry of an individual cavern. However, it is an exceedingly simple value to associate with the spatial position of each node (which, by definition, includes the elevation). As a mapped attribute, it is useful when comparing the spatial positioning of more than one cavern in a view, as it directly highlights differences in vertical position among a set of geometric (cavern) objects. Figure 8 illustrates such a comparison of vertical positions for two caverns.

Cavern Radius

The radius attribute is defined simply as the measured distance from the sonar-surveying tool to the "apparent reflection point" of the cavern wall. The radial distance, R, is simply

$$R_{(i,j)} \equiv Distance_{(i,j)} \tag{4}$$

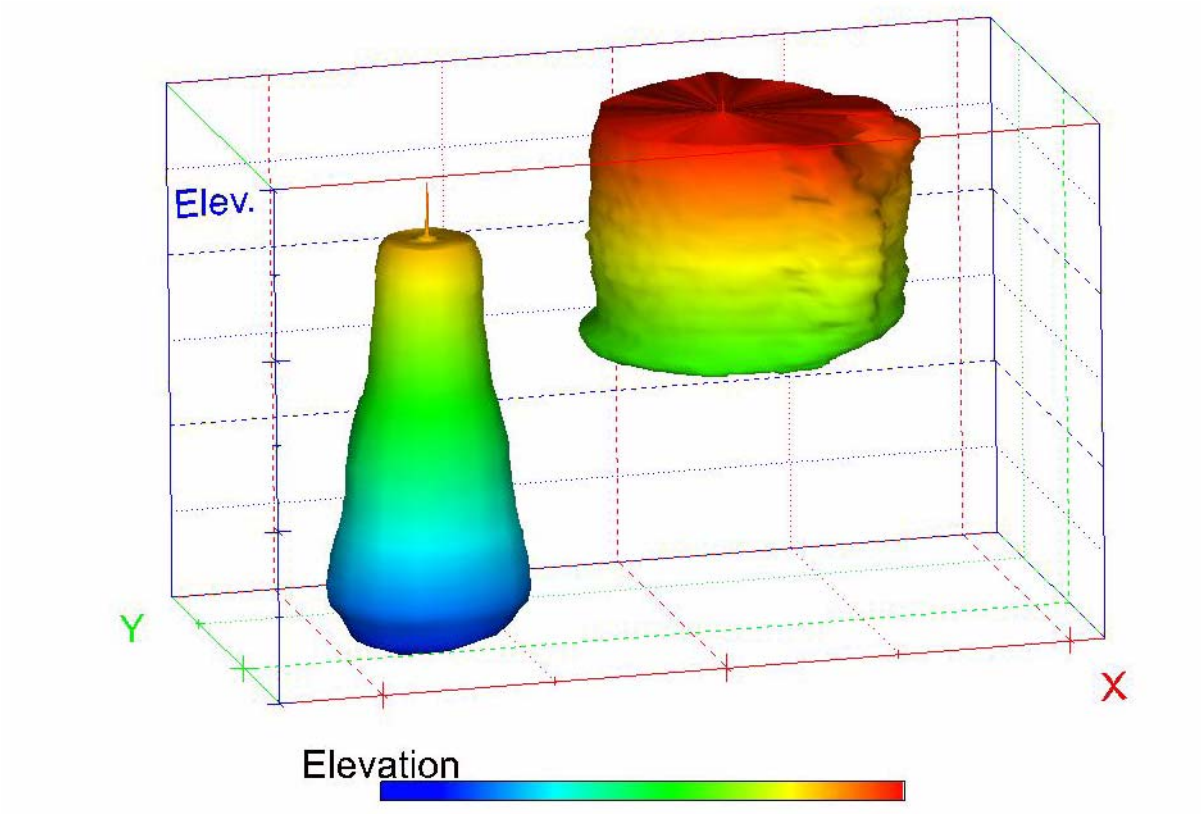

Figure 8. Two arbitrary caverns, located at different vertical positions, showing the elevation attribute. No scale.

where *i* indicates the particular azimuthal direction (measured from 0 degrees = north), for depth station *j*.

The number of azimuthal distances surveyed, for a particular sonar run, may vary from a minimum of eight (8) (for very old surveys, only) to a (known) maximum of 128. The actual number of radii is dependent upon both the age of the survey and the survey operator. Unless specified otherwise, the azimuthal survey directions are assumed to be evenly distributed over 360 degrees.

Note that we *assume* that the sonar reflection is from a "point" on the surface of the cavern wall, and that the wall at that point is virtually normal to the path of the incident sonar beam. Similarly, the sonar signal is assumed to travel as a single ray. In fact, the sonar beam is a wavefront, expanding outward with distance, and the reflecting surface may have a substantially more complicated geometry than that of a plane (i.e., fig. 5). Presumably most of the influence of these confounding factors have been incorporated, to a greater or a lesser extent, into the signal processing algorithms used by the sonar operator. A full discussion of these influences, as well as of the different orientation- and depth-control methods, employed by the survey operator, is beyond the scope of this report.

Centered Radius

The *radius* attribute, just described, is that distance value directly reported by the underlying sonar survey of the cavern. As such, the distance to the cavern wall from the sonar tool is affected by the positioning of the well, through which the tool is lowered into the cavern, with respect to the outline of the cavern itself. If the well collar, or more specifically, the casing shoe, from where the sonar tool hangs on its supporting wireline cable, is offset significantly with respect to the "center" of the cavern, the "radial" distances will vary markedly from one side of the cavern to the other, simply by virtue of the offset origin for the survey. The conceptual diagram of figures 2 and 3 show such an offset. To reduce the impact of such external influences, not directly related to the geometry of the cavern itself, we define what is termed the *centered radius* attribute.

The centered radius is computed by first finding the bounding coordinates of the overall cavern. After the *x, y,* and *z* coordinates of each apparent reflecting point on the cavern margin have been computed, the minimum and maximum *x* and *y* values, *Xmin, Xmax; Ymin, Ymax,* are identified, for the set of readings at each individual depth station. The averages of these maximum and minimum coordinate values are then taken, by definition, to represent the horizontal center of the cavern at this depth. Thus:

$$Xcen_{(j)} \equiv \frac{Xmax_{(j)} - Xmin_{(j)}}{2} \tag{5}$$

$$Ycen_{(j)} \equiv \frac{Ymax_{(j)} - Ymin_{(j)}}{2} \tag{6}$$

Using this defined center as the basis, it is then a simple matter to iterate through the list of reflection points, and to compute the "centered radial" distances from this constant *x-y* position, for each depth station, using the Pythagorean theorem. Thus:

$$Rcentered_{(i,j)} = \sqrt{(X_{(i,j)} - Xcen_{(j)})^2 - (Y_{(i,j)} - Ycen_{(j)})^2} \tag{7}$$

Figure 9 presents a comparison of the differences between the direct "radial" distance measurement and the equivalent centered radius distances for the same cavern. The cavern has been specifically selected, based on its markedly off-center access well.

Minimum Radius, Maximum Radius, and Average Radius

The minimum- (*Rmin*), maximum- (*Rmax*), and average-radius ($\bar{R}$) attributes are defined on a depth-by-depth basis, over the *j* depth stations surveyed. These values are computed simply as the minimum, maximum, and arithmetic average of the *Nradii* distance measurements reported by the sonar surveying tool at each individual depth station. Accordingly, these attribute values are constant for each surveyed depth level, *j*.

$$Rmin_{(j)} = Min(R_{(i,j)}), \tag{8}$$

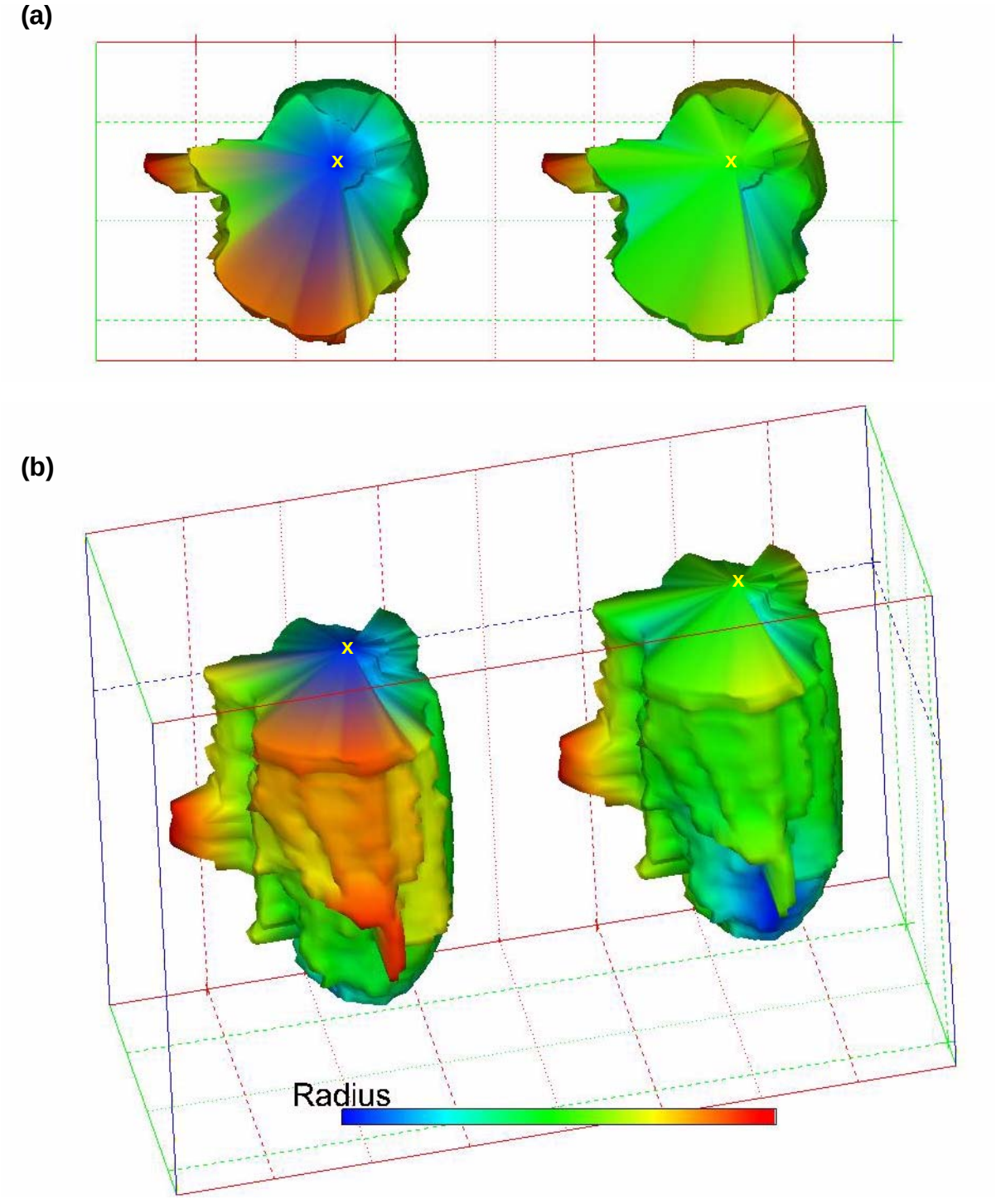

Figure 9. Comparison of the radius (left) and centered radius (right) attributes for a cavern for which the access well (x), through which the cavern was surveyed, is particularly off center. (a) Top view; (b) perspective view. No scale.

$$Rmax_{(j)} = Max(R_{(i,j)}), \tag{9}$$

and

$$\bar{R}_{(j)} = \frac{\sum_{i=1}^{Nradii} R_{(i,j)}}{Nradii} \tag{10}$$

The *overall* average cavern radius, across the entire vertical height of the cavern, may also be computed, as:

$$\bar{R}cavern = \frac{\sum_{j=1}^{Ndepth} \sum_{i=1}^{Nradii} R_{(i,j)}}{Ndepth \cdot Nradii} \tag{11}$$

This latter value is constant for each cavern. Thus, it is useful essentially when comparing more than one individual cavern, as within a cavern field. A simple example is shown in figure 10.

Radius Standard Deviation

It may be instructive to investigate the degree to which the *nradii* individual radial distance measurements, at any particular depth level, vary among each other. This variation provides one measure of cavern asymmetry, or deviation from a pure cylindrical form. A very simple, and relatively intuitive, measure of this consistence of cavern size is the *radius standard deviation*. This attribute is computed on a depth-by-depth basis.

We use the standard computational formula for a standard deviation, which avoids the need to compute the average radius, at each depth station, separately from, and prior to, computing the deviations of the individual values from that average. Thus:

$$Rsdev_{(j)} = \left[\frac{\sum_{i=1}^{Nradii} R_{(i,j)}^2 - \left(\sum_{i=1}^{Nradii} R_{(i,j)} \right)^2 / (Nradii)}{Nradii - 1} \right]^{\frac{1}{2}} \tag{12}$$

Out-of-Round Distance and Ratios

A somewhat more-involved cavern-geometry attribute is the so-called *out-of-round distance,* here indicated ΔR. This radial attribute is intended to highlight geometrical irregularities over the

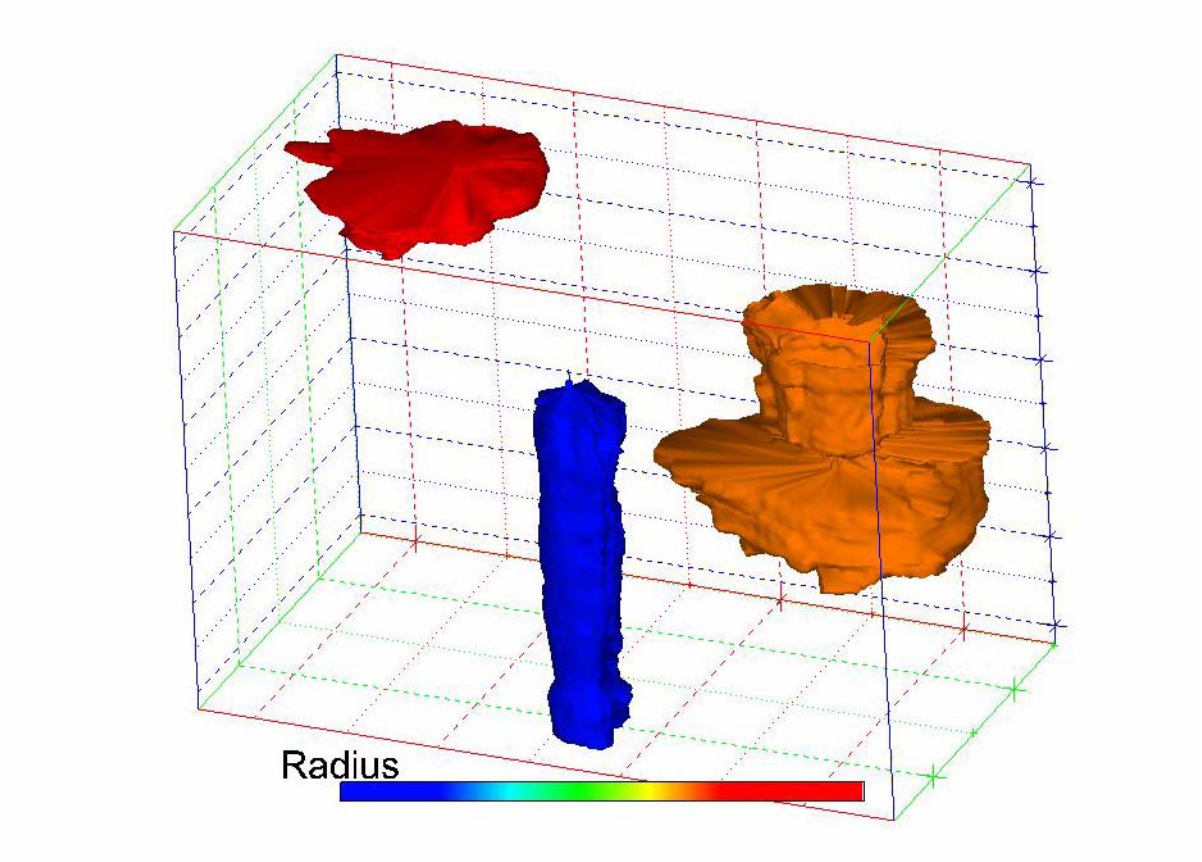

Figure 10. Example of the overall cavern radius attribute. The “overall” radius is constant for a given cavern. Note that the right-most cavern is shown as intermediate in overall radius, even though it appears significantly larger than the left-most cavern. The averaging of the vastly different radial measurements, across the total vertical height of the cavern, yields an overall radius value less than the corresponding measure for the much shorter left-most cavern.

vertical extent of the cavern. The values are computed as the difference between an individual centered-radial measurement and the average radius for the same depth level.

$$\Delta R_{(i,j)} = Rcentered_{(i,j)} - \overline{R}_{(j)} \tag{13}$$

Because any particular cavern, at a given depth, may be markedly large or smaller in diameter than at another depth, we may also evaluate the departures from “roundness” with respect to the average radius of the cavern at the same depth. The value, through which this type of deviation from symmetry is evaluated, is termed the *out-of-round ratio, ΔRratio*. This value is computed simply as the quotient of the actual out-of-round distances ($\Delta R_{(i,j)}$), and the average radius at that depth.

$$\Delta Rratio_{(j)} = \frac{\Delta R_{i,j}}{\bar{R}_{(j)}} \tag{14}$$

A separate measure of the overall out-of-round ratio for the entire cavern is computed using the individual out-of-round-distance deviations and the overall average diameter of the entire cavern. Thus:

$$\Delta Roverall_{(i,j)} = \frac{\Delta R_{(i,j)}}{\bar{R}cavern} \tag{15}$$

Figure 11 presents illustrations of the several out-of-round attributes. In this illustration, we present the out-of-round distance, in feet, in part (a) and the out-of-round ratio, as a fraction, in part (b). Recall that equation (14) computes the out-of-round ratio by dividing the out-of-round distances [fig. 11(a)] by the average cavern radius at that depth level, thus normalizing the deviations.

The overall out-of-round ratio, also a fraction, is shown in part (c) of the figure. Note that the color scales appear identical in parts (a) and (c), as the only difference between these two cavern attributes involves division of the individual deviation distances, part (a), by a constant. However, as the magnitudes of the attributes are significantly different, the two attributes provide different perspectives on how much the cavern departs from the idealized cylindrical form.

Part (d) of figure 11 presents a top view of this same cavern. The approximate orientation of the perspective views is shown by the arrow (from the northwest).

Pillar-to-Diameter Ratios and Minimum Inter-cavern Distances

Another, entirely different class of attributes may also be defined, which examine the geometrical relationship of one cavern to its neighbors. This class of cavern-relationship attributes are an expansion of more conventional assessments of cavern spacings and of their impact on cavern stability.

Conventionally, one way of examining the relationship between any given cavern and its nearest neighbors, which are usually the caverns of greatest interest, is through the so-called pillar-to-diameter ratio. The pillar-to-diameter ratio, P/D, is defined as the quotient of the minimum thickness of the pillar(s) of salt, separating the cavern of interest from adjacent caverns, divided by the "diameter" of that cavern. This ideal relationship is illustrated in figure 12. As the idealized form of an oil-storage cavern is a right-circular cylinder, it is quite easy to determine the two input values required for P/D from a map view of the caverns.

In practice, even carefully leached underground storage caverns depart from the idealized cylindrical form. Historically, this real-world condition has been acknowledged by using a measure of the average diameter of the cavern of interest as the denominator of the P/D ratio. The most straightforward method of deriving the average cavern diameter — conceptualized as the diameter of a cylindrical cavern of equivalent volume — is to extract that equivalent diameter by solving the algebraic expression for the volume of a cylinder ($V = \pi r^2 h$) for radius, and multiplying the radius by 2 to find the diameter.

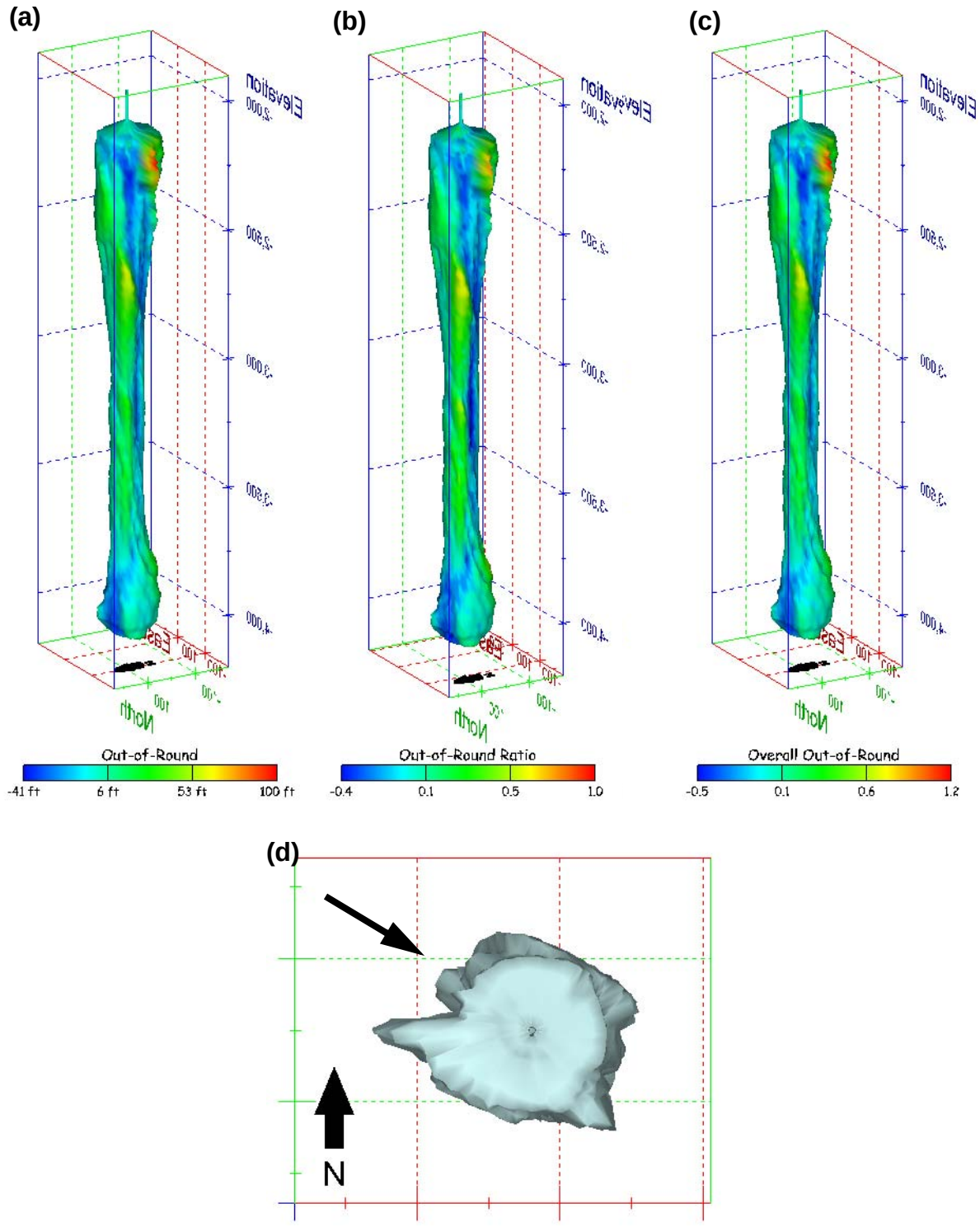

Figure 11. Examples of the three out-of-round attributes described in the text. (a) Out-of-round *distance*; (b) out-of-round *ratio*; (c) *overall* out-of-round ratio. (d) Top (map) view of cavern, showing approximate direction of perspective views (arrow). Note that whereas the color mapping is nearly identical, the scale values are markedly different. See text for discussion.

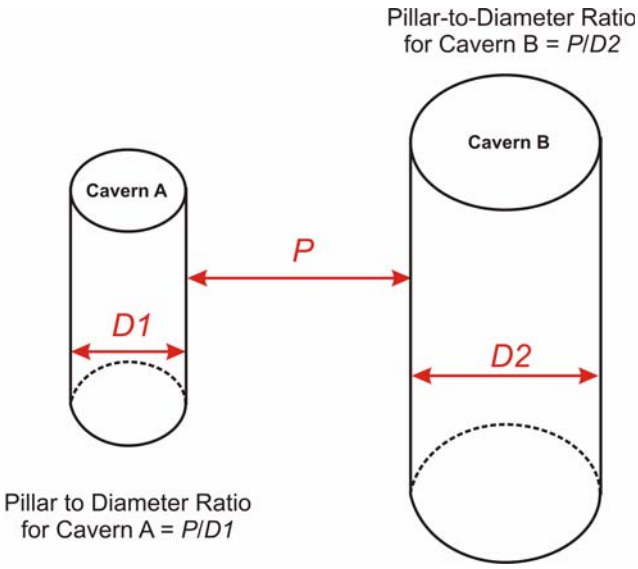

Figure 12. Geometrical relationships involved in the standard computation of the pillar-to-diameter ratio. Note that P:D for cavern A > P:D for cavern B.

However, whereas this approach to determining an average diameter works well for relatively well-formed caverns, usually leached specifically for storage purposes, the average-diameter methodology has increasingly severe limitations as the form of the cavern departs from that of a cylinder. As many SPR storage caverns are converted brine caverns, there are a wide variety of departures from the idealized cavern shape. For some caverns, the average cavern diameter, based upon equivalent volumes, simply is not an acceptable measure of cavern geometry.

Although there is no real substitute for a full 3-D geomechanical analysis for examining cavern stability, related to neighboring caverns, in detail, it is possible to use downhole sonar measurements to compute a "pillar-to-diameter ratio" in three dimensions. The 3-D P/D ratio thus becomes an attribute, which may be mapped onto the geometric form of the cavern, just as we have described for the more directly derived sonar attributes.

The 3-D P/D ratio attribute is thus defined as the minimum distance from *each* mesh node, on the cavern of interest, to *any* of the mesh nodes describing *any* of the neighboring caverns, divided by the average cavern diameter *at the depth of the particular mesh node*. This may be written, in terms of the nomenclature we have been using above, as:

$$[P/D]_{i,\,j,\,k^*} = \frac{\text{MIN}\,[\;Dist\,[\;(x,y,z)_{i1,\,j1,\,k^*}\;,\;(x,y,z)_{i2,\,j2,\,k2}]\;]}{2\;\bar{R}_{j,\,k^*}} \qquad (16)$$

where k^* indicates the cavern of interest, and *Dist*[...] is shorthand for the computed (Pythagorean) distance between the mesh node described by indices i and j on the base cavern (k^*) and all the other mesh nodes on caverns $k2 = 1$ to *Ncavern* neighboring caverns. As implied by equation (16), the calculation of 3-D P/D is complex and computationally intensive.

This three-dimensional pillar-to-diameter relationship is illustrated in figure 13. As suggested by the numerous dashed arrows, the pillar distances, *P*, from each particular point under consideration on the sonar mesh constituting the base cavern, must be computed to each and every (relevant) point on the sonar mesh constituting *each* neighboring cavern. The minimum pillar distance, P_{min}, is then selected and divided by the average diameter, "*D*", associated with the current point of interest. Once this three-dimensional P:D value has been computed and stored, the search moves to the next point of consideration on the sonar mesh of the base cavern, and the process is repeated.

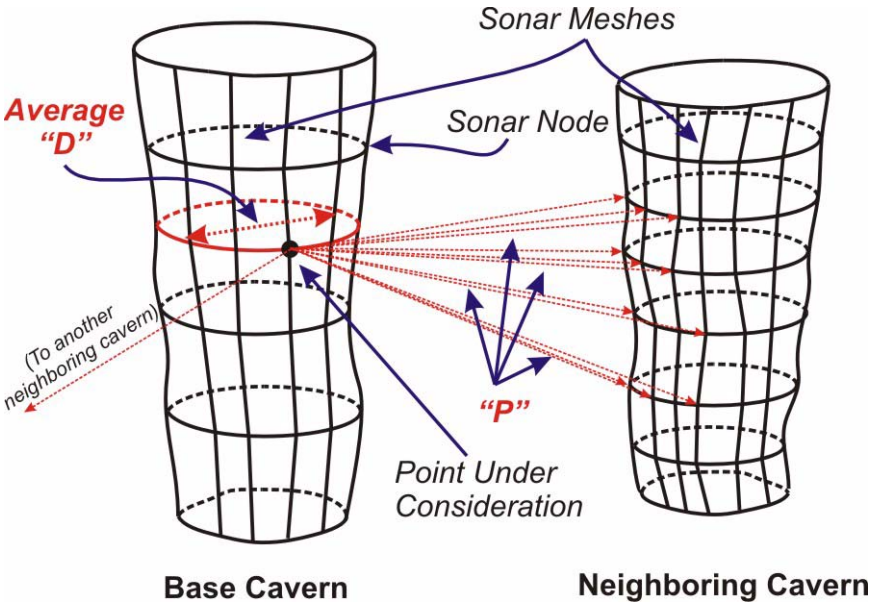

Figure 13. Conceptual illustration of the concepts underlying the definition and calculation of the three-dimensional pillar-to-diameter ratio.Compare to figure 12.

Snider and Stein (2006) and Rudeen and Snider (2007) have developed computer algorithms that minimize the computations necessary to find P_{min}, by screening the mesh(es) describing the nearest-neighboring caverns to eliminate grid nodes that cannot possibly be related to the minimum distance between the two cavern walls. Examples of such screened-out mesh nodes include points on the backside of the neighboring cavern, or nodes near the base of the neighbor cavern when examining nodes near the top of the cavern of interest.

The resulting computer program [Rudeen and Snider (2007)], implementing these sorting, searching, and computing algorithms, makes practical the use of the three-dimensional pillar-to-diameter as a mappable attribute for this atlas. We present illustrations of cavern geometries showing both the minimum distance, in absolute terms, and as the P/D ratio.

Note that the minimum distance, *Pmin*, will be the same for any two specific nodes involved on caverns "A" and "B", whether comparing cavern "A" to cavern "B", or vice versa. However, the P/D values associated with those two nodes will almost certainly be different. The divisor for

one node, say on cavern "A," will be the average diameter at its depth, whereas the divisor for the ratio associated with the other node will be the average diameter for the other cavern, "B" [equation (16)].

RESULTS: THE SONAR ATLAS

The Big Hill cavern field is shown in map view in figure 14. The dates of the most recent available sonar surveys, which are used in this report, are given in table 1.

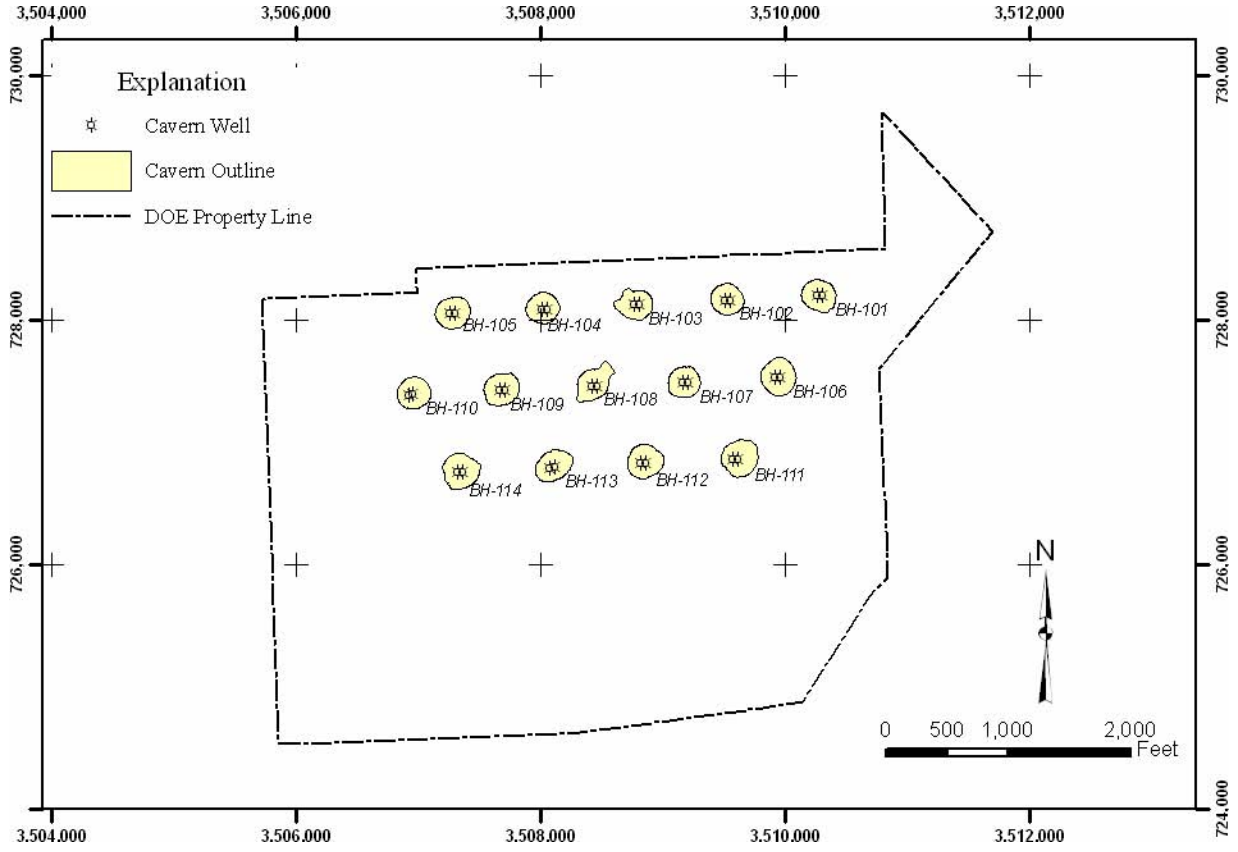

Figure 14. Index map showing positions of the Big Hill caverns within the DOE SPR property boundary

Table 1: Dates of Big Hill Sonar Surveys Presented in Atlas

Cavern	Date	Operator
BH-101A	12-Oct-00	Sonarwire, Inc.
BH-102A	19-Nov-03	Sonarwire, Inc.
BH-103A	15-Sep-04	Socon Cavity Control
BH-104A	01-Oct-02	Sonarwire, Inc.
BH-105A	23-Mar-99	Sonarwire, Inc.
BH-106A	23-Feb-05	Socon Cavity Control

Table 1: Dates of Big Hill Sonar Surveys Presented in Atlas (Continued)

Cavern	Date	Operator
BH-107A	28-Nov-00	Sonarwire, Inc.
BH-108A	09-Mar-05	Socon Cavity Control
BH-109A	08-Mar-05	Socon Cavity Control
BH-110A	01-Mar-05	Socon Cavity Control
BH-111A	02-Mar-05	Socon Cavity Control
BH-112A	04-Apr-05	Socon Cavity Control
BH-113A	02-Feb-05	Socon Cavity Control
BH-114A	08-Oct-03	Socon Cavity Control

Cavern Geometry

The actual images showing the geometry of the various caverns are presented below. A consistent presentation format has been adopted. The intention of this format is to facilitate comparisons between and among the different caverns and the different attributes for each cavern.

First, a top (map) view of the cavern is presented at the beginning of each cavern section. Second, we present (1) the measured radius, (2) the centered radius, (3) the averaged radius, (4) the minimum radius, and (5) the maximum radius. Next, we present the various measures of departure from the idealized cylindrical form: (6) the radius standard deviation, (7) the out-of-round distance, (8) the out-of-round ratio, and (9) the overall out-of-round ratio. Finally, we present the measures of each cavern in relationship to the other caverns in the field. The first part of this relationship involves (10) the distance from each point of the external surface of the cavern to the closest point on any neighboring cavern. The second part of this relationship involves (12) the three-dimensional pillar-to-diameter ratio.

Each of these computed cavern attributes is presented from four quadrants of the compass: southwest, southeast, northeast, and northwest. The angle of inclination of the perspective views is constant at from 20 degrees above the horizontal. After reviewing many, many sonar images, these view angles appear to capture the overall image of the caverns in a fairly satisfactory manner, for a static, printed format.

Some brief comments on the presentation, itself, are appropriate. The spatial axes shown for each sonar image are generated auby the computer modeling program. As such, there is only minimal control over the positioning of the axis labels and the coordinate values. As the cavern views, described in the preceding paragraph, rotate through 360 degrees, the labels rotate also. Thus in some images, the labels will be “reversed”. They are always shown “properly” from the south.

Some clipping of the various images has also been necessary to fit the various images into the page format of this report. This effect has been minimized. However, where the choice was between a larger image of the cavern, proper, and including the entire image (especially axis labels) in the visible portion of the figure, we opted for the larger cavern image. Mental compensation for these two unavoidable visualization artifacts should be fairly easy and intuitive.

Velocity of Sound

One of the “cavern” attributes contained in *some* sonar survey files is the measured velocity of sound, as recorded by the sonar tool during its vertical transit of the cavern. We present, as the final image in each cavern set, a horizontal view showing this measured velocity. The view is from due south.

Note that the velocity profile is a function of the fill state of the cavern at the time of the survey. Note, also, that the velocity profile is not provided by all sonar vendors. The result is that we are unable to present a meaningful illustratin of this type for a number of the caverns.

The Interactive Sonar Atlas

Additional details and greater insight into the cavern geometries may be gained through use of the digital images, included on the compact disk contained in the pocket at the back of this report volume. These digital files contain the same set of cavern attributes as the printed illustrations. The user may step through the various display attributes one at a time.

However, the format of the files allows the user to view and manipulate each image, as may be desired. The cavern models may be rotated to view the images from any desired direction, using the mouse. Additionally, the images may be panned across the computer screen, and zoomed in or out to any desired magnification. Finally, the user may print any particular view, or save the image to a digital image file for later use. The cavern identification, as well as the visible attriubute, are indicated on the screen, in order to ensure positive identification of the particular view.

Installation instructions for the visualization software are included in the Appendix. The appendix also contains more detailed instructions for using the visualization software and manipulating the viewer.

The viewer is proprietary software of C Tech Development Co. (www.ctech.com). However, the software may also be used in “unlicensed” mode. In unlicensed mode, only files that have been written containing a special binary code are viewable. Other files cannot be loaded or viewed. In essence, then, the “license” is portable with the model files, themselves. Sandia National Laboratories is able to write these binary codes into each and every model file, thus facilitating use of such models by anyone, without the need to purchase a separate license for the player, itself.

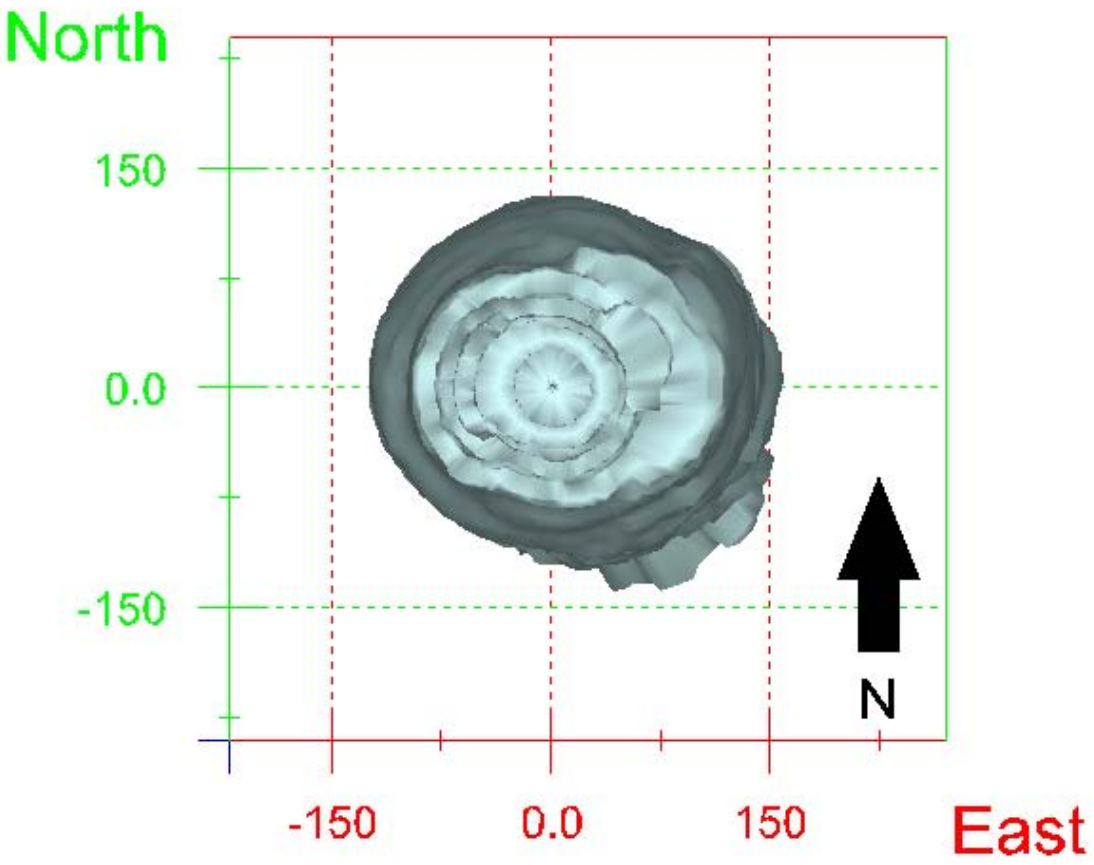

Figure 15. Map view sonar images of cavern BH-101, showing the basic geometry of the cavern. Grid squares represent 150 ft.

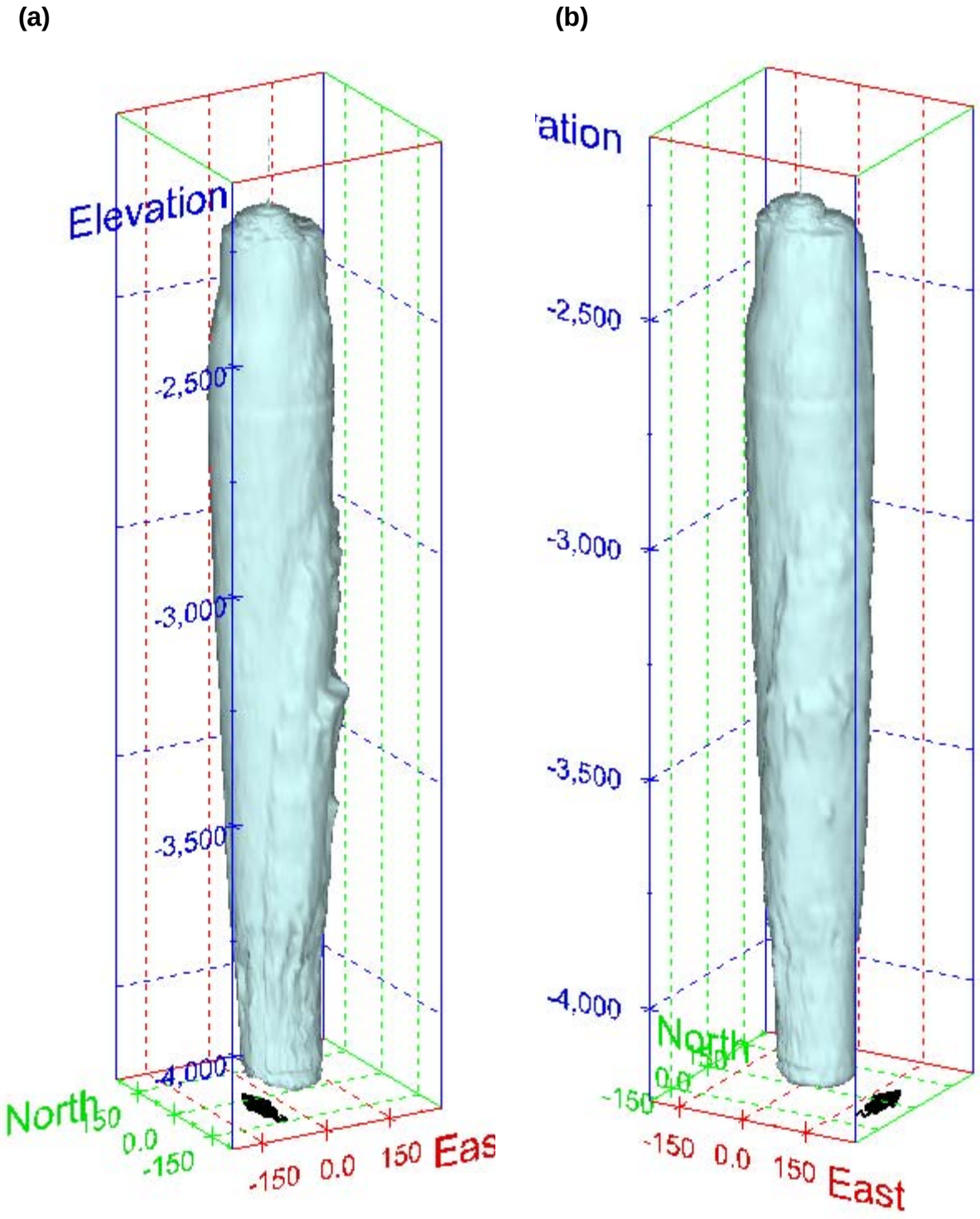

Figure 16. Sonar images of cavern BH-101, showing the basic geometric shape of the cavern. View from (a) azimuth 210°, elevation 20°; (b) azimuth 150°, elevation 20°.

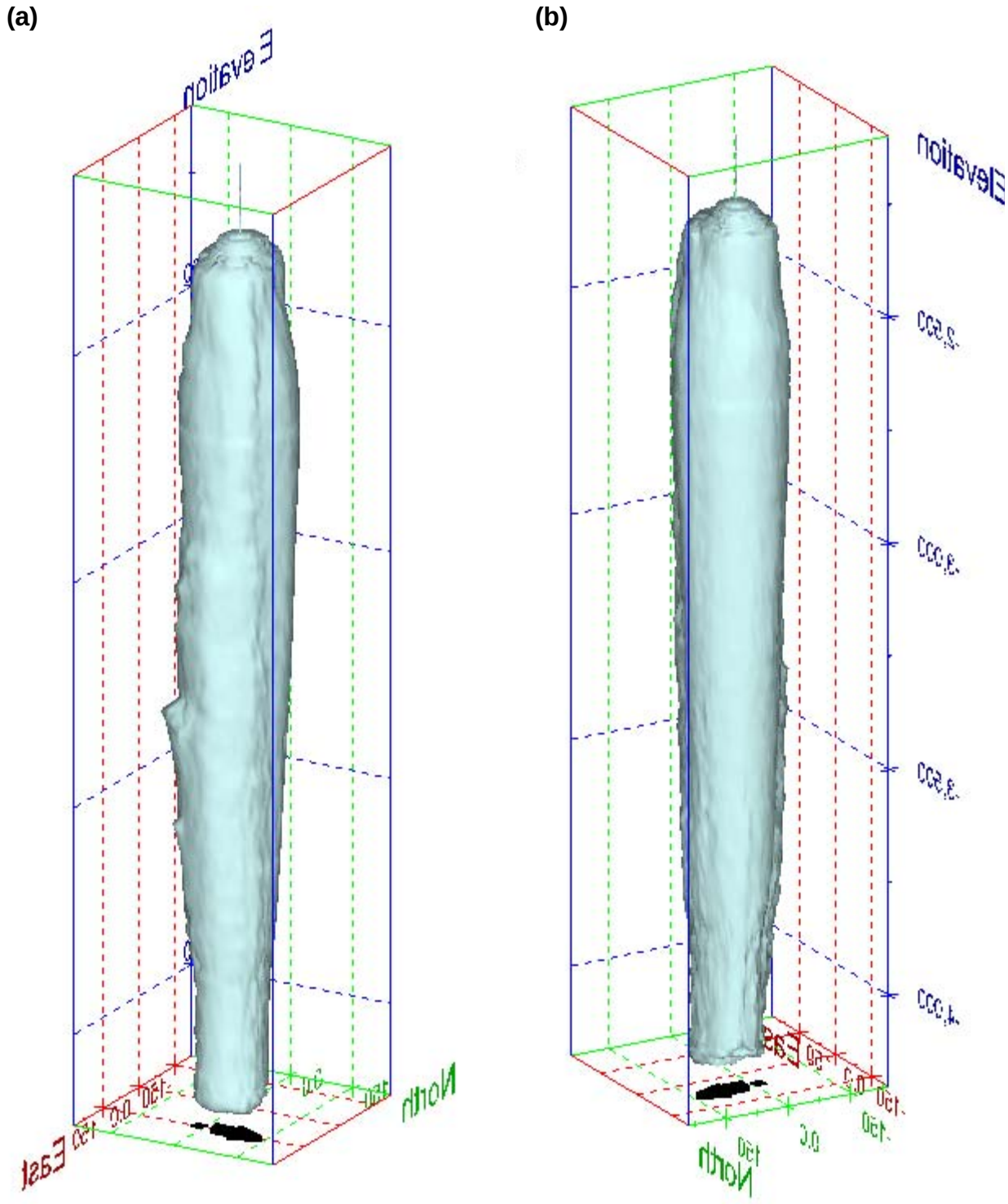

Figure 17. Sonar images of cavern BH-101, showing the basic geometric shape of the cavern. View from (a) azimuth 60°, elevation 20°; (b) azimuth 300°, elevation 20°.

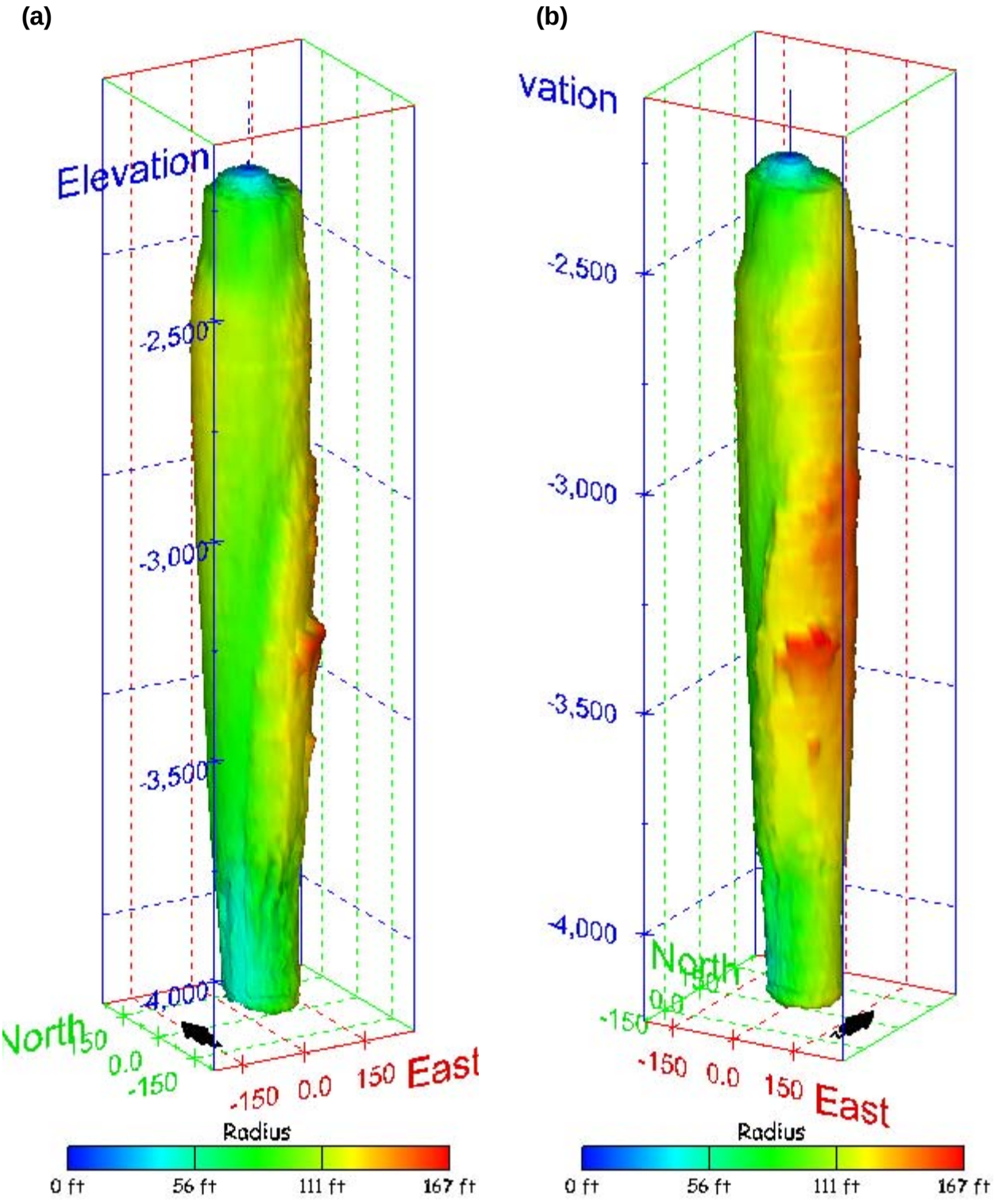

Figure 18. Sonar images of cavern BH-101, showing the geometry of the cavern colored by measured radius. View from (a) azimuth 210°, elevation 20°; (b) azimuth 150°, elevation 20°.

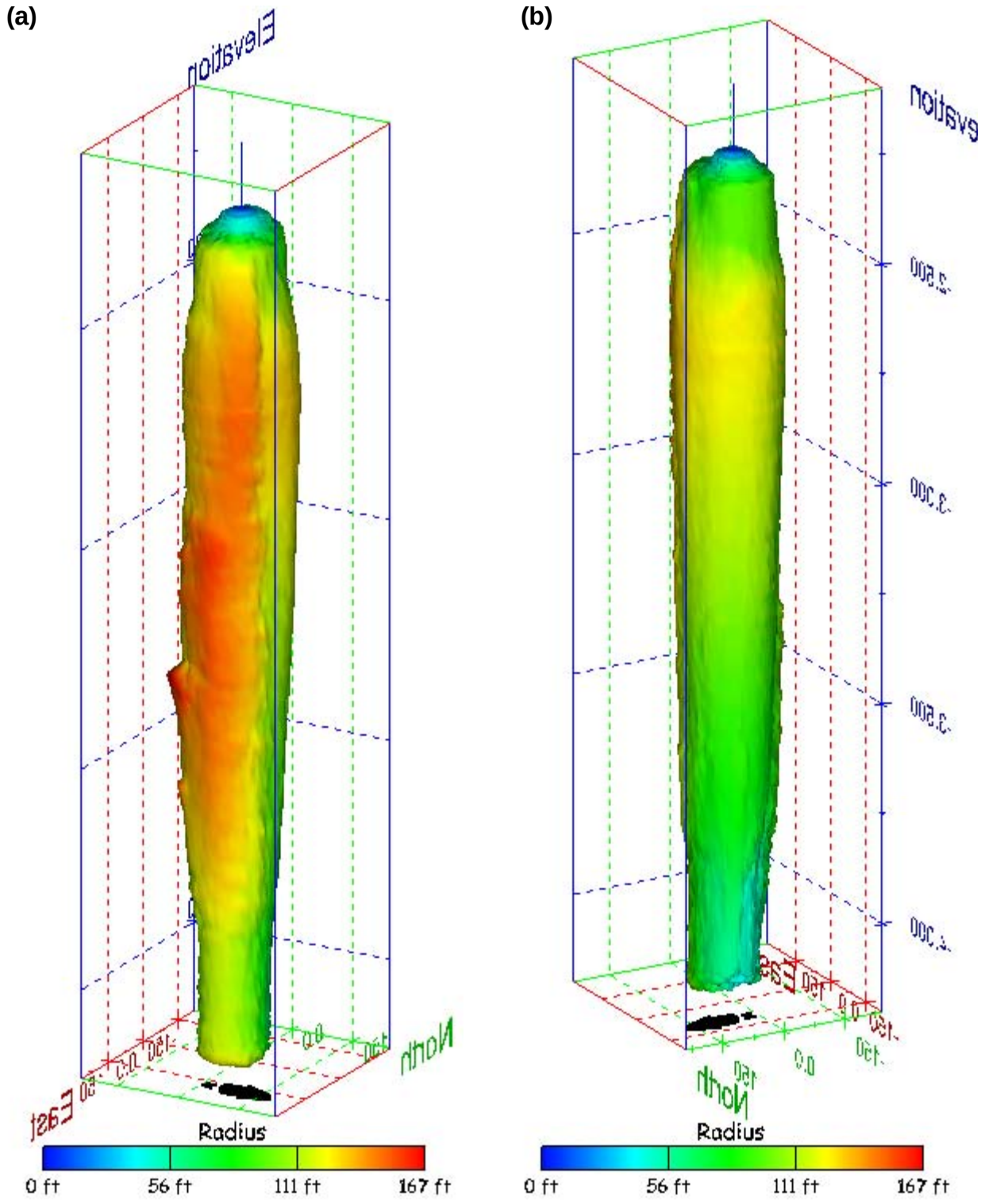

Figure 19. Sonar images of cavern BH-101, showing the geometry of the cavern colored by measured radius. View from (a) azimuth 60°, elevation 20°; (b) azimuth 300°, elevation 20°.

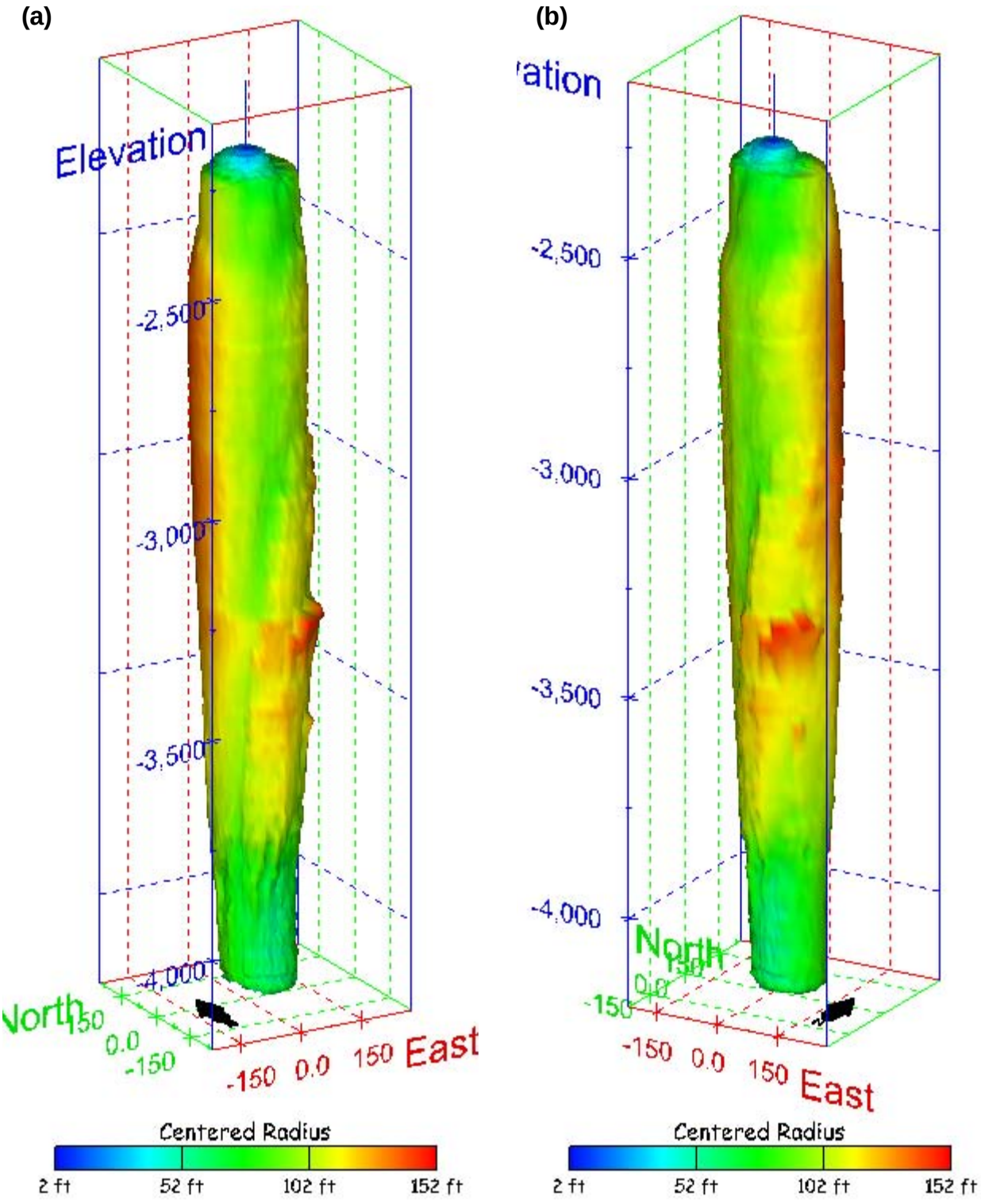

Figure 20. Sonar images of cavern BH-101, showing the geometry of the cavern colored by centered radius.View from (a) azimuth 210°, elevation 20°; (b) azimuth 150°, elevation 20°.

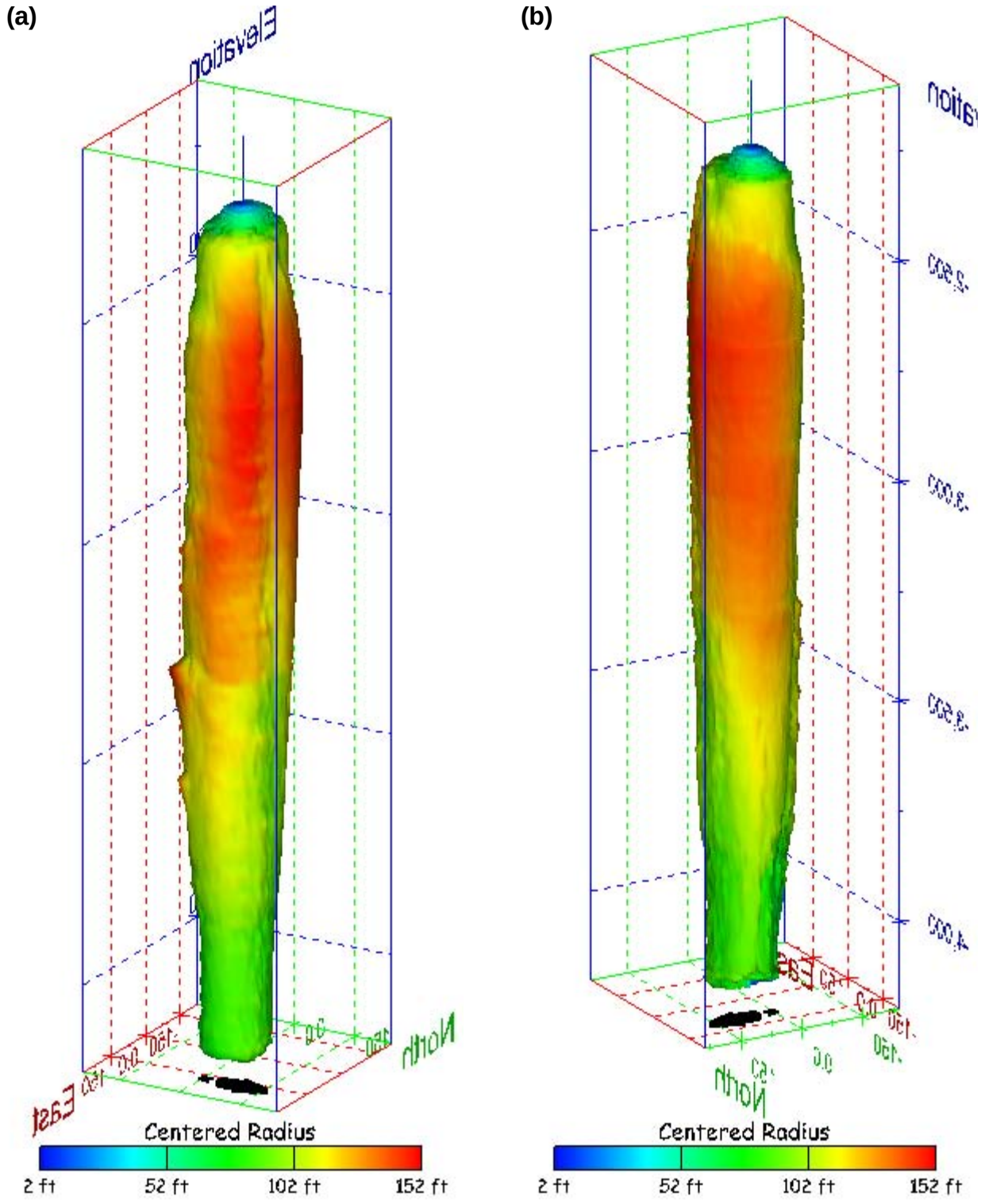

Figure 21. Sonar images of cavern BH-101, showing the geometry of the cavern colored by centered radius. View from (a) azimuth 60°, elevation 20°; (b) azimuth 300°, elevation 20°.

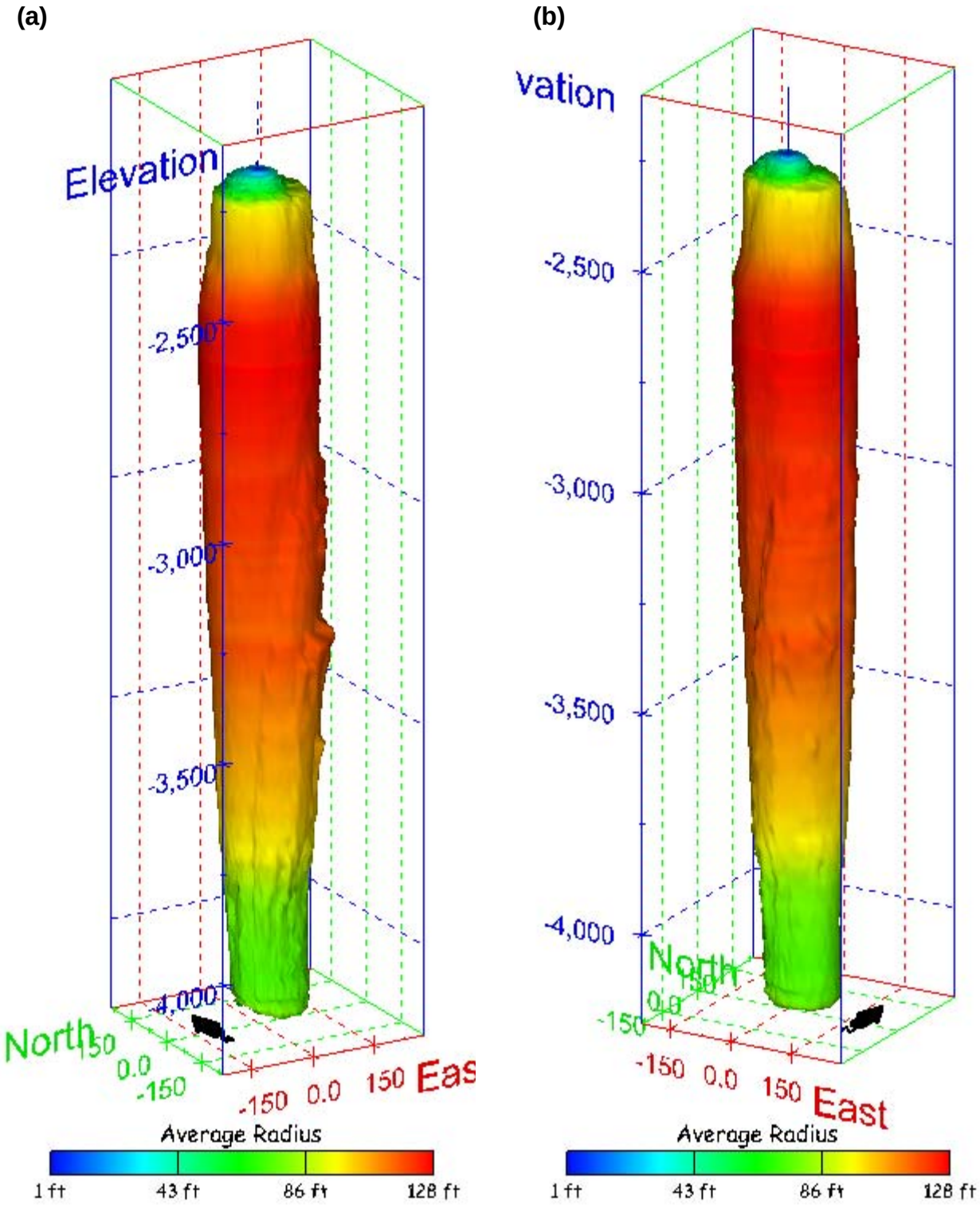

Figure 22. Sonar images of cavern BH-101, showing the geometry of the cavern colored by average radius. View from (a) azimuth 210°, elevation 20°; (b) azimuth 150°, elevation 20°.

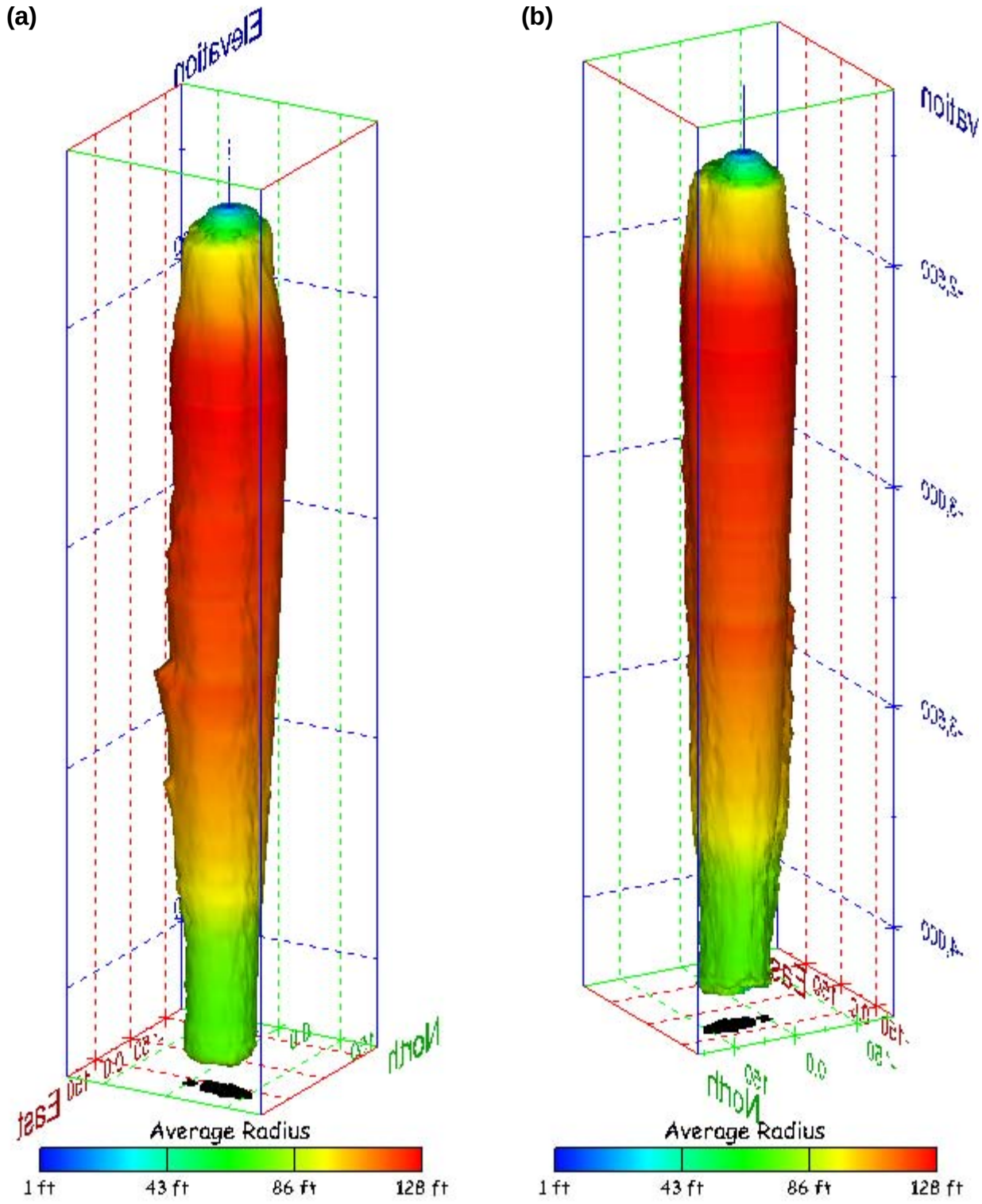

Figure 23. Sonar images of cavern BH-101, showing the geometry of the cavern colored by average radius. View from (a) azimuth 60°, elevation 20°; (b) azimuth 300°, elevation 20°.

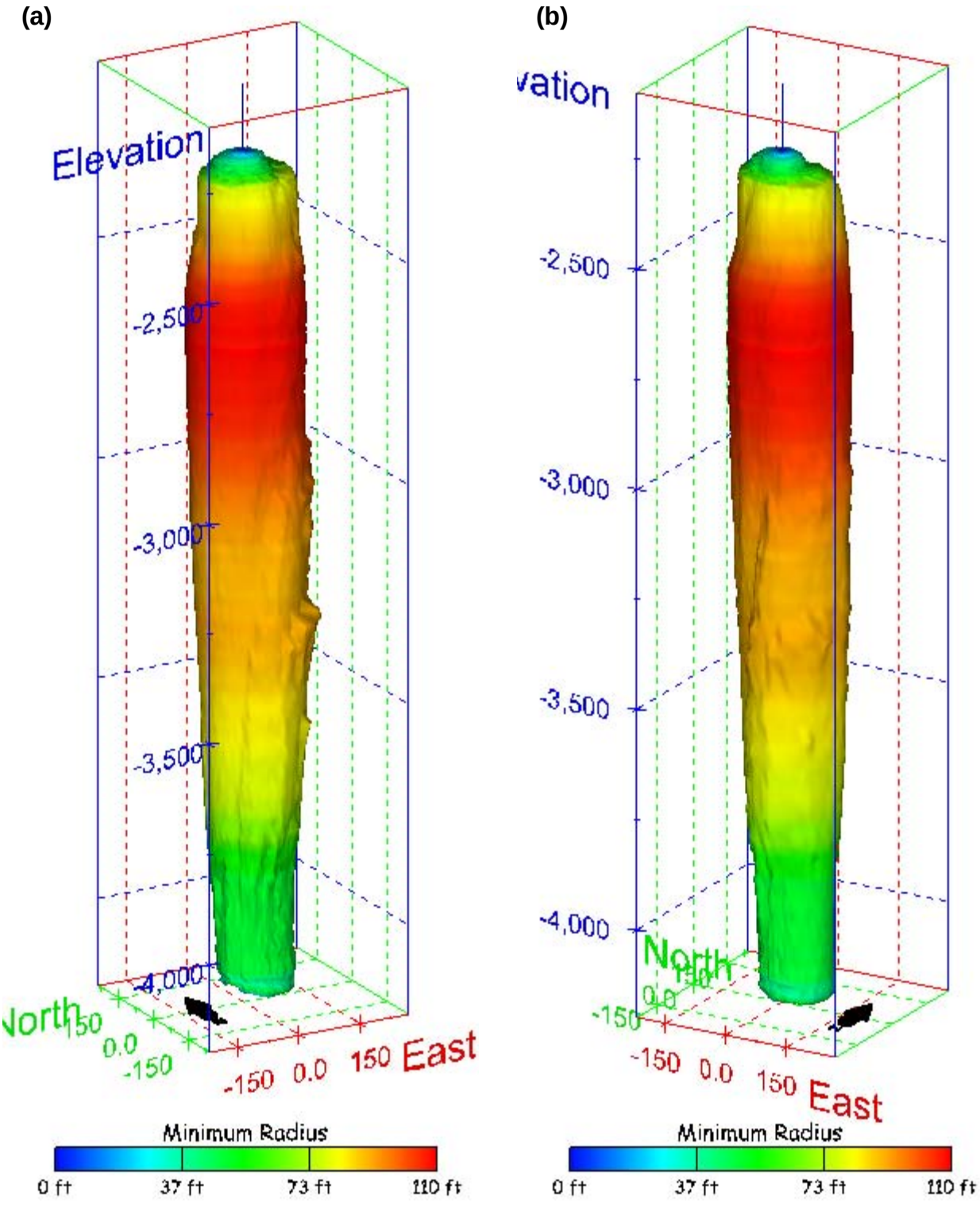

Figure 24. Sonar images of cavern BH-101, showing the geometry of the cavern colored by minimum radius. View from (a) azimuth 210°, elevation 20°; (b) azimuth 150°, elevation 20°.

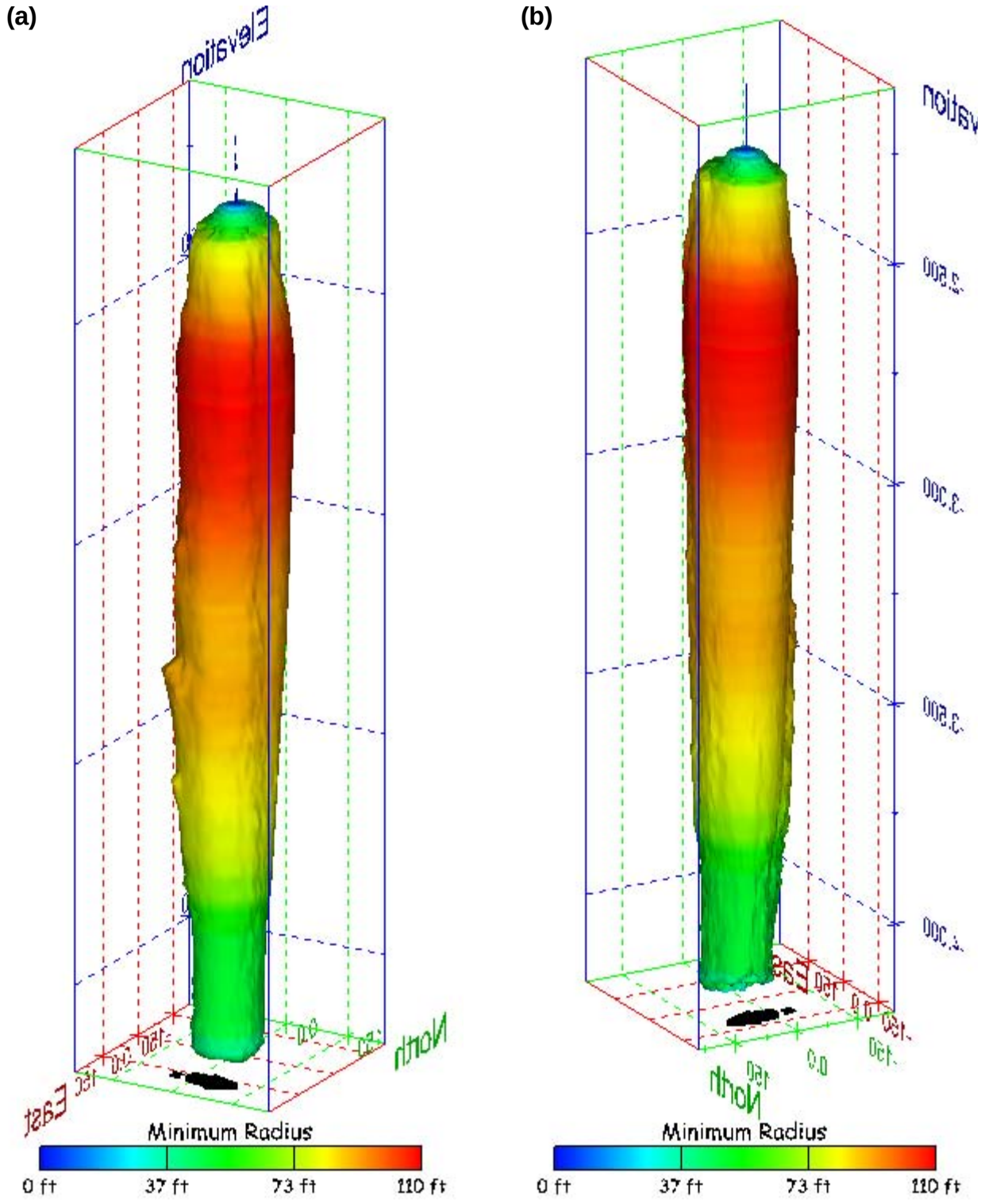

Figure 25. Sonar images of cavern BH-101, showing the geometry of the cavern colored by minimum radius. View from (a) azimuth 60°, elevation 20°; (b) azimuth 300°, elevation 20°.

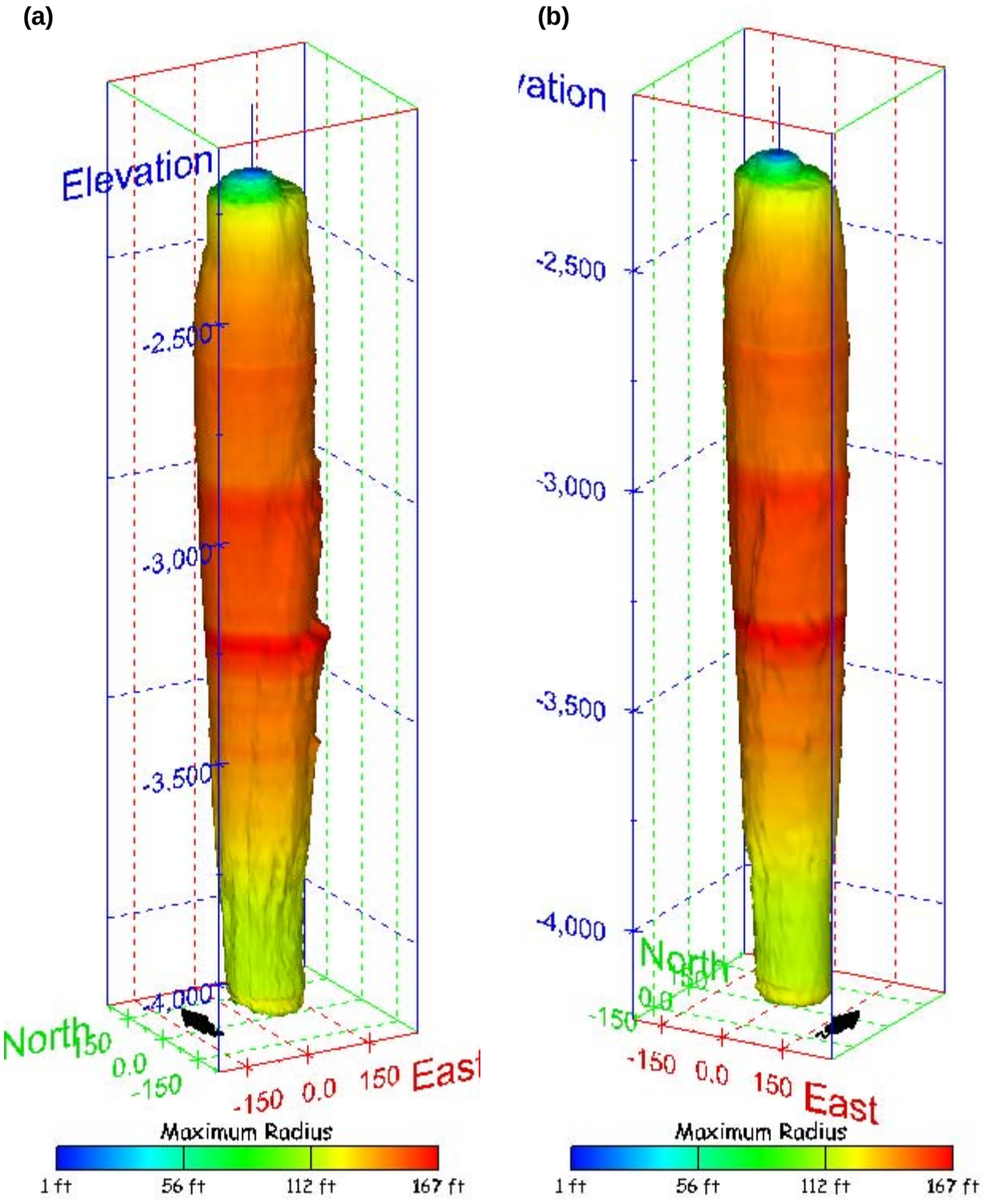

Figure 26. Sonar images of cavern BH-101, showing the geometry of the cavern colored by maximum radius. View from (a) azimuth 210°, elevation 20°; (b) azimuth 150°, elevation 20°.

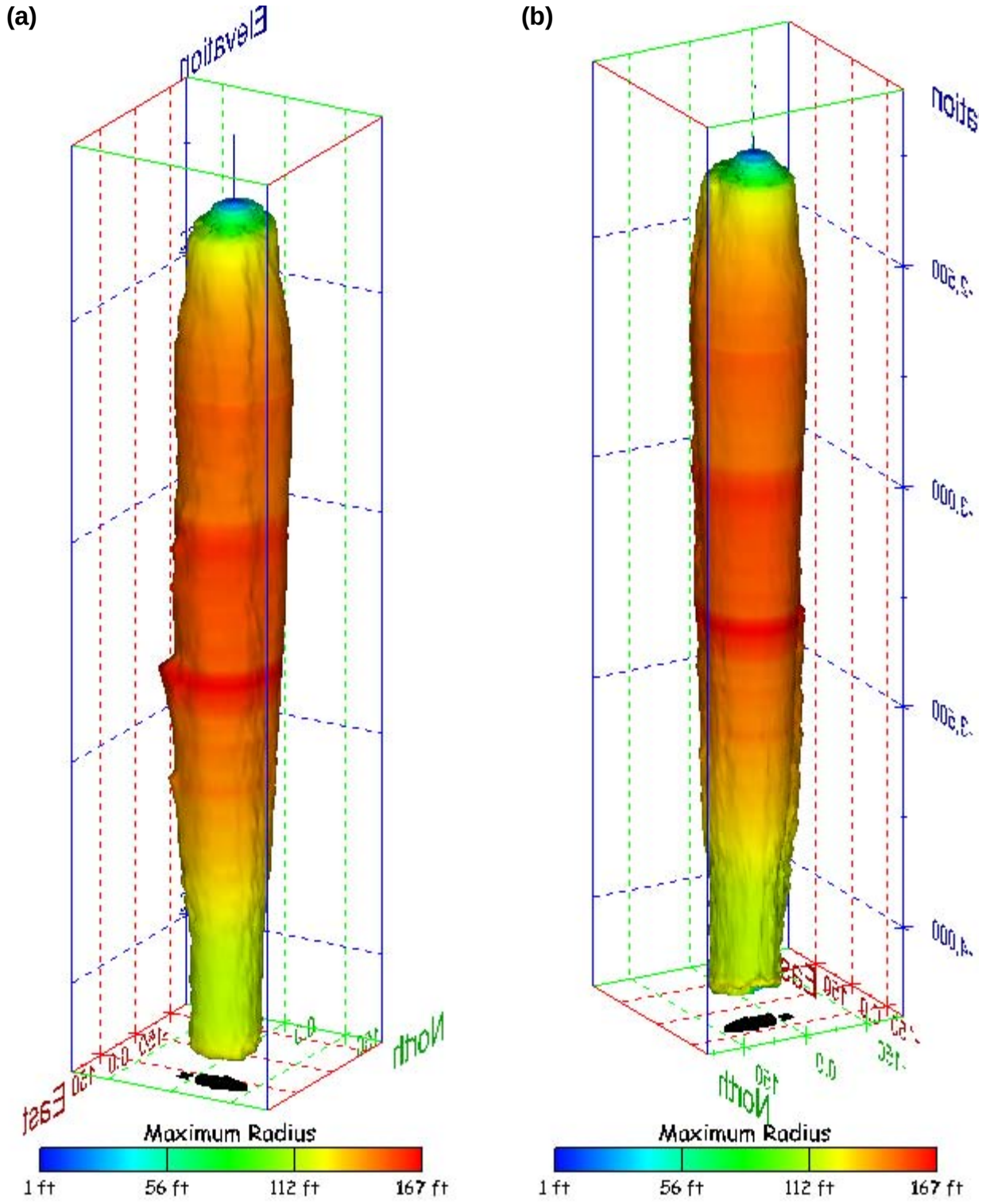

Figure 27. Sonar images of cavern BH-101, showing the geometry of the cavern colored by maximum radius. View from (a) azimuth 60°, elevation 20°; (b) azimuth 300°, elevation 20°.

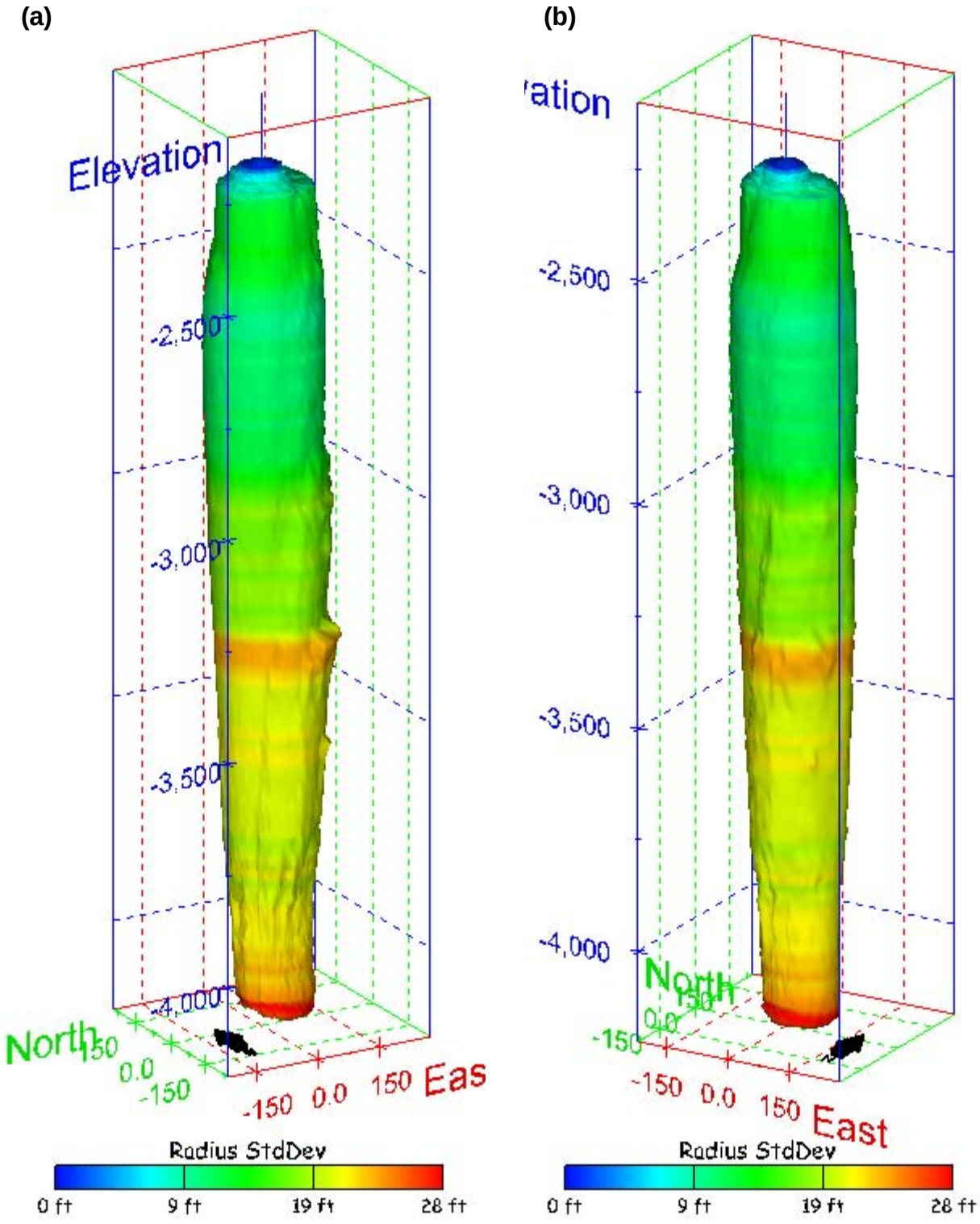

Figure 28. Sonar images of cavern BH-101, showing the geometry of the cavern colored by radius standard deviation. View from (a) azimuth 210°, elevation 20°; (b) azimuth 150°, elevation 20°.

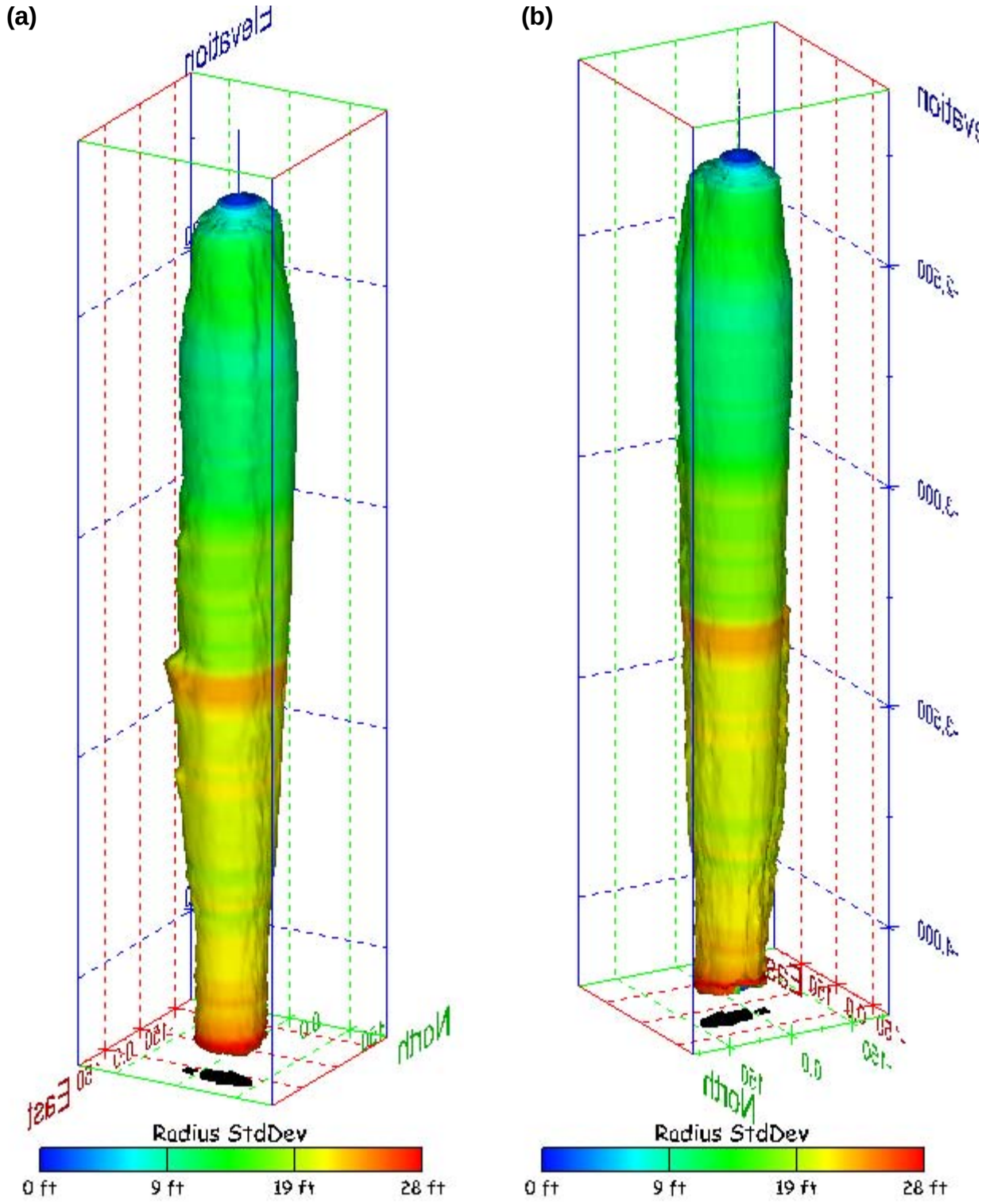

Figure 29. Sonar images of cavern BH-101, showing the geometry of the cavern colored by radius standard deviation. View from (a) azimuth 60°, elevation 20°; (b) azimuth 300°, elevation 20°.

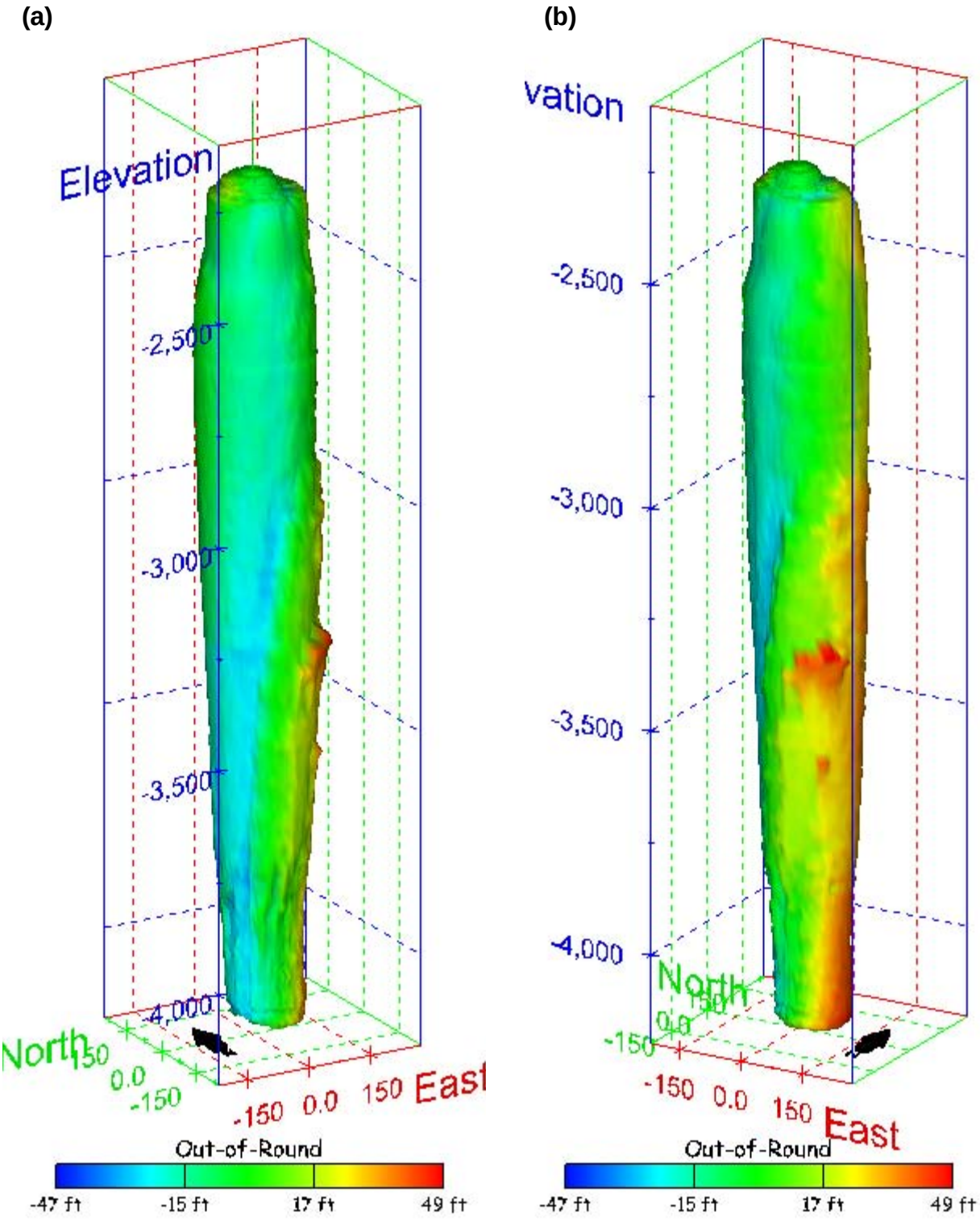

Figure 30. Sonar images of cavern BH-101, showing the geometry of the cavern colored by out-of-round distance. View from (a) azimuth 210°, elevation 20°; (b) azimuth 150°, elevation 20°.

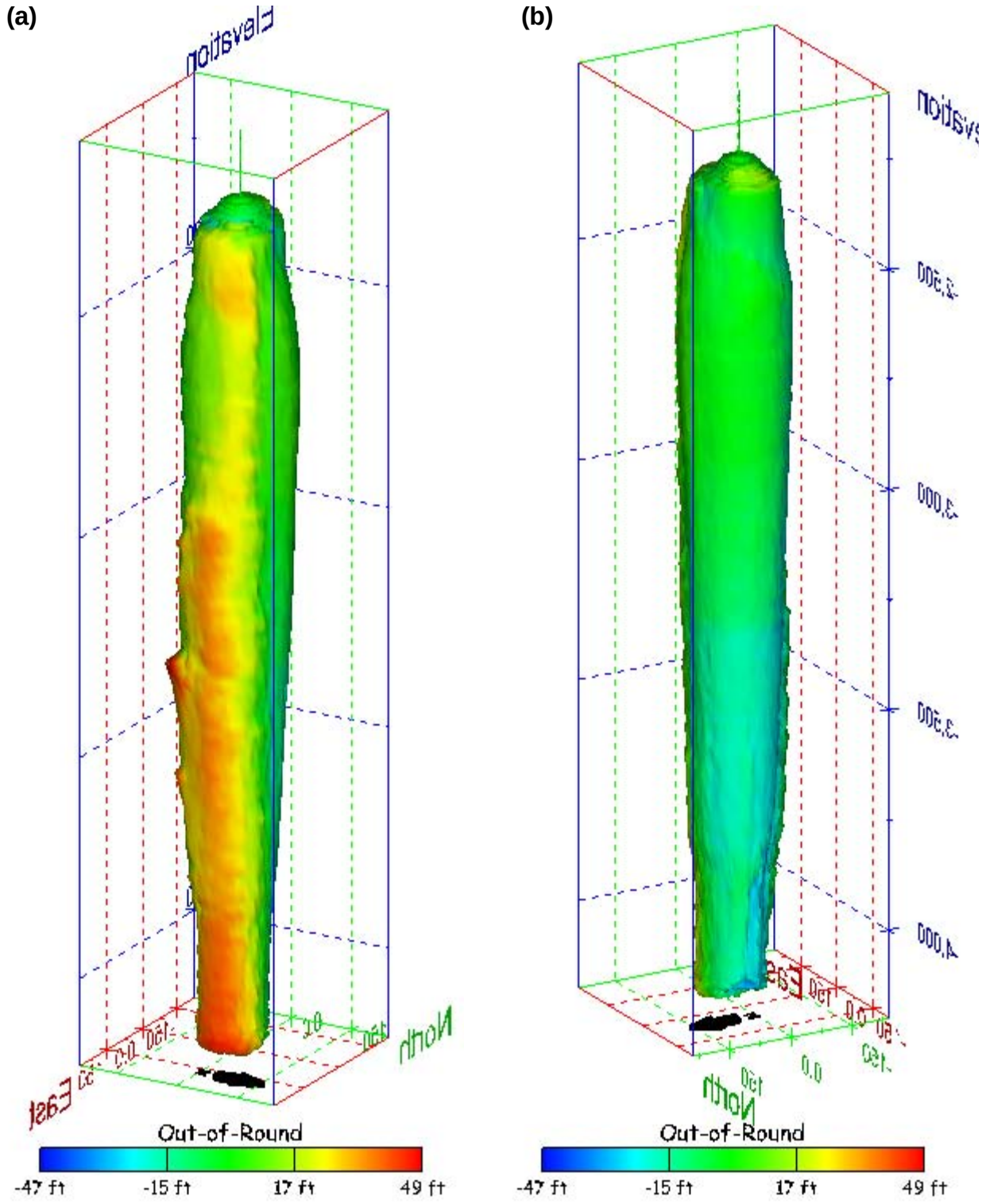

Figure 31. Sonar images of cavern BH-101, showing the geometry of the cavern colored by out-of-round distance. View from (a) azimuth 60°, elevation 20°; (b) azimuth 300°, elevation 20°.

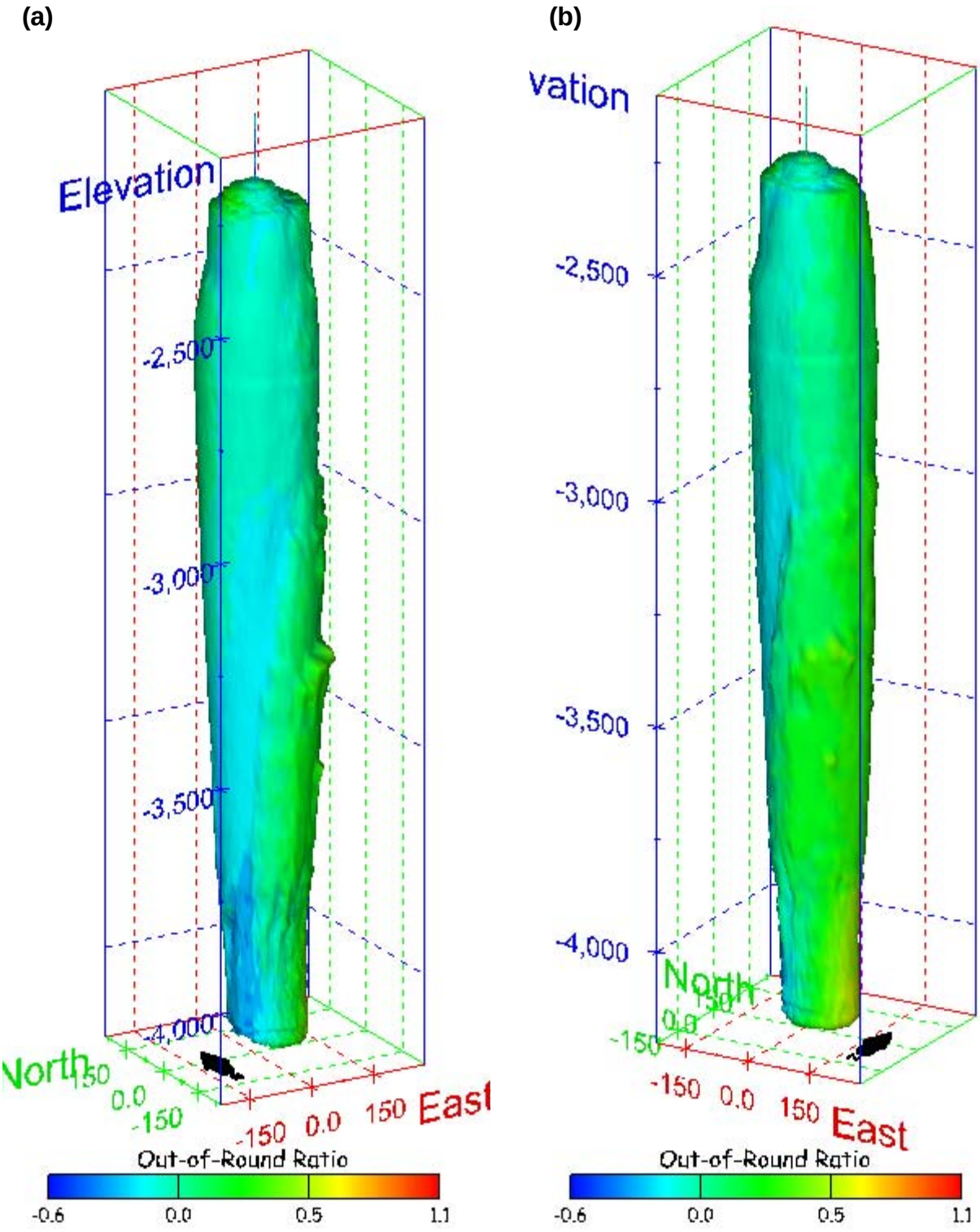

Figure 32. Sonar images of cavern BH-101, showing the geometry of the cavern colored by out-of-round ratio. View from (a) azimuth 210°, elevation 20°; (b) azimuth 150°, elevation 20°.

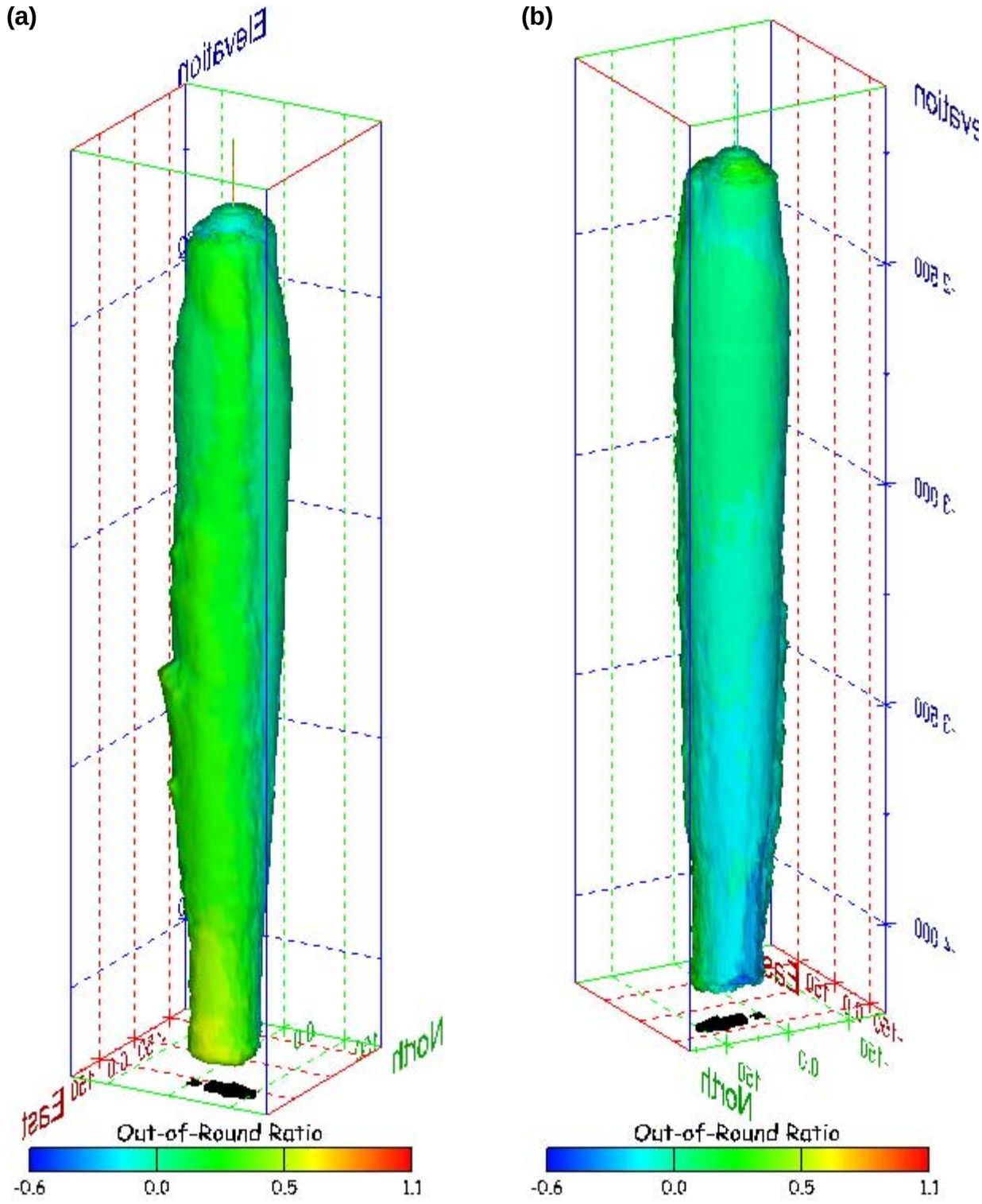

Figure 33. Sonar images of cavern BH-101, showing the geometry of the cavern colored by out-of-round ratio. View from (a) azimuth 60°, elevation 20°; (b) azimuth 300°, elevation 20°.

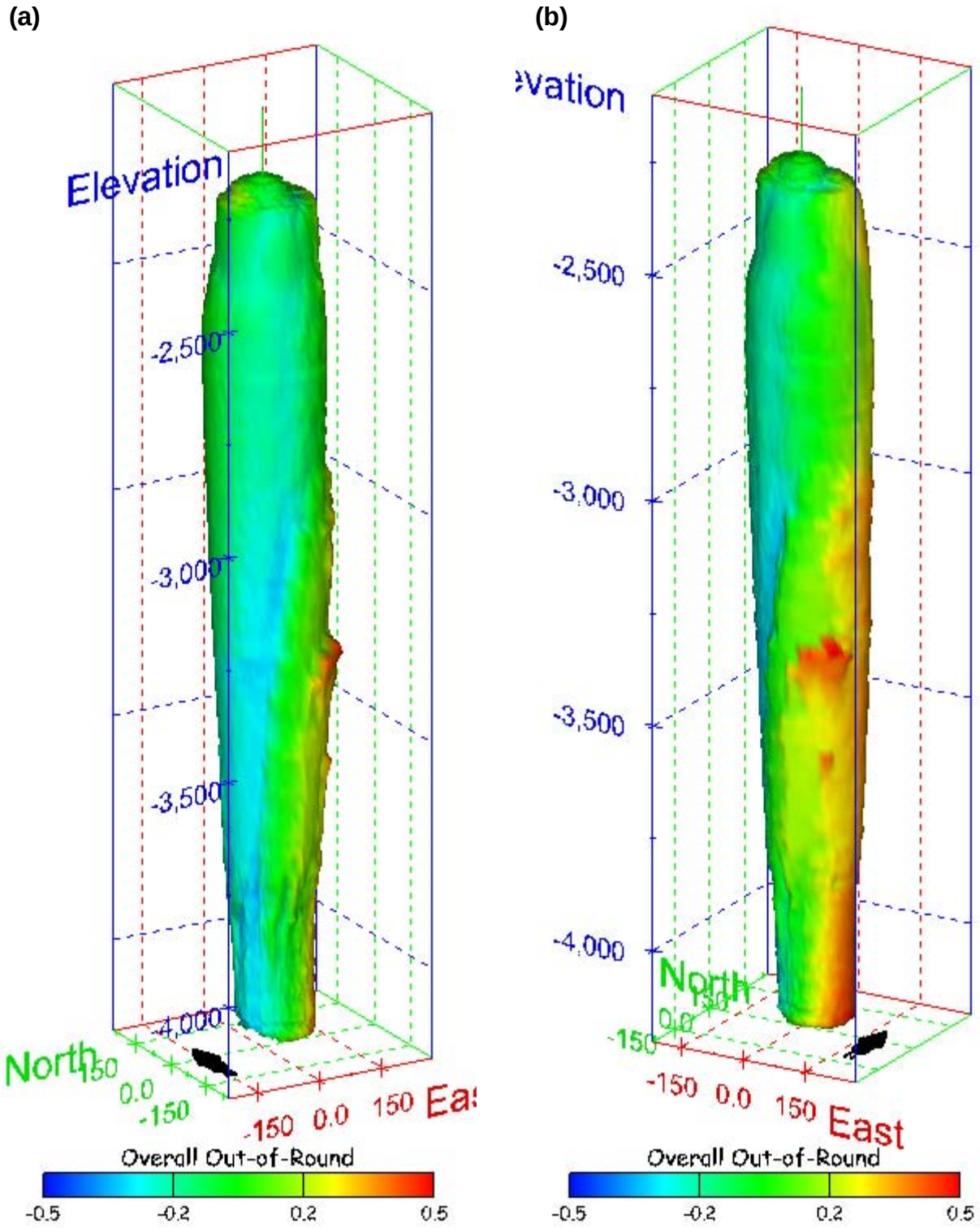

Figure 34. Sonar images of cavern BH-101, showing the geometry of the cavern colored by overall out-of-round ratio. View from (a) azimuth 210°, elevation 20°; (b) azimuth 150°, elevation 20°.

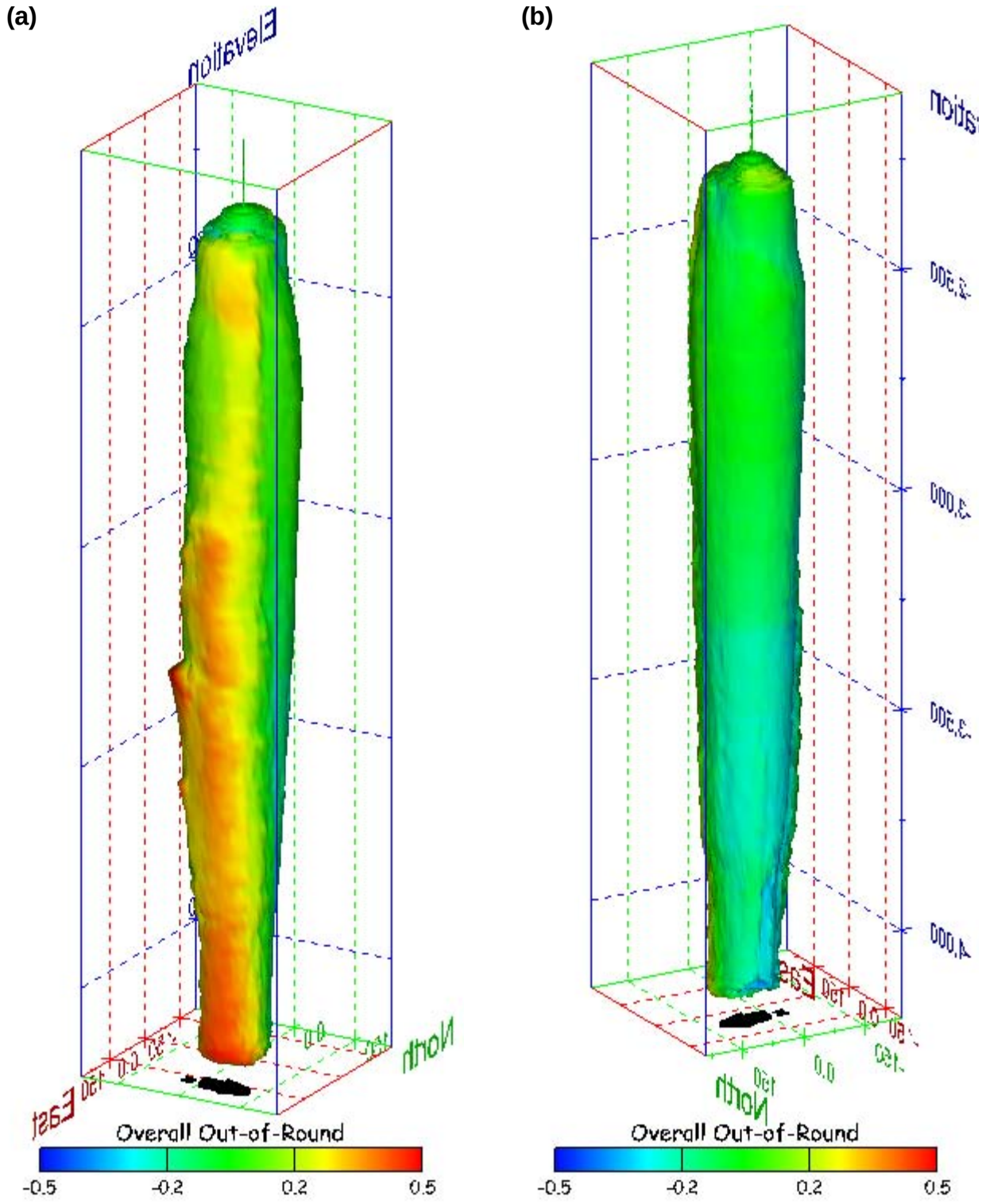

Figure 35. Sonar images of cavern BH-101, showing the geometry of the cavern colored by overall out-of-round ratio. View from (a) azimuth 60°, elevation 20°; (b) azimuth 300°, elevation 20°.

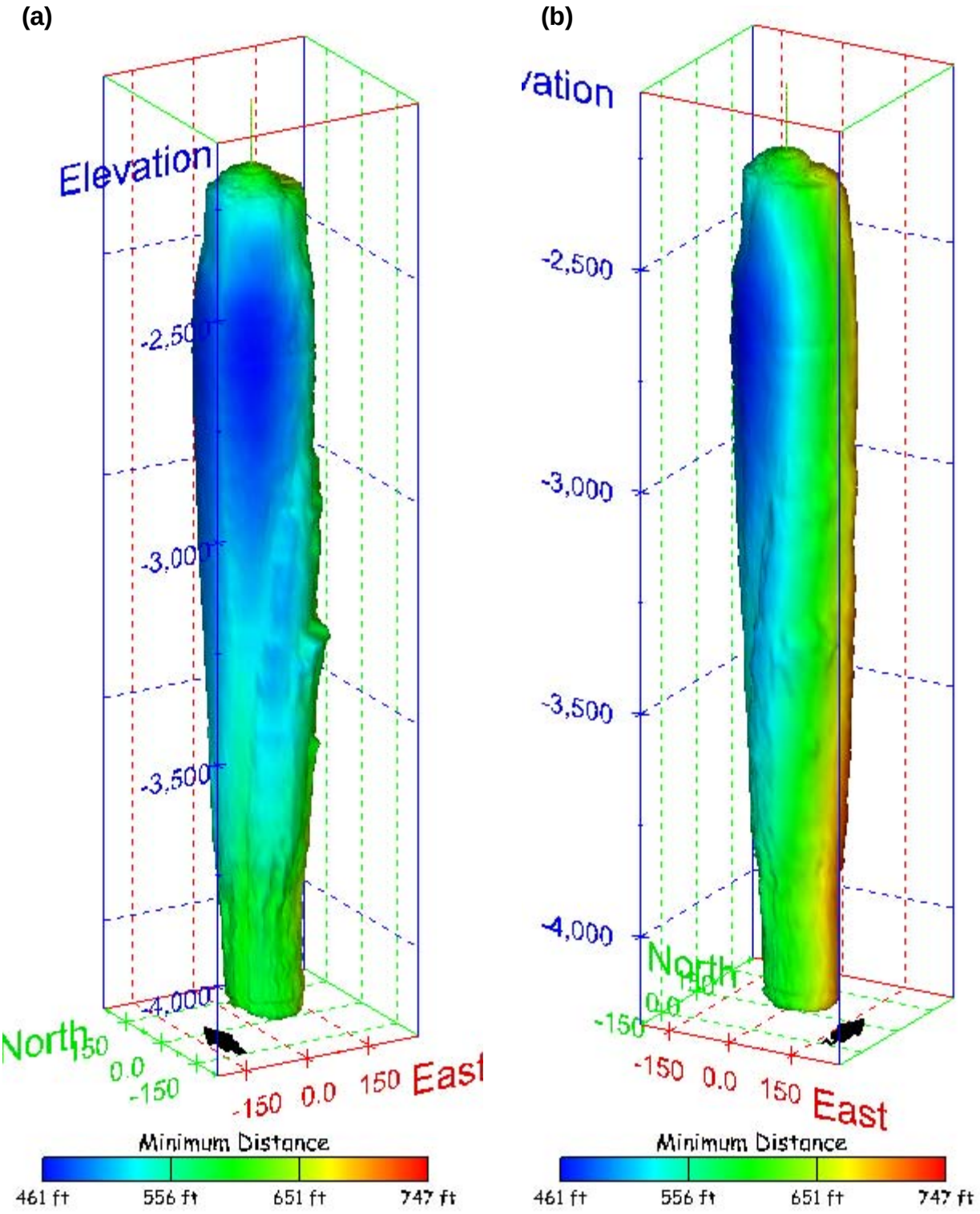

Figure 36. Sonar images of cavern BH-101, showing the geometry of the cavern colored by the minimum distance to the nearest neighboring cavern. View from (a) azimuth 210°, elevation 20°; (b) azimuth 150°, elevation 20°.

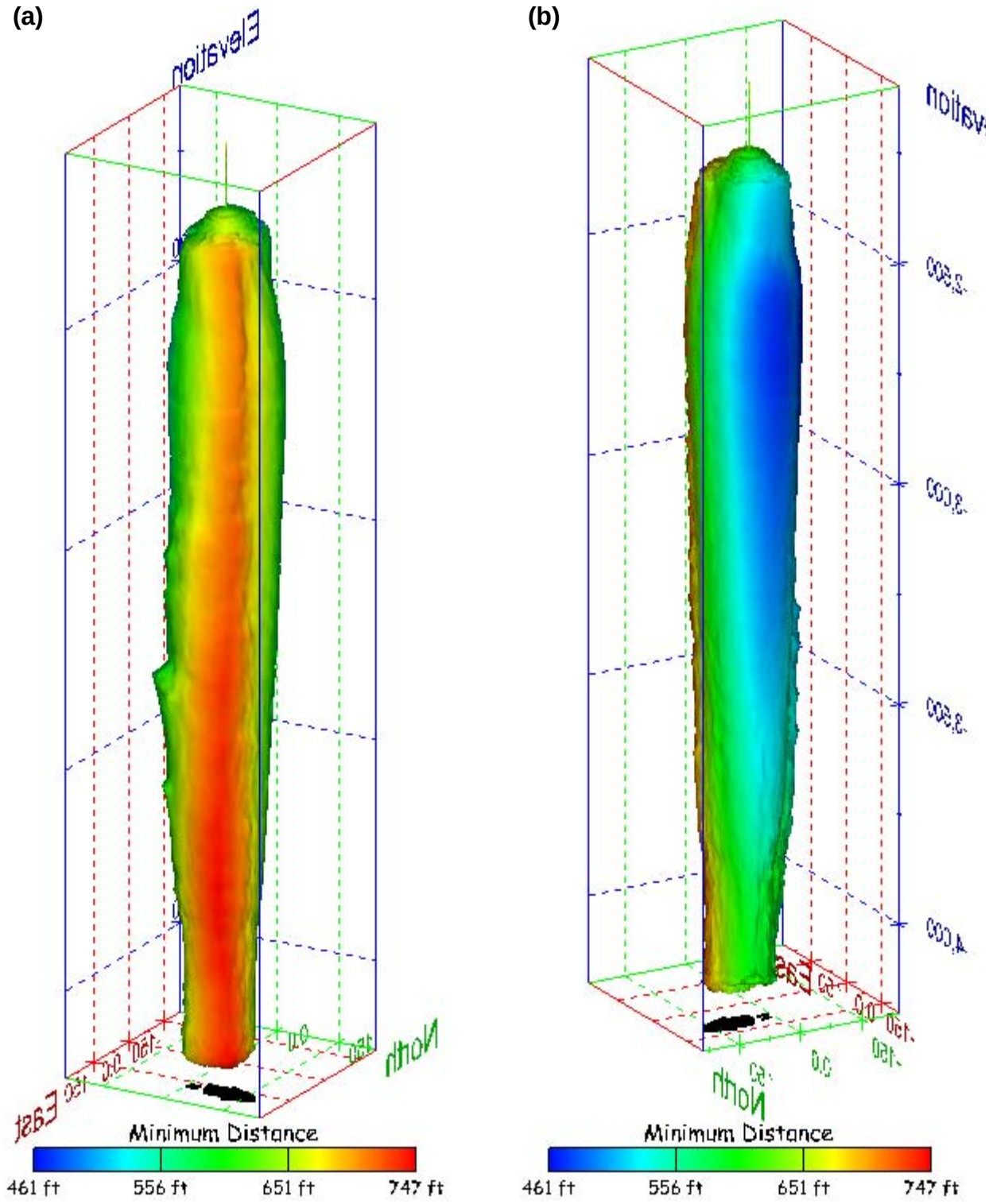

Figure 37. Sonar images of cavern BH-101, showing the geometry of the cavern colored by minimum distance to the nearest neighboring cavern. View from (a) azimuth 60°, elevation 20°; (b) azimuth 300°, elevation 20°.

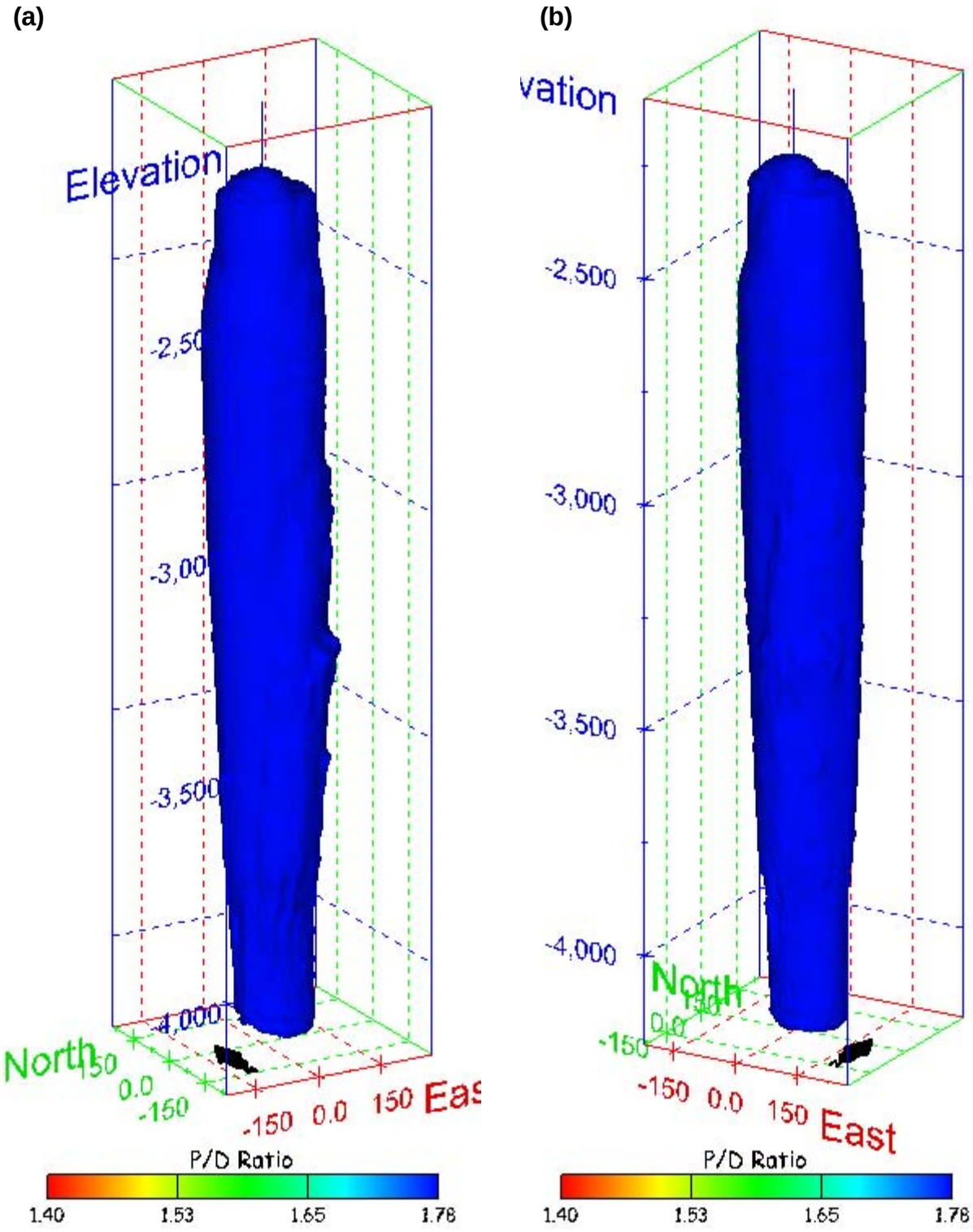

Figure 38. Sonar images of cavern BH-101, showing the geometry of the cavern colored by three-dimensional pillar-to-diameter ratio. View from (a) azimuth 210°, elevation 20°; (b) azimuth 150°, elevation 20°.

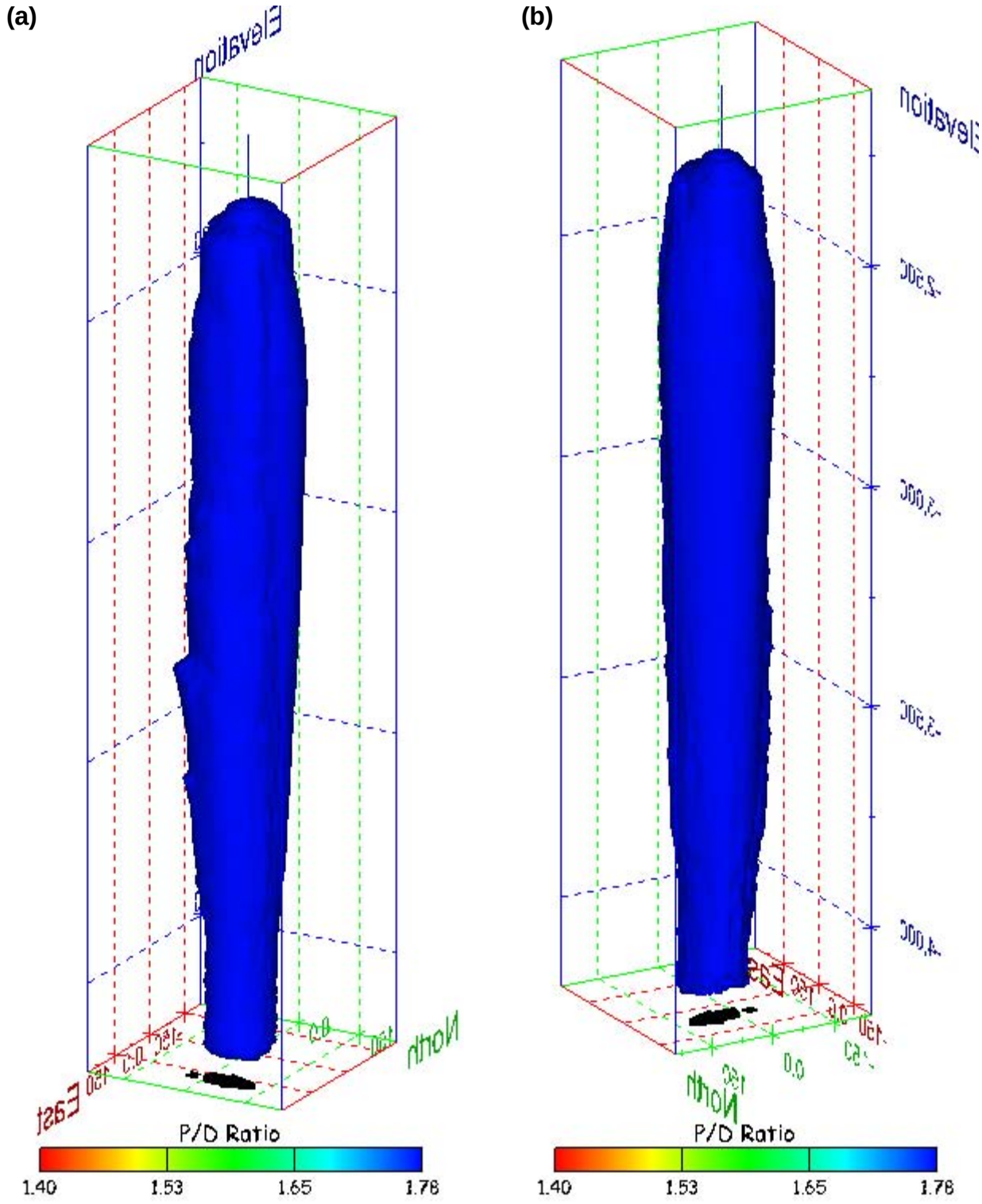

Figure 39. Sonar images of cavern BH-101, showing the geometry of the cavern colored by three-dimensional pillar-to-diameter ratio. View from (a) azimuth 60°, elevation 20°; (b) azimuth 300°, elevation 20°.

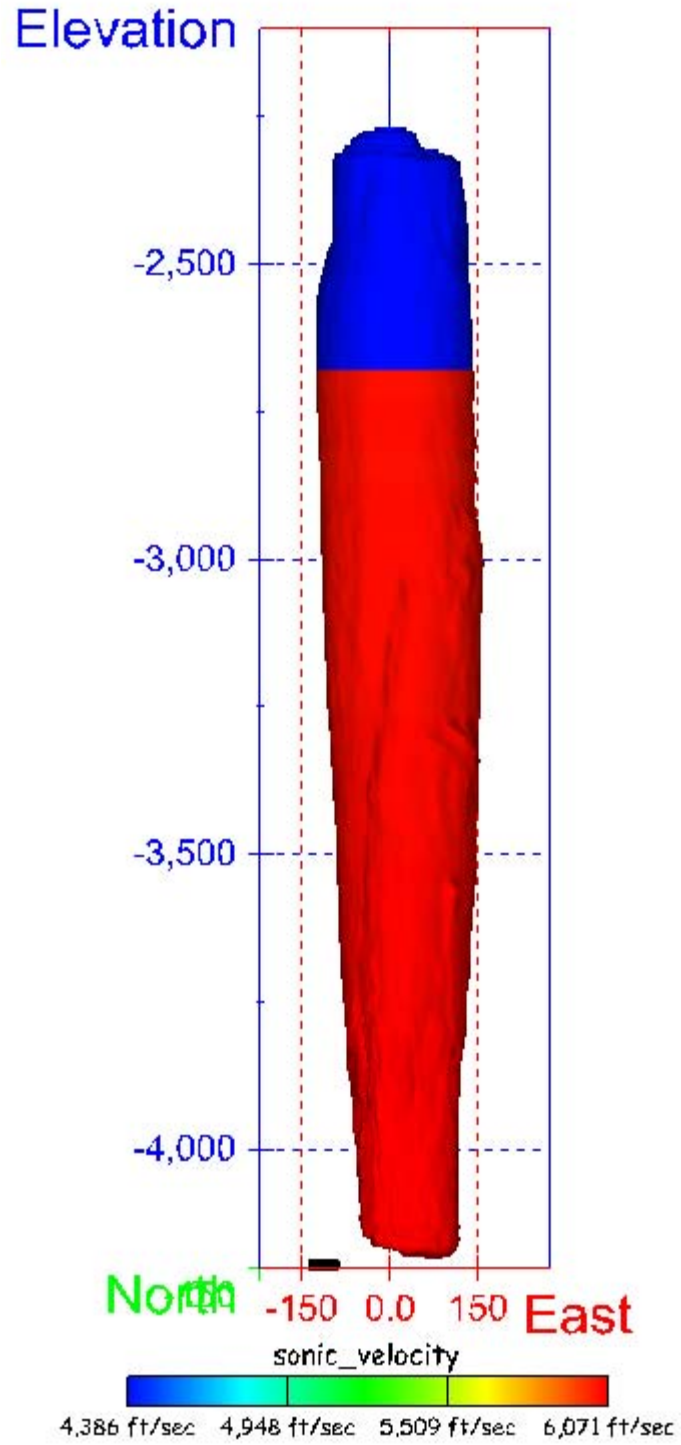

Figure 40. Sonar image of cavern BH-101, showing the geometry of the cavern colored by the reported velocity of sound on the survey date of October 2000. View from due south, elevation zero.

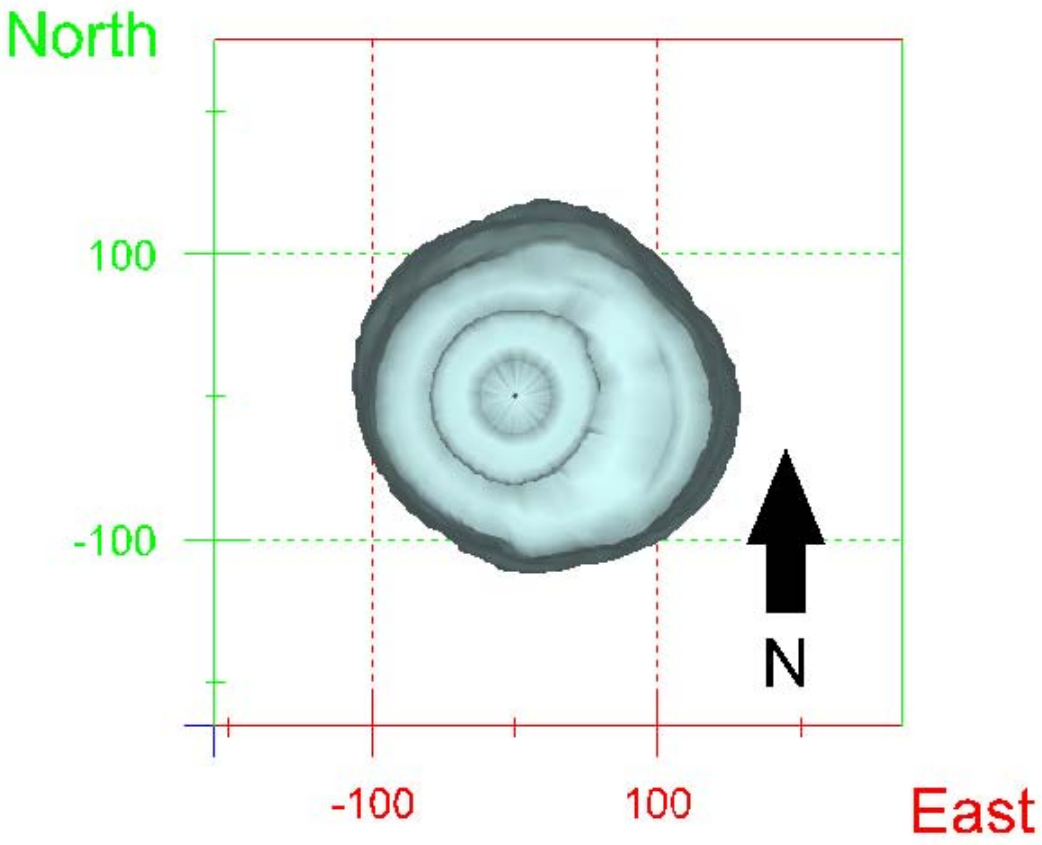

Figure 41. Map view sonar image of cavern BH-102, showing the basic geometry of the cavern. Grid squares represent 200 ft.

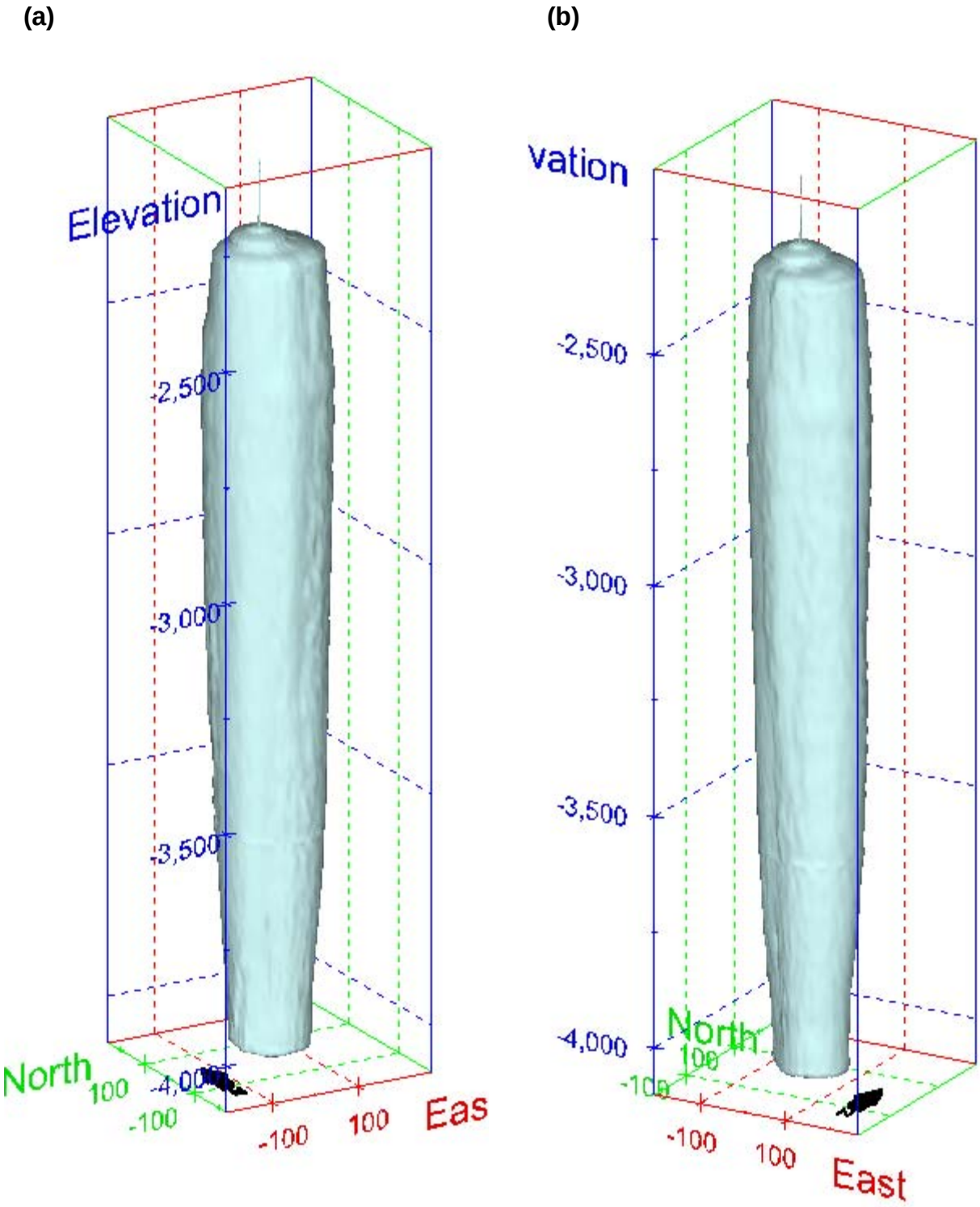

Figure 42. Sonar images of cavern BH-102, showing the basic geometric shape of the cavern. View from (a) azimuth 210°, elevation 20°; (b) azimuth 150°, elevation 20°.

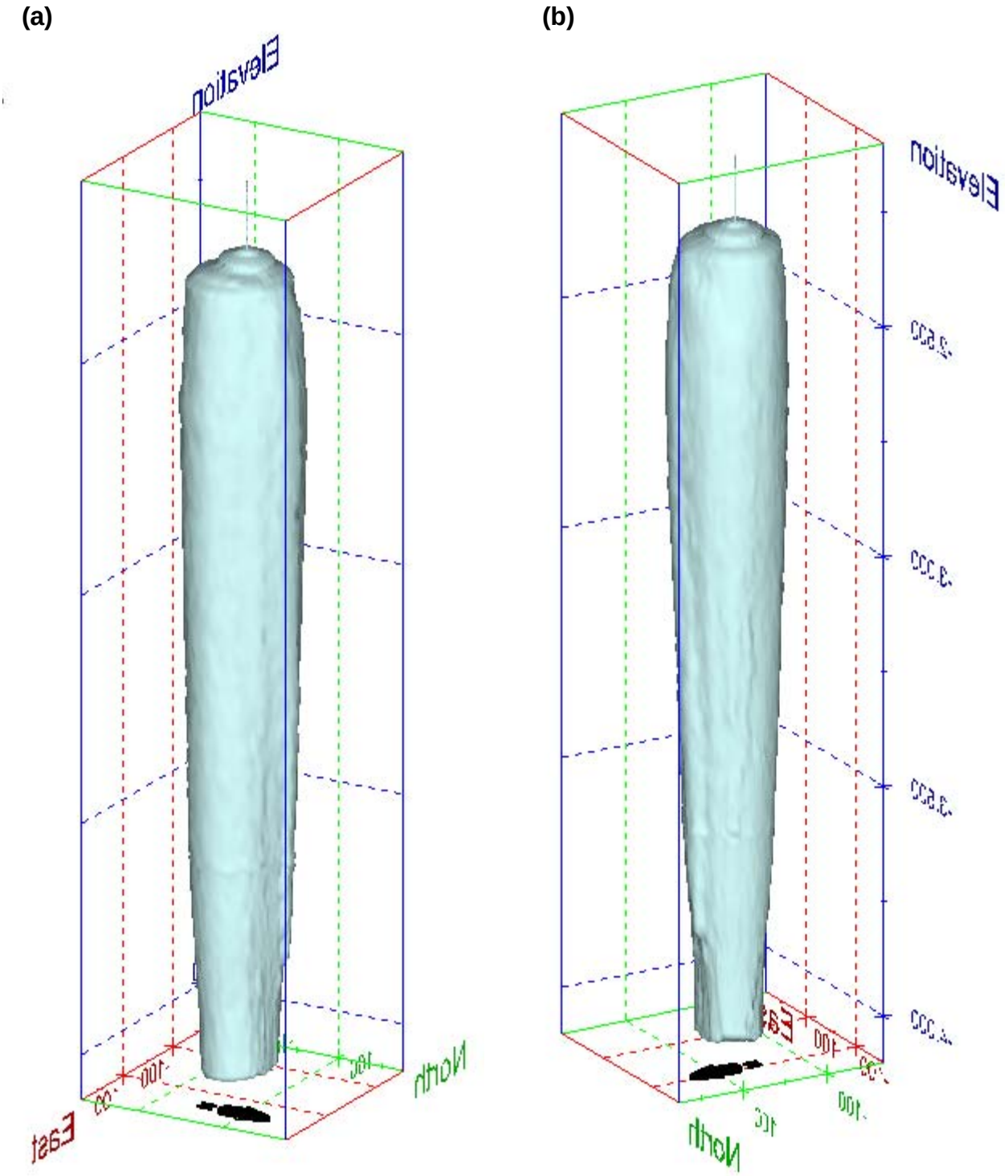

Figure 43. Sonar images of cavern BH-102, showing the basic geometric shape of the cavern. View from (a) azimuth 60°, elevation 20°; (b) azimuth 300°, elevation 20°.

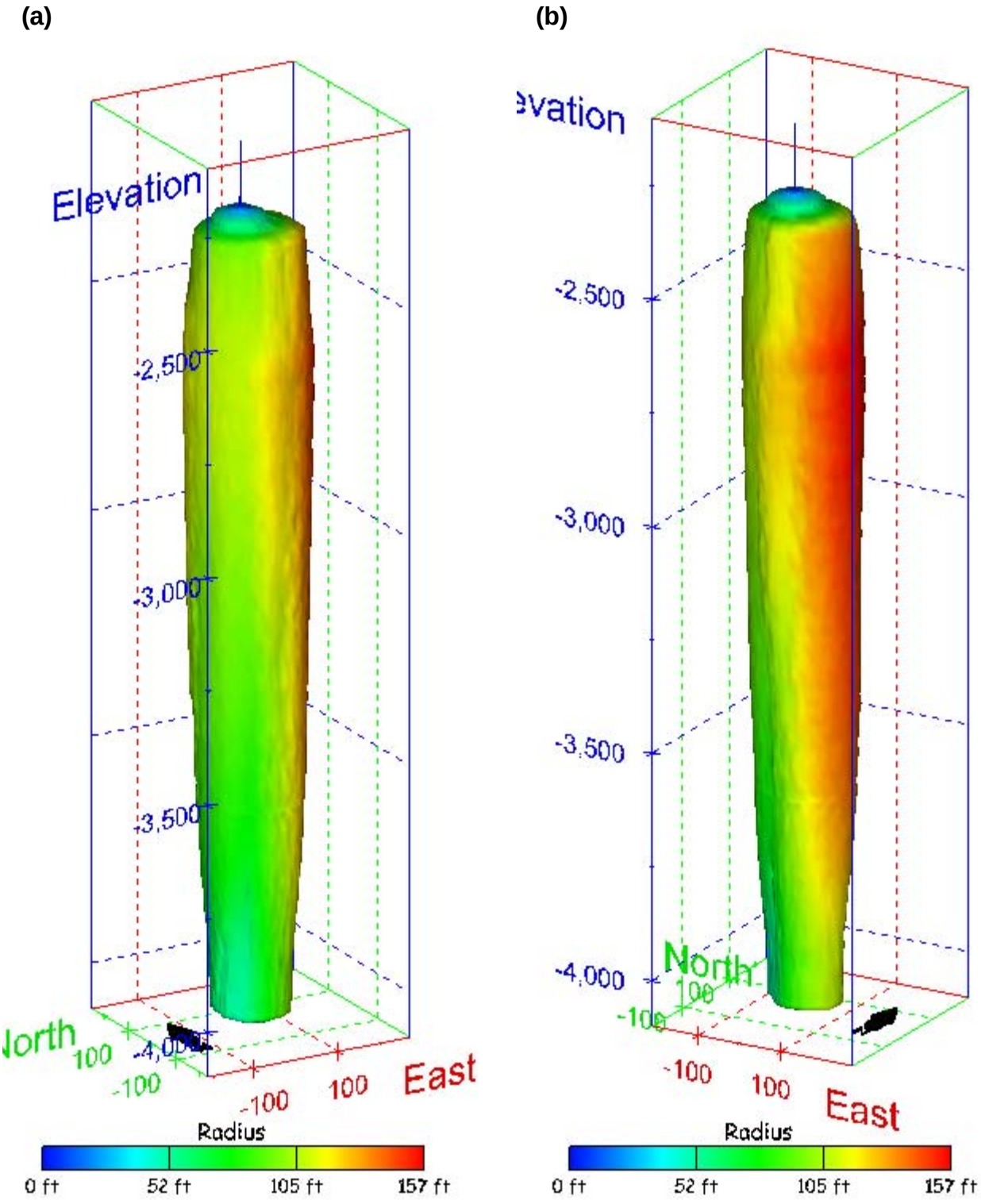

Figure 44. Sonar images of cavern BH-102, showing the geometry of the cavern colored by measured radius. View from (a) azimuth 210°, elevation 20°; (b) azimuth 150°, elevation 20°.

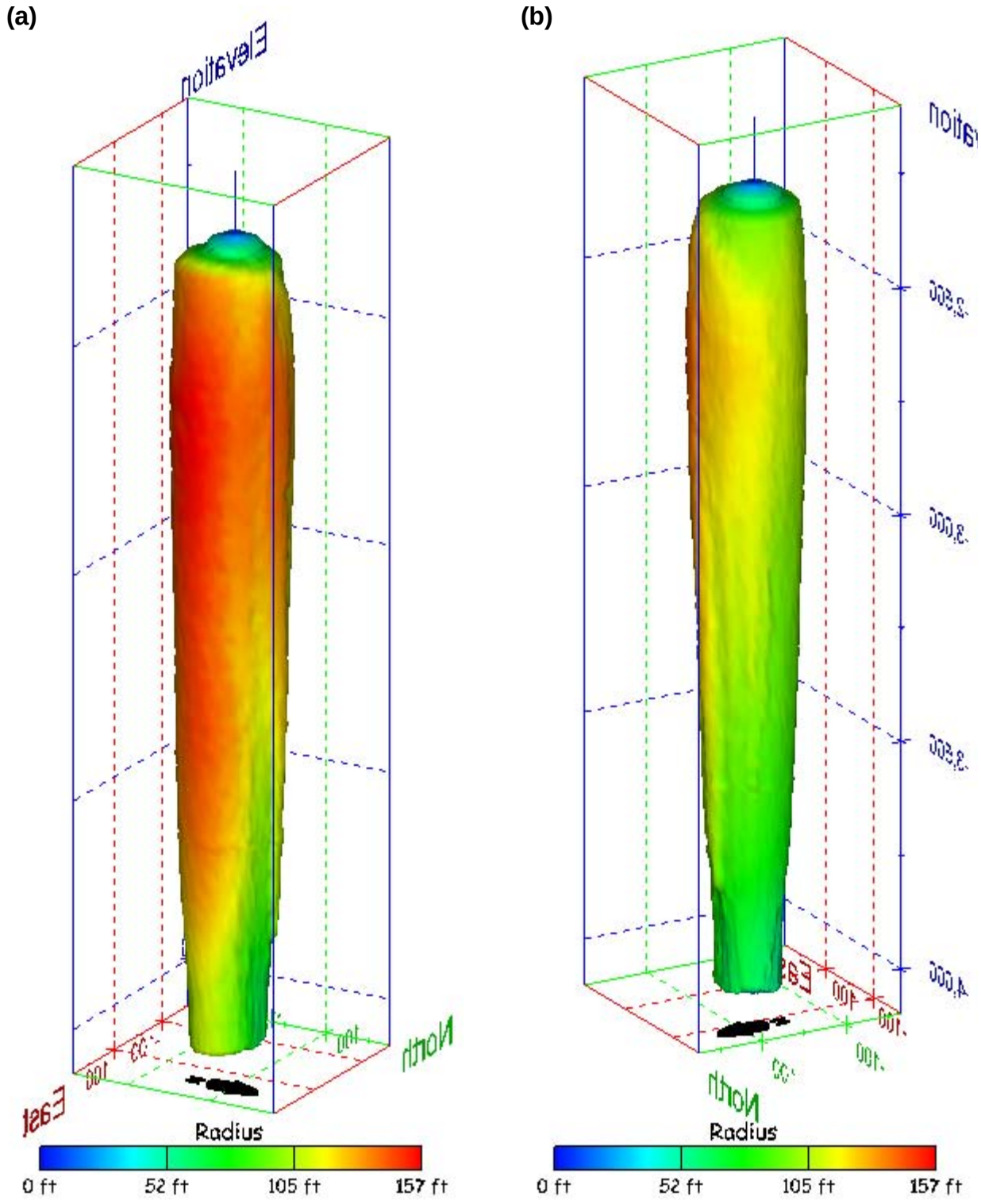

Figure 45. Sonar images of cavern BH-102, showing the geometry of the cavern colored by measured radius. View from (a) azimuth 60°, elevation 20°; (b) azimuth 300°, elevation 20°.

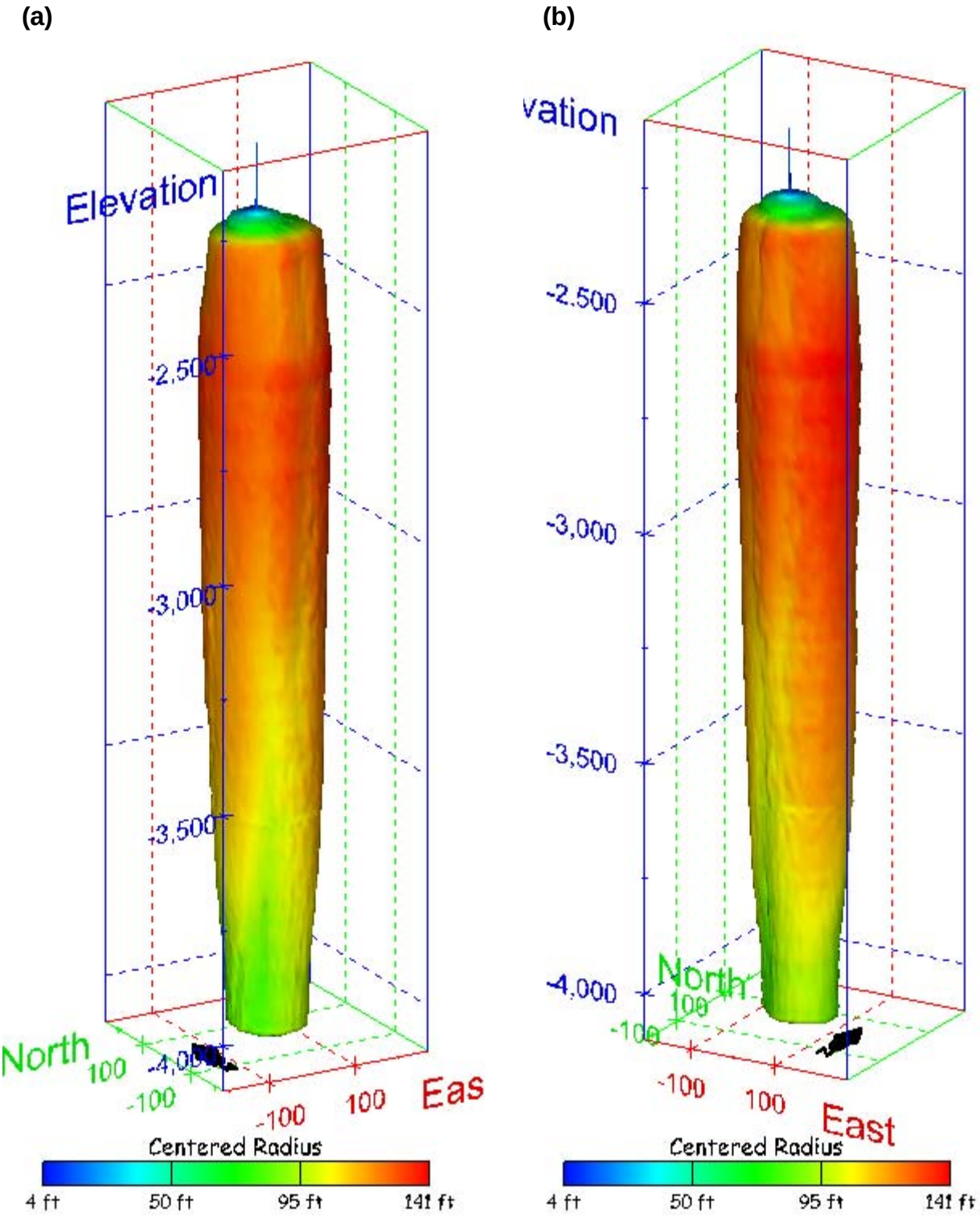

Figure 46. Sonar images of cavern BH-102, showing the geometry of the cavern colored by centered radius. View from (a) azimuth 210°, elevation 20°; (b) azimuth 150°, elevation 20°.

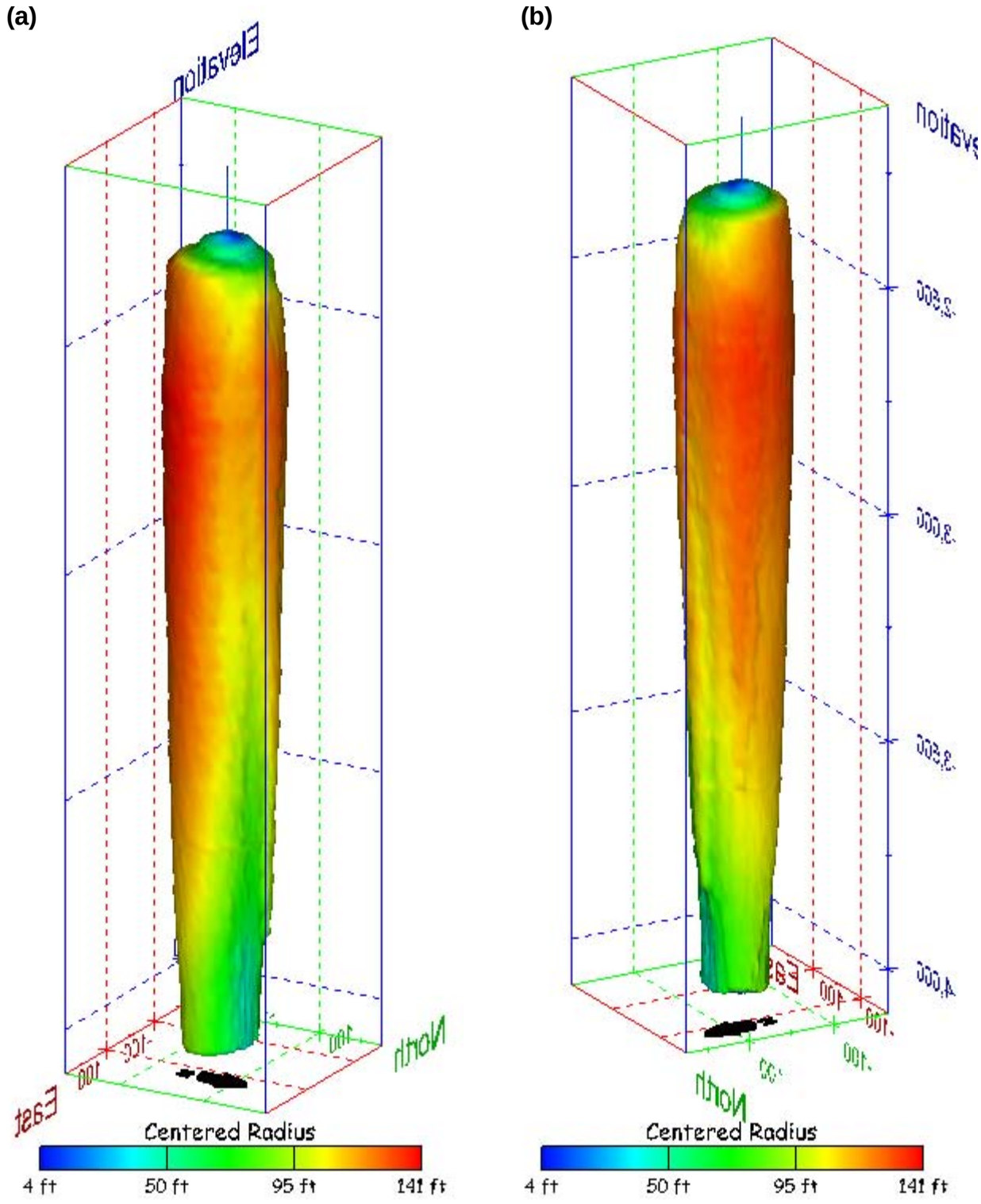

Figure 47. Sonar images of cavern BH-102, showing the geometry of the cavern colored by centered radius. View from (a) azimuth 60°, elevation 20°; (b) azimuth 300°, elevation 20°.

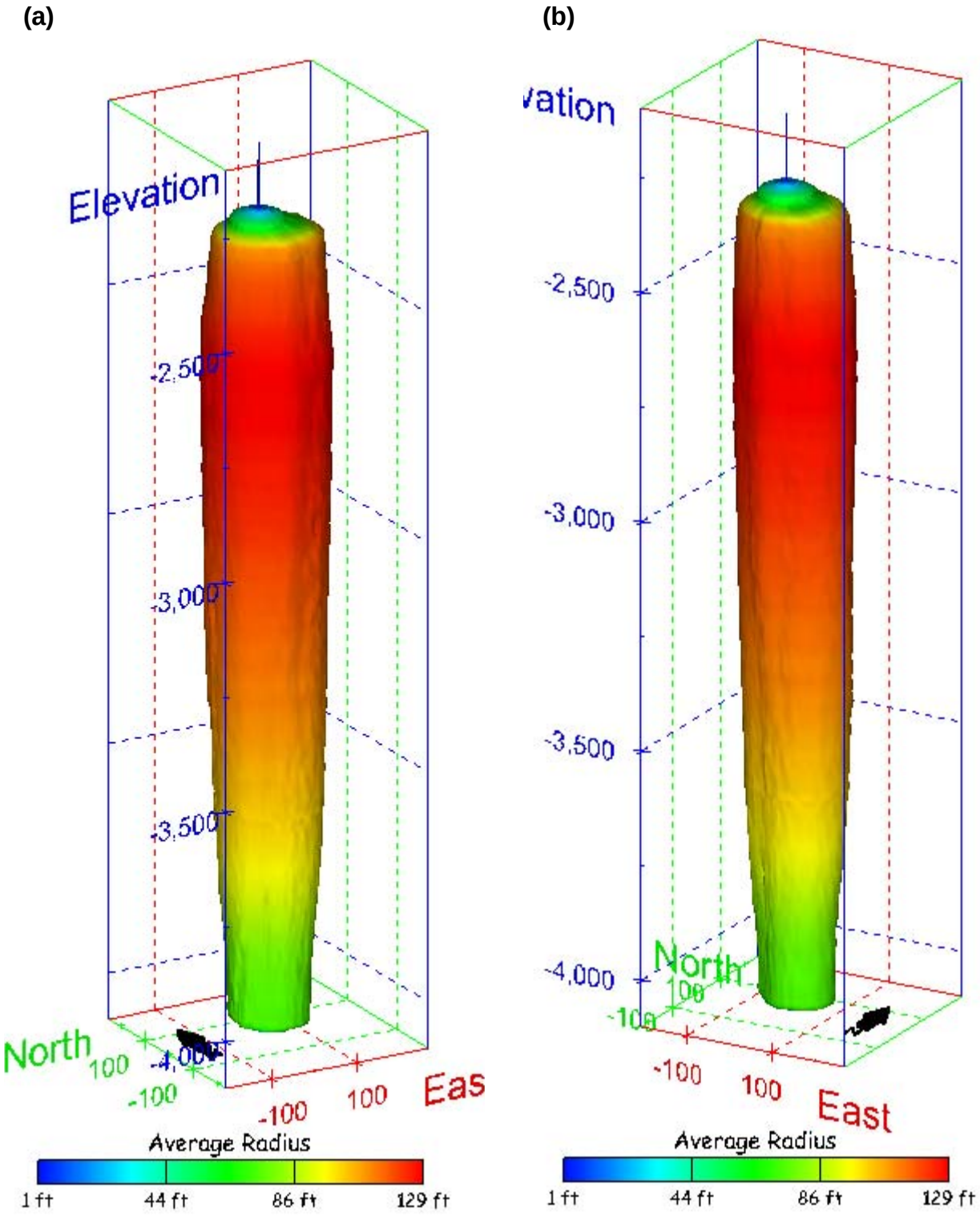

Figure 48. Sonar images of cavern BH-102, showing the geometry of the cavern colored by average radius. View from (a) azimuth 210°, elevation 20°; (b) azimuth 150°, elevation 20°.

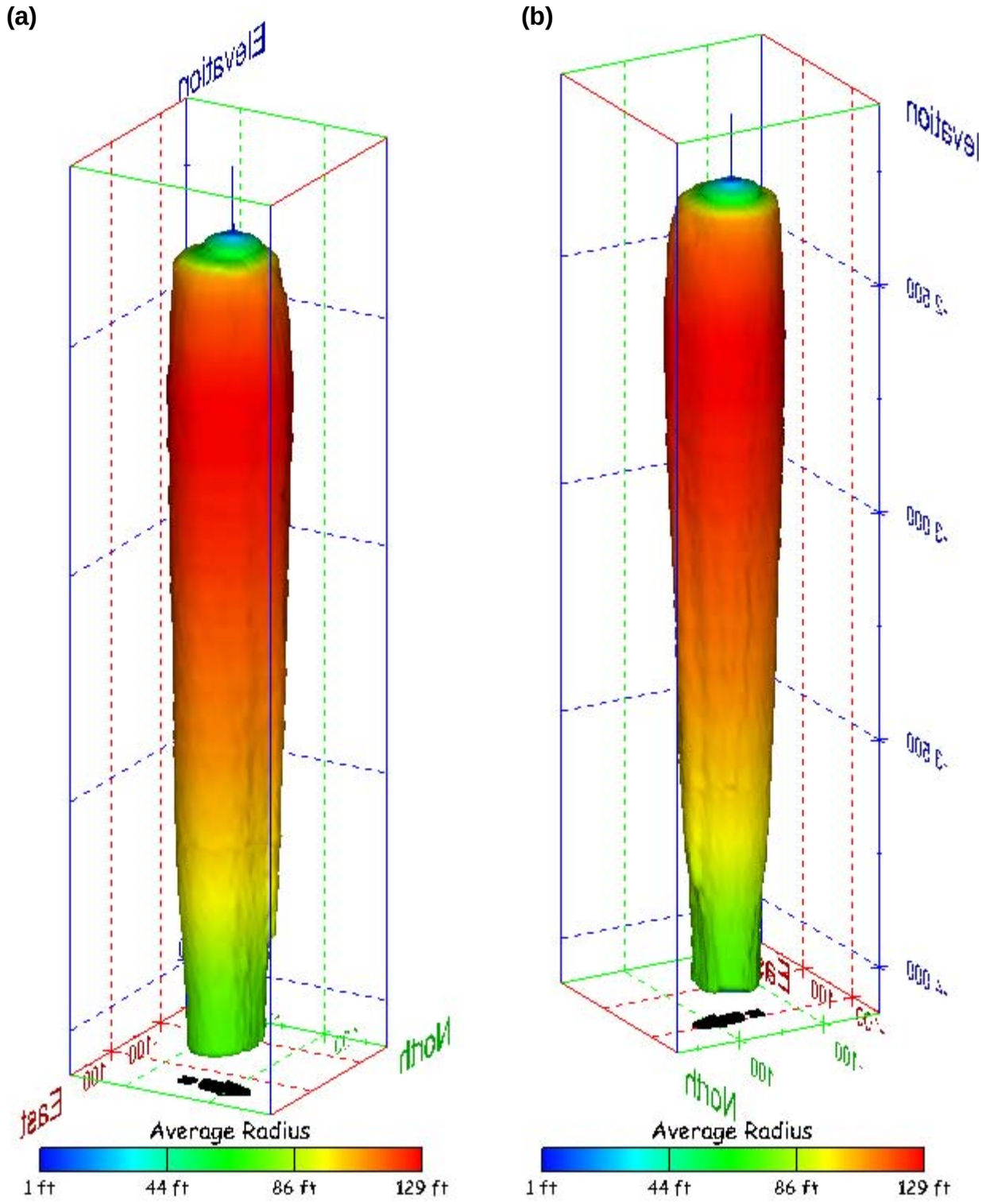

Figure 49. Sonar images of cavern BH-102, showing the geometry of the cavern colored by average radius. View from (a) azimuth 60°, elevation 20°; (b) azimuth 300°, elevation 20°.

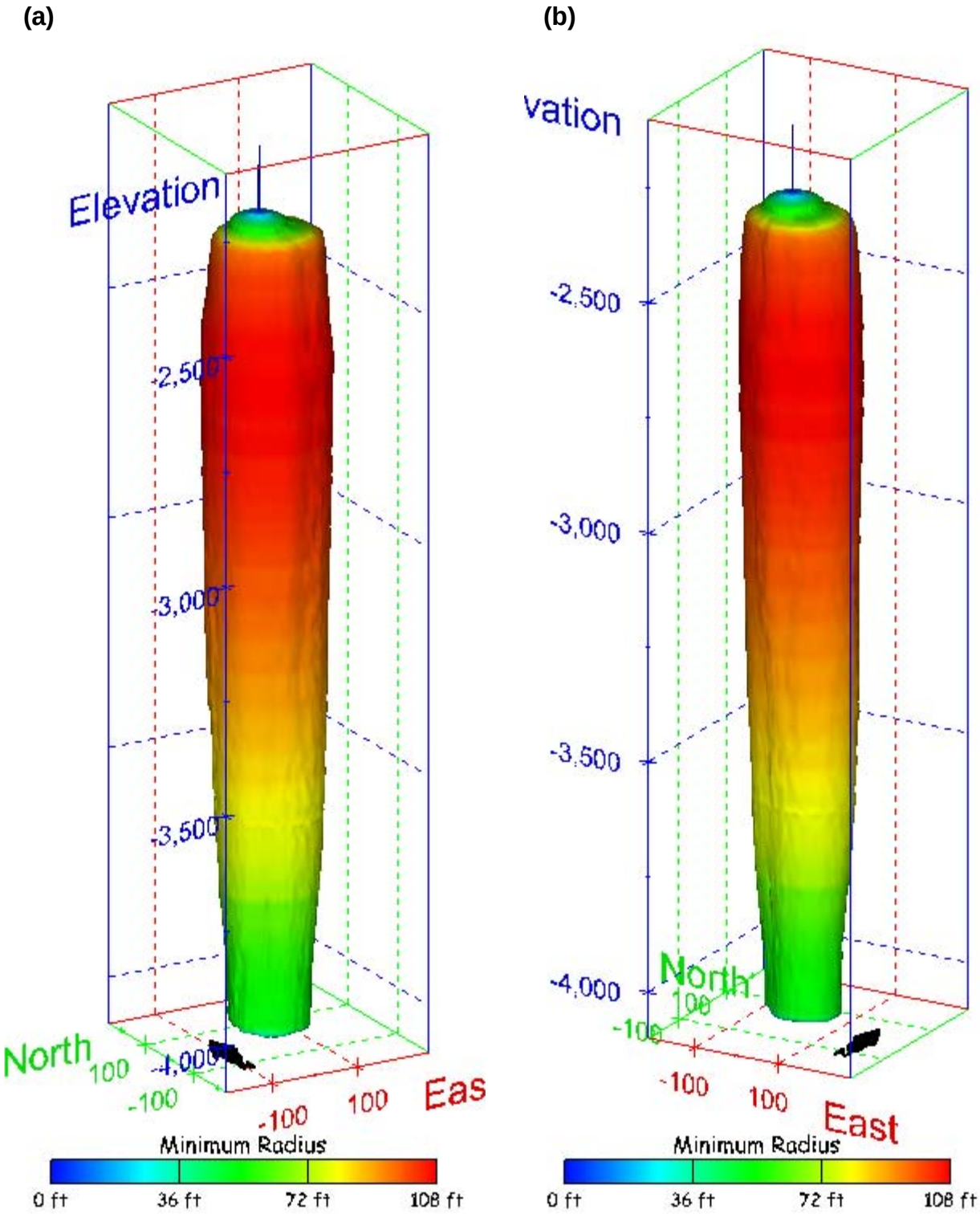

Figure 50. Sonar images of cavern BH-102, showing the geometry of the cavern colored by minimum radius. View from (a) azimuth 210°, elevation 20°; (b) azimuth 150°, elevation 20°.

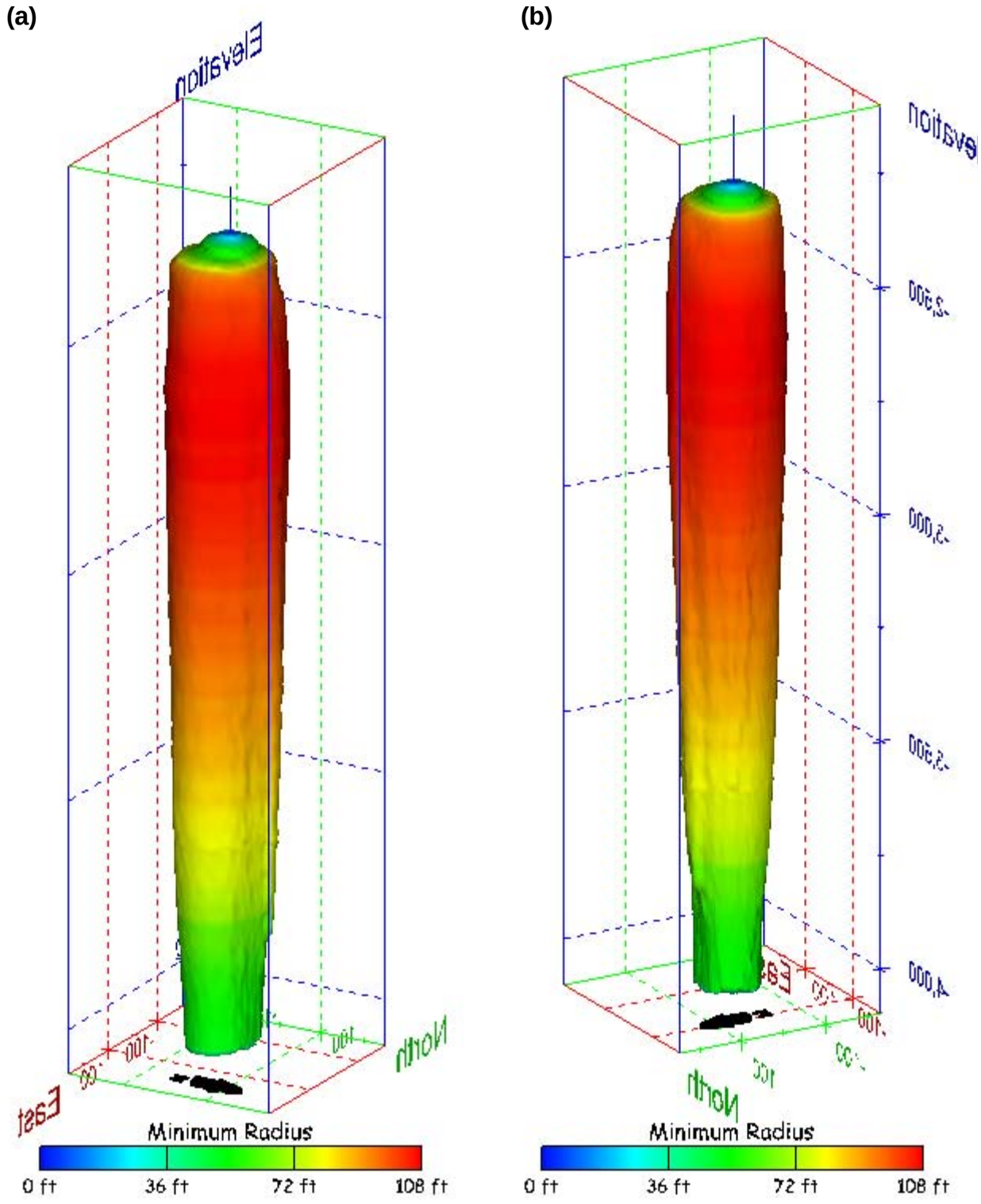

Figure 51. Sonar images of cavern BH-102, showing the geometry of the cavern colored by minimum radius. View from (a) azimuth 60°, elevation 20°; (b) azimuth 300°, elevation 20°.

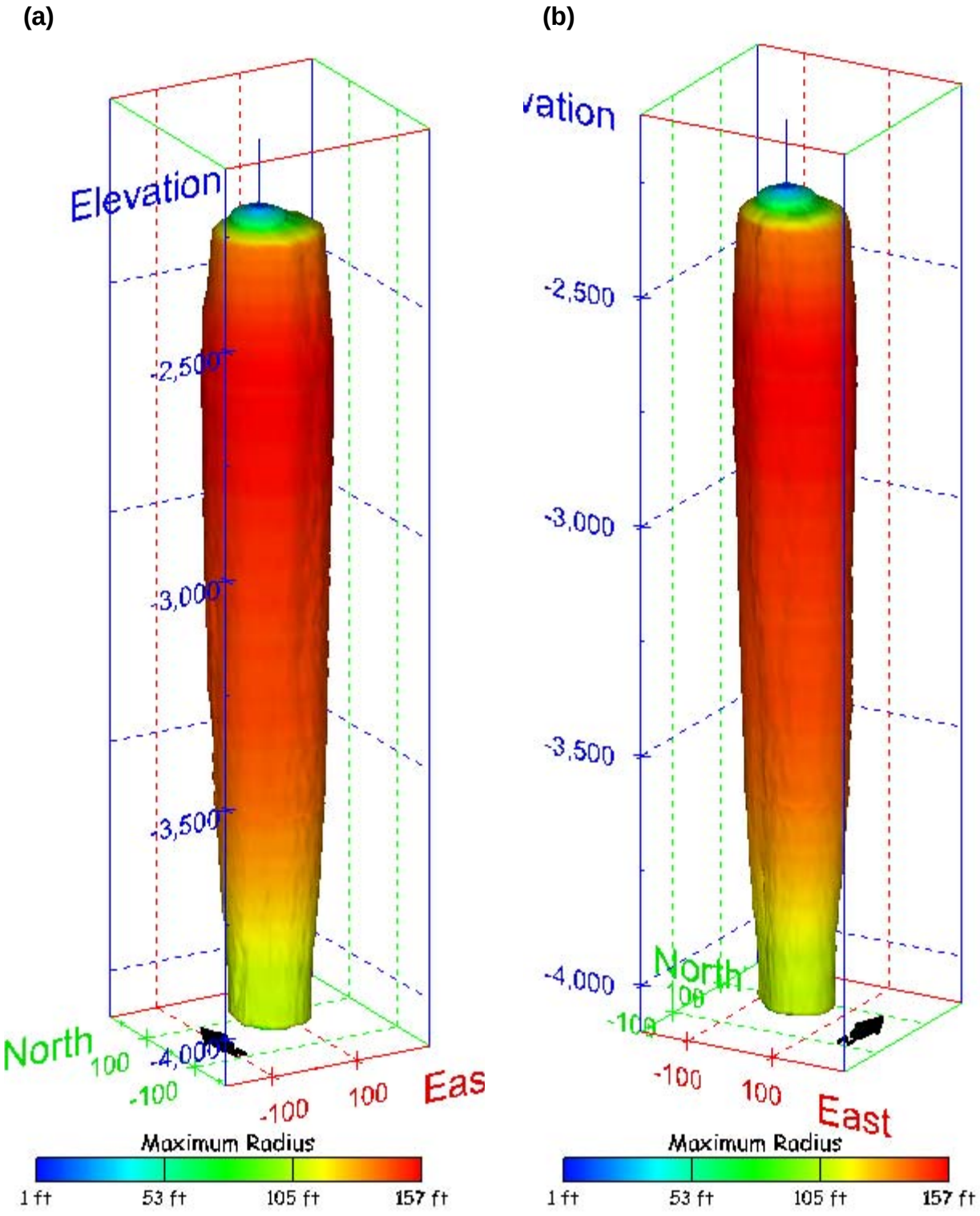

Figure 52. Sonar images of cavern BH-102, showing the geometry of the cavern colored by maximum radius. View from (a) azimuth 210°, elevation 20°; (b) azimuth 150°, elevation 20°.

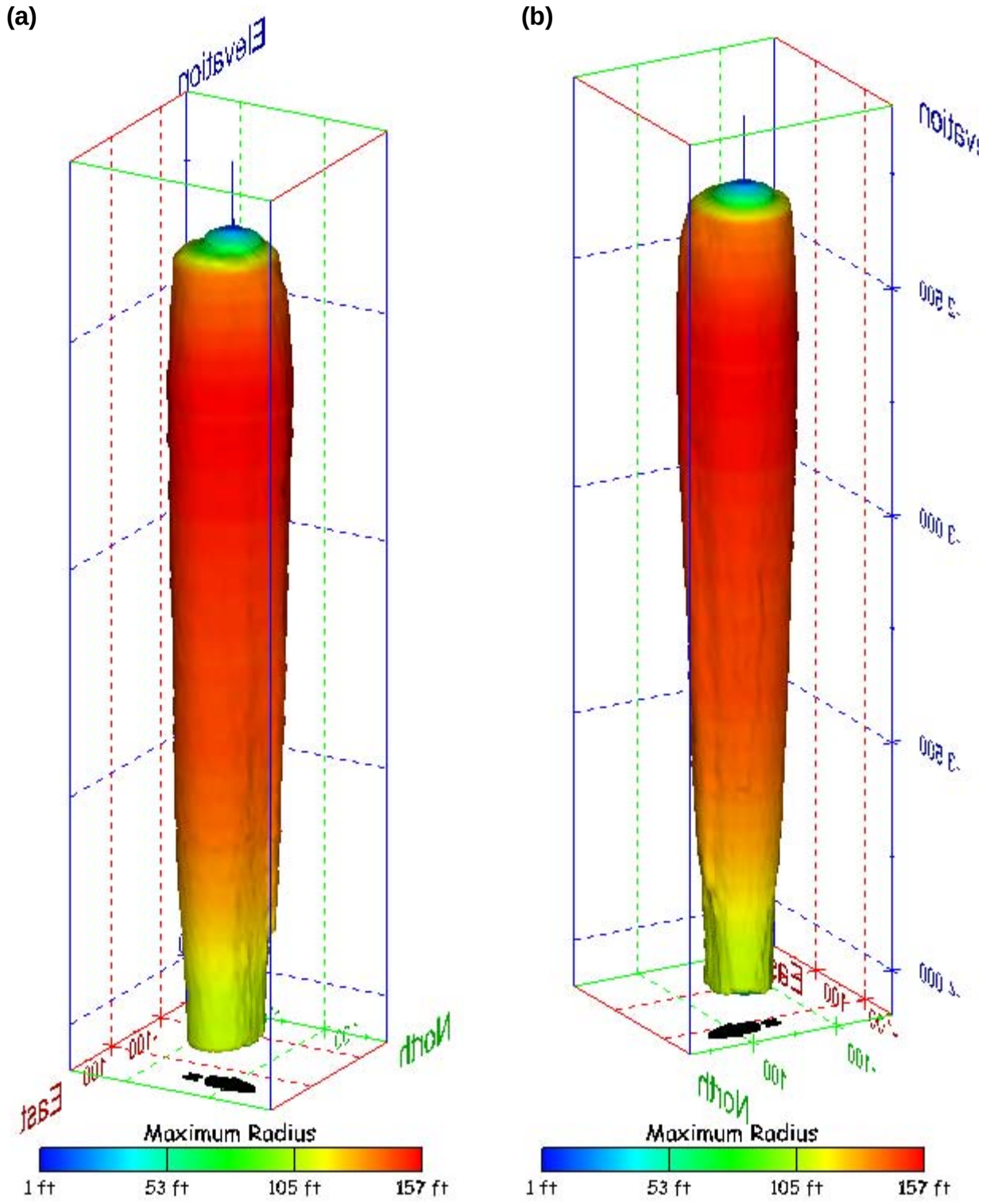

Figure 53. Sonar images of cavern BH-102, showing the geometry of the cavern colored by maximum radius. View from (a) azimuth 60°, elevation 20°; (b) azimuth 300°, elevation 20°.

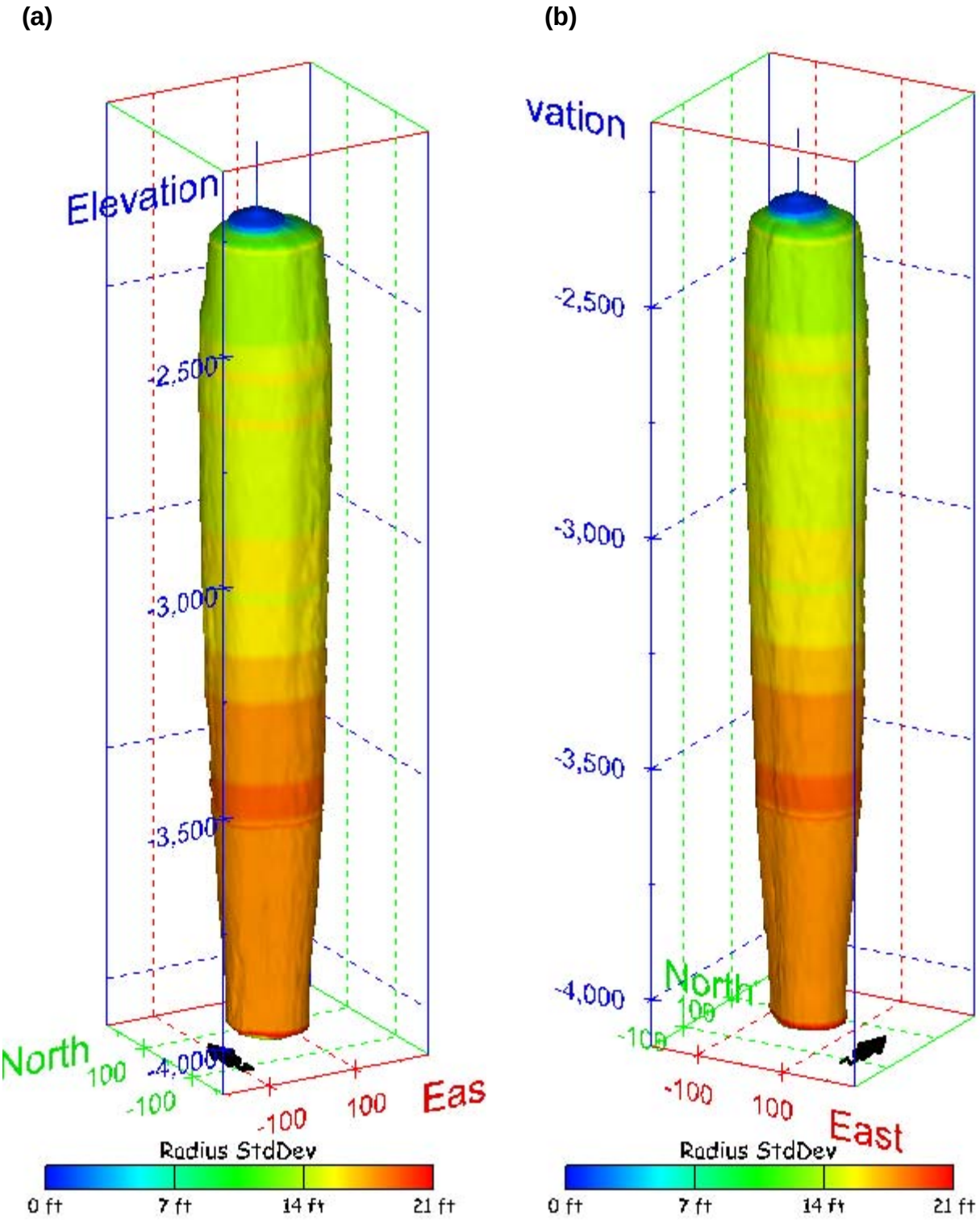

Figure 54. Sonar images of cavern BH-102, showing the geometry of the cavern colored by radius standard deviation. View from (a) azimuth 210°, elevation 20°; (b) azimuth 150°, elevation 20°.

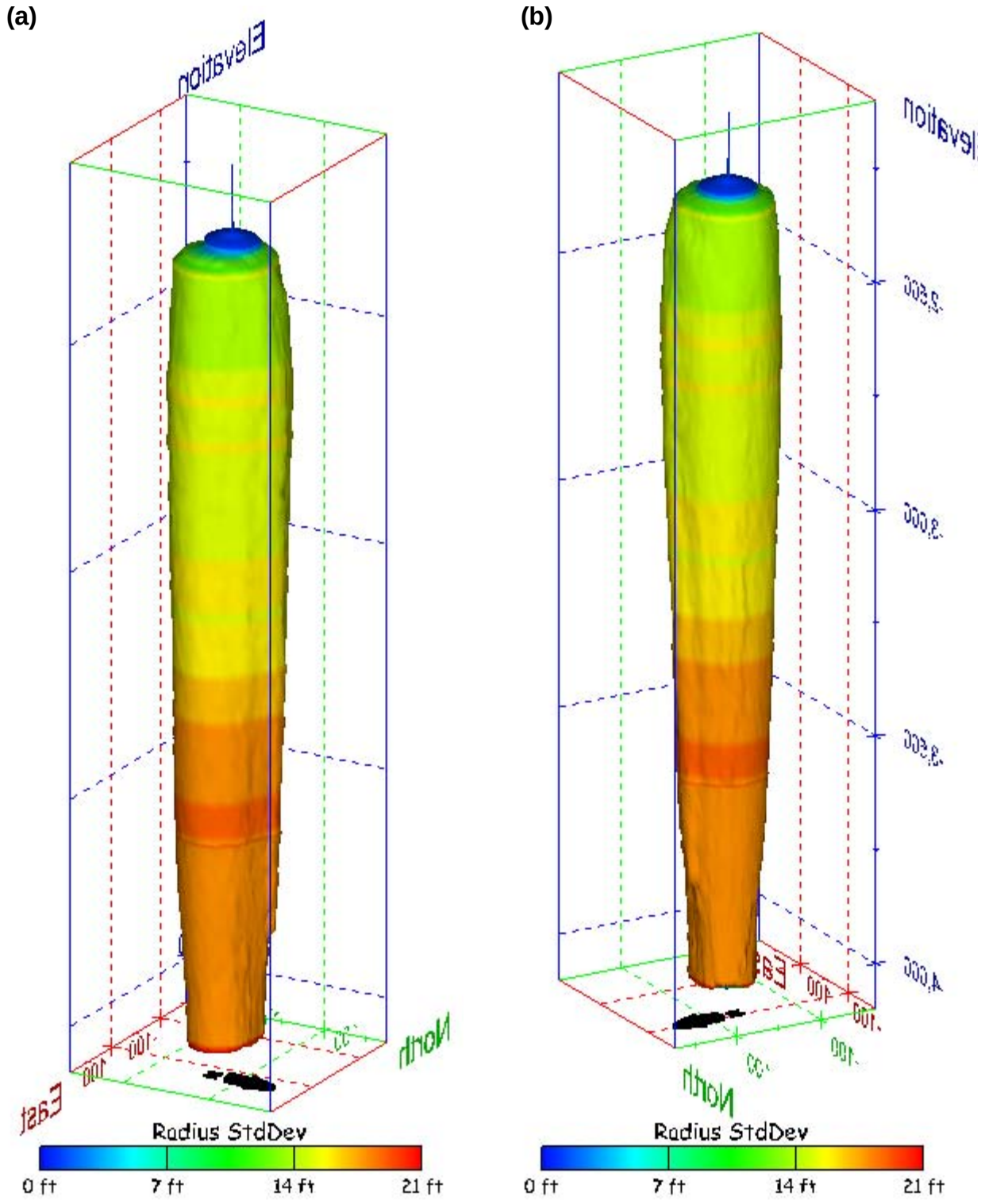

Figure 55. Sonar images of cavern BH-102, showing the geometry of the cavern colored by radius standard deviation. View from (a) azimuth 60°, elevation 20°; (b) azimuth 300°, elevation 20°.

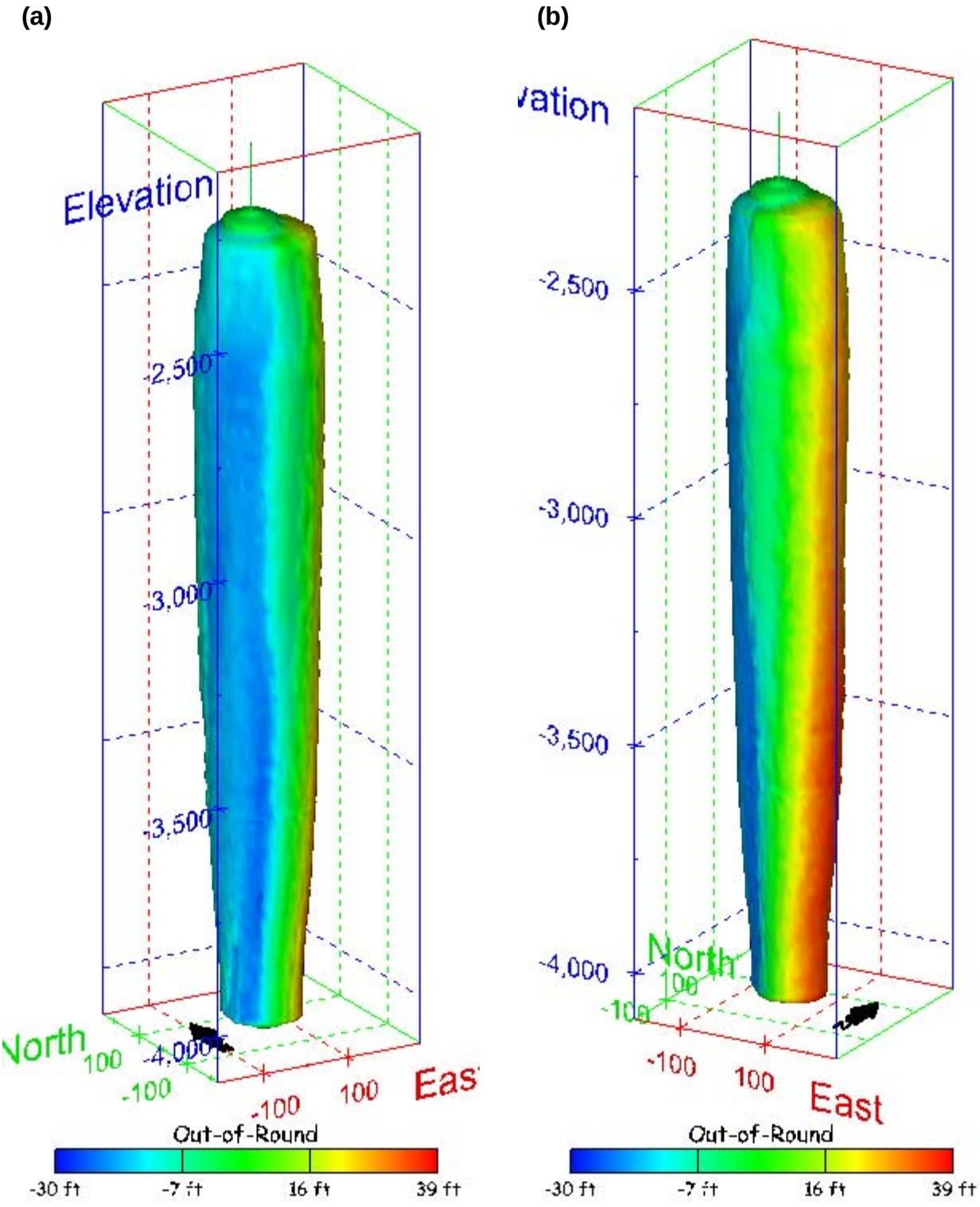

Figure 56. Sonar images of cavern BH-102, showing the geometry of the cavern colored by out-of-round distance. View from (a) azimuth 210°, elevation 20°; (b) azimuth 150°, elevation 20°.

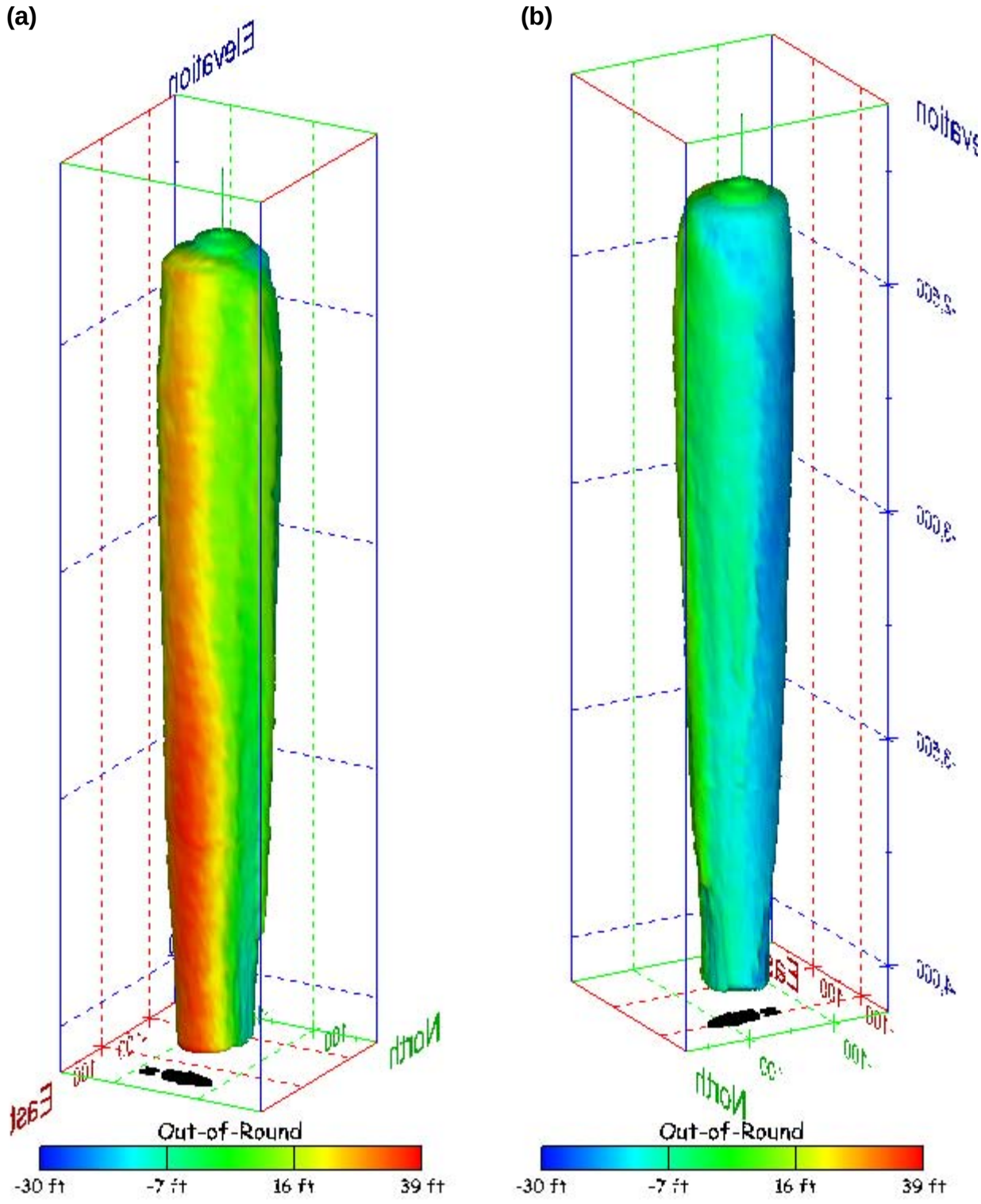

Figure 57. Sonar images of cavern BH-102, showing the geometry of the cavern colored by out-of-round distance. View from (a) azimuth 60°, elevation 20°; (b) azimuth 300°, elevation 20°.

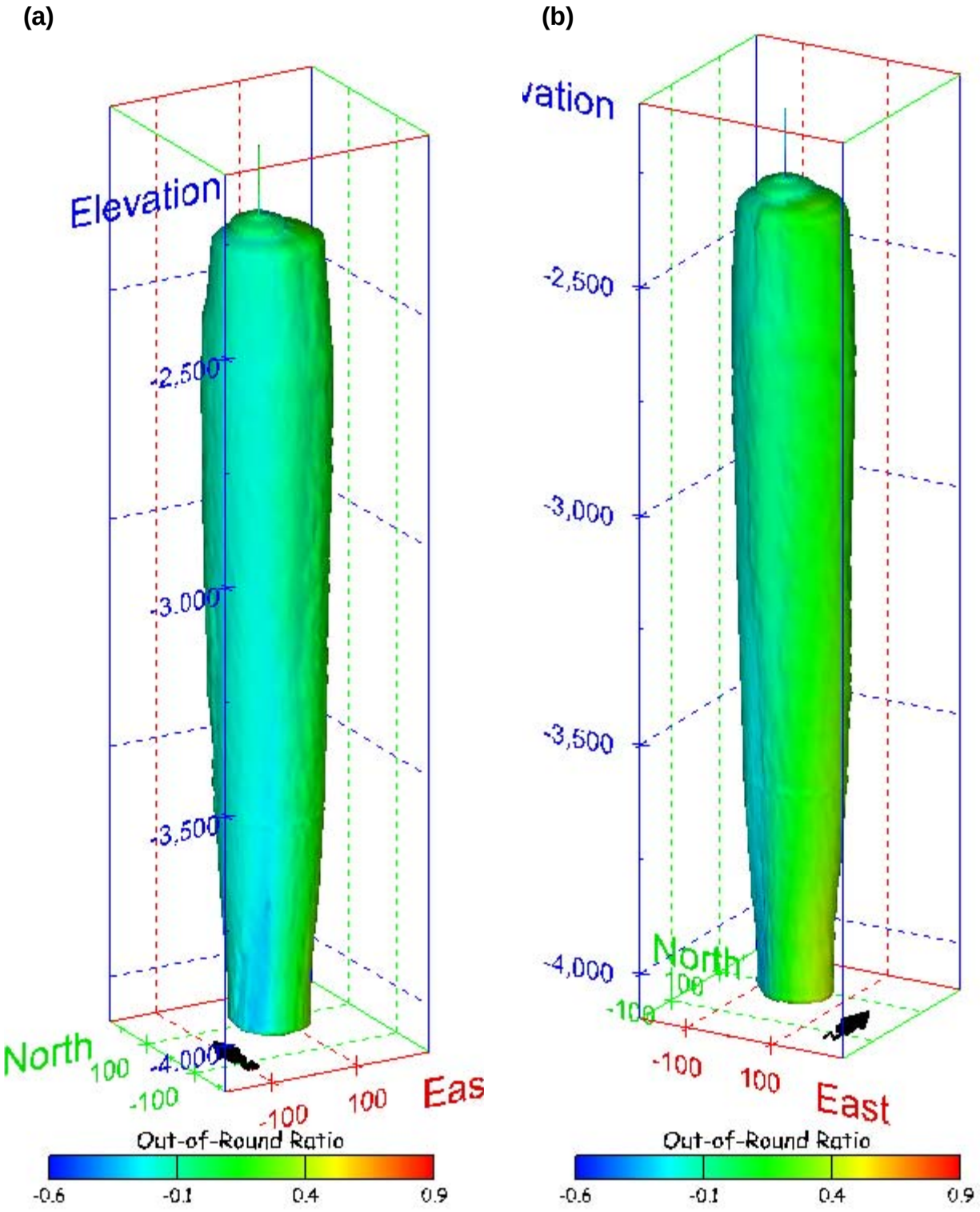

Figure 58. Sonar images of cavern BH-102, showing the geometry of the cavern colored by out-of-round ratio. View from (a) azimuth 210°, elevation 20°; (b) azimuth 150°, elevation 20°.

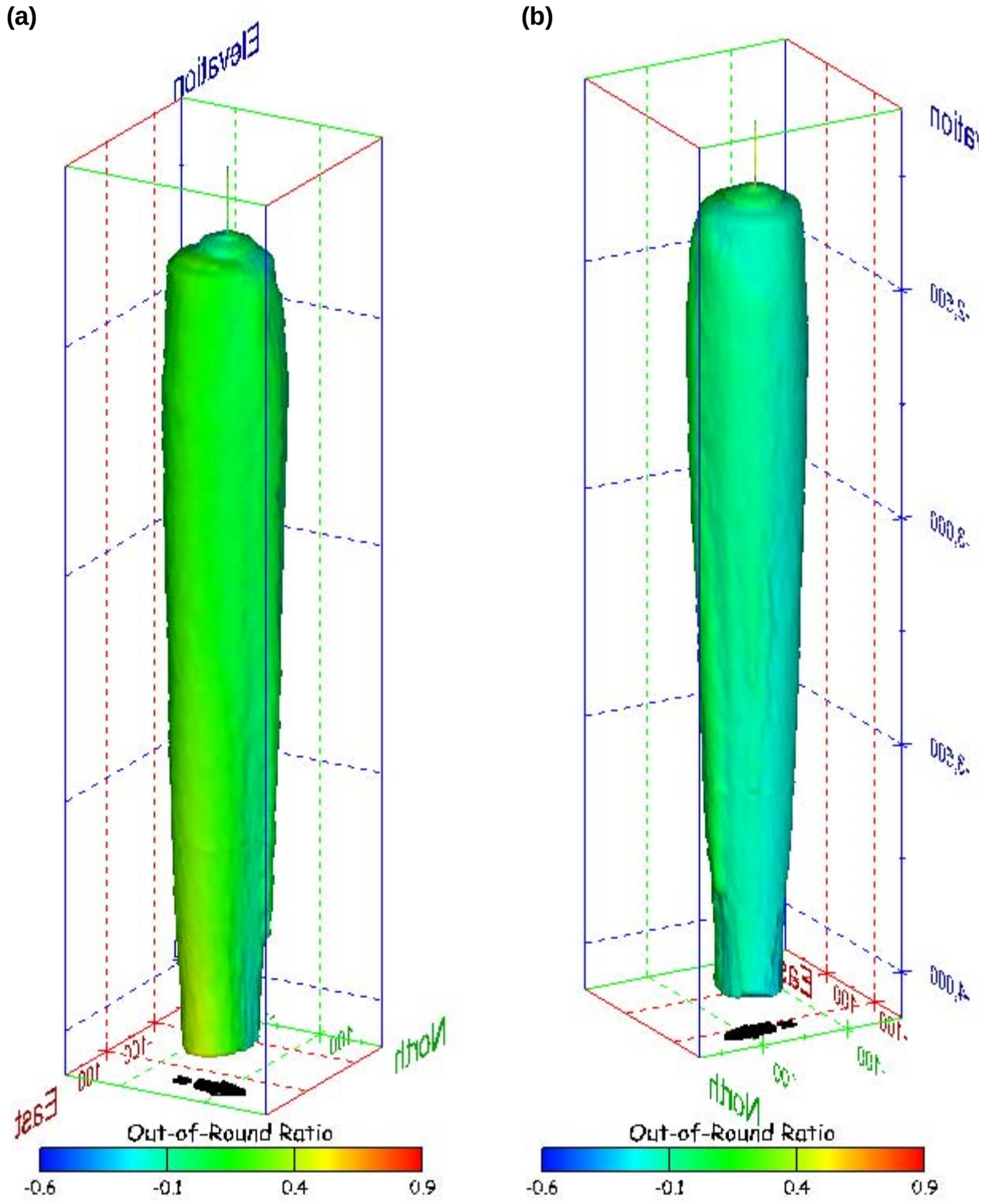

Figure 59. Sonar images of cavern BH-102, showing the geometry of the cavern colored by out-of-round ratio. View from (a) azimuth 60°, elevation 20°; (b) azimuth 300°, elevation 20°.

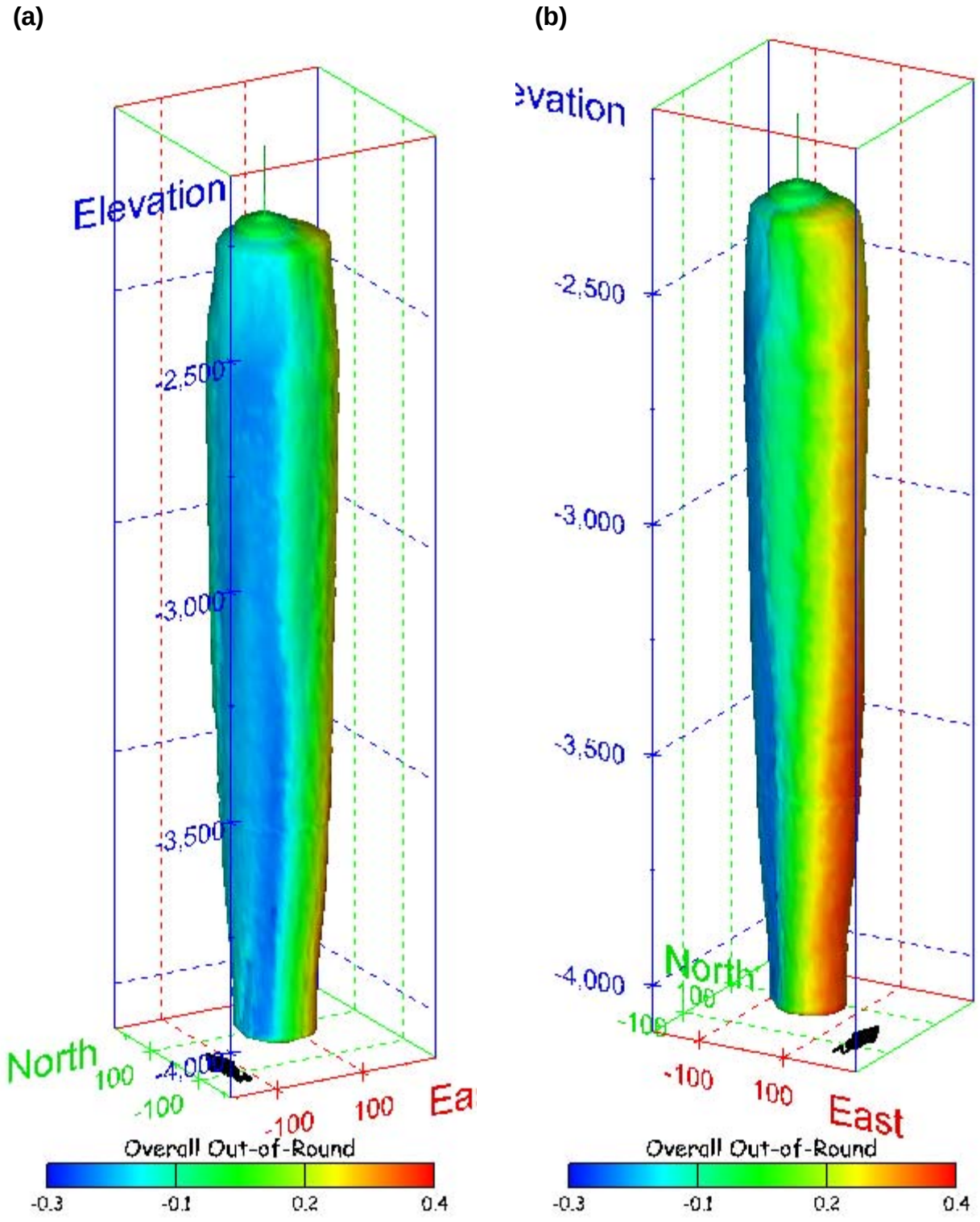

Figure 60. Sonar images of cavern BH-102, showing the geometry of the cavern colored by overall out-of-round ratio. View from (a) azimuth 210°, elevation 20°; (b) azimuth 150°, elevation 20°.

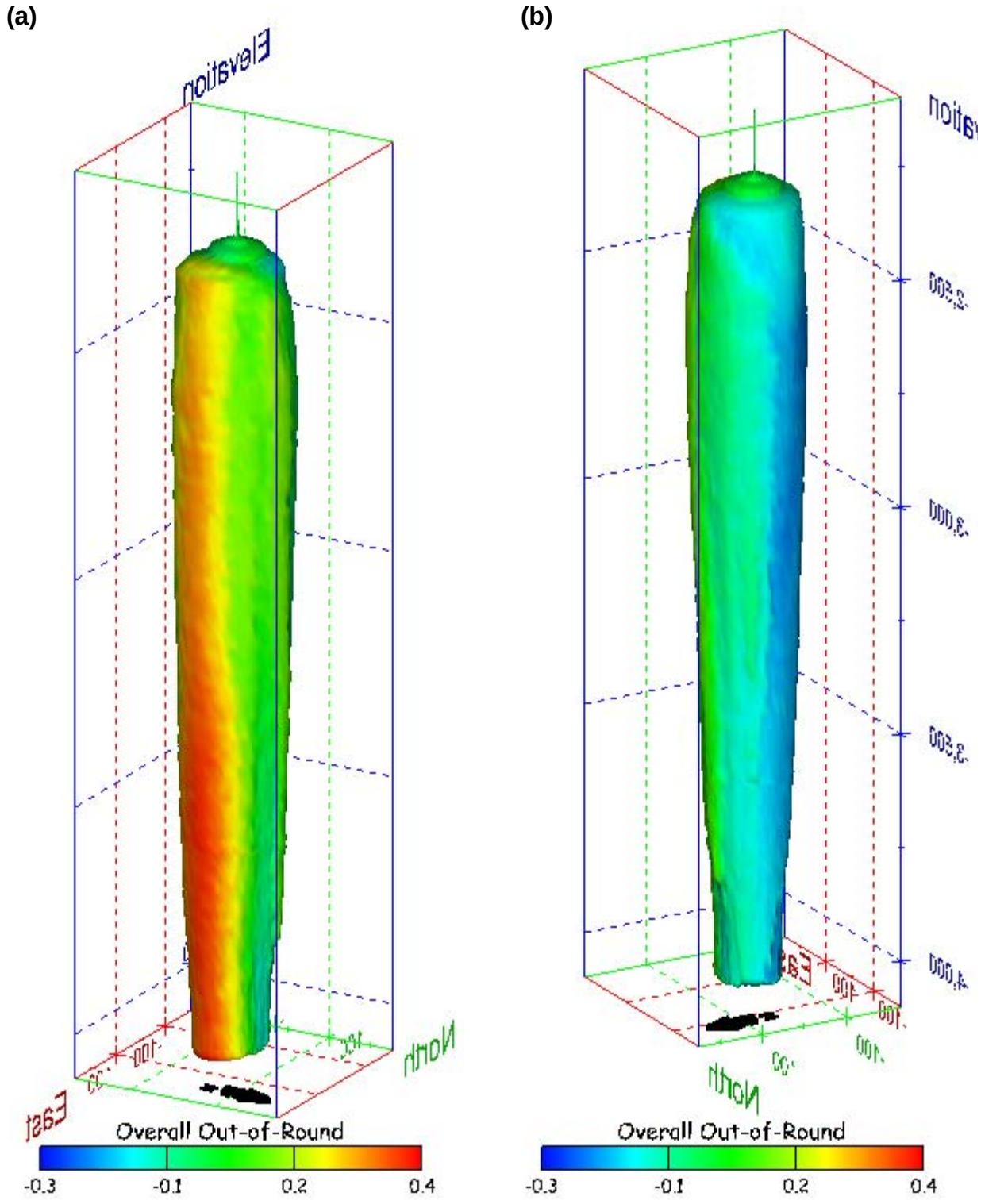

Figure 61. Sonar images of cavern BH-102, showing the geometry of the cavern colored by overall out-of-round ratio. View from (a) azimuth 60°, elevation 20°; (b) azimuth 300°, elevation 20°.

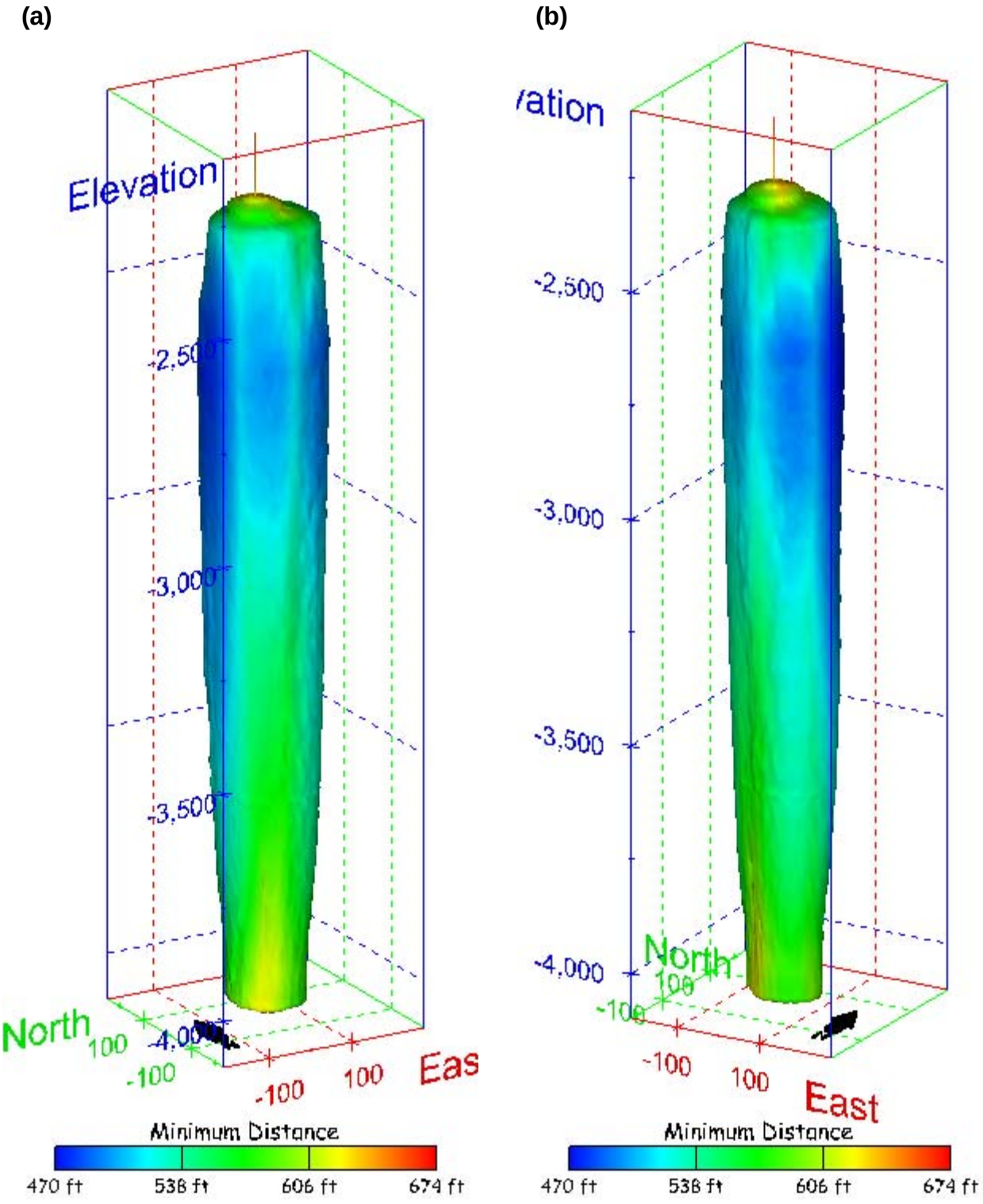

Figure 62. Sonar images of cavern BH-102, showing the geometry of the cavern colored by the minimum distance to the nearest neighboring cavern. View from (a) azimuth 210°, elevation 20°; (b) azimuth 150°, elevation 20°.

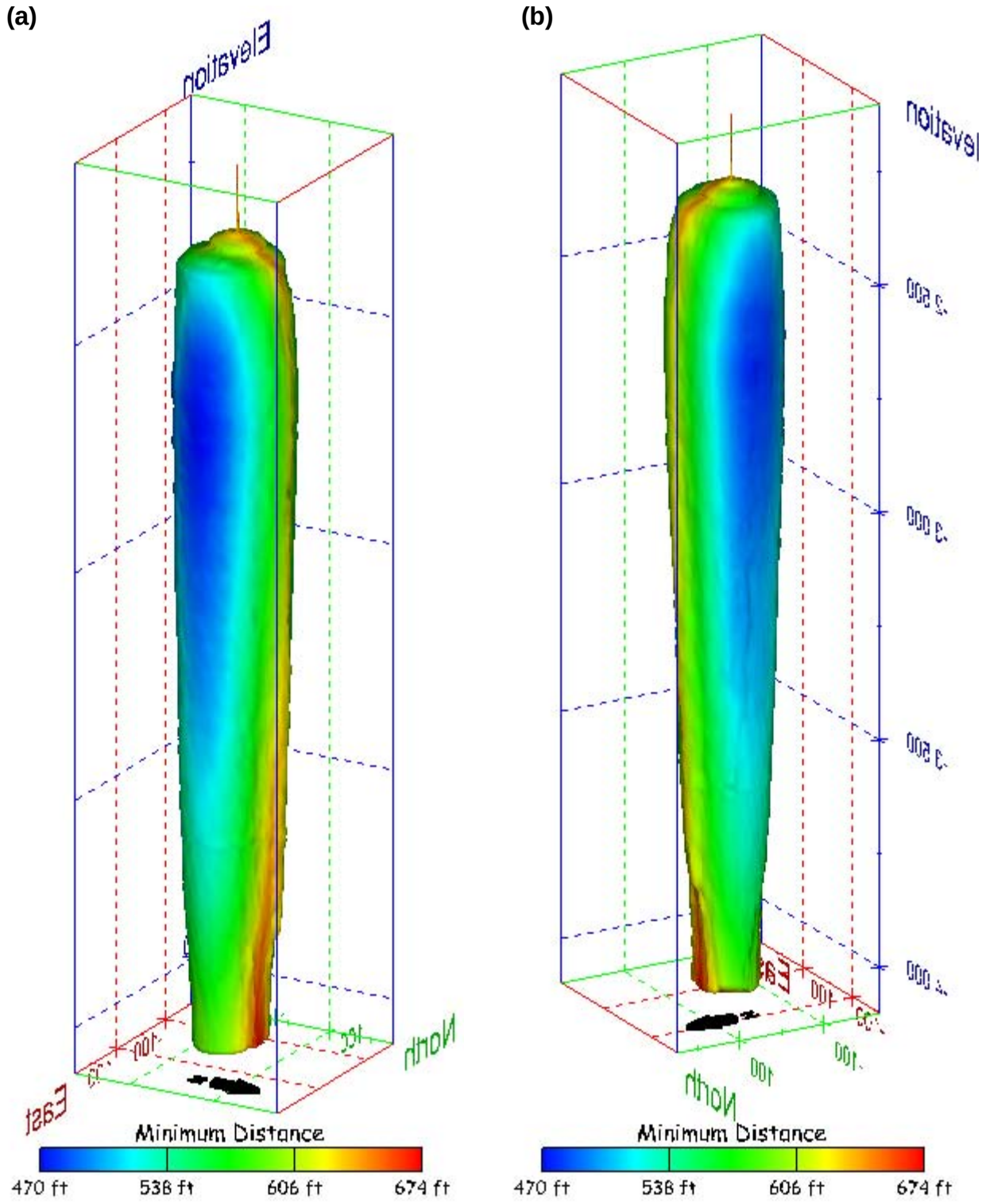

Figure 63. Sonar images of cavern BH-102, showing the geometry of the cavern colored by minimum distance to the nearest neighboring cavern. View from (a) azimuth 60°, elevation 20°; (b) azimuth 300°, elevation 20°.

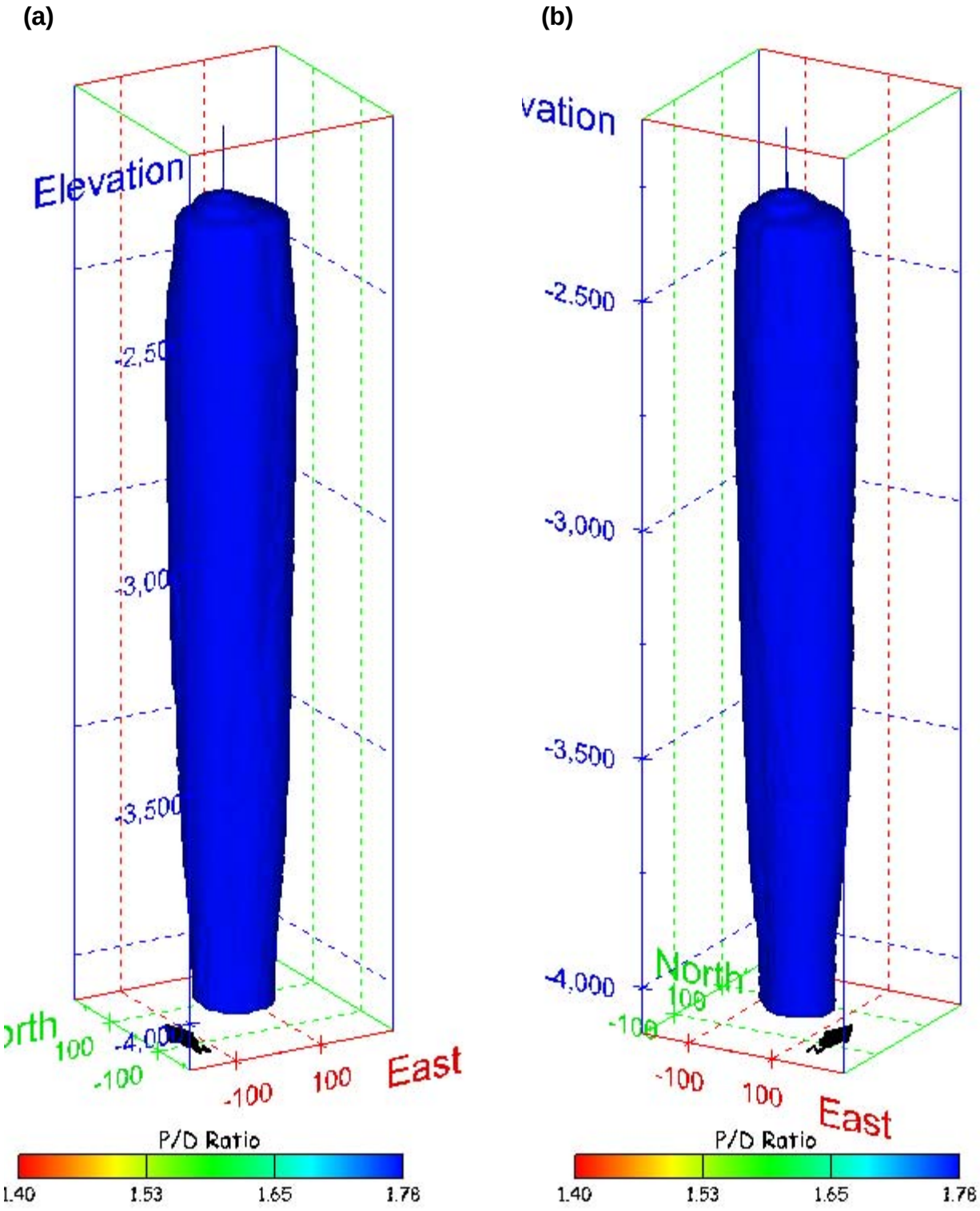

Figure 64. Sonar images of cavern BH-102, showing the geometry of the cavern colored by three-dimensional pillar-to-diameter ratio. View from (a) azimuth 210°, elevation 20°; (b) azimuth 150°, elevation 20°.

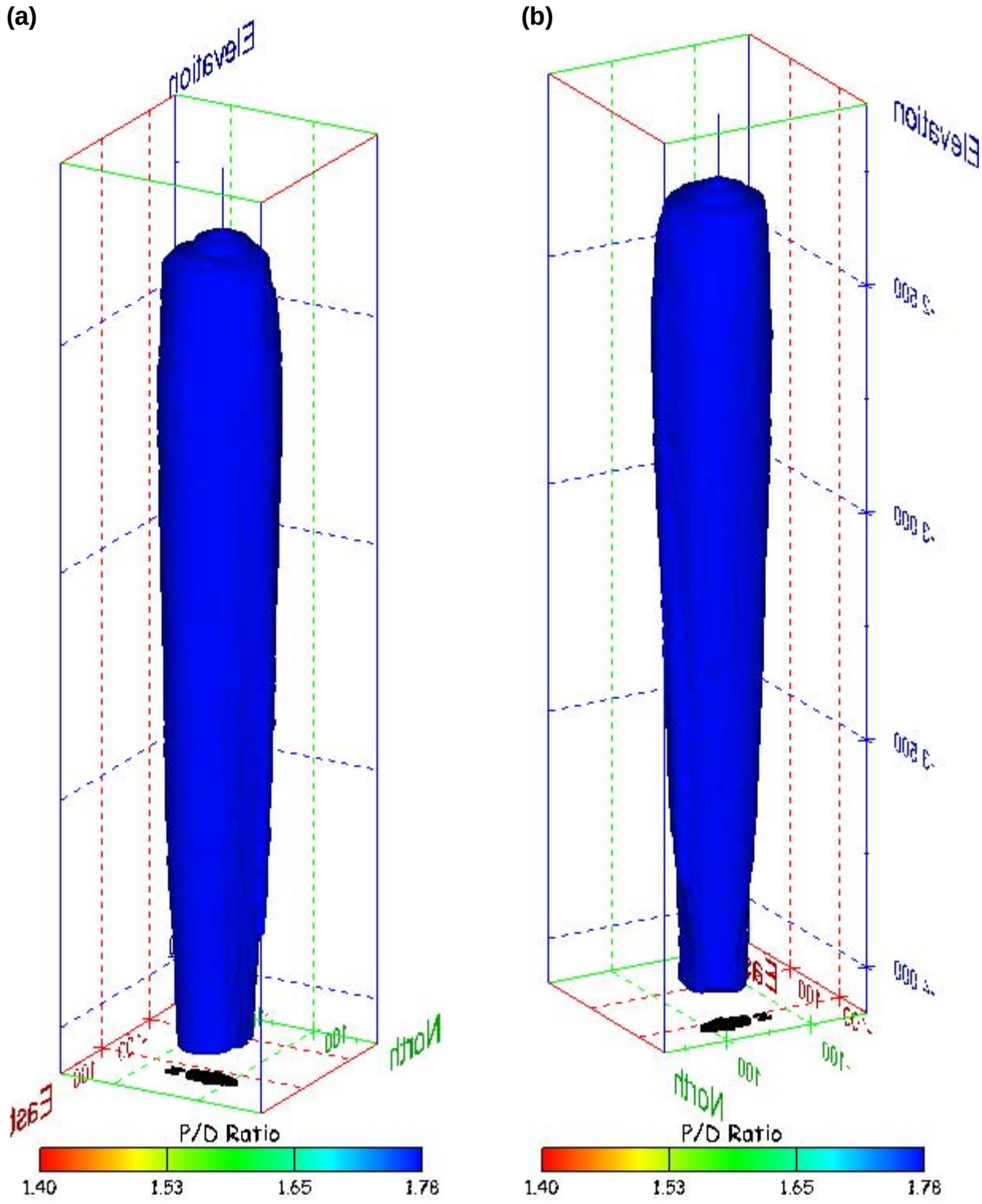

Figure 65. Sonar images of cavern BH-102, showing the geometry of the cavern colored by three-dimensional pillar-to-diameter ratio. View from (a) azimuth 760°, elevation 20°; (b) azimuth 300°, elevation 20°.

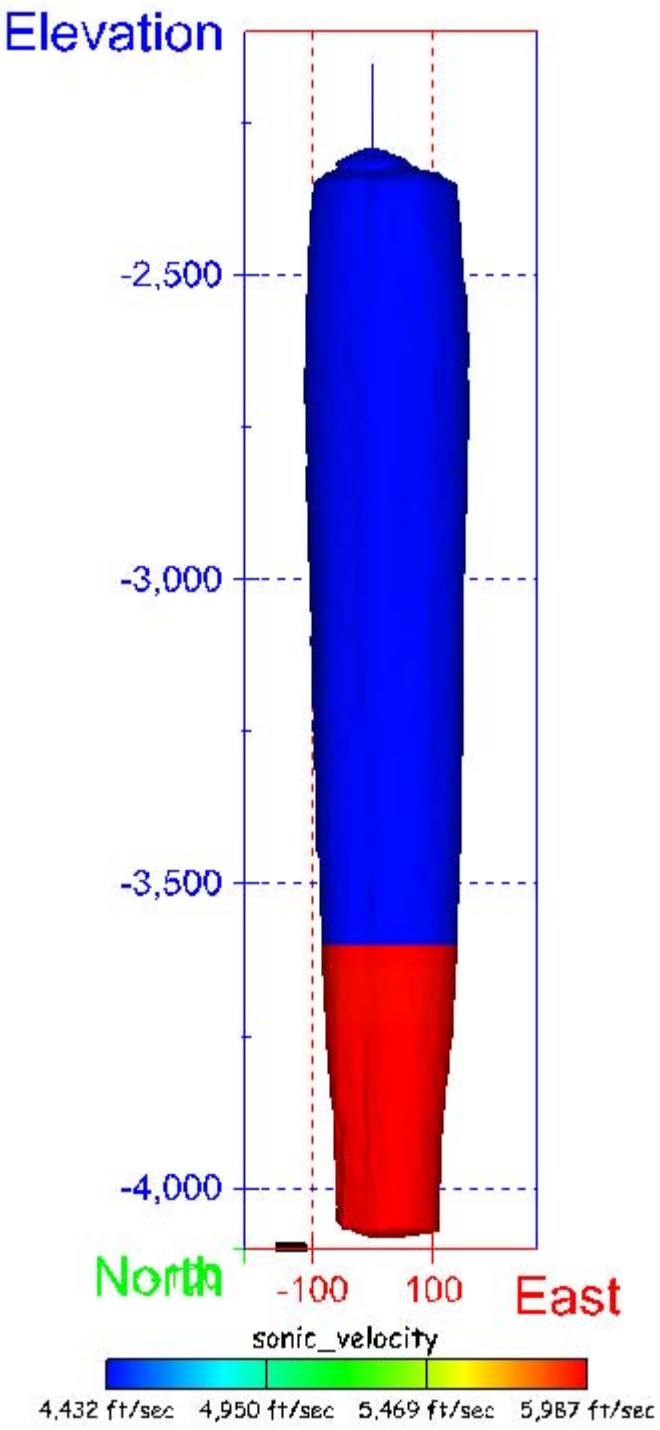

Figure 66. Sonar image of cavern BH-102, showing the geometry of the cavern colored by the reported velocity of sound on the survey date of November 2003. View from due south, elevation zero.

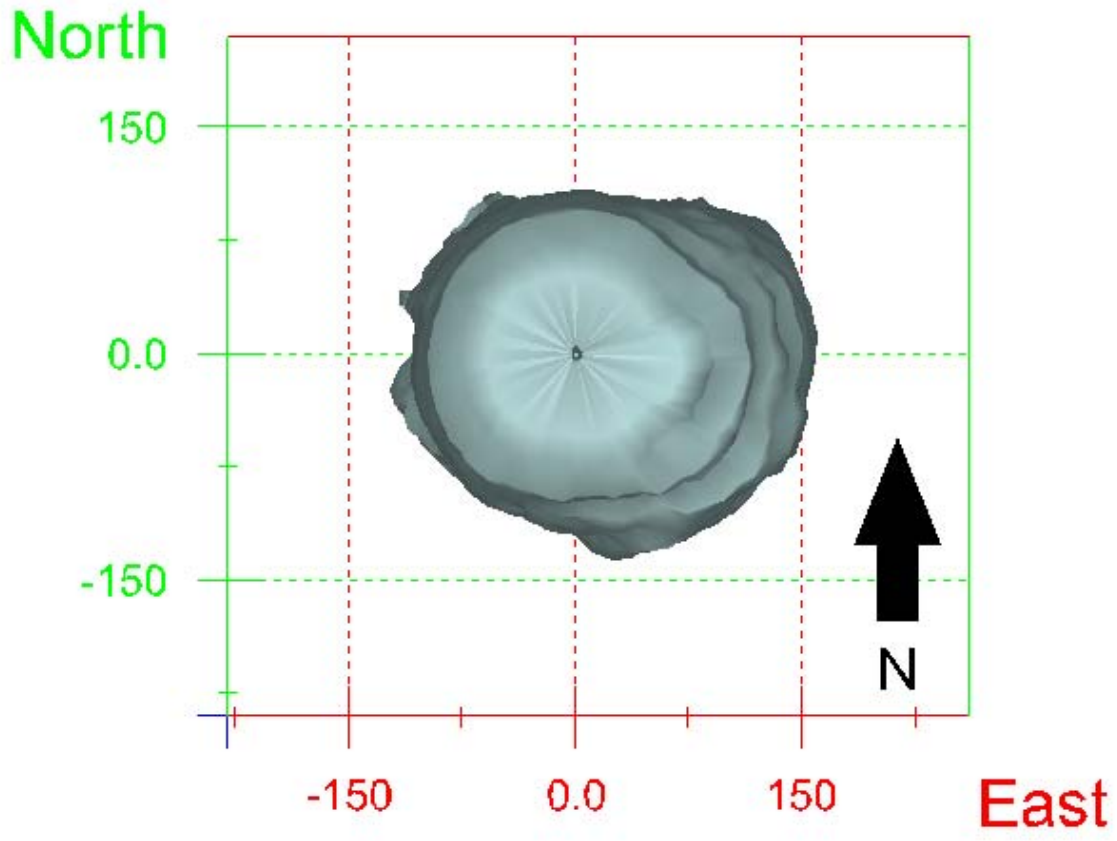

Figure 67. Map view sonar image of cavern BH-103, showing the basic geometry of the cavern. Grid squares represent 150 ft.

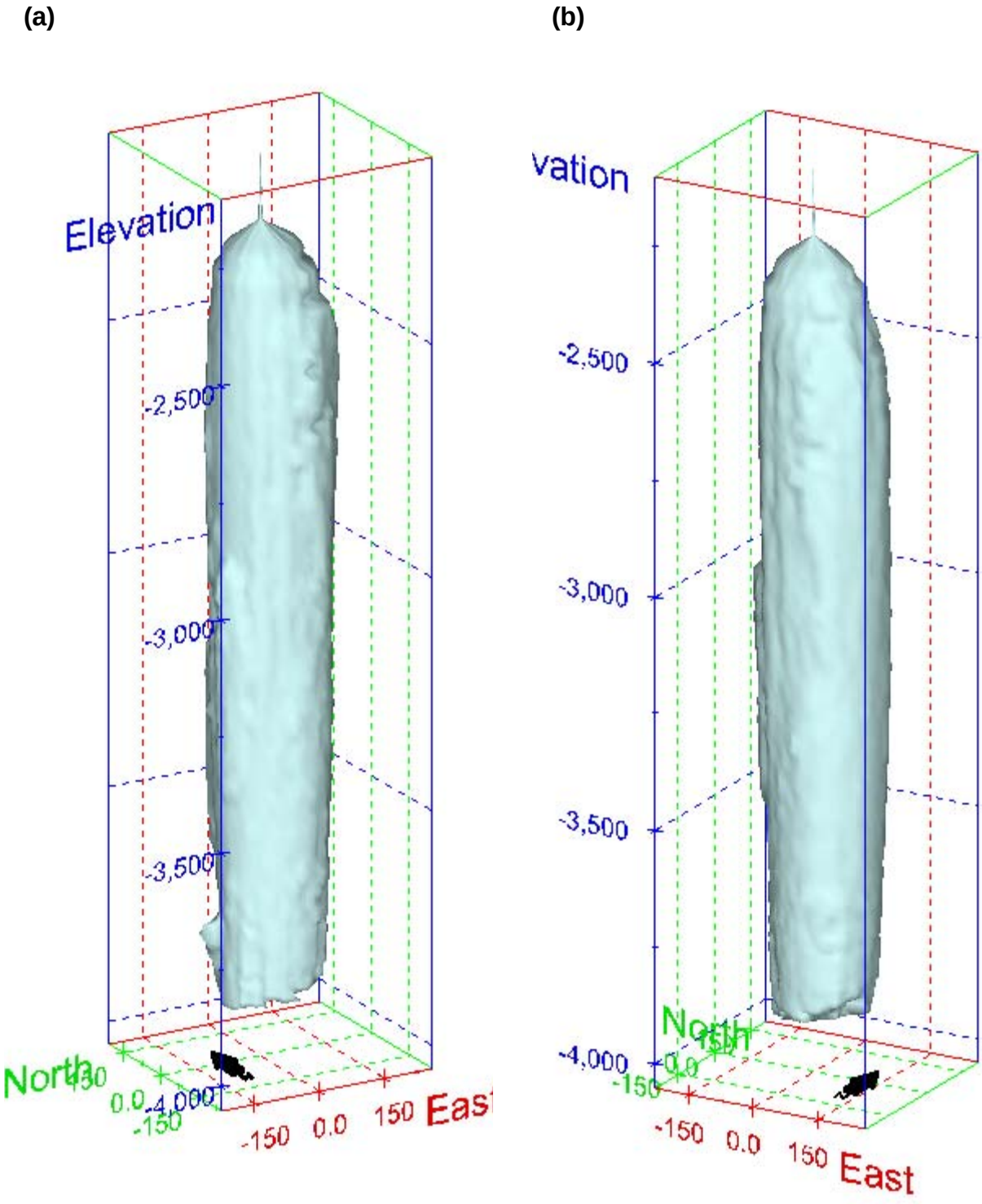

Figure 68. Sonar images of cavern BH-103, showing the basic geometric shape of the cavern. View from (a) azimuth 210°, elevation 20°; (b) azimuth 150°, elevation 20°.

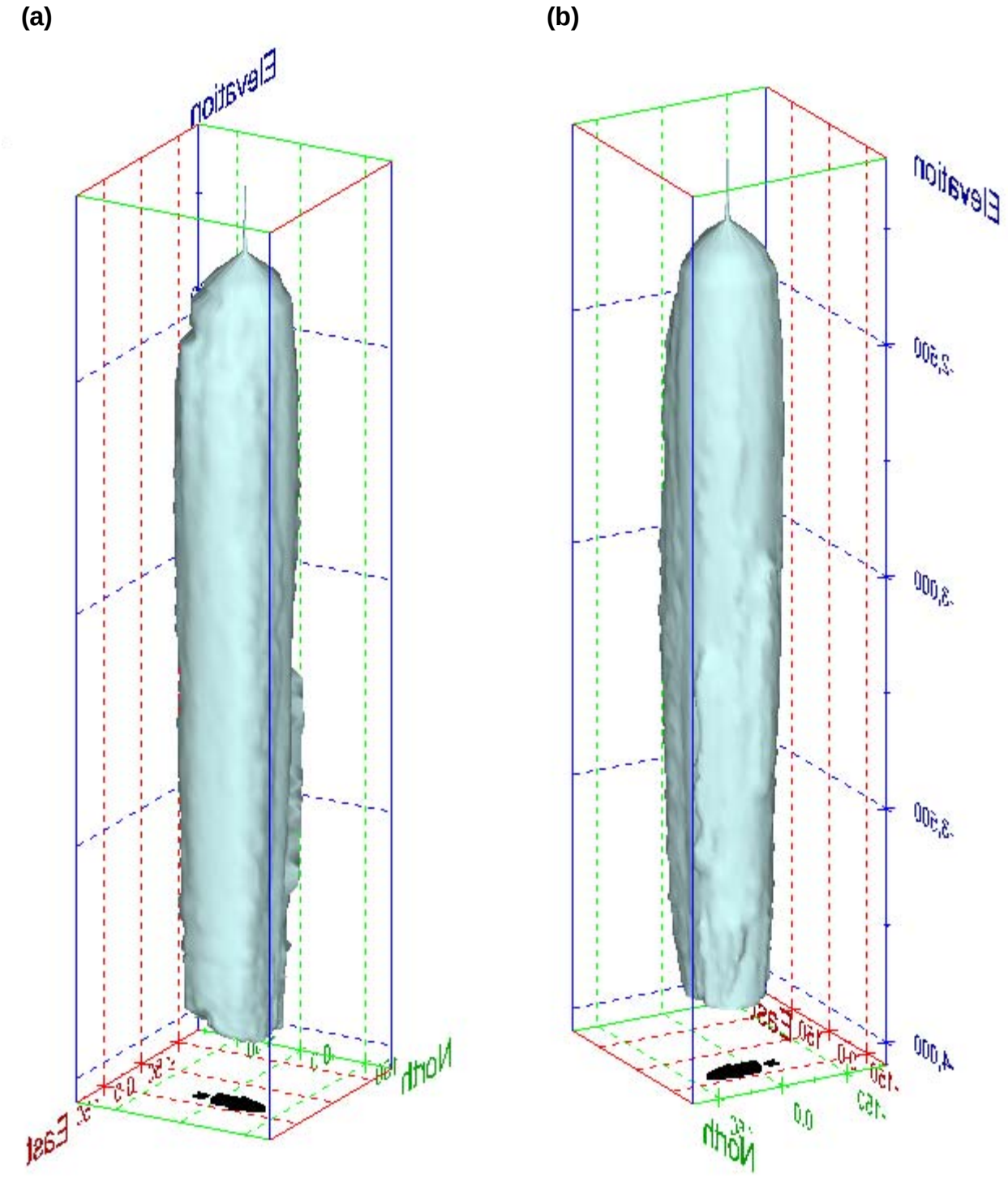

Figure 69. Sonar images of cavern BH-103, showing the basic geometric shape of the cavern. View from (a) azimuth 60°, elevation 20°; (b) azimuth 300°, elevation 20°.

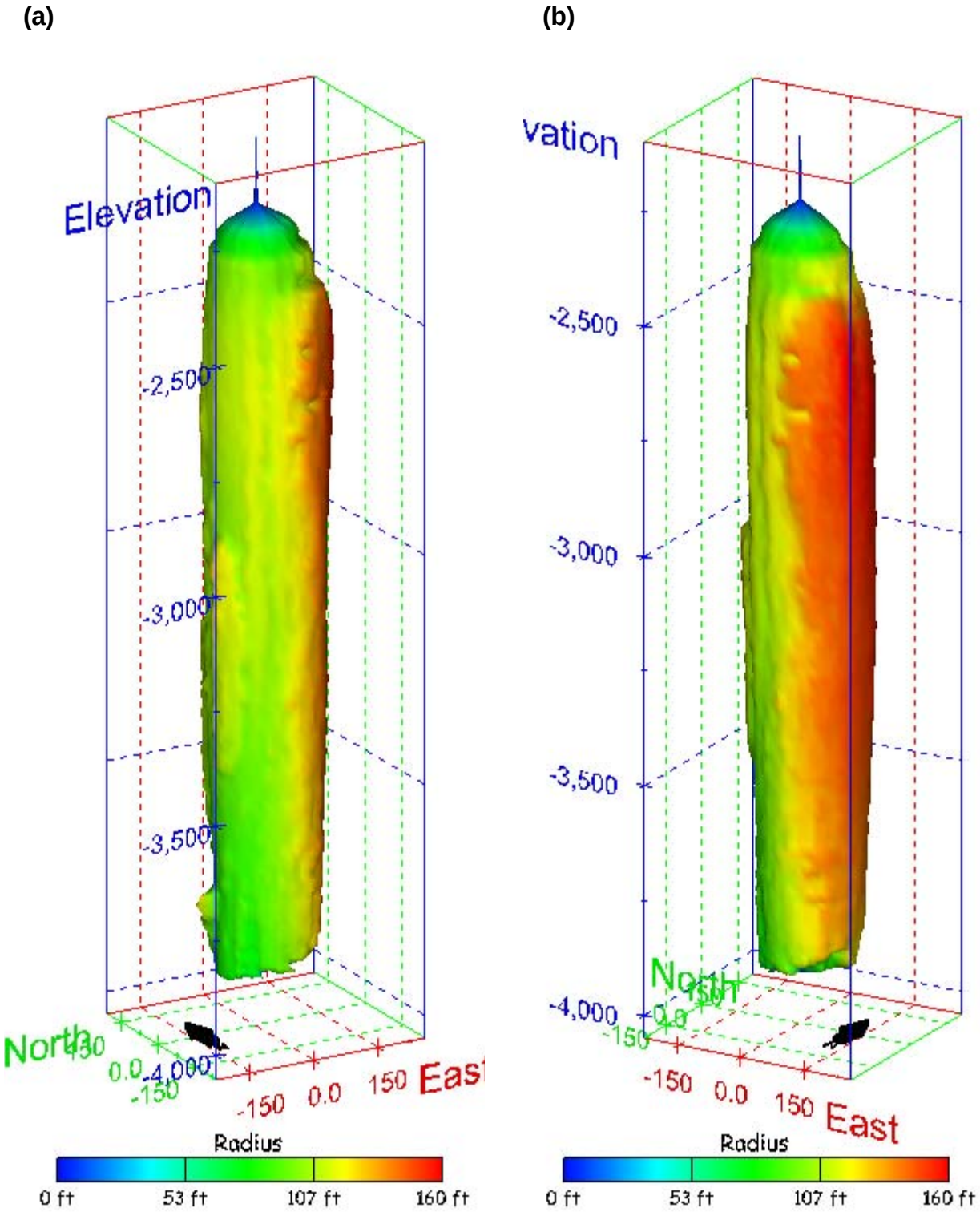

Figure 70. Sonar images of cavern BH-103, showing the geometry of the cavern colored by measured radius. View from (a) azimuth 210°, elevation 20°; (b) azimuth 150°, elevation 20°.

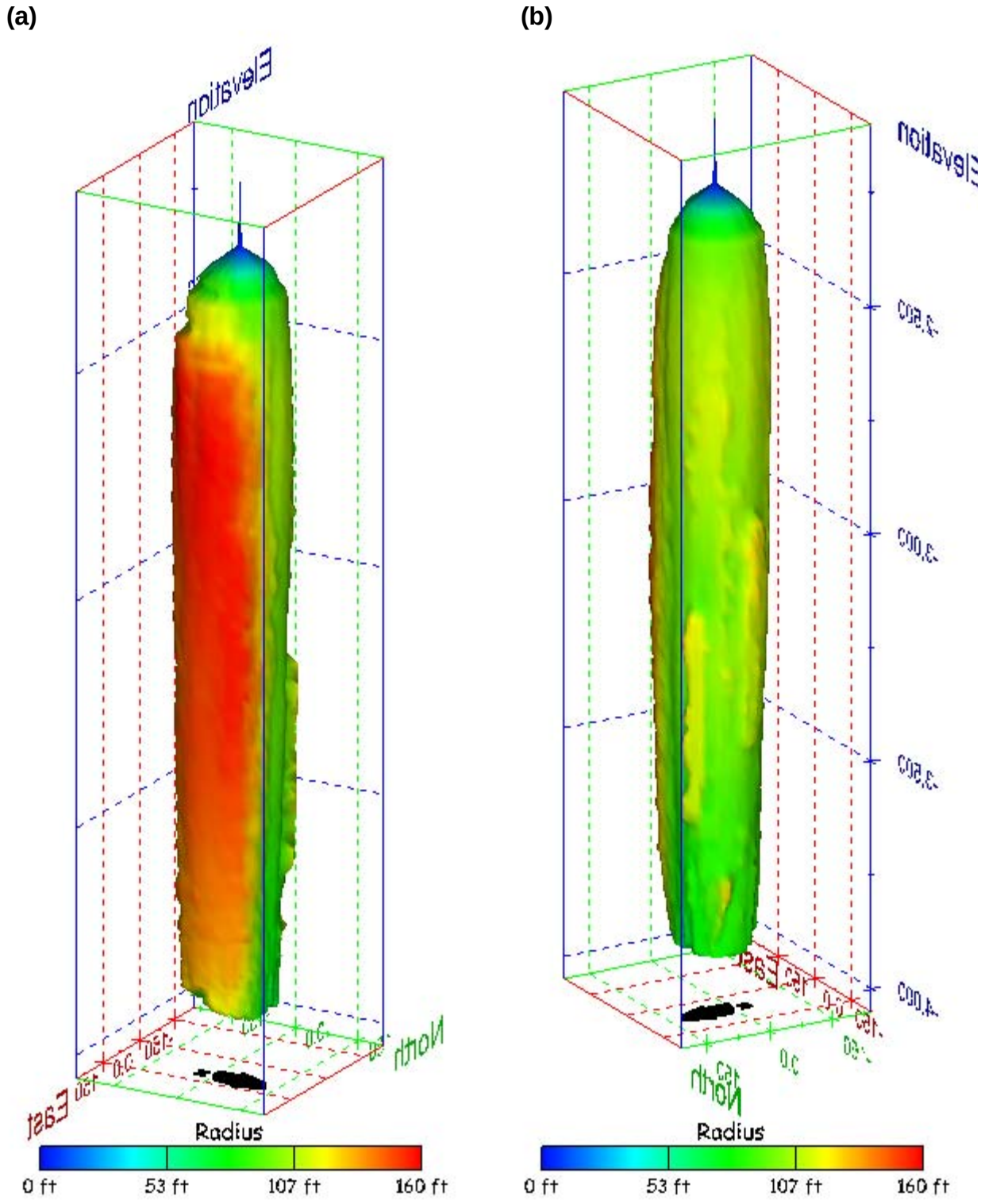

Figure 71. Sonar images of cavern BH-103, showing the geometry of the cavern colored by measured radius. View from (a) azimuth 60°, elevation 20°; (b) azimuth 300°, elevation 20°.

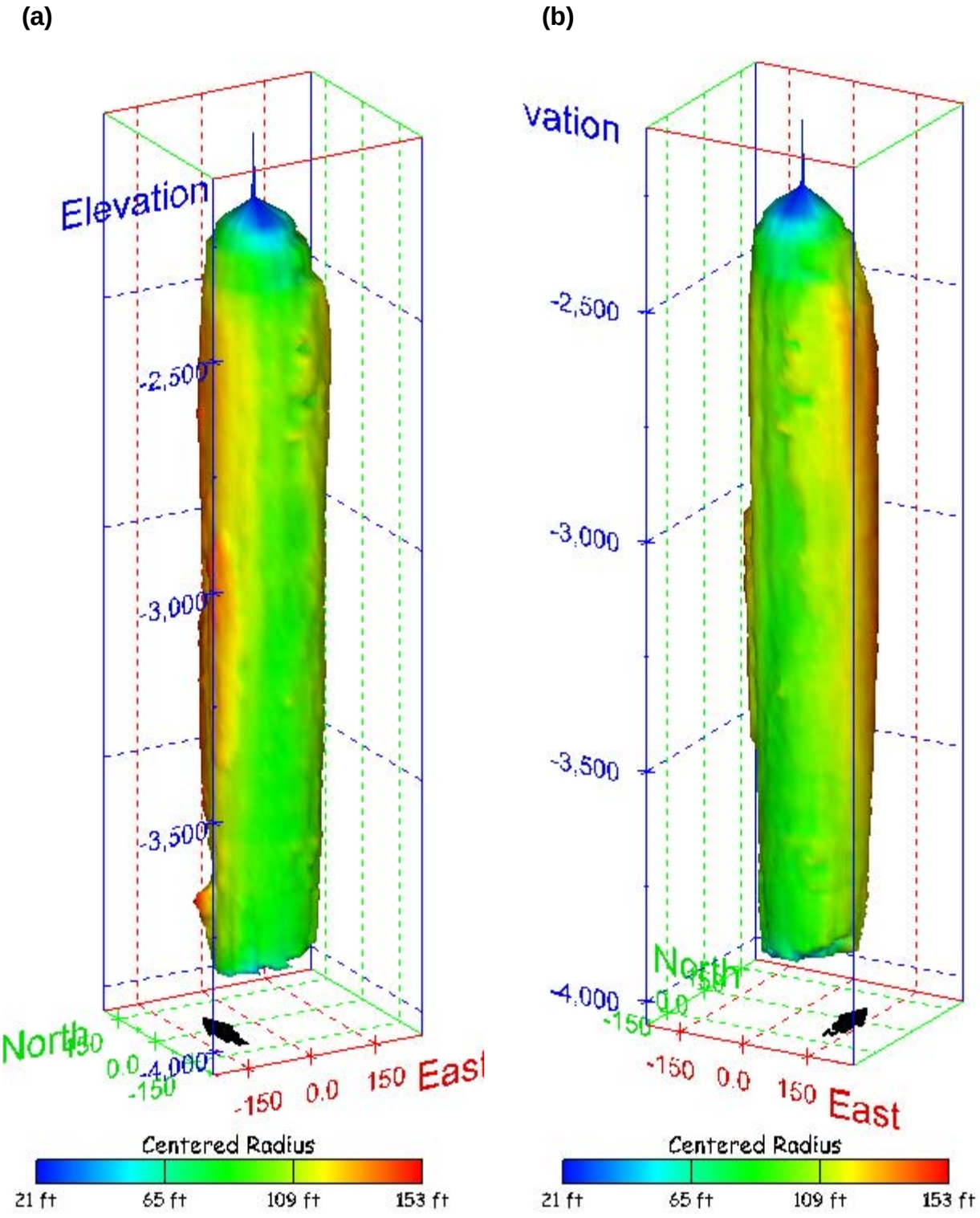

Figure 72. Sonar images of cavern BH-103, showing the geometry of the cavern colored by centered radius. View from (a) azimuth 210°, elevation 20°; (b) azimuth 150°, elevation 20°.

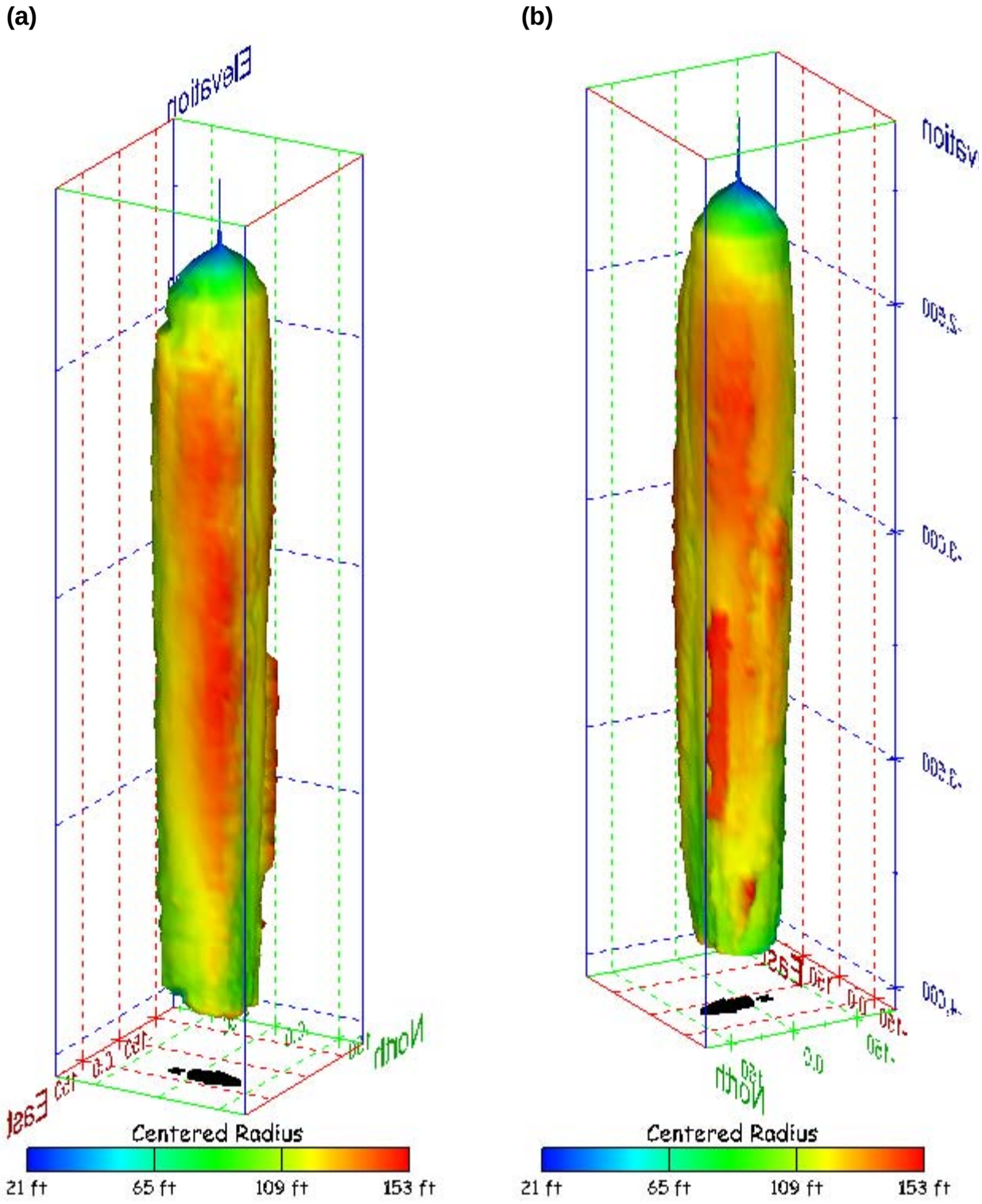

Figure 73. Sonar images of cavern BH-103, showing the geometry of the cavern colored by centered radius. View from (a) azimuth 60°, elevation 20°; (b) azimuth 300°, elevation 20°.

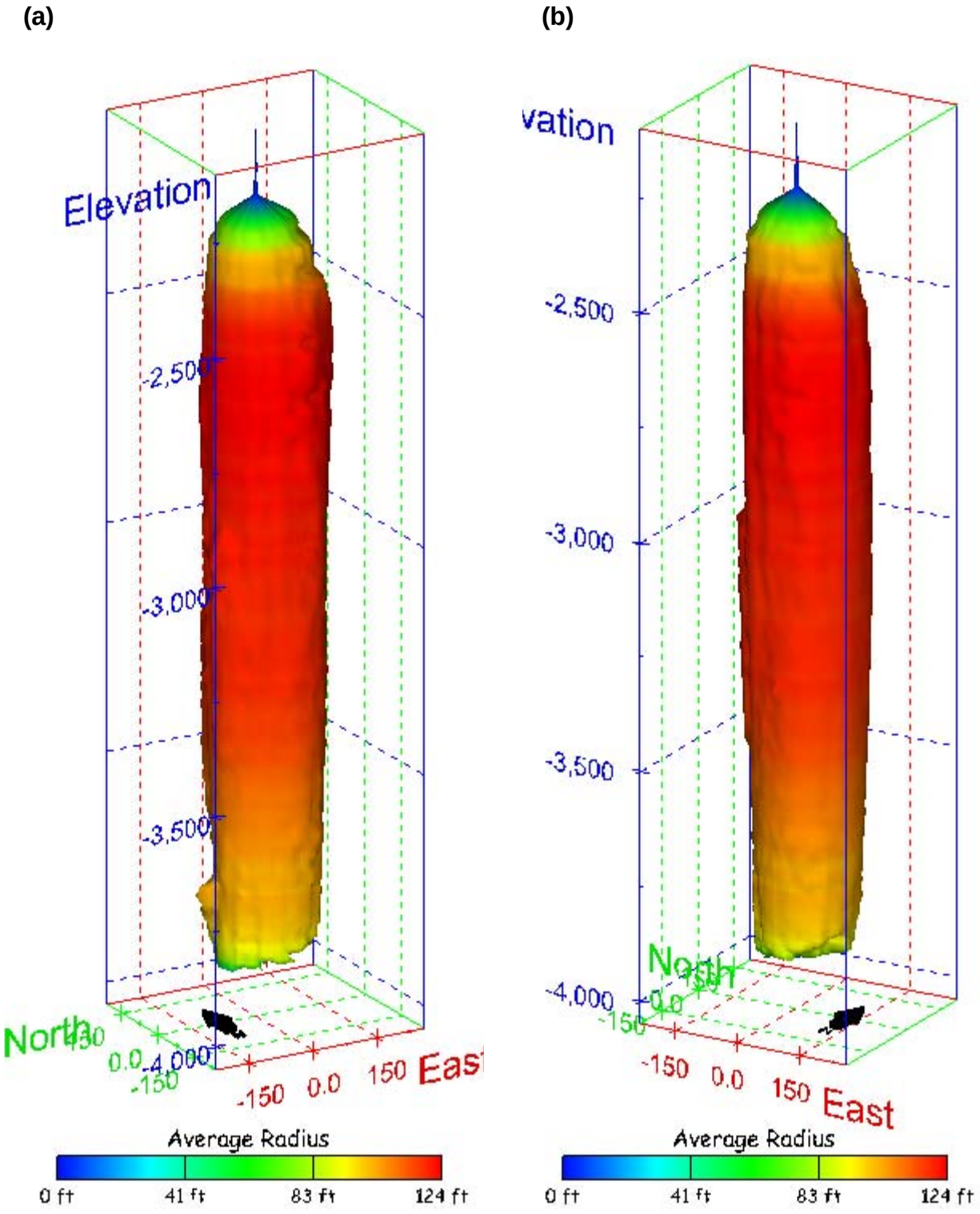

Figure 74. Sonar images of cavern BH-103, showing the geometry of the cavern colored by average radius. View from (a) azimuth 210°, elevation 20°; (b) azimuth 150°, elevation 20°.

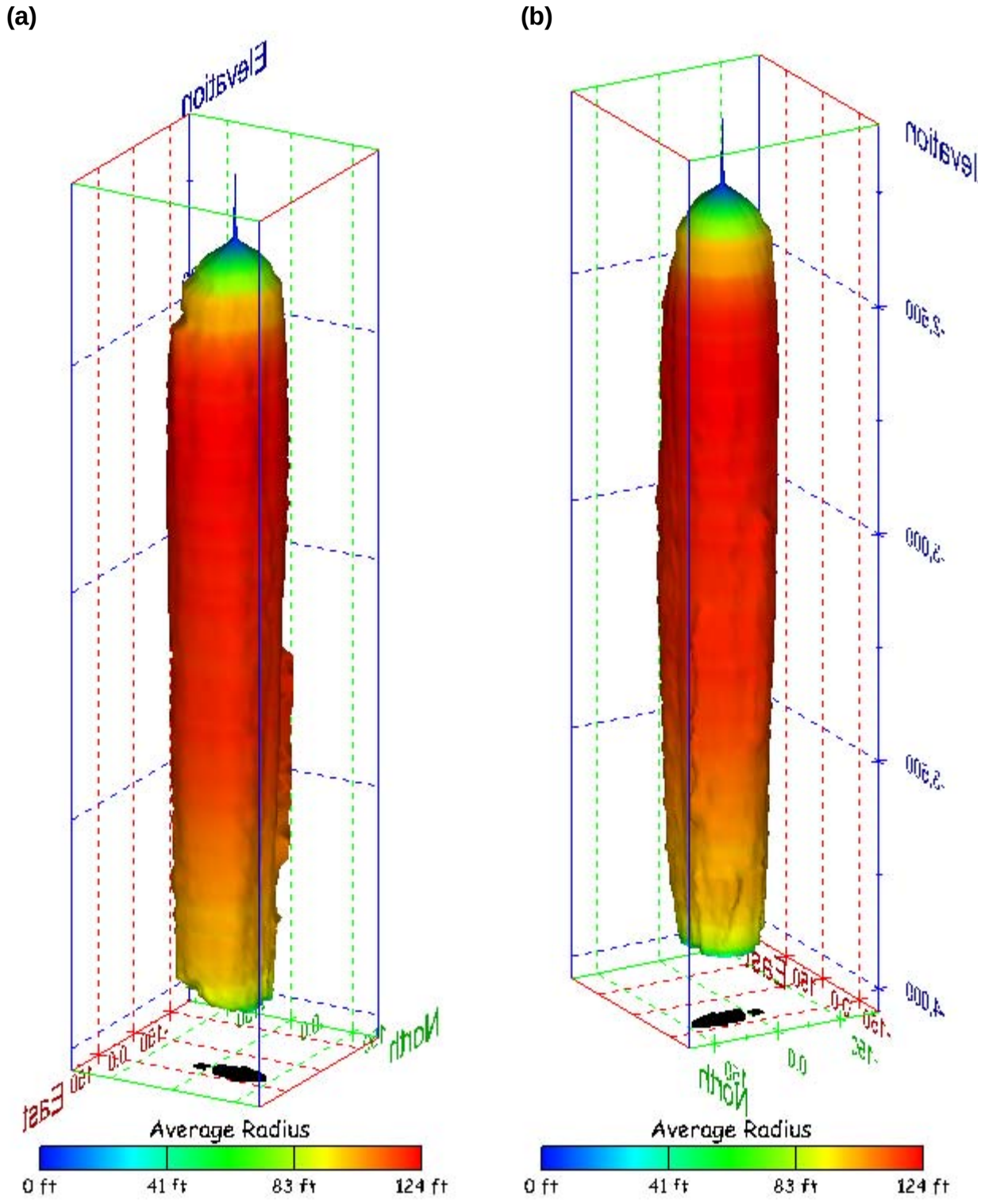

Figure 75. Sonar images of cavern BH-103, showing the geometry of the cavern colored by average radius. View from (a) azimuth 60°, elevation 20°; (b) azimuth 300°, elevation 20°.

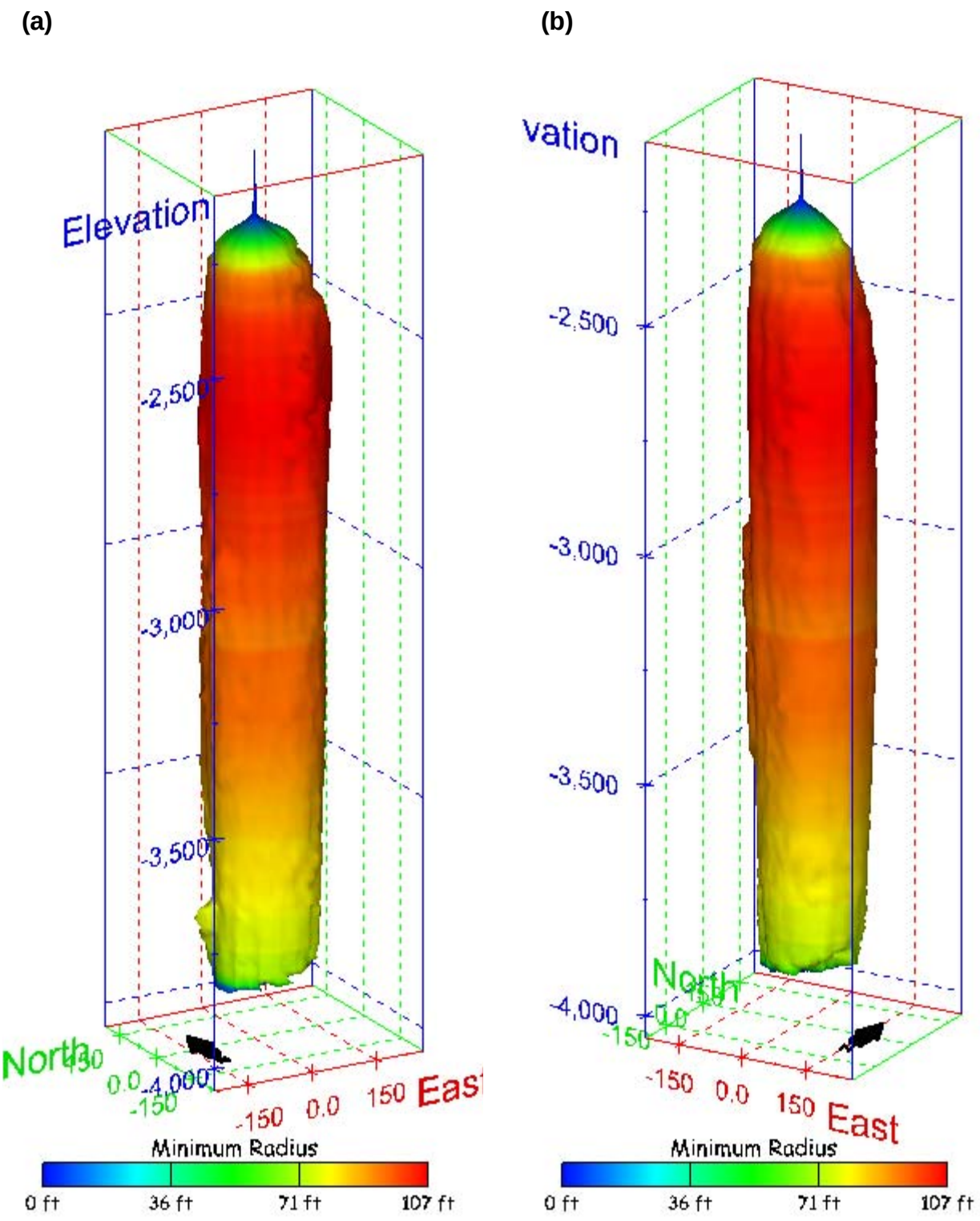

Figure 76. Sonar images of cavern BH-103, showing the geometry of the cavern colored by minimum radius. View from (a) azimuth 210°, elevation 20°; (b) azimuth 150°, elevation 20°.

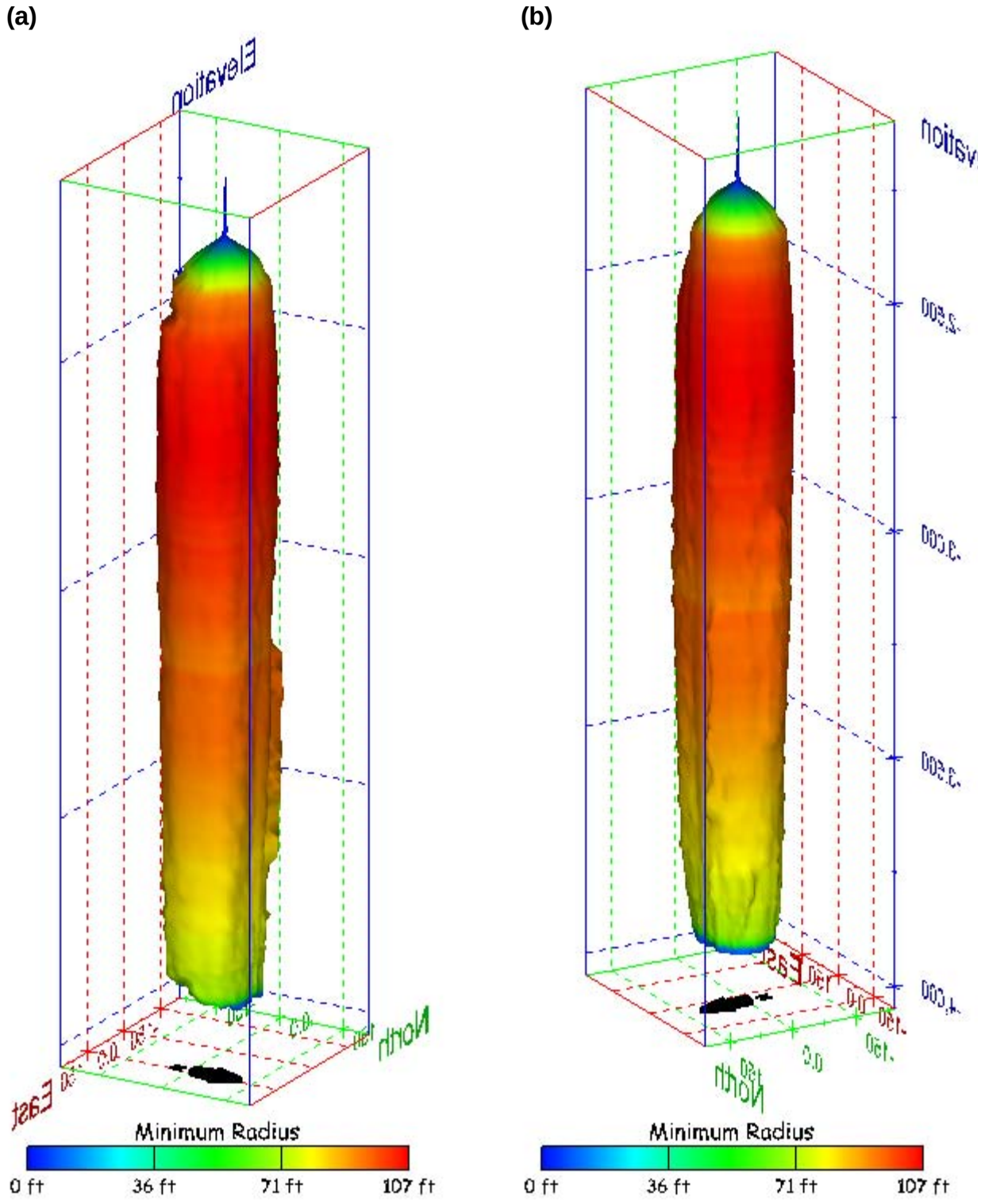

Figure 77. Sonar images of cavern BH-103, showing the geometry of the cavern colored by minimum radius. View from (a) azimuth 60°, elevation 20°; (b) azimuth 300°, elevation 20°.

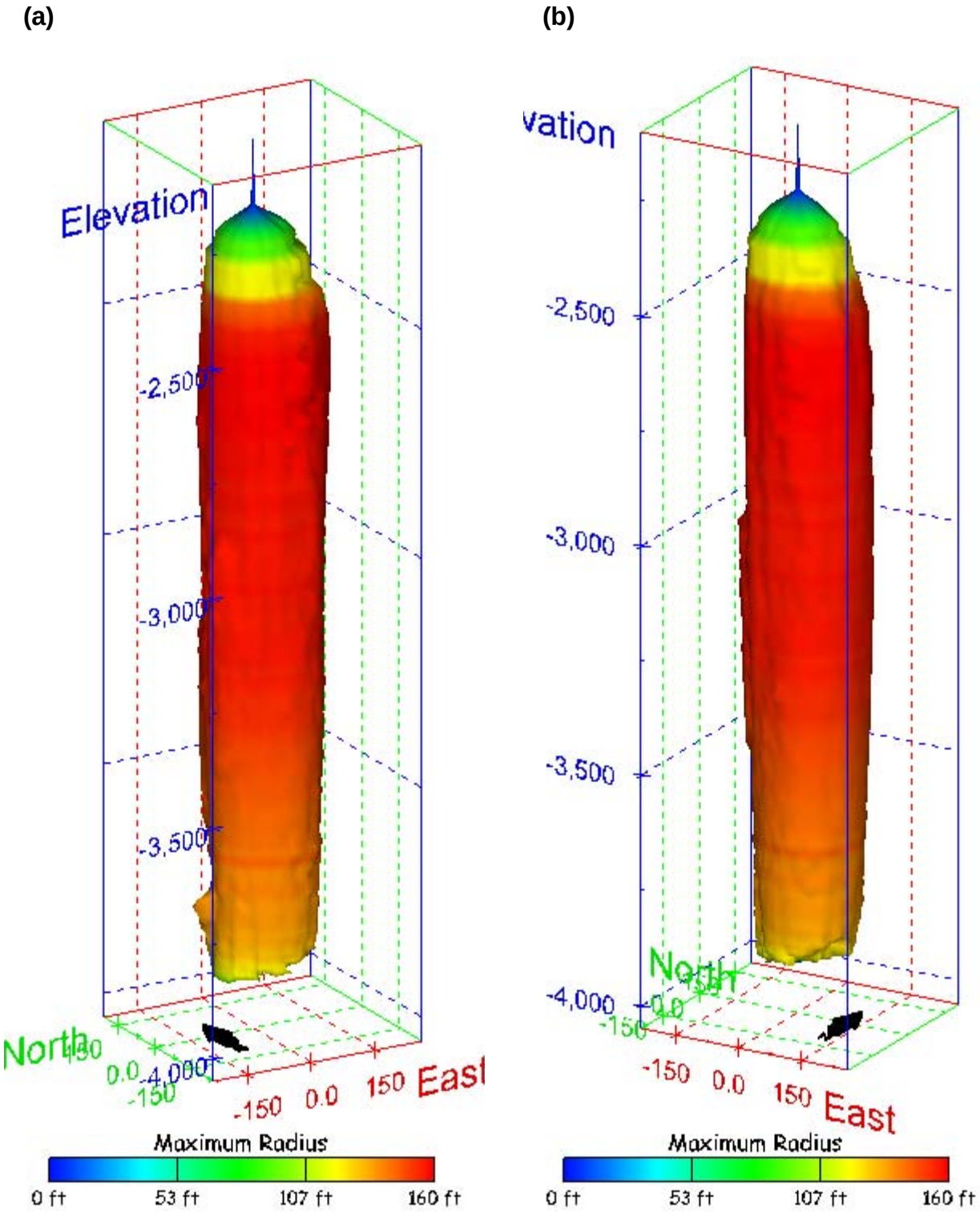

Figure 78. Sonar images of cavern BH-103, showing the geometry of the cavern colored by maximum radius. View from (a) azimuth 210°, elevation 20°; (b) azimuth 150°, elevation 20°.

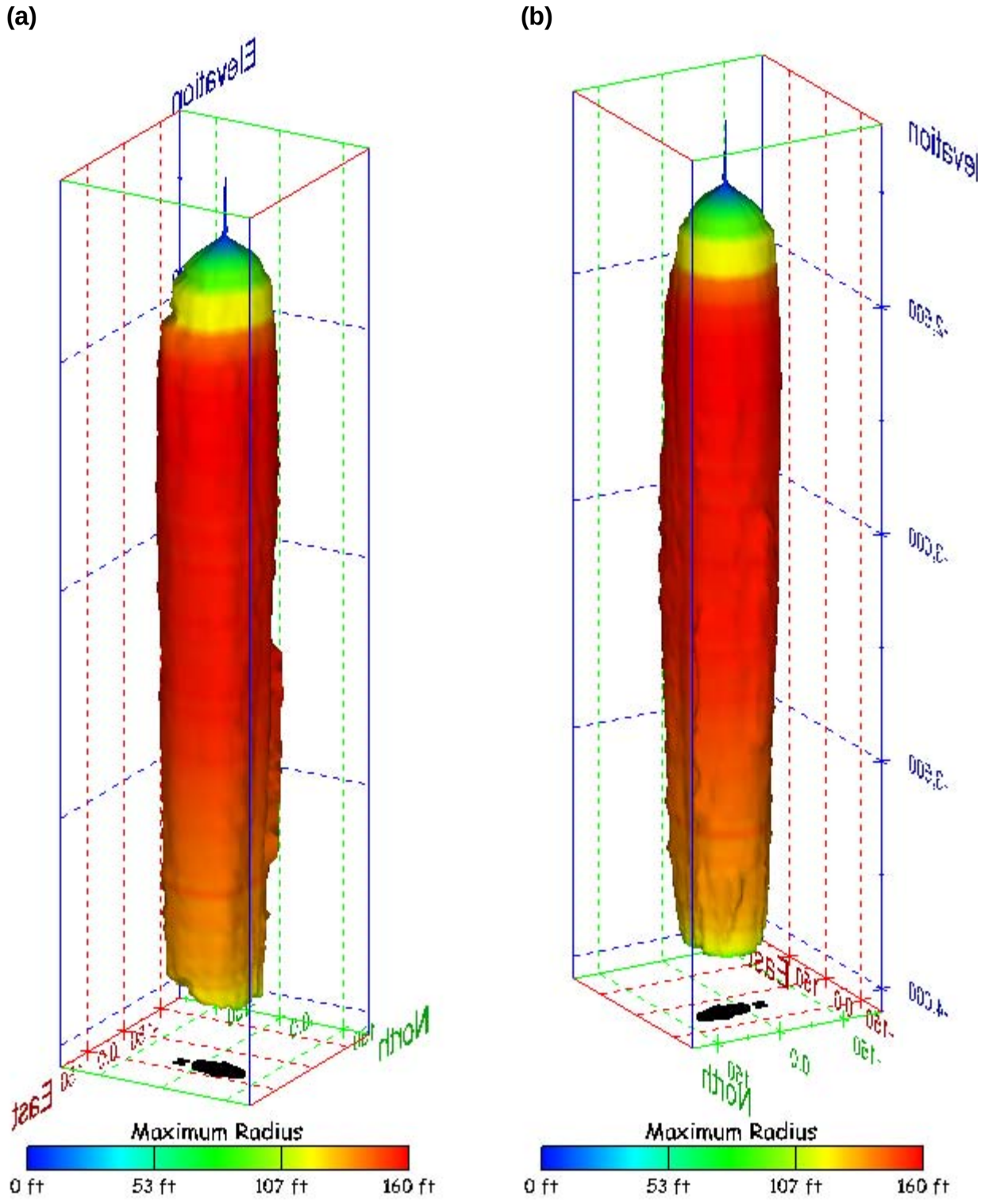

Figure 79. Sonar images of cavern BH-103, showing the geometry of the cavern colored by maximum radius. View from (a) azimuth 60°, elevation 20°; (b) azimuth 300°, elevation 20°.

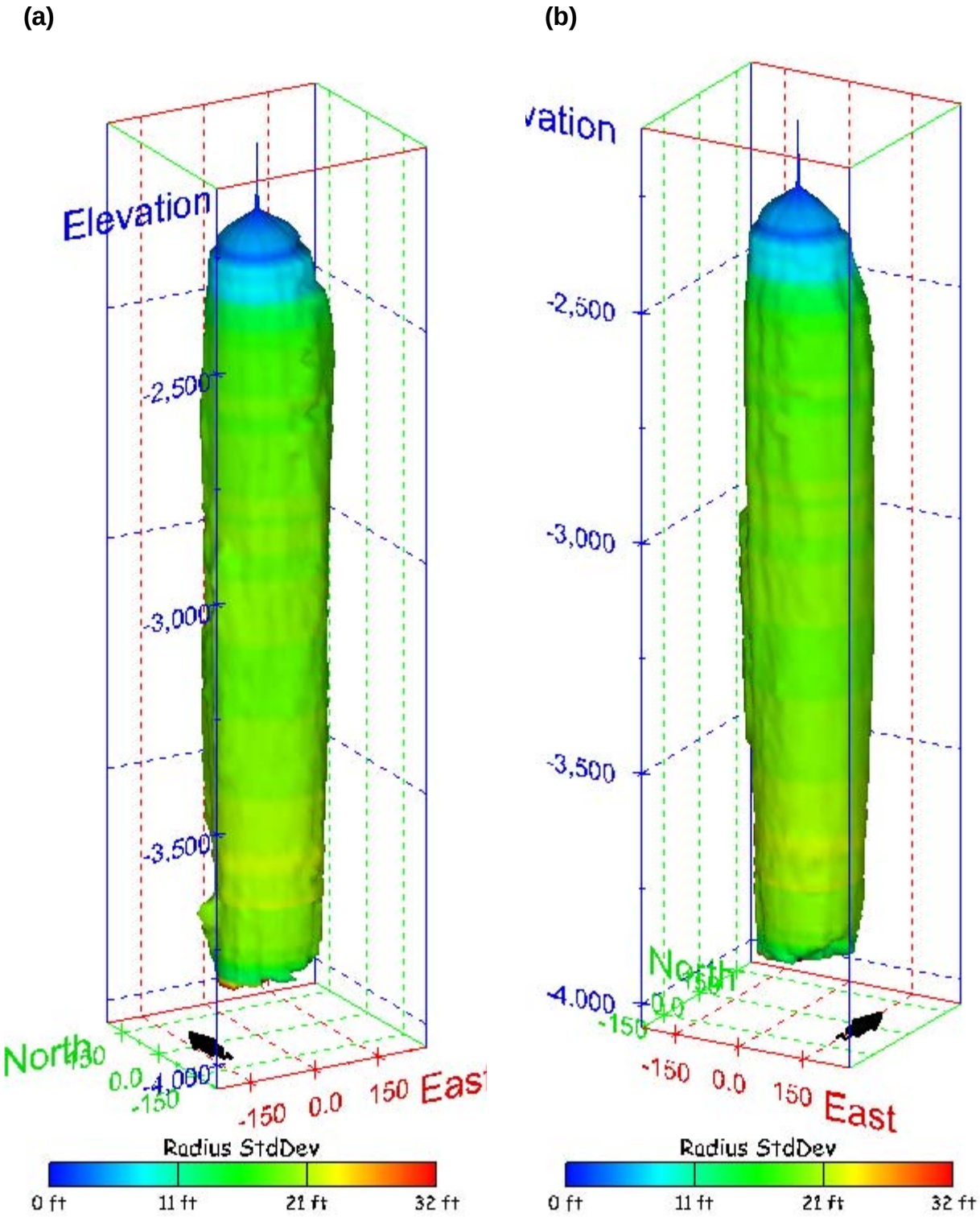

Figure 80. Sonar images of cavern BH-103, showing the geometry of the cavern colored by radius standard deviation. View from (a) azimuth 210°, elevation 20°; (b) azimuth 150°, elevation 20°.

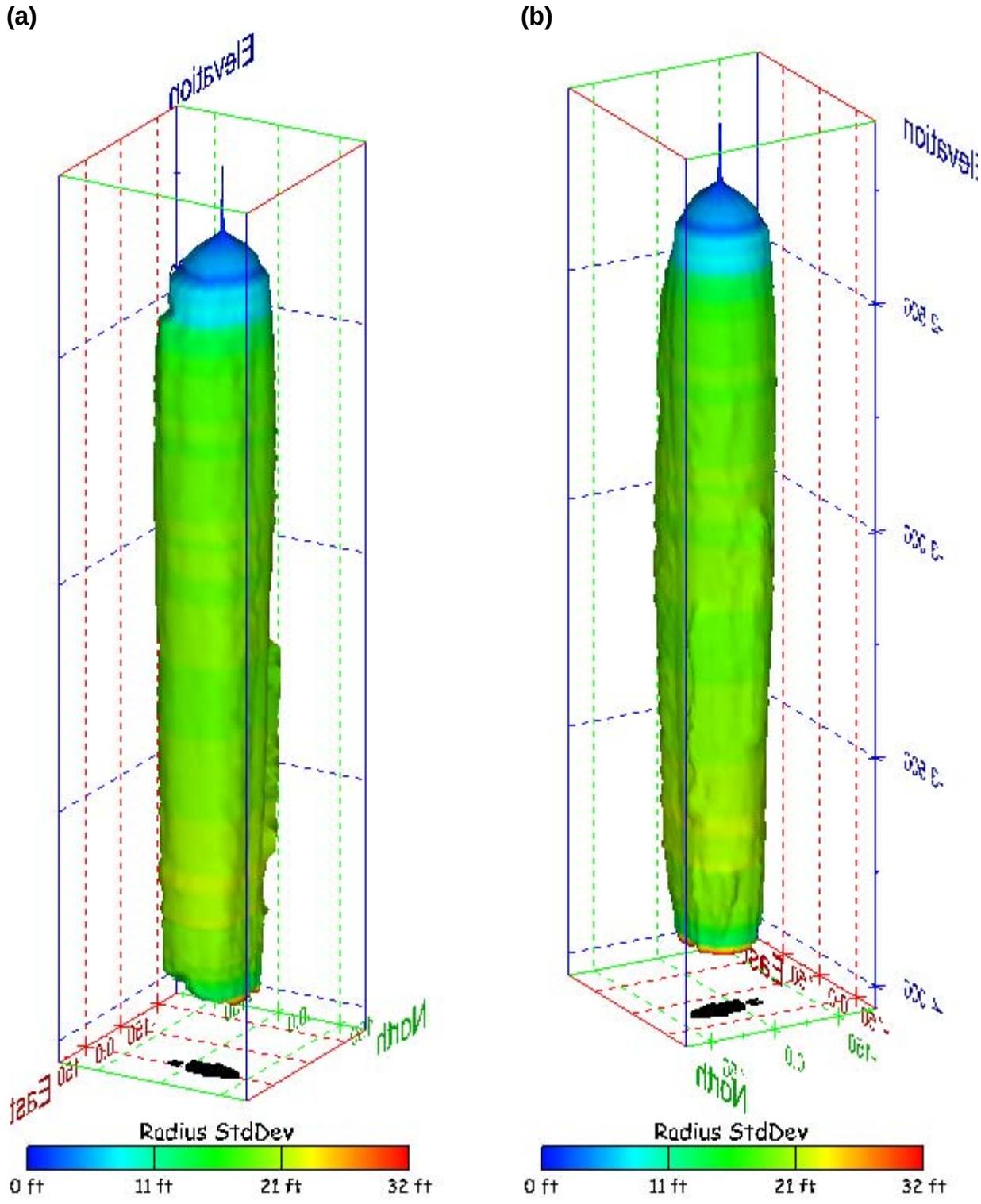

Figure 81. Sonar images of cavern BH-103, showing the geometry of the cavern colored by radius standard deviation. View from (a) azimuth 60°, elevation 20°; (b) azimuth 300°, elevation 20°.

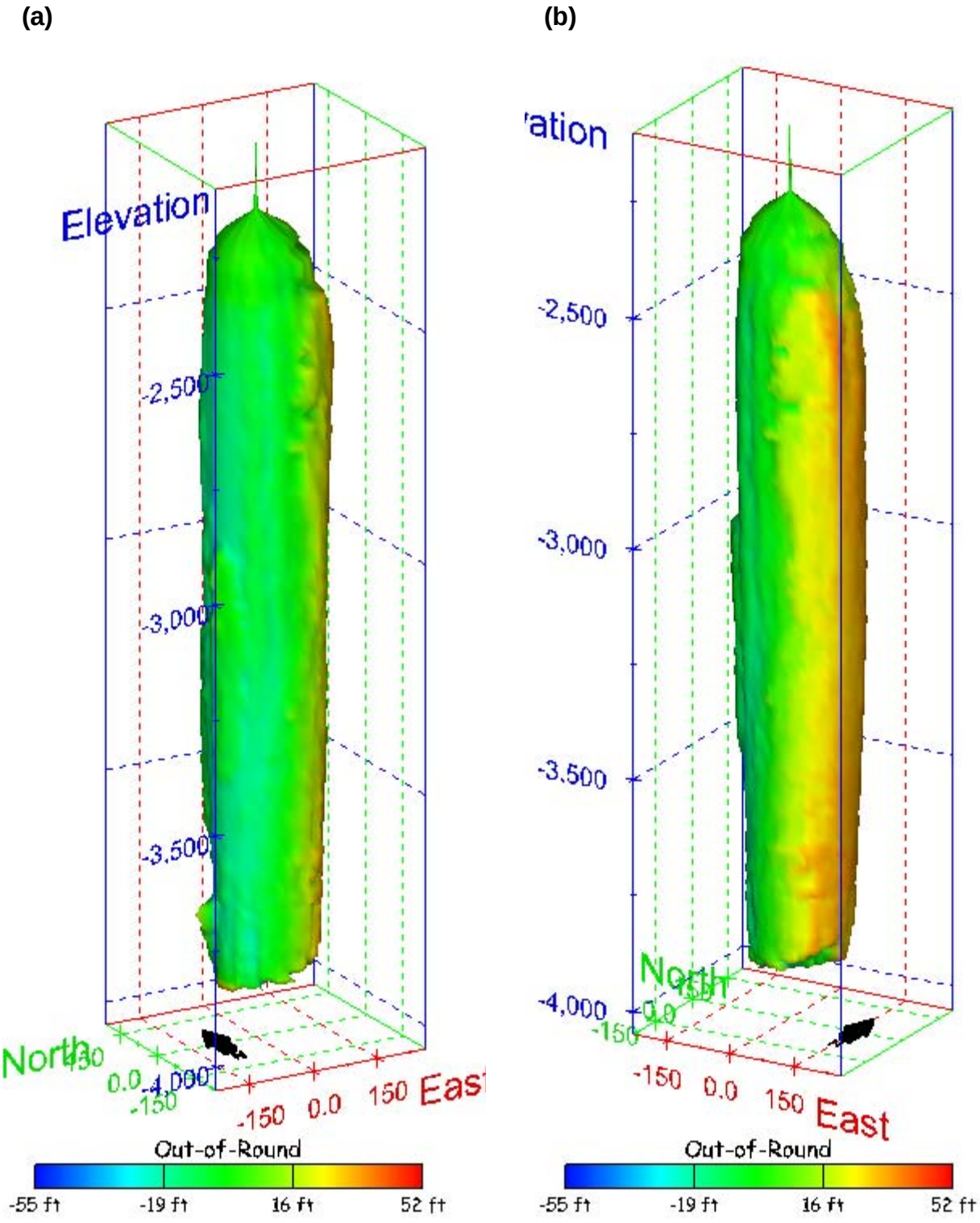

Figure 82. Sonar images of cavern BH-103, showing the geometry of the cavern colored by out-of-round distance. View from (a) azimuth 210°, elevation 20°; (b) azimuth 150°, elevation 20°.

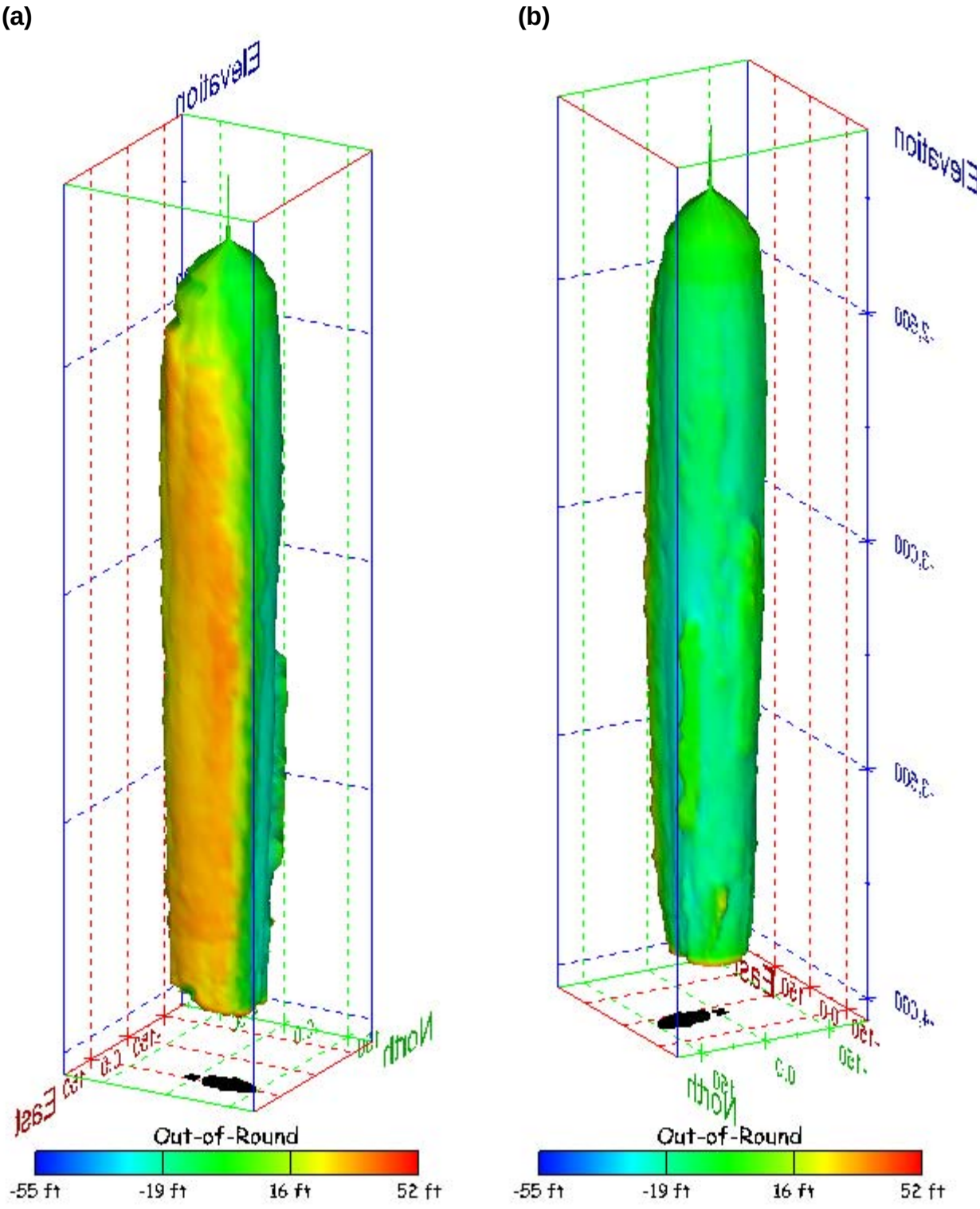

Figure 83. Sonar images of cavern BH-103, showing the geometry of the cavern colored by out-of-round distance. View from (a) azimuth 60°, elevation 20°; (b) azimuth 300°, elevation 20°.

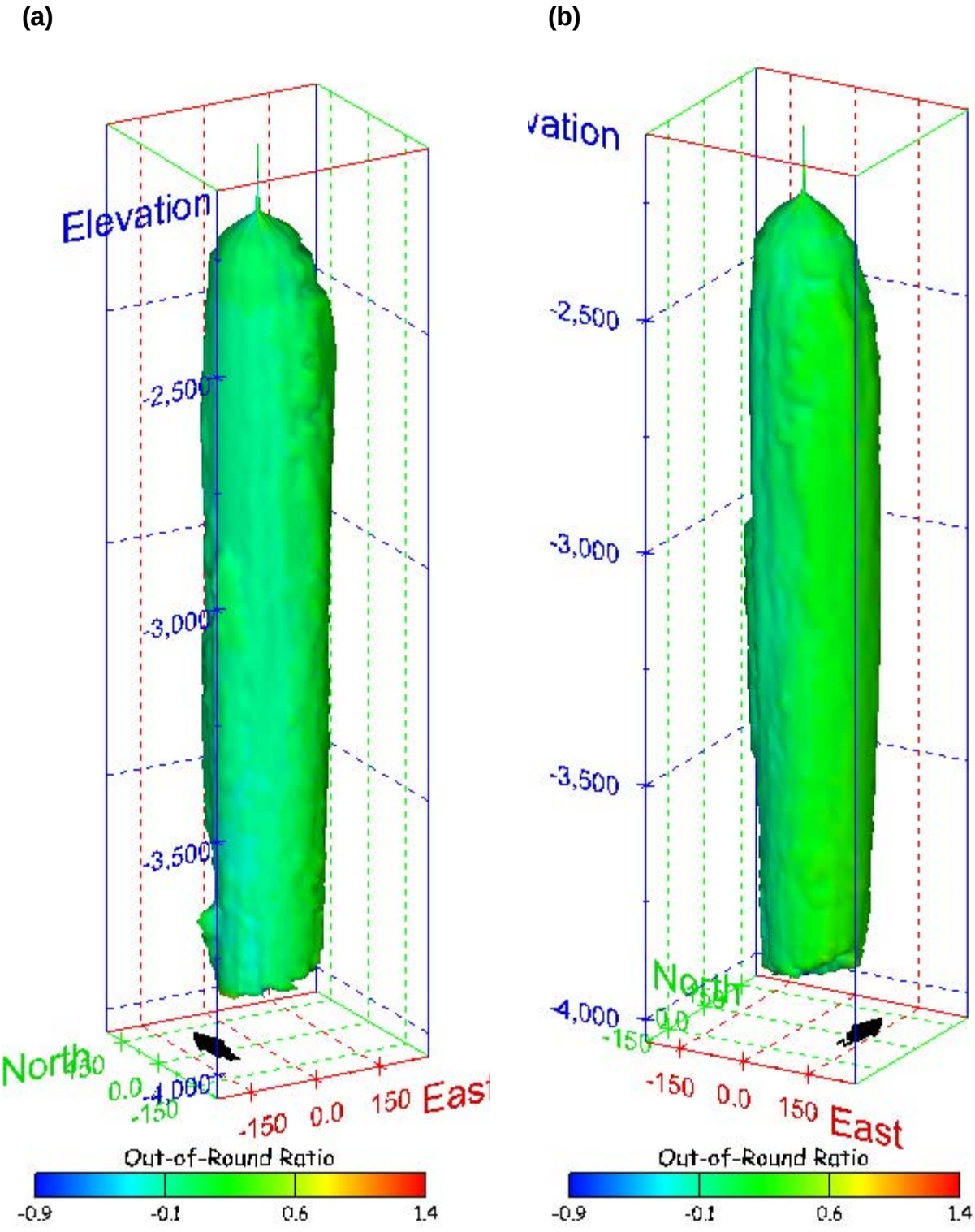

Figure 84. Sonar images of cavern BH-103, showing the geometry of the cavern colored by out-of-round ratio. View from (a) azimuth 210°, elevation 20°; (b) azimuth 150°, elevation 20°.

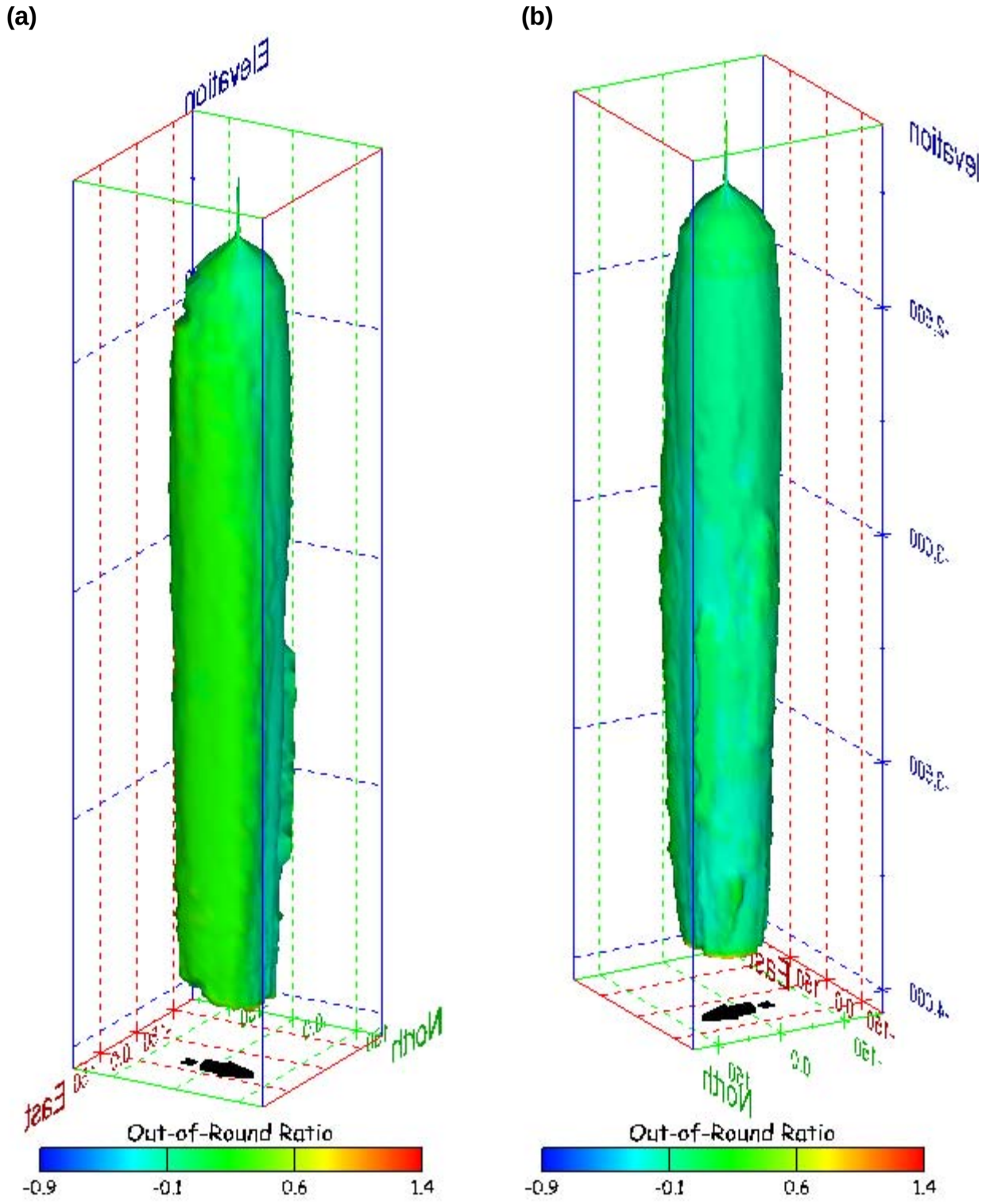

Figure 85. Sonar images of cavern BH-103, showing the geometry of the cavern colored by out-of-round ratio. View from (a) azimuth 60°, elevation 20°; (b) azimuth 300°, elevation 20°.

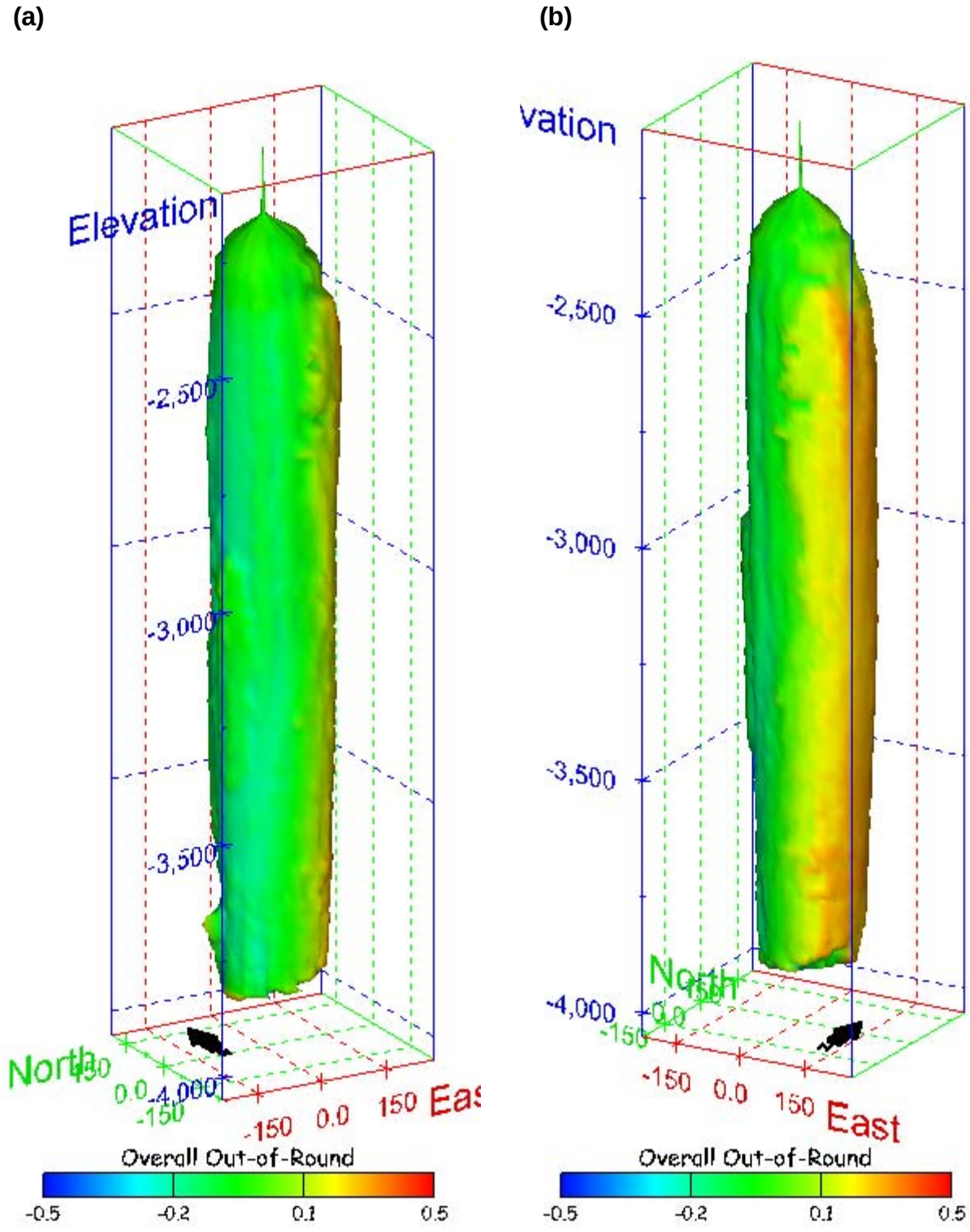

Figure 86. Sonar images of cavern BH-103, showing the geometry of the cavern colored by overall out-of-round ratio. View from (a) azimuth 210°, elevation 20°; (b) azimuth 150°, elevation 20°.

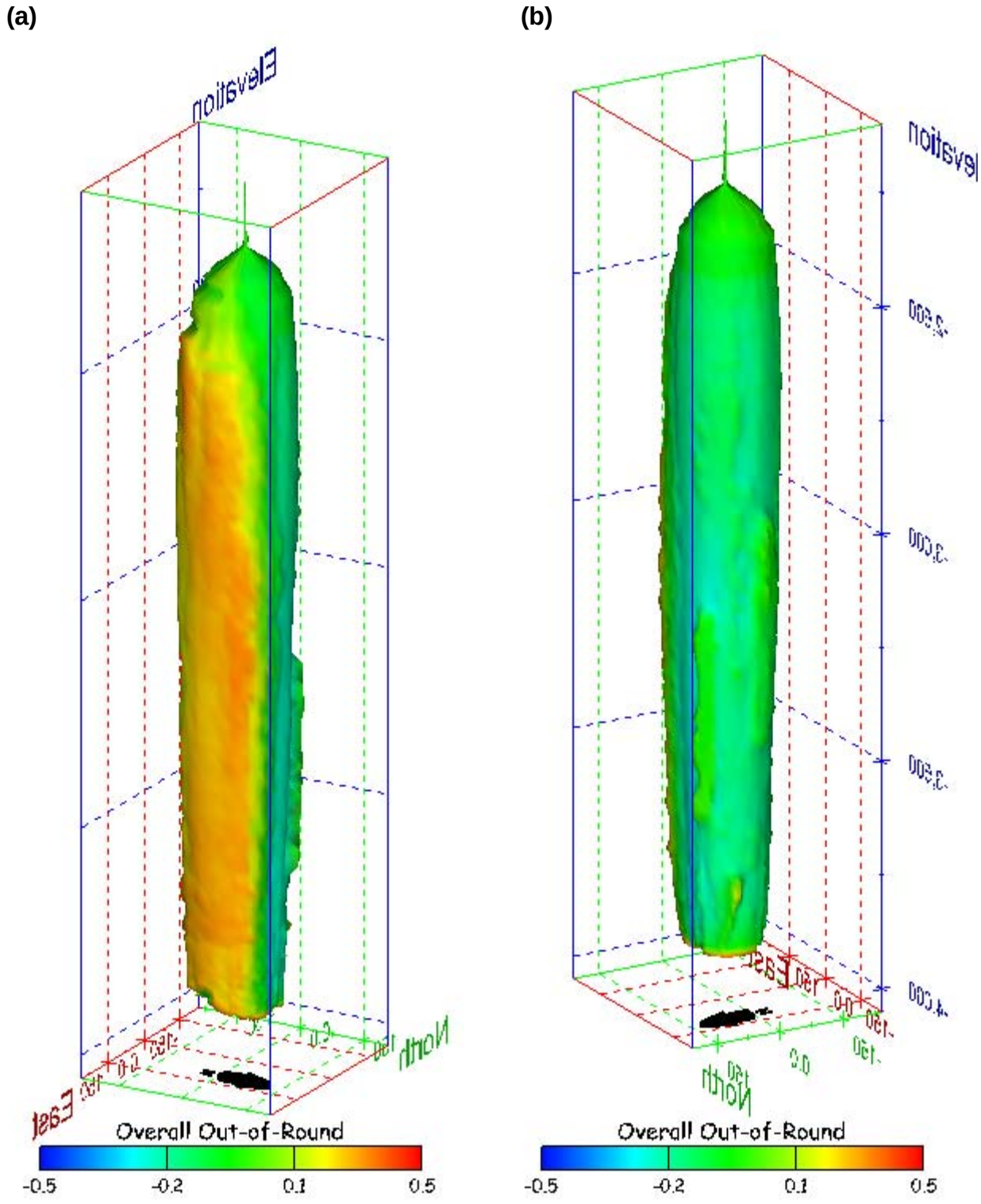

Figure 87. Sonar images of cavern BH-103, showing the geometry of the cavern colored by overall out-of-round ratio. View from (a) azimuth 60°, elevation 20°; (b) azimuth 300°, elevation 20°.

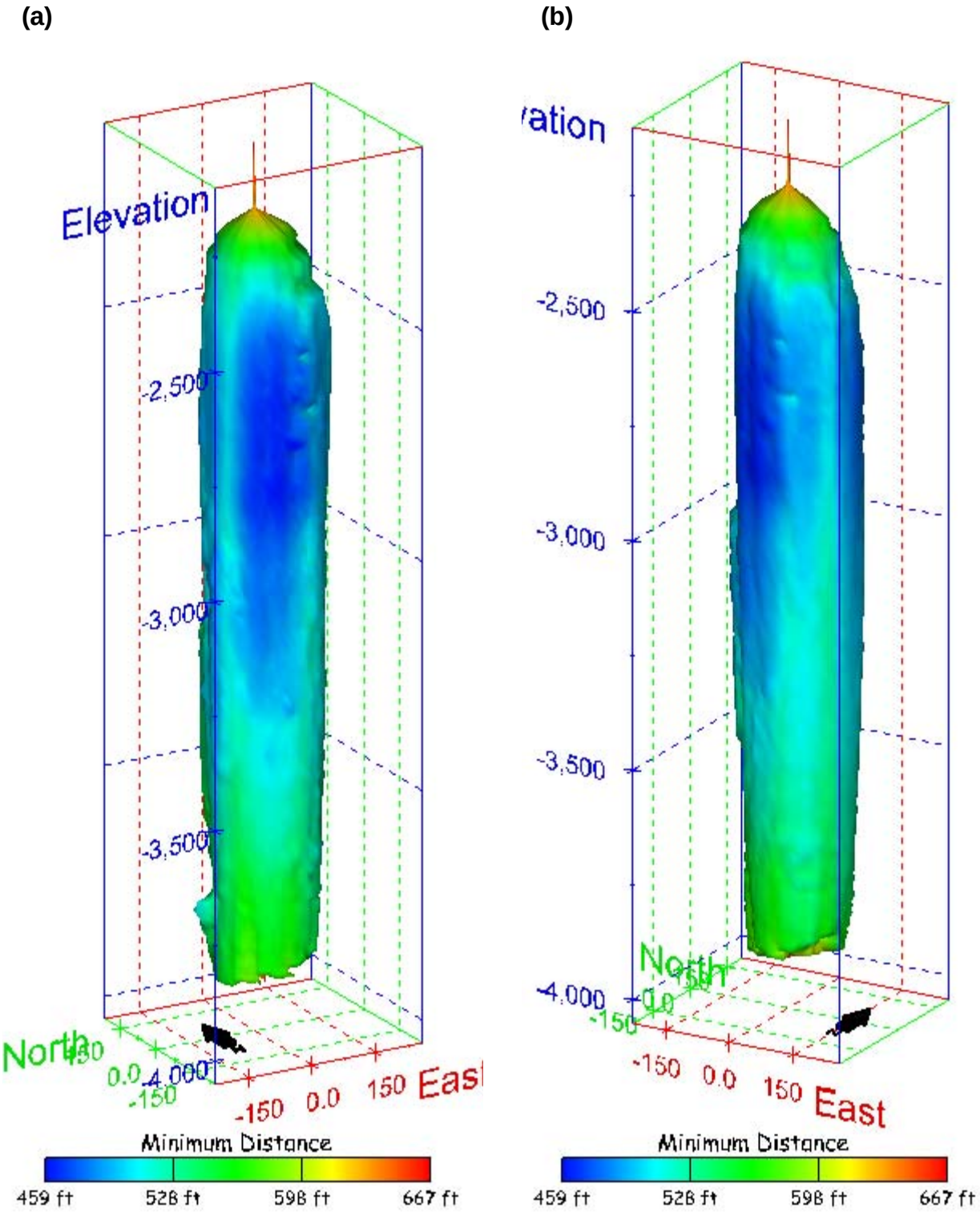

Figure 88. Sonar images of cavern BH-103, showing the geometry of the cavern colored by the minimum distance to the nearest neighboring cavern. View from (a) azimuth 210°, elevation 20°; (b) azimuth 150°, elevation 20°.

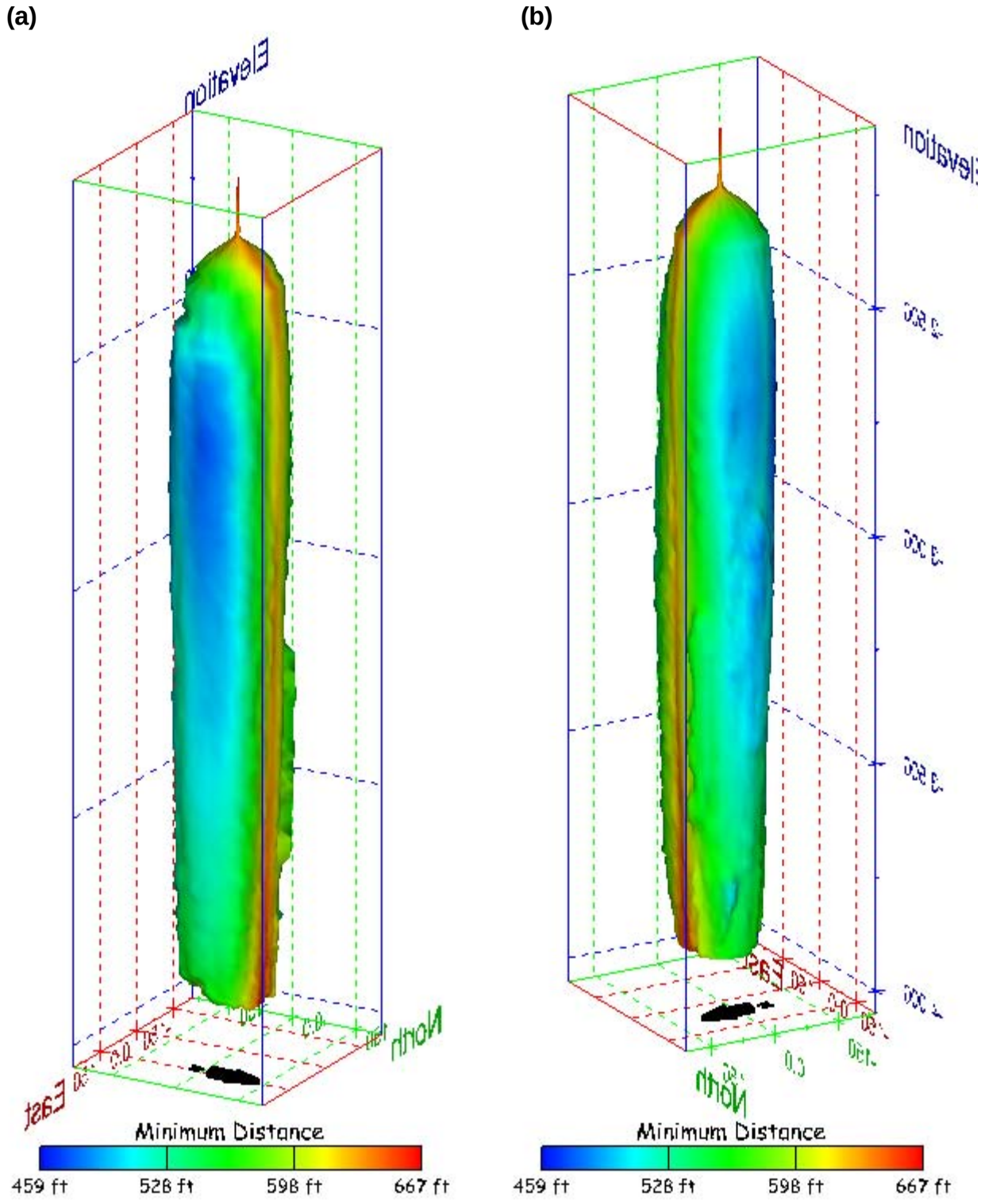

Figure 89. Sonar images of cavern BH-103, showing the geometry of the cavern colored by minimum distance to the nearest neighboring cavern. View from (a) azimuth 60°, elevation 20°; (b) azimuth 300°, elevation 20°.

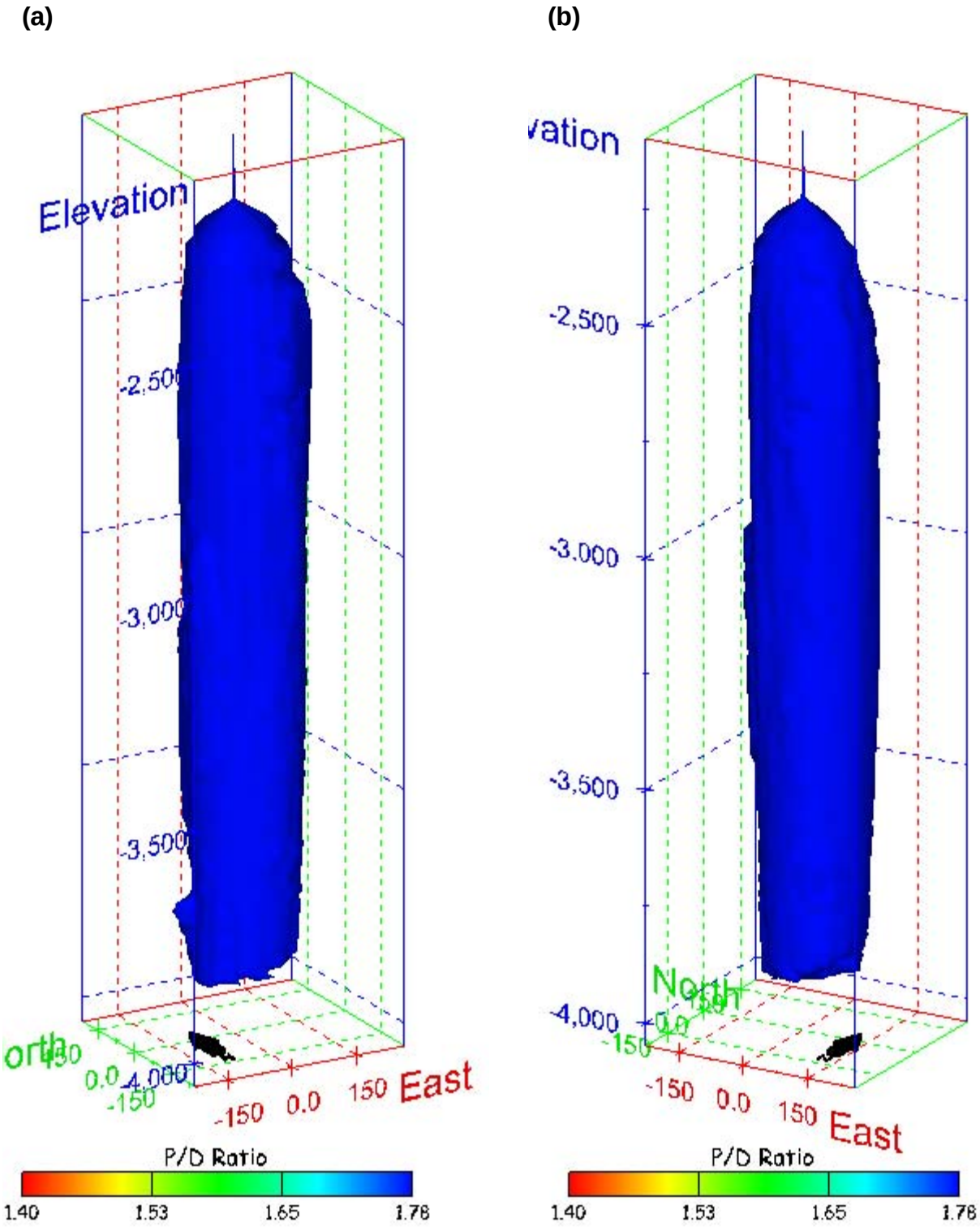

Figure 90. Sonar images of cavern BH-103, showing the geometry of the cavern colored by three-dimensional pillar-to-diameter ratio. View from (a) azimuth 210°, elevation 20°; (b) azimuth 150°, elevation 20°.

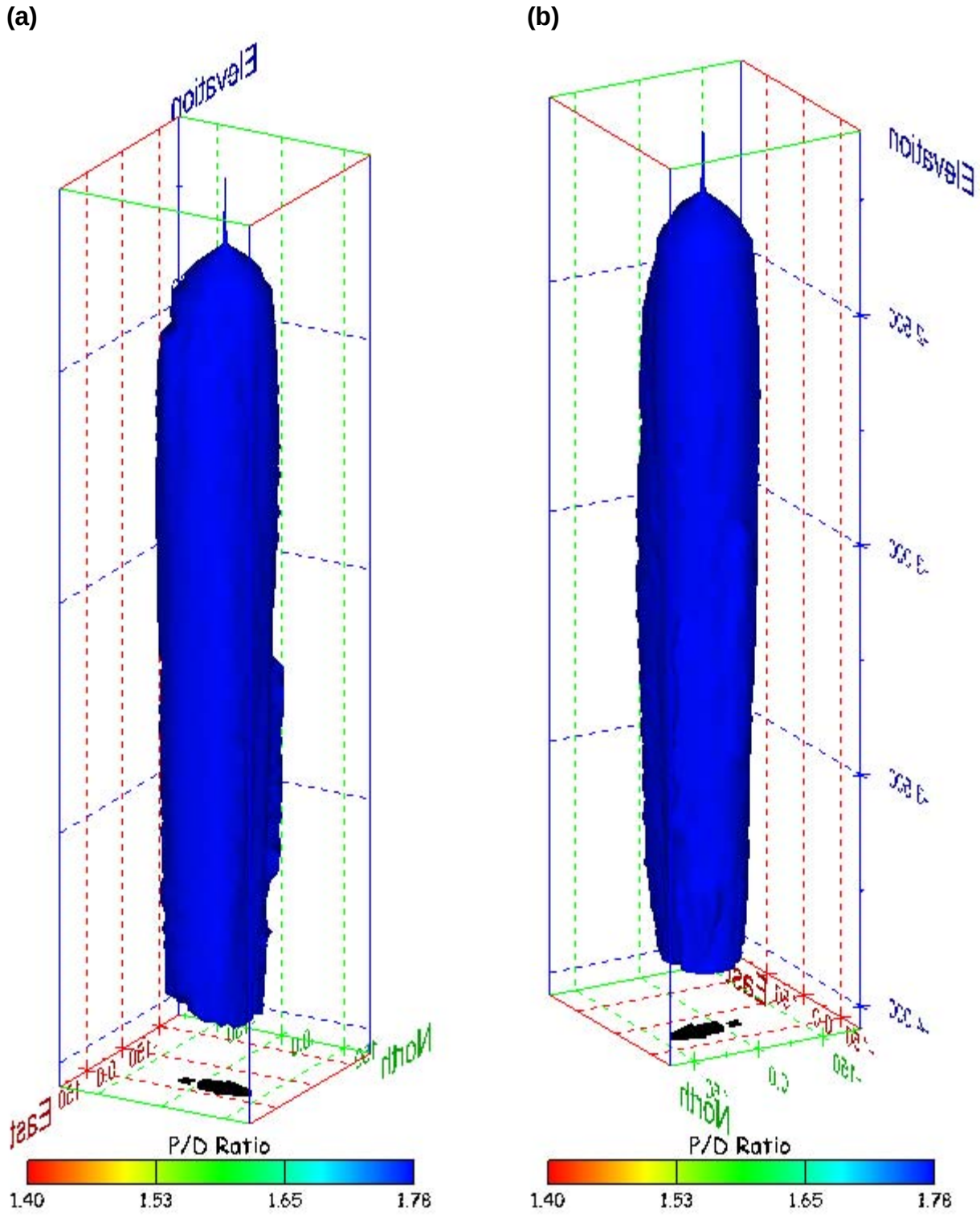

Figure 91. Sonar images of cavern BH-103, showing the geometry of the cavern colored by three-dimensional pillar-to-diameter ratio. View from (a) azimuth 60°, elevation 20°; (b) azimuth 300°, elevation 20°.

No Sonic Velocity Data Available for Socon Surveys

Figure 92. Sonar image of cavern BH-103, showing the geometry of the cavern colored by the reported velocity of sound on the survey date of September 2004. View from due south, elevation zero.

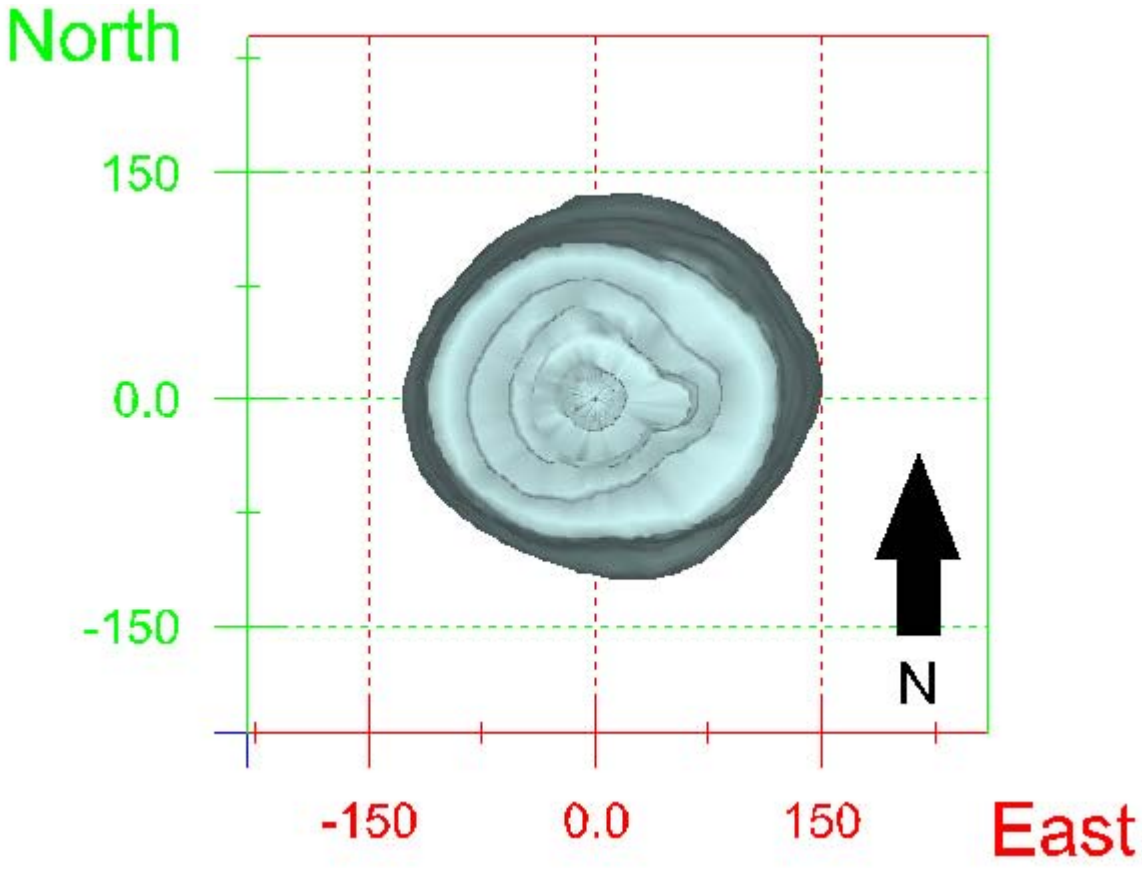

Figure 93. Map view sonar image of cavern BH-104, showing the basic geometry of the cavern. Grid squares represent 150 ft.

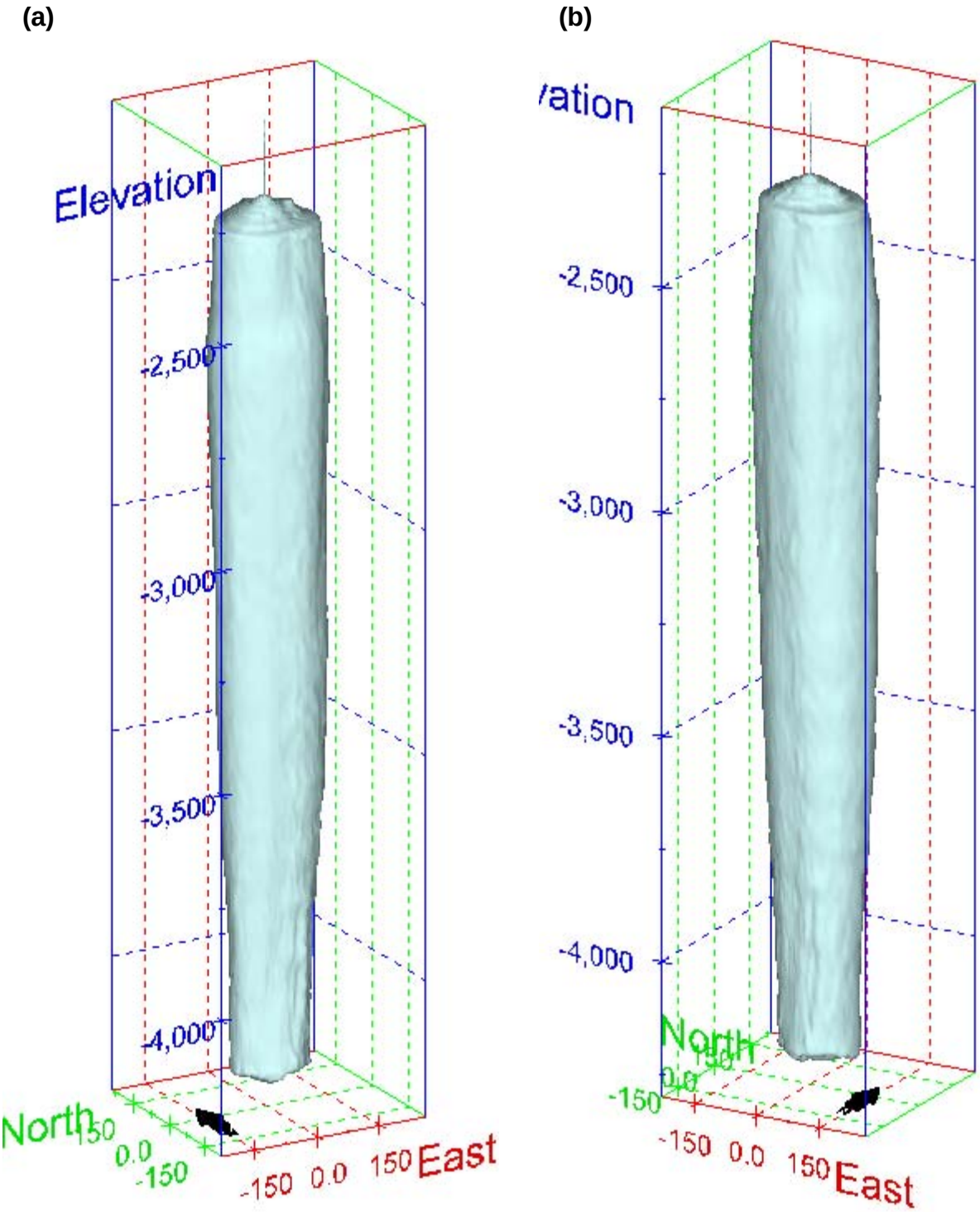

Figure 94. Sonar images of cavern BH-104, showing the basic geometric shape of the cavern. View from (a) azimuth 210°, elevation 20°; (b) azimuth 150°, elevation 20°.

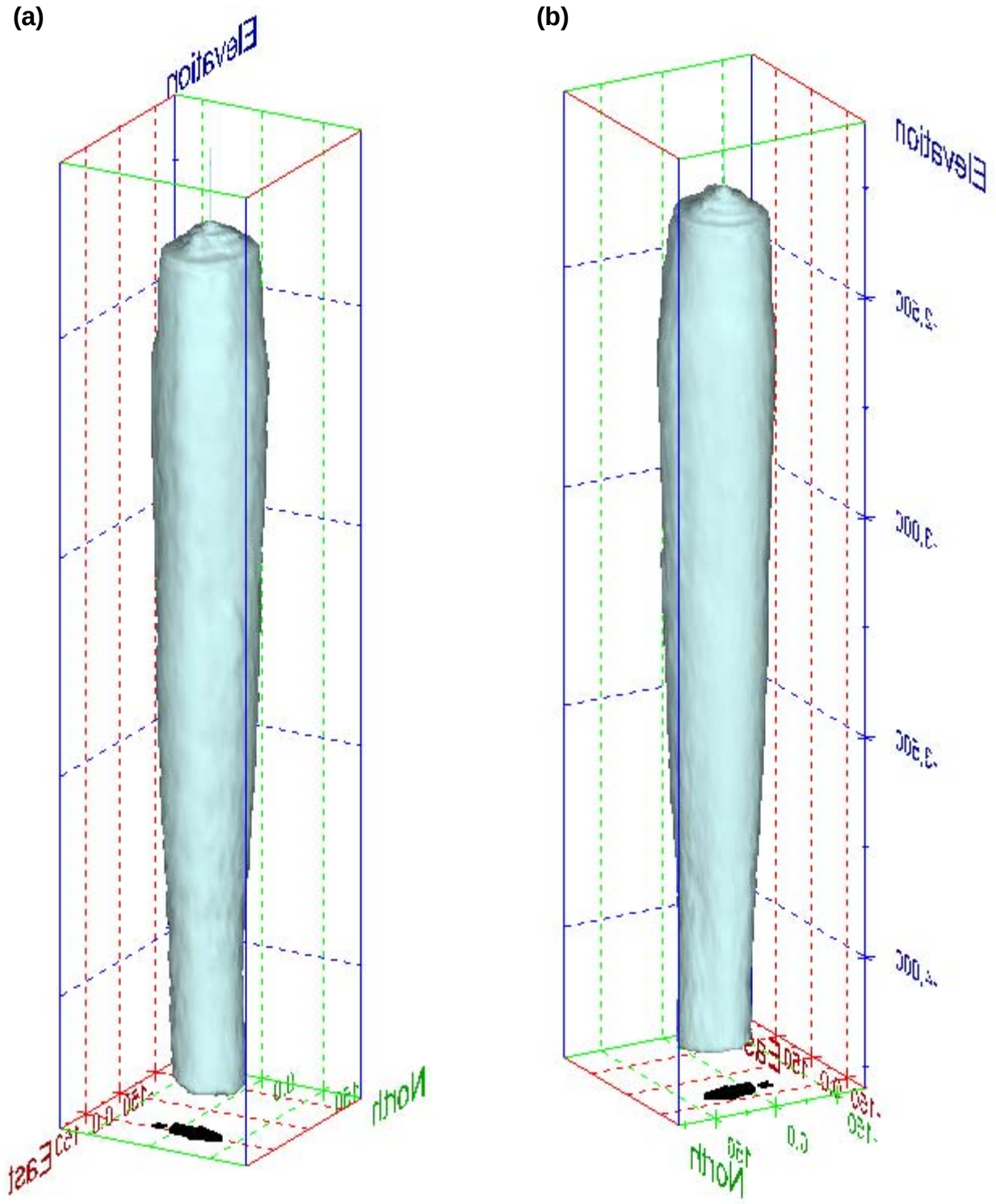

Figure 95. Sonar images of cavern BH-104, showing the basic geometric shape of the cavern. View from (a) azimuth 60°, elevation 20°; (b) azimuth 300°, elevation 20°.

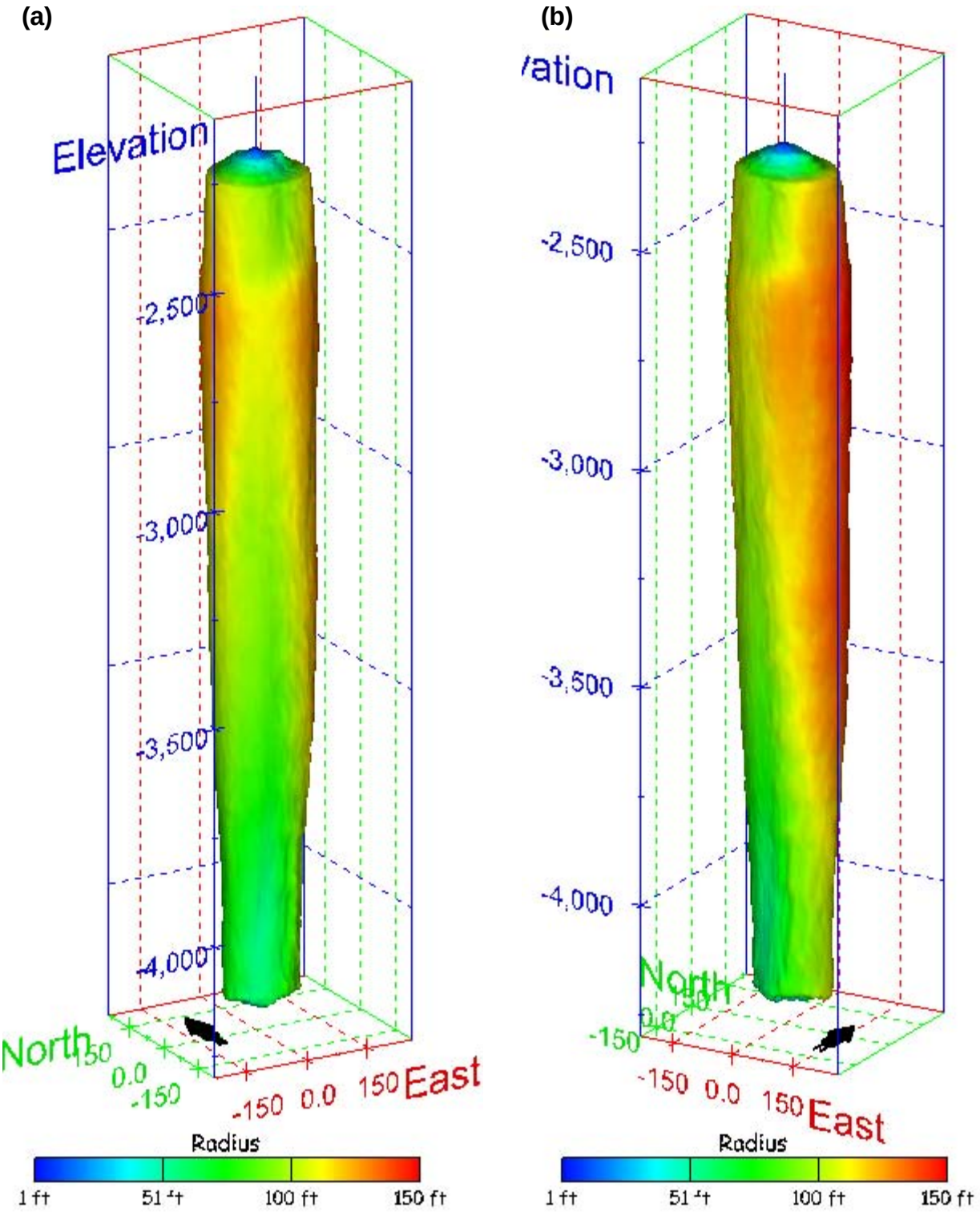

Figure 96. Sonar images of cavern BH-104, showing the geometry of the cavern colored by measured radius. View from (a) azimuth 210°, elevation 20°; (b) azimuth 150°, elevation 20°.

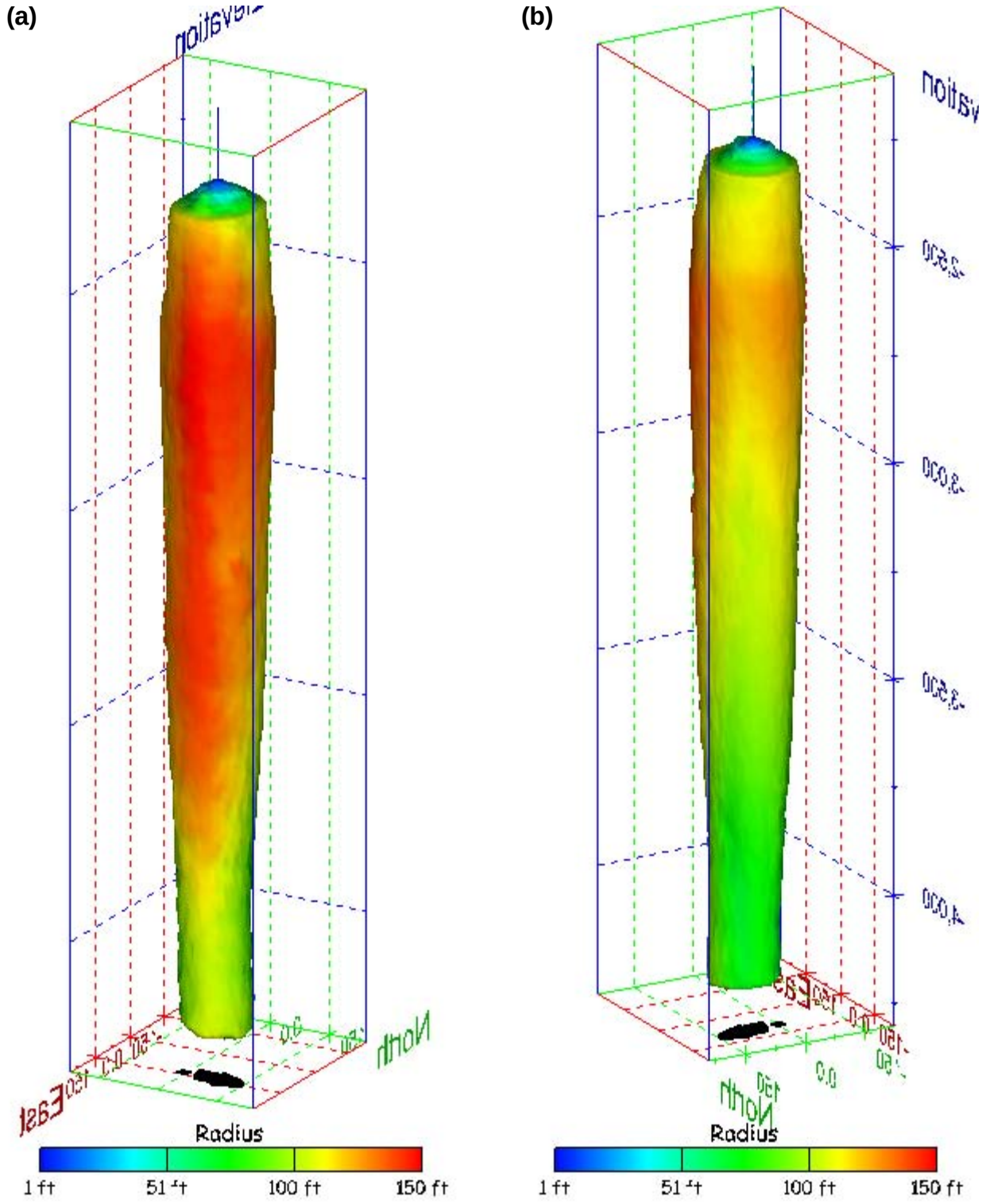

Figure 97. Sonar images of cavern BH-104, showing the geometry of the cavern colored by measured radius. View from (a) azimuth 60°, elevation 20°; (b) azimuth 300°, elevation 20°.

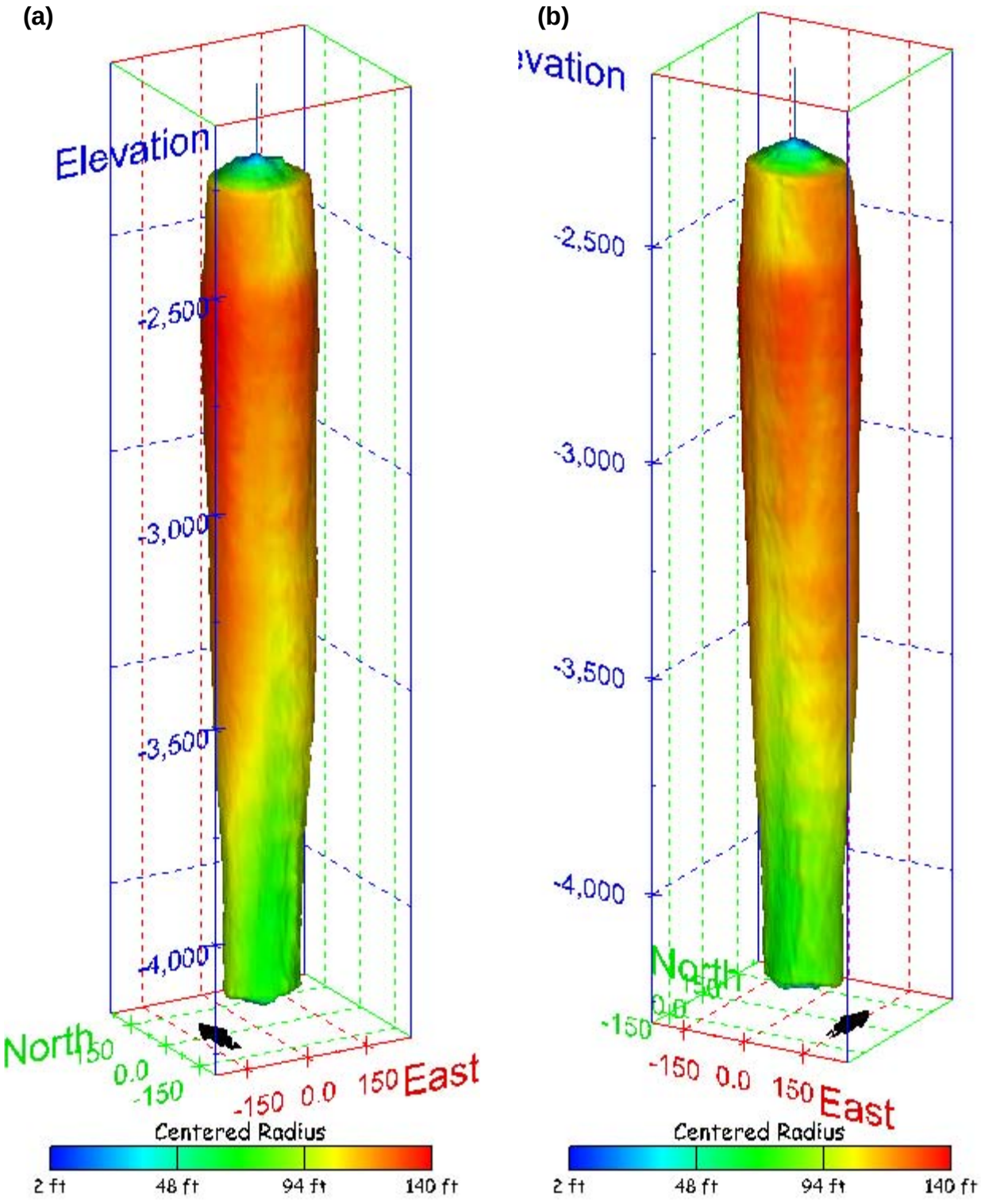

Figure 98. Sonar images of cavern BH-104, showing the geometry of the cavern colored by centered radius. View from (a) azimuth °, elevation 20°; (b) azimuth 150°, elevation 20°.

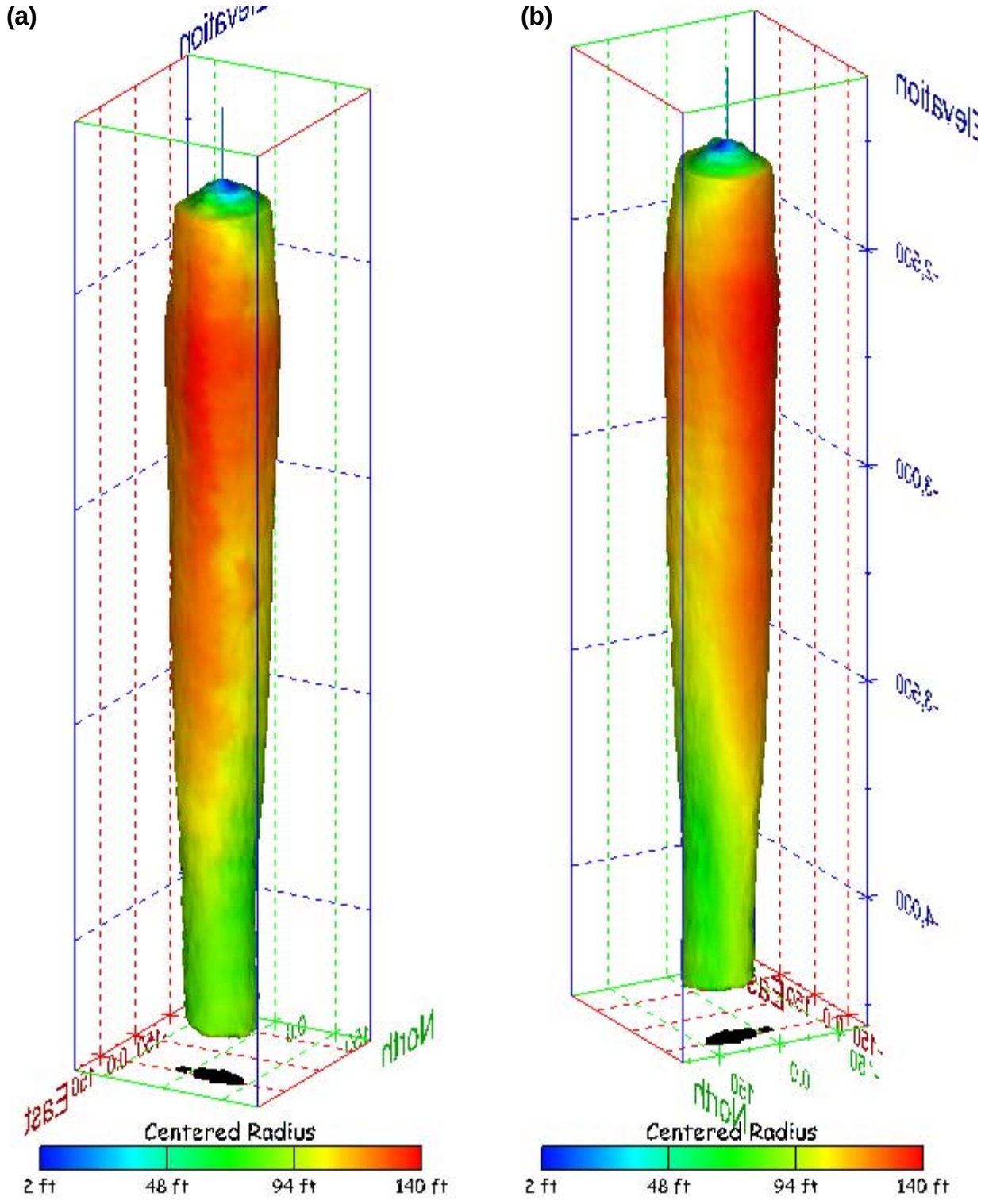

Figure 99. Sonar images of cavern BH-104, showing the geometry of the cavern colored by centered radius. View from (a) azimuth 60°, elevation 20°; (b) azimuth 300°, elevation 20°.

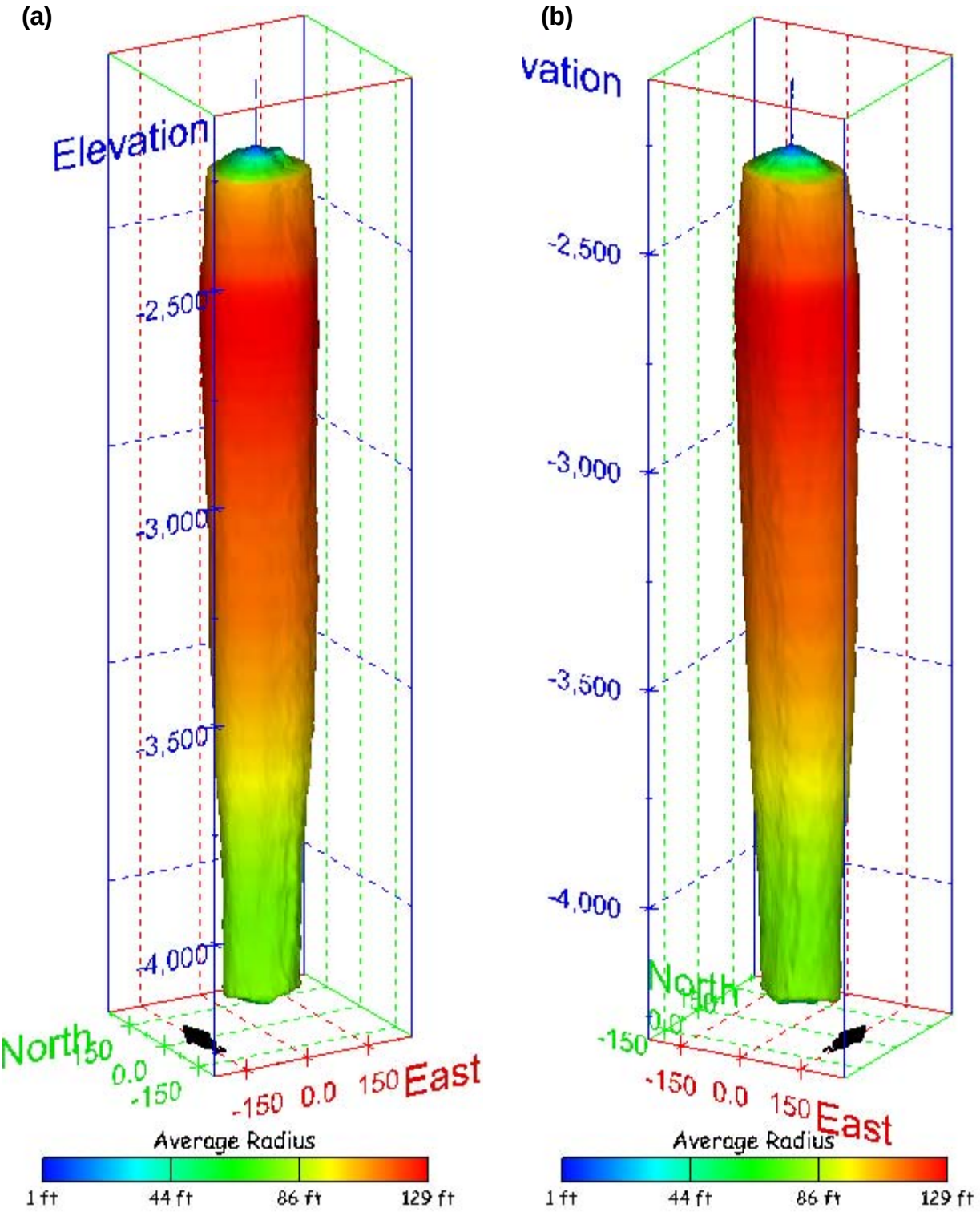

Figure 100. Sonar images of cavern BH-104, showing the geometry of the cavern colored by average radius. View from (a) azimuth 210°, elevation 20°; (b) azimuth 150°, elevation 20°.

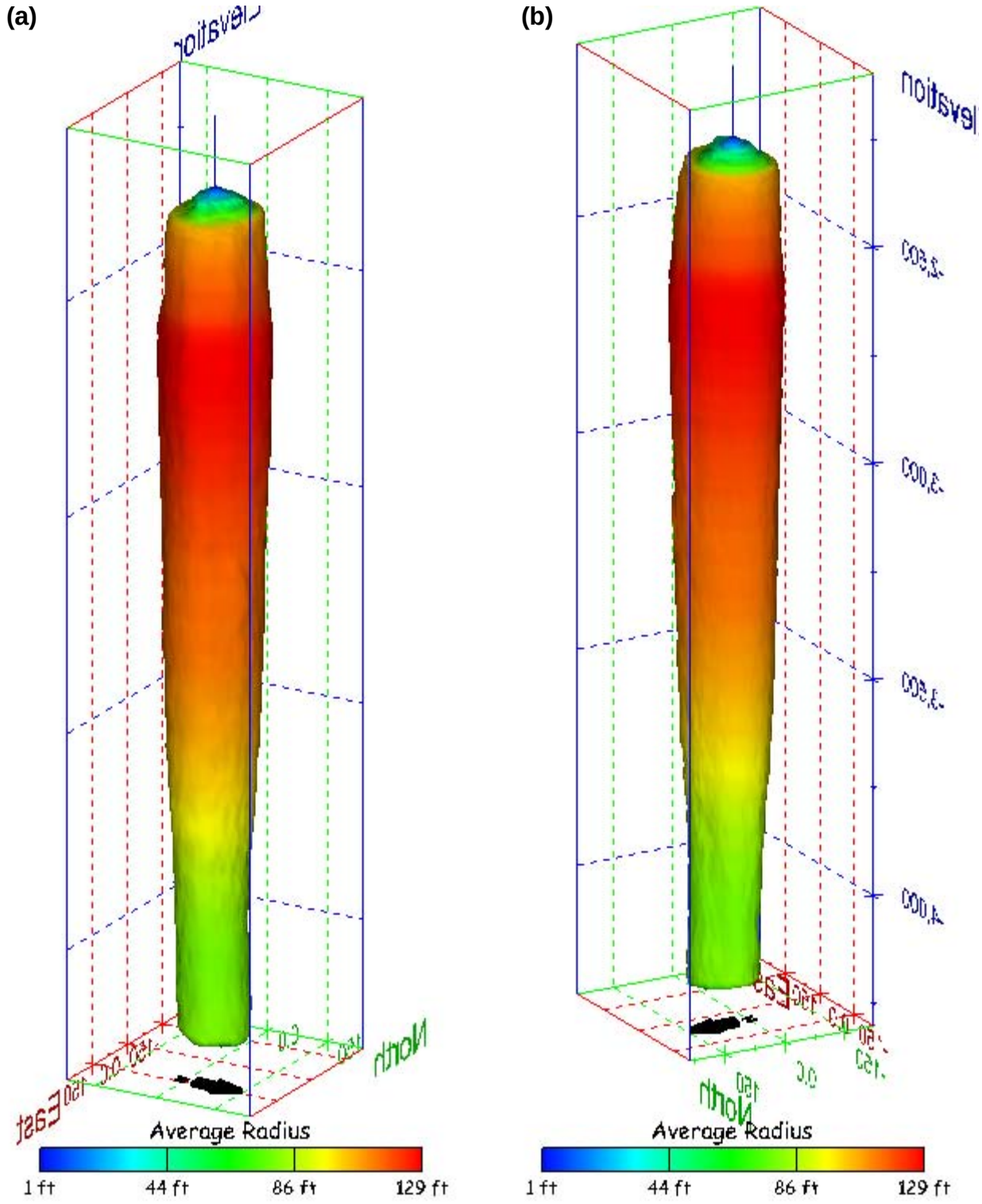

Figure 101. Sonar images of cavern BH-104, showing the geometry of the cavern colored by average radius. View from (a) azimuth 60°, elevation 20°; (b) azimuth 300°, elevation 20°.

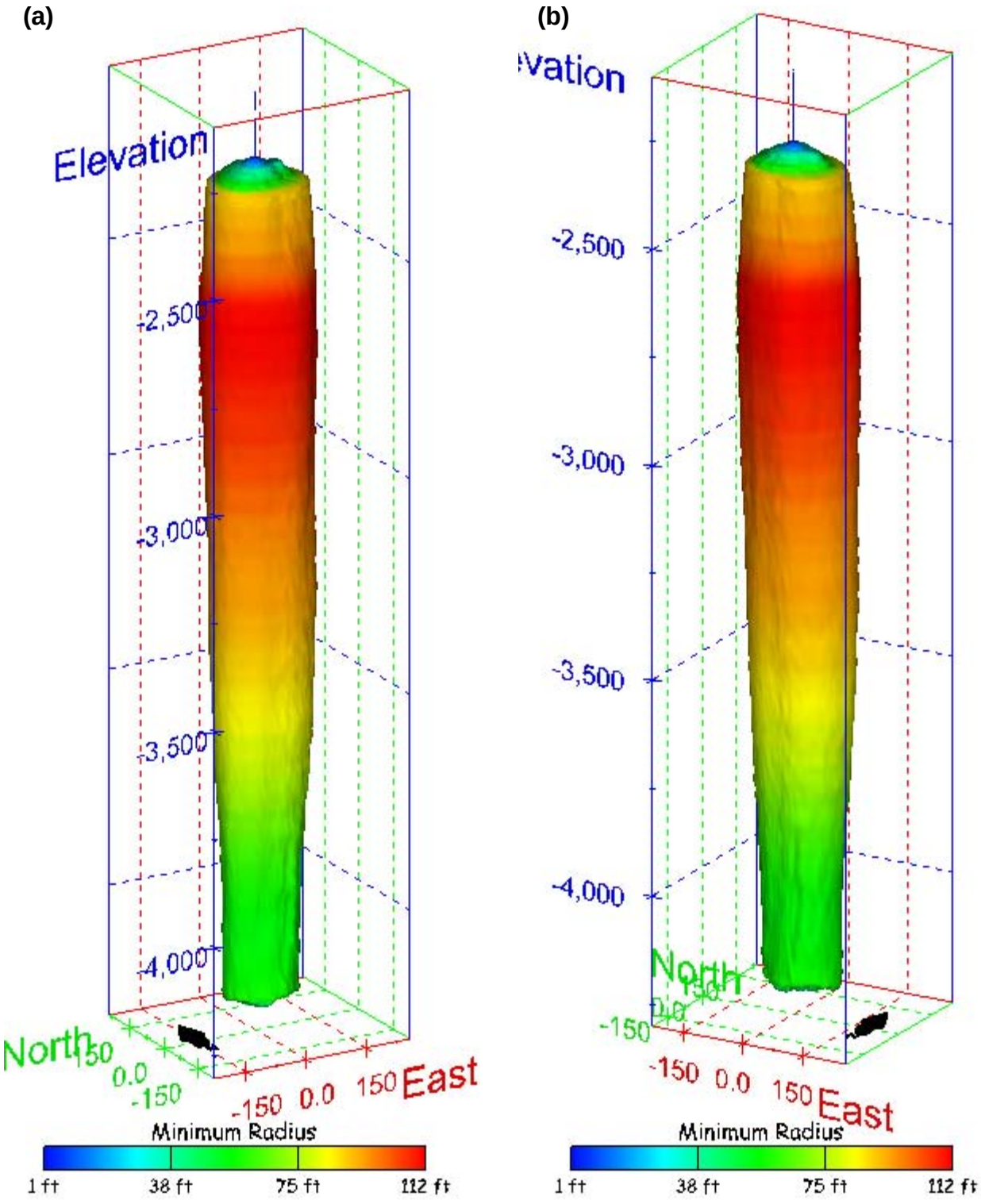

Figure 102. Sonar images of cavern BH-104, showing the geometry of the cavern colored by minimum radius. View from (a) azimuth 210°, elevation 20°; (b) azimuth 150°, elevation 20°.

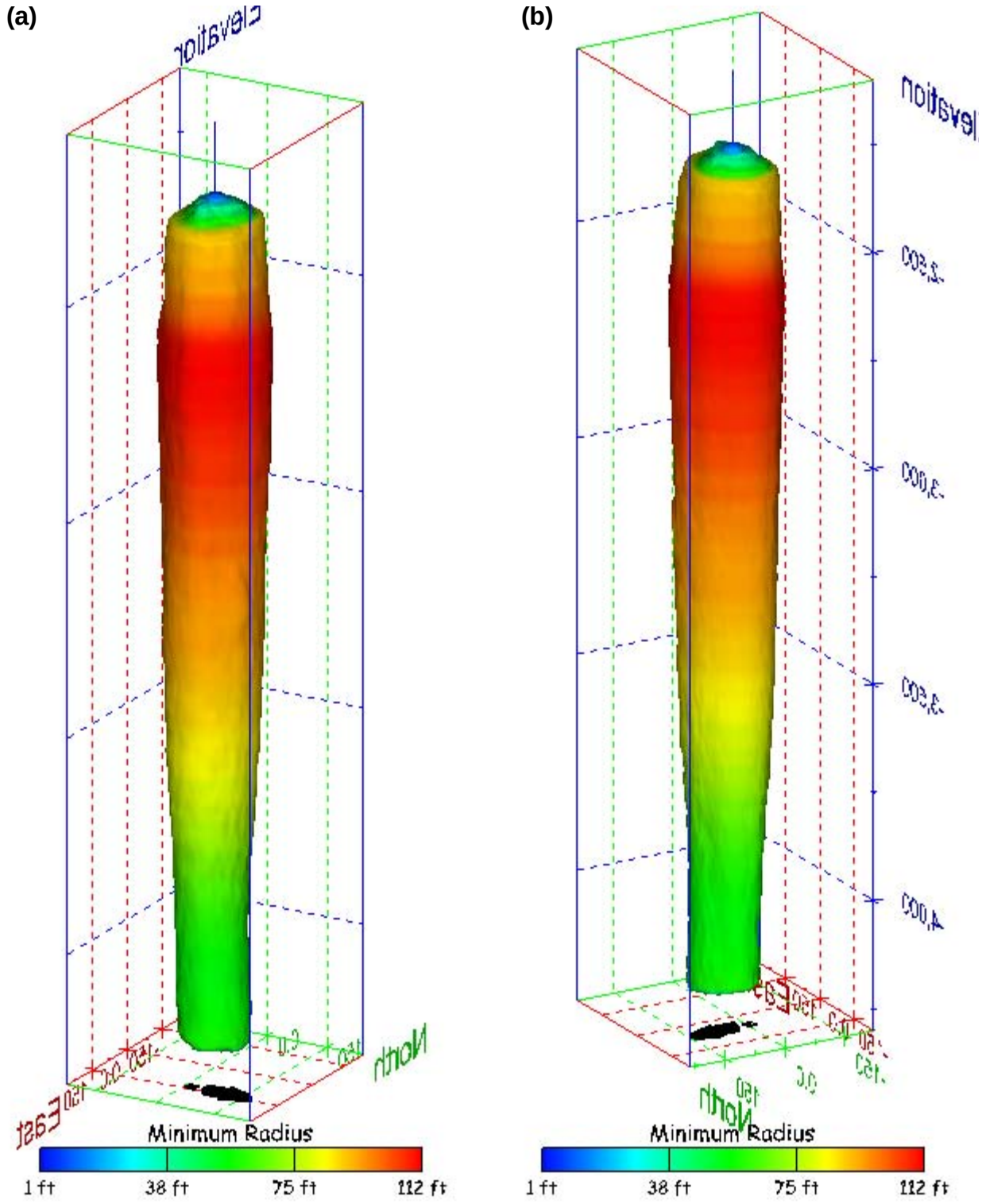

Figure 103. Sonar images of cavern BH-104, showing the geometry of the cavern colored by minimum radius. View from (a) azimuth 60°, elevation 20°; (b) azimuth 300°, elevation 20°.

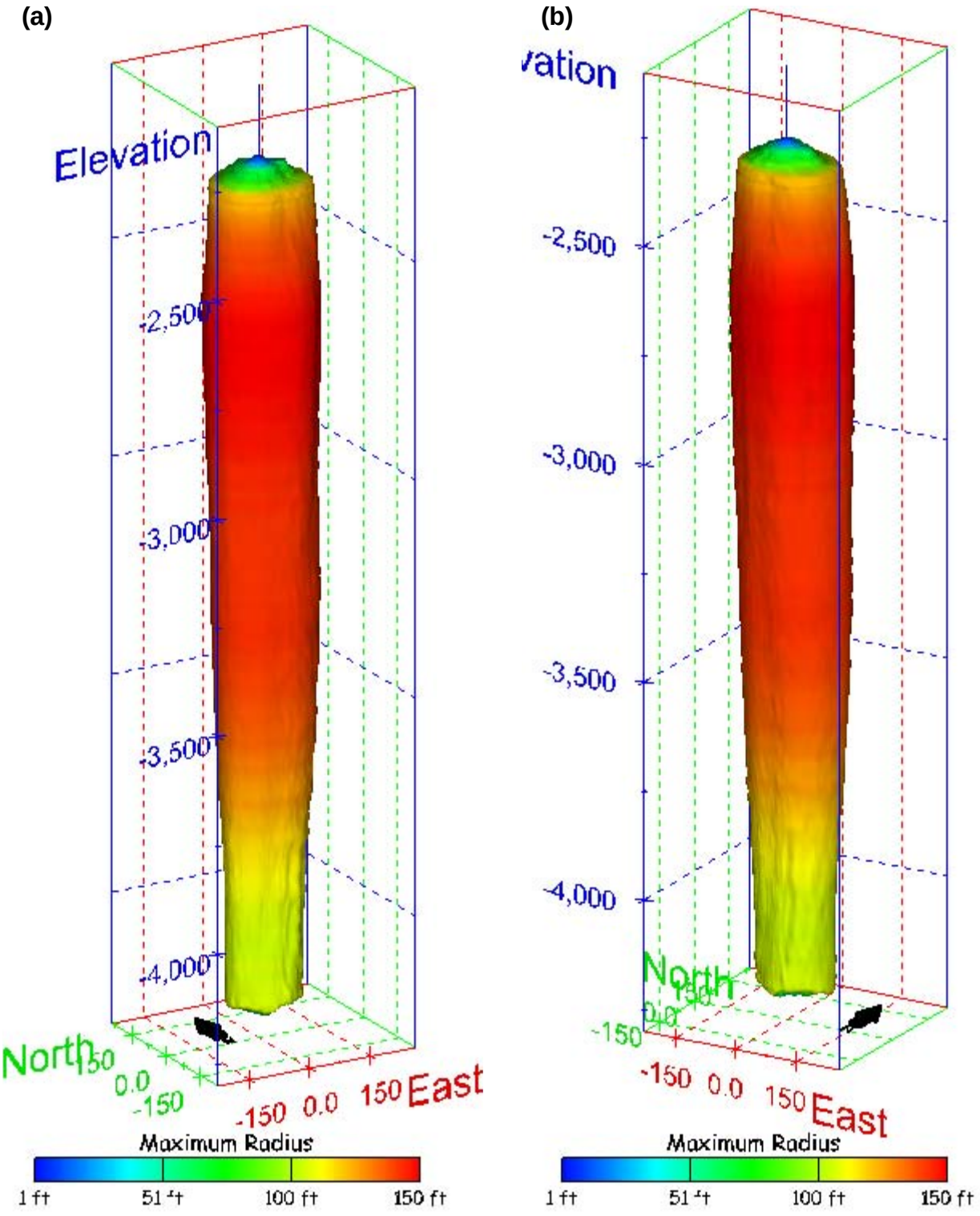

Figure 104. Sonar images of cavern BH-104, showing the geometry of the cavern colored by maximum radius. View from (a) azimuth 210°, elevation 20°; (b) azimuth 150°, elevation 20°.

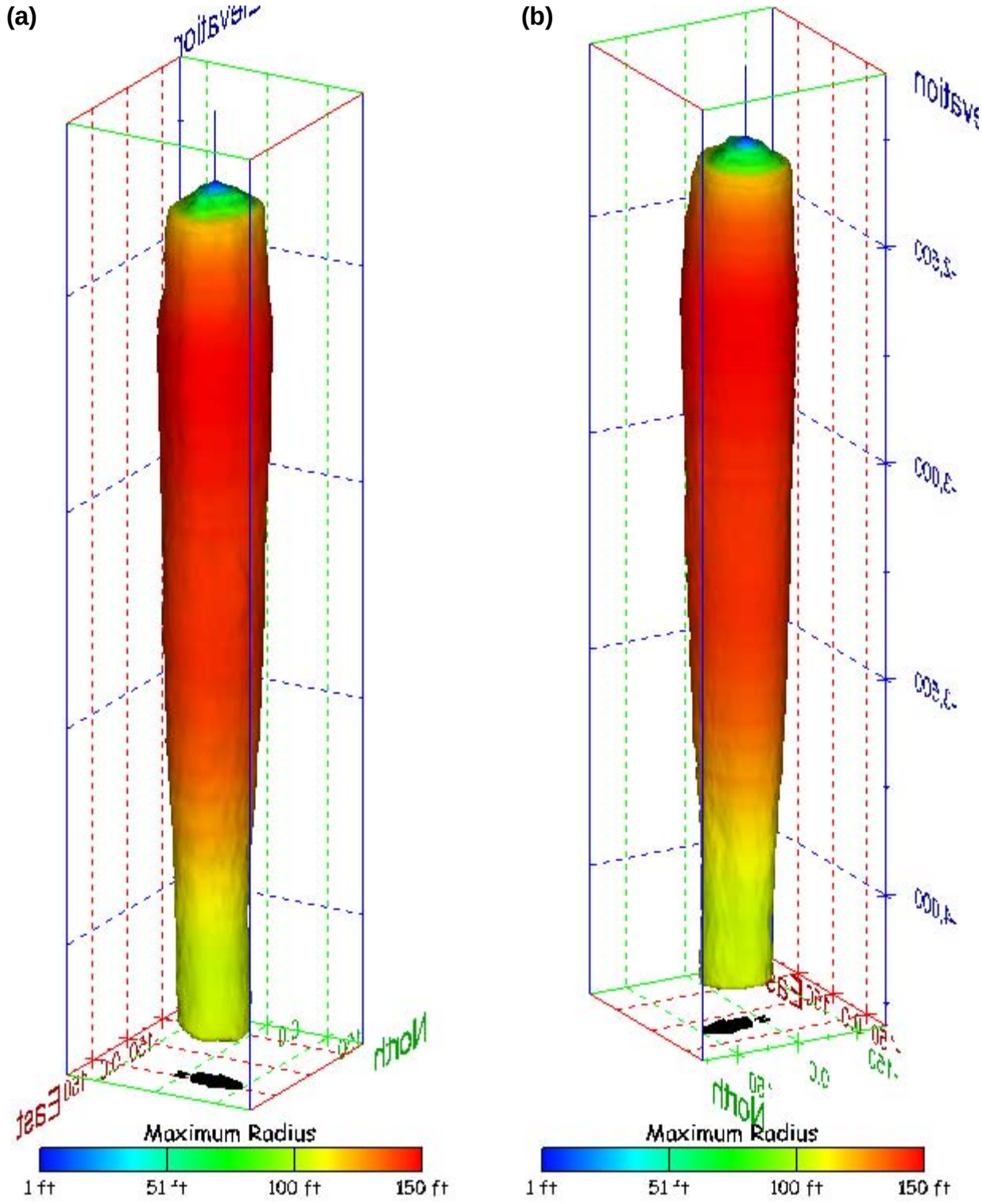

Figure 105. Sonar images of cavern BH-104, showing the geometry of the cavern colored by maximum radius. View from (a) azimuth 60°, elevation 20°; (b) azimuth 300°, elevation 20°.

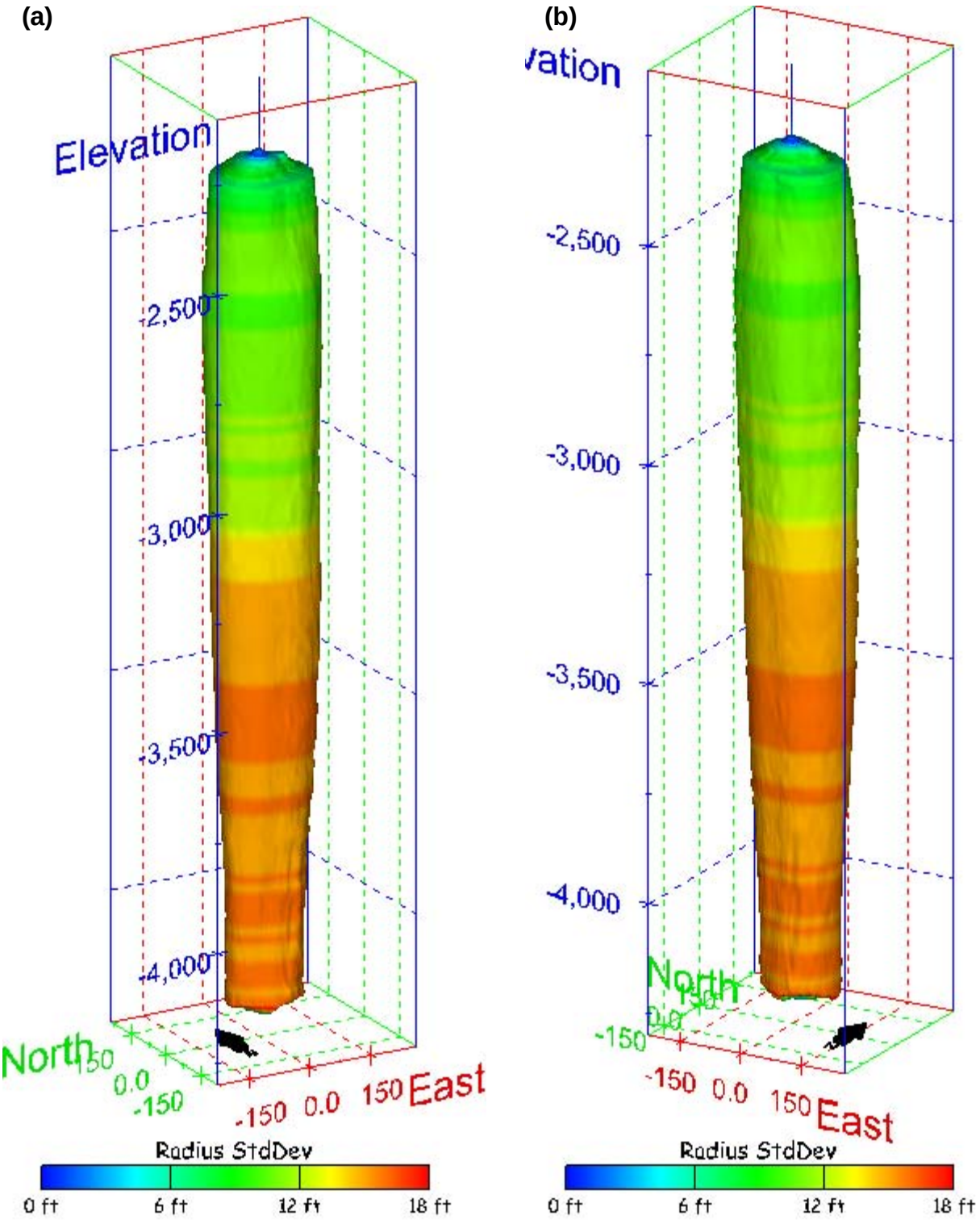

Figure 106. Sonar images of cavern BH-104, showing the geometry of the cavern colored by radius standard deviation. View from (a) azimuth 210°, elevation 20°; (b) azimuth 150°, elevation 20°.

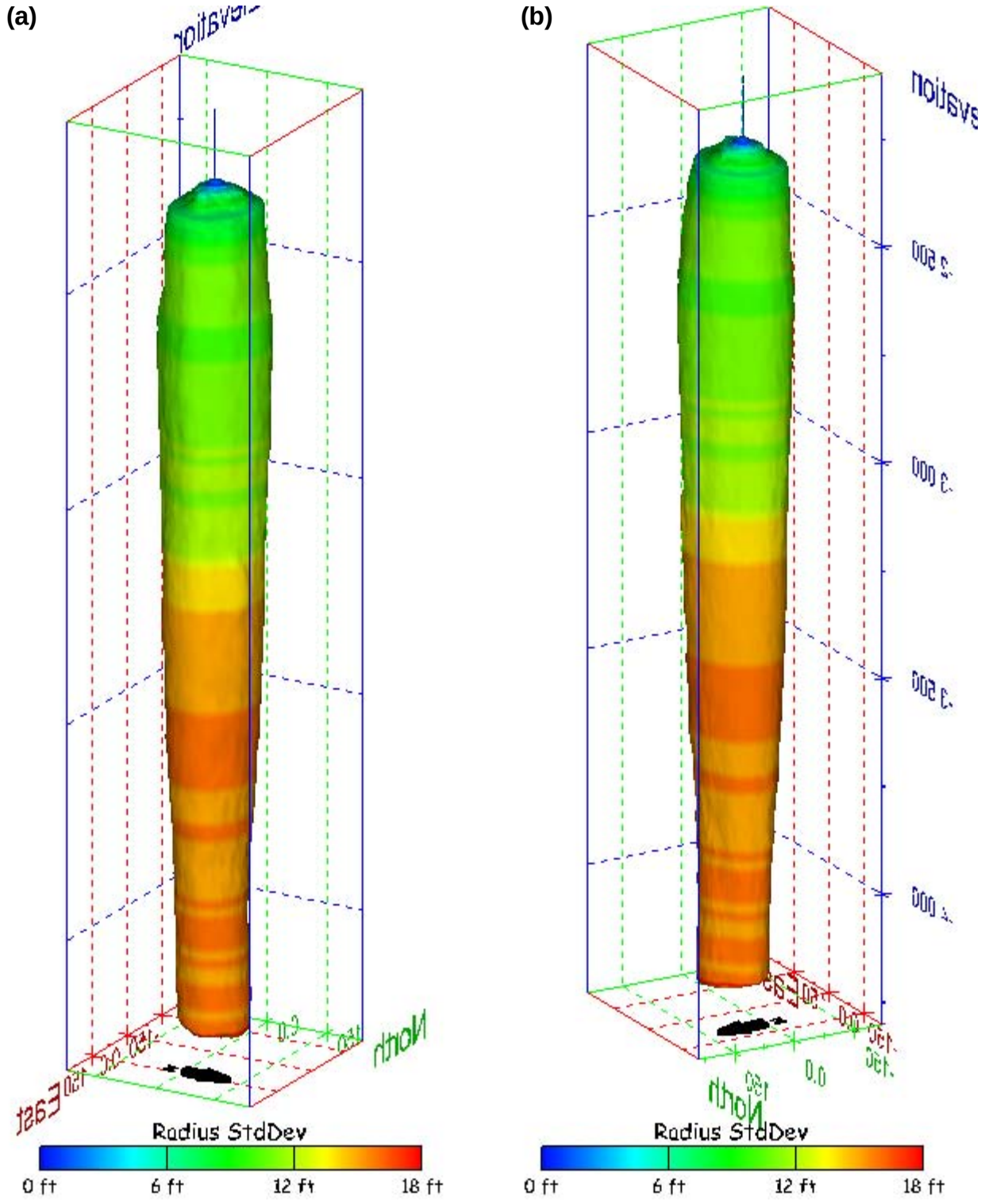

Figure 107. Sonar images of cavern BH-104, showing the geometry of the cavern colored by radius standard deviation.View from (a) azimuth 60°, elevation 20°; (b) azimuth 300°, elevation 20°.

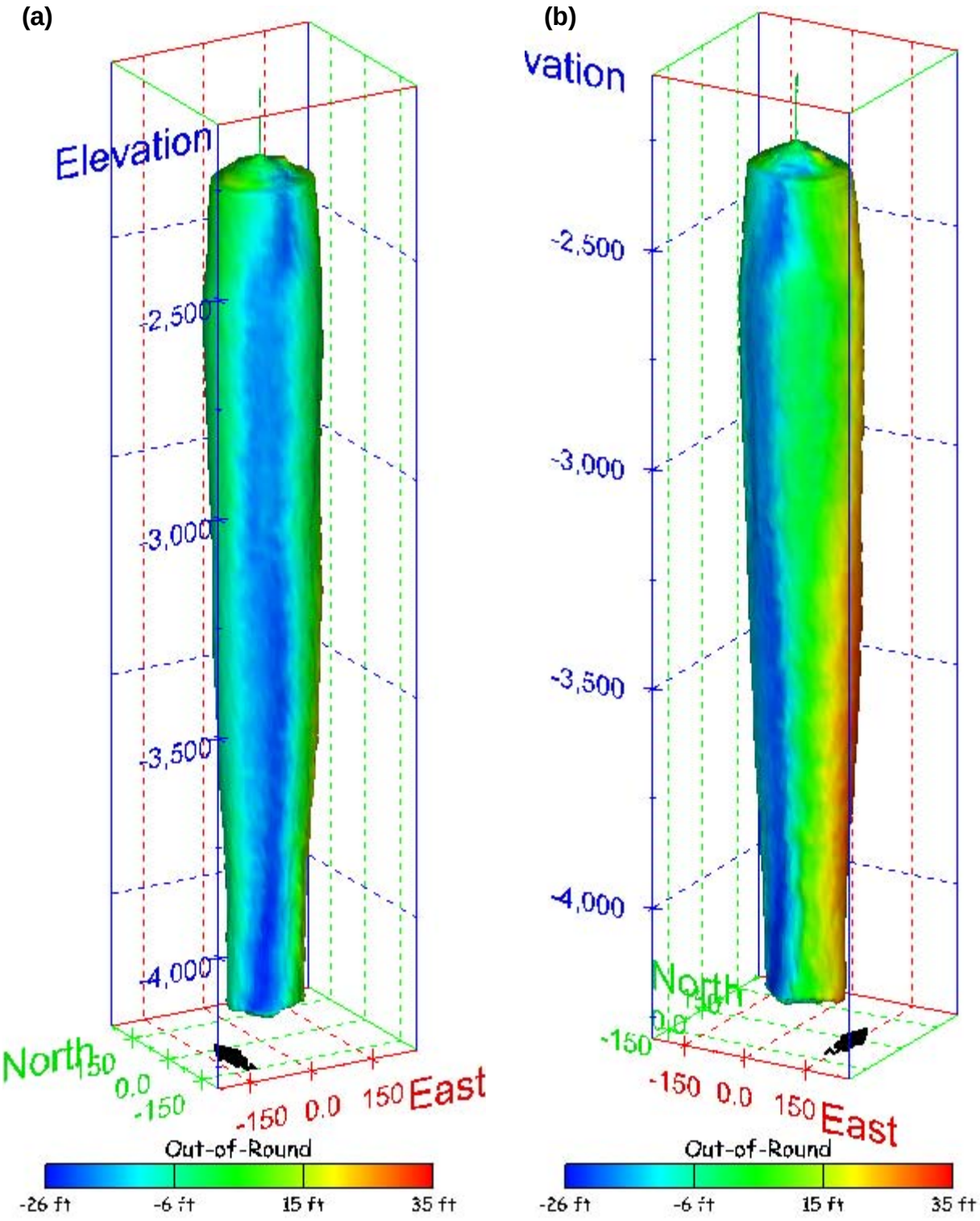

Figure 108. Sonar images of cavern BH-104, showing the geometry of the cavern colored by out-of-round distance. View from (a) azimuth 210°, elevation 20°; (b) azimuth 150°, elevation 20°.

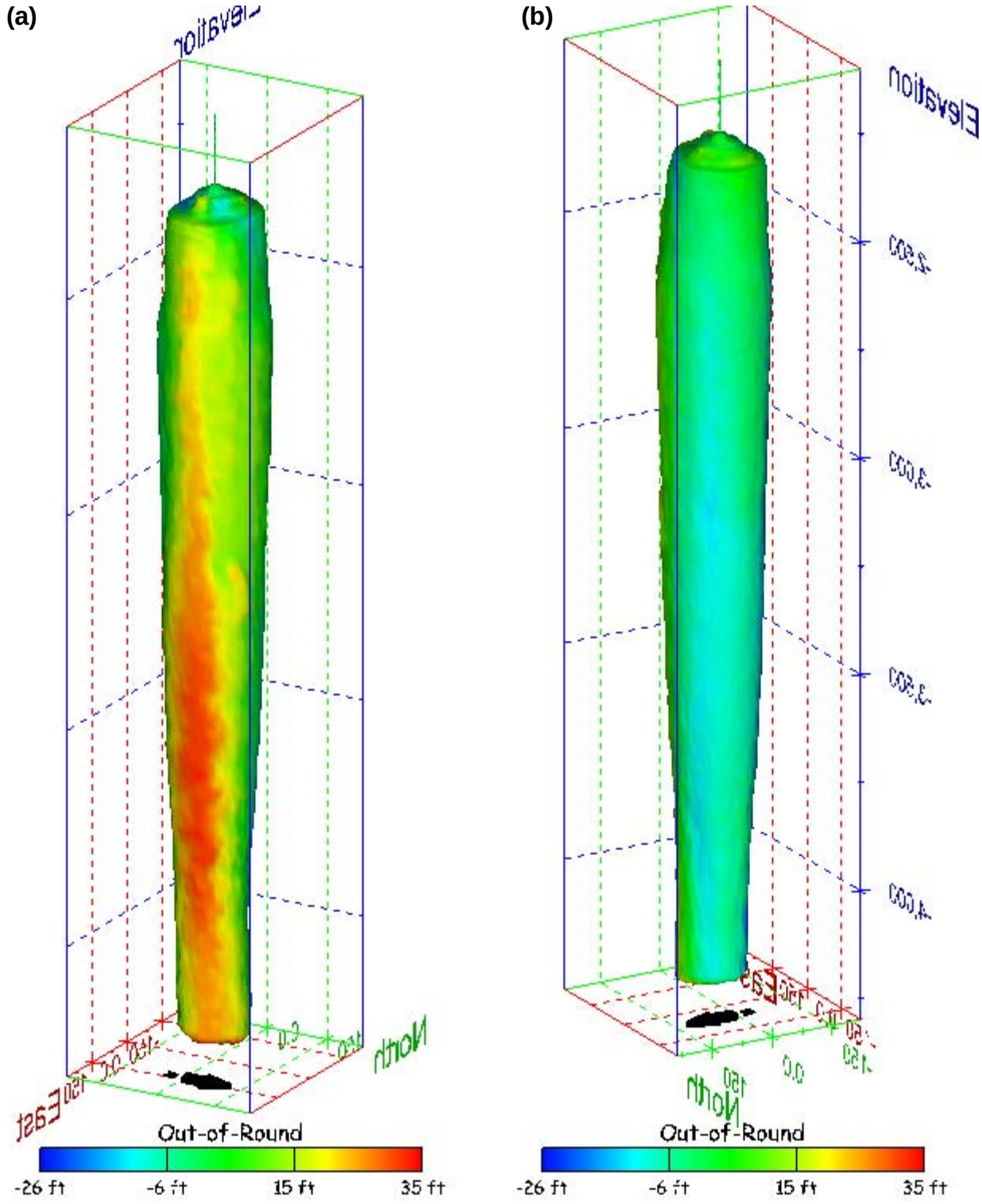

Figure 109. Sonar images of cavern BH-104, showing the geometry of the cavern colored by out-of-round distance. View from (a) azimuth 60°, elevation 20°; (b) azimuth 300°, elevation 20°.

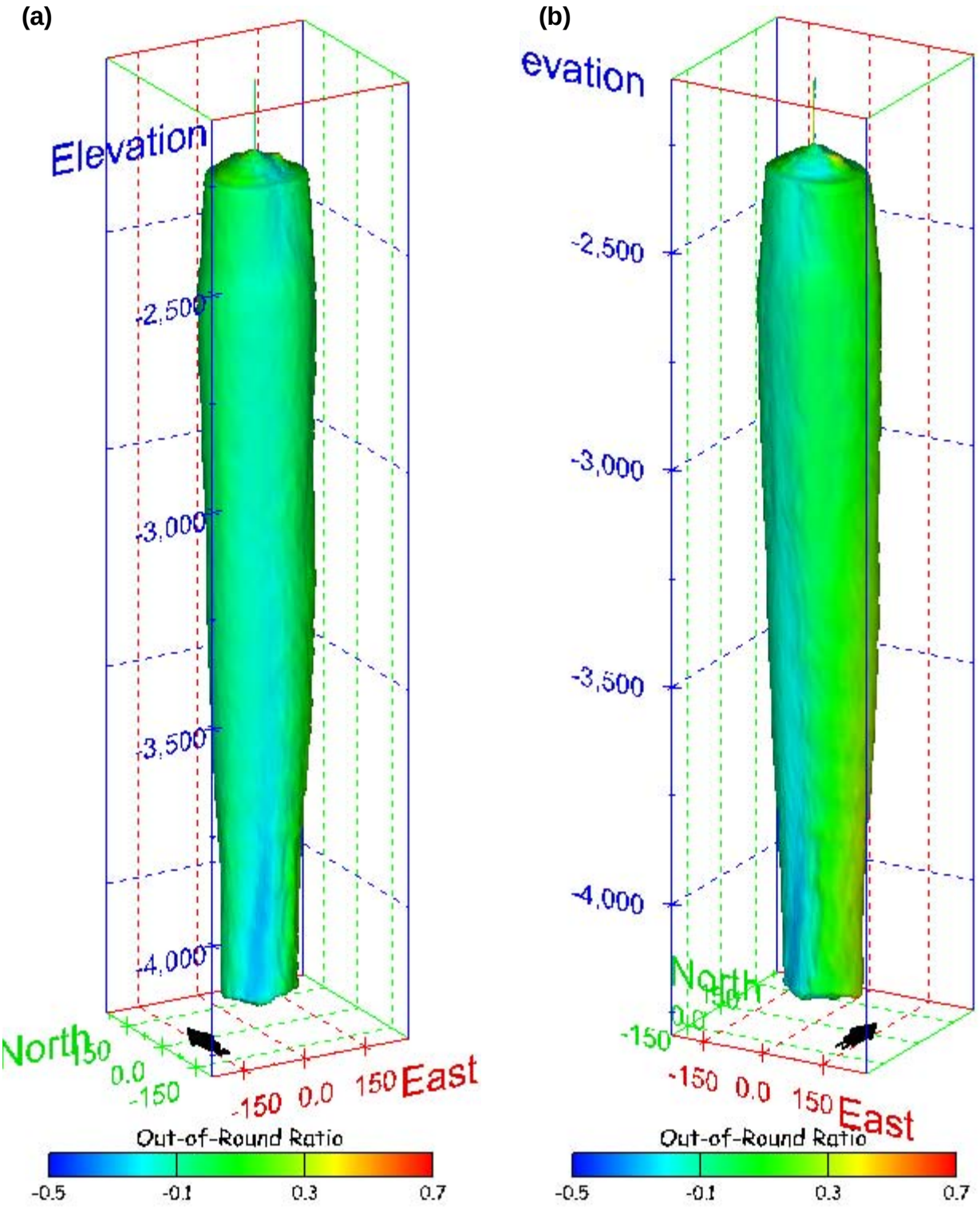

Figure 110. Sonar images of cavern BH-104, showing the geometry of the cavern colored by out-of-round ratio. View from (a) azimuth 210°, elevation 20°; (b) azimuth 150°, elevation 20°.

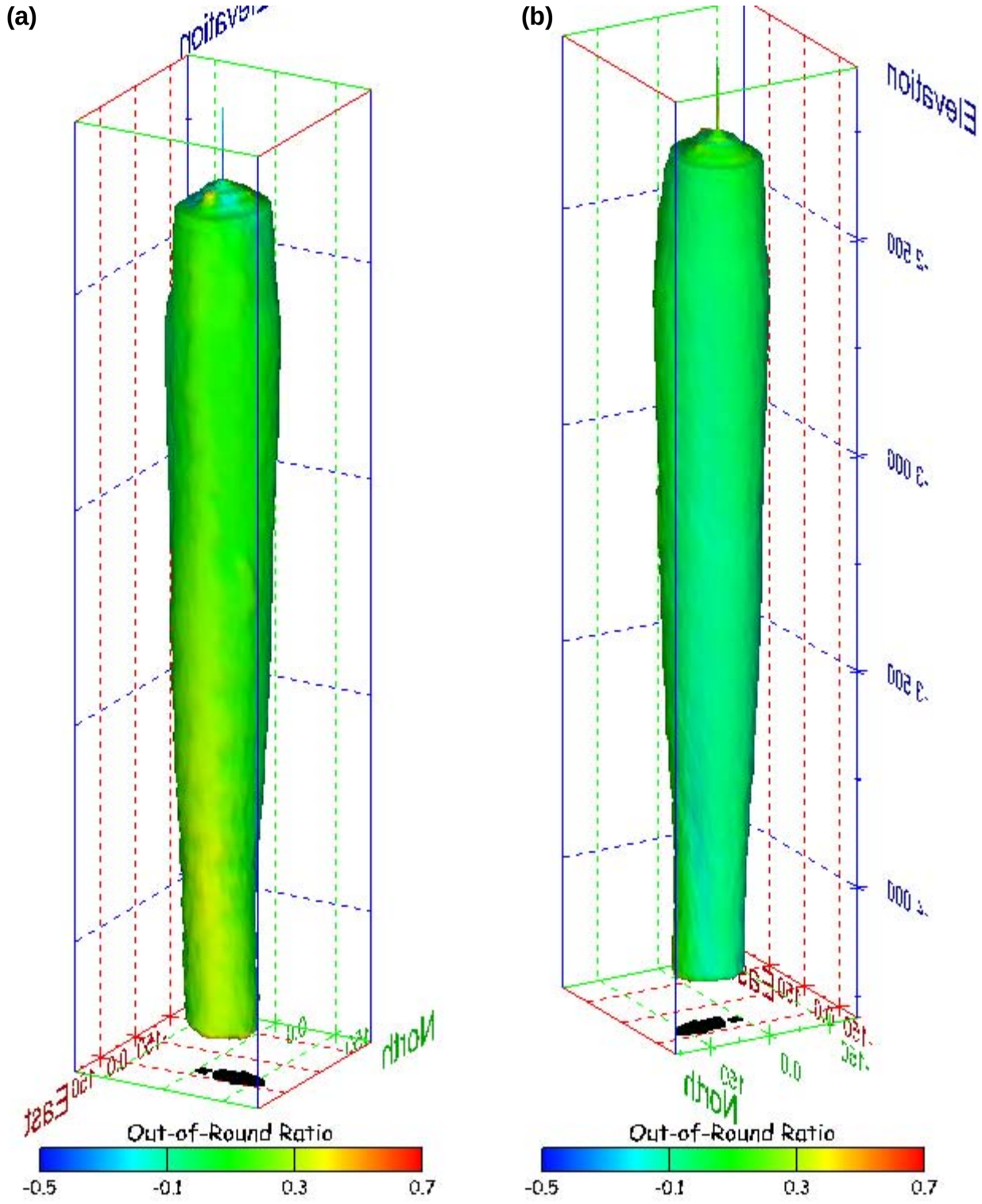

Figure 111. Sonar images of cavern BH-104, showing the geometry of the cavern colored by out-of-round ratio. View from (a) azimuth 60°, elevation 20°; (b) azimuth 300°, elevation 20°.

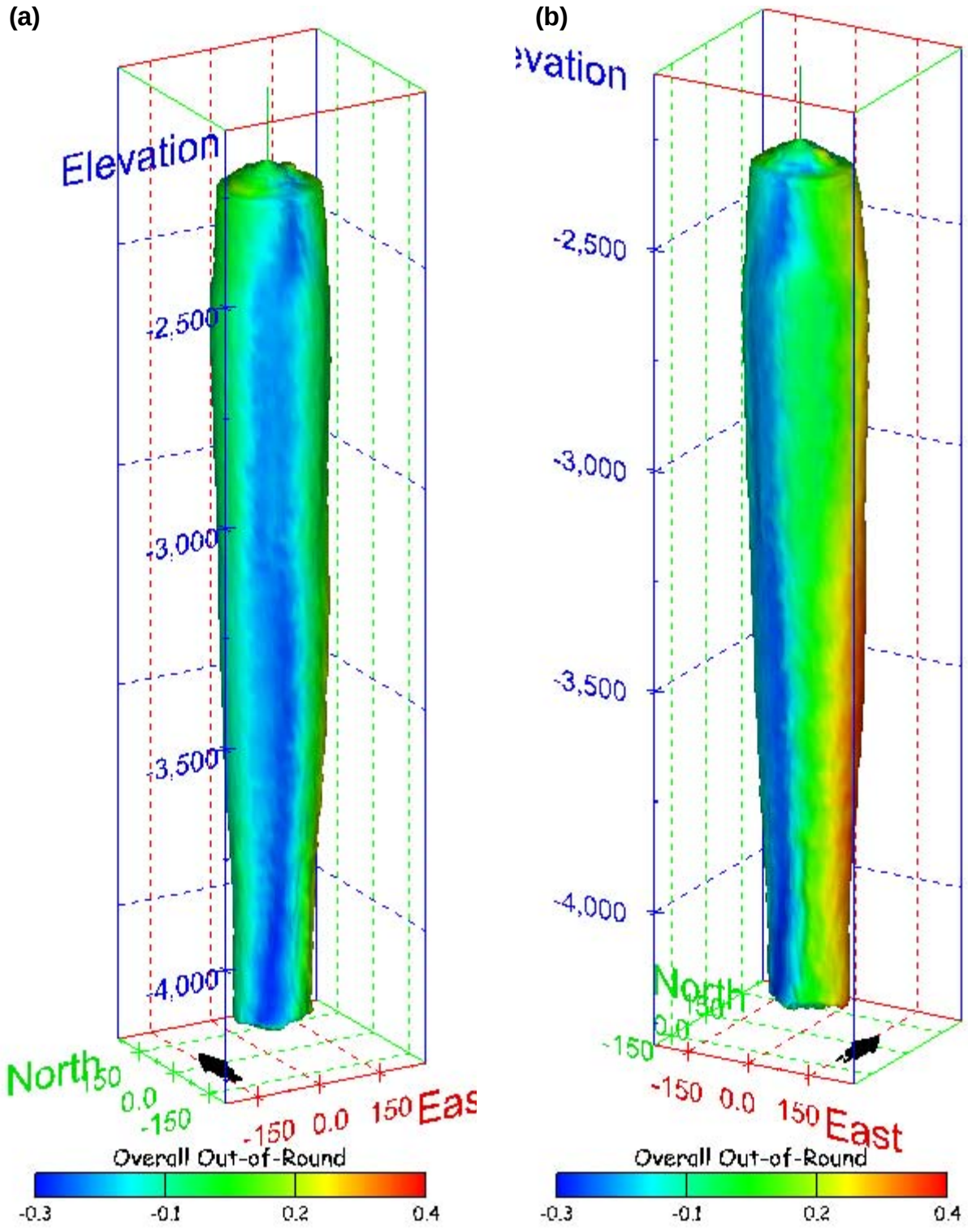

Figure 112. Sonar images of cavern BH-104, showing the geometry of the cavern colored by overall out-of-round ratio. View from (a) azimuth 210°, elevation 20°; (b) azimuth 150°, elevation 20°.

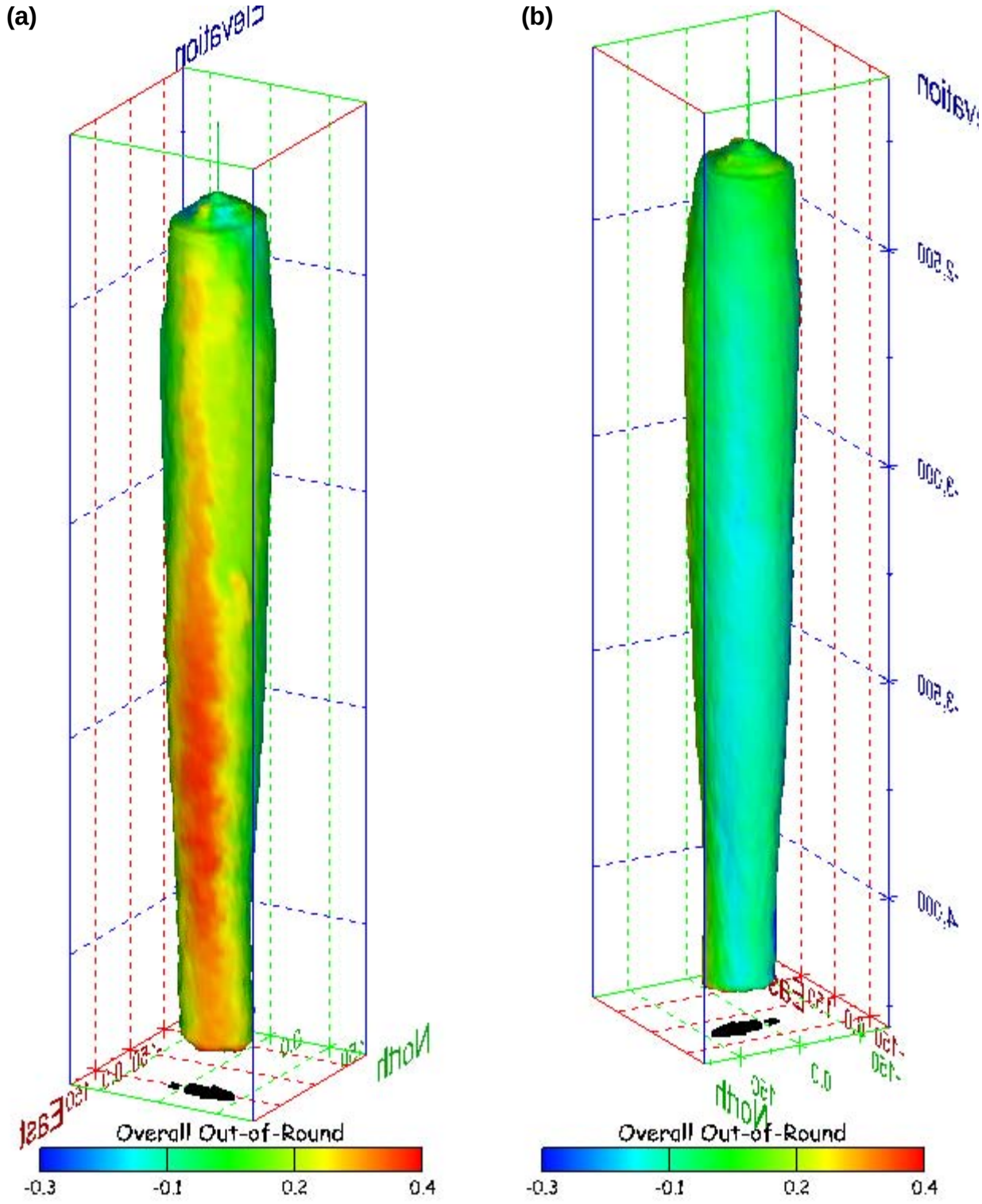

Figure 113. Sonar images of cavern BH-104, showing the geometry of the cavern colored by overall out-of-round ratio. View from (a) azimuth 60°, elevation 20°; (b) azimuth 300°, elevation 20°.

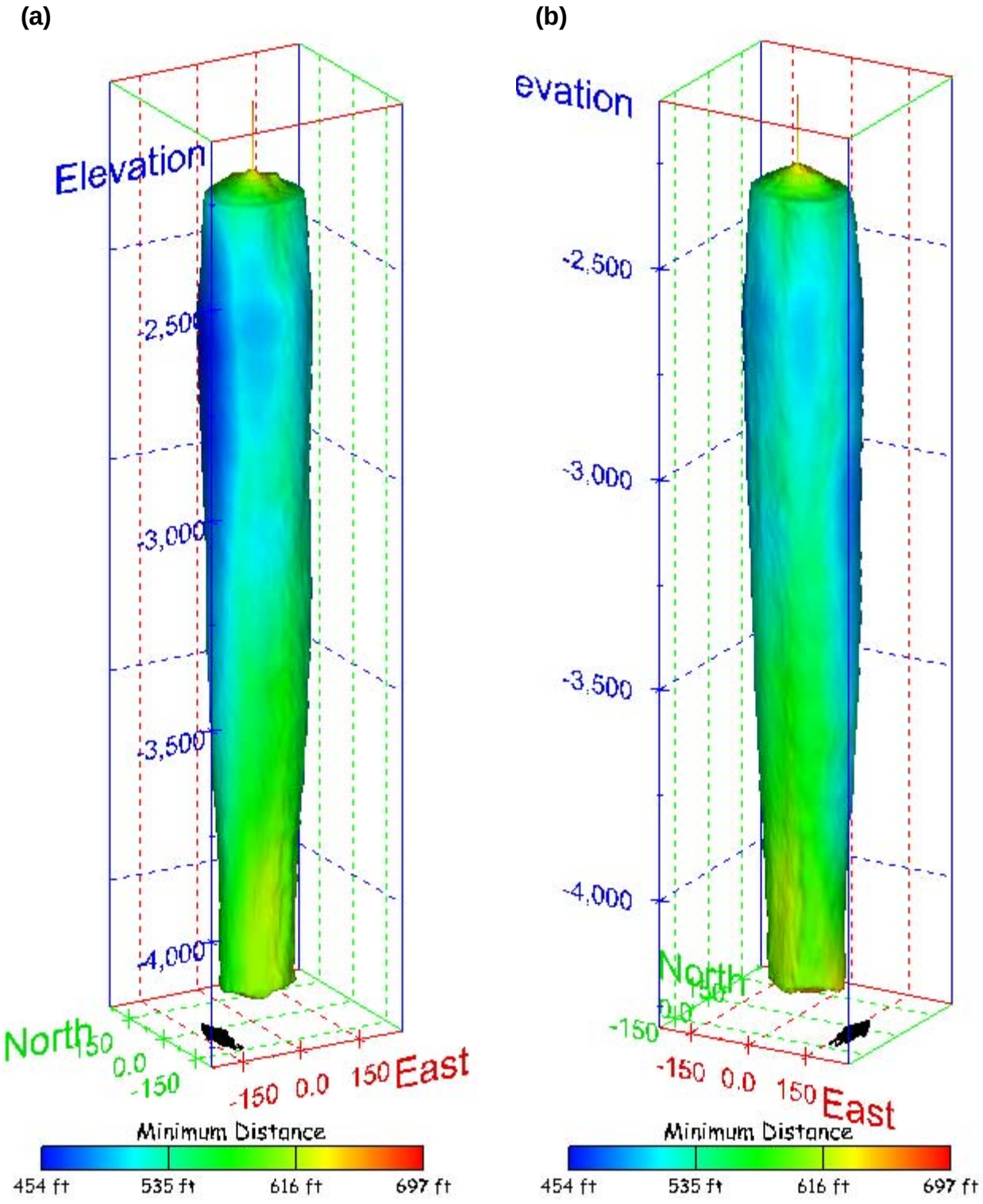

Figure 114. Sonar images of cavern BH-104, showing the geometry of the cavern colored by the minimum distance to the nearest neighboring cavern. View from (a) azimuth 210°, elevation 20°; (b) azimuth 150°, elevation 20°.

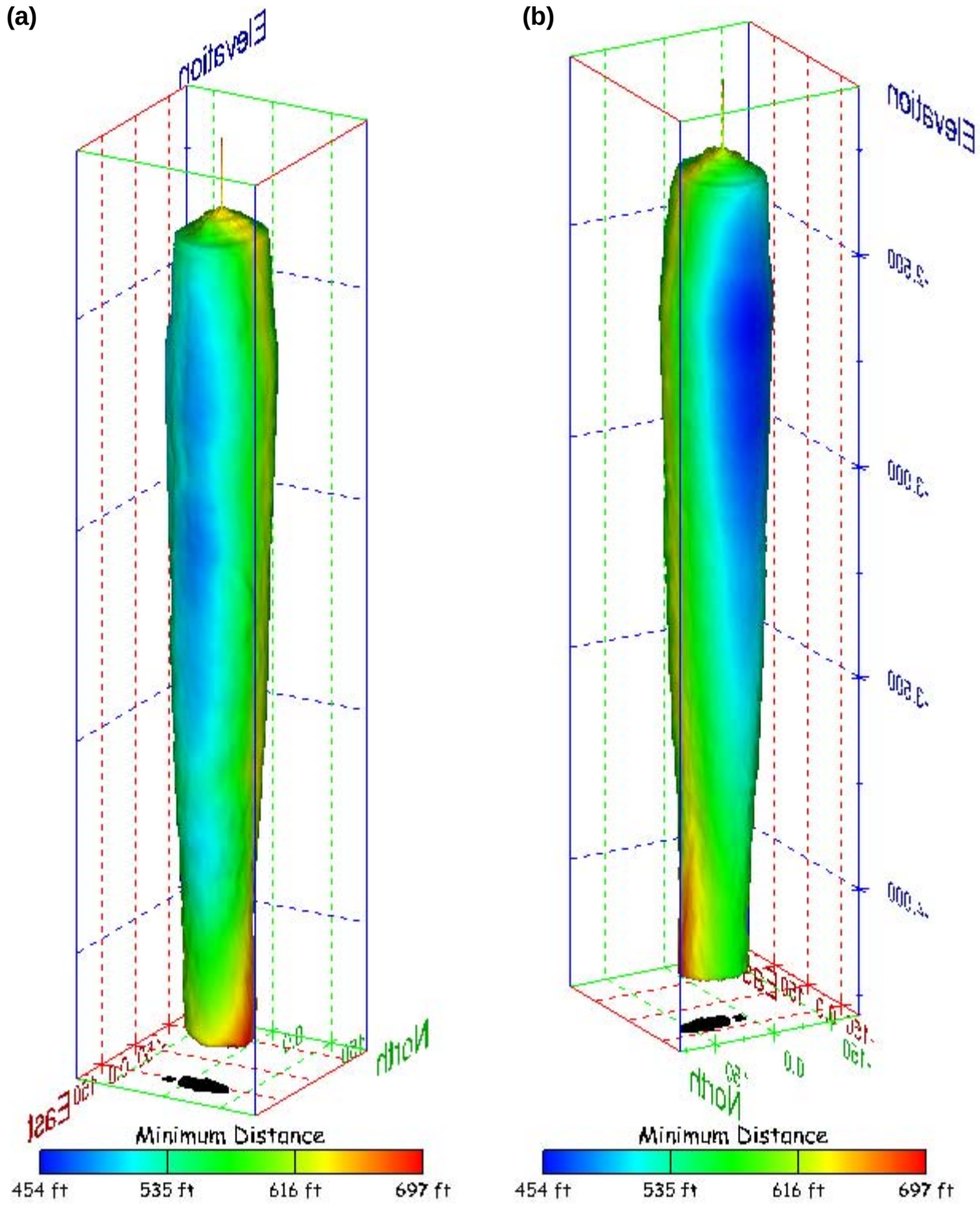

Figure 115. Sonar images of cavern BH-104, showing the geometry of the cavern colored by minimum distance to the nearest neighboring cavern. View from (a) azimuth 60°, elevation 20°; (b) azimuth 300°, elevation 20°.

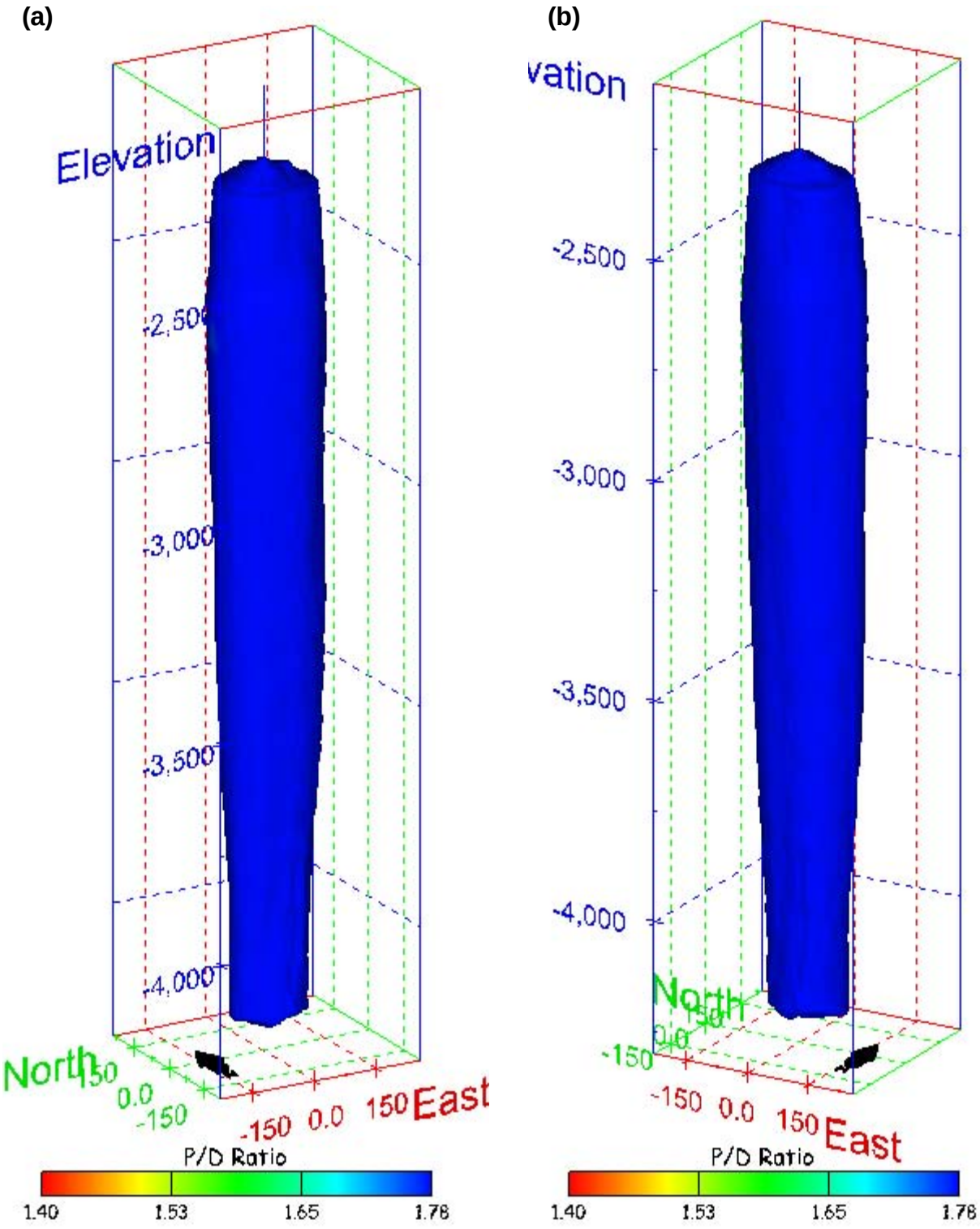

Figure 116. Sonar images of cavern BH-104, showing the geometry of the cavern colored by three-dimensional pillar-to-diameter ratio. View from (a) azimuth 210°, elevation 20°; (b) azimuth 150°, elevation 20°.

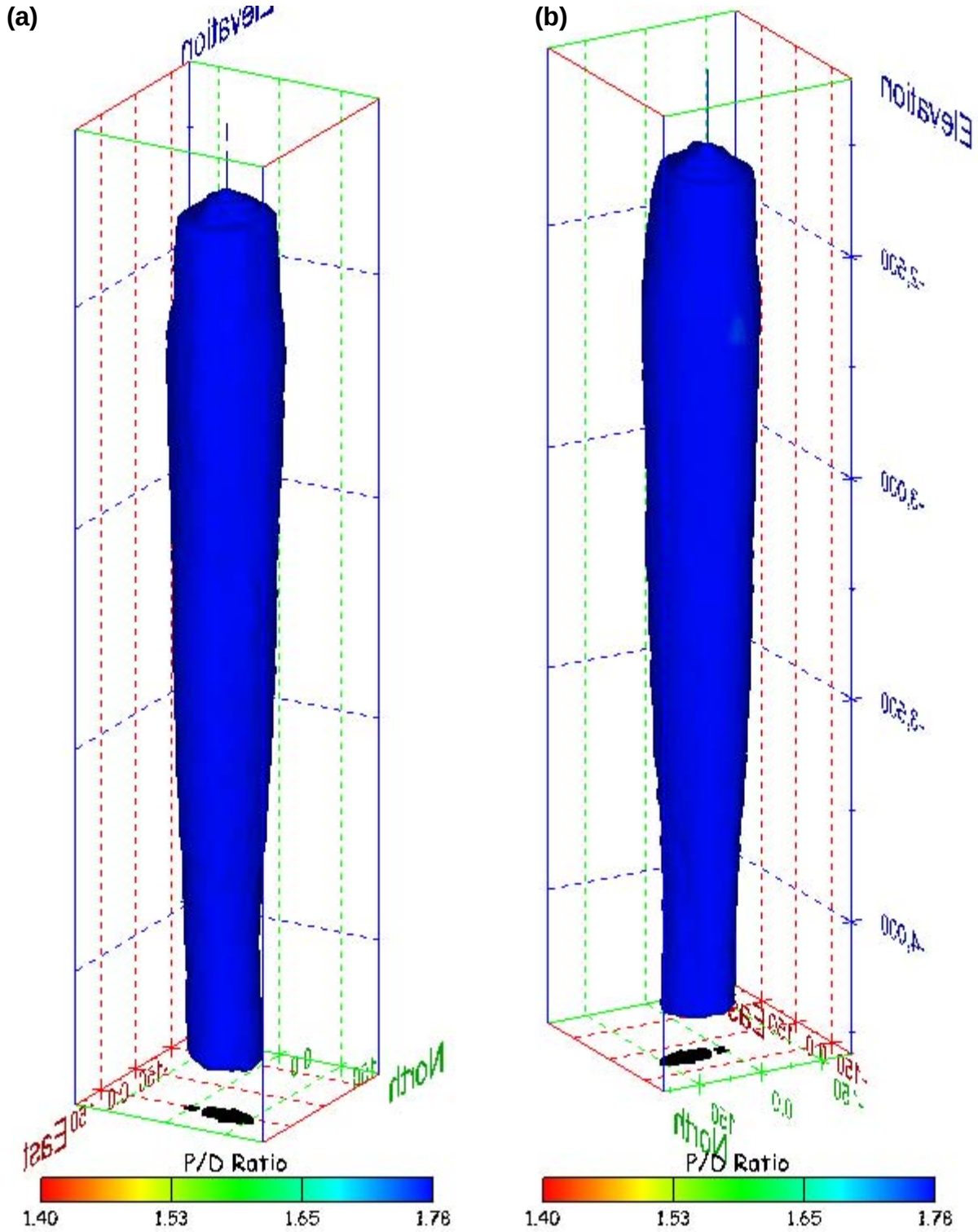

Figure 117. Sonar images of cavern BH-104, showing the geometry of the cavern colored by three-dimensional pillar-to-diameter ratio. View from (a) azimuth 60°, elevation 20°; (b) azimuth 300°, elevation 20°.

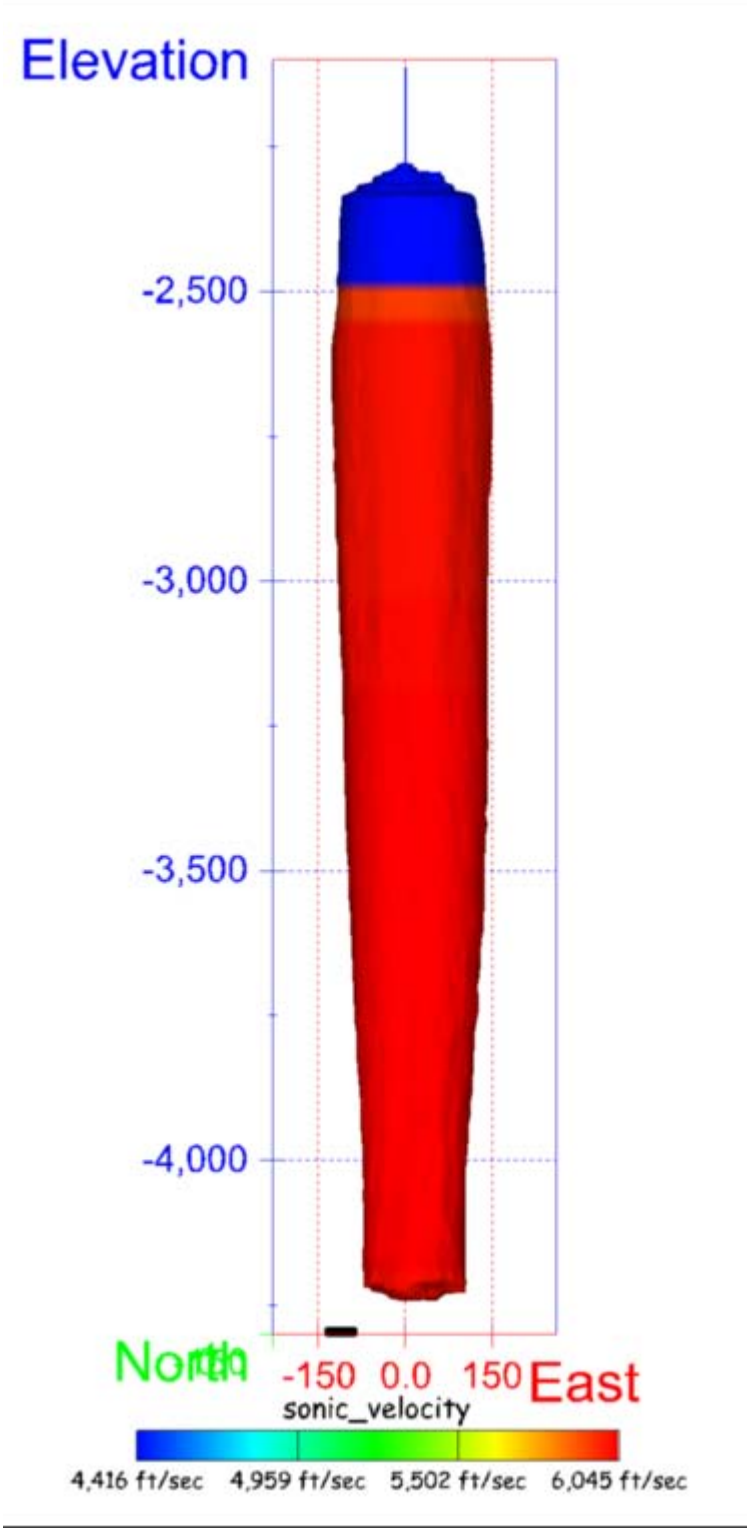

Figure 118. Sonar image of cavern BH-104, showing the geometry of the cavern colored by the reported velocity of sound on the survey date of October 2002. View from due south, elevation zero.

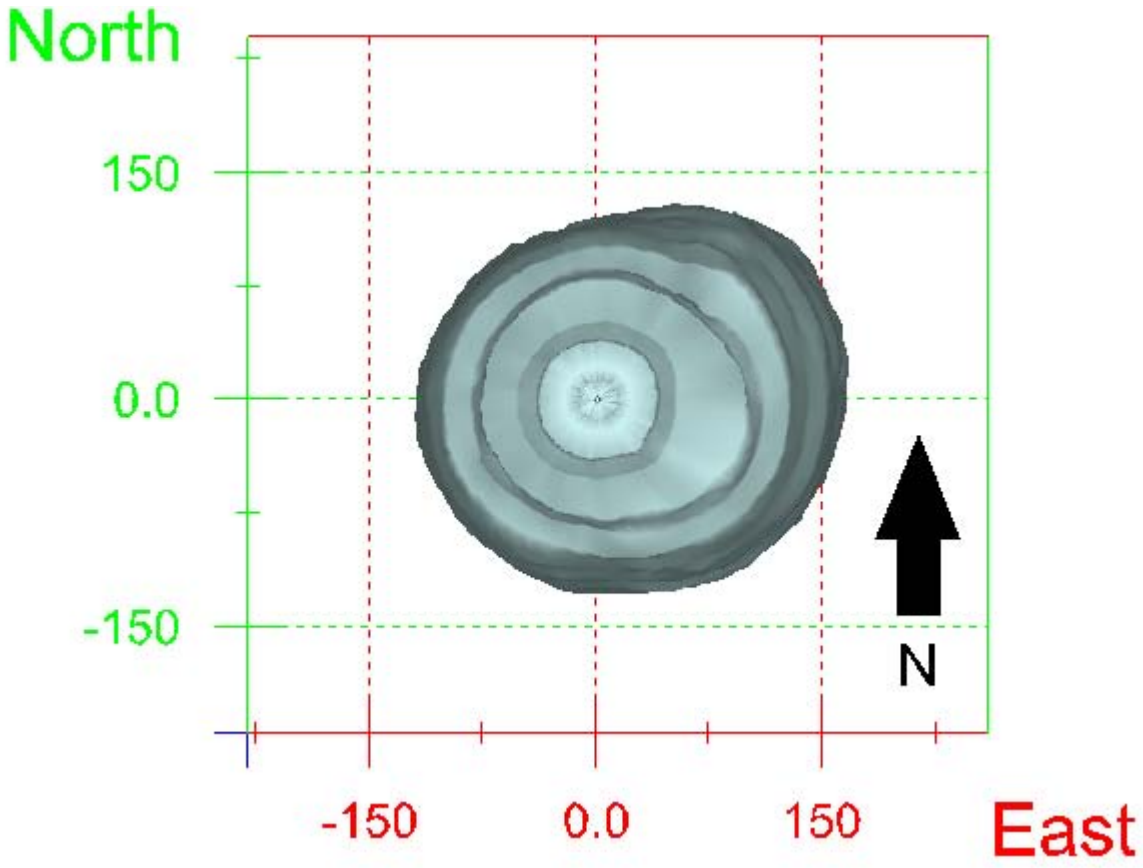

Figure 119. Map view sonar image of cavern BH-105, showing the basic geometry of the cavern. Grid squares represent 150 ft.

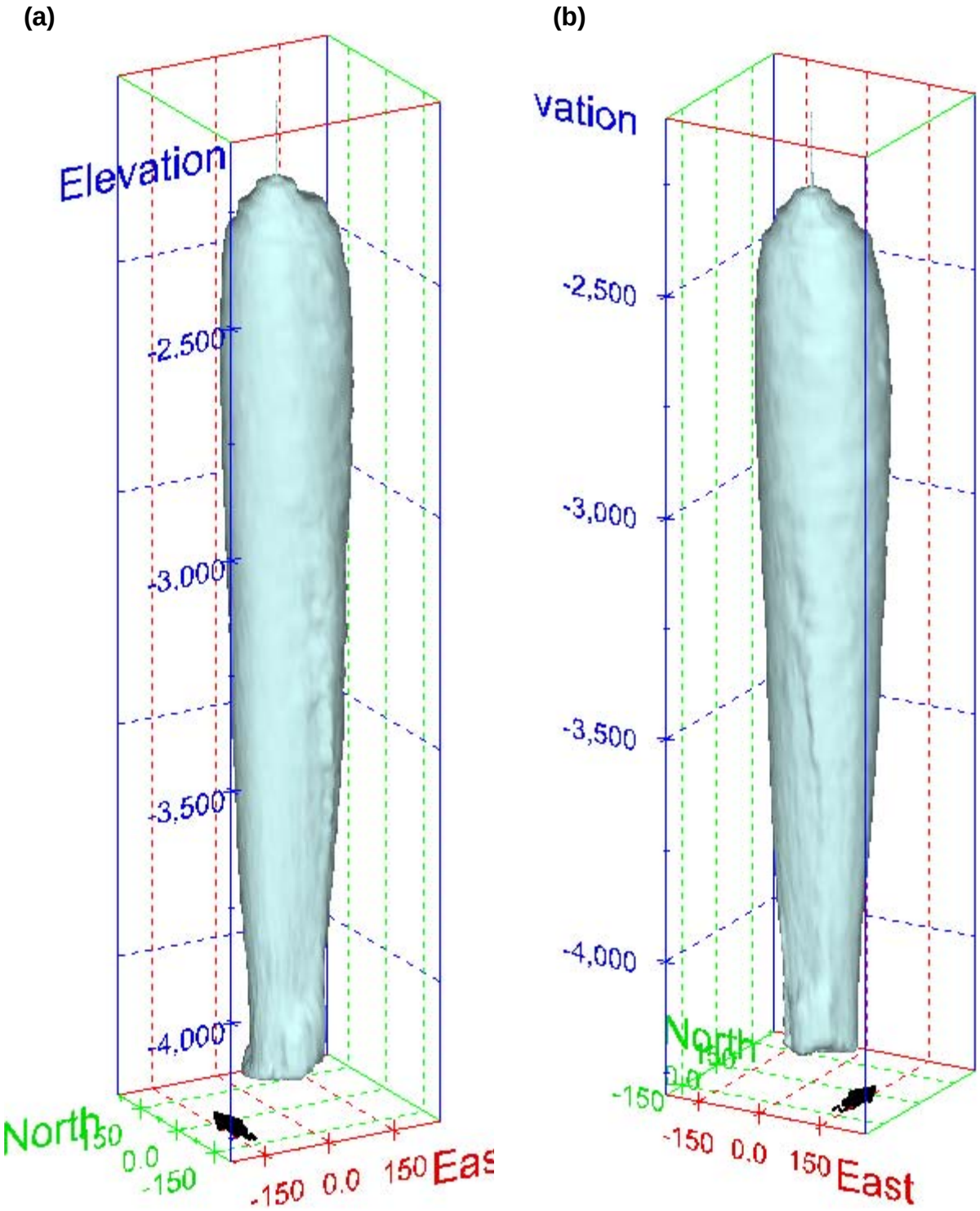

Figure 120. Sonar images of cavern BH-105, showing the basic geometric shape of the cavern. View from (a) azimuth 210°, elevation 20°; (b) azimuth 150°, elevation 20°.

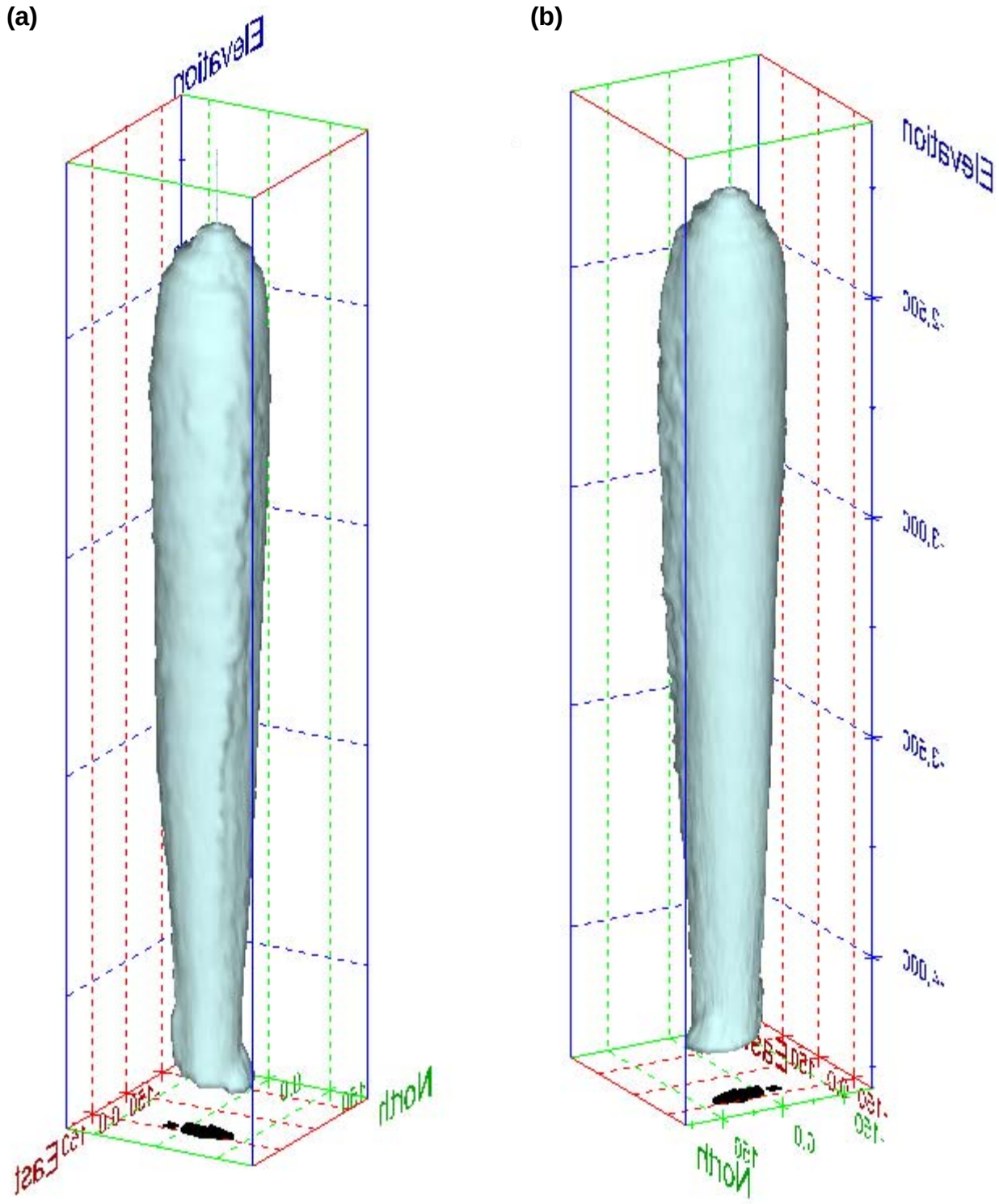

Figure 121. Sonar images of cavern BH-105, showing the basic geometric shape of the cavern. View from (a) azimuth 60°, elevation 20°; (b) azimuth 300°, elevation 20°.

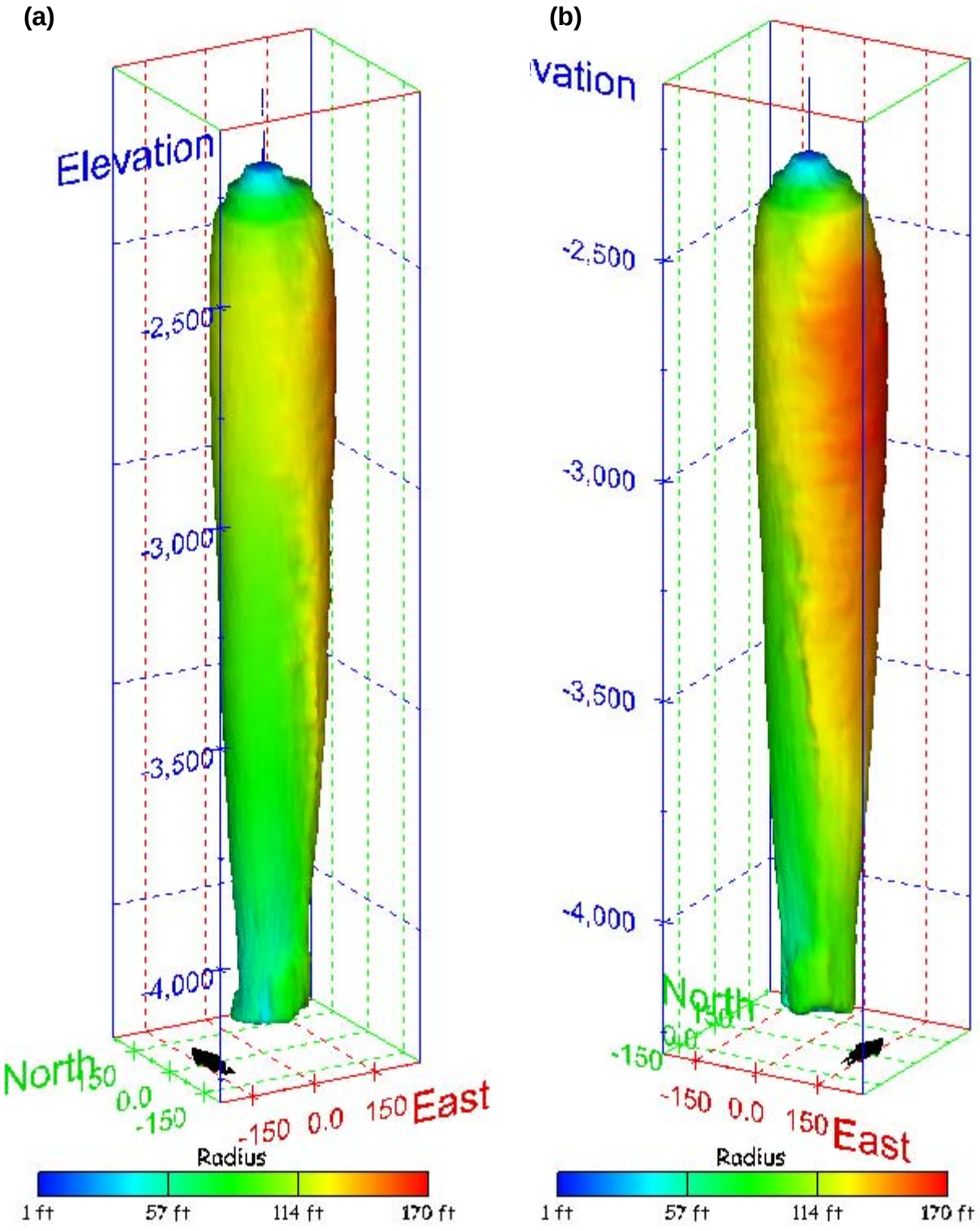

Figure 122. Sonar images of cavern BH-105, showing the geometry of the cavern colored by measured radius. View from (a) azimuth 210°, elevation 20°; (b) azimuth 150°, elevation 20°.

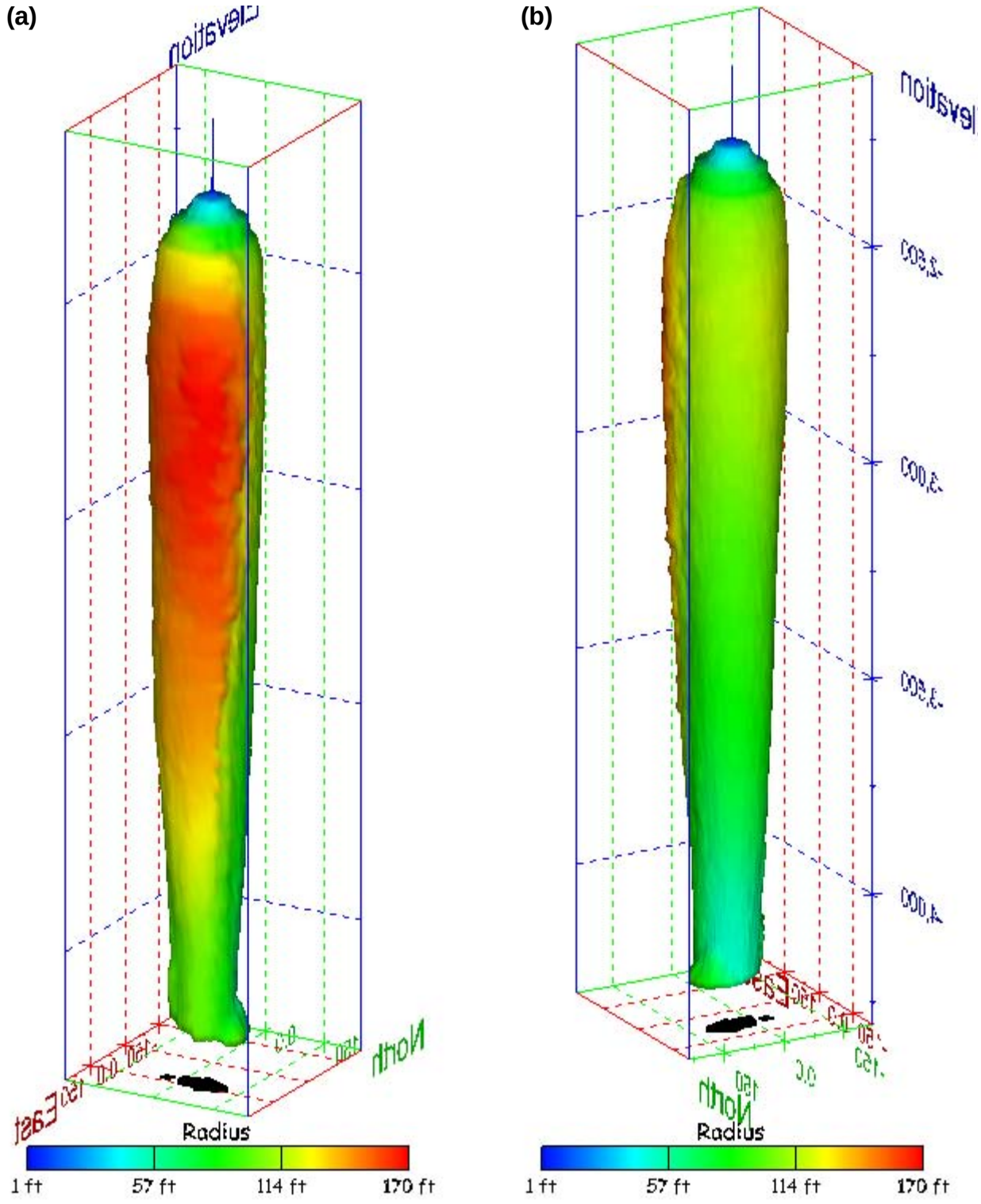

Figure 123. Sonar images of cavern BH-105, showing the geometry of the cavern colored by measured radius. View from (a) azimuth 60°, elevation 20°; (b) azimuth 300°, elevation 20°.

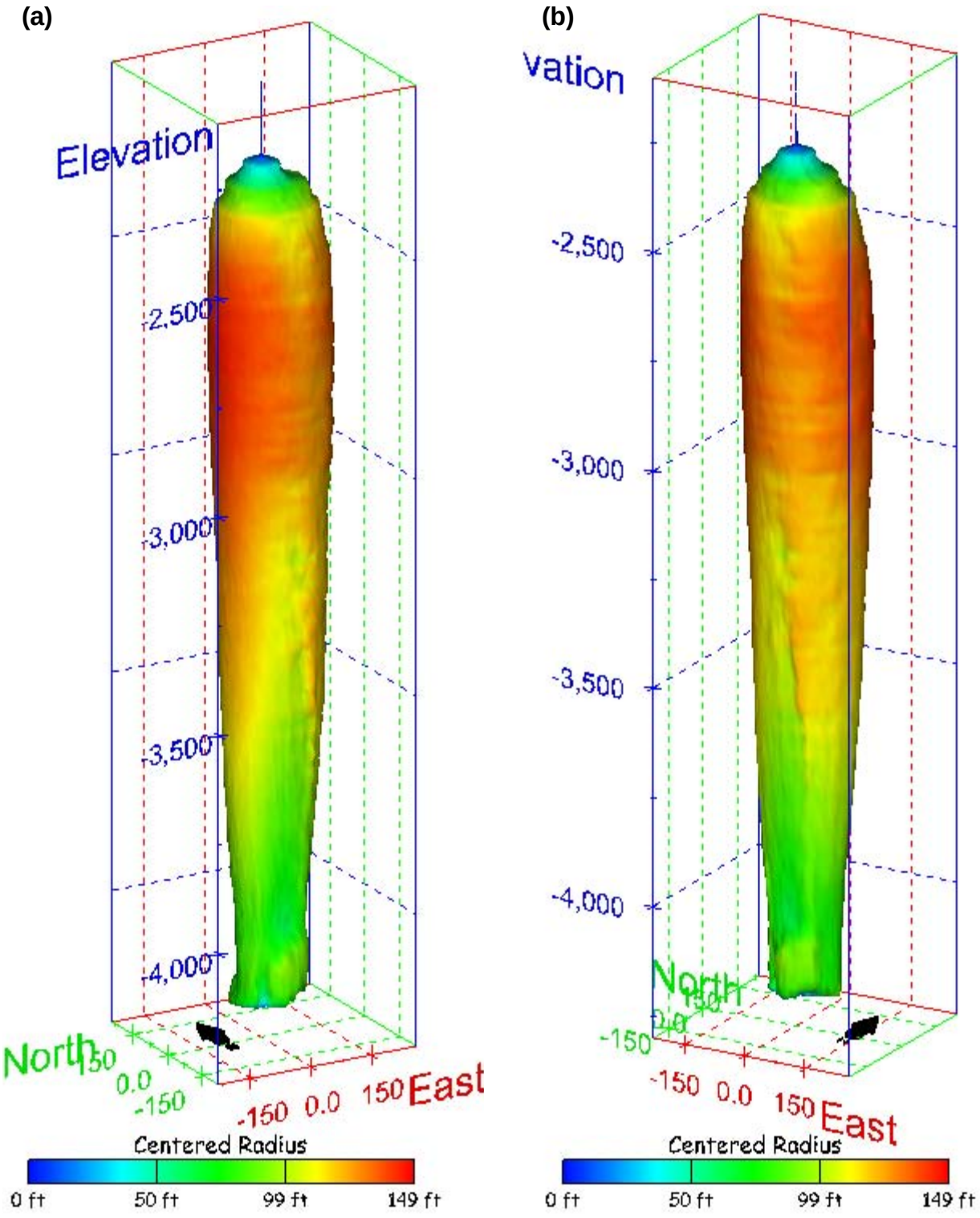

Figure 124. Sonar images of cavern BH-105, showing the geometry of the cavern colored by centered radius. View from (a) azimuth 210°, elevation 20°; (b) azimuth 150°, elevation 20°.

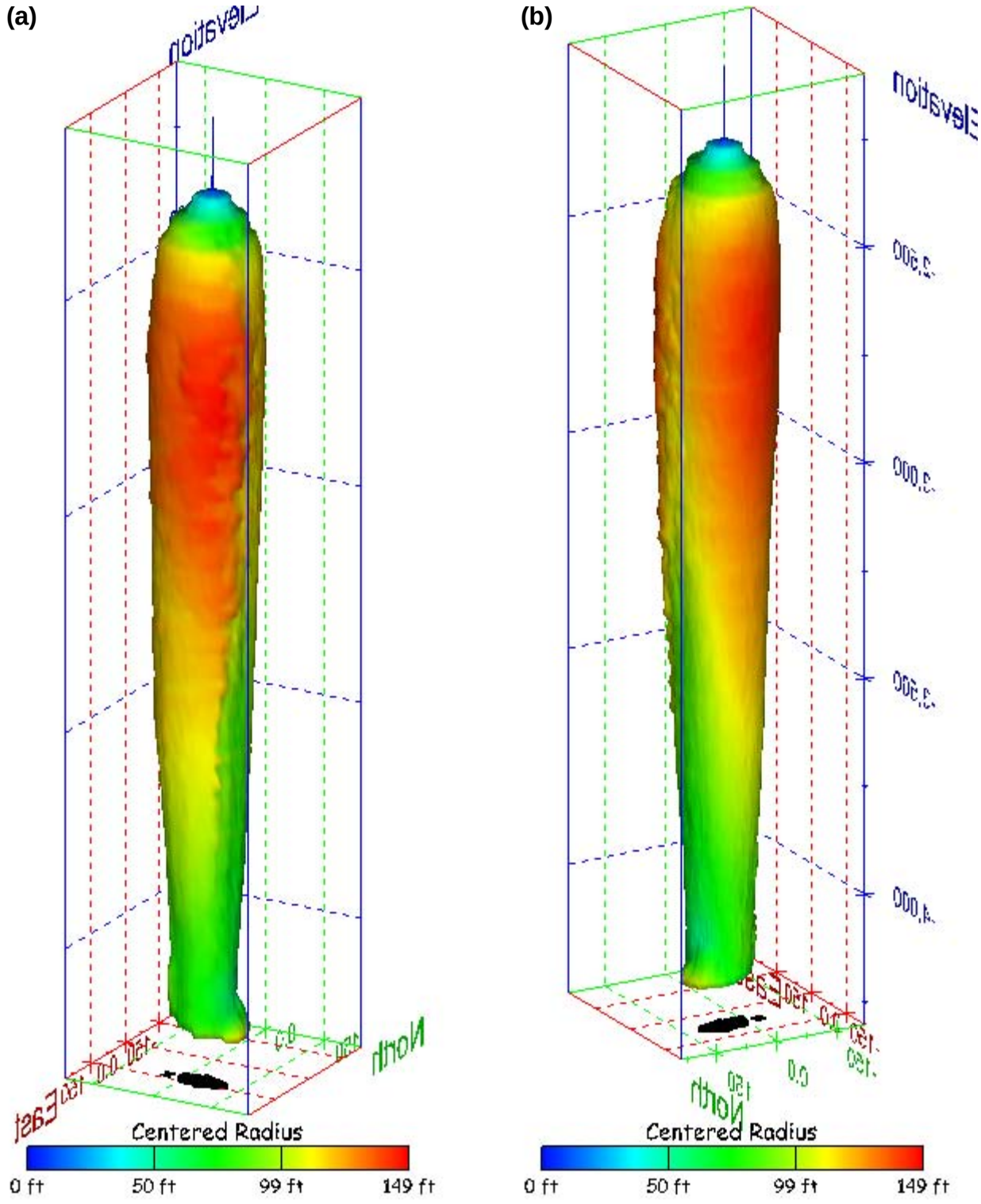

Figure 125. Sonar images of cavern BH-105, showing the geometry of the cavern colored by centered radius. View from (a) azimuth 60°, elevation 20°; (b) azimuth 300°, elevation 20°.

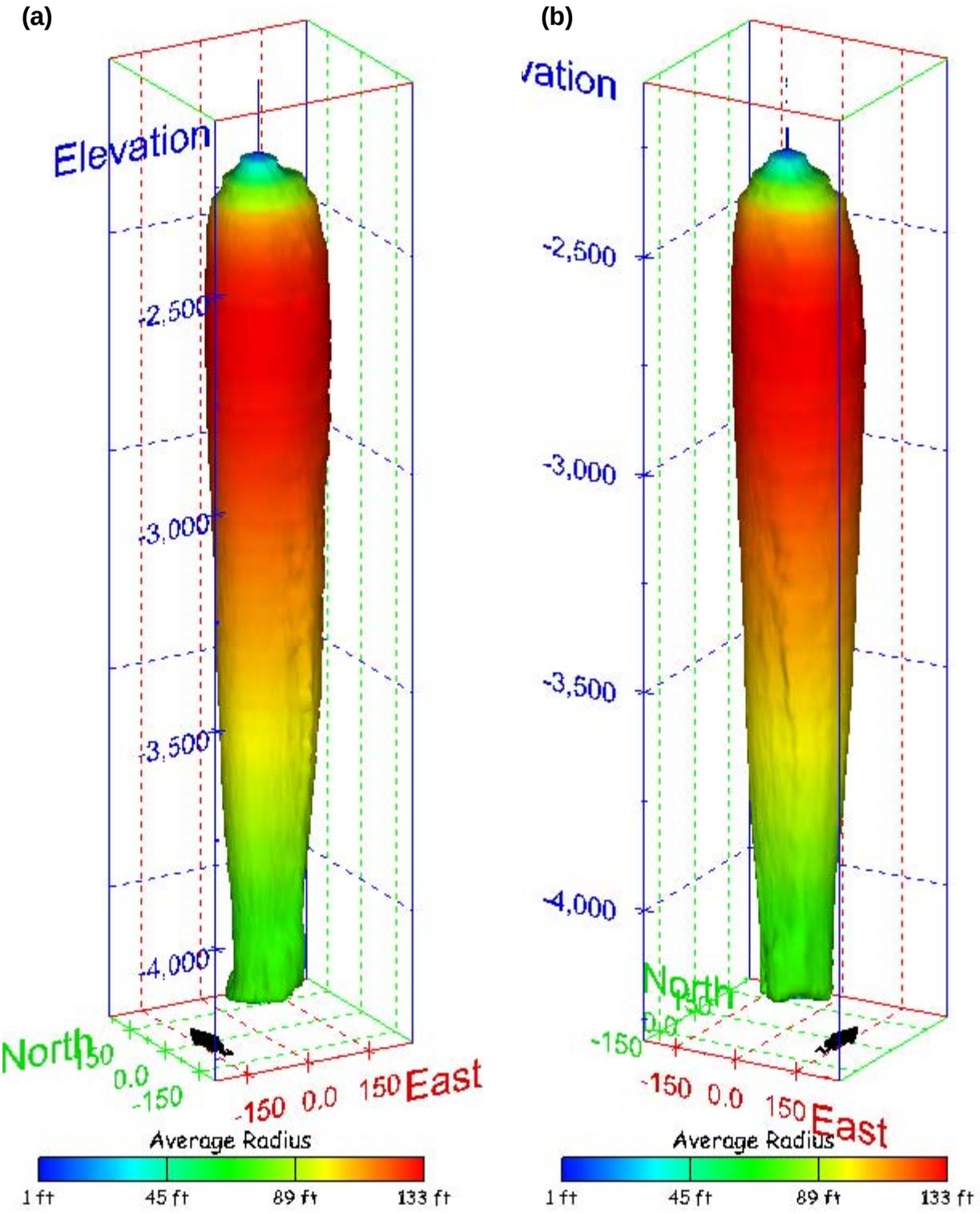

Figure 126. Sonar images of cavern BH-105, showing the geometry of the cavern colored by average radius. View from (a) azimuth 210°, elevation 20°; (b) azimuth 150°, elevation 20°.

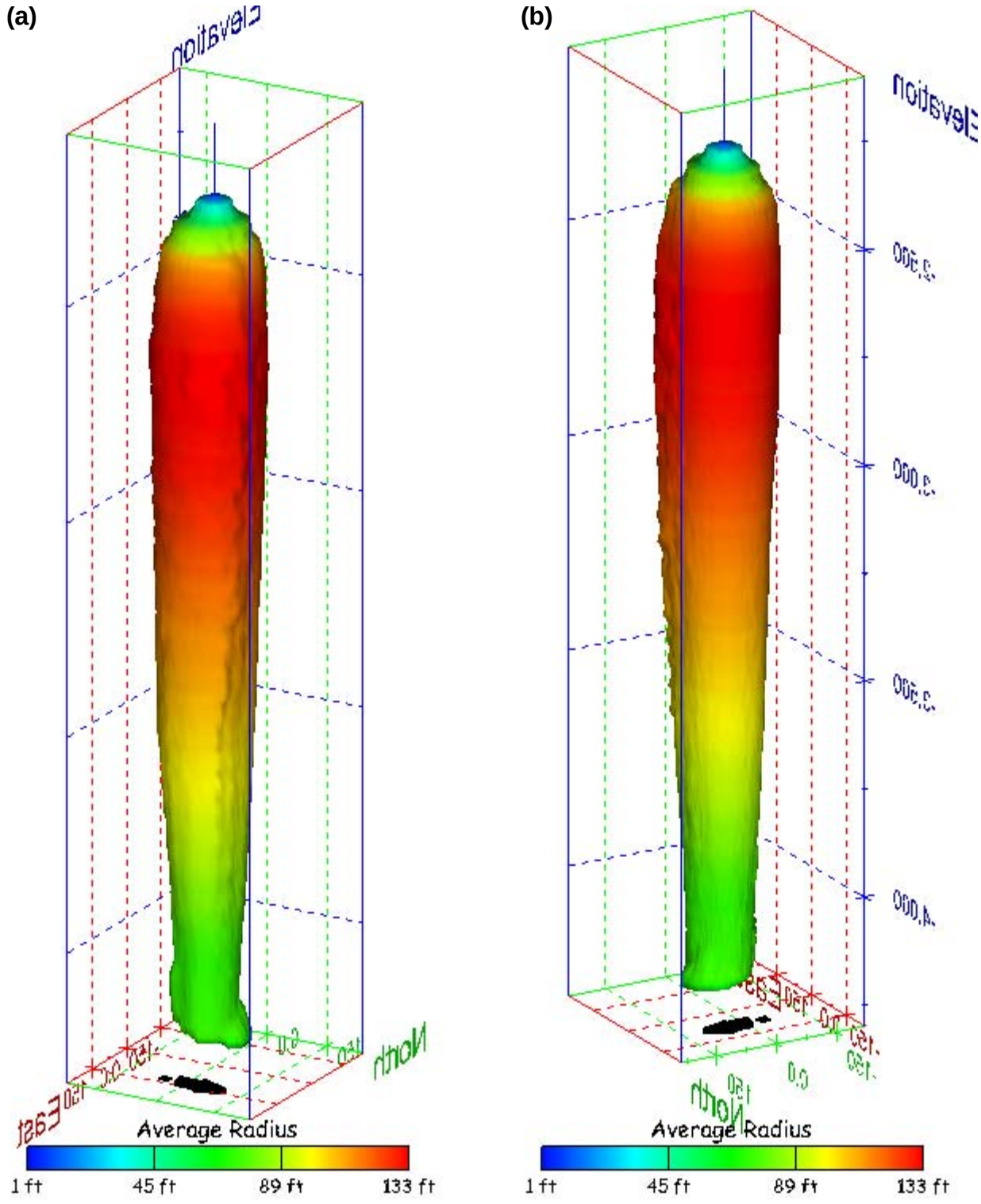

Figure 127. Sonar images of cavern BH-105, showing the geometry of the cavern colored by average radius. View from (a) azimuth 60°, elevation 20°; (b) azimuth 300°, elevation 20°.

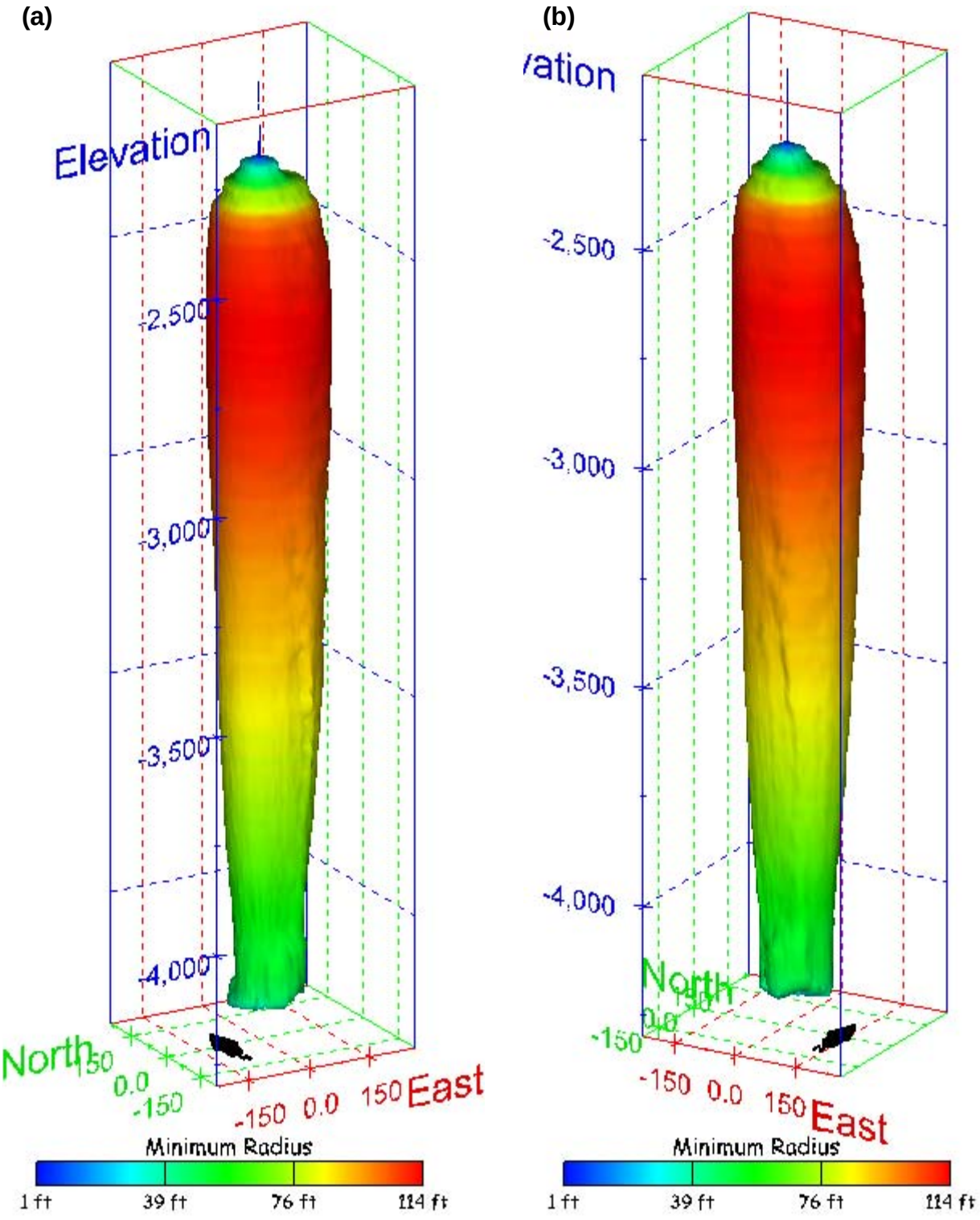

Figure 128. Sonar images of cavern BH-105, showing the geometry of the cavern colored by minimum radius. View from (a) azimuth 210°, elevation 20°; (b) azimuth 150°, elevation 20°.

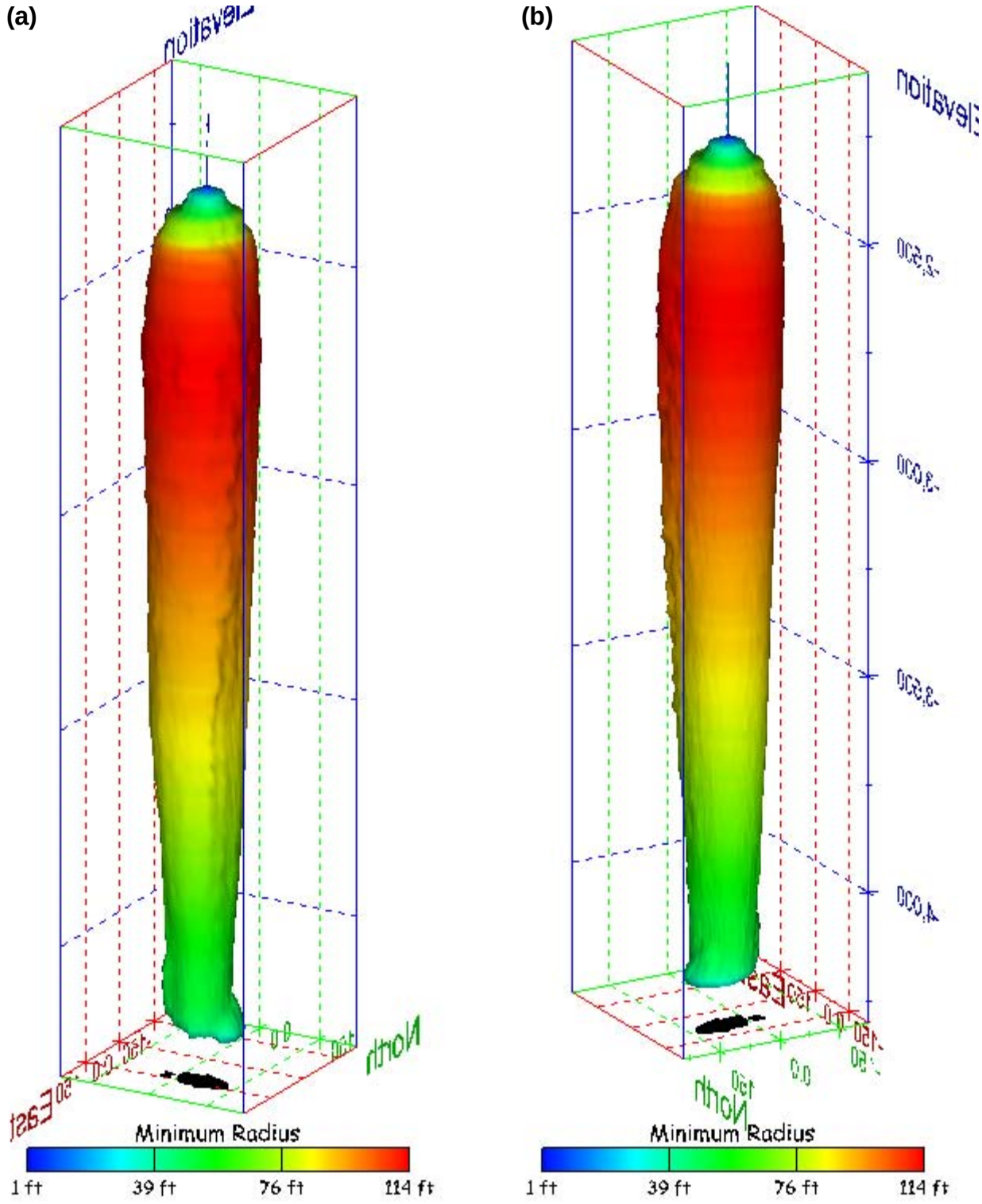

Figure 129. Sonar images of cavern BH-105, showing the geometry of the cavern colored by minimum radius. View from (a) azimuth 60°, elevation 20°; (b) azimuth 300°, elevation 20°.

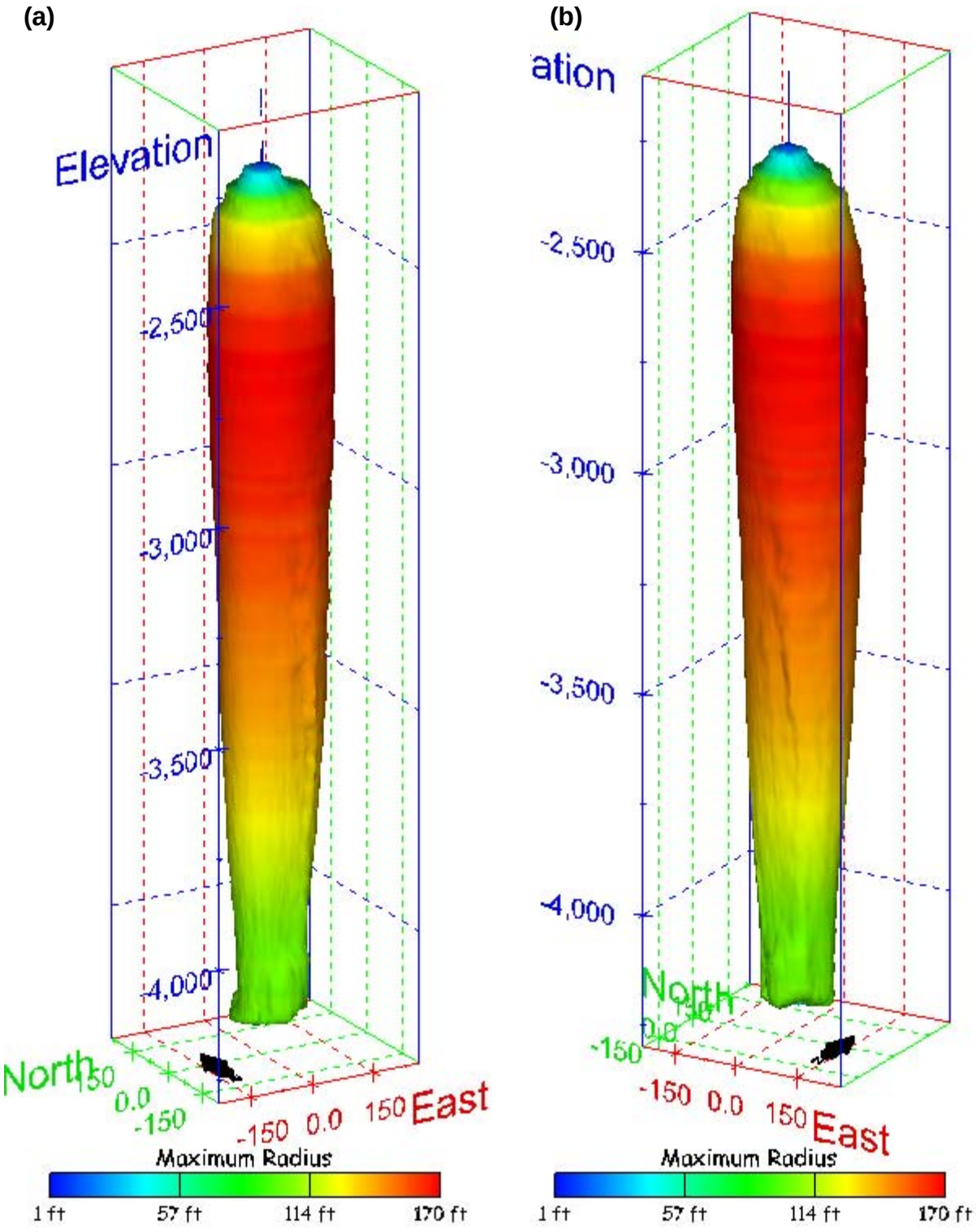

Figure 130. Sonar images of cavern BH-105, showing the geometry of the cavern colored by maximum radius. View from (a) azimuth 210°, elevation 20°; (b) azimuth 150°, elevation 20°.

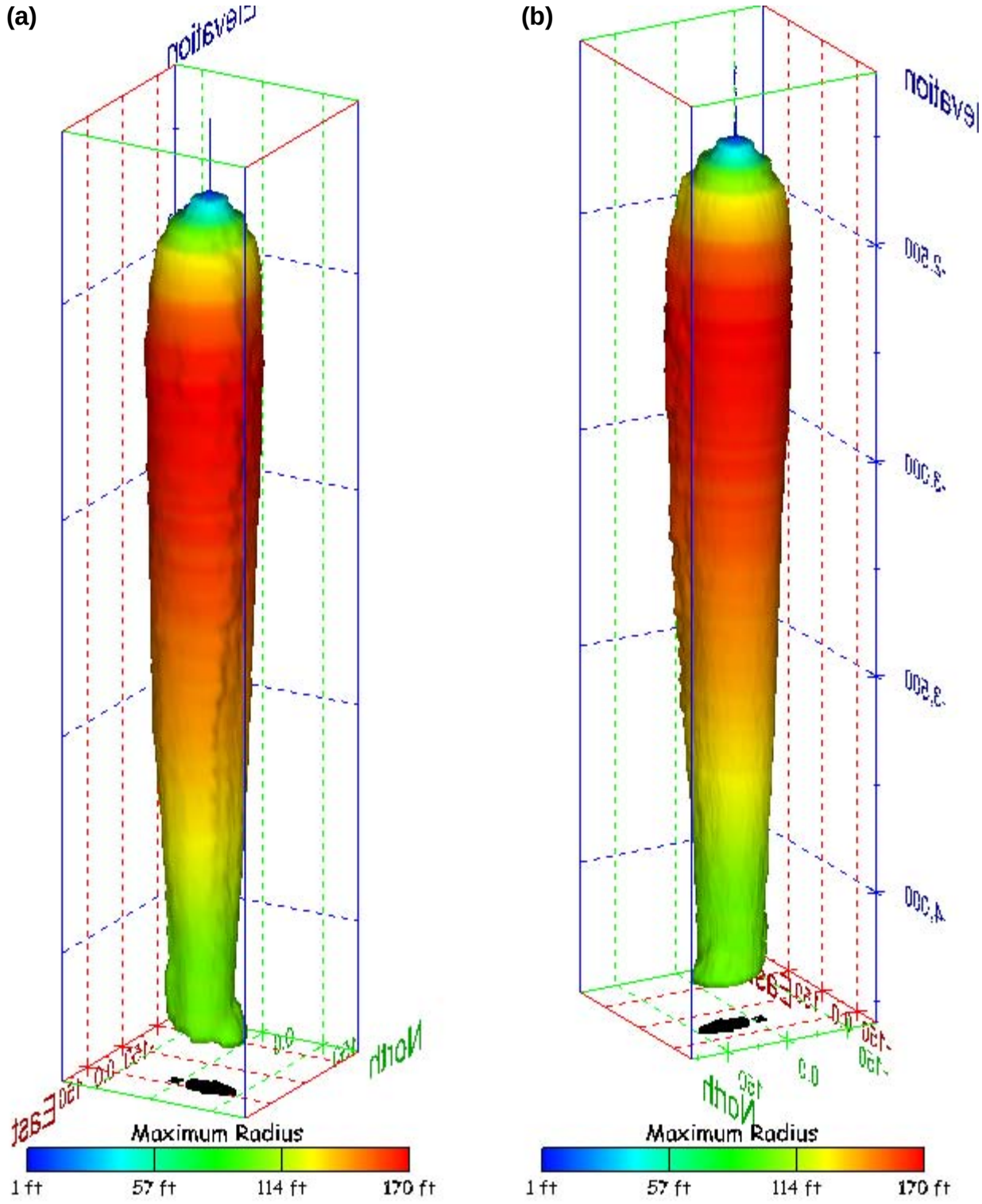

Figure 131. Sonar images of cavern BH-105, showing the geometry of the cavern colored by maximum radius. View from (a) azimuth 60°, elevation 20°; (b) azimuth 300°, elevation 20°.

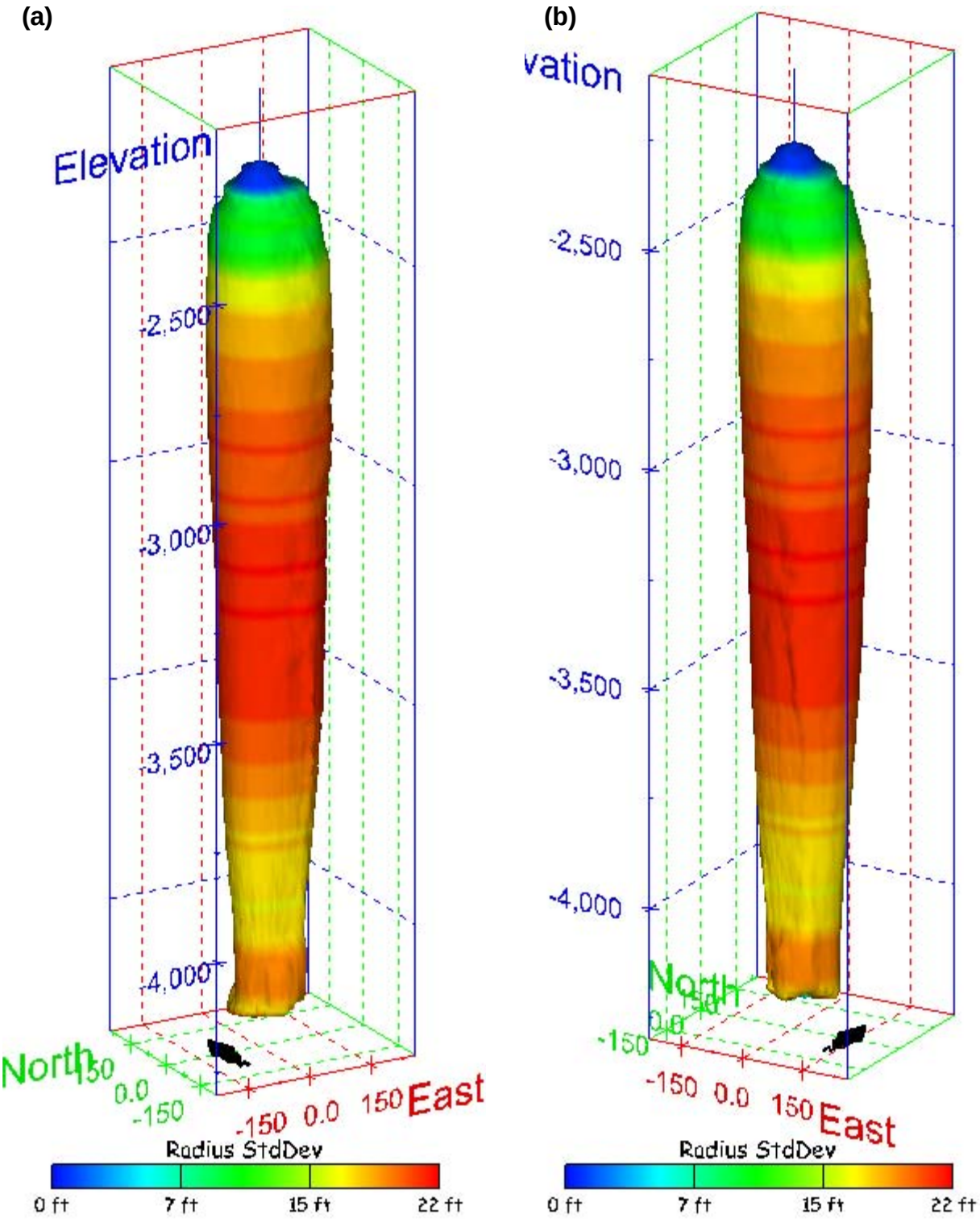

Figure 132. Sonar images of cavern BH-105, showing the geometry of the cavern colored by radius standard deviation. View from (a) azimuth 210°, elevation 20°; (b) azimuth 150°, elevation 20°.

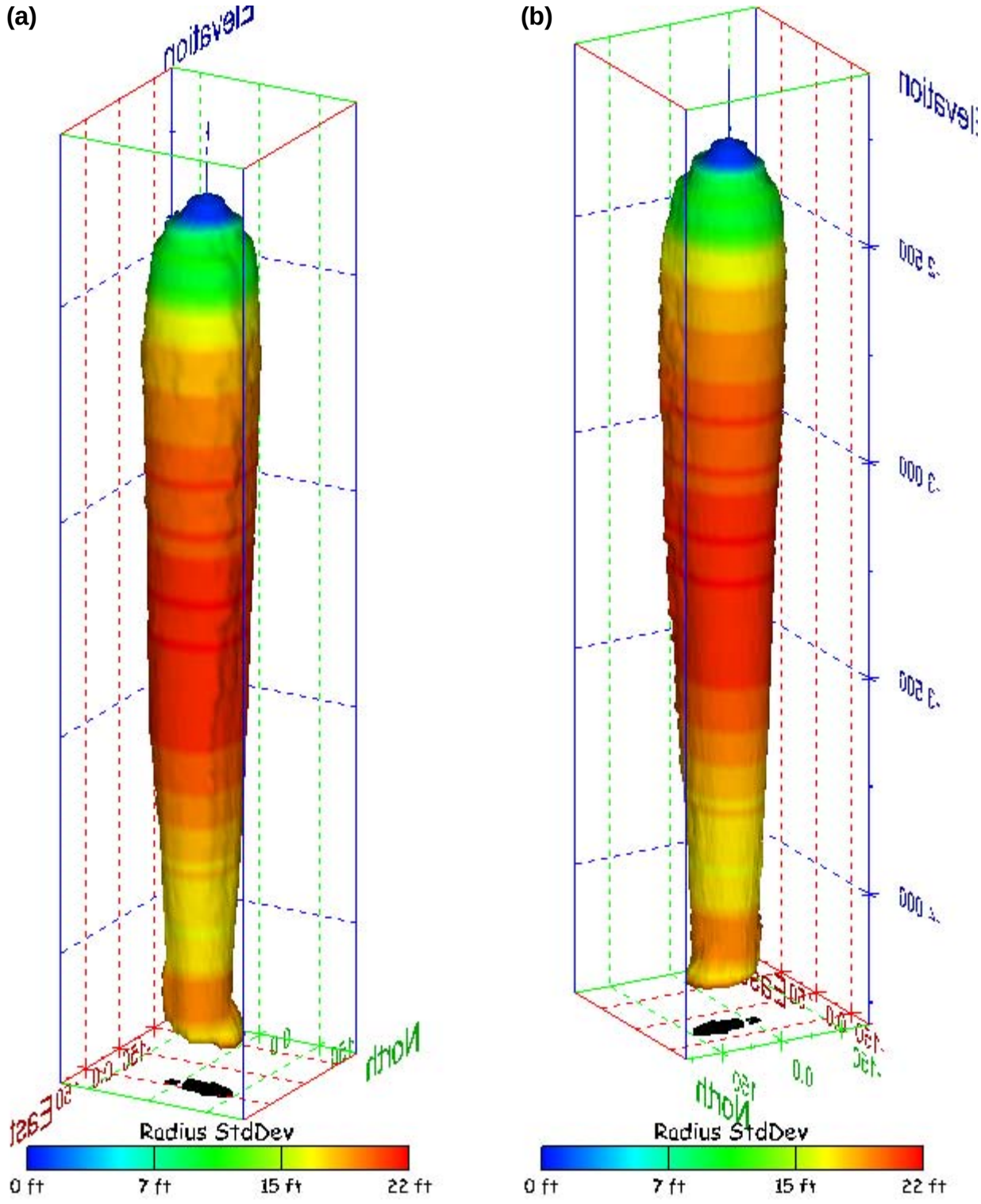

Figure 133. Sonar images of cavern BH-105, showing the geometry of the cavern colored by radius standard deviation. View from (a) azimuth 60°, elevation 20°; (b) azimuth 300°, elevation 20°.

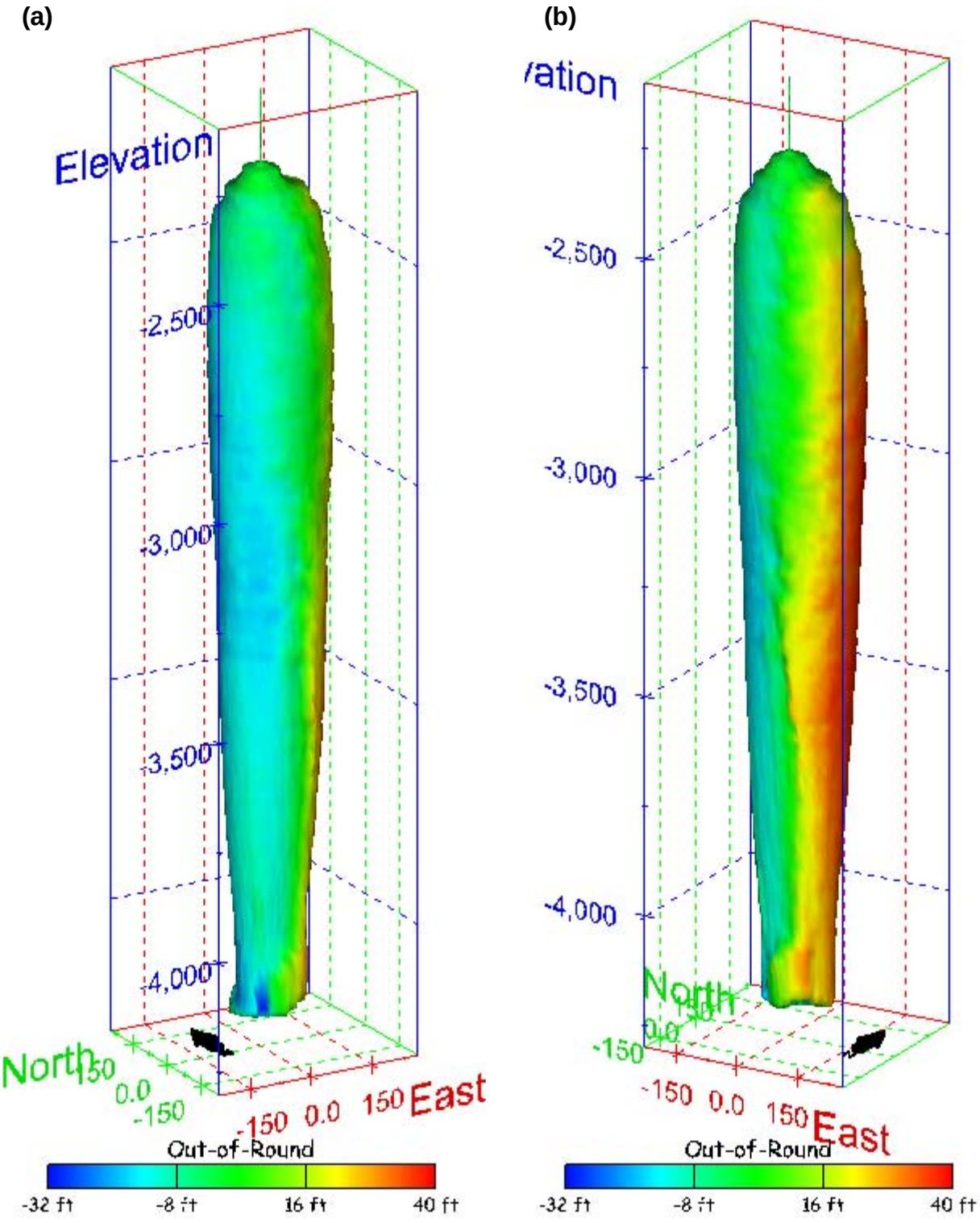

Figure 134. Sonar images of cavern BH-105, showing the geometry of the cavern colored by out-of-round distance. View from (a) azimuth 210°, elevation 20°; (b) azimuth 150°, elevation 20°.

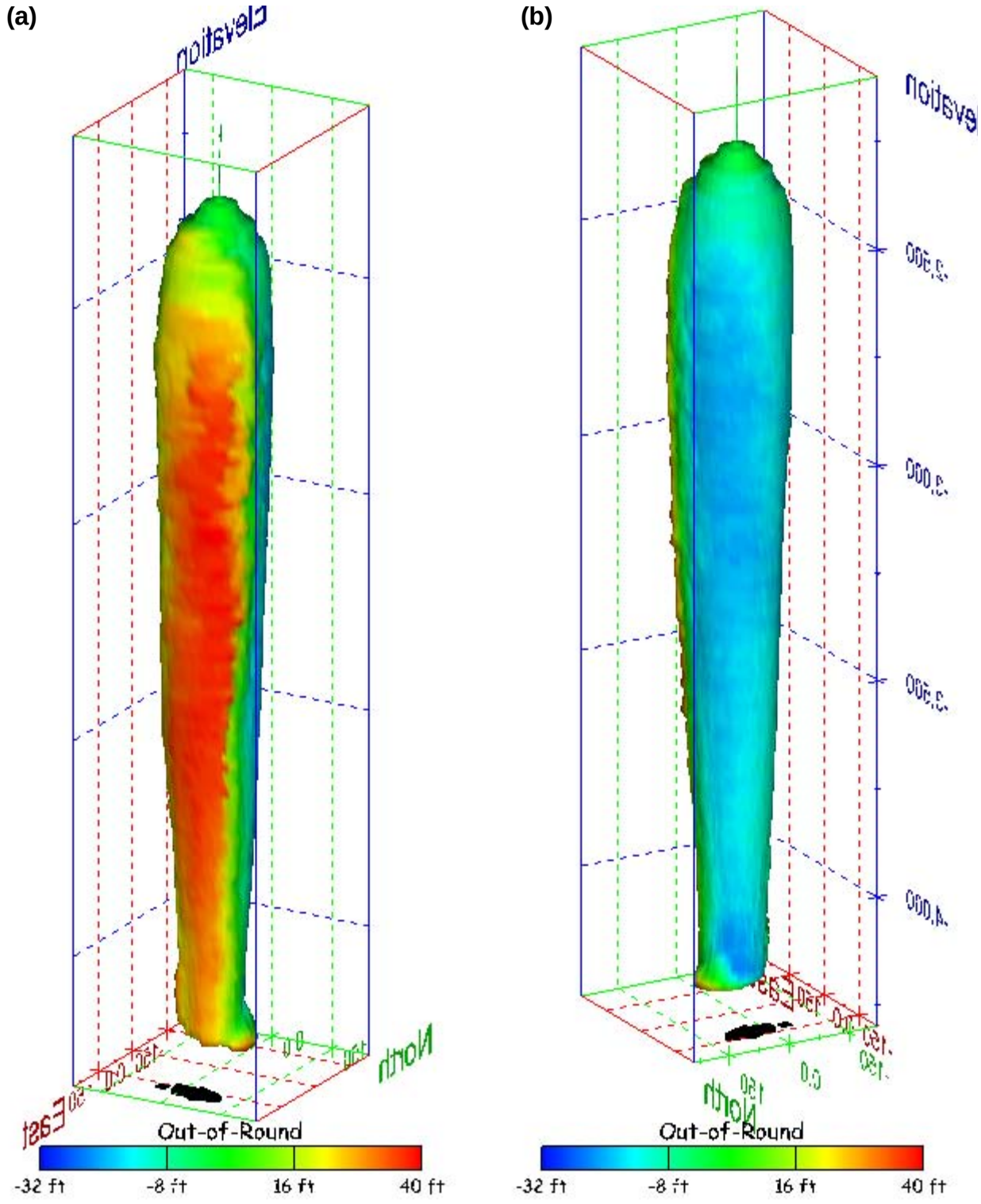

Figure 135. Sonar images of cavern BH-105, showing the geometry of the cavern colored by out-of-round distance. View from (a) azimuth 60°, elevation 20°; (b) azimuth 300°, elevation 20°.

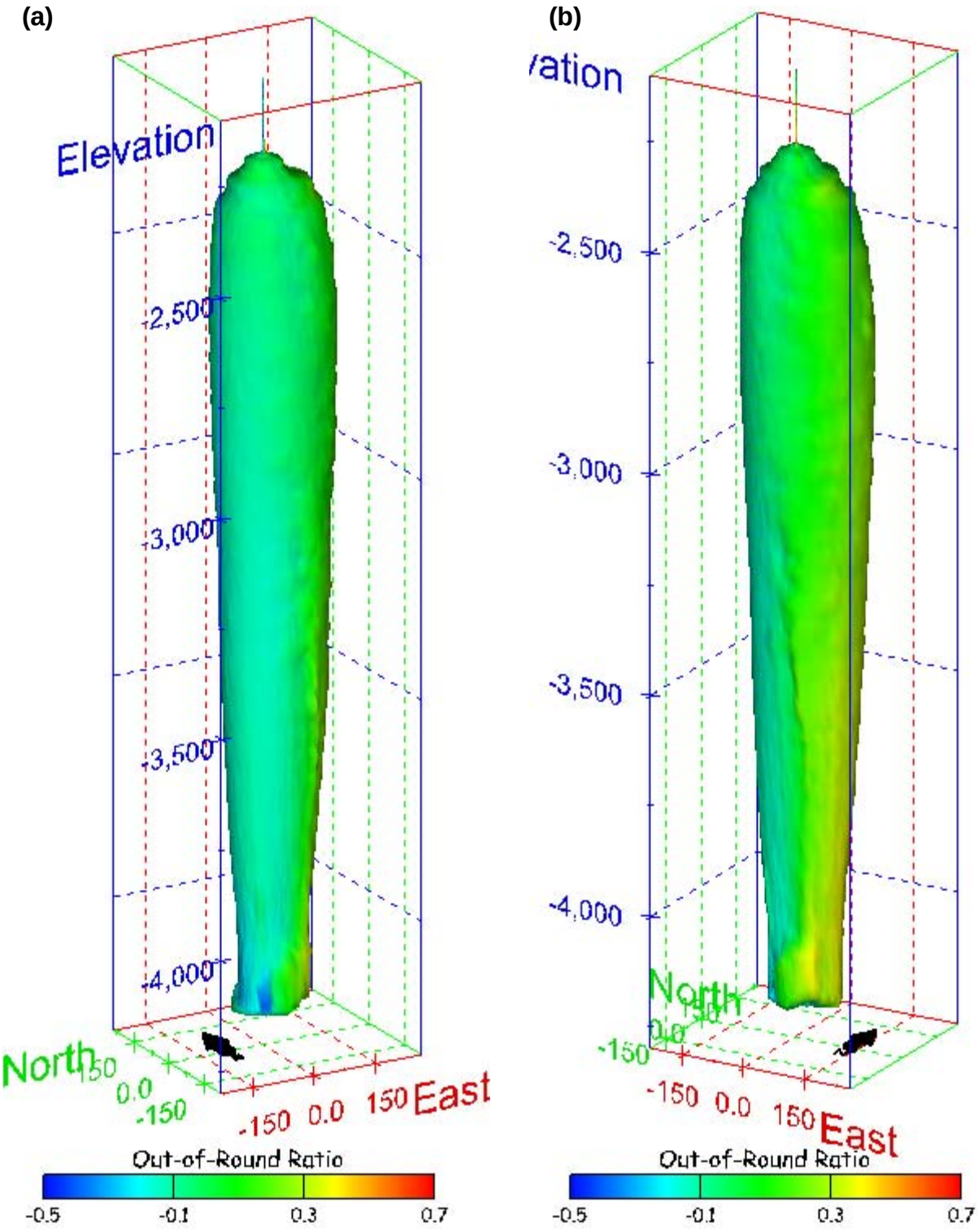

Figure 136. Sonar images of cavern BH-105, showing the geometry of the cavern colored by out-of-round ratio. View from (a) azimuth 210°, elevation 20°; (b) azimuth 150°, elevation 20°.

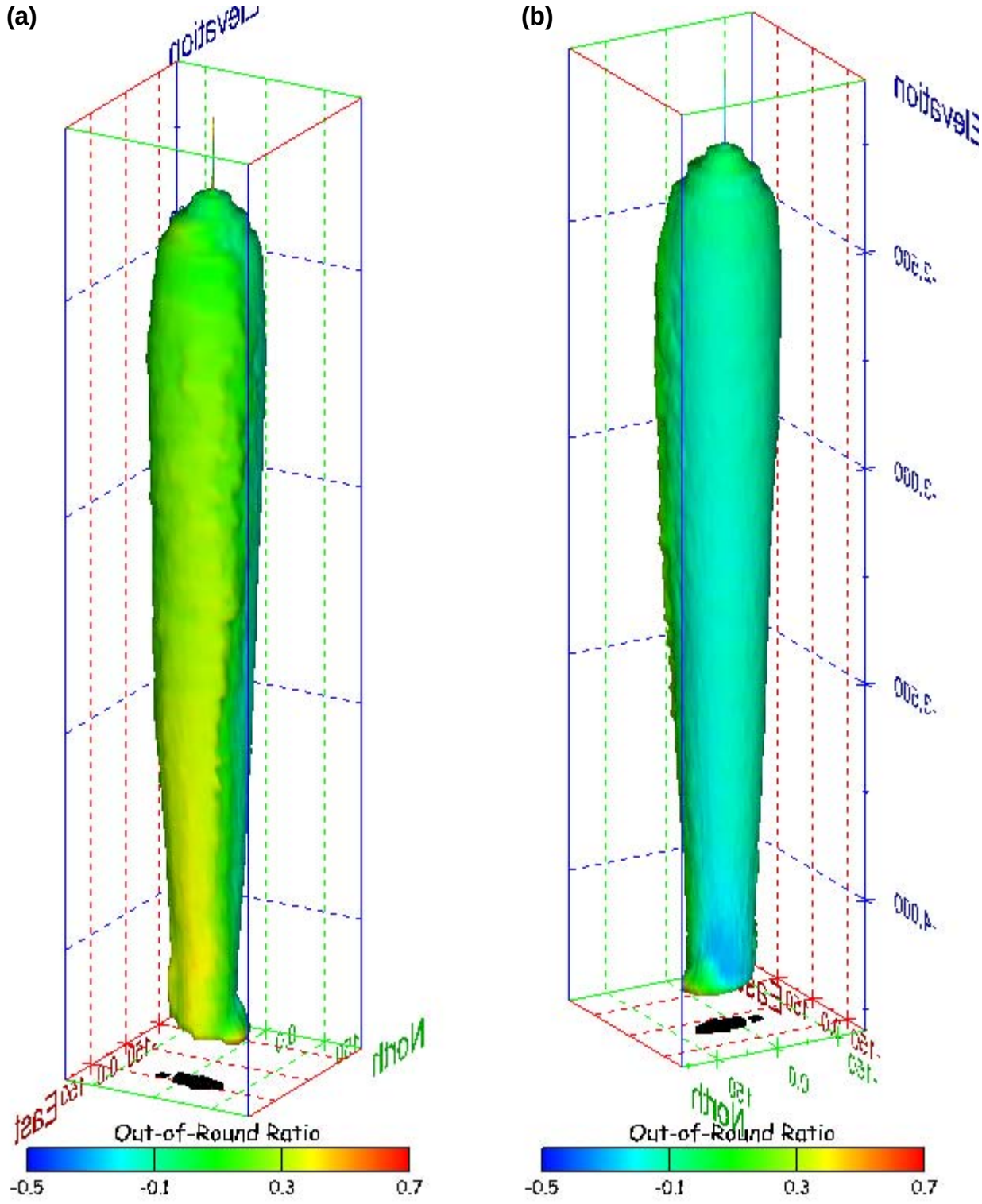

Figure 137. Sonar images of cavern BH-105, showing the geometry of the cavern colored by out-of-round ratio. View from (a) azimuth 60°, elevation 20°; (b) azimuth 300°, elevation 20°.

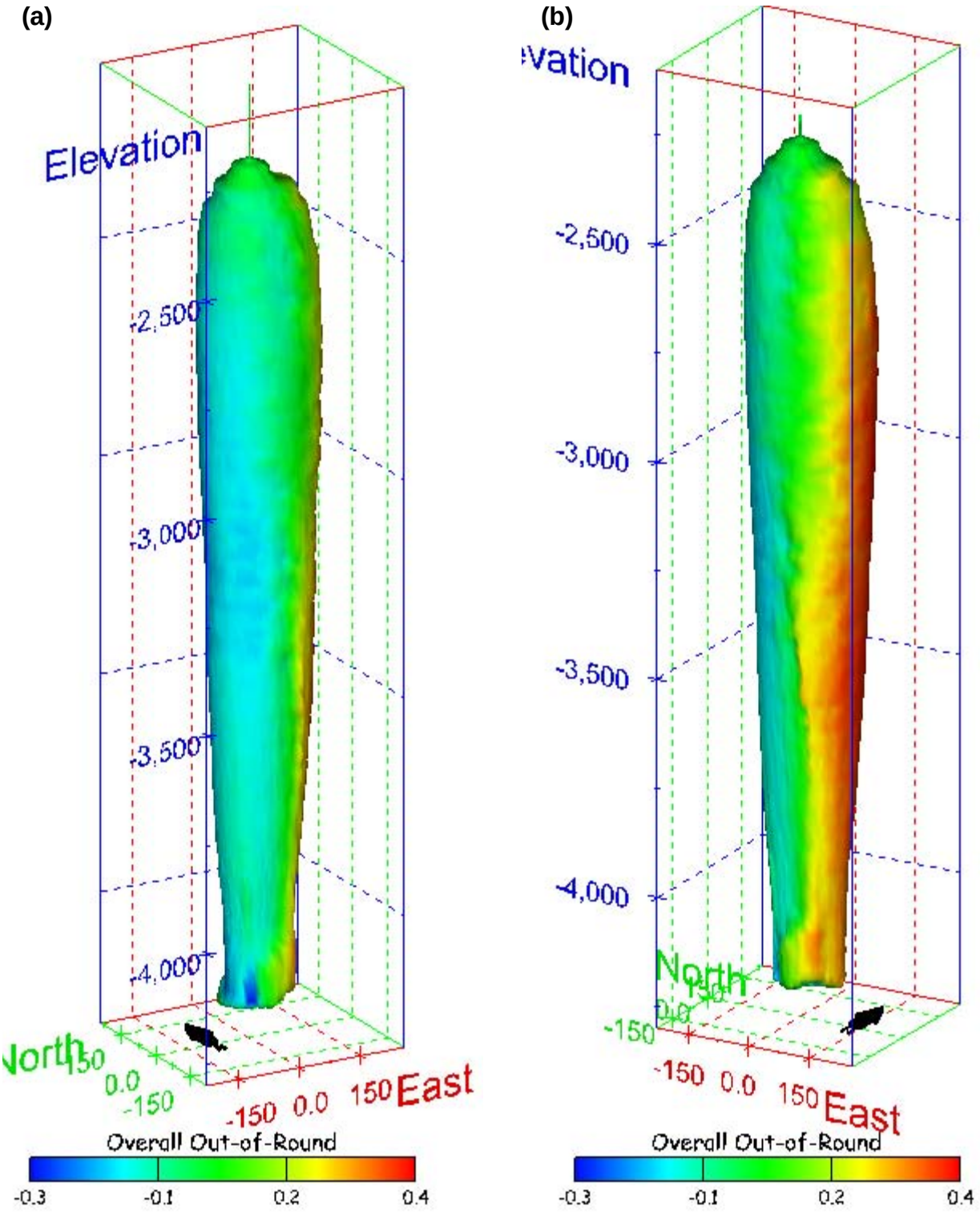

Figure 138. Sonar images of cavern BH-105, showing the geometry of the cavern colored by overall out-of-round ratio. View from (a) azimuth 210°, elevation 20°; (b) azimuth 150°, elevation 20°.

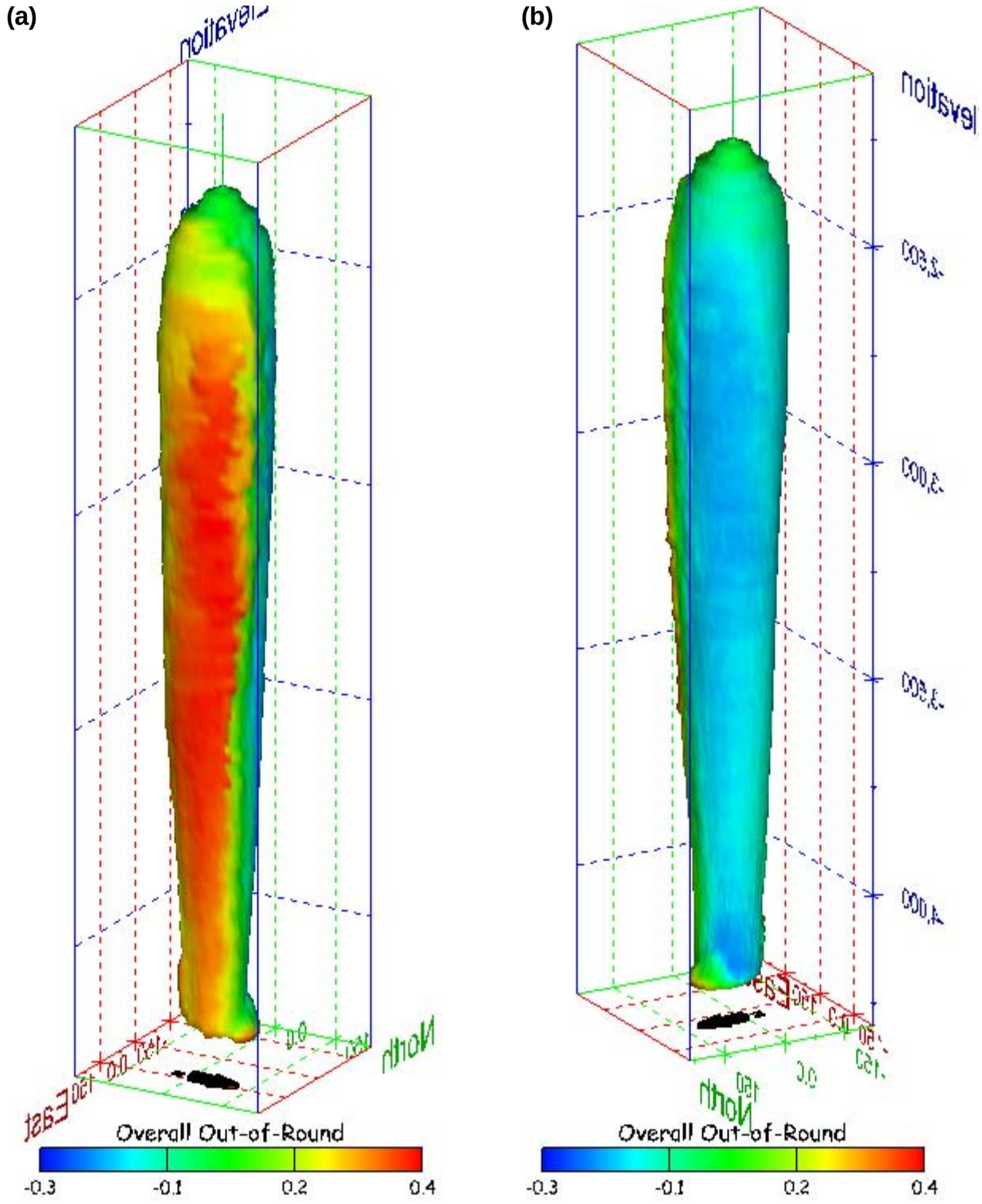

Figure 139. Sonar images of cavern BH-105, showing the geometry of the cavern colored by overall out-of-round ratio. View from (a) azimuth 60°, elevation 20°; (b) azimuth 300°, elevation 20°.

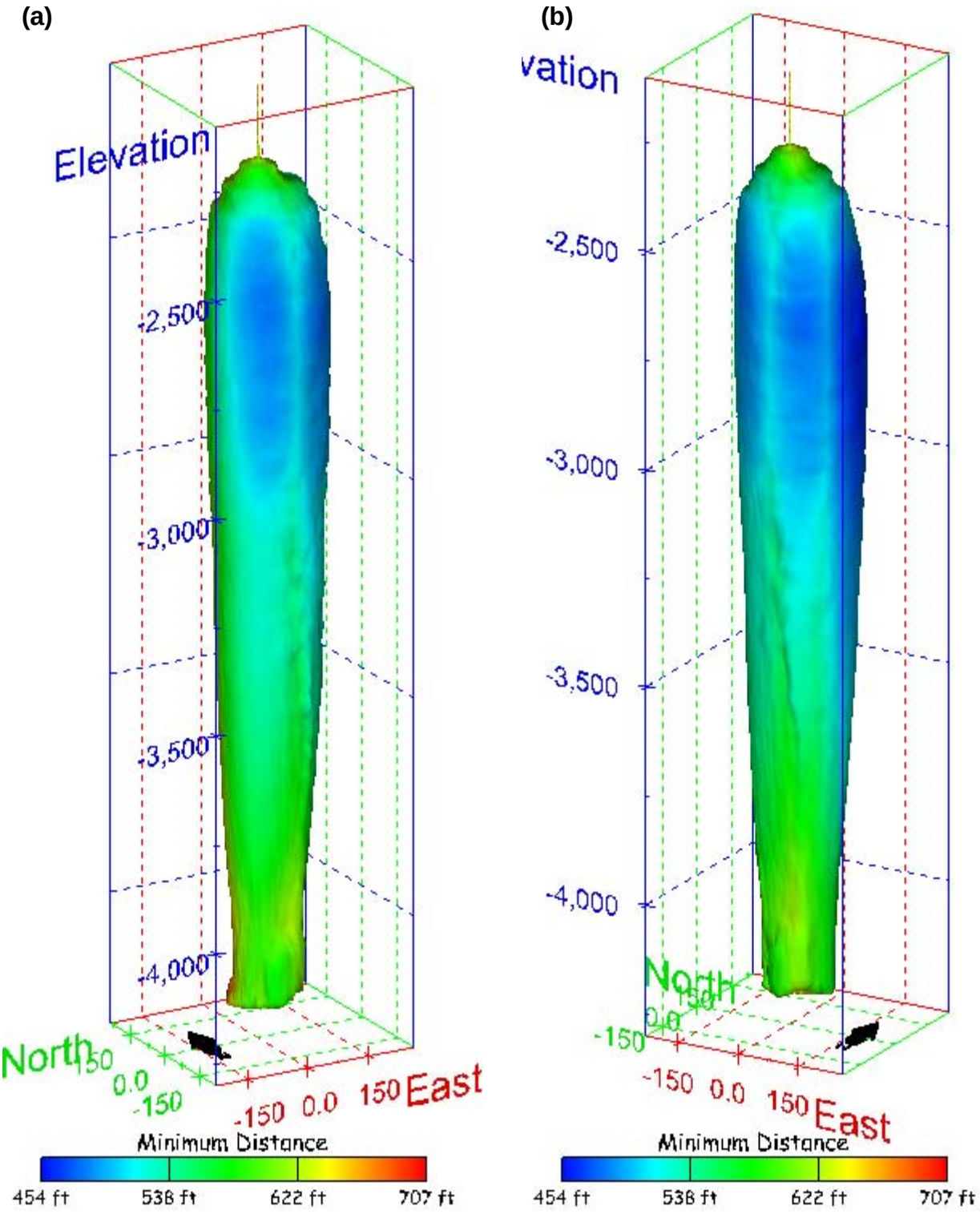

Figure 140. Sonar images of cavern BH-105, showing the geometry of the cavern colored by the minimum distance to the nearest neighboring cavern. View from (a) azimuth 210°, elevation 20°; (b) azimuth 150°, elevation 20°.

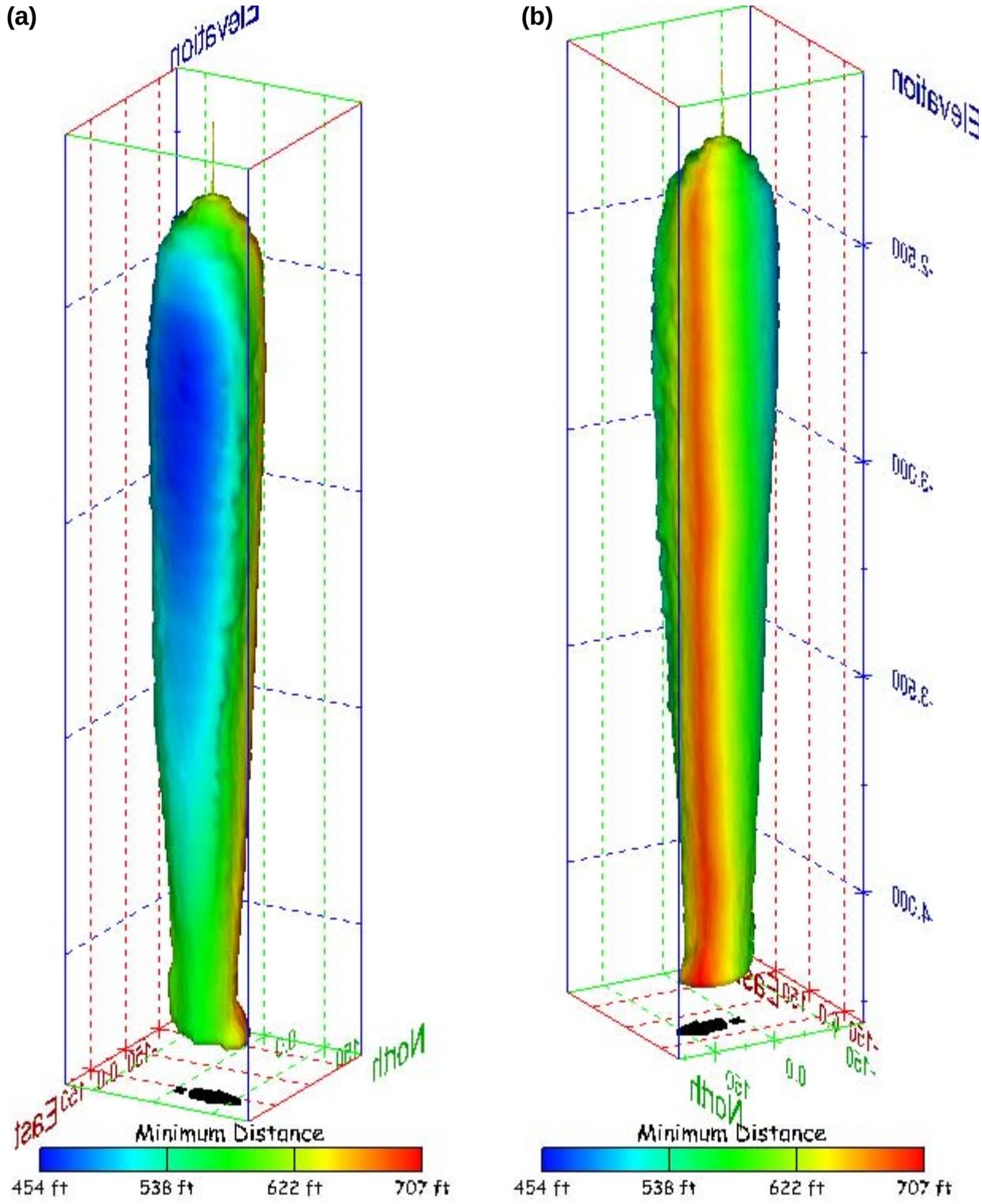

Figure 141. Sonar images of cavern BH-105, showing the geometry of the cavern colored by minimum distance to the nearest neighboring cavern. View from (a) azimuth 60°, elevation 20°; (b) azimuth 300°, elevation 20°.

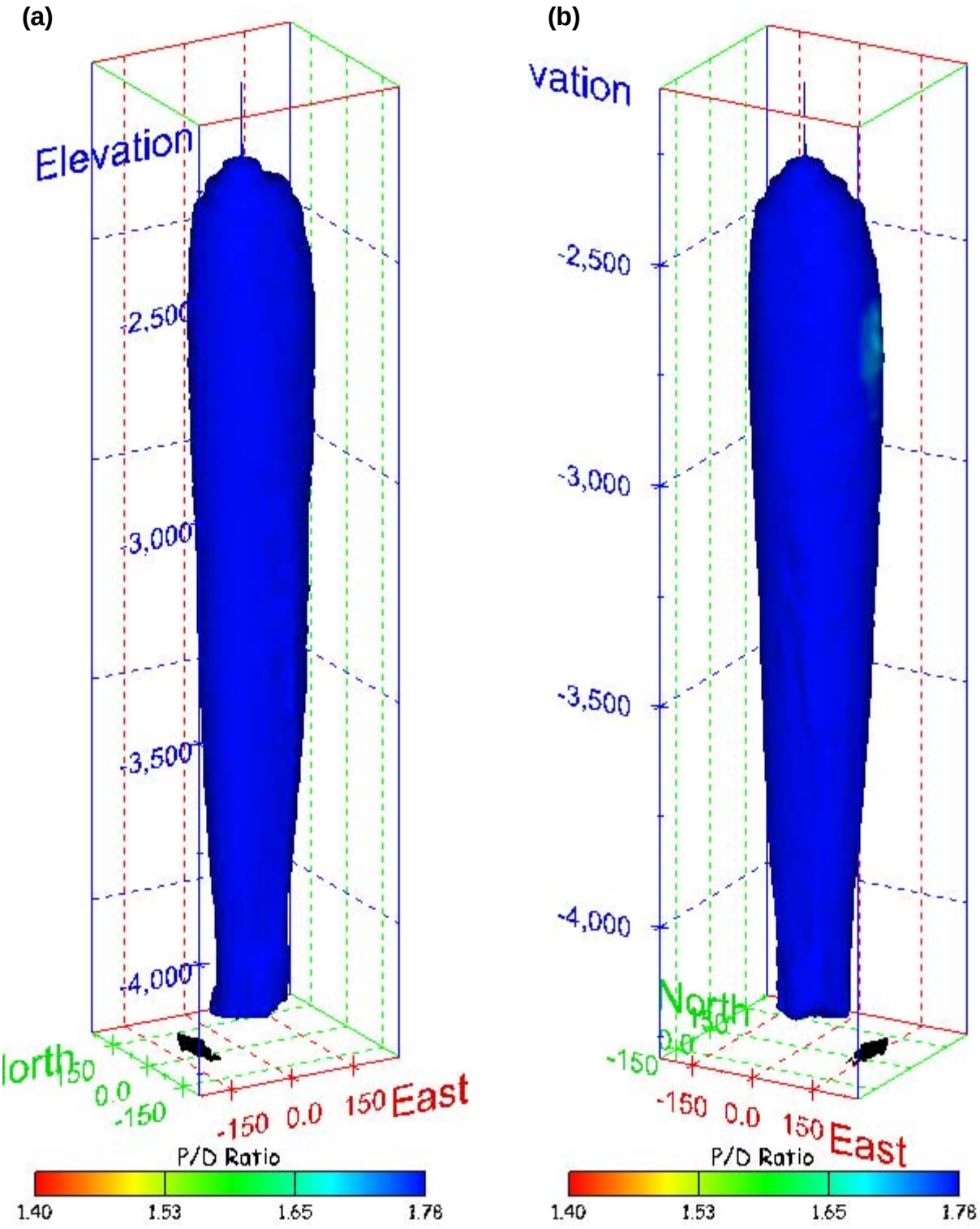

Figure 142. Sonar images of cavern BH-105, showing the geometry of the cavern colored by three-dimensional pillar-to-diameter ratio. View from (a) azimuth 210°, elevation 20°; (b) azimuth 150°, elevation 20°.

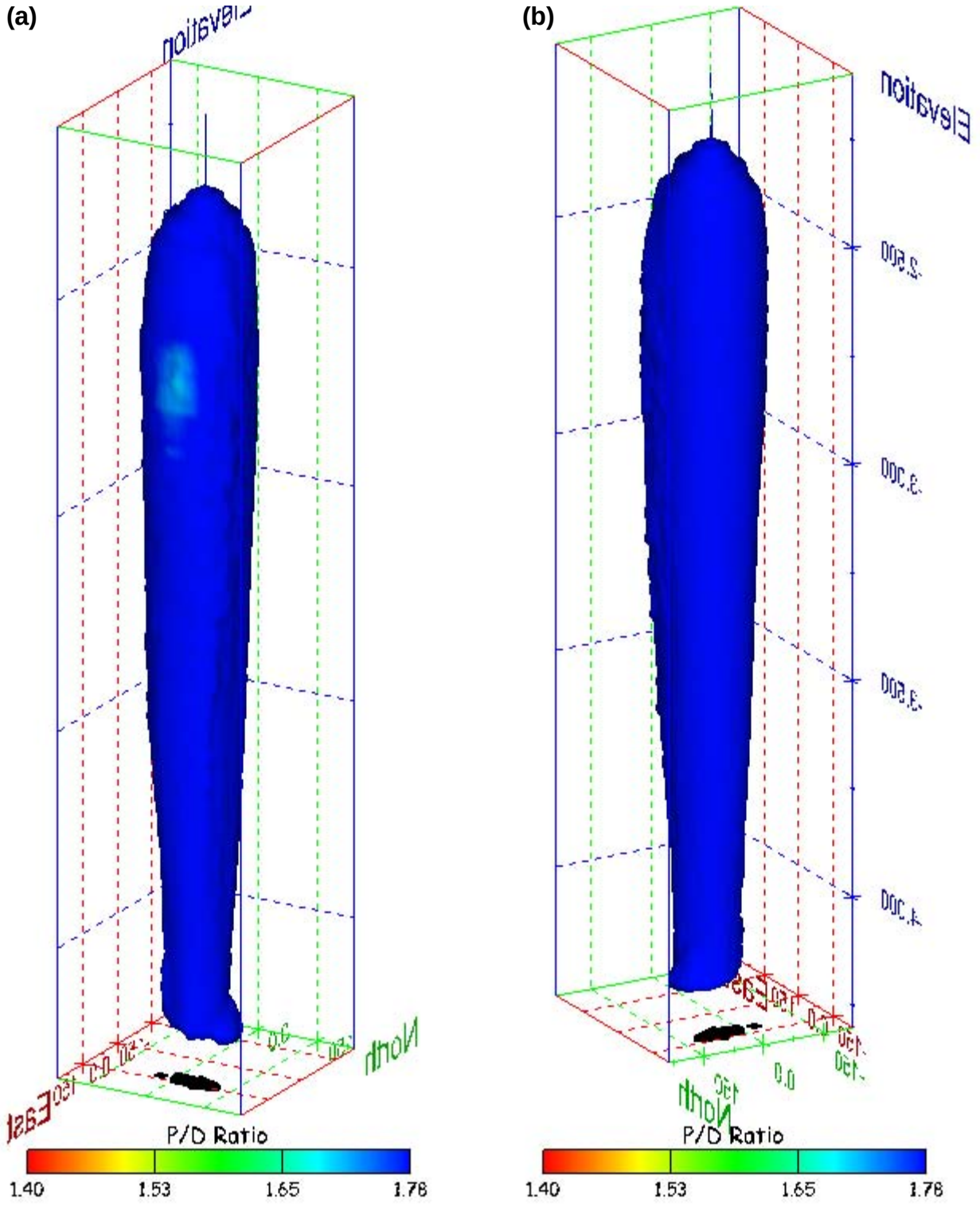

Figure 143. Sonar images of cavern BH-105, showing the geometry of the cavern colored by three-dimensional pillar-to-diameter ratio. View from (a) azimuth 60°, elevation 20°; (b) azimuth 300°, elevation 20°.

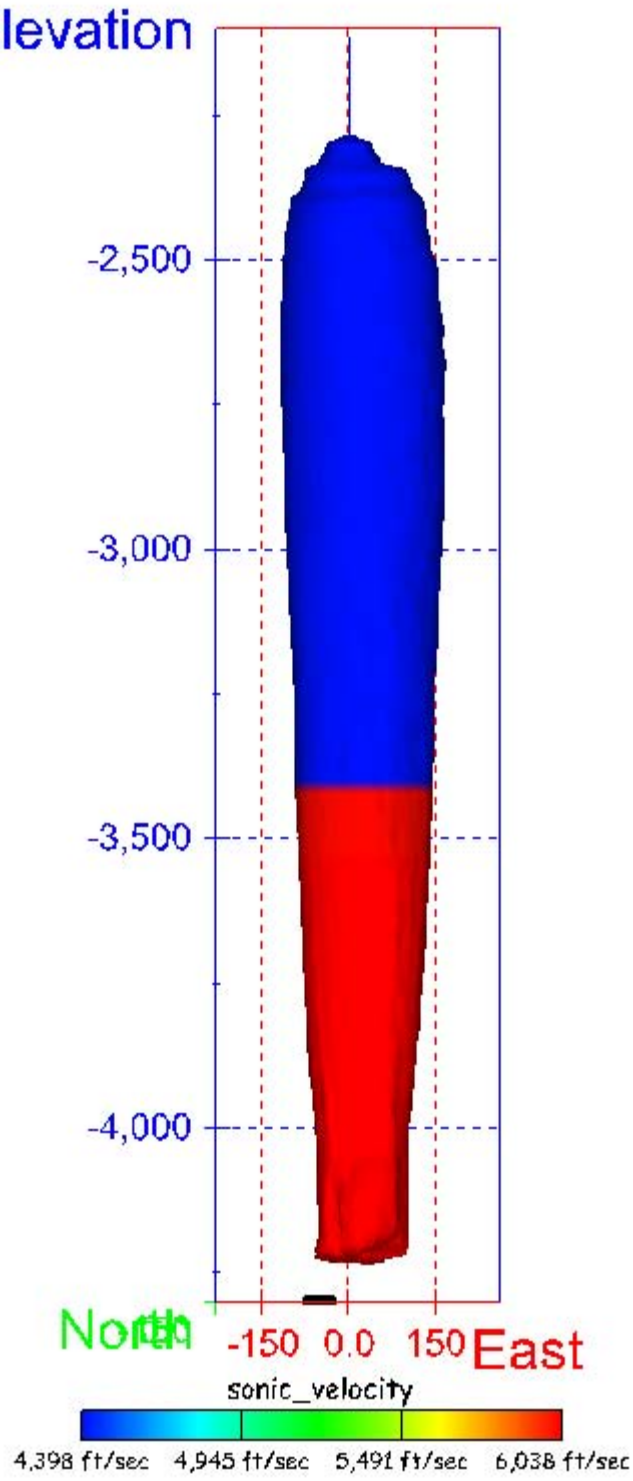

Figure 144. Sonar image of cavern BH-105, showing the geometry of the cavern colored by the reported velocity of sound on the survey date of March 1999. View from due south, elevation zero.

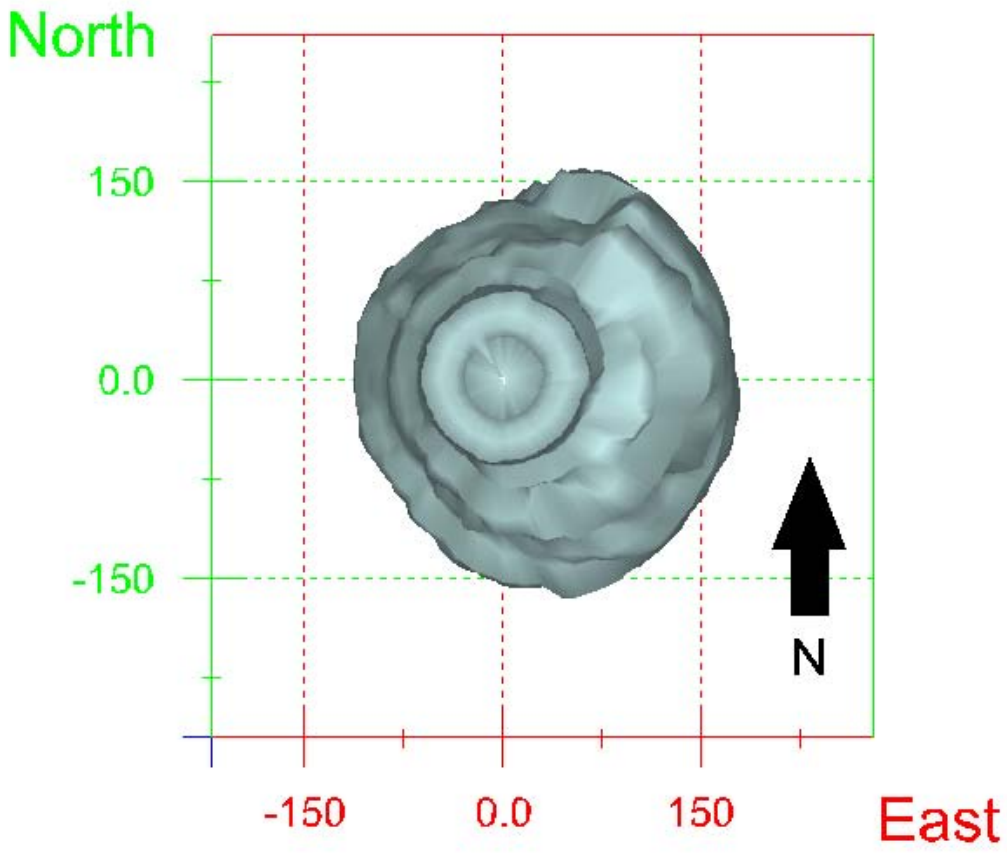

Figure 145. Map view sonar image of cavern BH-106, showing the basic geometry of the cavern. Grid squares represent 150 ft.

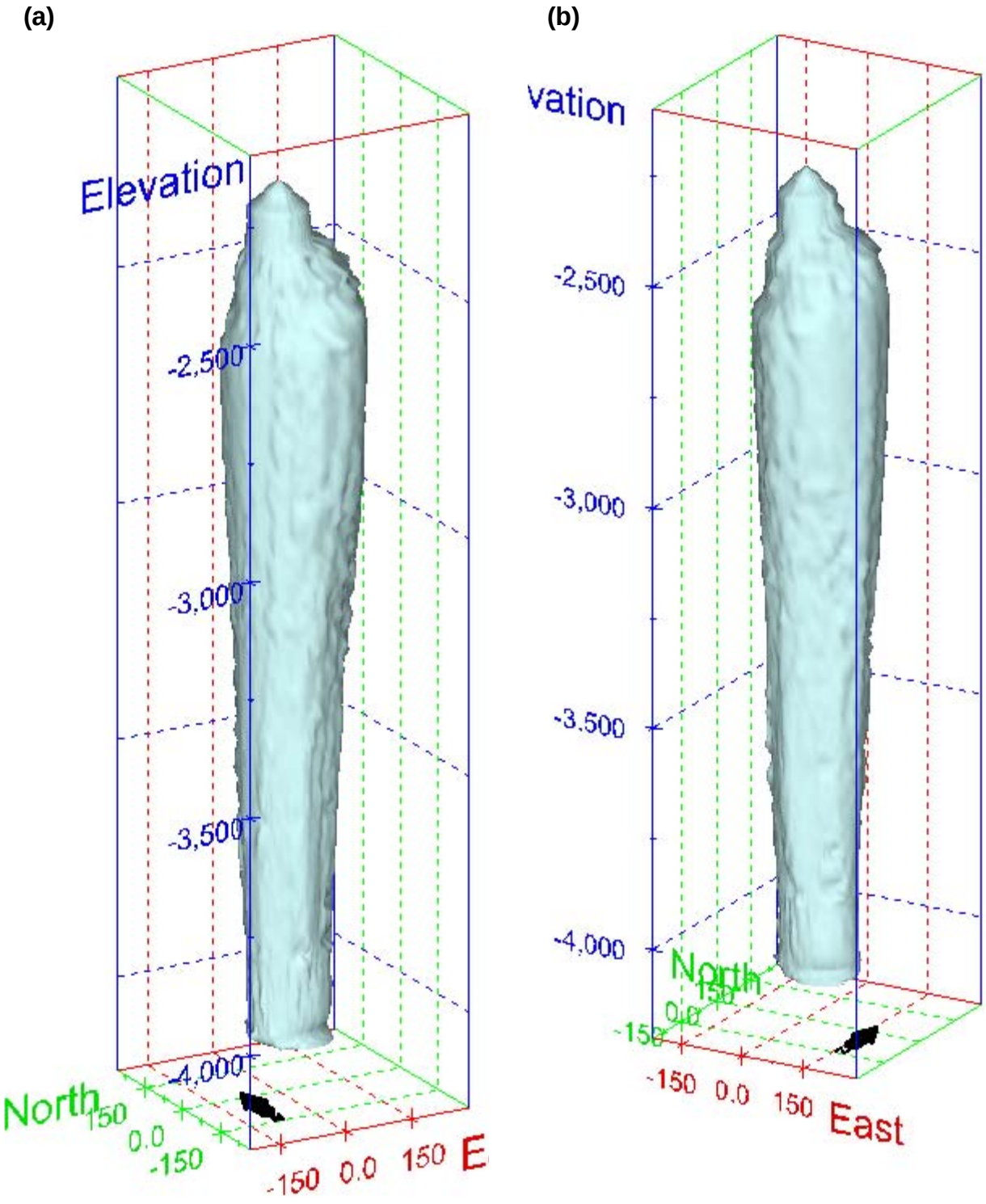

Figure 146. Sonar images of cavern BH-106, showing the basic geometric shape of the cavern. View from (a) azimuth 210°, elevation 20°; (b) azimuth 150°, elevation 20°.

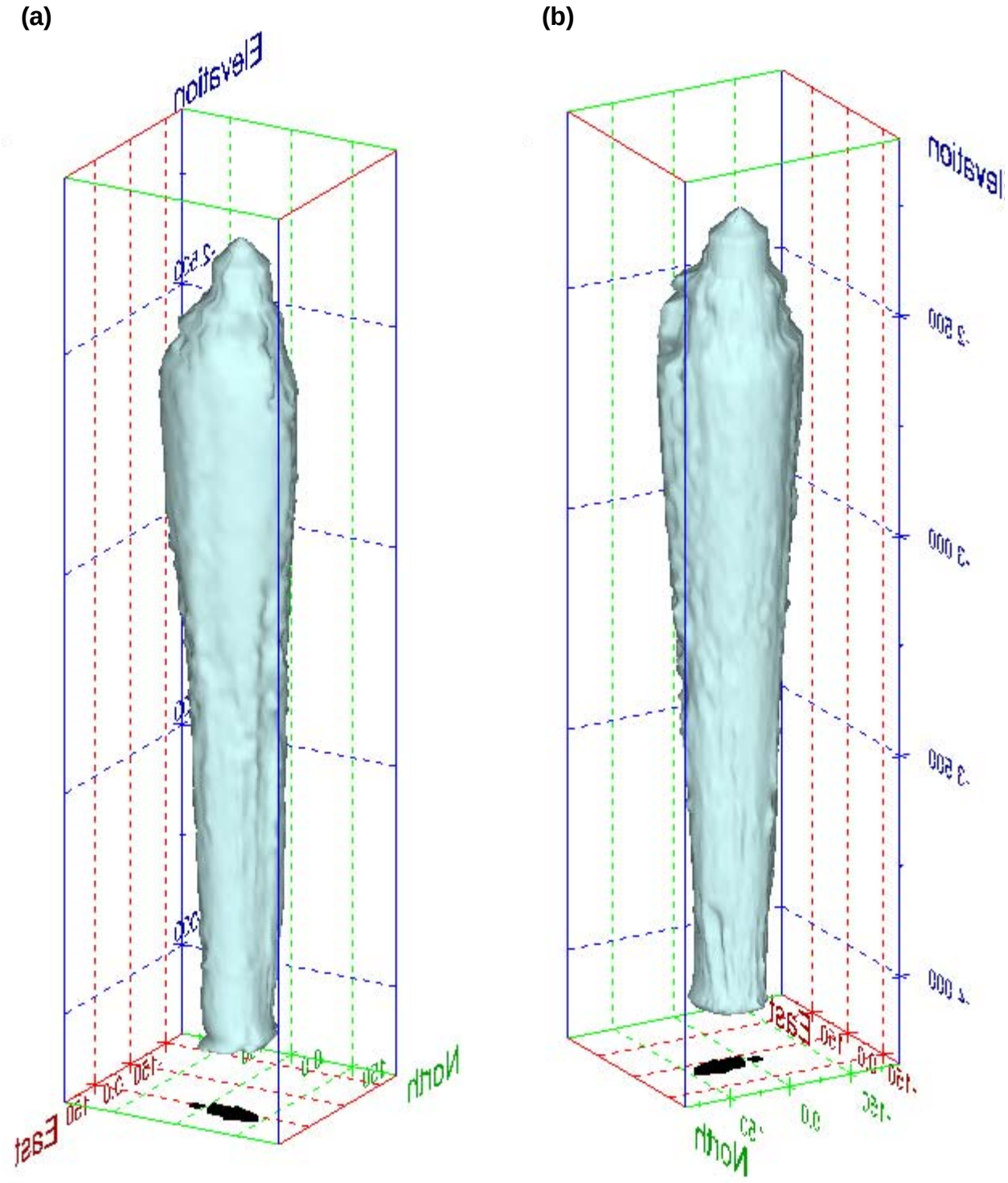

Figure 147. Sonar images of cavern BH-106, showing the basic geometric shape of the cavern. View from (a) azimuth 60°, elevation 20°; (b) azimuth 300°, elevation 20°.

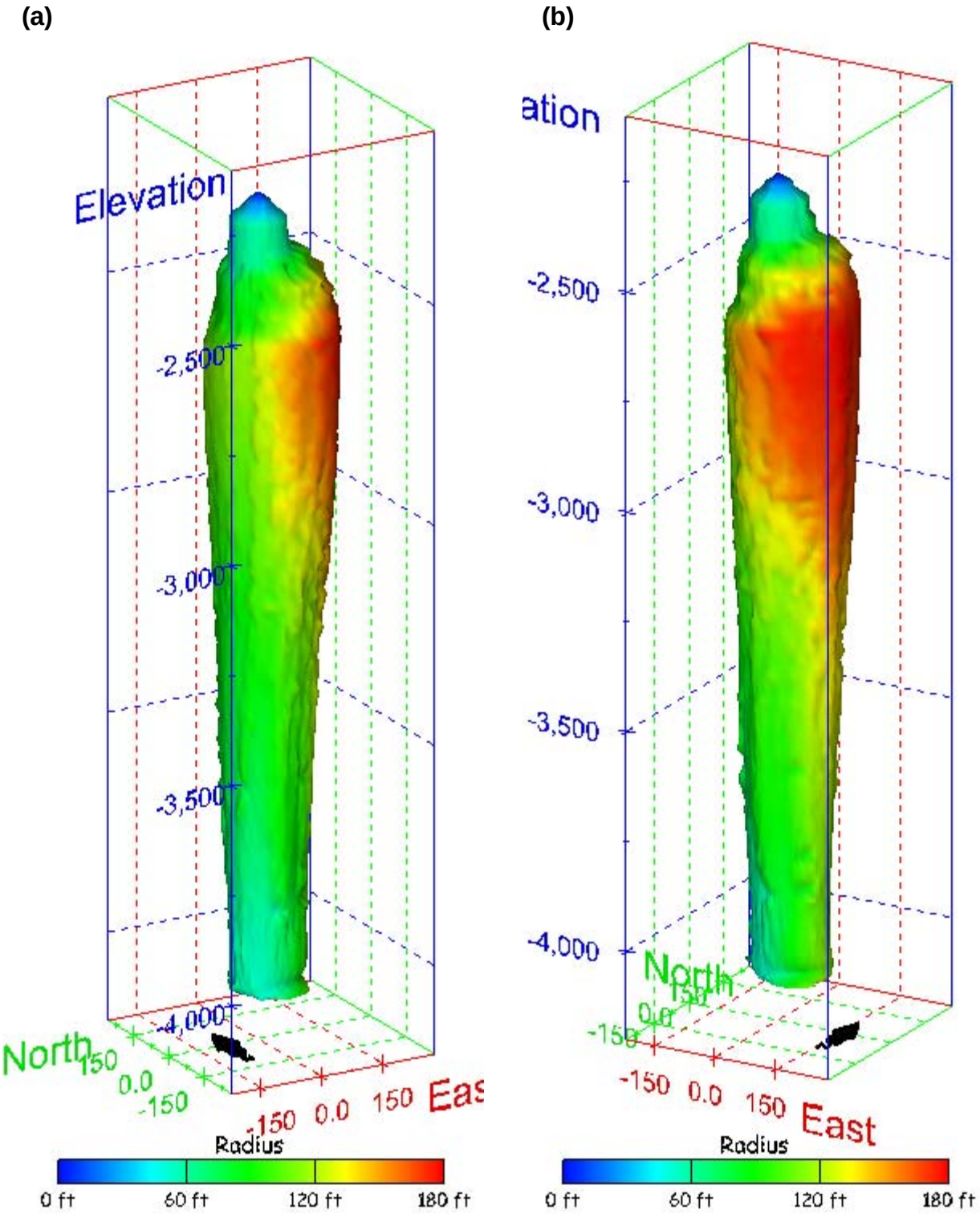

Figure 148. Sonar images of cavern BH-106, showing the geometry of the cavern colored by measured radius. View from (a) azimuth 210°, elevation 20°; (b) azimuth 150°, elevation 20°.

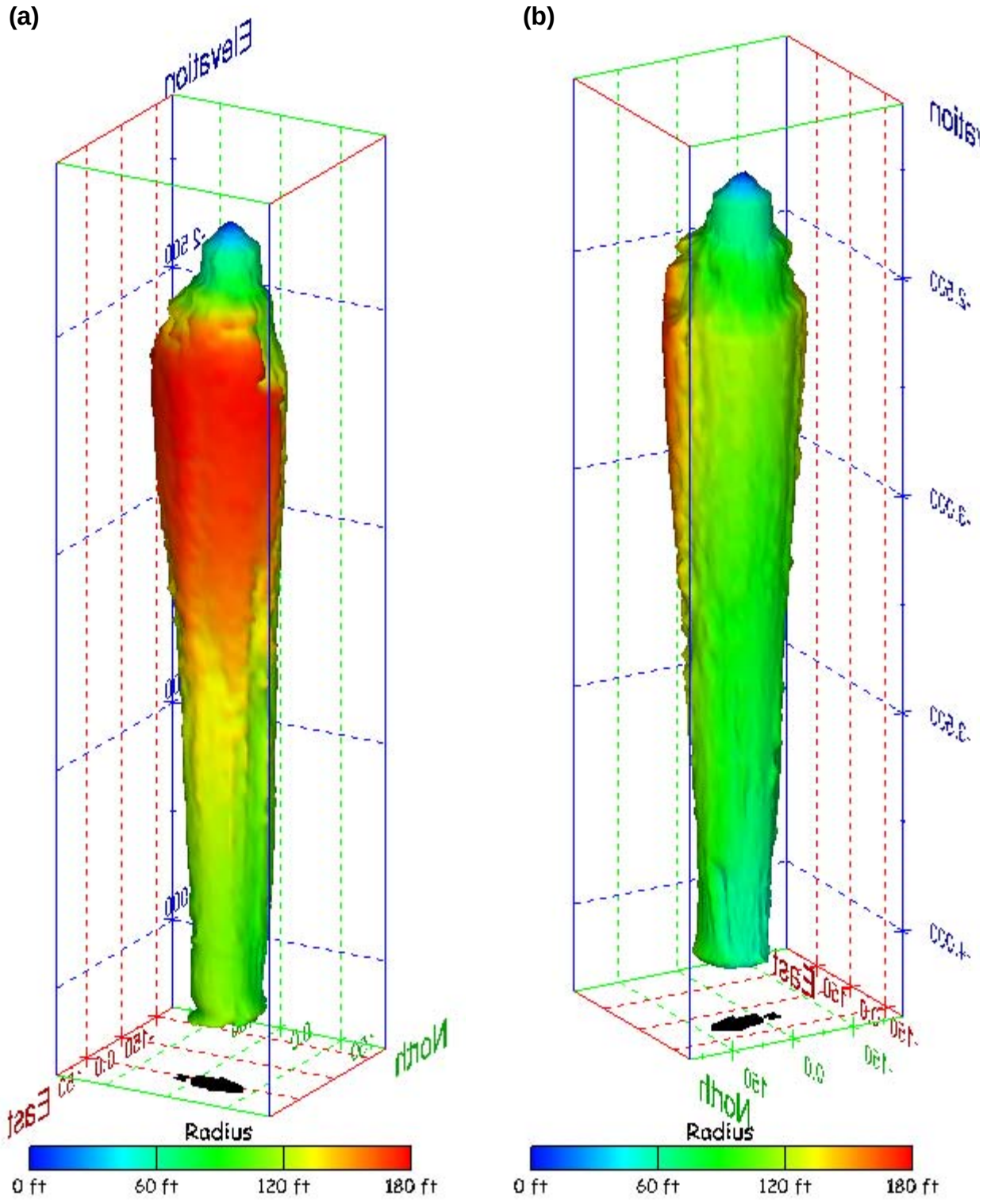

Figure 149. Sonar images of cavern BH-106, showing the geometry of the cavern colored by measured radius. View from (a) azimuth 60°, elevation 20°; (b) azimuth 300°, elevation 20°.

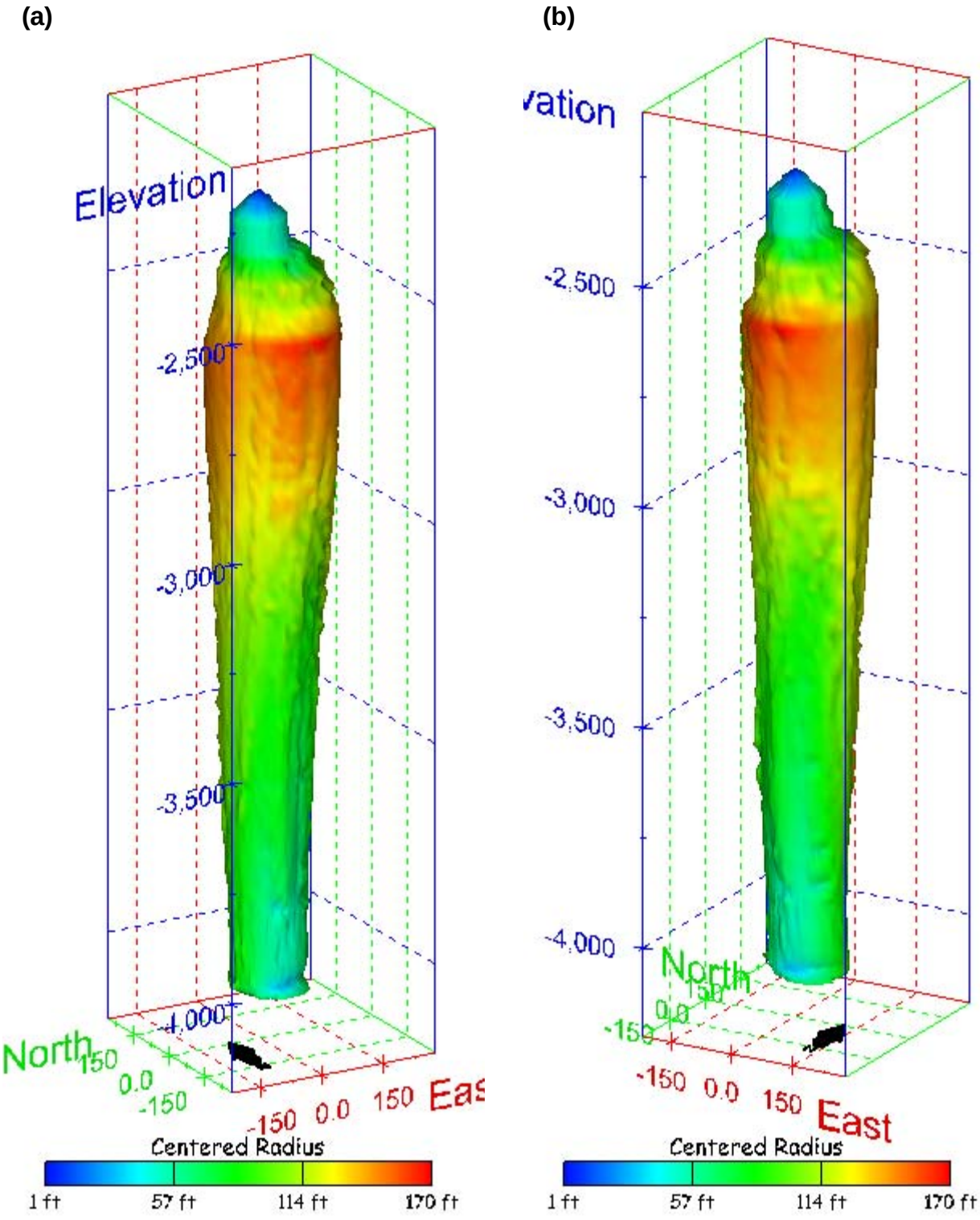

Figure 150. Sonar images of cavern BH-106, showing the geometry of the cavern colored by centered radius. View from (a) azimuth 210°, elevation 20°; (b) azimuth 150°, elevation 20°.

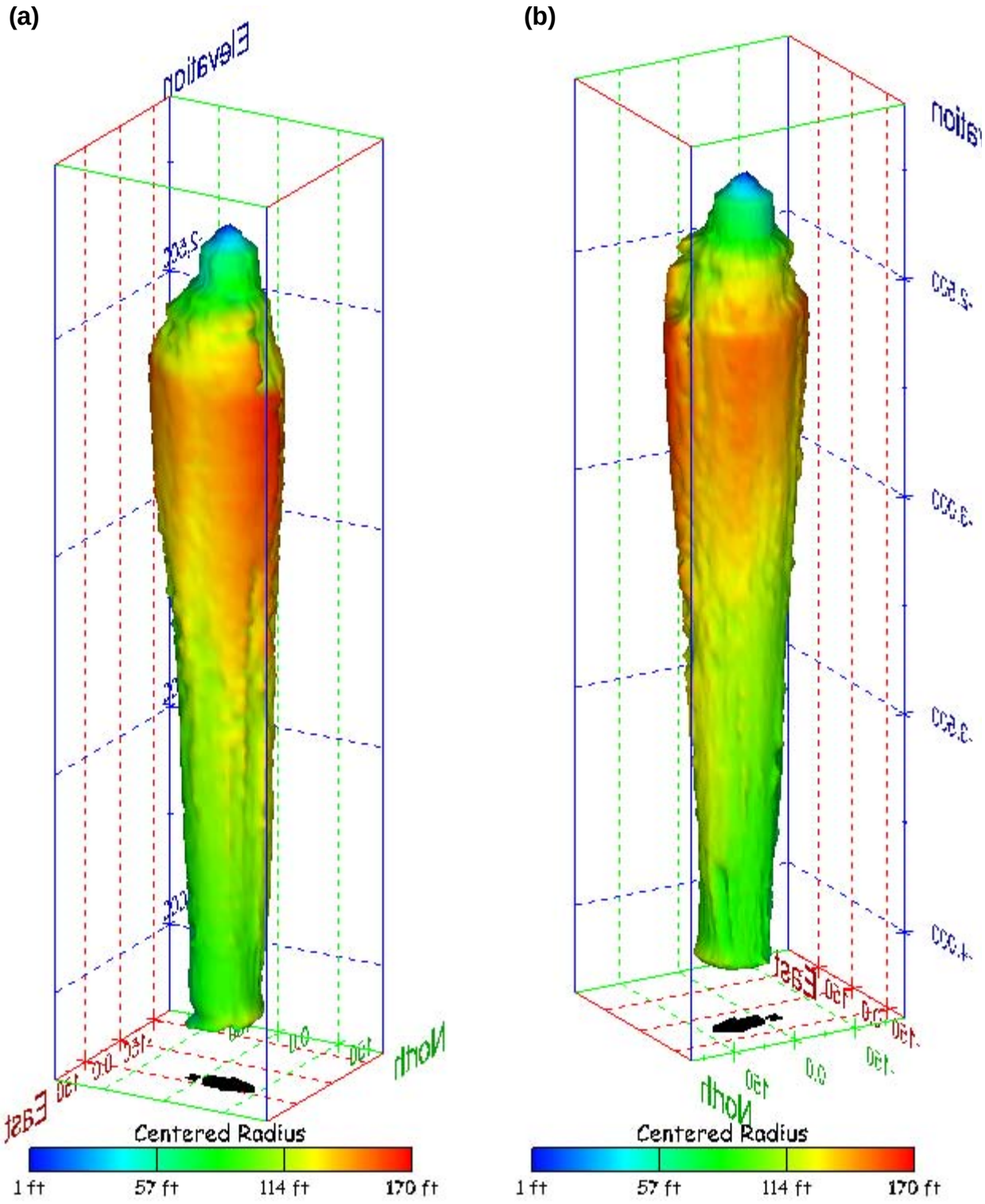

Figure 151. Sonar images of cavern BH-106, showing the geometry of the cavern colored by centered radius. View from (a) azimuth 60°, elevation 20°; (b) azimuth 300°, elevation 20°.

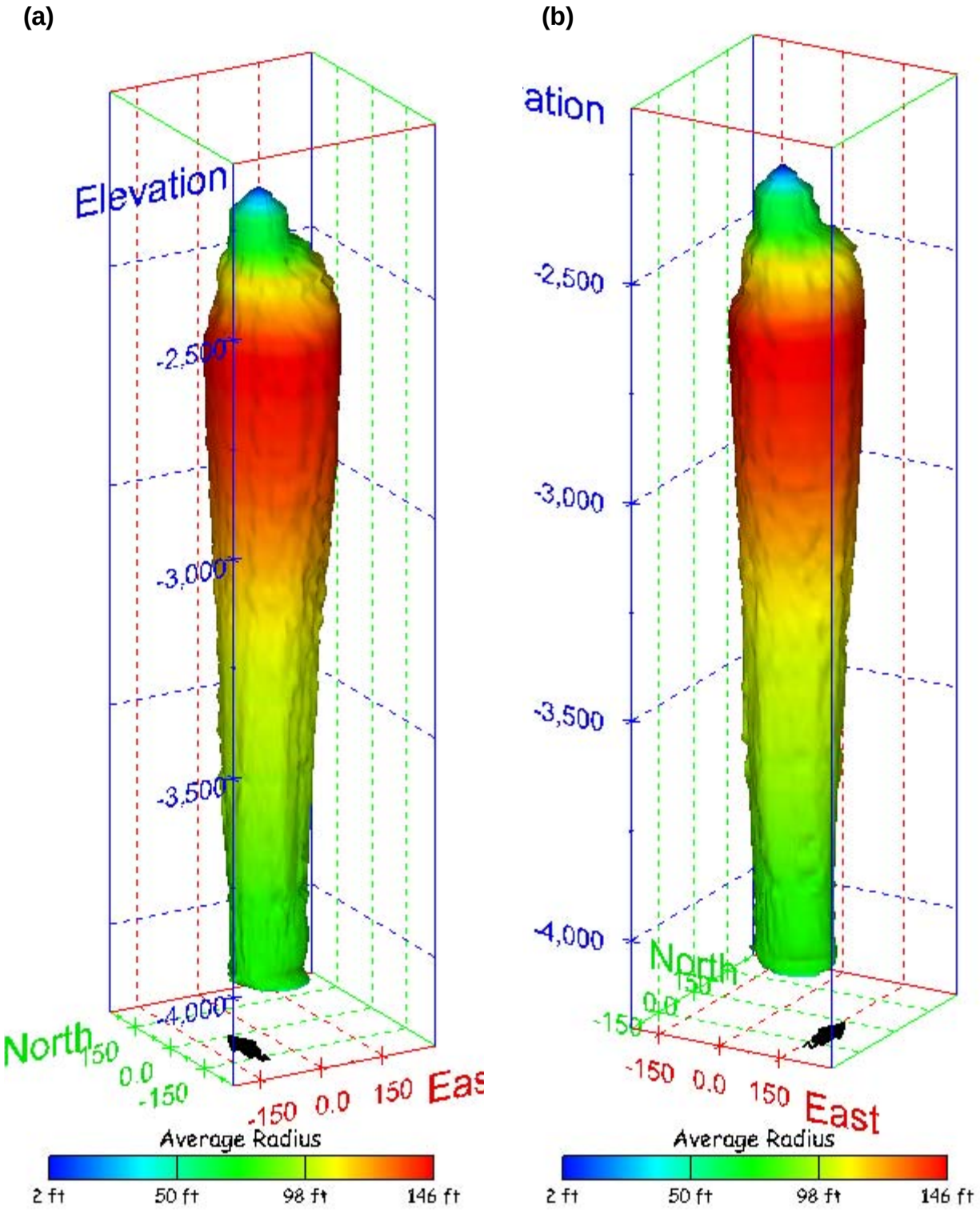

Figure 152. Sonar images of cavern BH-106, showing the geometry of the cavern colored by average radius. View from (a) azimuth 210°, elevation 20°; (b) azimuth 150°, elevation 20°.

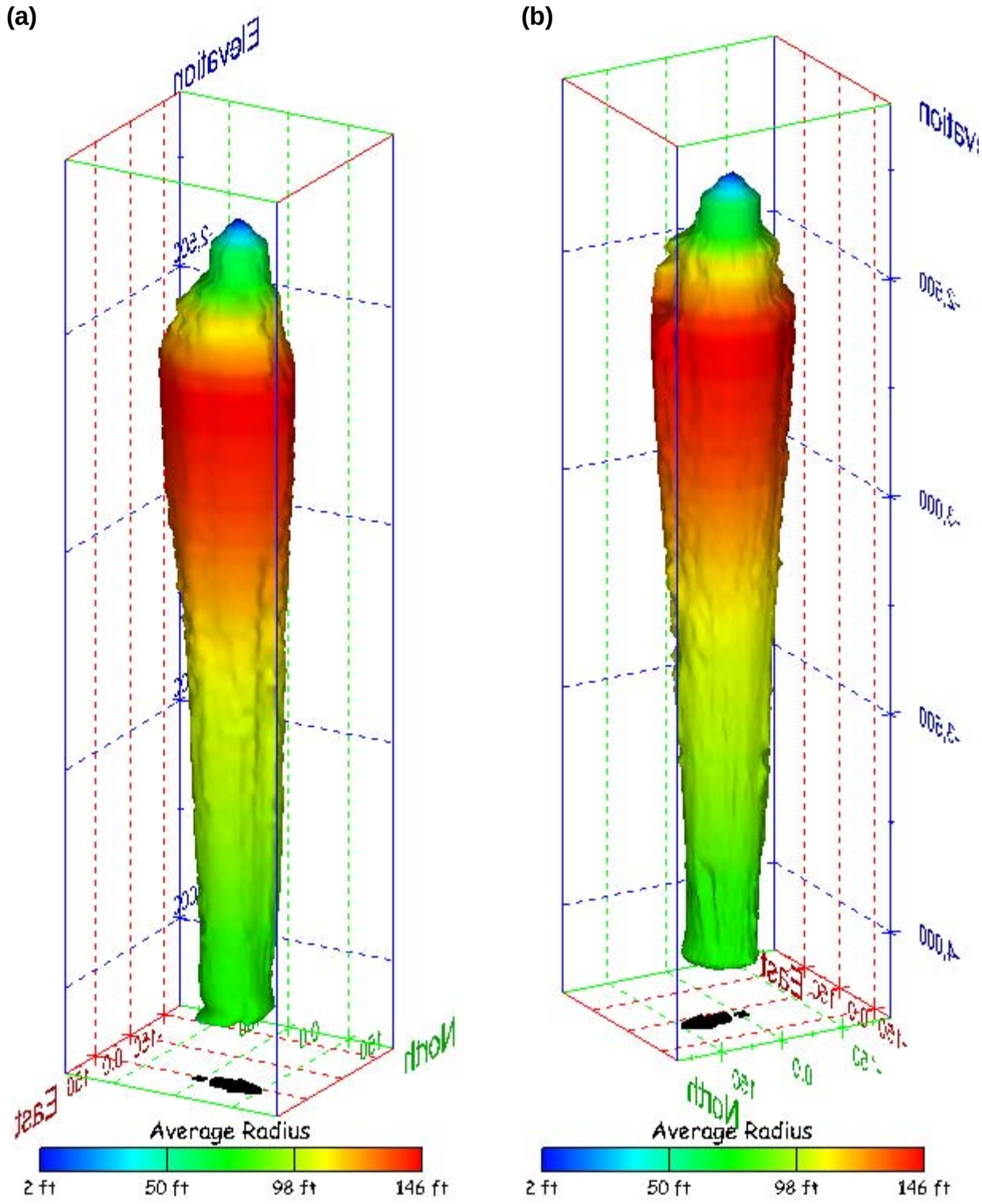

Figure 153. Sonar images of cavern BH-106, showing the geometry of the cavern colored by average radius. View from (a) azimuth 60°, elevation 20°; (b) azimuth 300°, elevation 20°.

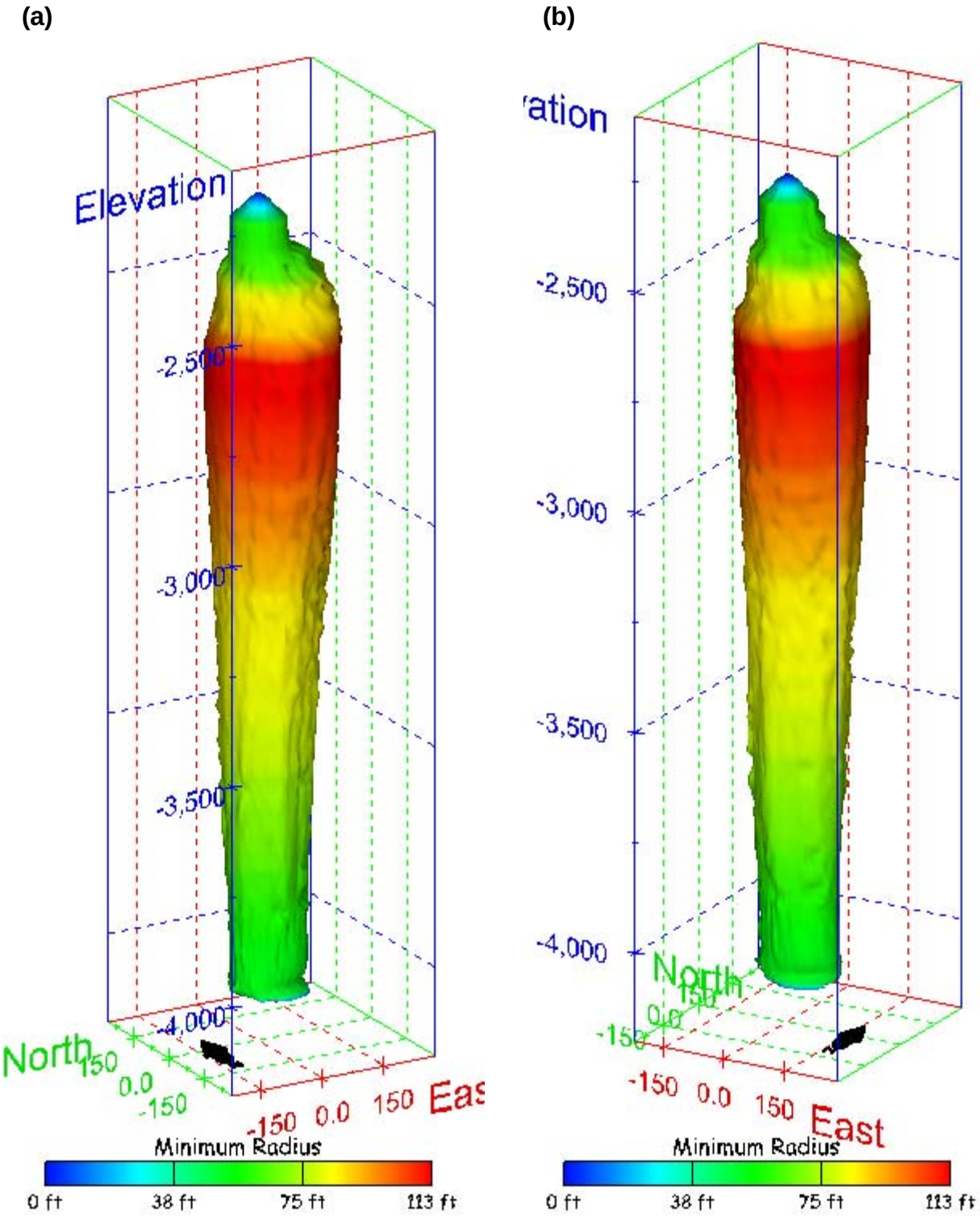

Figure 154. Sonar images of cavern BH-106, showing the geometry of the cavern colored by minimum radius. View from (a) azimuth 210°, elevation 20°; (b) azimuth 150°, elevation 20°.

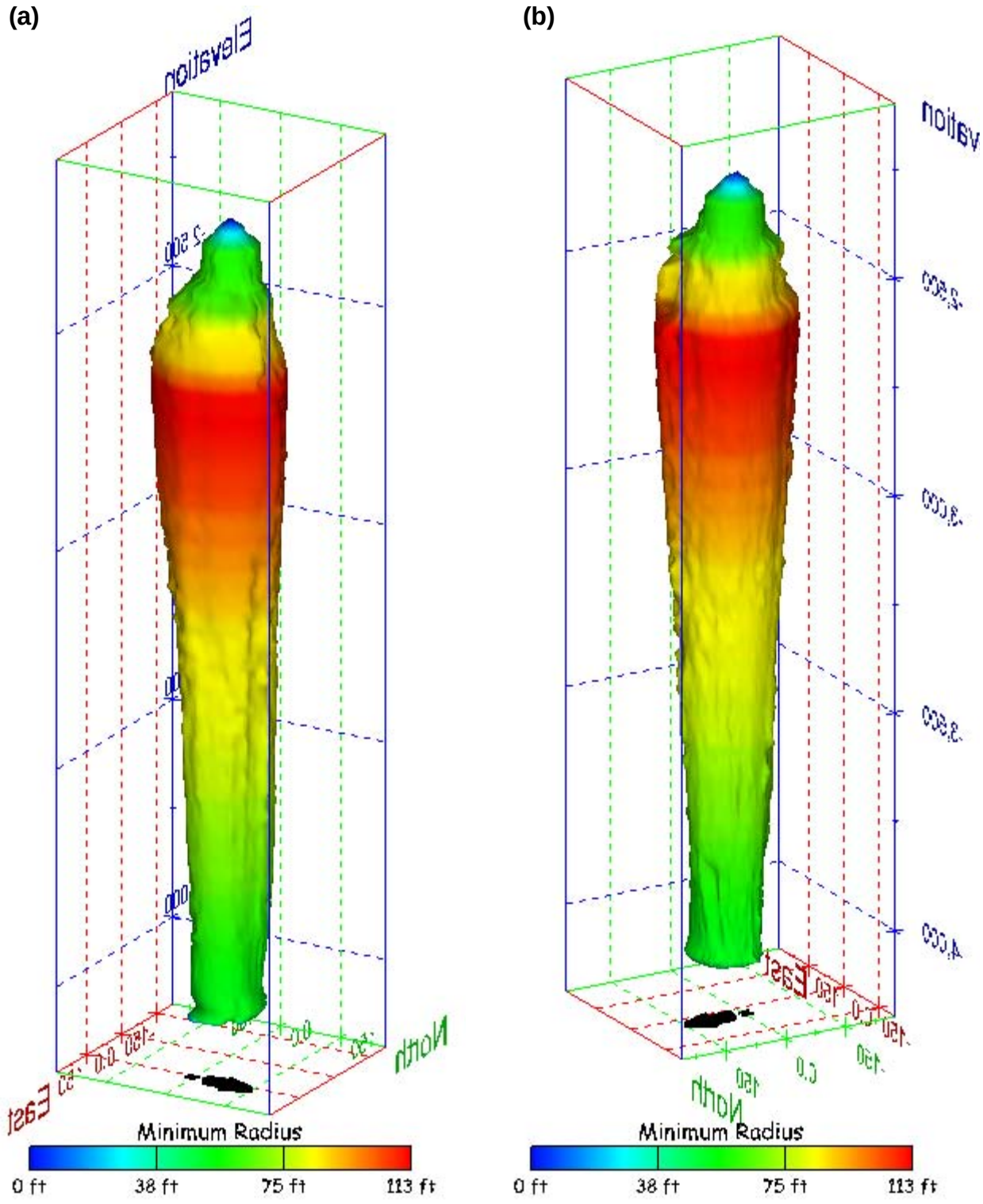

Figure 155. Sonar images of cavern BH-106, showing the geometry of the cavern colored by minimum radius. View from (a) azimuth 60°, elevation 20°; (b) azimuth 300°, elevation 20°.

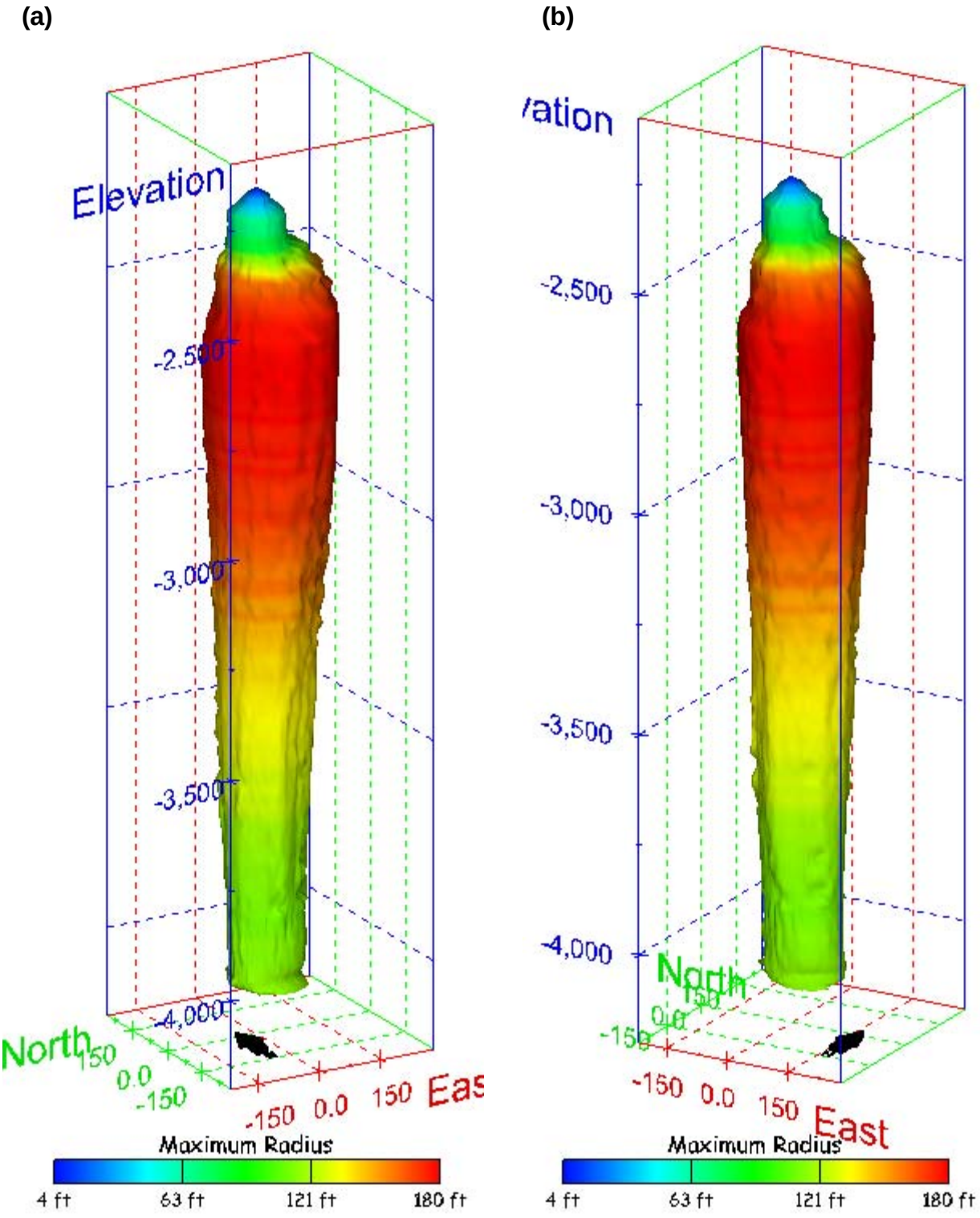

Figure 156. Sonar images of cavern BH-106, showing the geometry of the cavern colored by maximum radius. View from (a) azimuth 210°, elevation 20°; (b) azimuth 150°, elevation 20°.

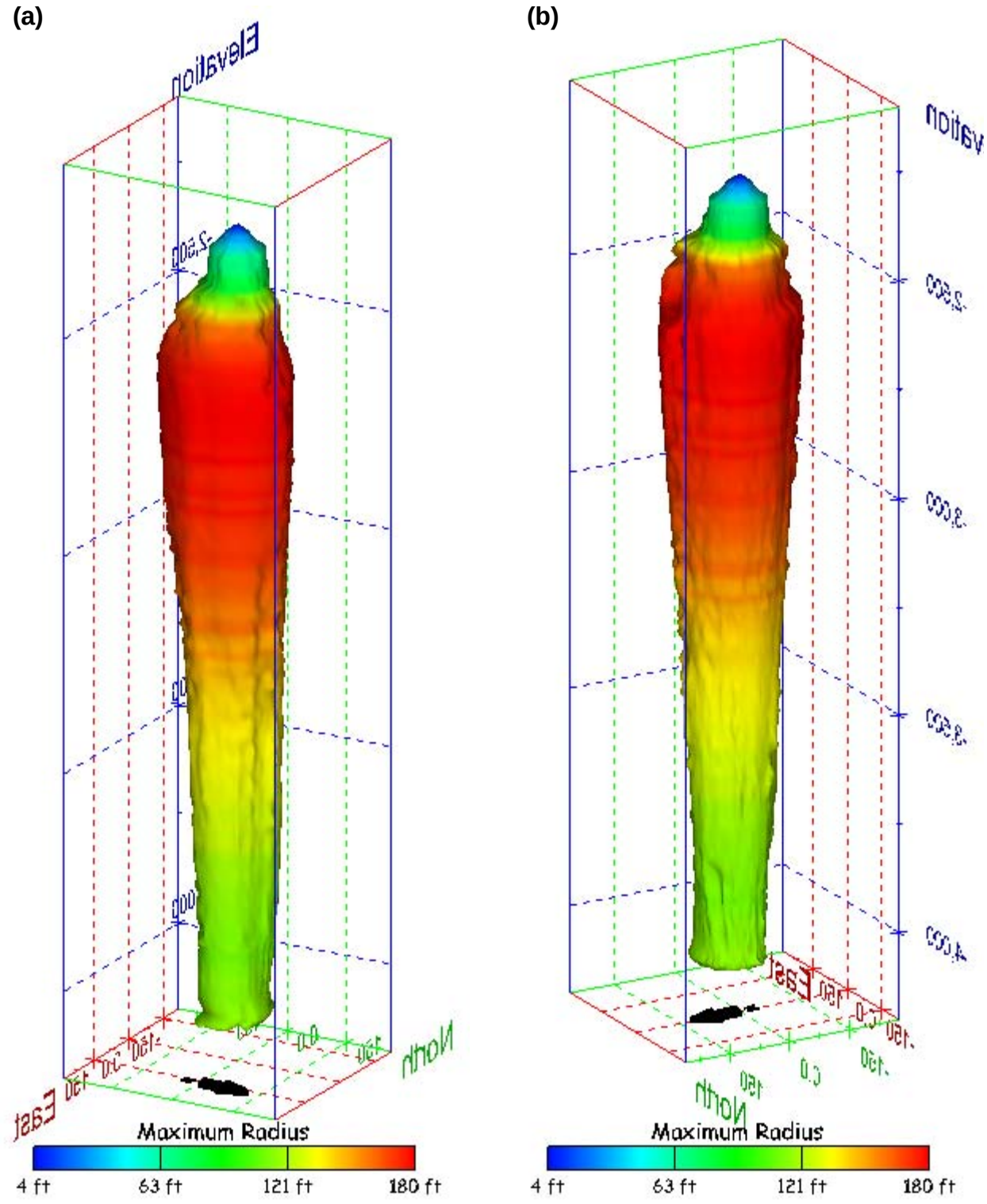

Figure 157. Sonar images of cavern BH-106, showing the geometry of the cavern colored by maximum radius. View from (a) azimuth 60°, elevation 20°; (b) azimuth 300°, elevation 20°.

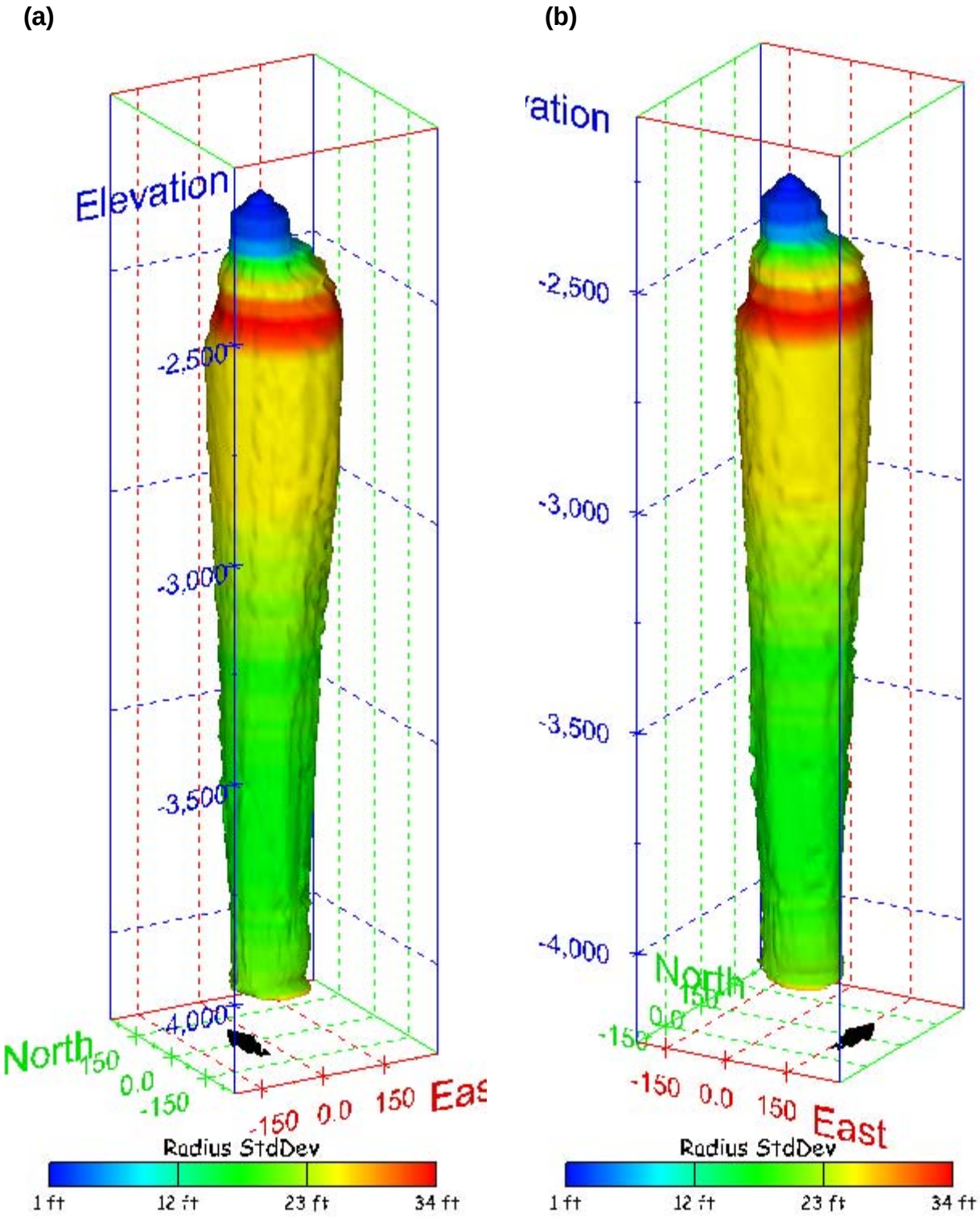

Figure 158. Sonar images of cavern BH-106, showing the geometry of the cavern colored by radius standard deviation. View from (a) azimuth 210°, elevation 20°; (b) azimuth 150°, elevation 20°.

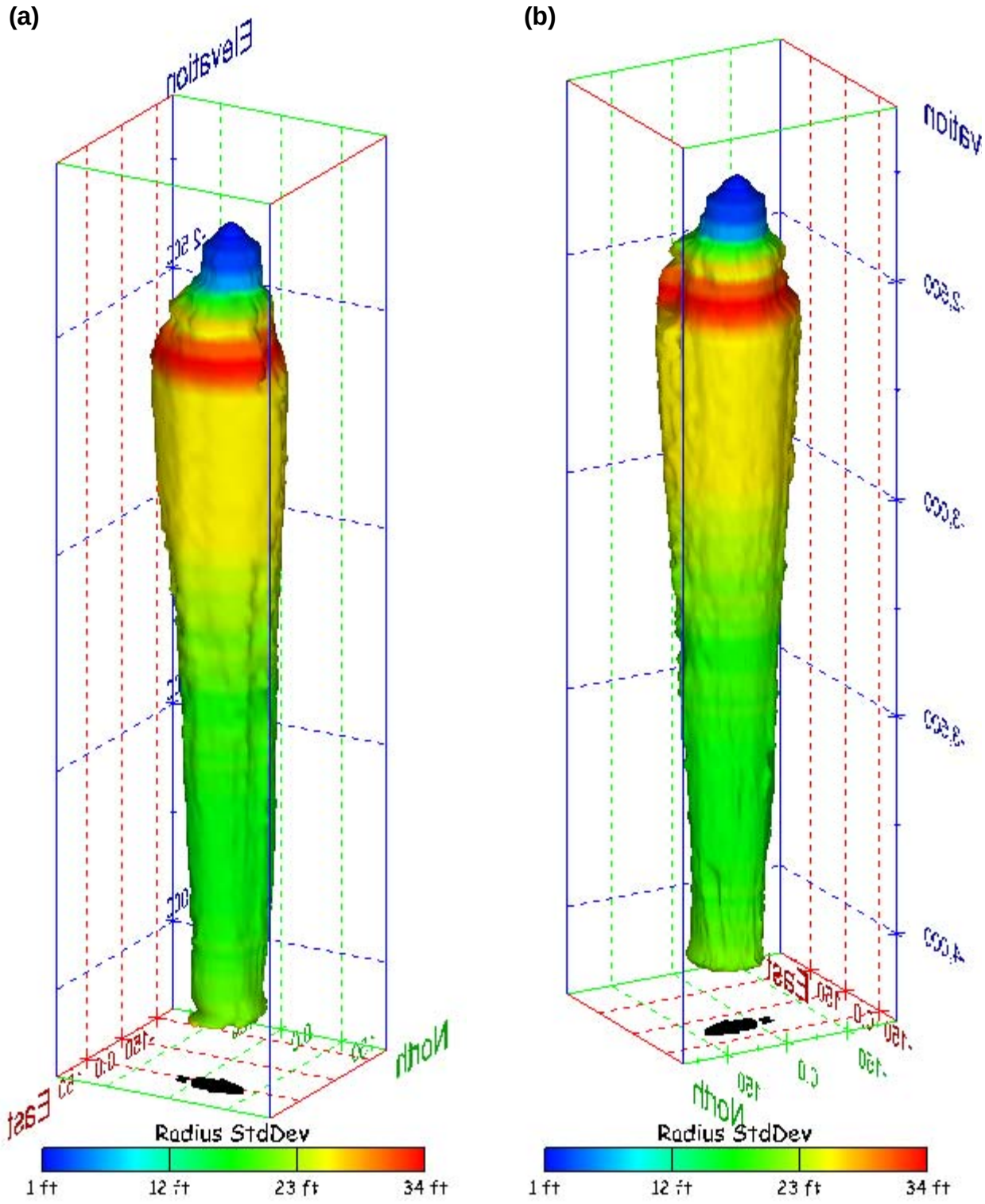

Figure 159. Sonar images of cavern BH-106, showing the geometry of the cavern colored by radius standard deviation. View from (a) azimuth 60°, elevation 20°; (b) azimuth 300°, elevation 20°.

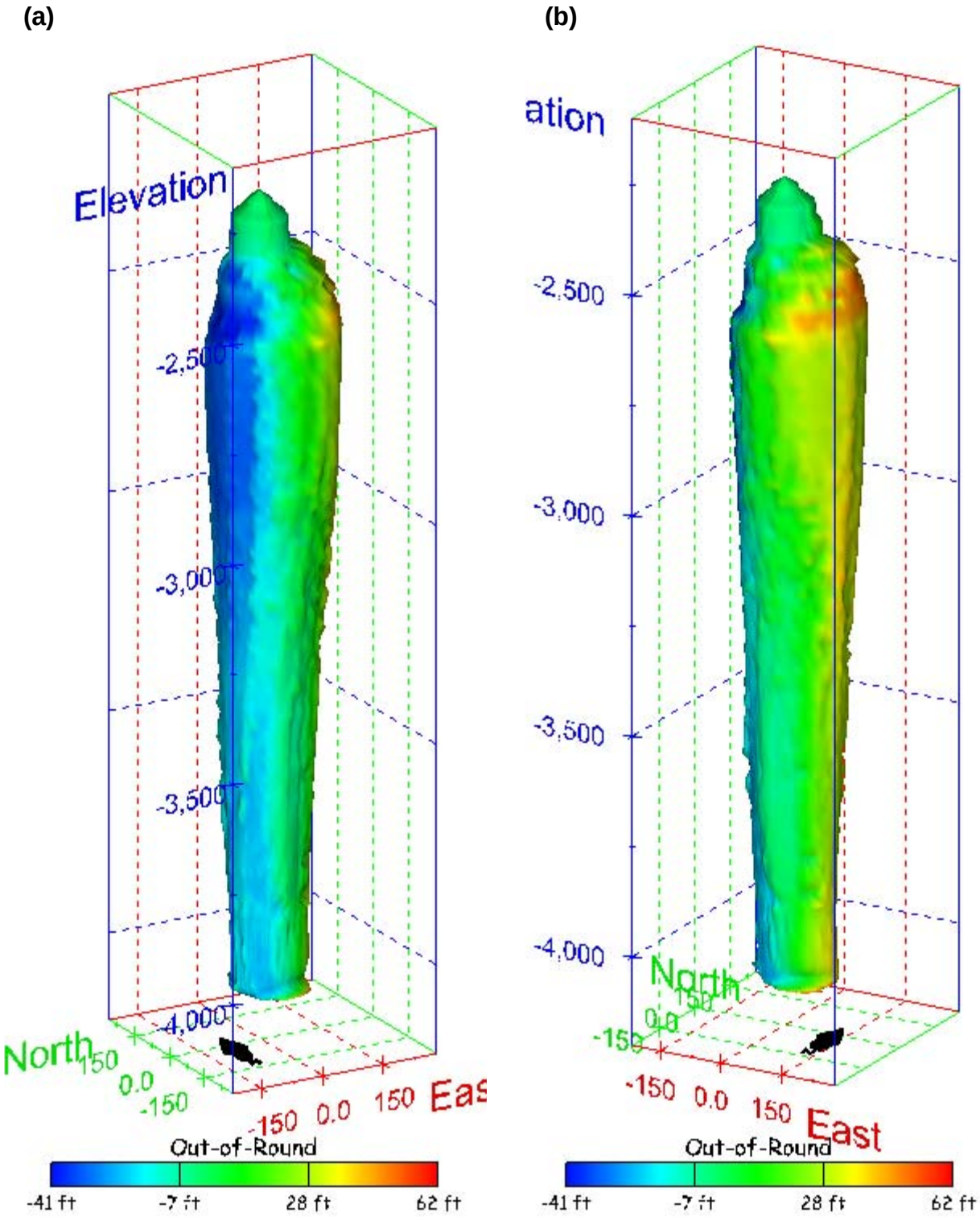

Figure 160. Sonar images of cavern BH-106, showing the geometry of the cavern colored by out-of-round distance. View from (a) azimuth 210°, elevation 20°; (b) azimuth 150°, elevation 20°.

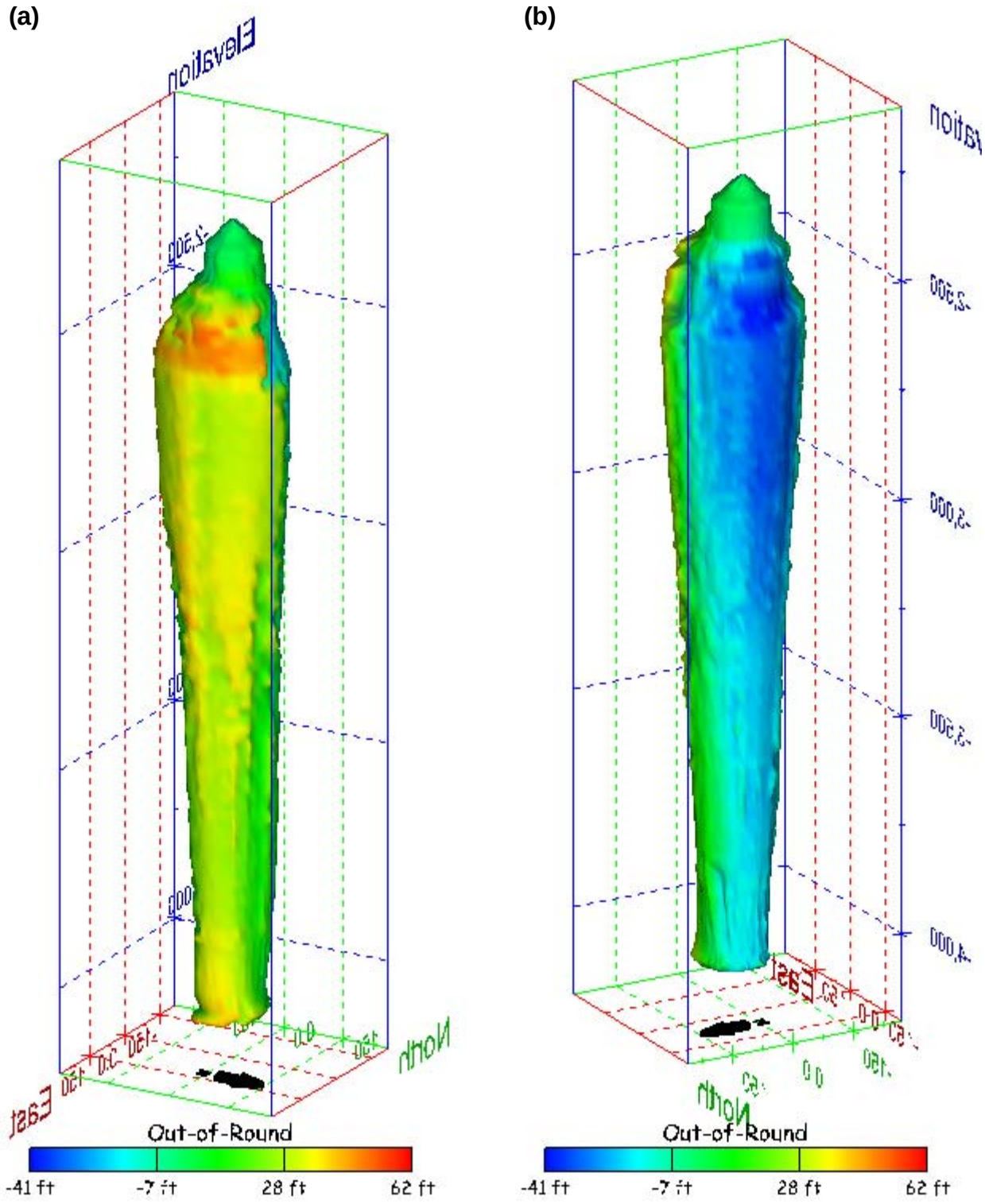

Figure 161. Sonar images of cavern BH-106, showing the geometry of the cavern colored by out-of-round distance. View from (a) azimuth 60°, elevation 20°; (b) azimuth 300°, elevation 20°.

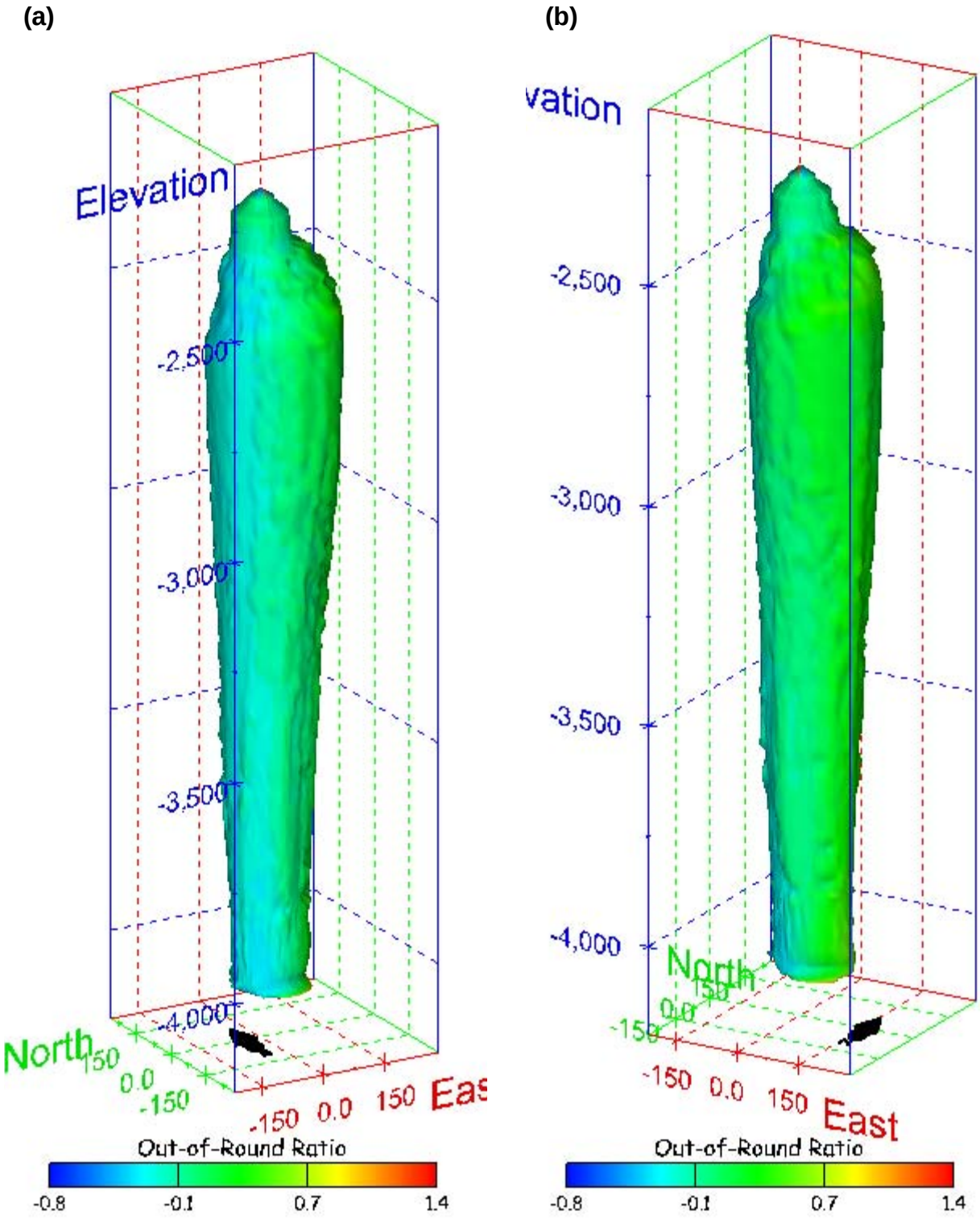

Figure 162. Sonar images of cavern BH-106, showing the geometry of the cavern colored by out-of-round ratio. View from (a) azimuth 210°, elevation 20°; (b) azimuth 150°, elevation 20°.

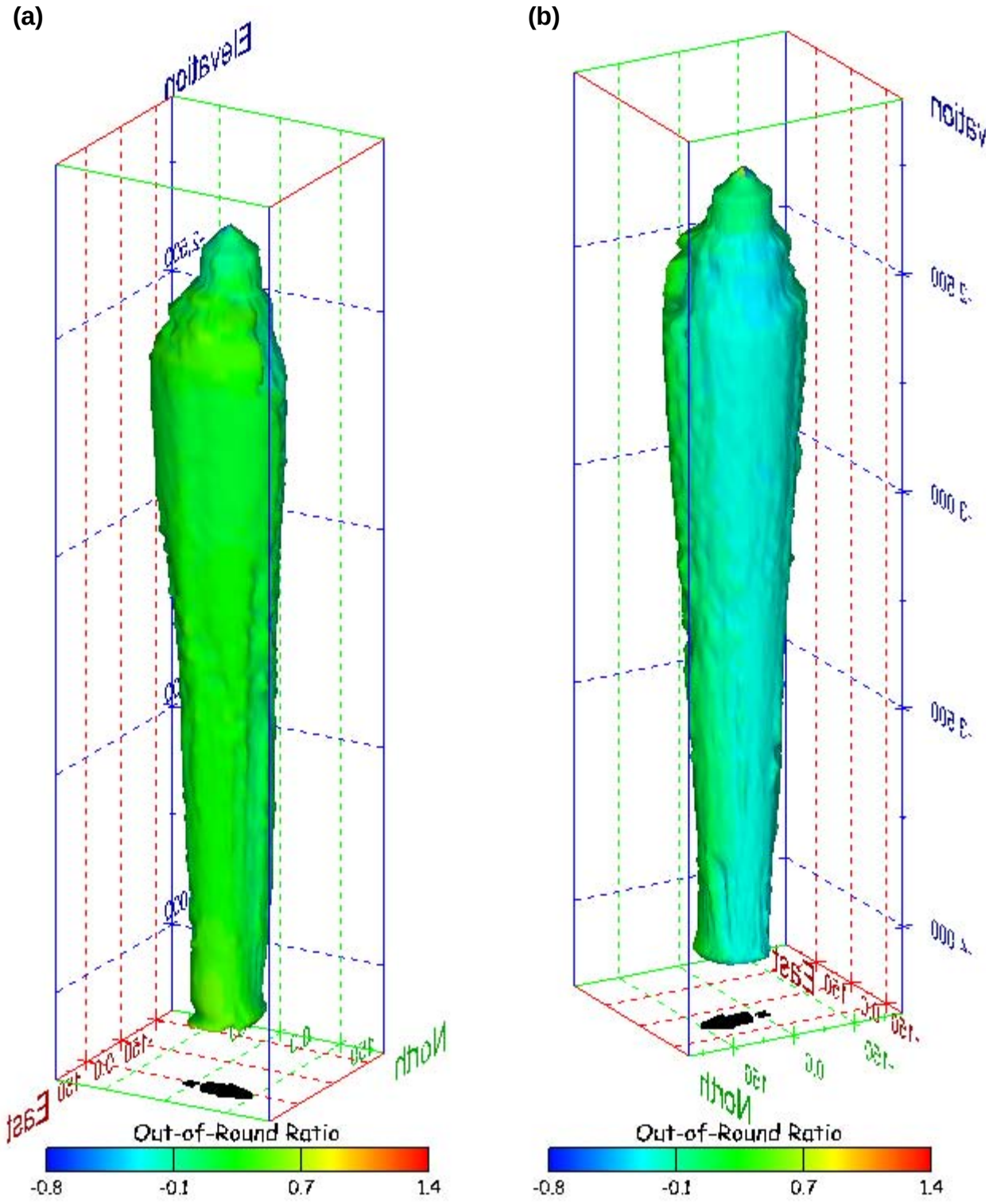

Figure 163. Sonar images of cavern BH-106, showing the geometry of the cavern colored by out-of-round ratio. View from (a) azimuth 60°, elevation 20°; (b) azimuth 300°, elevation 20°.

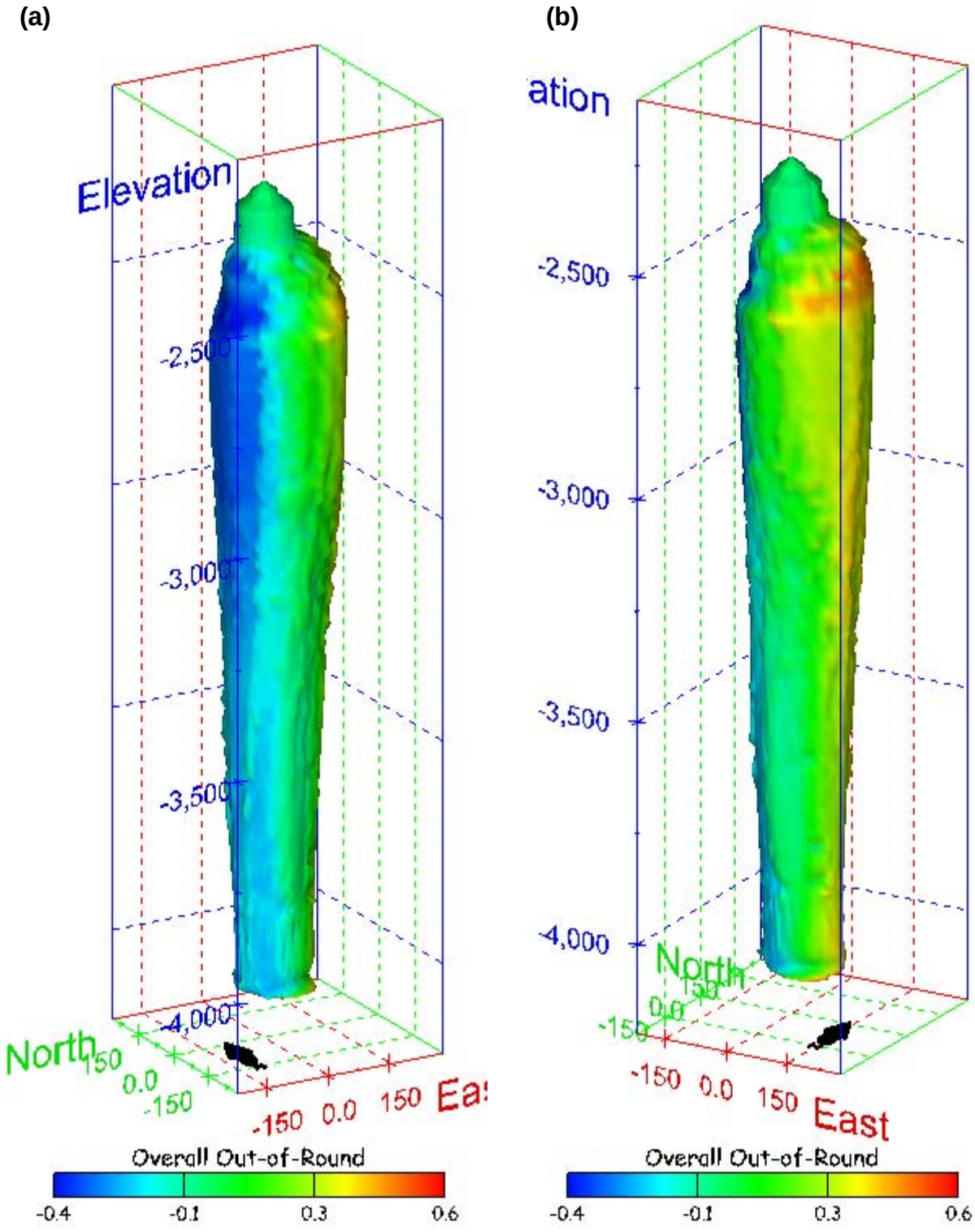

Figure 164. Sonar images of cavern BH-106, showing the geometry of the cavern colored by overall out-of-round ratio. View from (a) azimuth 210°, elevation 20°; (b) azimuth 150°, elevation 20°.

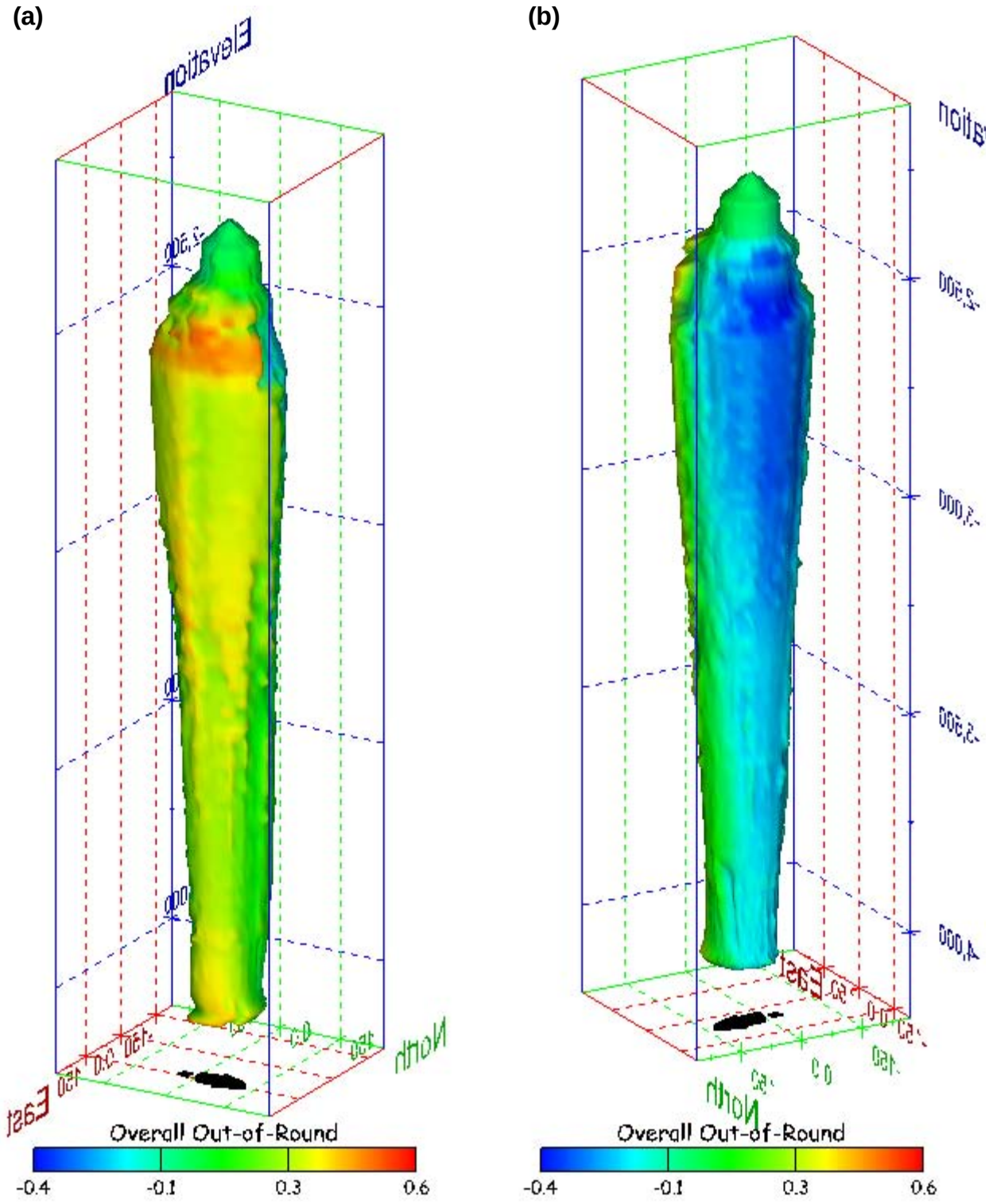

Figure 165. Sonar images of cavern BH-106, showing the geometry of the cavern colored by overall out-of-round ratio. View from (a) azimuth 60°, elevation 20°; (b) azimuth 300°, elevation 20°.

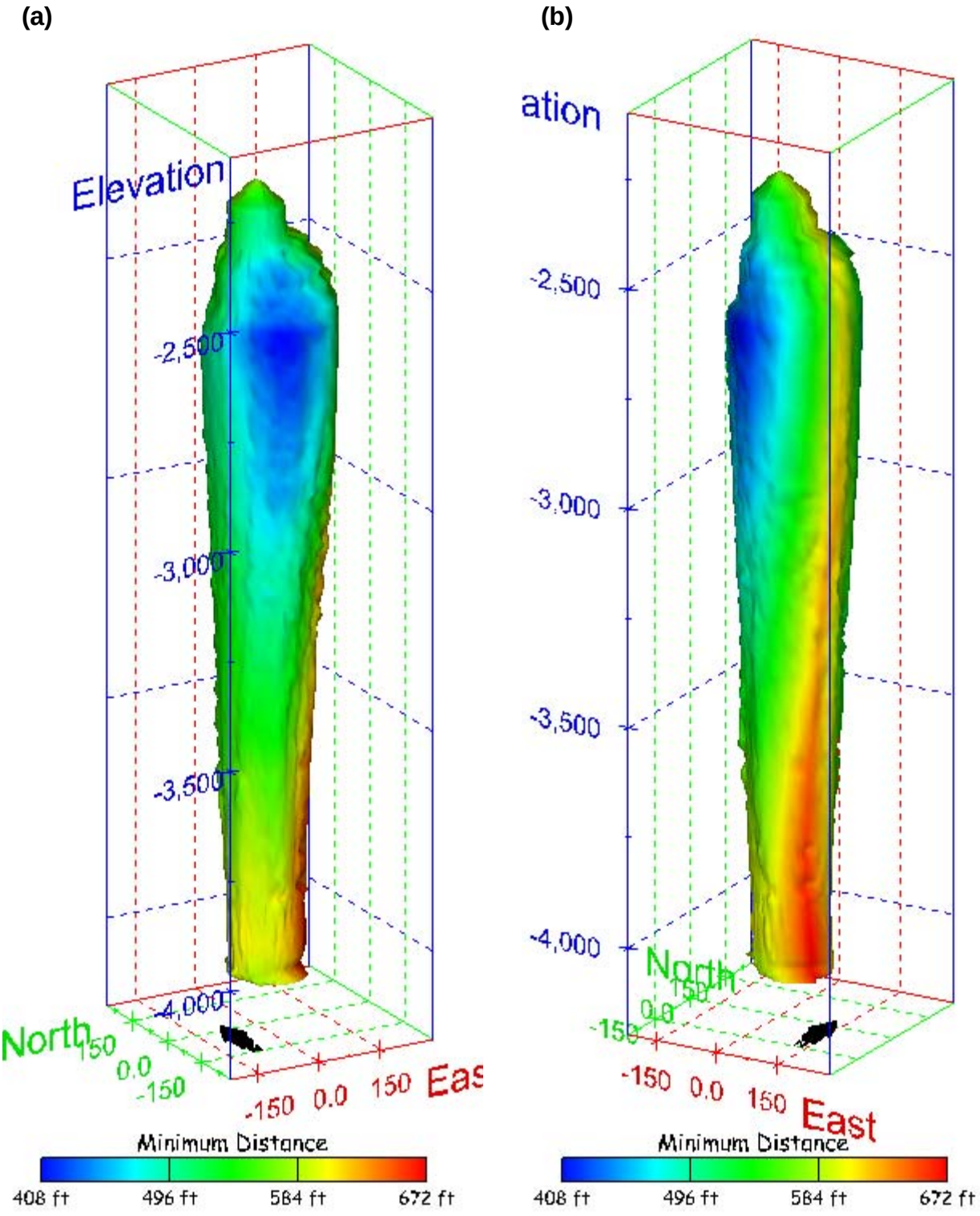

Figure 166. Sonar images of cavern BH-106, showing the geometry of the cavern colored by the minimum distance to the nearest neighboring cavern. View from (a) azimuth 210°, elevation 20°; (b) azimuth 150°, elevation 20°.

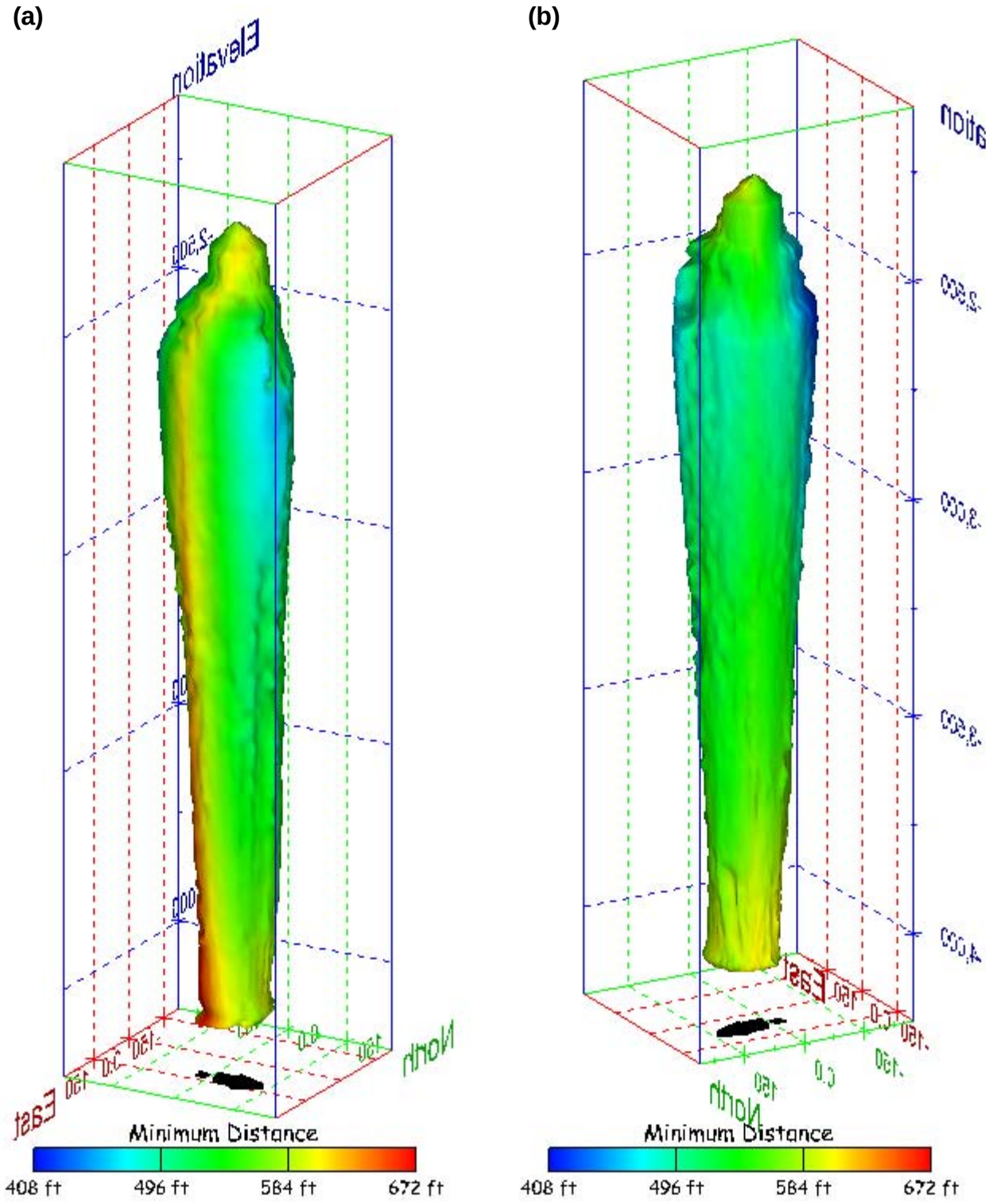

Figure 167. Sonar images of cavern BH-106, showing the geometry of the cavern colored by minimum distance to the nearest neighboring cavern. View from (a) azimuth 60°, elevation 20°; (b) azimuth 300°, elevation 20°.

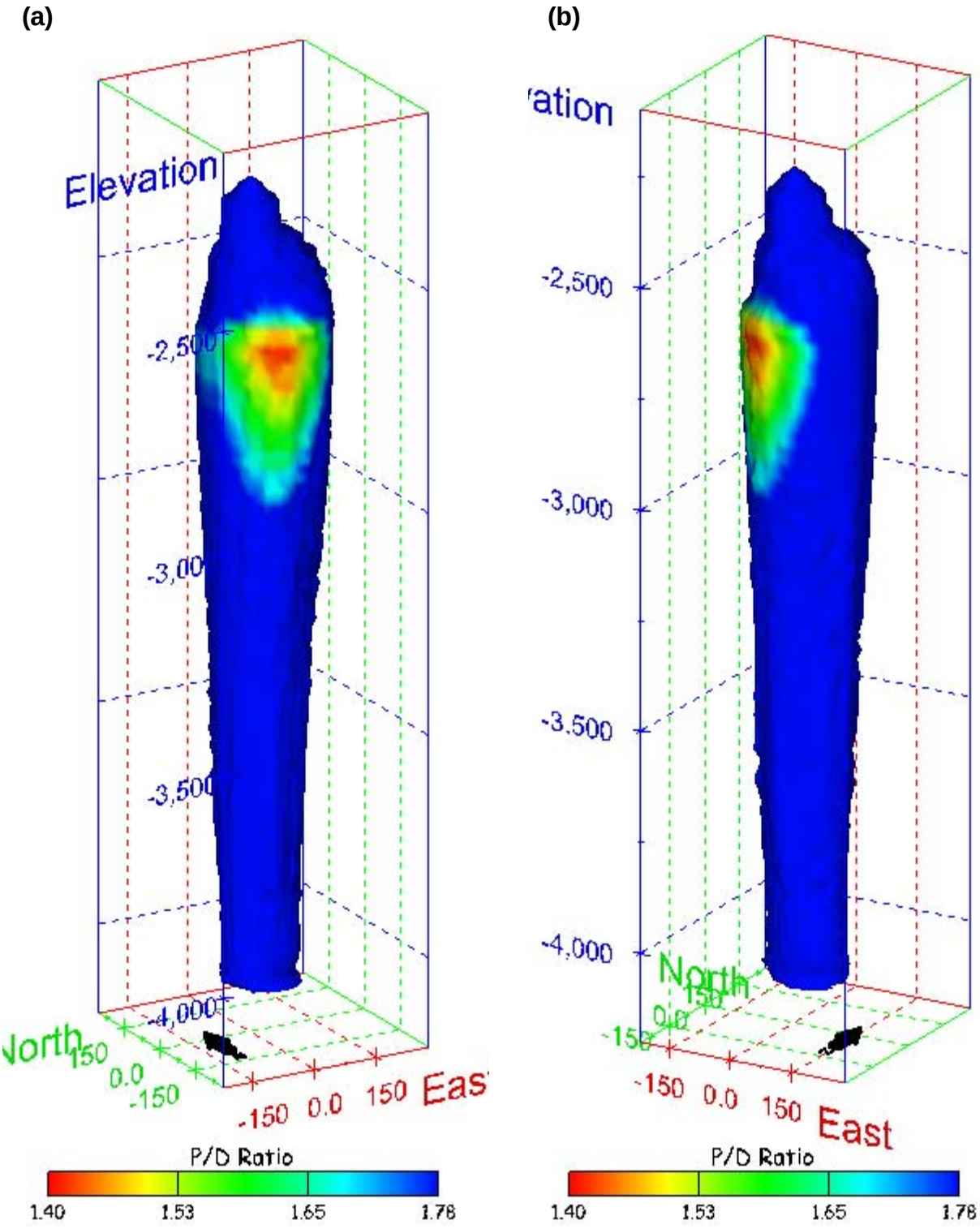

Figure 168. Sonar images of cavern BH-106, showing the geometry of the cavern colored by three-dimensional pillar-to-diameter ratio. View from (a) azimuth 210°, elevation 20°; (b) azimuth 150°, elevation 20°.

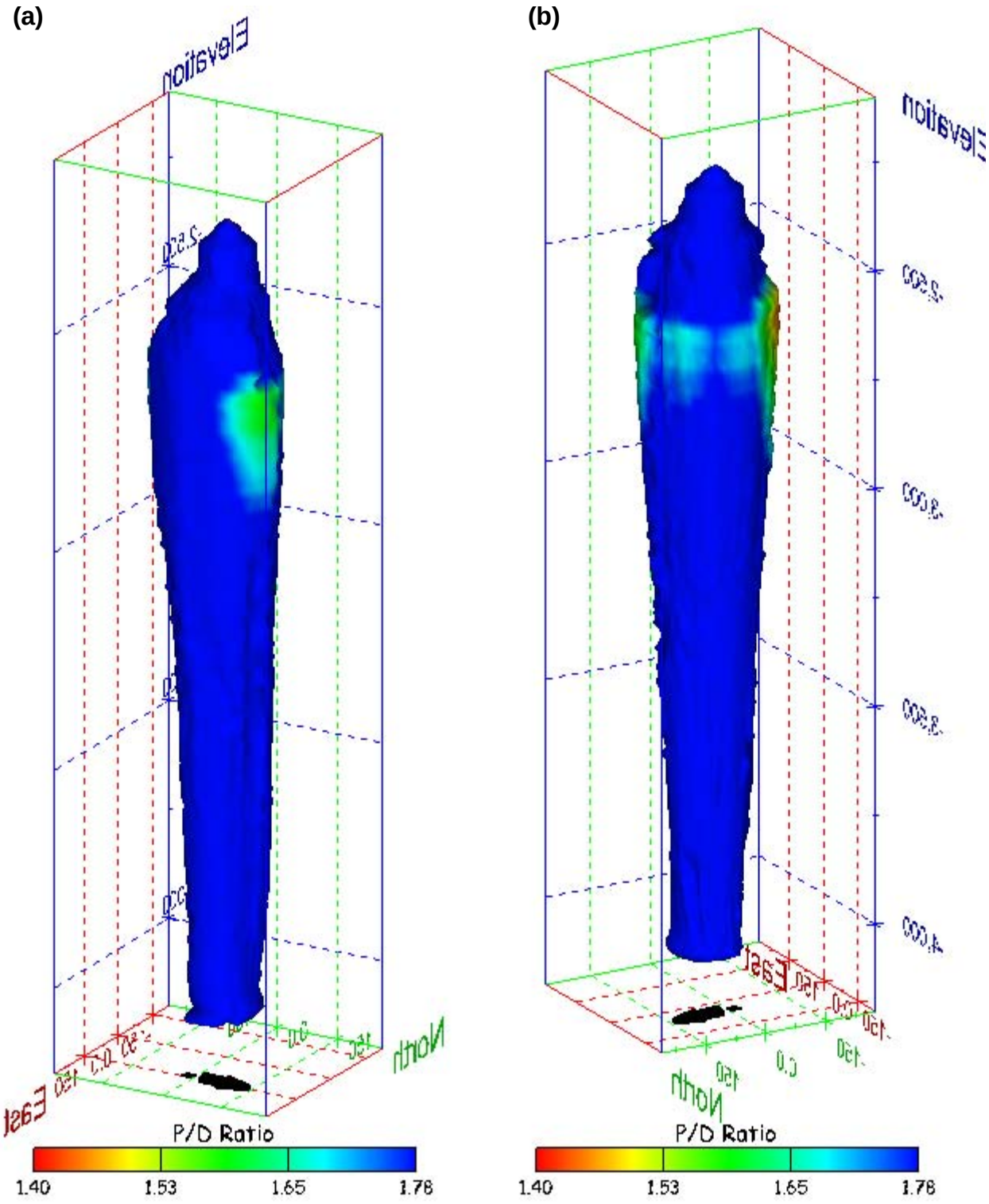

Figure 169. Sonar images of cavern BH-106, showing the geometry of the cavern colored by three-dimensional pillar-to-diameter ratio. View from (a) azimuth 60°, elevation 20°; (b) azimuth 300°, elevation 20°.

No Sonic Velocity Data Available for Socon Surveys

Figure 170. Sonar image of cavern BH-106, showing the geometry of the cavern colored by the reported velocity of sound on the survey date of February 2005. View from due south, elevation zero.

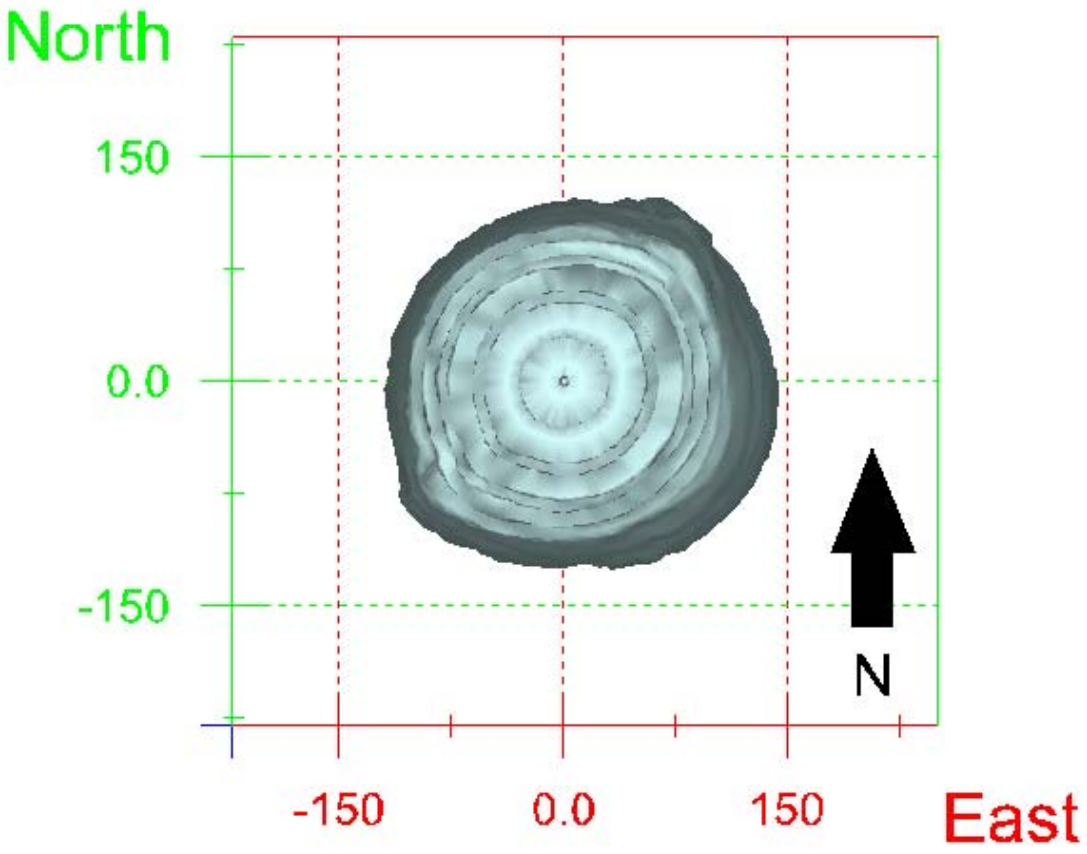

Figure 171. Map view sonar image of cavern BH-107, showing the basic geometry of the cavern. Grid squares represent 150 ft.

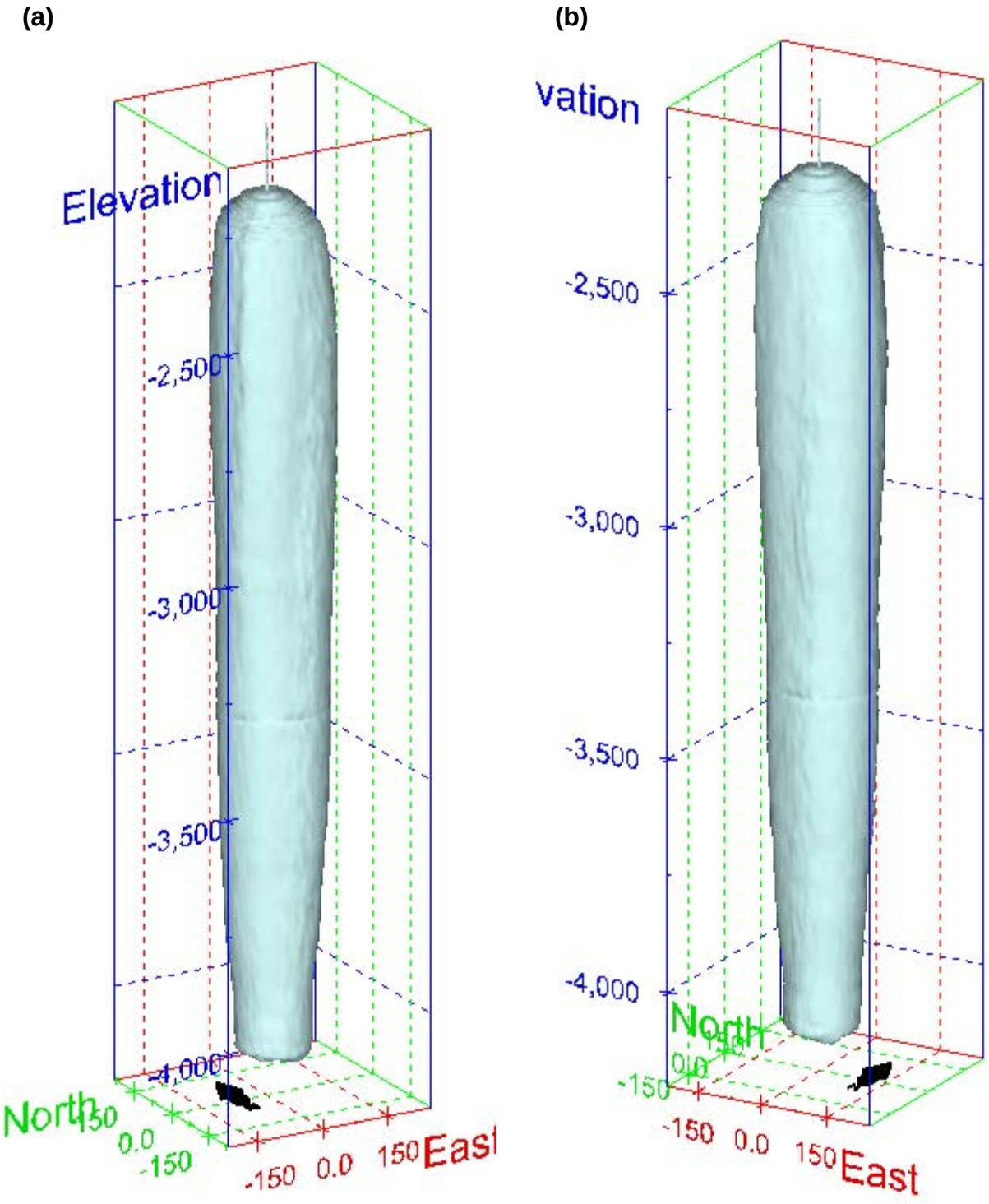

Figure 172. Sonar images of cavern BH-107, showing the basic geometric shape of the cavern. View from (a) azimuth 210°, elevation 20°; (b) azimuth 150°, elevation 20°.

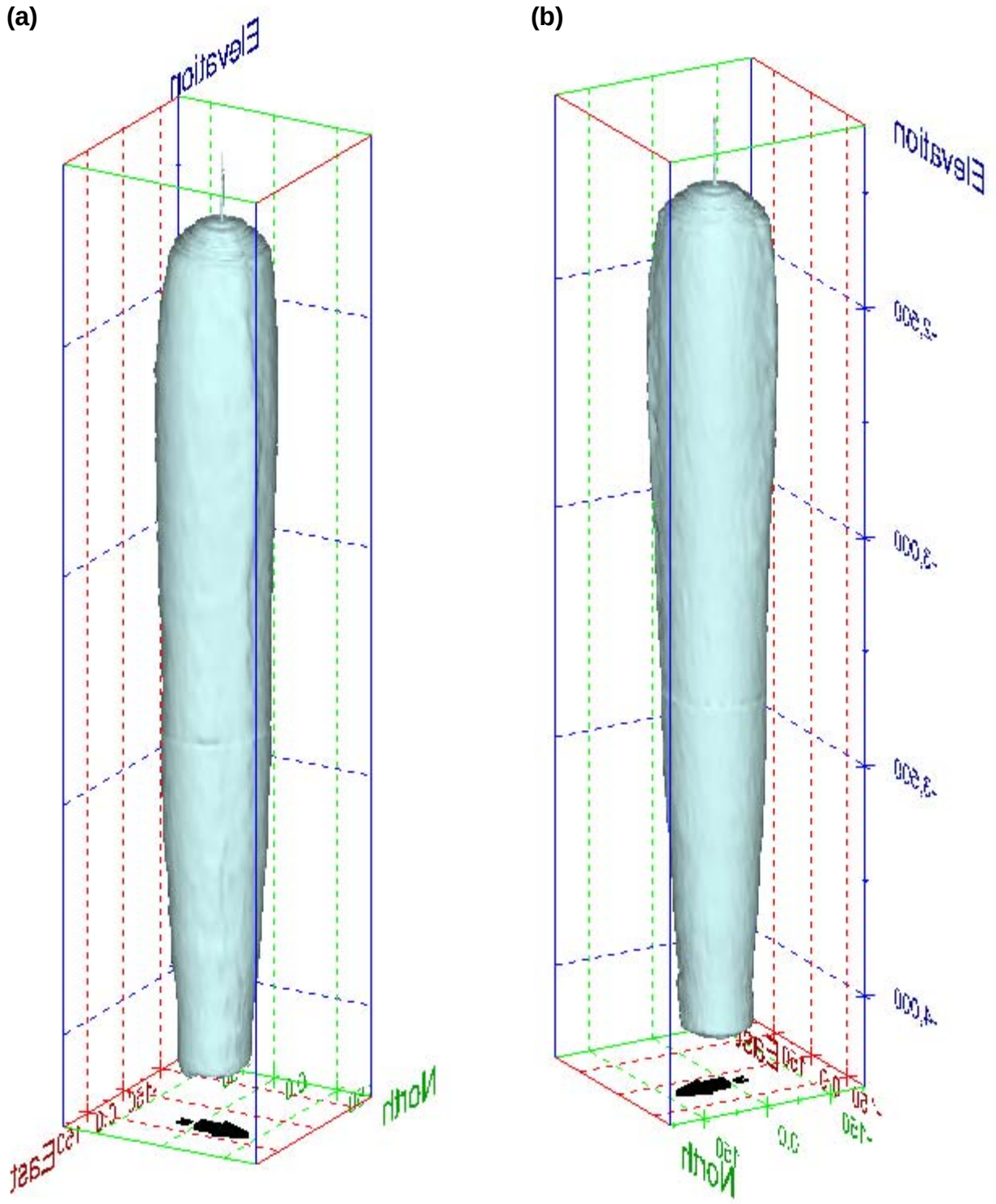

Figure 173. Sonar images of cavern BH-107, showing the basic geometric shape of the cavern. View from (a) azimuth 60°, elevation 20°; (b) azimuth 300°, elevation 20°.

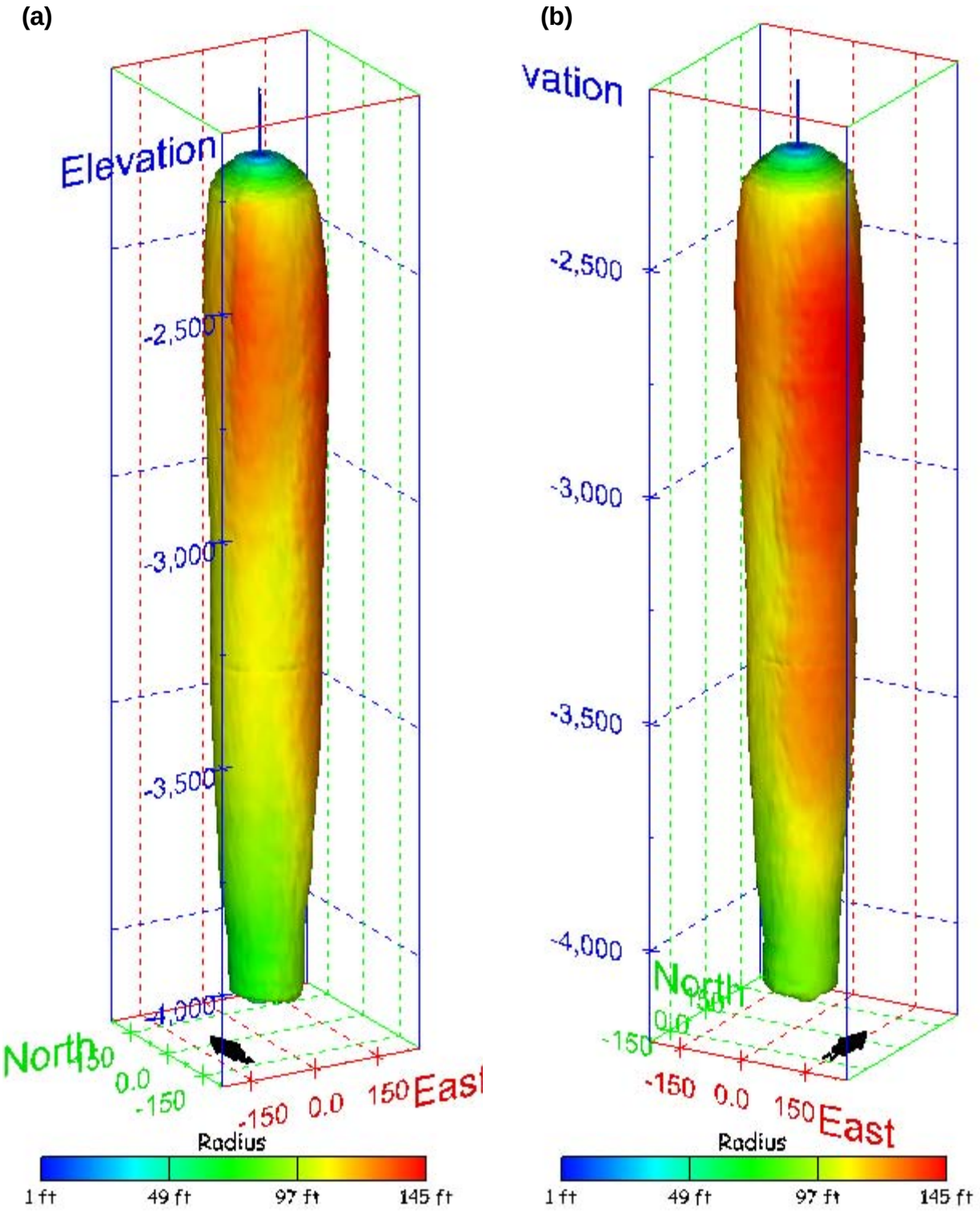

Figure 174. Sonar images of cavern BH-107, showing the geometry of the cavern colored by measured radius. View from (a) azimuth 210°, elevation 20°; (b) azimuth 150°, elevation 20°.

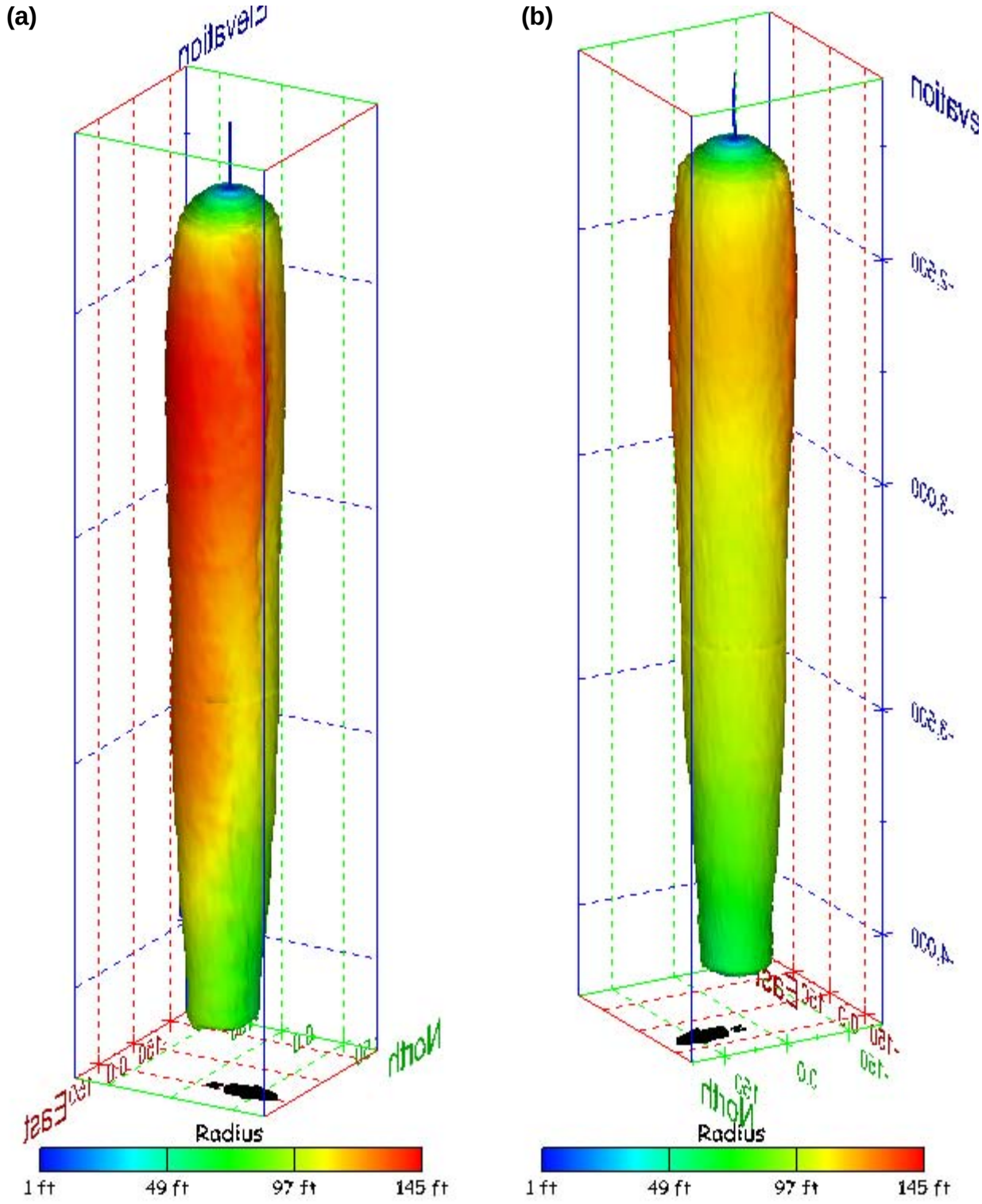

Figure 175. Sonar images of cavern BH-107, showing the geometry of the cavern colored by measured radius. View from (a) azimuth 0°, elevation 20°; (b) azimuth 300°, elevation 20°.

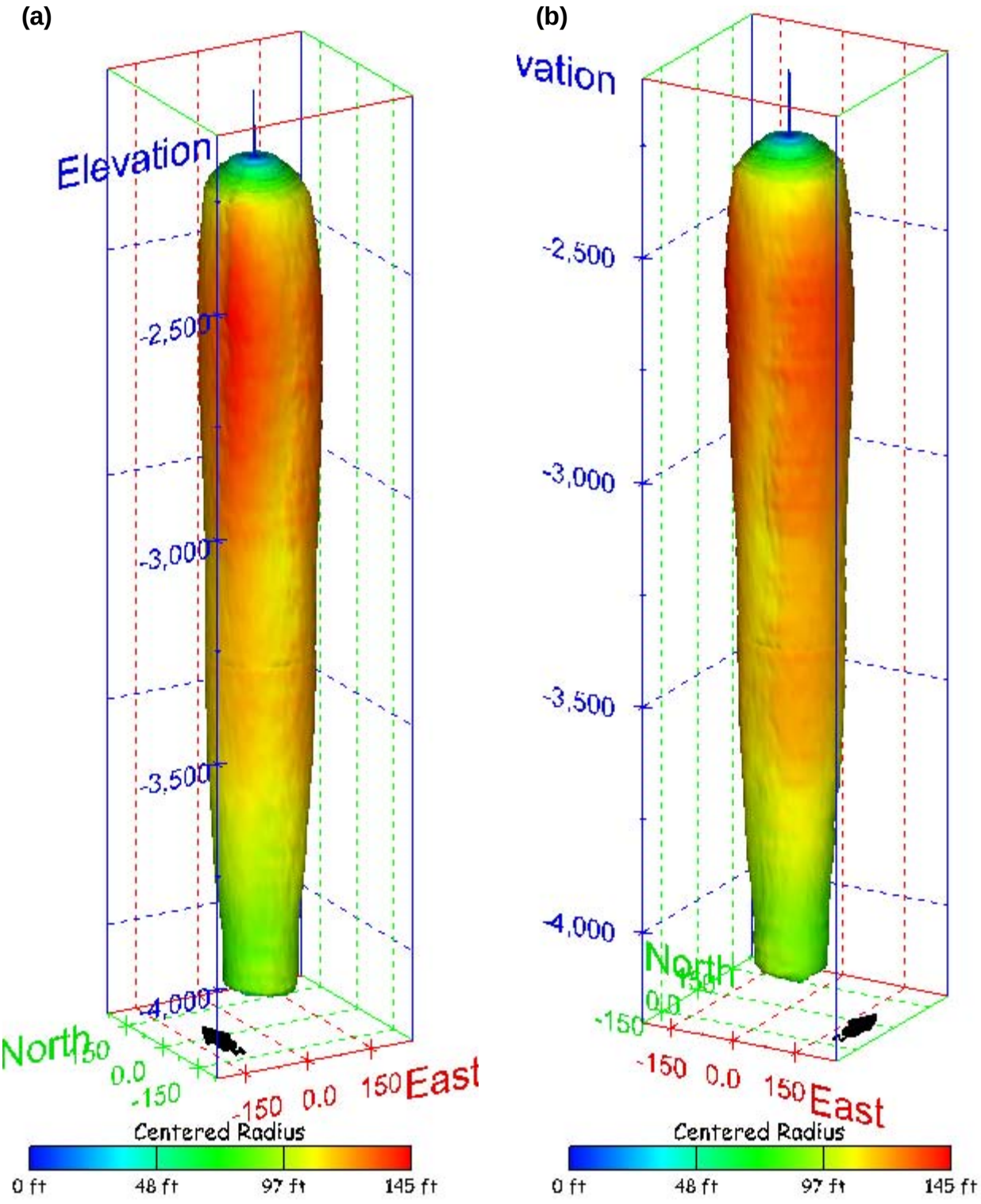

Figure 176. Sonar images of cavern BH-107, showing the geometry of the cavern colored by centered radius. View from (a) azimuth 210°, elevation 20°; (b) azimuth 150°, elevation 20°.

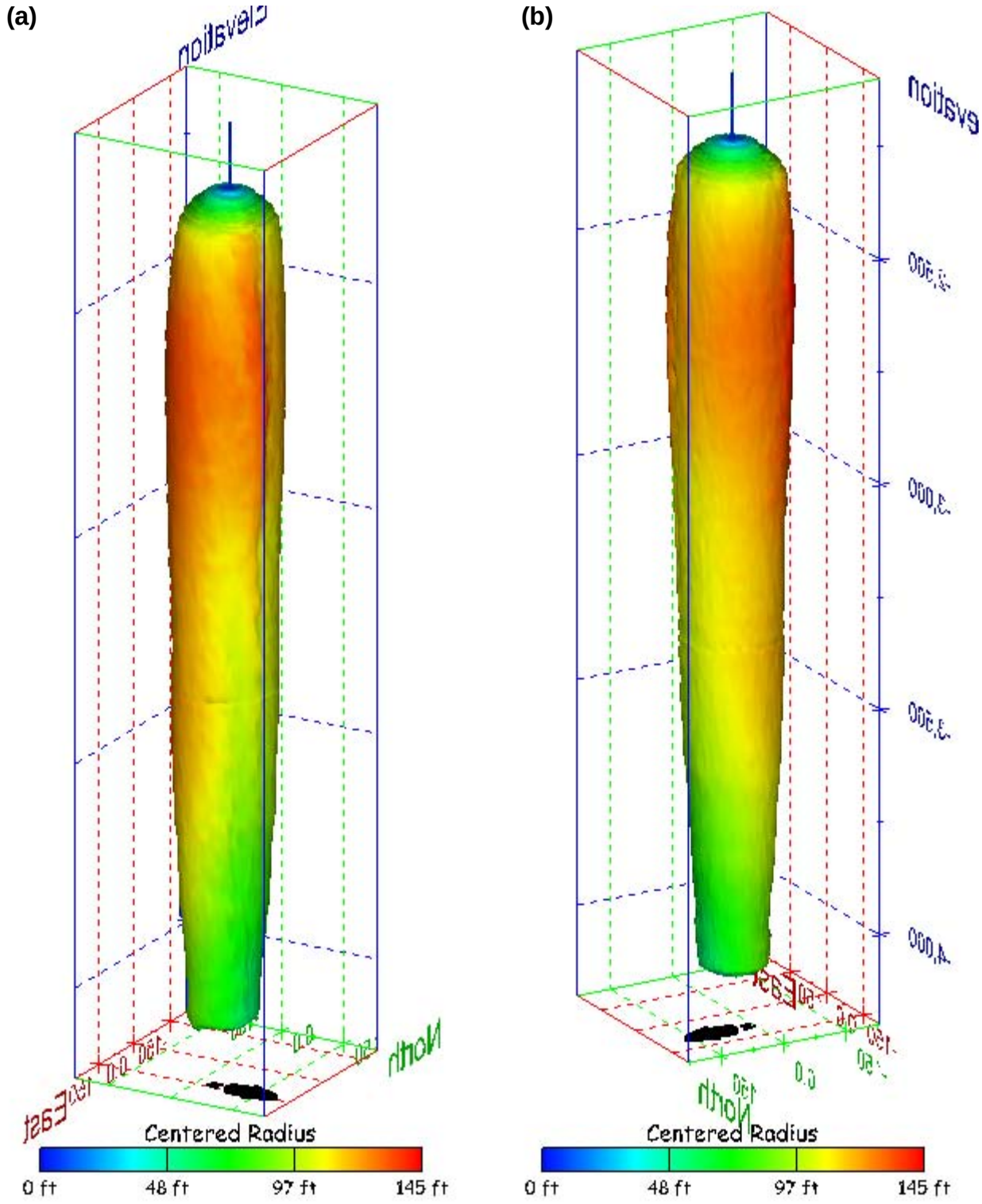

Figure 177. Sonar images of cavern BH-107, showing the geometry of the cavern colored by centered radius. View from (a) azimuth 60°, elevation 20°; (b) azimuth 300°, elevation 20°.

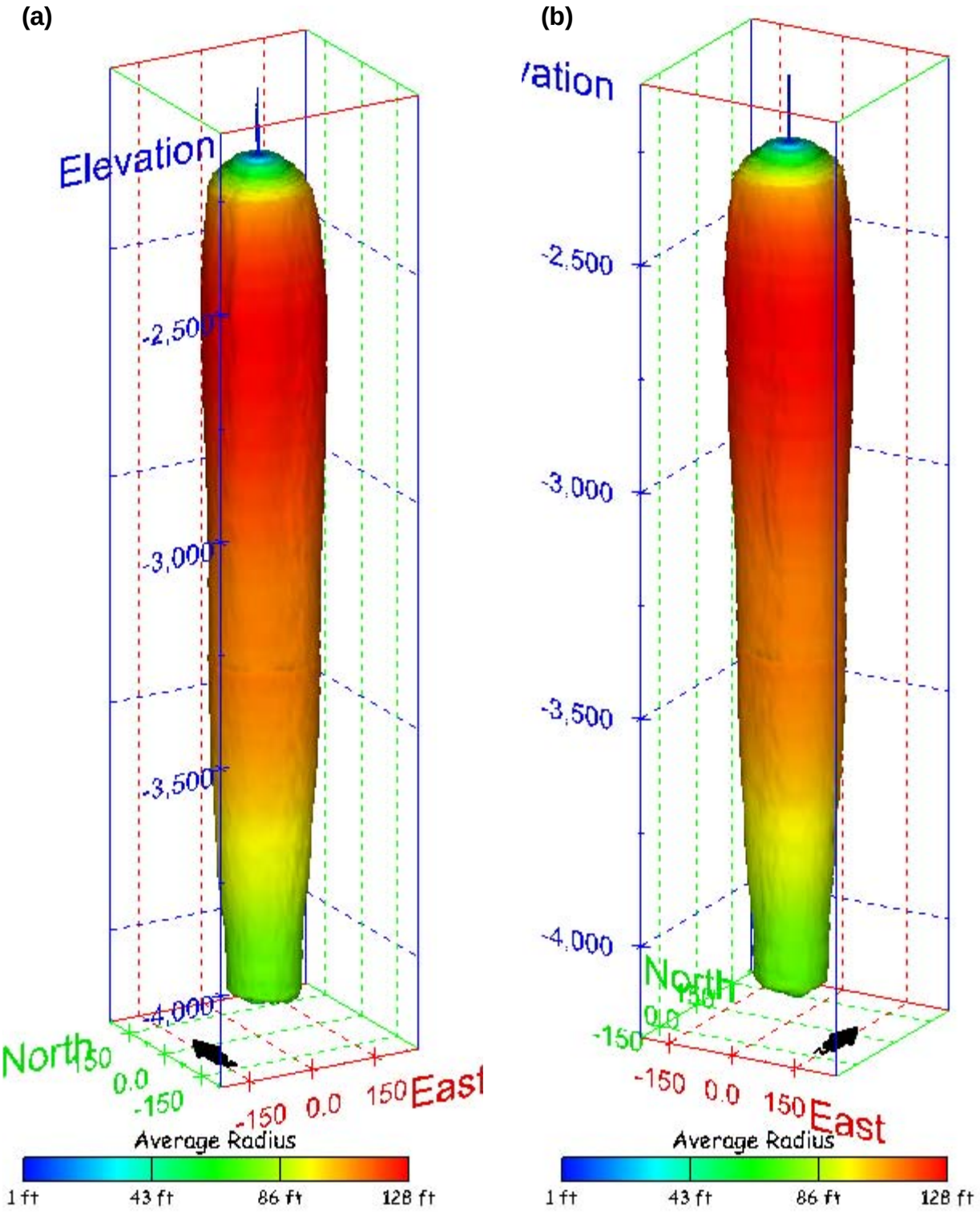

Figure 178. Sonar images of cavern BH-107, showing the geometry of the cavern colored by average radius. View from (a) azimuth 210°, elevation 20°; (b) azimuth 150°, elevation 20°.

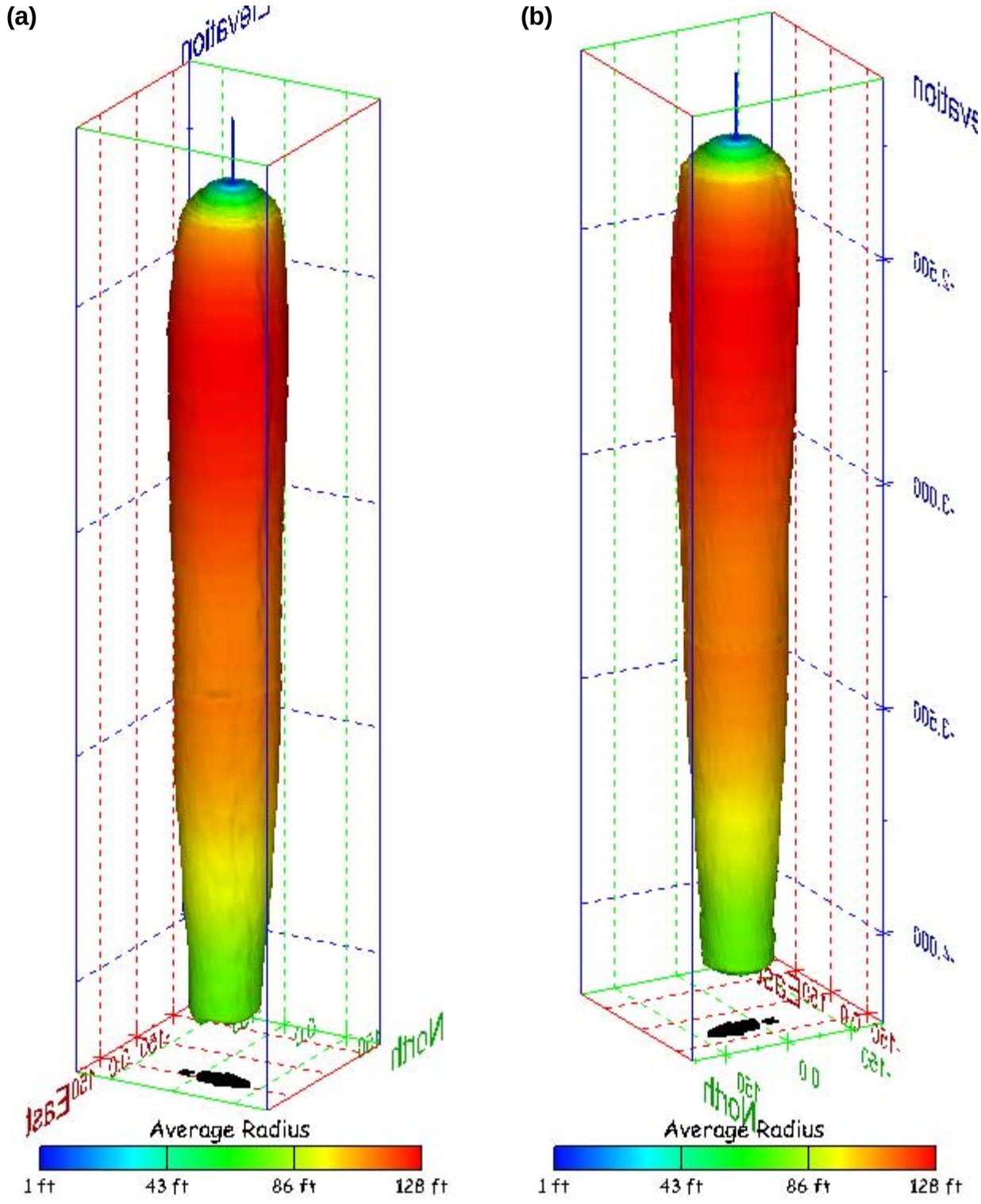

Figure 179. Sonar images of cavern BH-107, showing the geometry of the cavern colored by average radius. View from (a) azimuth 60°, elevation 20°; (b) azimuth 300°, elevation 20°.

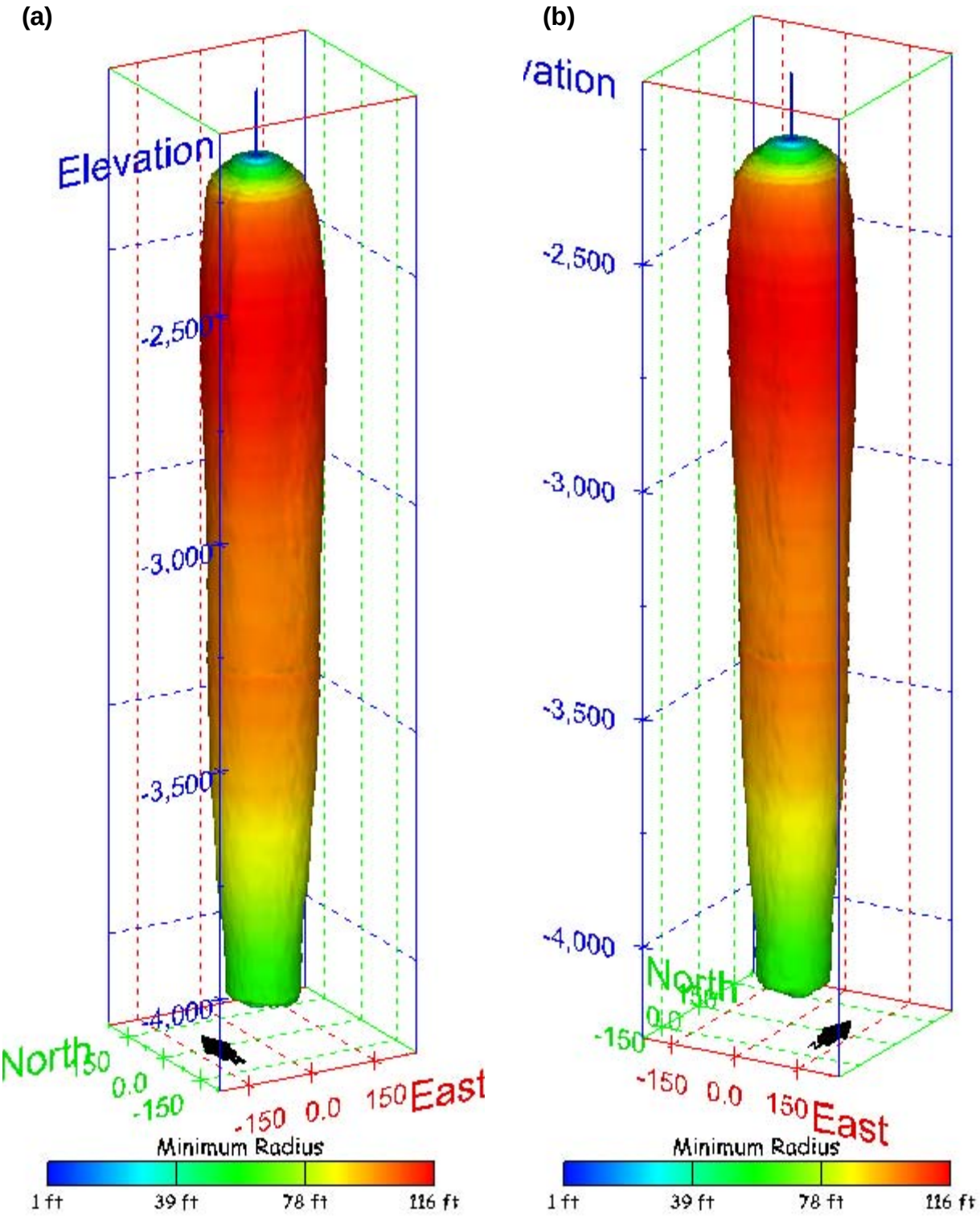

Figure 180. Sonar images of cavern BH-107, showing the geometry of the cavern colored by minimum radius. View from (a) azimuth 210°, elevation 20°; (b) azimuth 150°, elevation 20°.

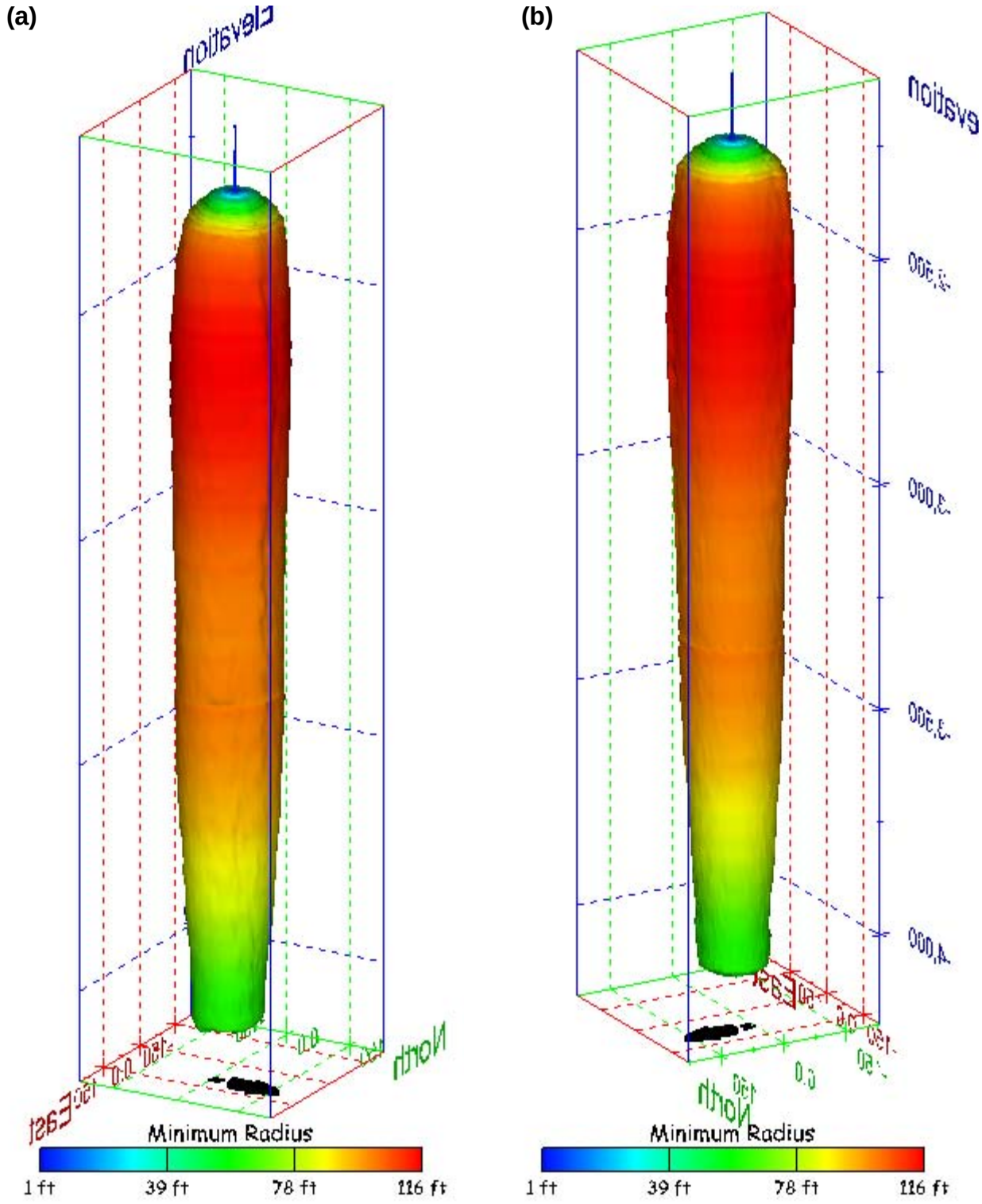

Figure 181. Sonar images of cavern BH-107, showing the geometry of the cavern colored by minimum radius. View from (a) azimuth 60°, elevation 20°; (b) azimuth 300°, elevation 20°.

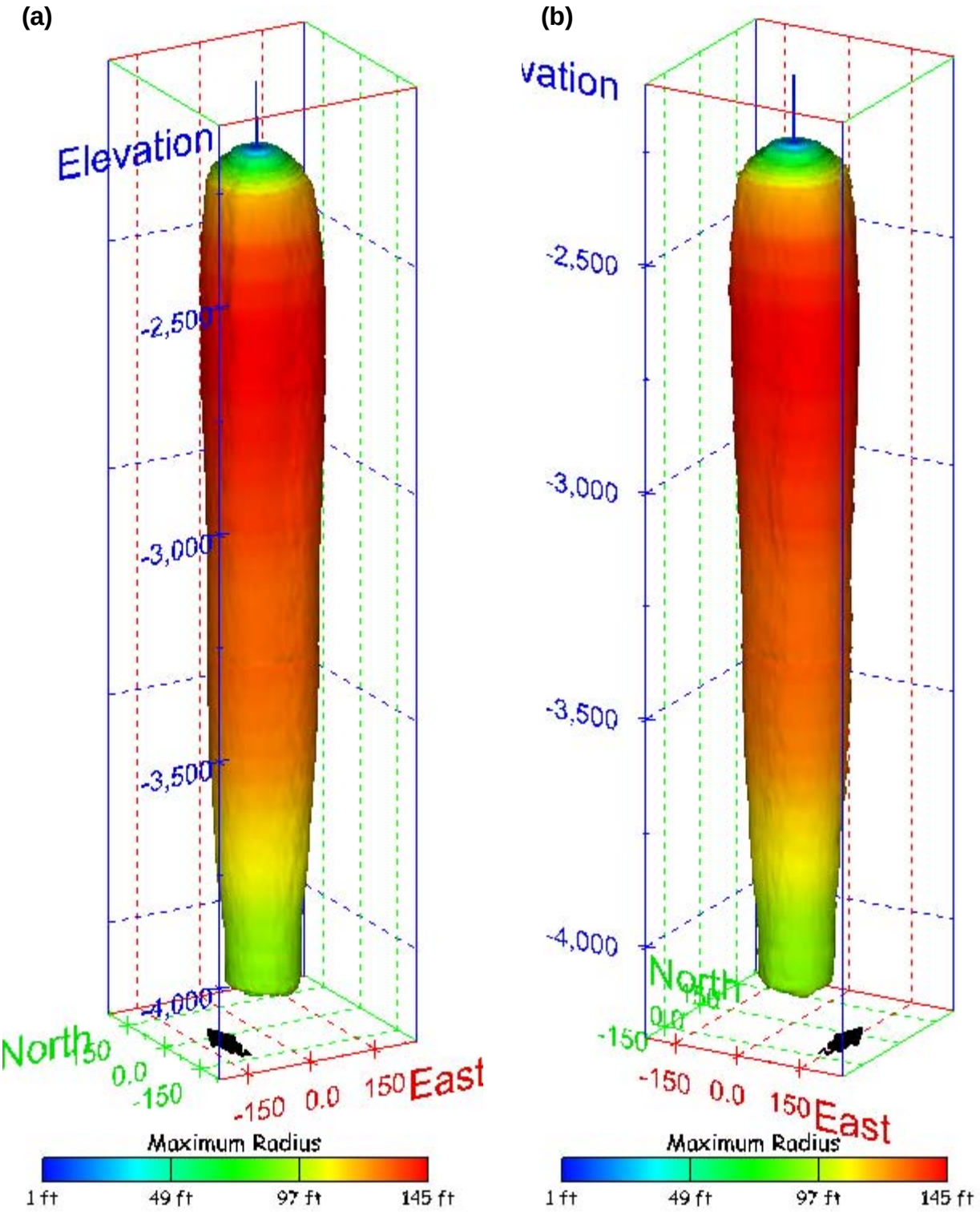

Figure 182. Sonar images of cavern BH-107, showing the geometry of the cavern colored by maximum radius. View from (a) azimuth 210°, elevation 20°; (b) azimuth 150°, elevation 20°.

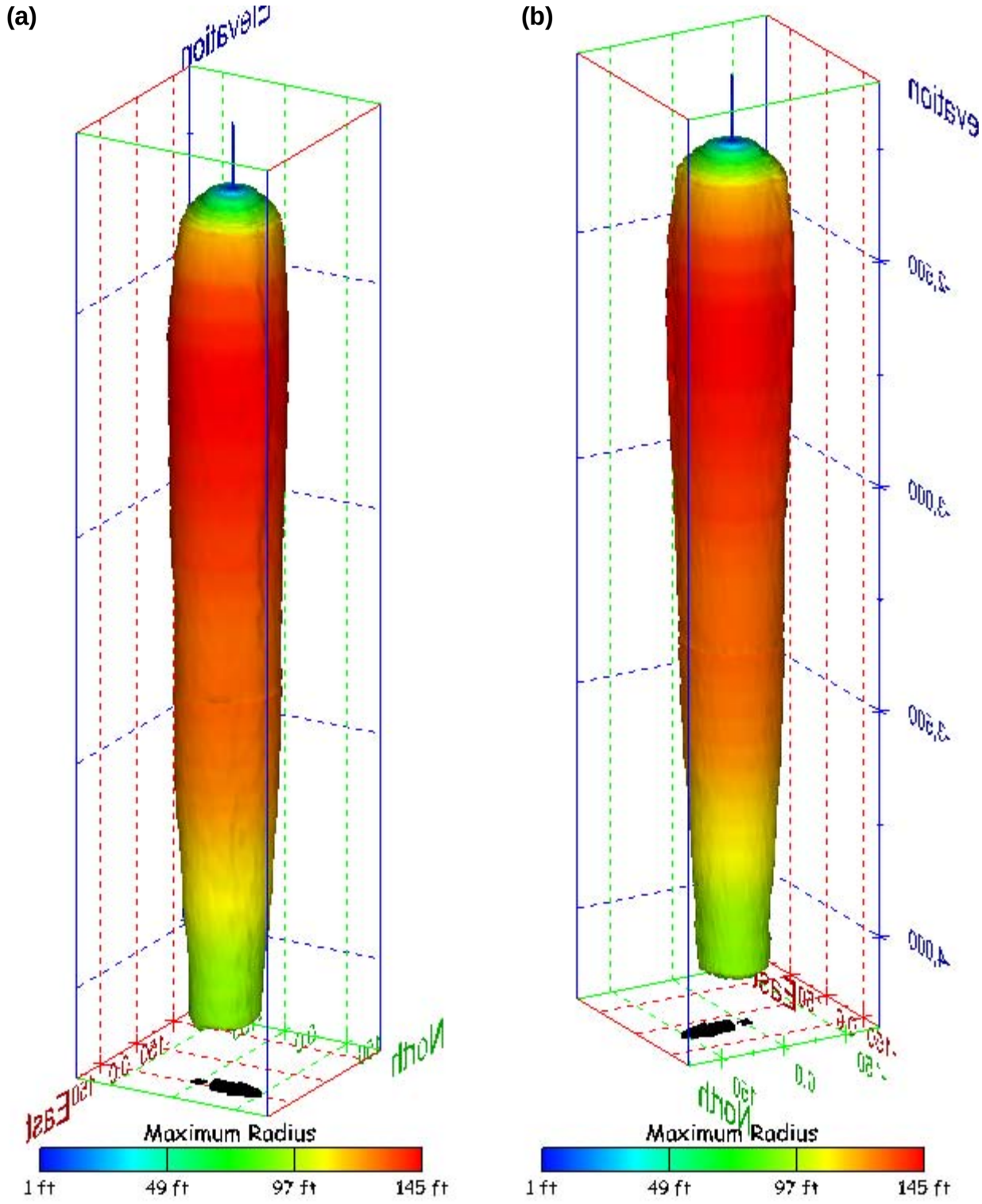

Figure 183. Sonar images of cavern BH-107, showing the geometry of the cavern colored by maximum radius. View from (a) azimuth 60°, elevation 20°; (b) azimuth 300°, elevation 20°.

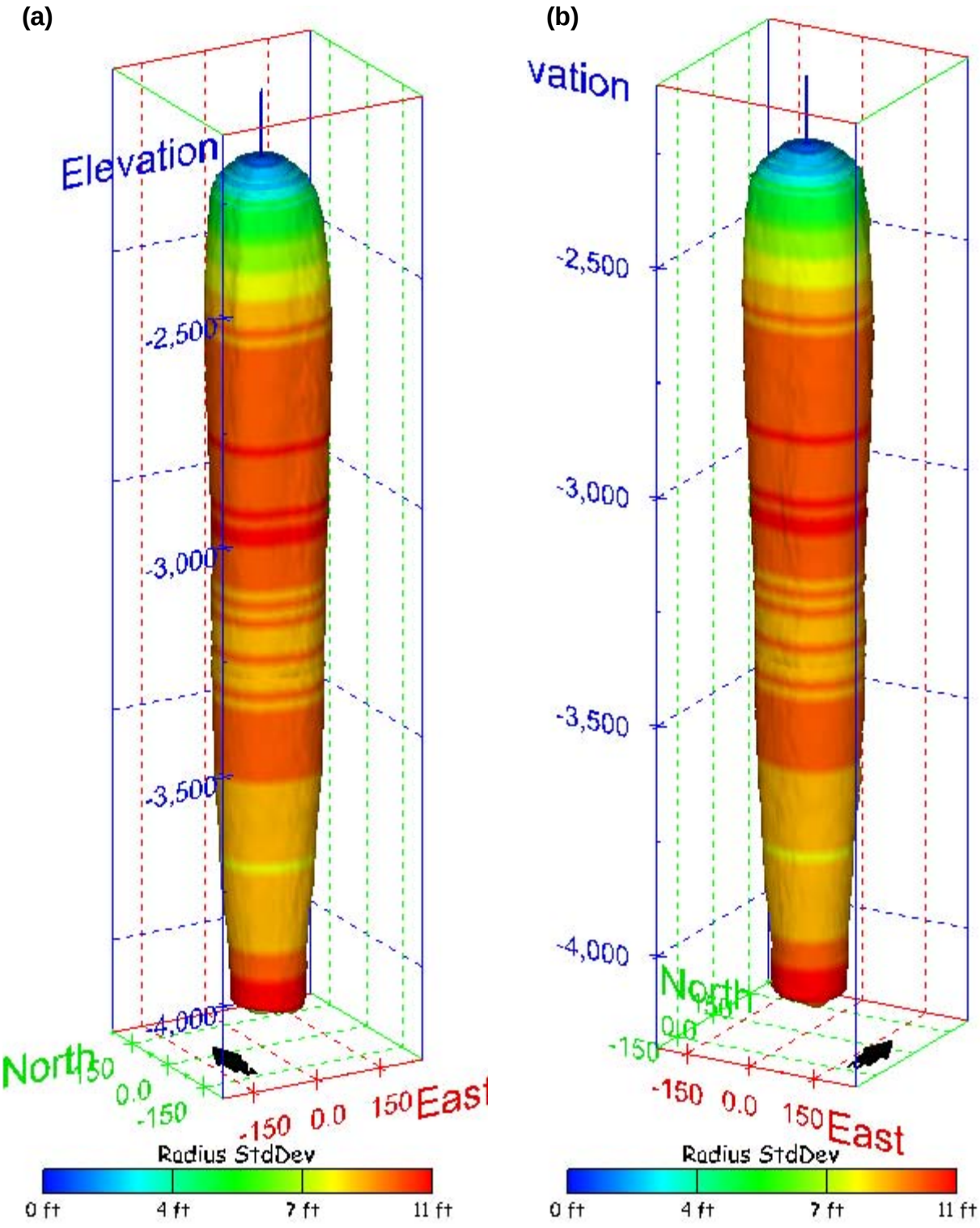

Figure 184. Sonar images of cavern BH-107, showing the geometry of the cavern colored by radius standard deviation. View from (a) azimuth 210°, elevation 20°; (b) azimuth 150°, elevation 20°.

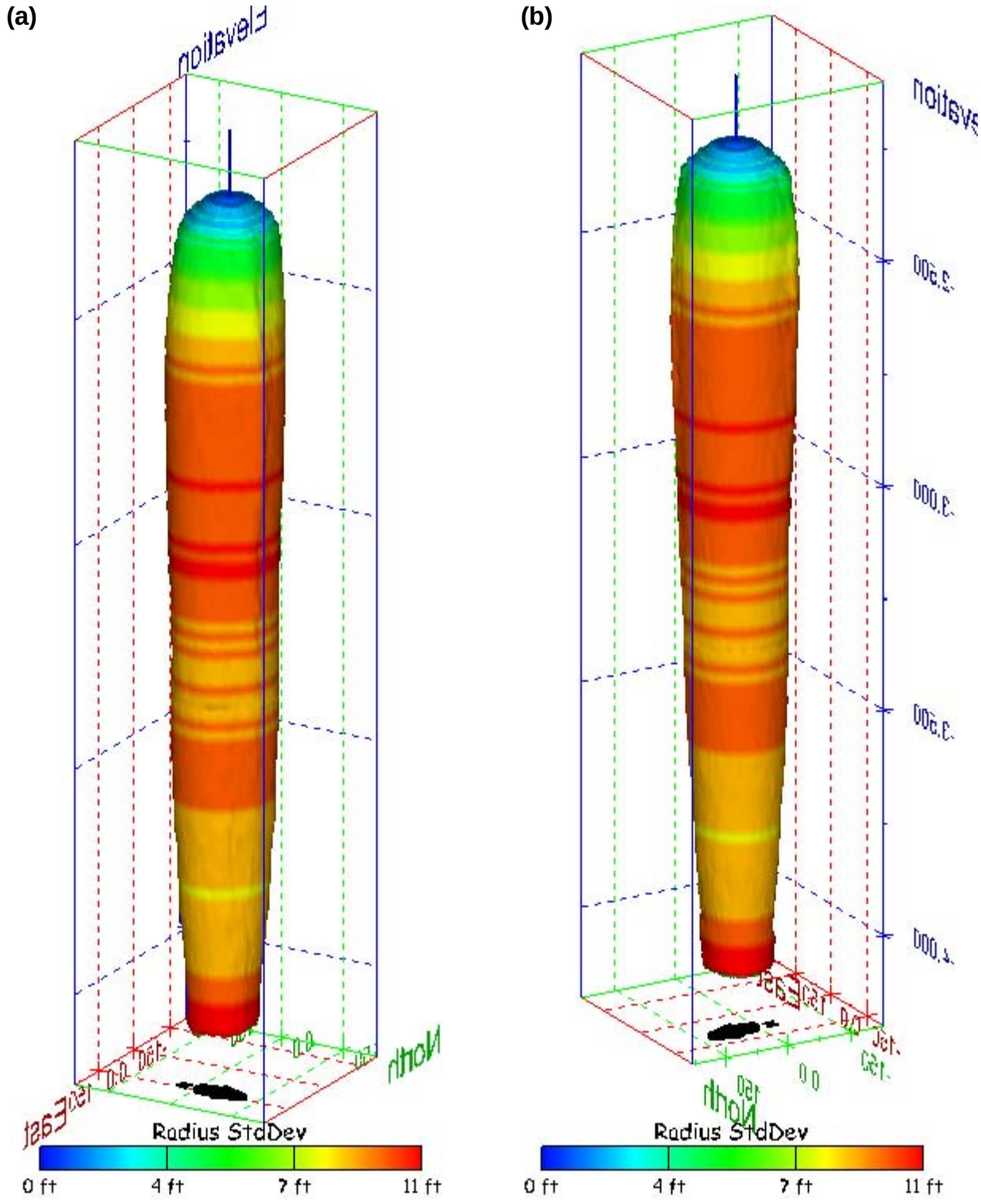

Figure 185. Sonar images of cavern BH-107, showing the geometry of the cavern colored by radius standard deviation. View from (a) azimuth 60°, elevation 20°; (b) azimuth 300°, elevation 20°.

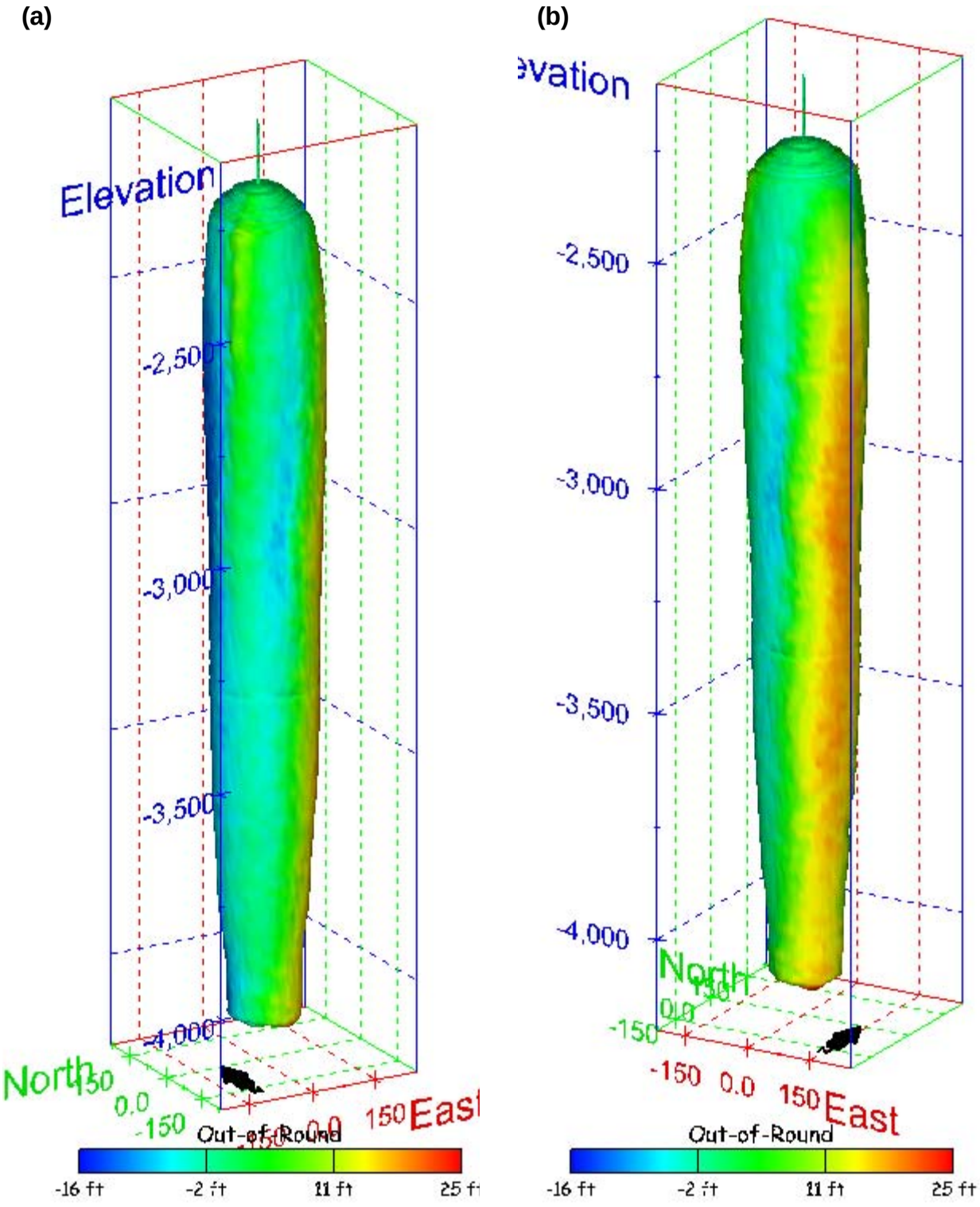

Figure 186. Sonar images of cavern BH-107, showing the geometry of the cavern colored by out-of-round distance. View from (a) azimuth 210°, elevation 20°; (b) azimuth 150°, elevation 20°.

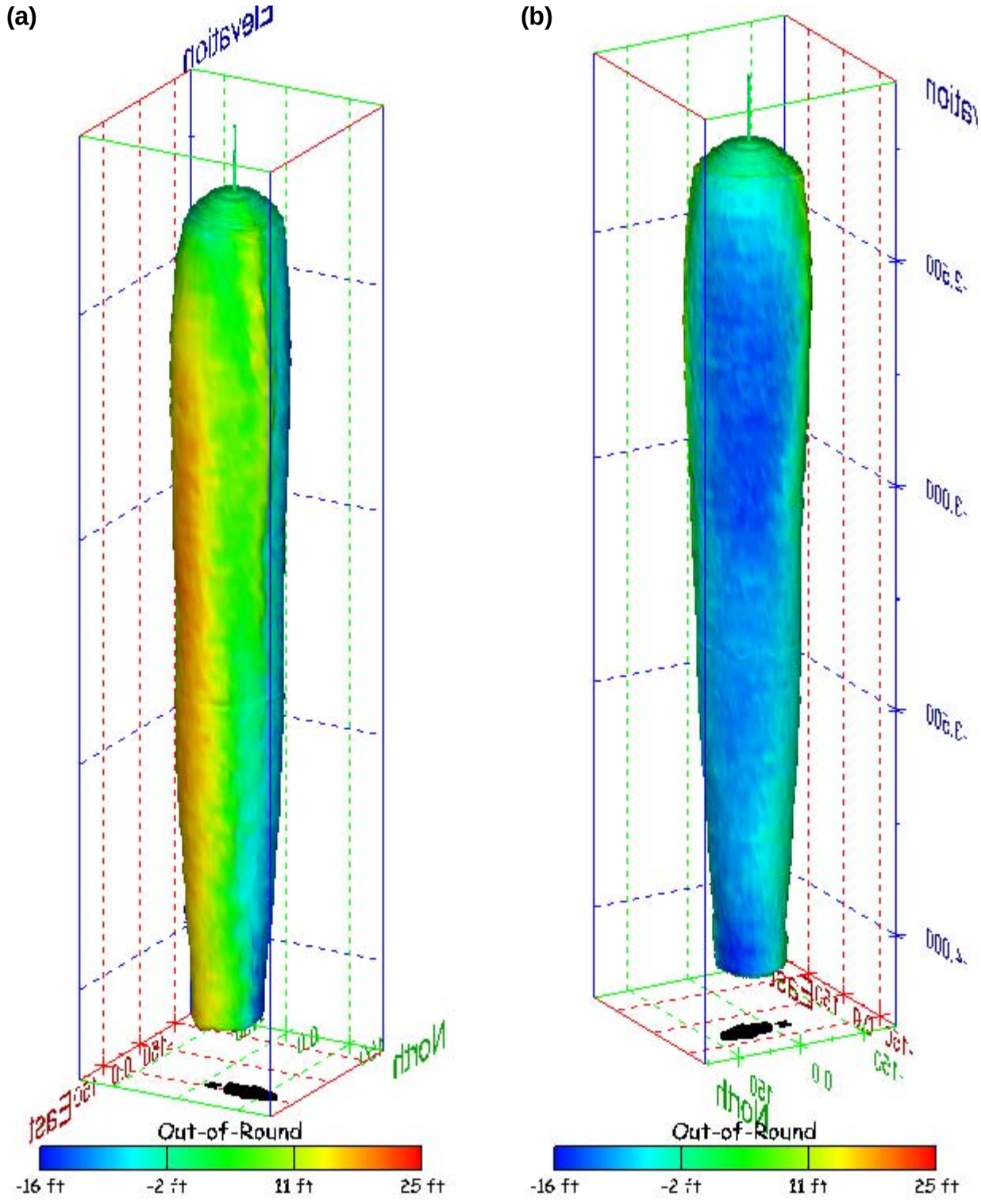

Figure 187. Sonar images of cavern BH-107, showing the geometry of the cavern colored by out-of-round distance. View from (a) azimuth 60°, elevation 20°; (b) azimuth 300°, elevation 20°.

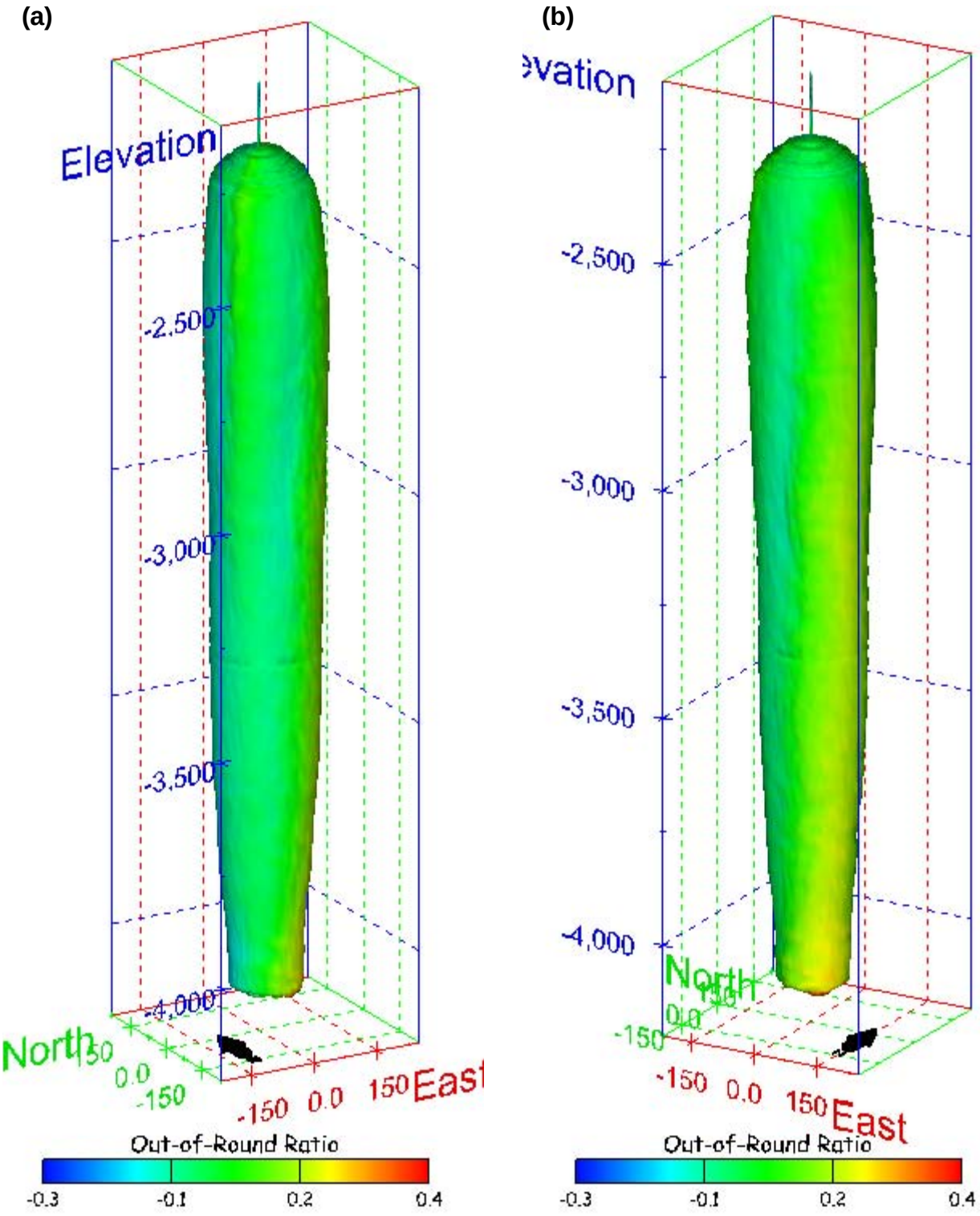

Figure 188. Sonar images of cavern BH-107, showing the geometry of the cavern colored by out-of-round ratio. View from (a) azimuth 210°, elevation 20°; (b) azimuth 150°, elevation 20°.

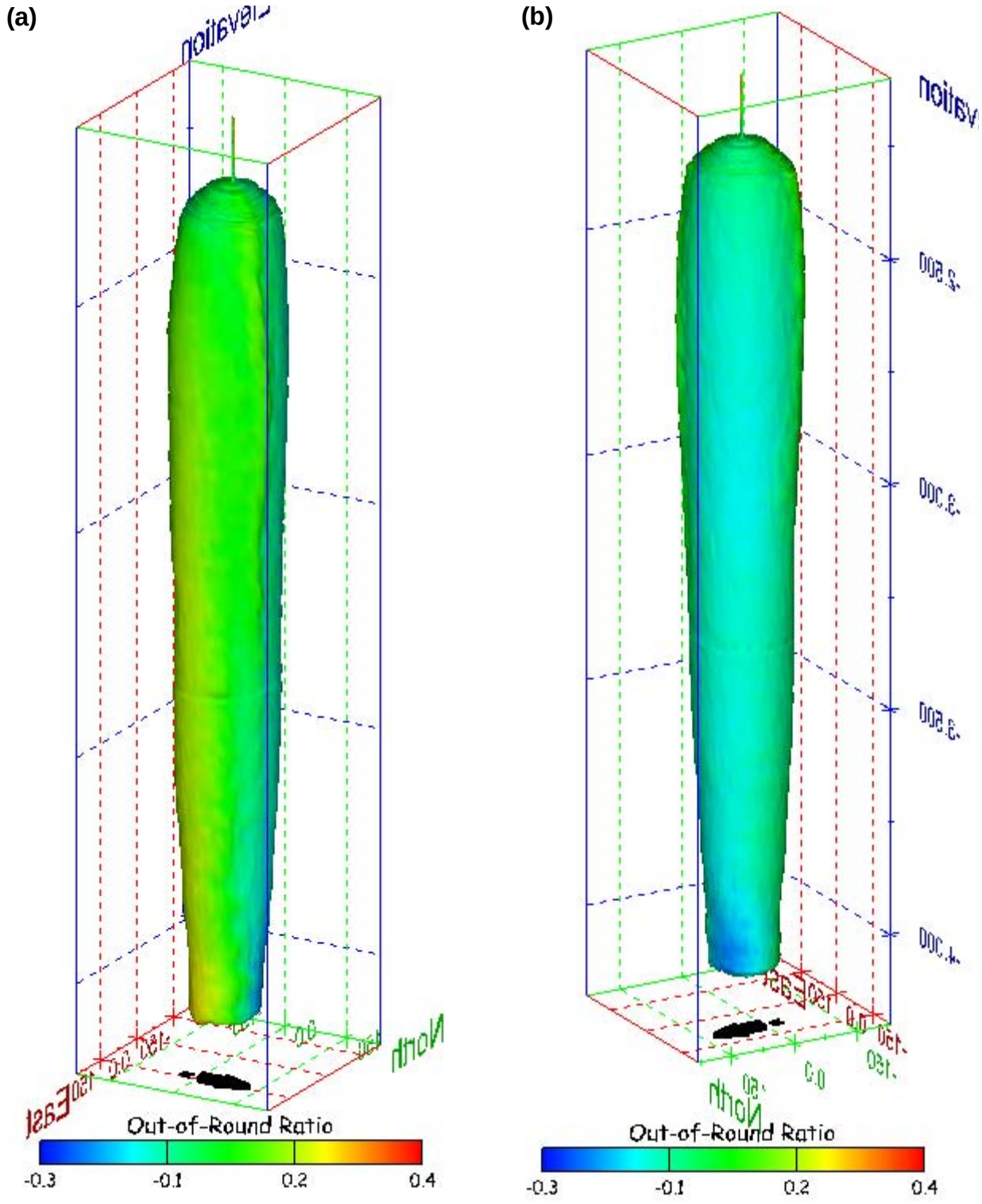

Figure 189. Sonar images of cavern BH-107, showing the geometry of the cavern colored by out-of-round ratio. View from (a) azimuth 60°, elevation 20°; (b) azimuth 300°, elevation 20°.

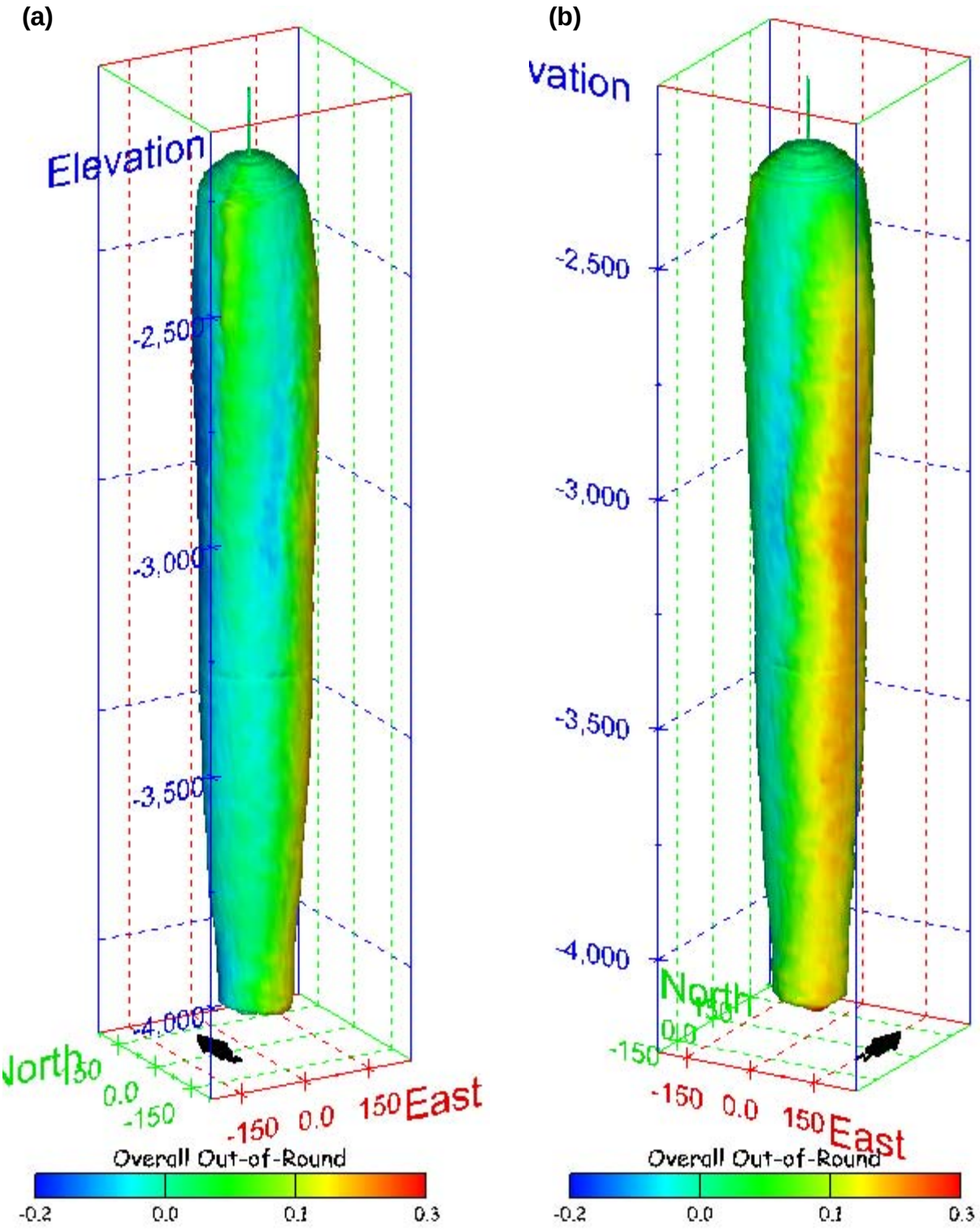

Figure 190. Sonar images of cavern BH-107, showing the geometry of the cavern colored by overall out-of-round ratio. View from (a) azimuth 210°, elevation 20°; (b) azimuth 150°, elevation 20°.

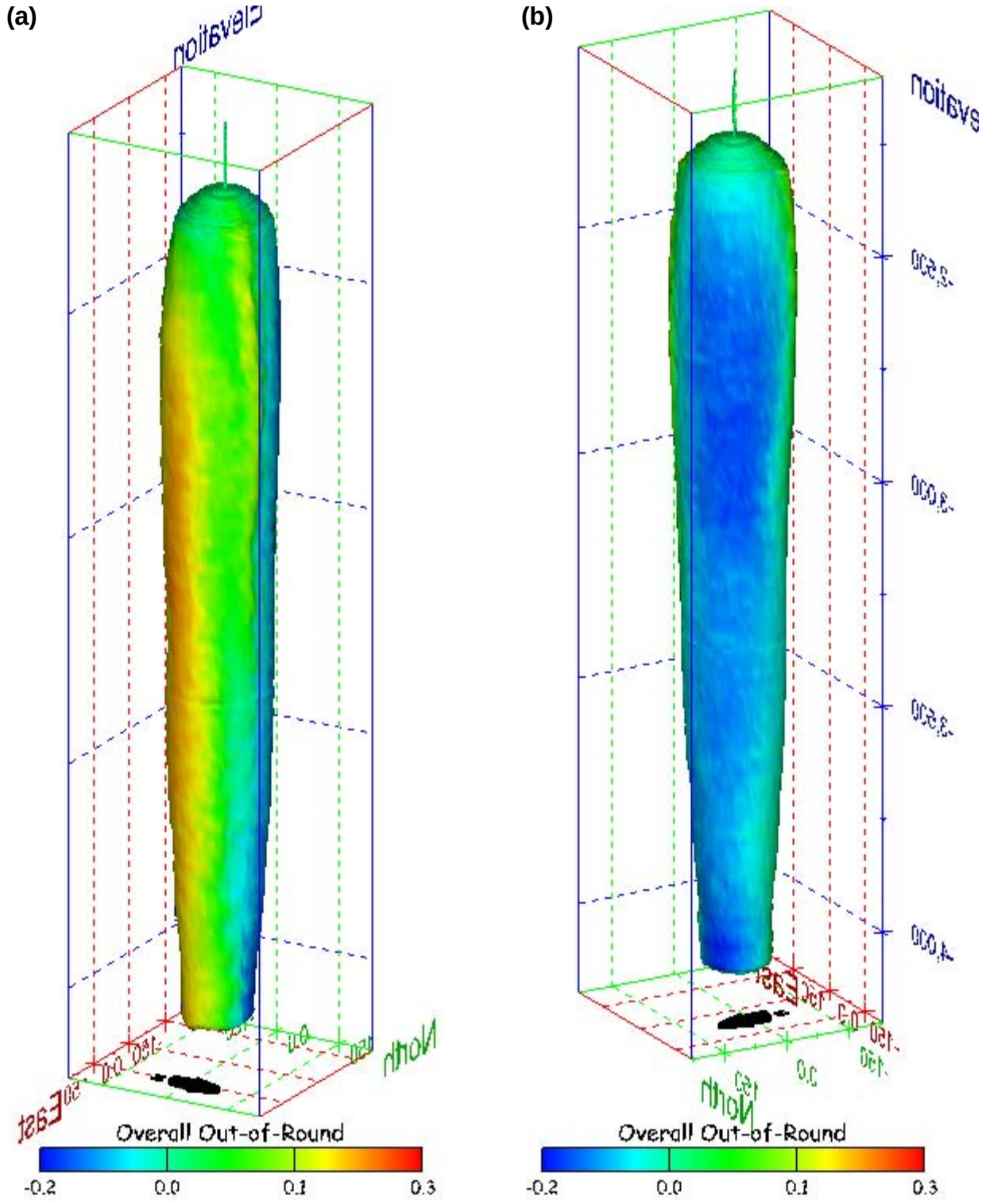

Figure 191. Sonar images of cavern BH-107, showing the geometry of the cavern colored by overall out-of-round ratio. View from (a) azimuth 60°, elevation 20°; (b) azimuth 300°, elevation 20°.

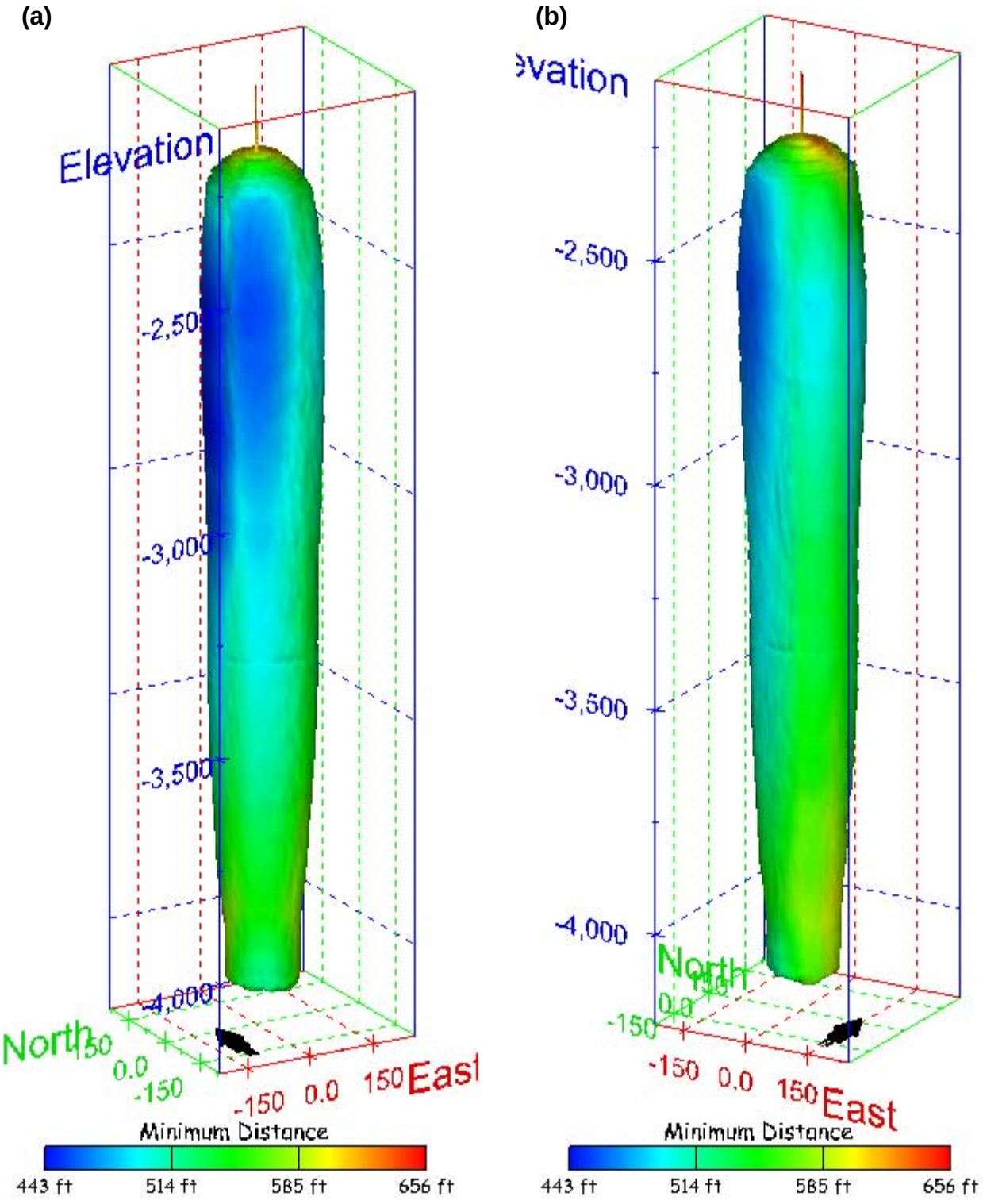

Figure 192. Sonar images of cavern BH-107, showing the geometry of the cavern colored by the minimum distance to the nearest neighboring cavern. View from (a) azimuth 210°, elevation 20°; (b) azimuth 150°, elevation 20°.

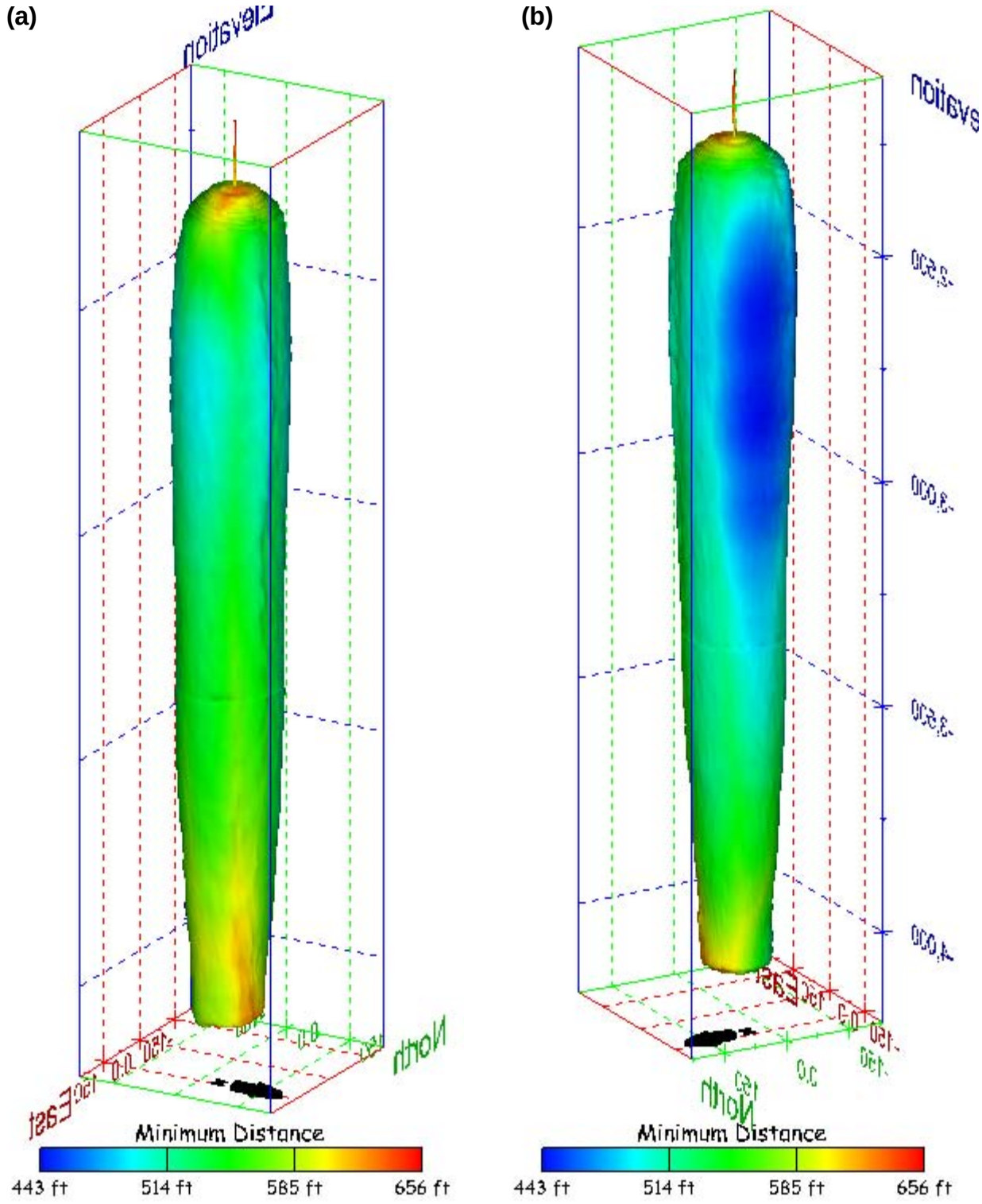

Figure 193. Sonar images of cavern BH-107, showing the geometry of the cavern colored by minimum distance to the nearest neighboring cavern. View from (a) azimuth 60°, elevation 20°; (b) azimuth 300°, elevation 20°.

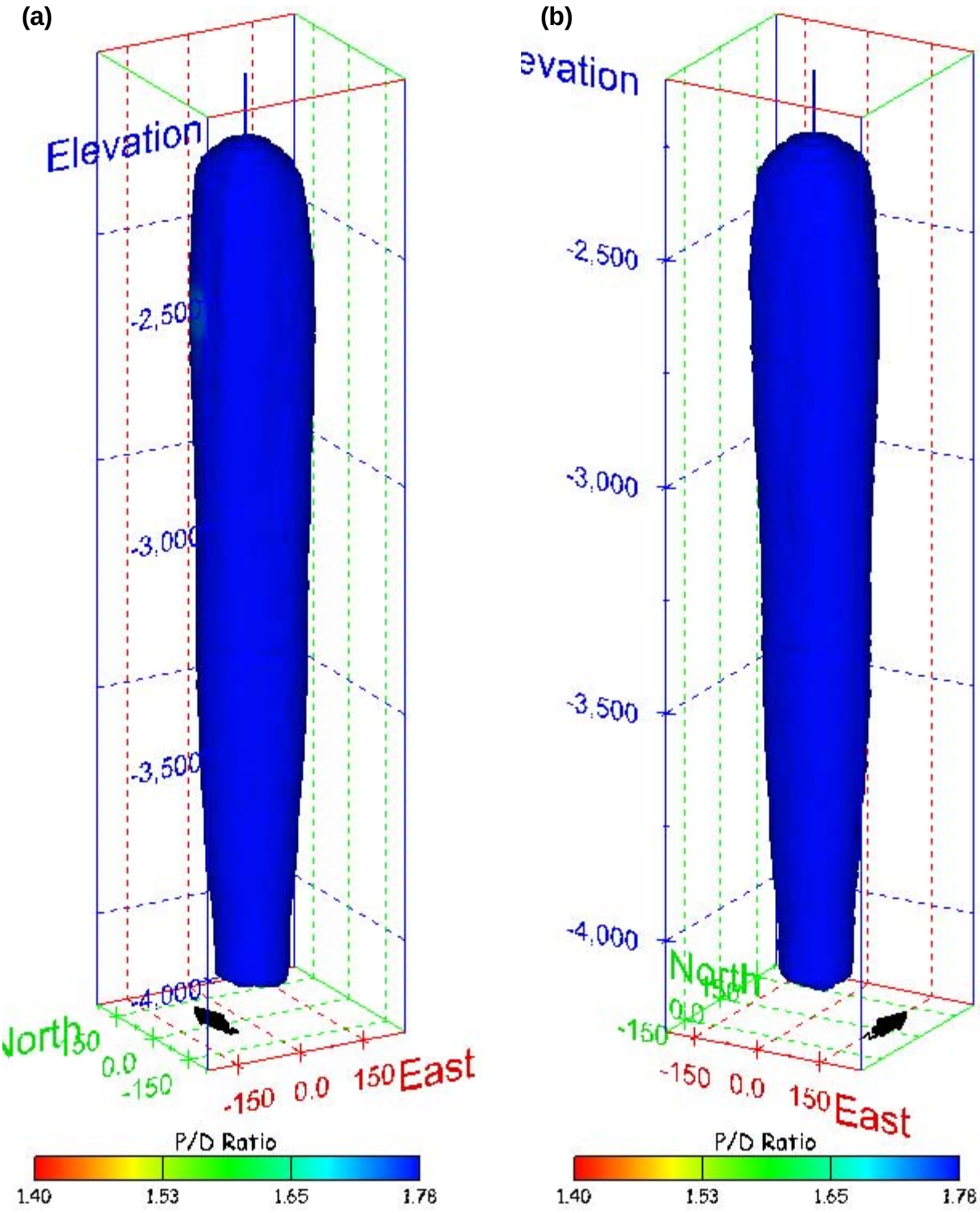

Figure 194. Sonar images of cavern BH-107, showing the geometry of the cavern colored by three-dimensional pillar-to-diameter ratio. View from (a) azimuth 210°, elevation 20°; (b) azimuth 150°, elevation 20°.

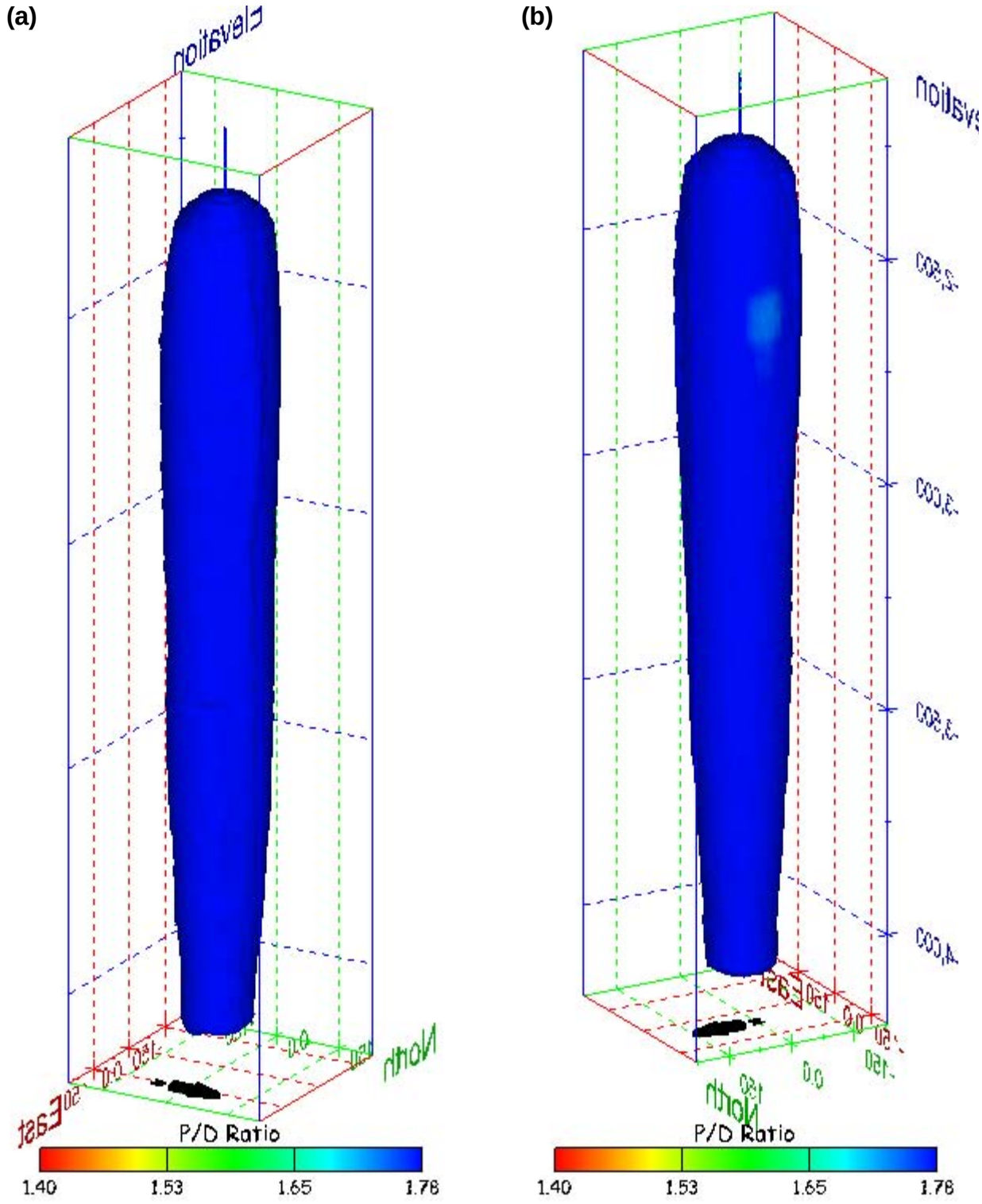

Figure 195. Sonar images of cavern BH-107, showing the geometry of the cavern colored by three-dimensional pillar-to-diameter ratio. View from (a) azimuth 60°, elevation 20°; (b) azimuth 300°, elevation 20°.

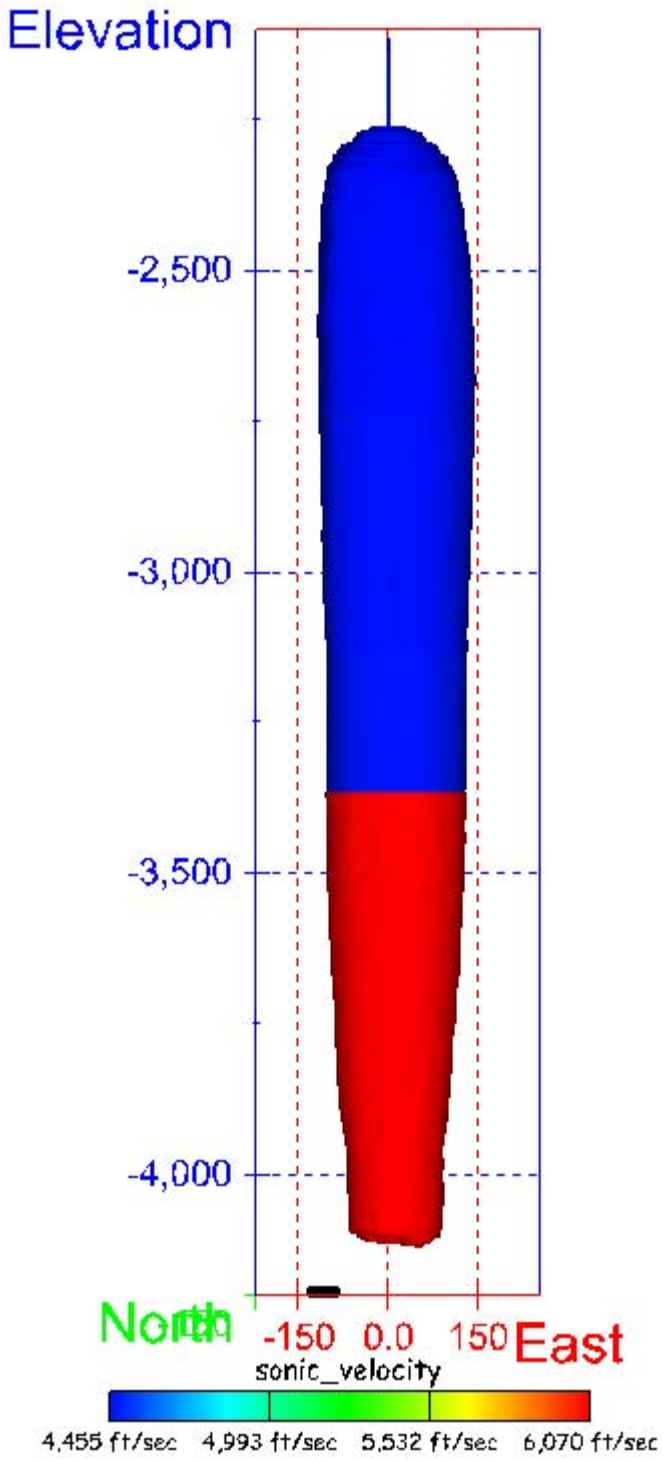

Figure 196. Sonar image of cavern BH-107, showing the geometry of the cavern colored by the reported velocity of sound on the survey date of November 2000. View from due south, elevation zero.

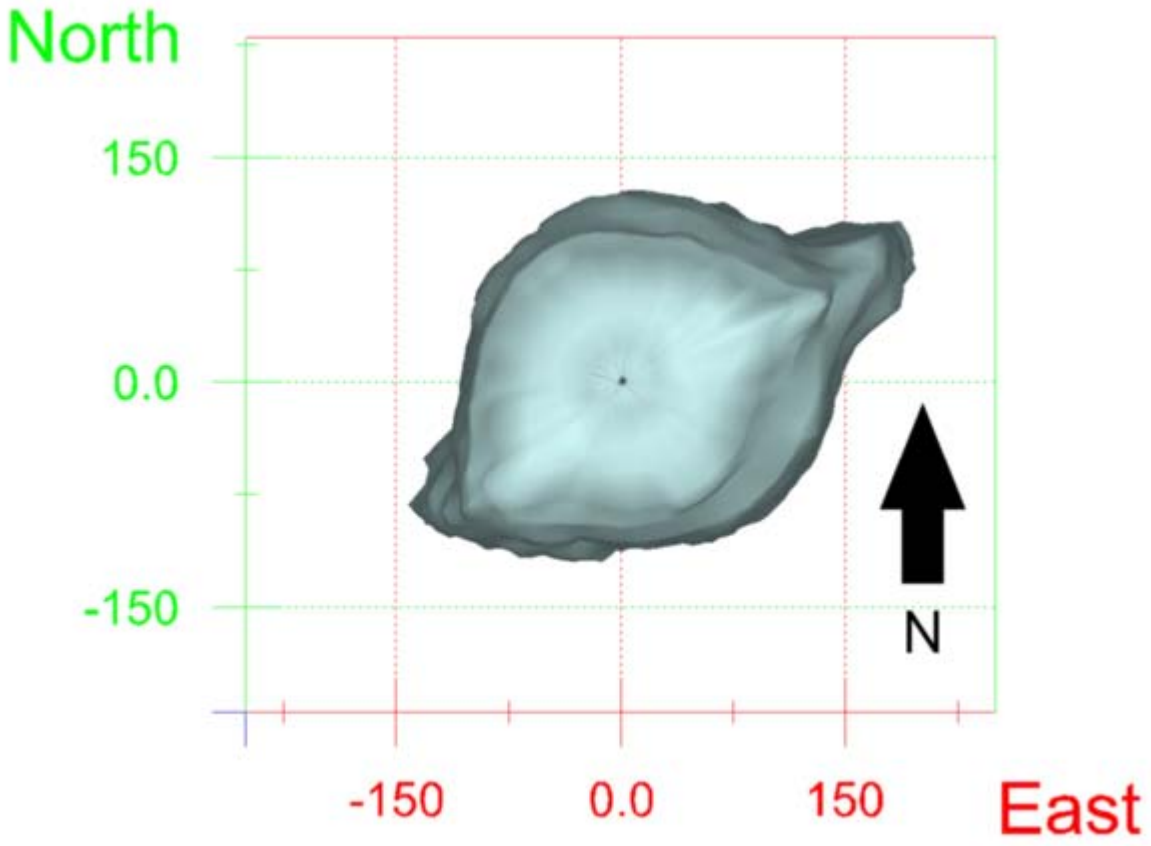

Figure 197. Map view sonar image of cavern BH-108, showing the basic geometry of the cavern. Grid squares represent 150 ft.

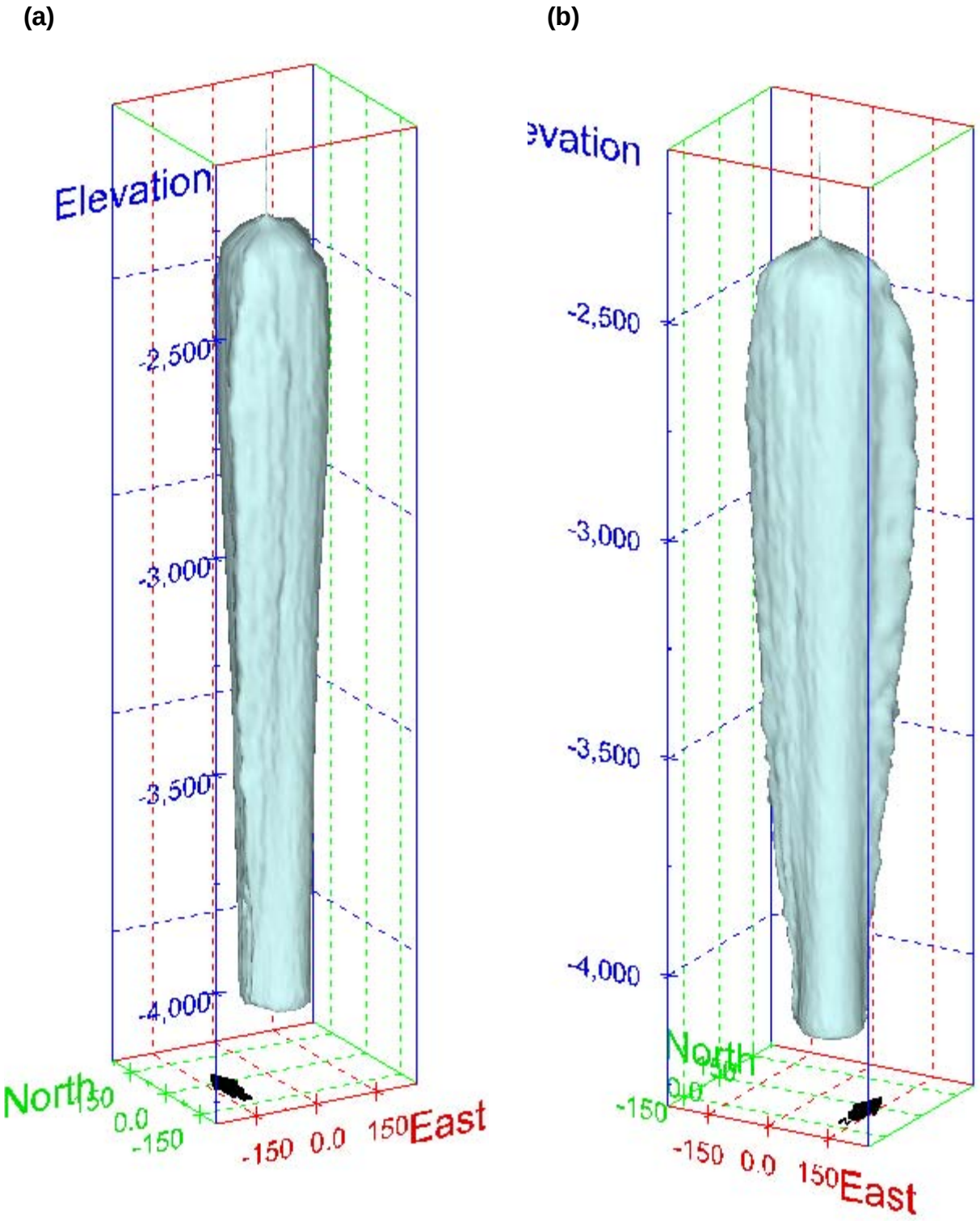

Figure 198. Sonar images of cavern BH-108, showing the basic geometric shape of the cavern. View from (a) azimuth 210°, elevation 20°; (b) azimuth 150°, elevation 20°.

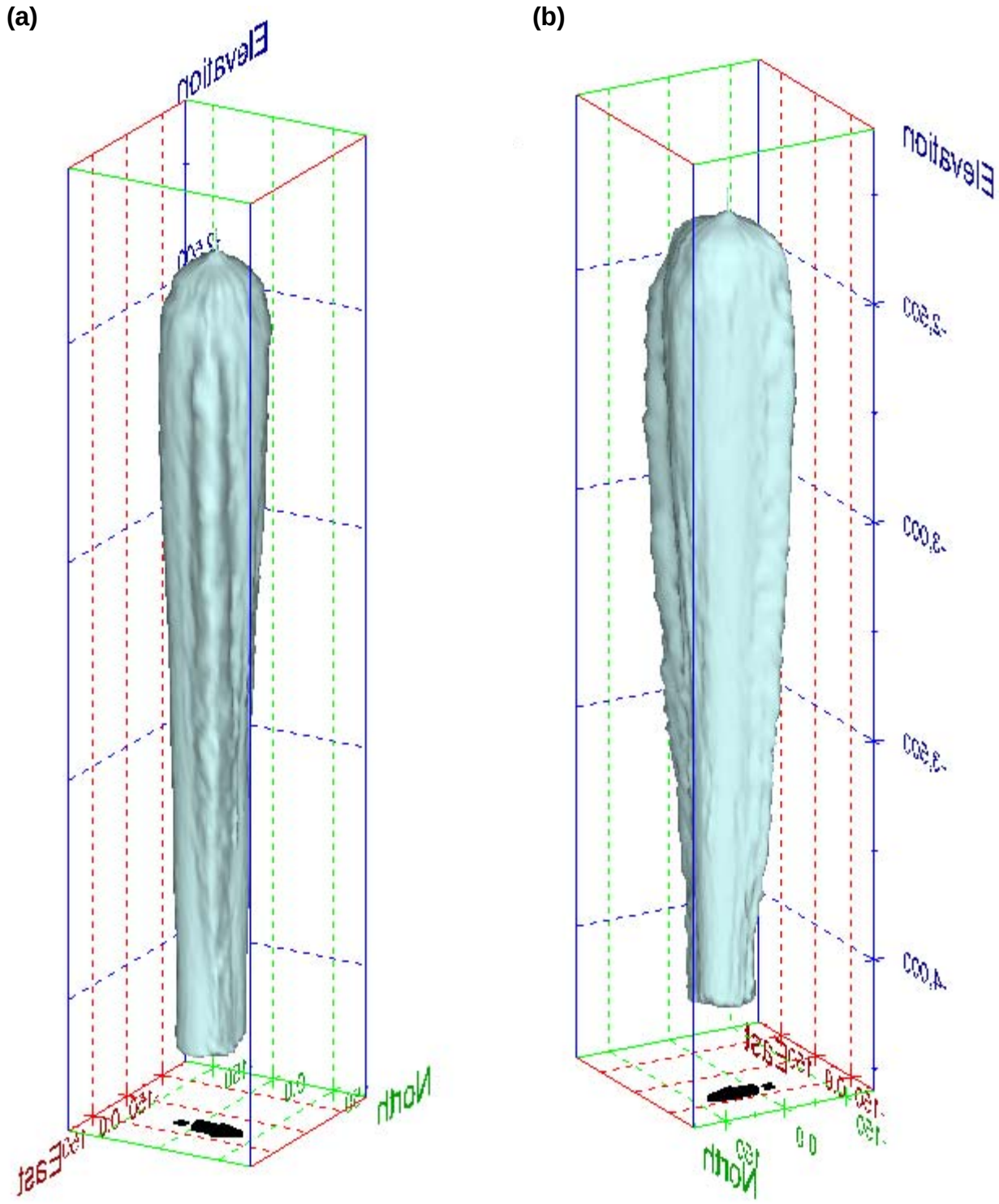

Figure 199. Sonar images of cavern BH-108, showing the basic geometric shape of the cavern. View from (a) azimuth 60°, elevation 20°; (b) azimuth 300°, elevation 20°.

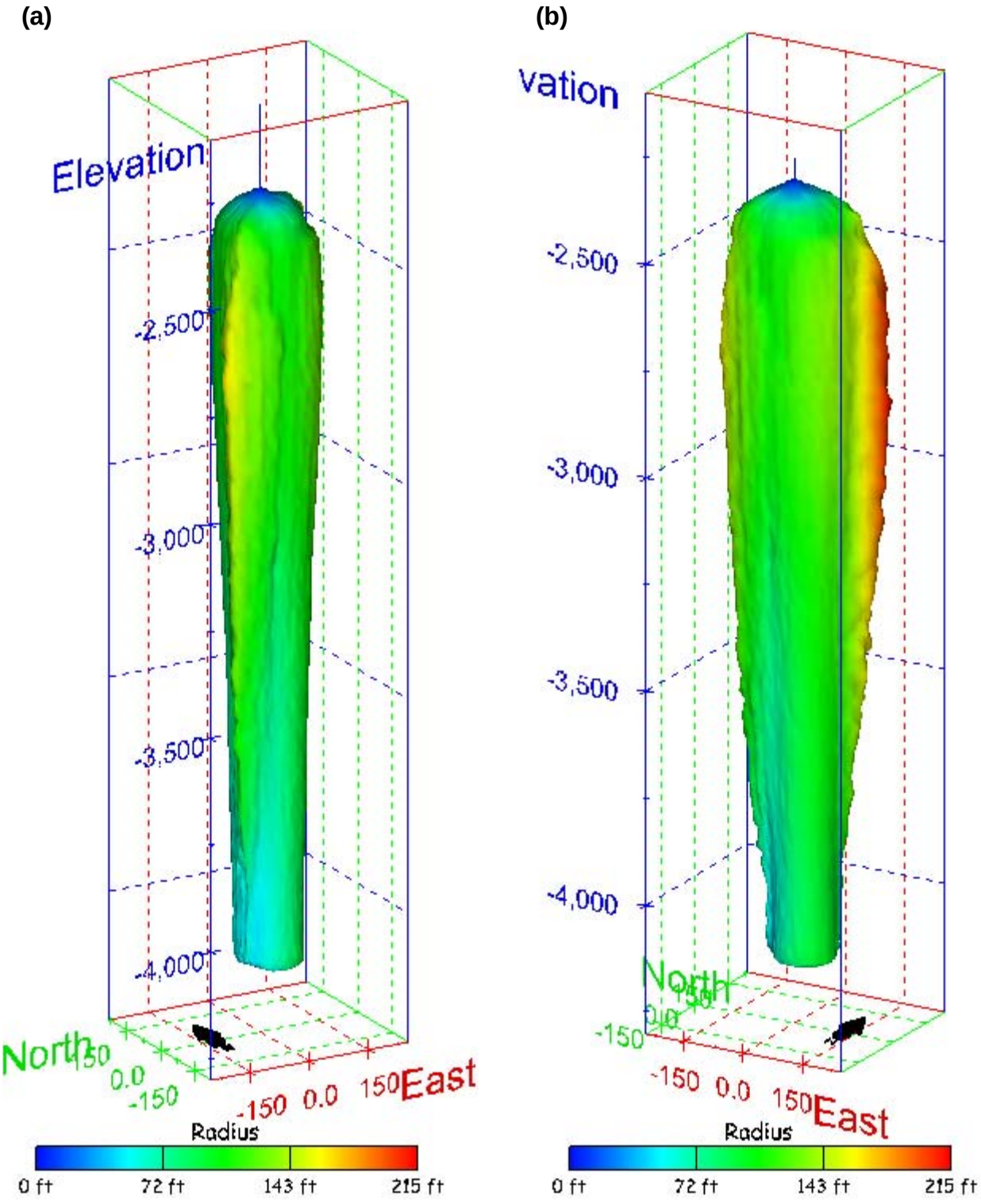

Figure 200. Sonar images of cavern BH-108, showing the geometry of the cavern colored by measured radius. View from (a) azimuth 210°, elevation 20°; (b) azimuth 150°, elevation 20°.

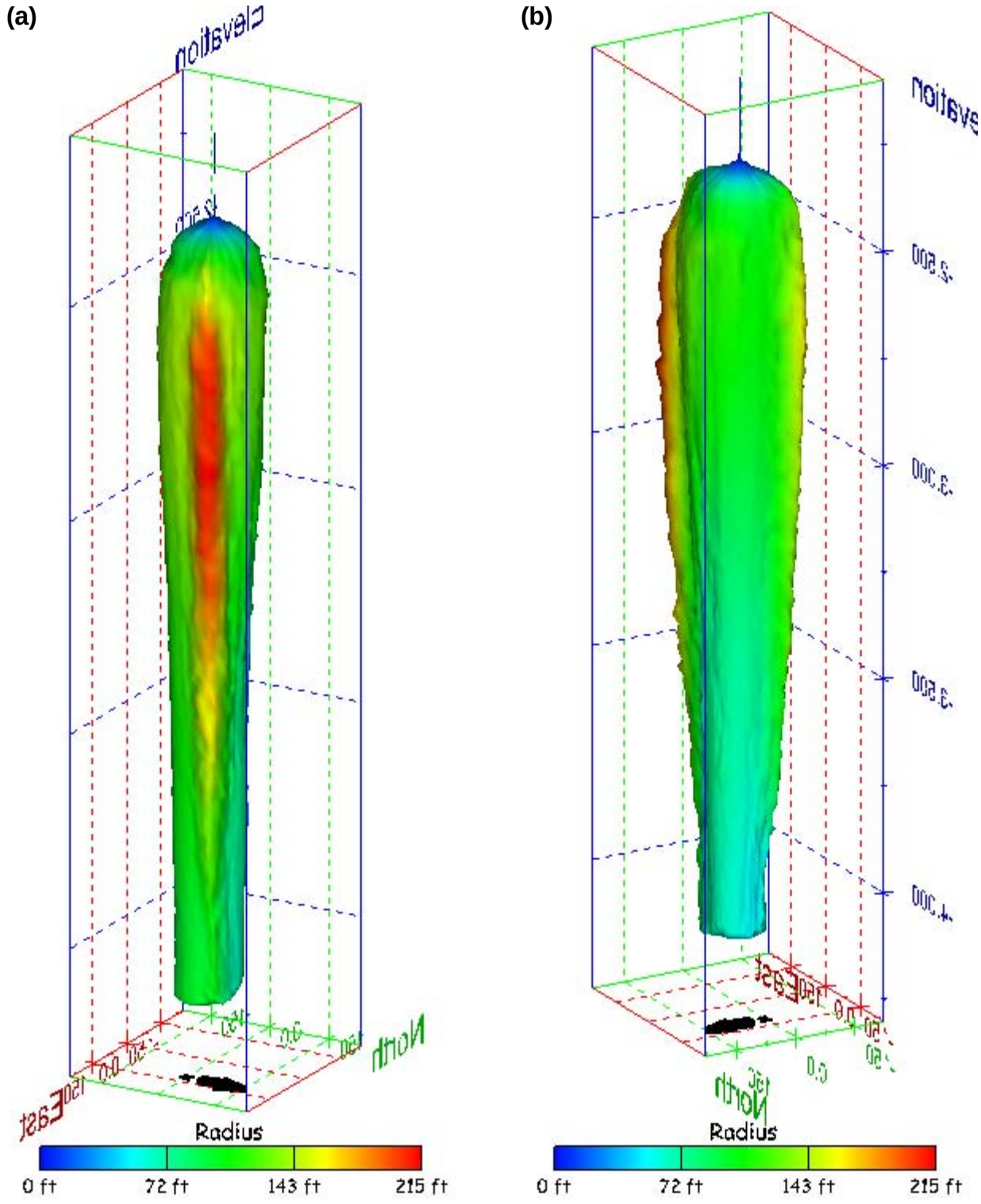

Figure 201. Sonar images of cavern BH-108, showing the geometry of the cavern colored by measured radius. View from (a) azimuth 60°, elevation 20°; (b) azimuth 300°, elevation 20°.

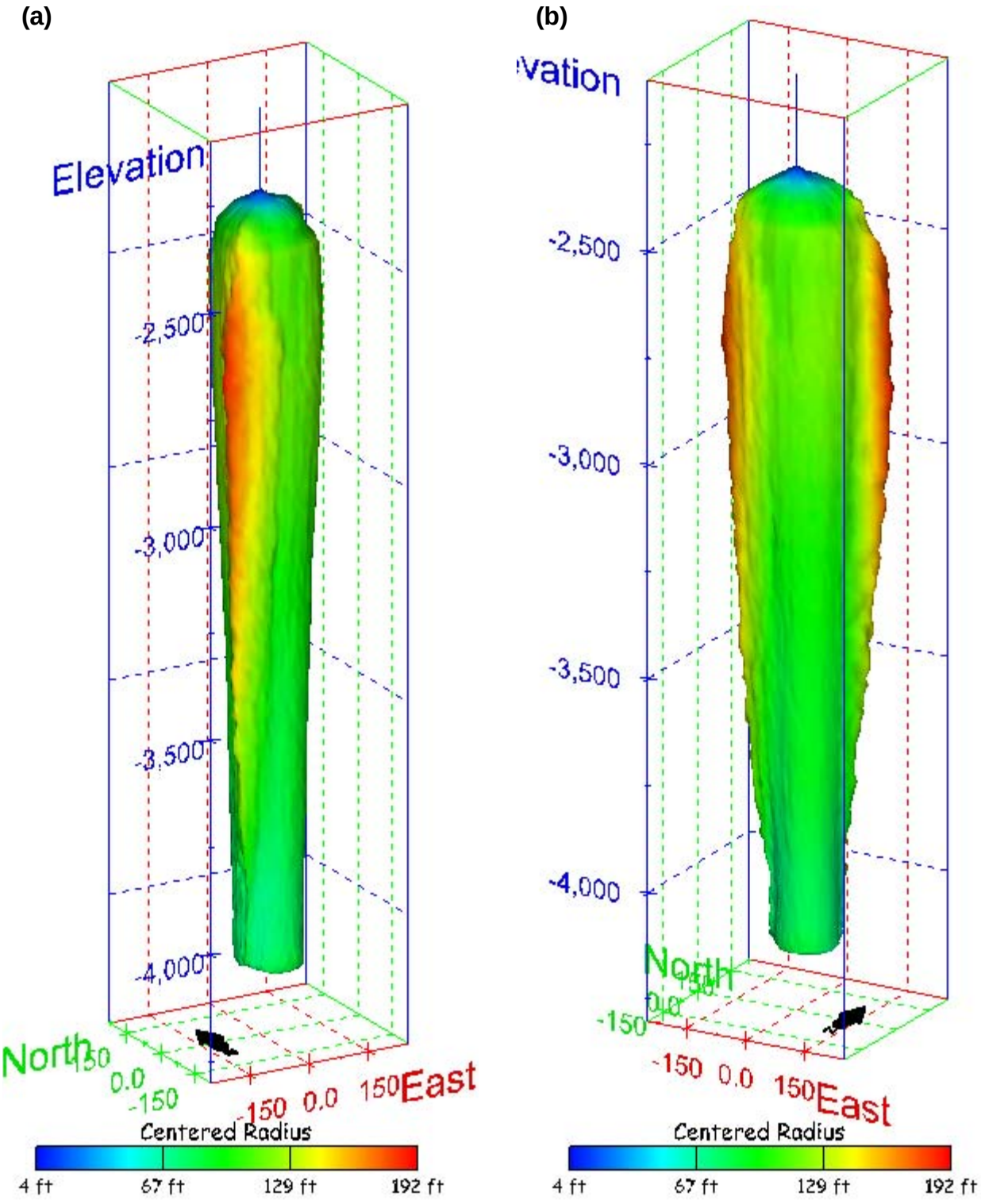

Figure 202. Sonar images of cavern BH-108, showing the geometry of the cavern colored by centered radius. View from (a) azimuth 210°, elevation 20°; (b) azimuth 150°, elevation 20°.

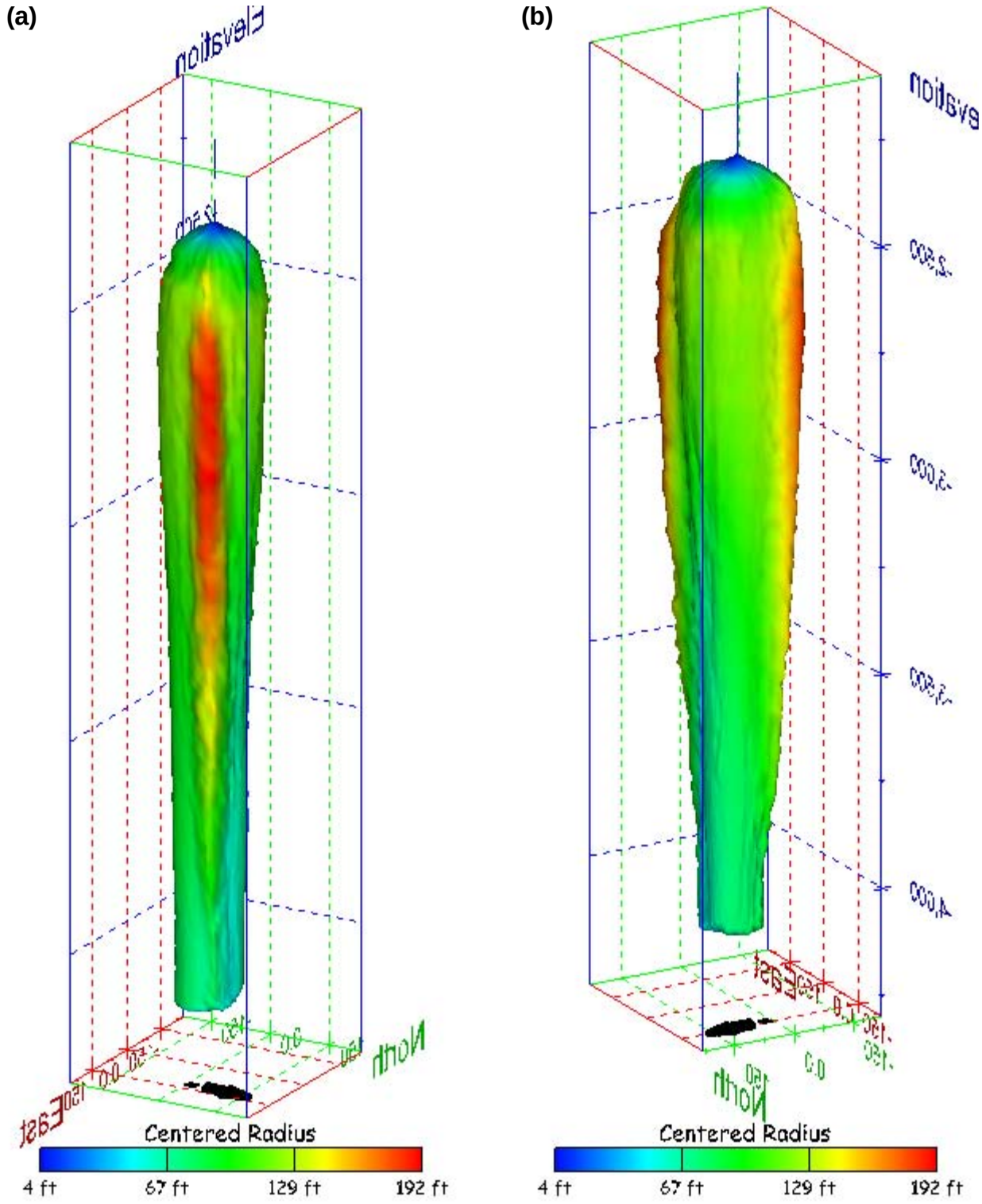

Figure 203. Sonar images of cavern BH-108, showing the geometry of the cavern colored by centered radius. View from (a) azimuth 60°, elevation 20°; (b) azimuth 300°, elevation 20°.

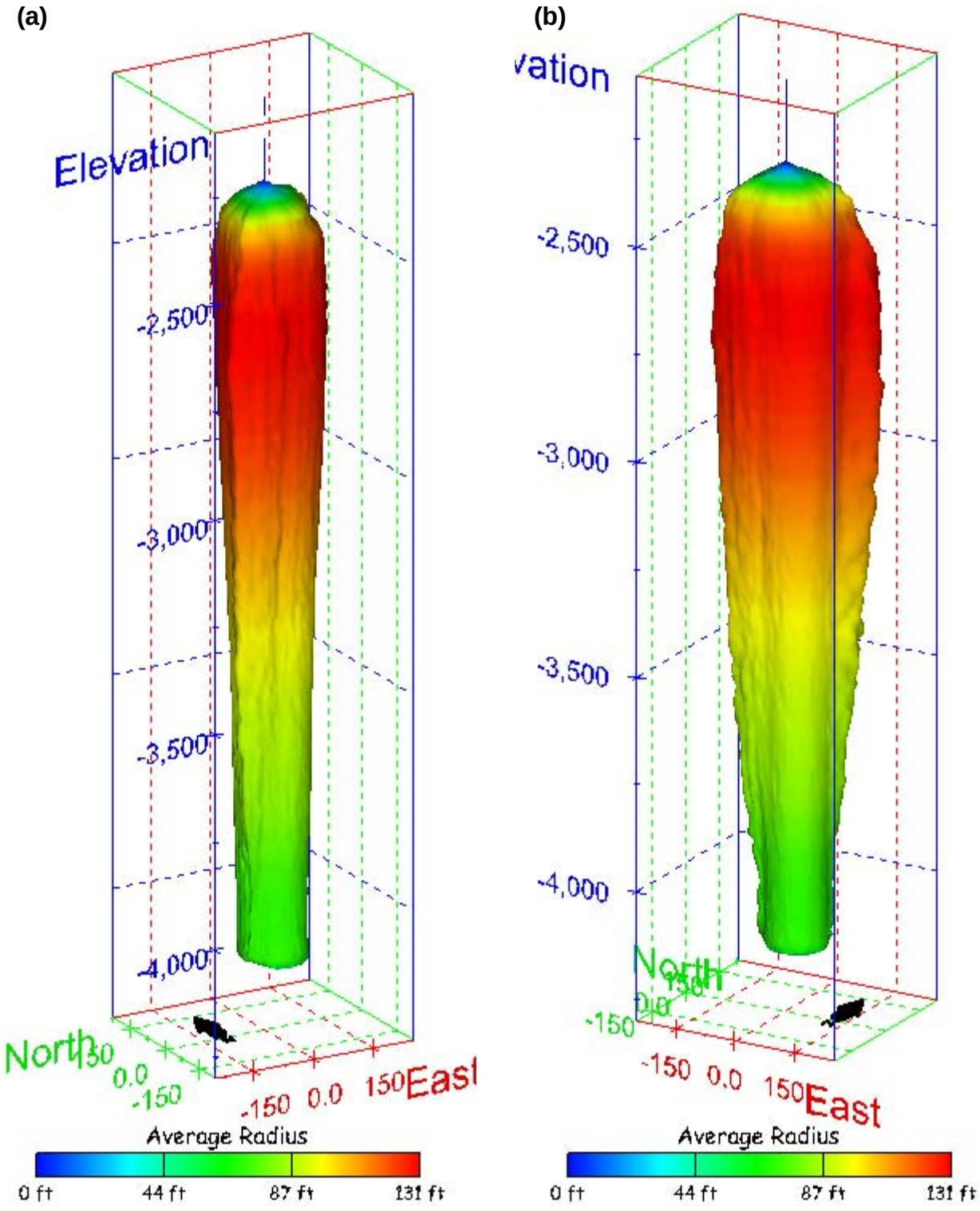

Figure 204. Sonar images of cavern BH-108, showing the geometry of the cavern colored by average radius. View from (a) azimuth 210°, elevation 20°; (b) azimuth 150°, elevation 20°.

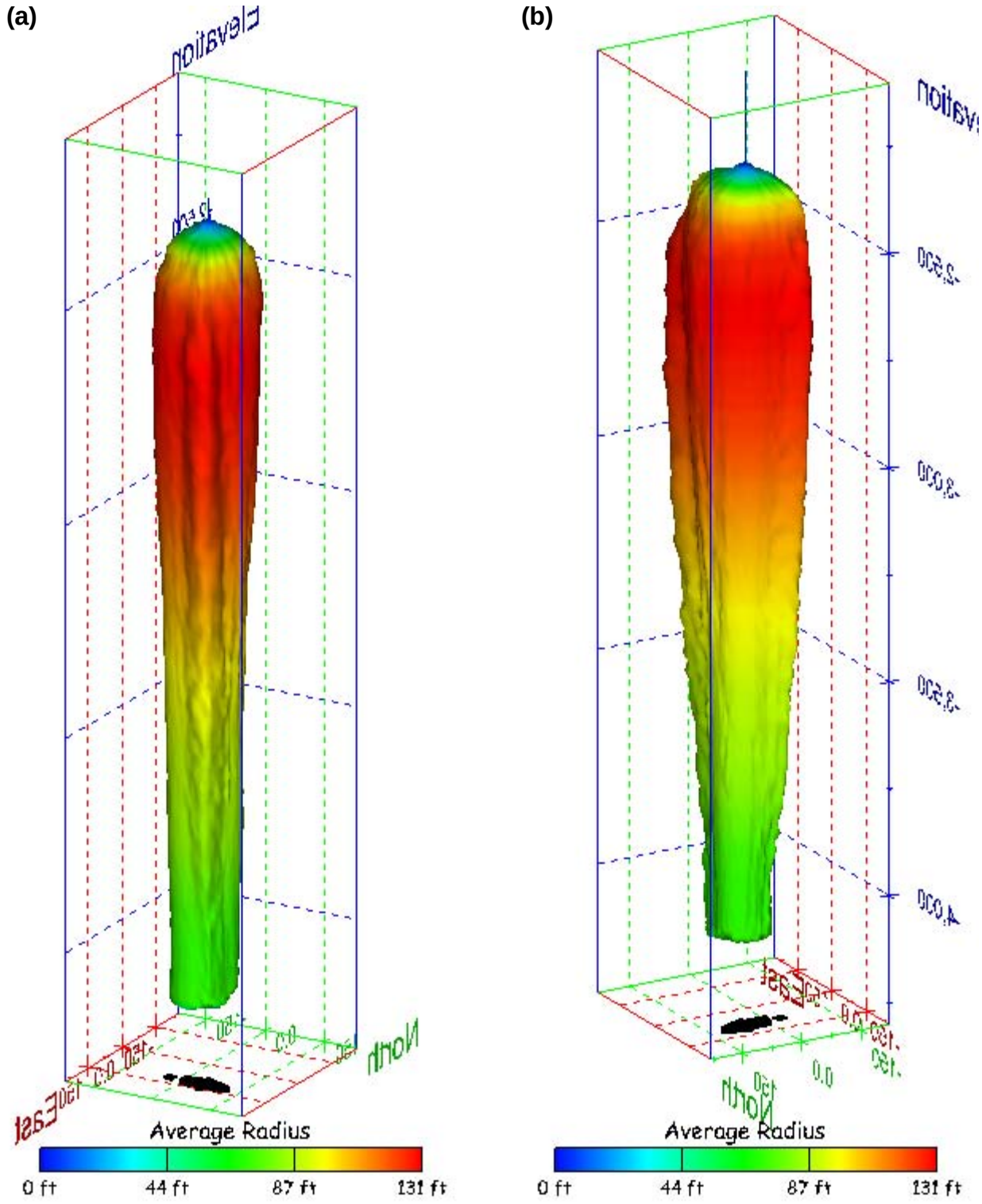

Figure 205. Sonar images of cavern BH-108, showing the geometry of the cavern colored by average radius. View from (a) azimuth 60°, elevation 20°; (b) azimuth 300°, elevation 20°.

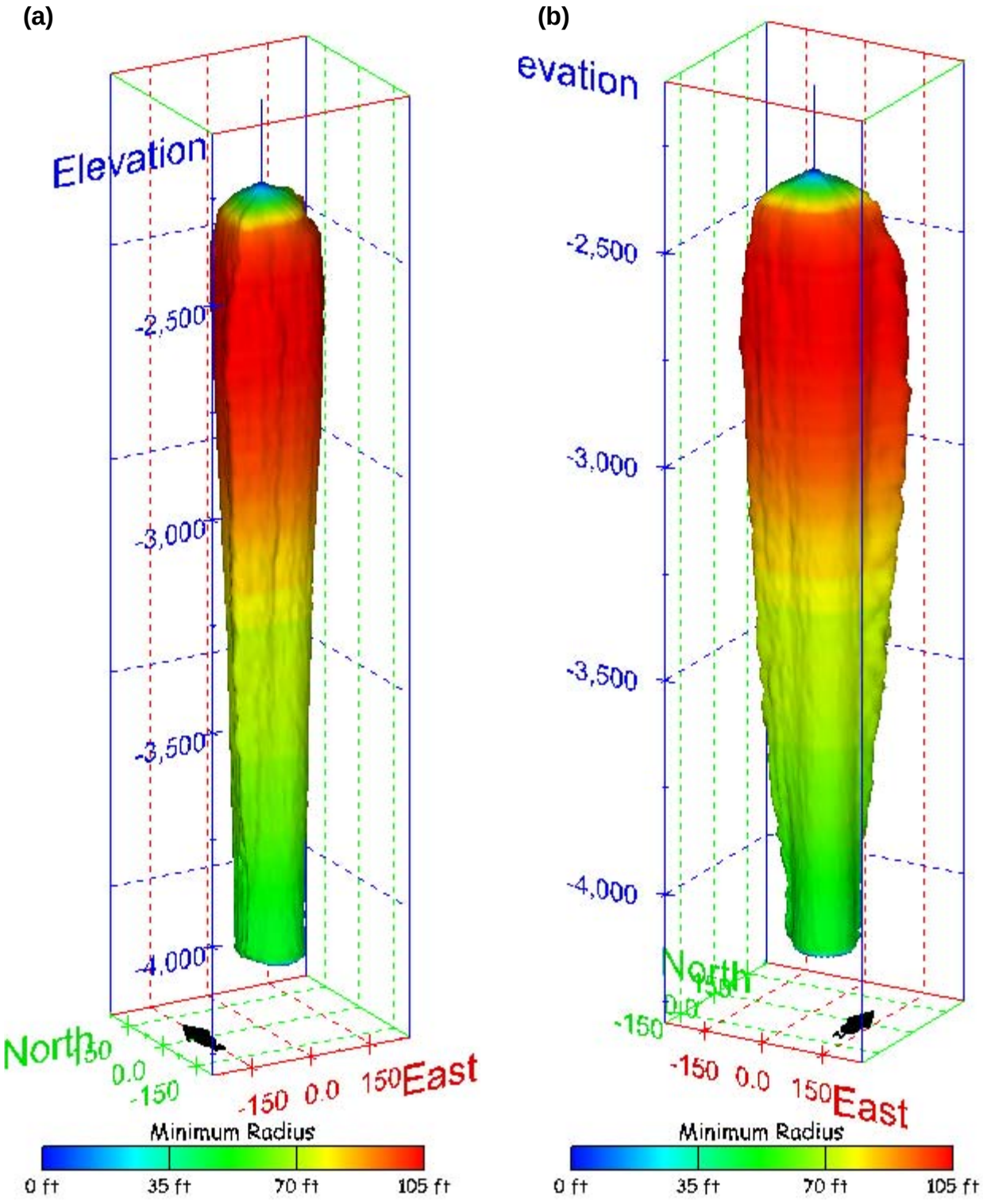

Figure 206. Sonar images of cavern BH-108, showing the geometry of the cavern colored by minimum radius. View from (a) azimuth 210°, elevation 20°; (b) azimuth 150°, elevation 20°.

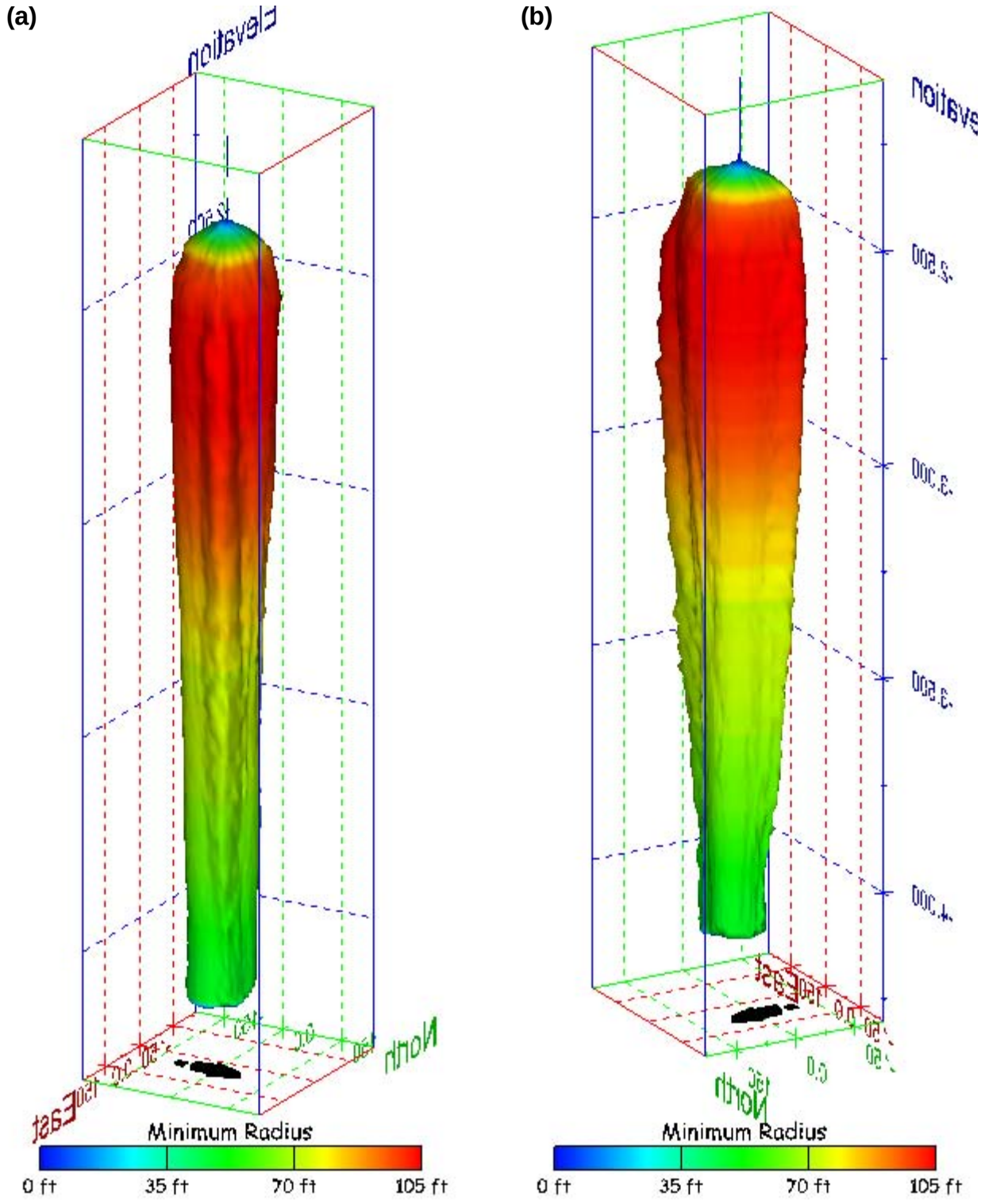

Figure 207. Sonar images of cavern BH-108, showing the geometry of the cavern colored by minimum radius. View from (a) azimuth 60°, elevation 20°; (b) azimuth 300°, elevation 20°.

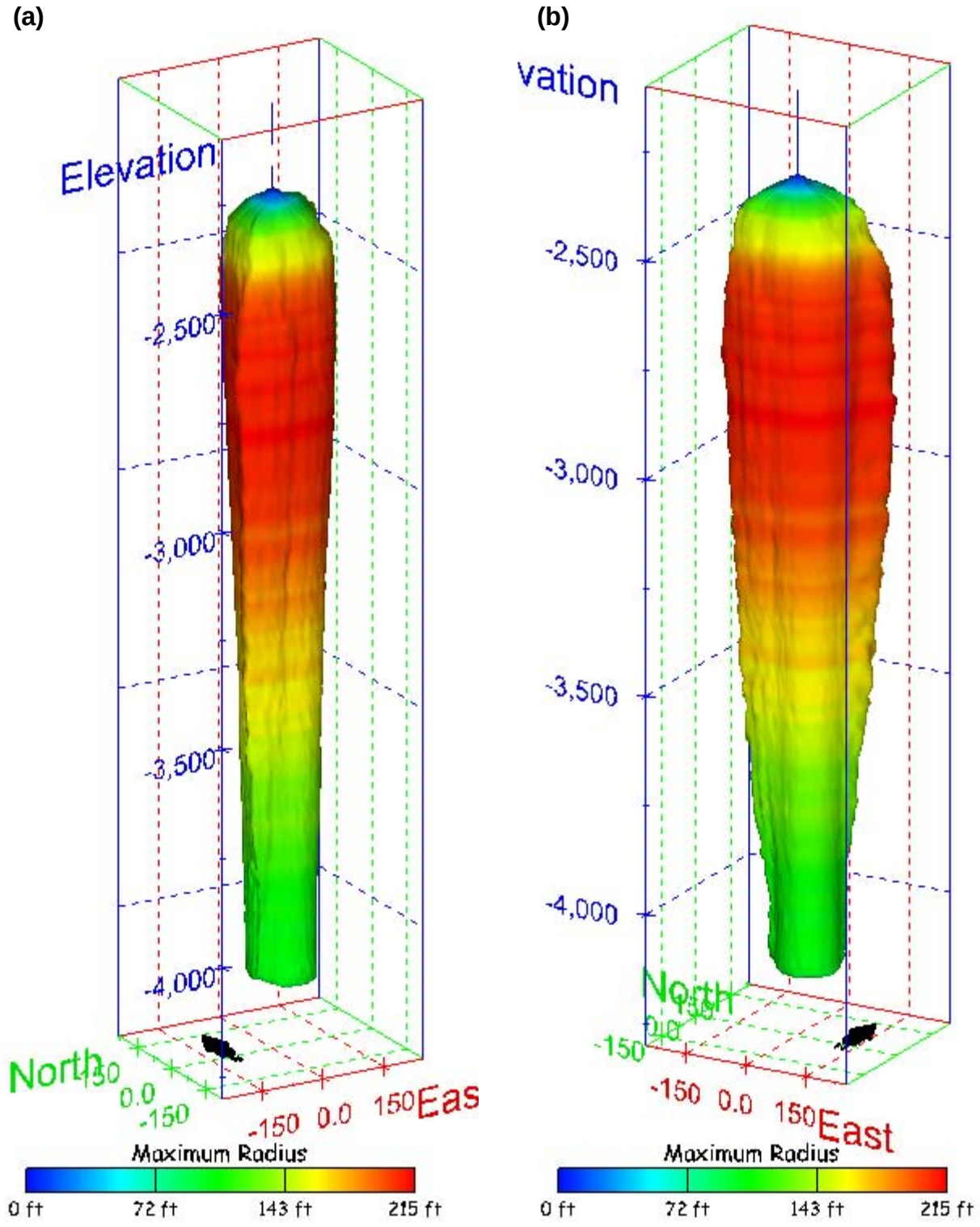

Figure 208. Sonar images of cavern BH-108, showing the geometry of the cavern colored by maximum radius. View from (a) azimuth 210°, elevation 20°; (b) azimuth 150°, elevation 20°.

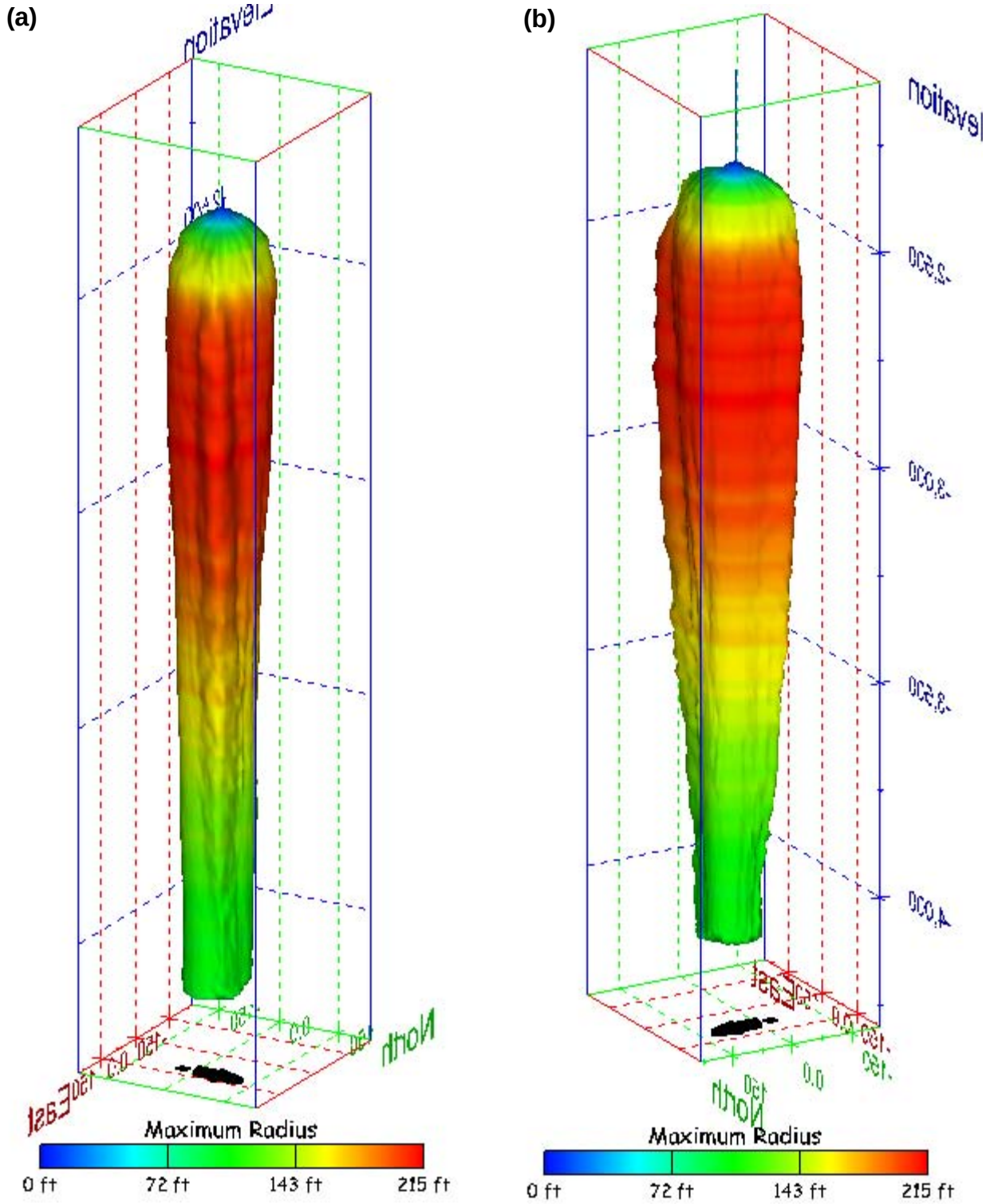

Figure 209. Sonar images of cavern BH-108, showing the geometry of the cavern colored by maximum radius. View from (a) azimuth 60°, elevation 20°; (b) azimuth 300°, elevation 20°.

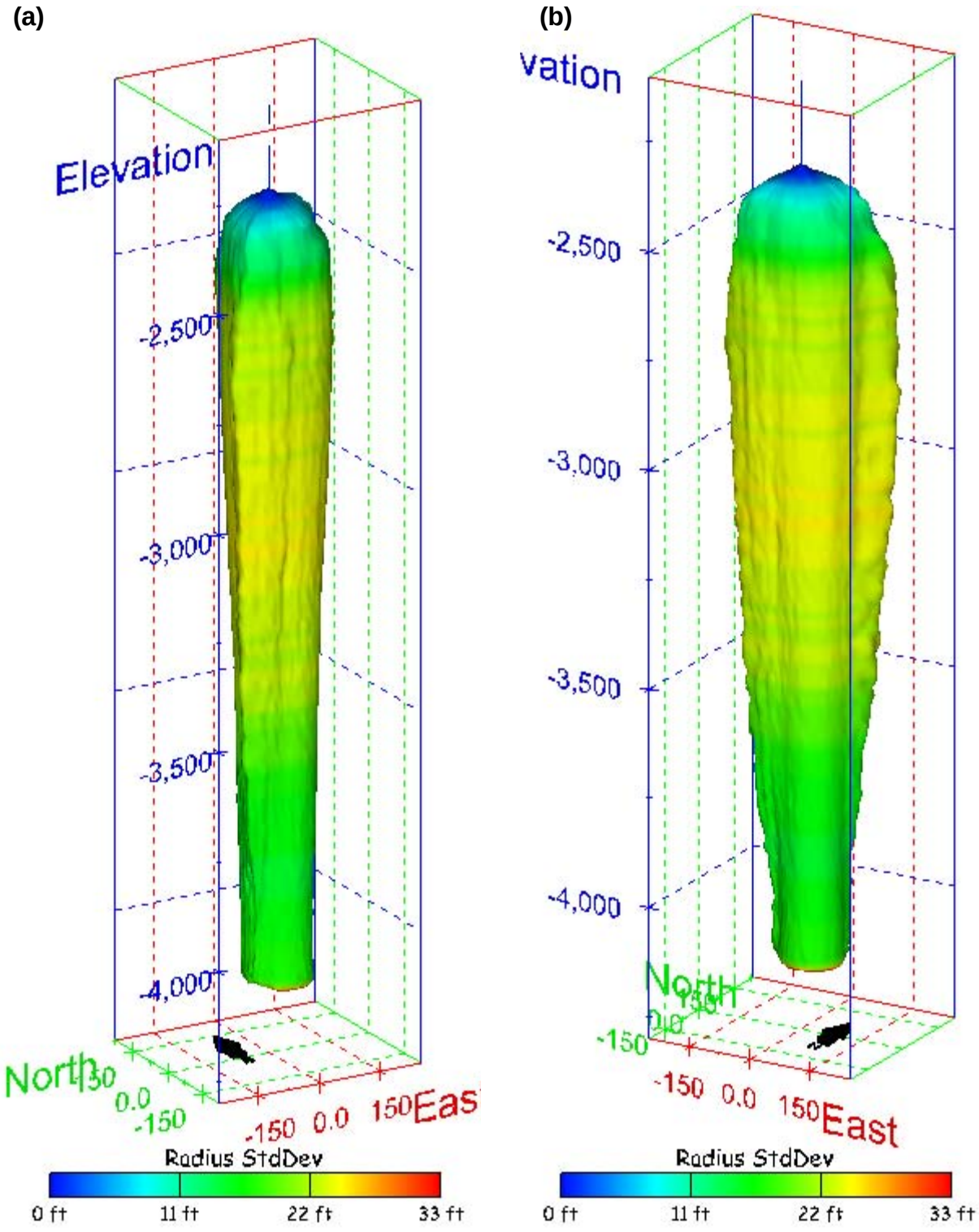

Figure 210. Sonar images of cavern BH-108, showing the geometry of the cavern colored by radius standard deviation. View from (a) azimuth 210°, elevation 20°; (b) azimuth 150°, elevation 20°.

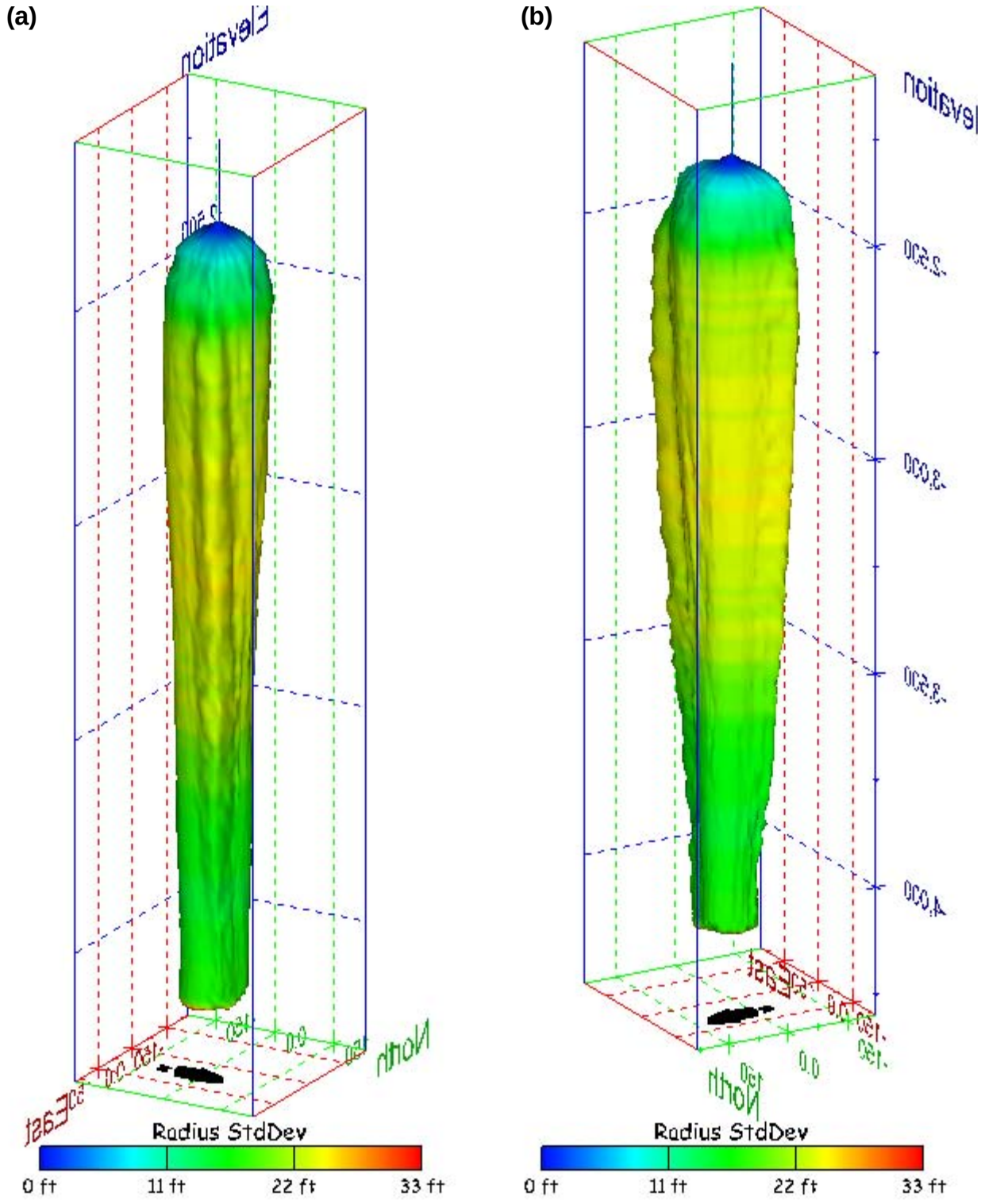

Figure 211. Sonar images of cavern BH-108, showing the geometry of the cavern colored by radius standard deviation. View from (a) azimuth 60°, elevation 20°; (b) azimuth 300°, elevation 20°.

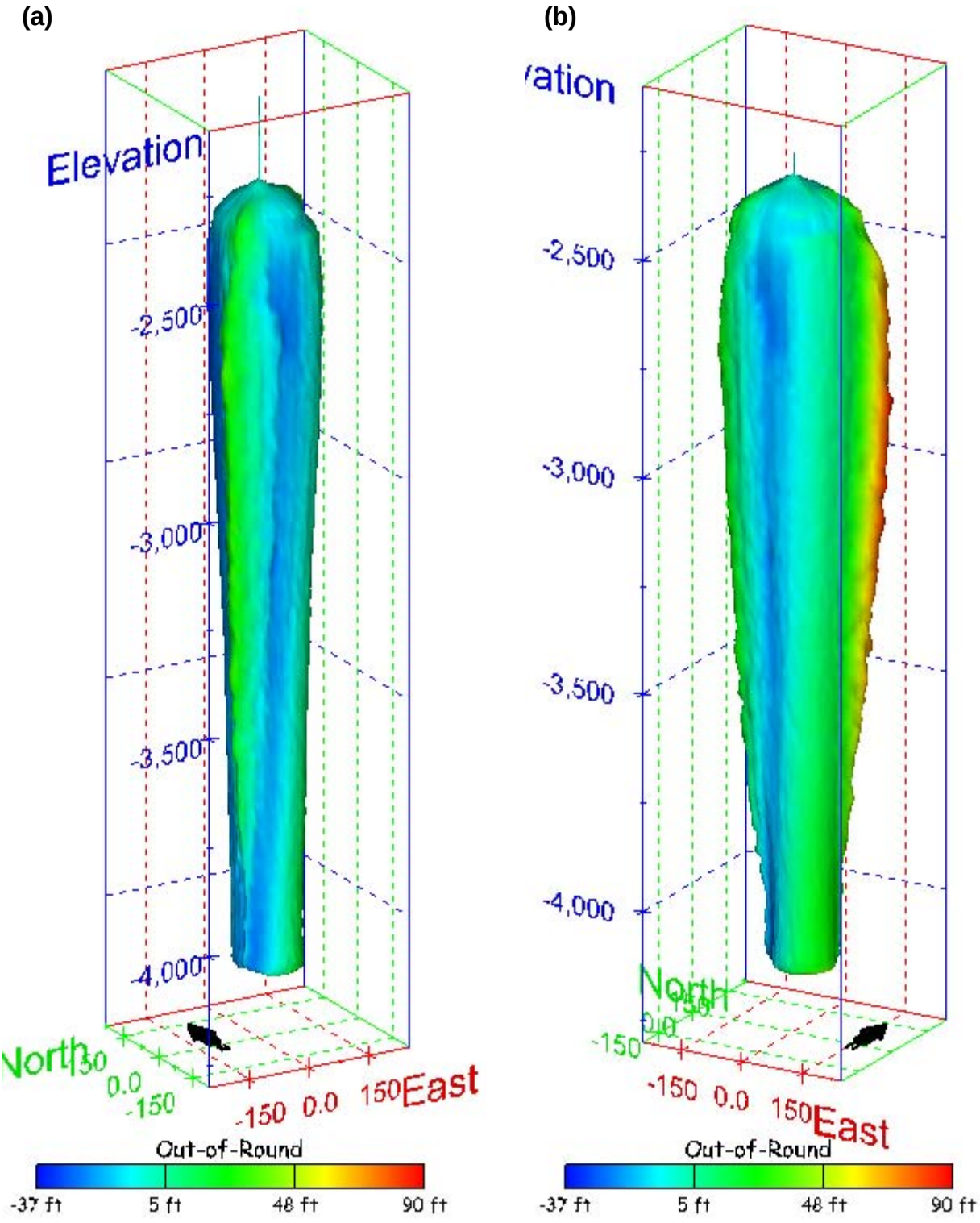

Figure 212. Sonar images of cavern BH-108, showing the geometry of the cavern colored by out-of-round distance. View from (a) azimuth 210°, elevation 20°; (b) azimuth 150°, elevation 20°.

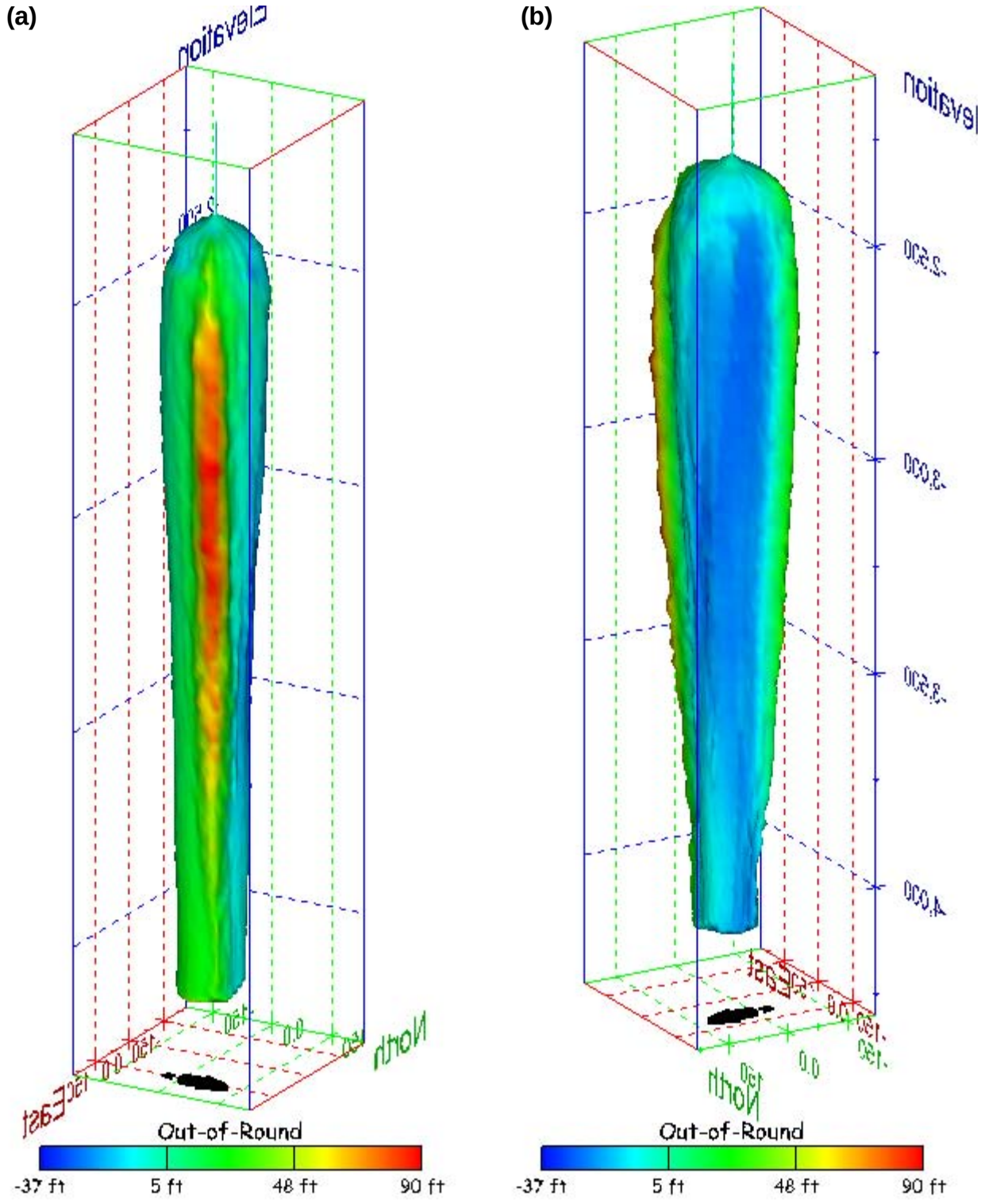

Figure 213. Sonar images of cavern BH-108, showing the geometry of the cavern colored by out-of-round distance. View from (a) azimuth 60°, elevation 20°; (b) azimuth 300°, elevation 20°.

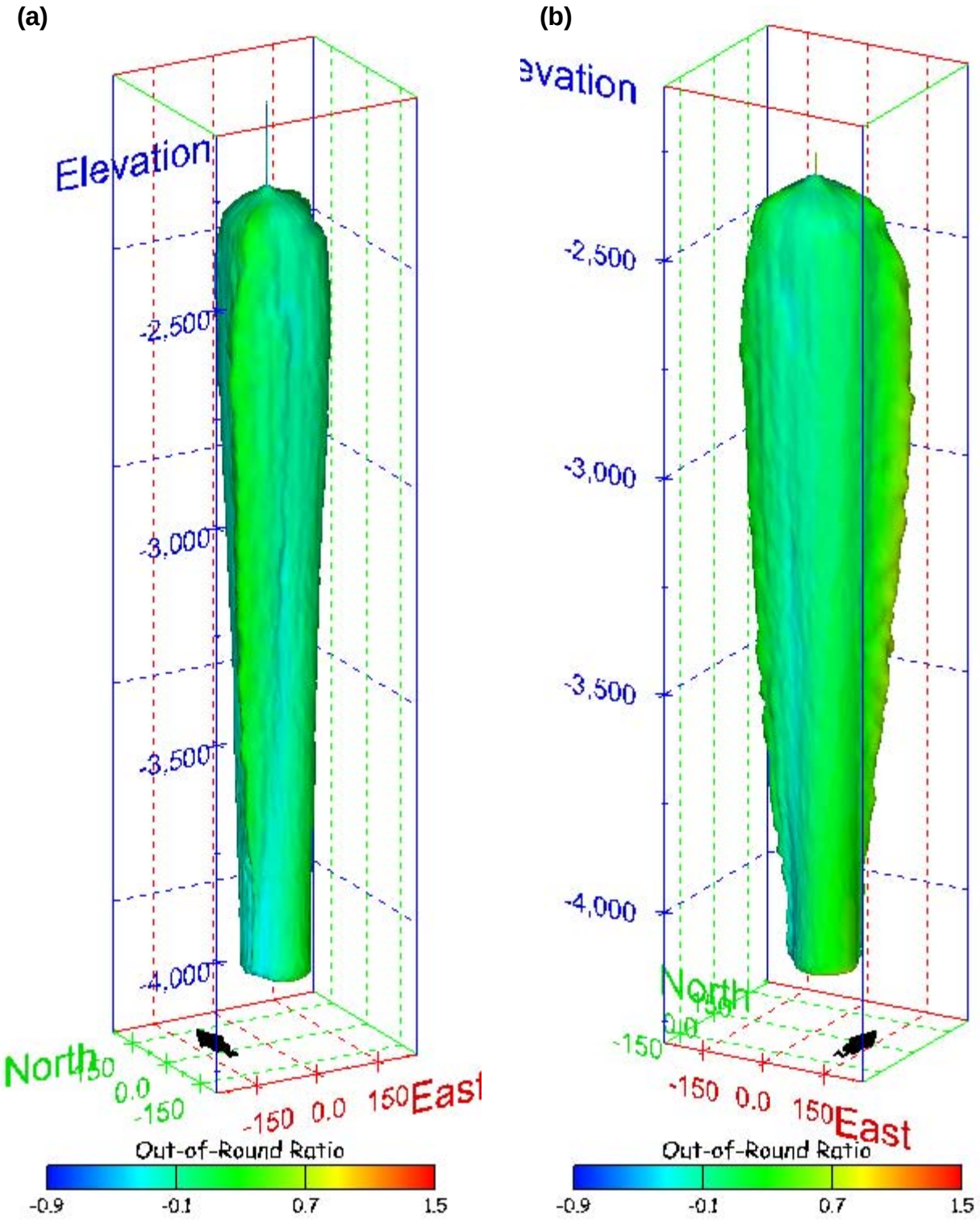

Figure 214. Sonar images of cavern BH-108, showing the geometry of the cavern colored by out-of-round ratio. View from (a) azimuth 210°, elevation 20°; (b) azimuth 150°, elevation 20°.

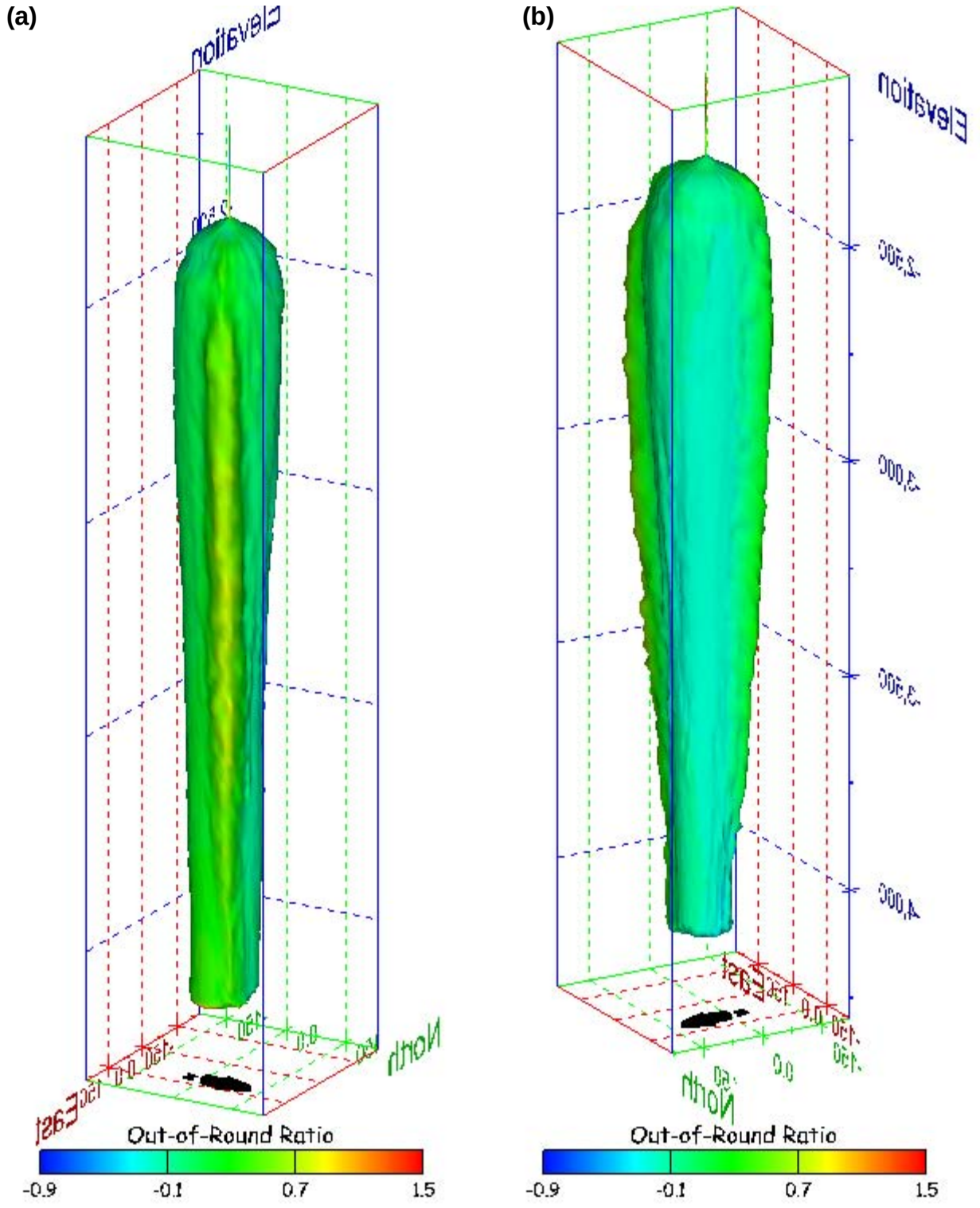

Figure 215. Sonar images of cavern BH-108, showing the geometry of the cavern colored by out-of-round ratio. View from (a) azimuth 60°, elevation 20°; (b) azimuth 300°, elevation 20°.

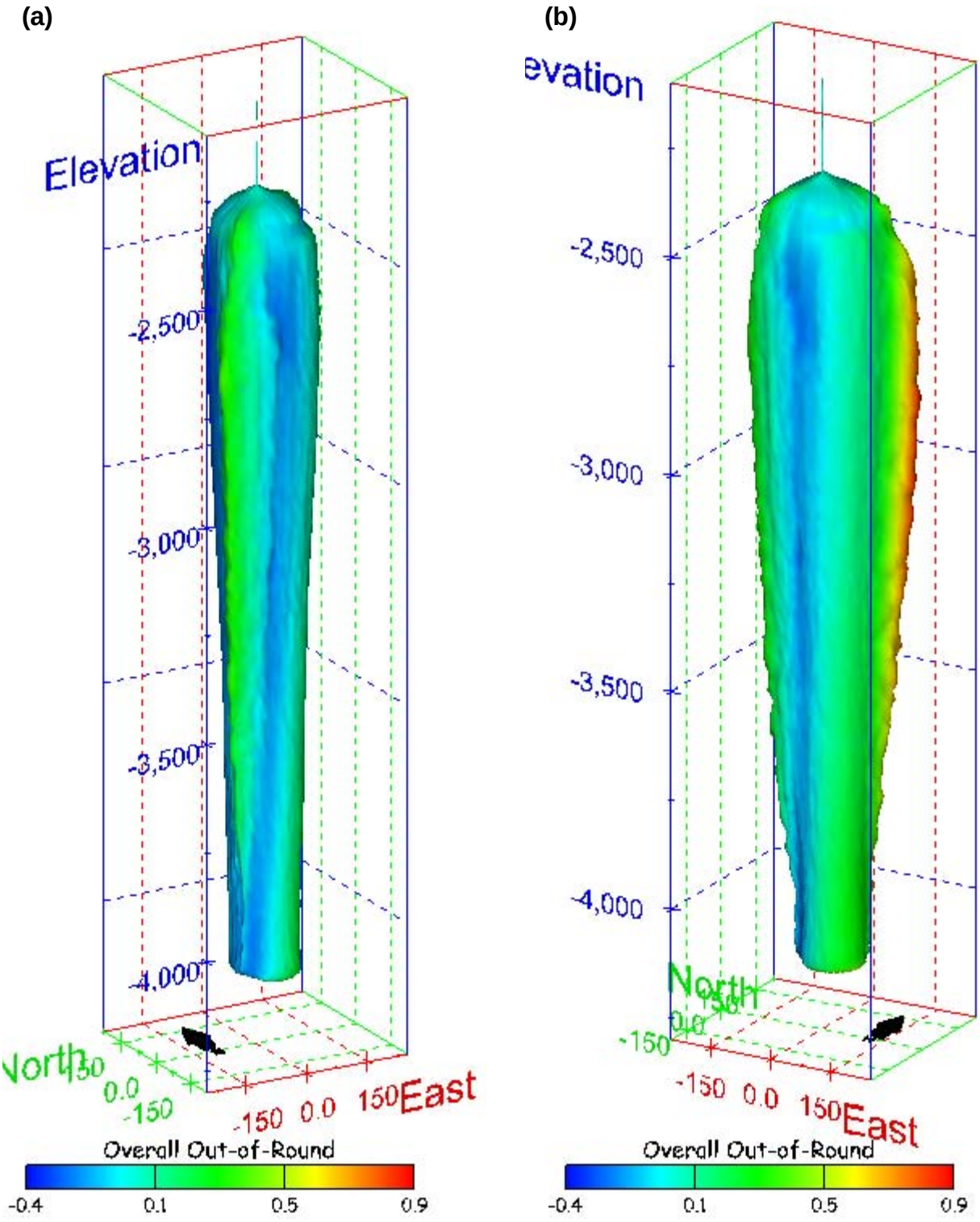

Figure 216. Sonar images of cavern BH-108, showing the geometry of the cavern colored by overall out-of-round ratio. View from (a) azimuth 210°, elevation 20°; (b) azimuth 150°, elevation 20°.

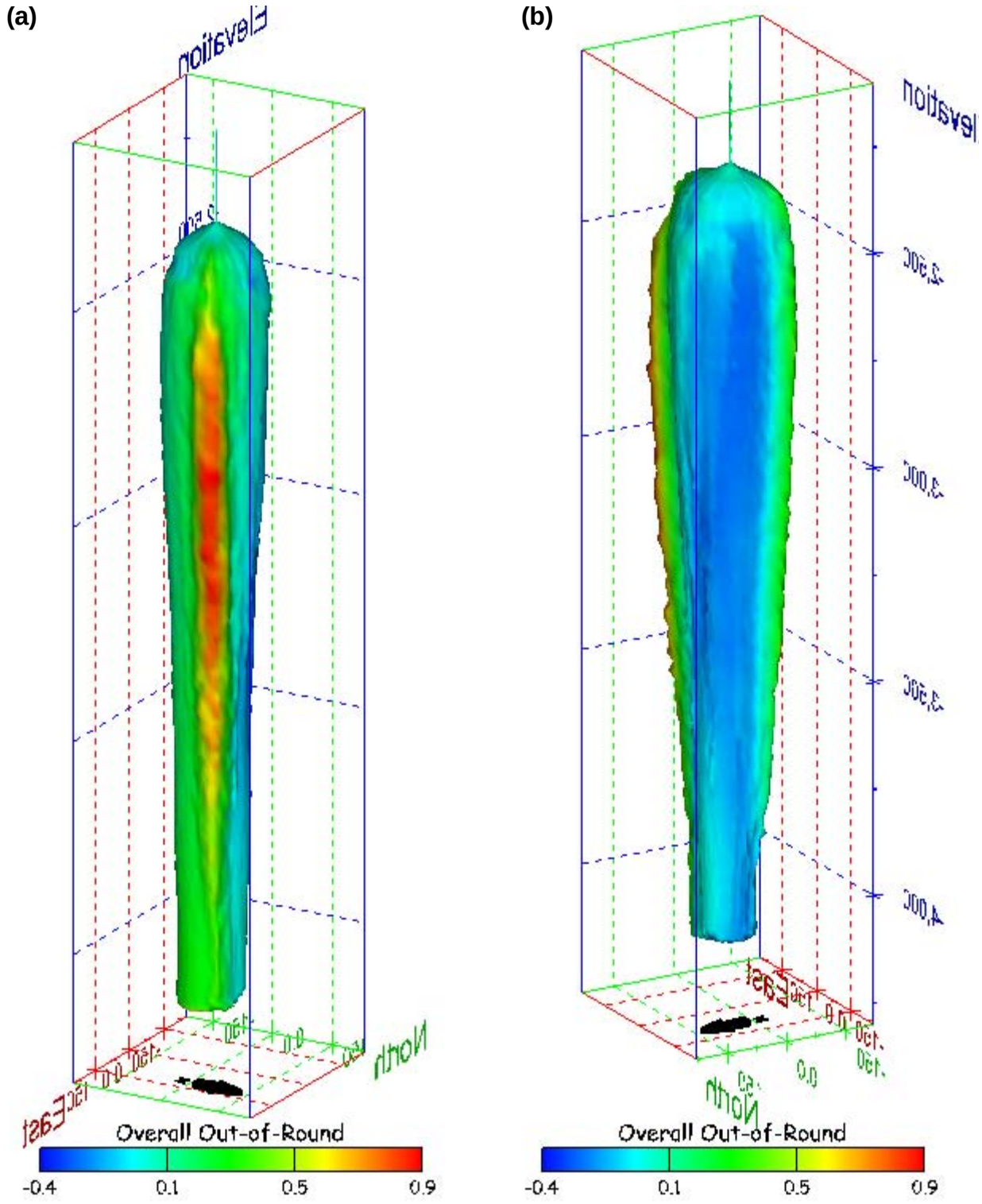

Figure 217. Sonar images of cavern BH-108, showing the geometry of the cavern colored by overall out-of-round ratio. View from (a) azimuth 60°, elevation 20°; (b) azimuth 300°, elevation 20°.

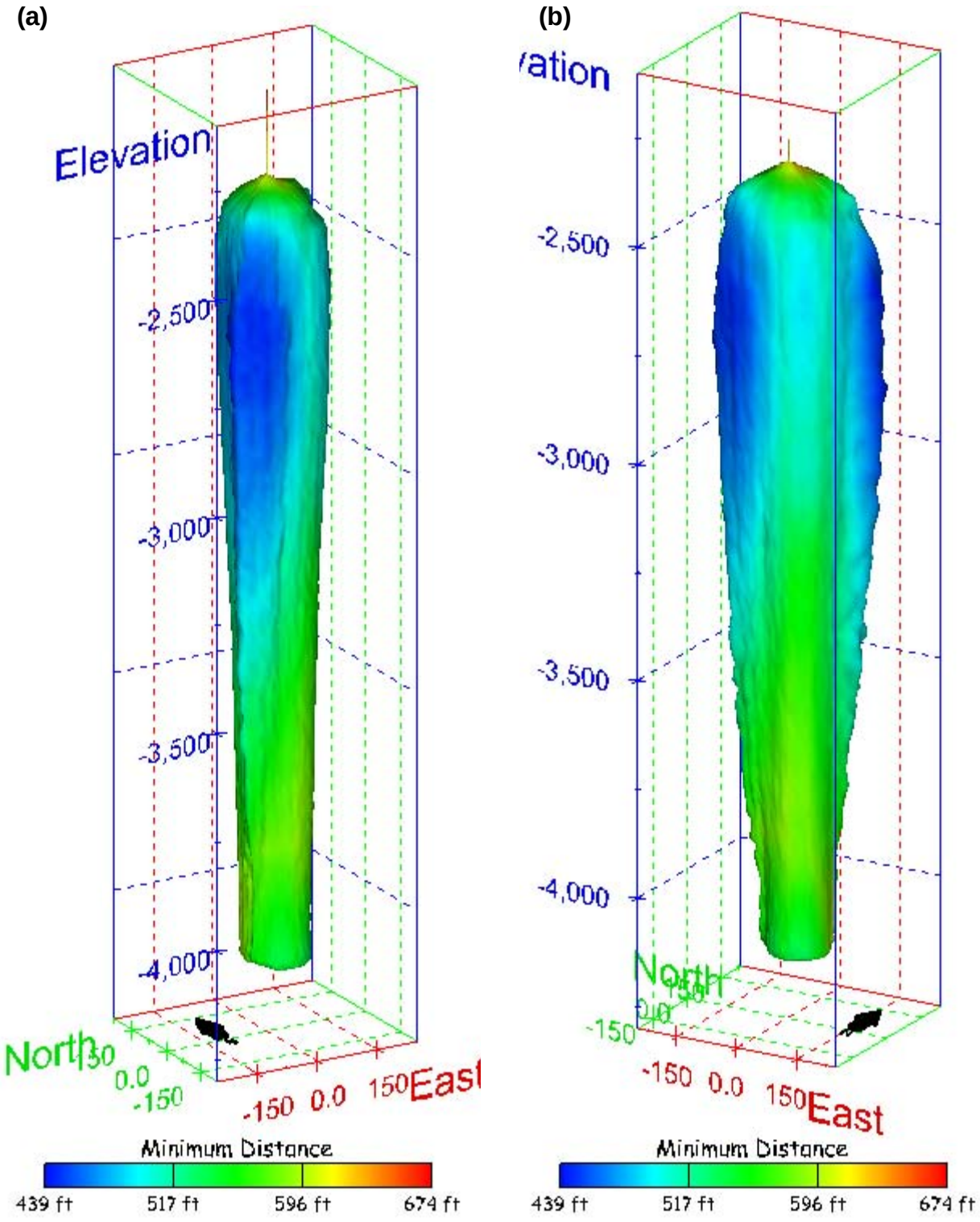

Figure 218. Sonar images of cavern BH-108, showing the geometry of the cavern colored by the minimum distance to the nearest neighboring cavern. View from (a) azimuth 210°, elevation 20°; (b) azimuth 150°, elevation 20°.

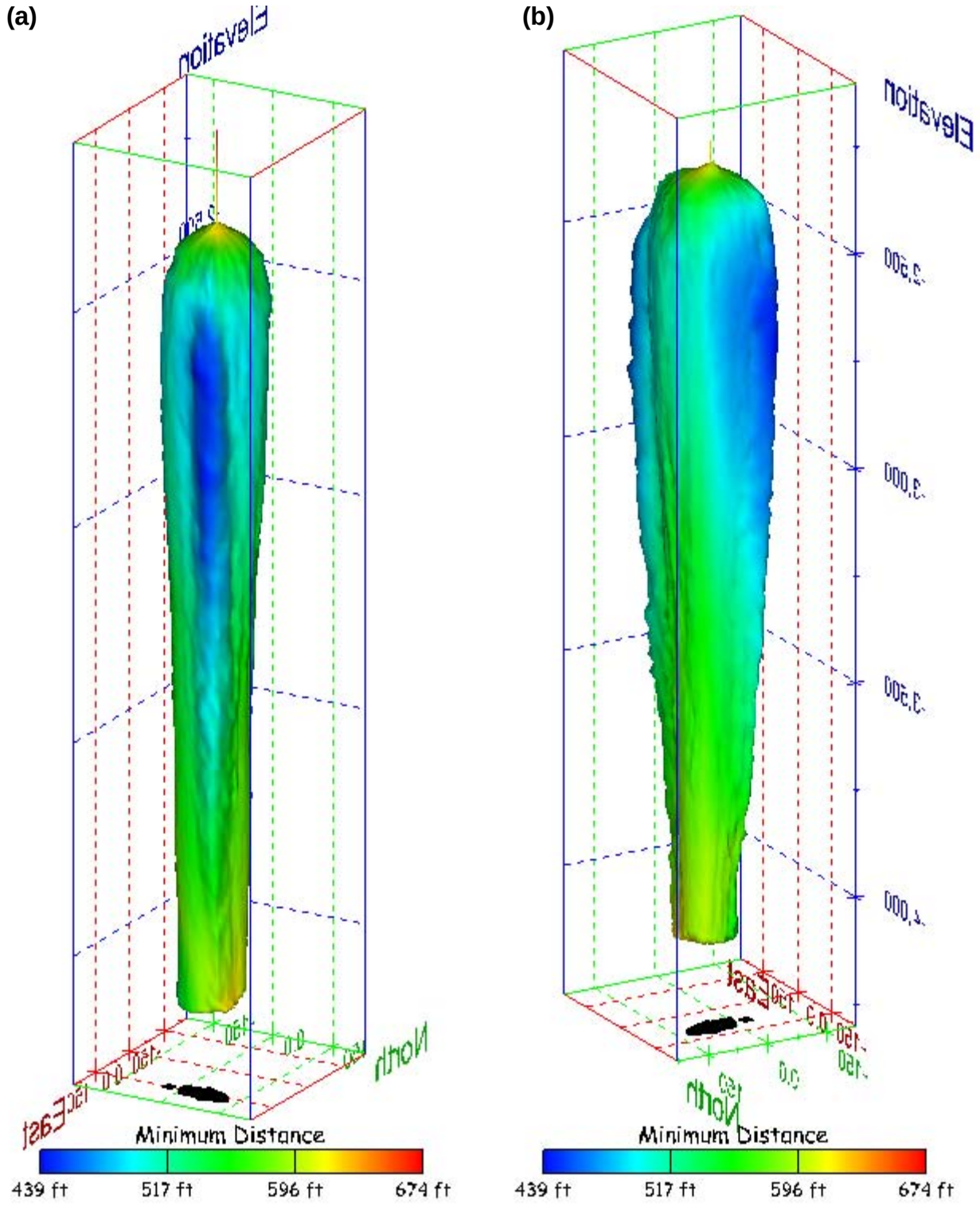

Figure 219. Sonar images of cavern BH-108, showing the geometry of the cavern colored by minimum distance to the nearest neighboring cavern. View from (a) azimuth 60°, elevation 20°; (b) azimuth 300°, elevation 20°.

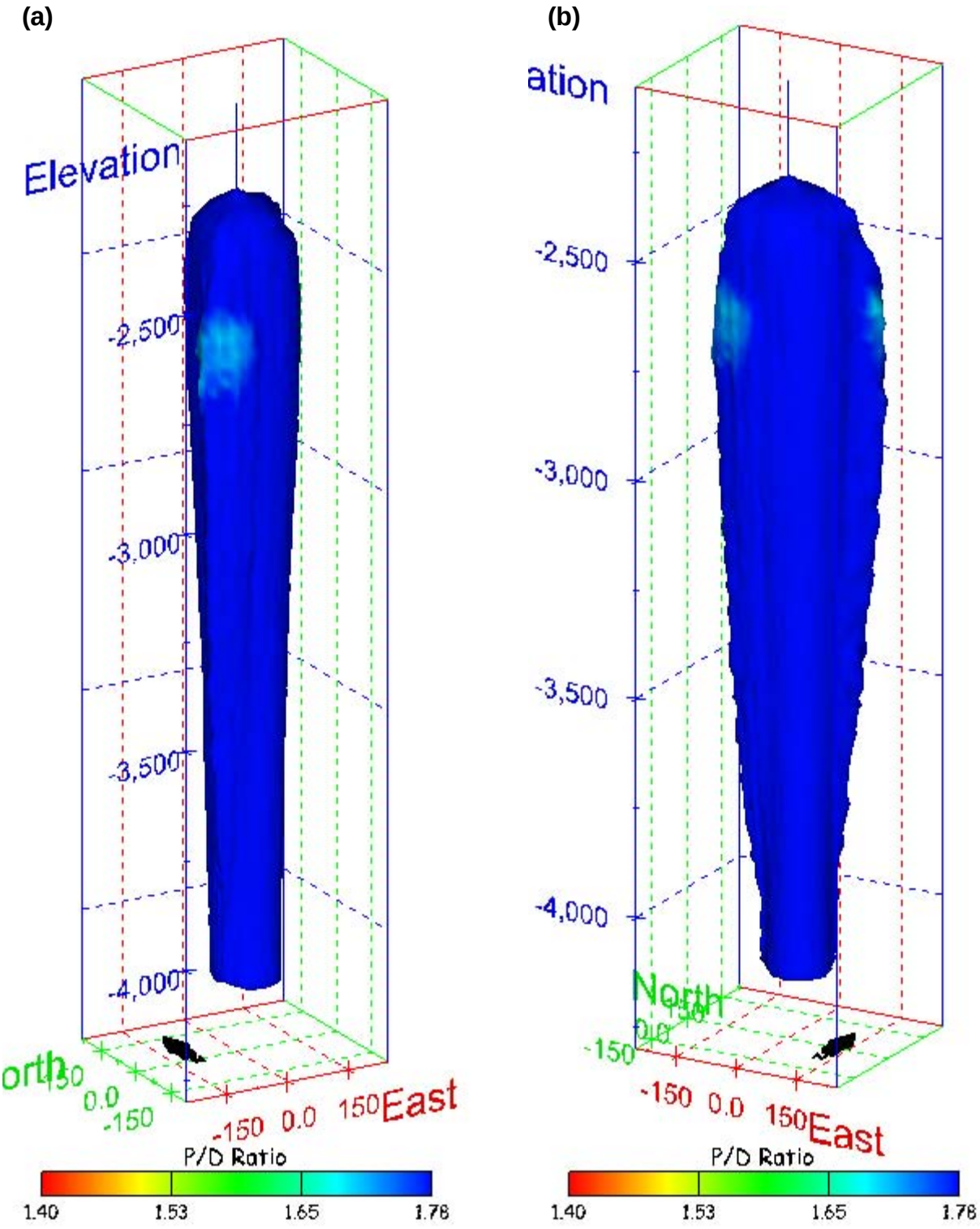

Figure 220. Sonar images of cavern BH-108, showing the geometry of the cavern colored by three-dimensional pillar-to-diameter ratio. View from (a) azimuth 210°, elevation 20°; (b) azimuth 150°, elevation 20°.

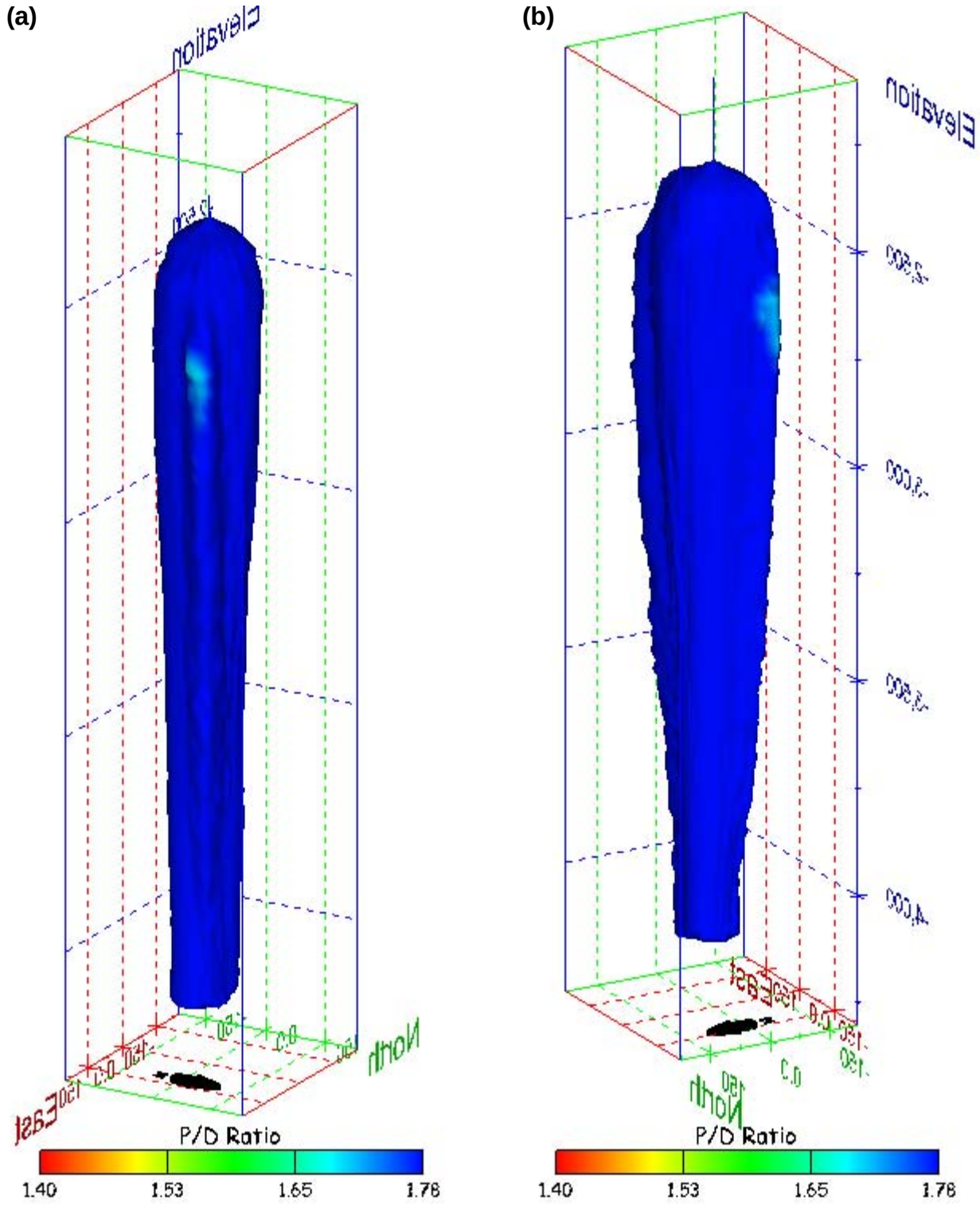

Figure 221. Sonar images of cavern BH-108, showing the geometry of the cavern colored by three-dimensional pillar-to-diameter ratio. View from (a) azimuth 60°, elevation 20°; (b) azimuth 300°, elevation 20°.

No Sonic Velocity Data Available for Socon Surveys

Figure 222. Sonar image of cavern BH-108, showing the geometry of the cavern colored by the reported velocity of sound on the survey date of March 2005. View from due south, elevation zero.

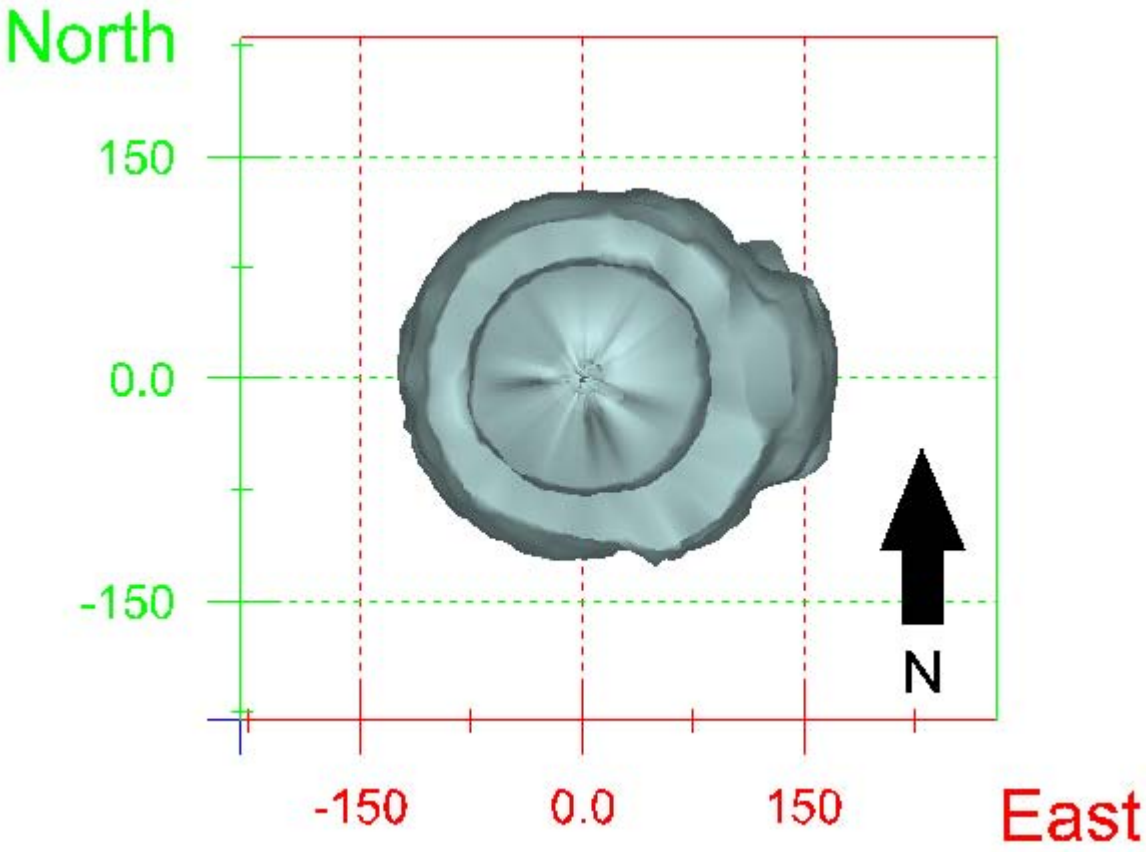

Figure 223. Map view sonar image of cavern BH-109, showing the basic geometry of the cavern. Grid squares represent 150 ft.

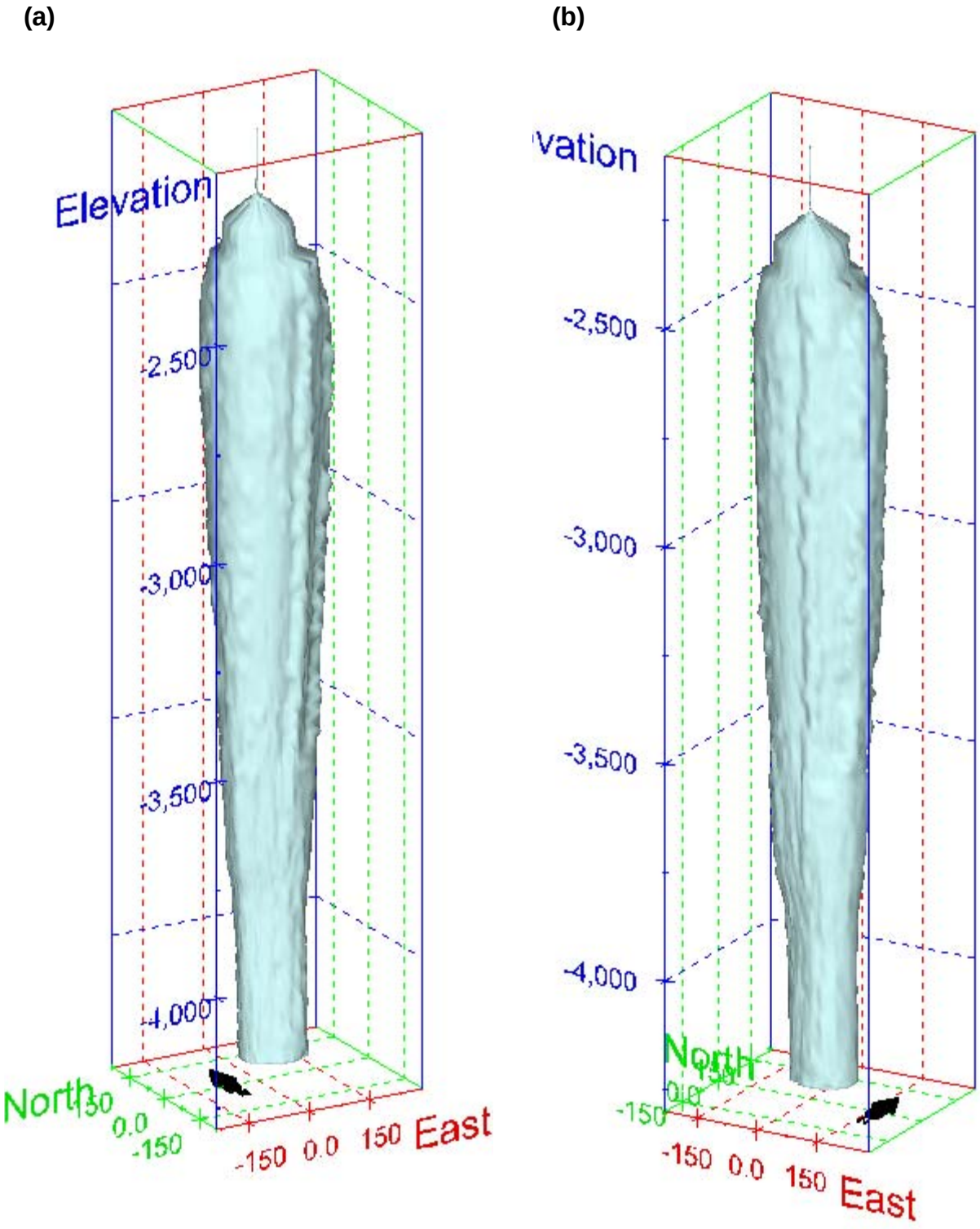

Figure 224. Sonar images of cavern BH-109, showing the basic geometric shape of the cavern. View from (a) azimuth 210°, elevation 20°; (b) azimuth 150°, elevation 20°.

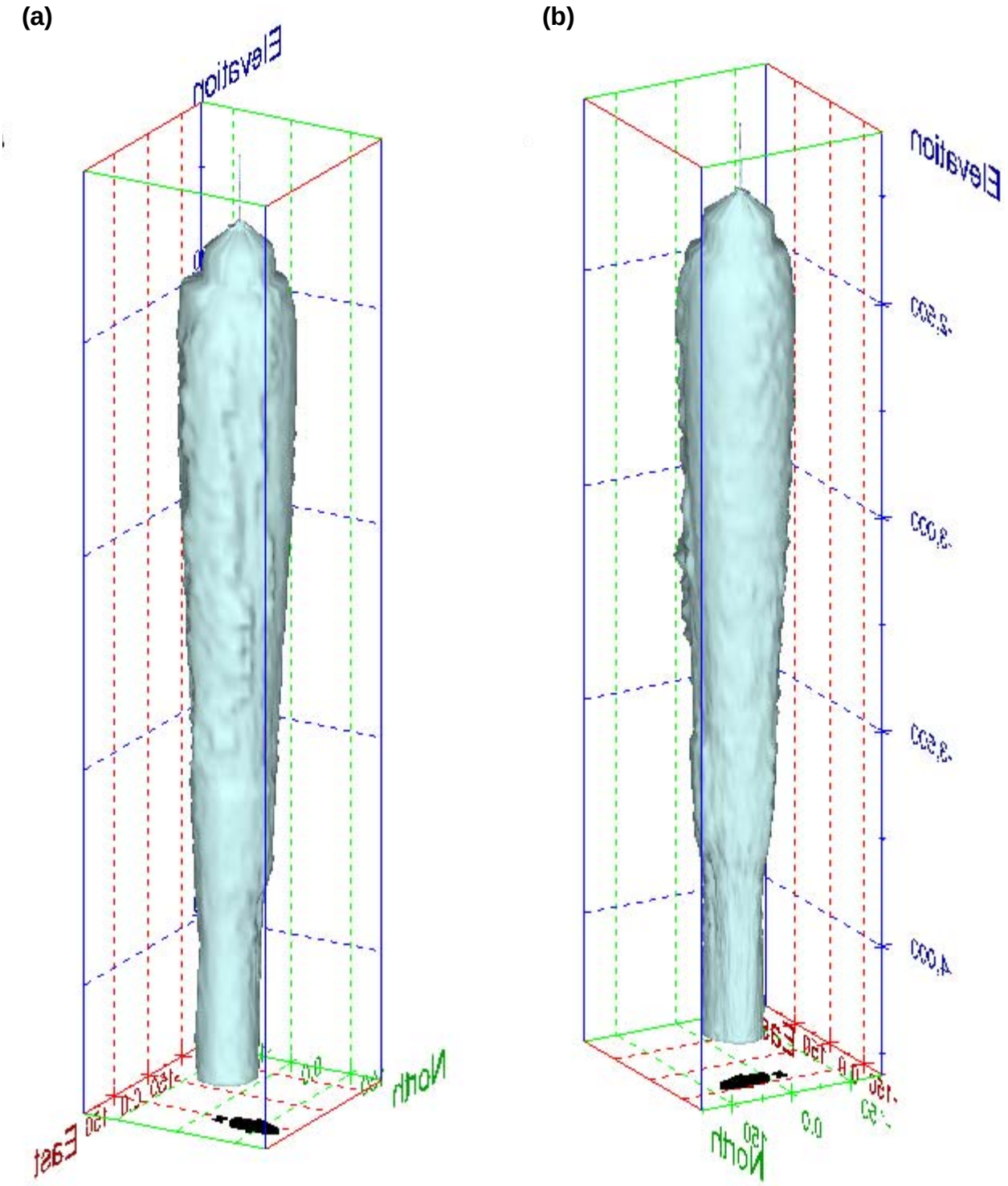

Figure 225. Sonar images of cavern BH-109, showing the basic geometric shape of the cavern. View from (a) azimuth 60°, elevation 20°; (b) azimuth 300°, elevation 20°.

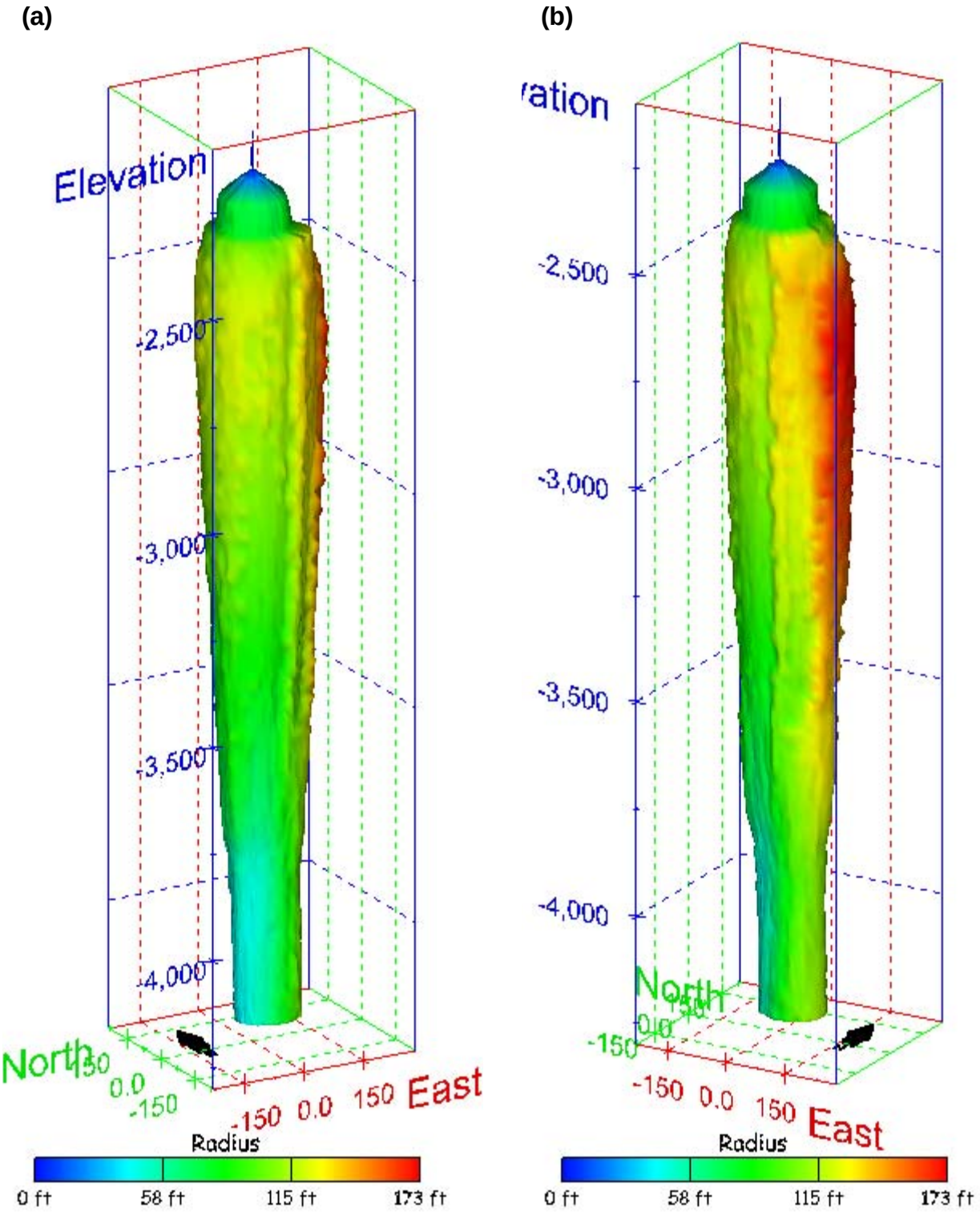

Figure 226. Sonar images of cavern BH-109, showing the geometry of the cavern colored by measured radius. View from (a) azimuth 210°, elevation 20°; (b) azimuth 150°, elevation 20°.

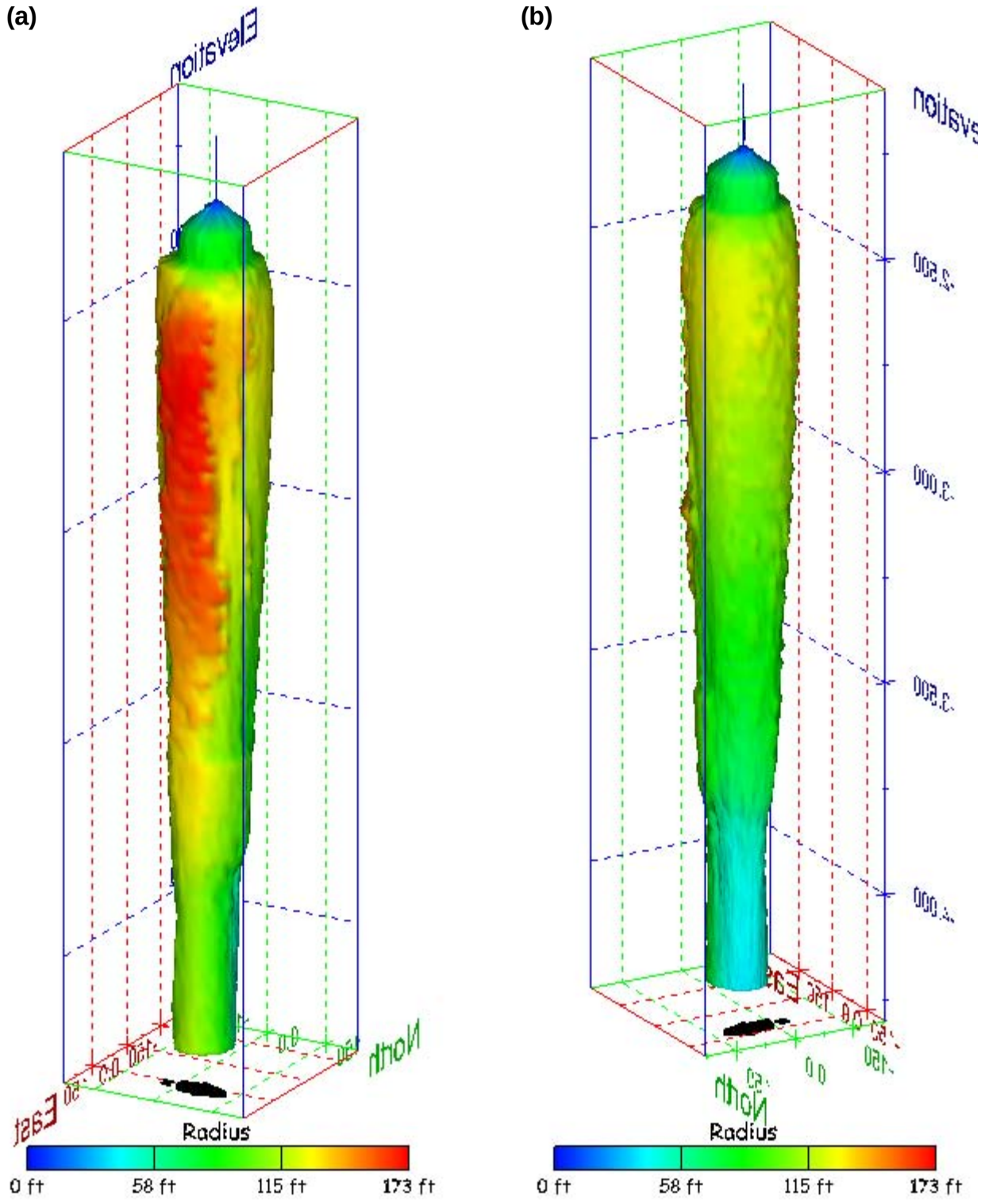

Figure 227. Sonar images of cavern BH-109, showing the geometry of the cavern colored by measured radius. View from (a) azimuth 60°, elevation 20°; (b) azimuth 300°, elevation 20°.

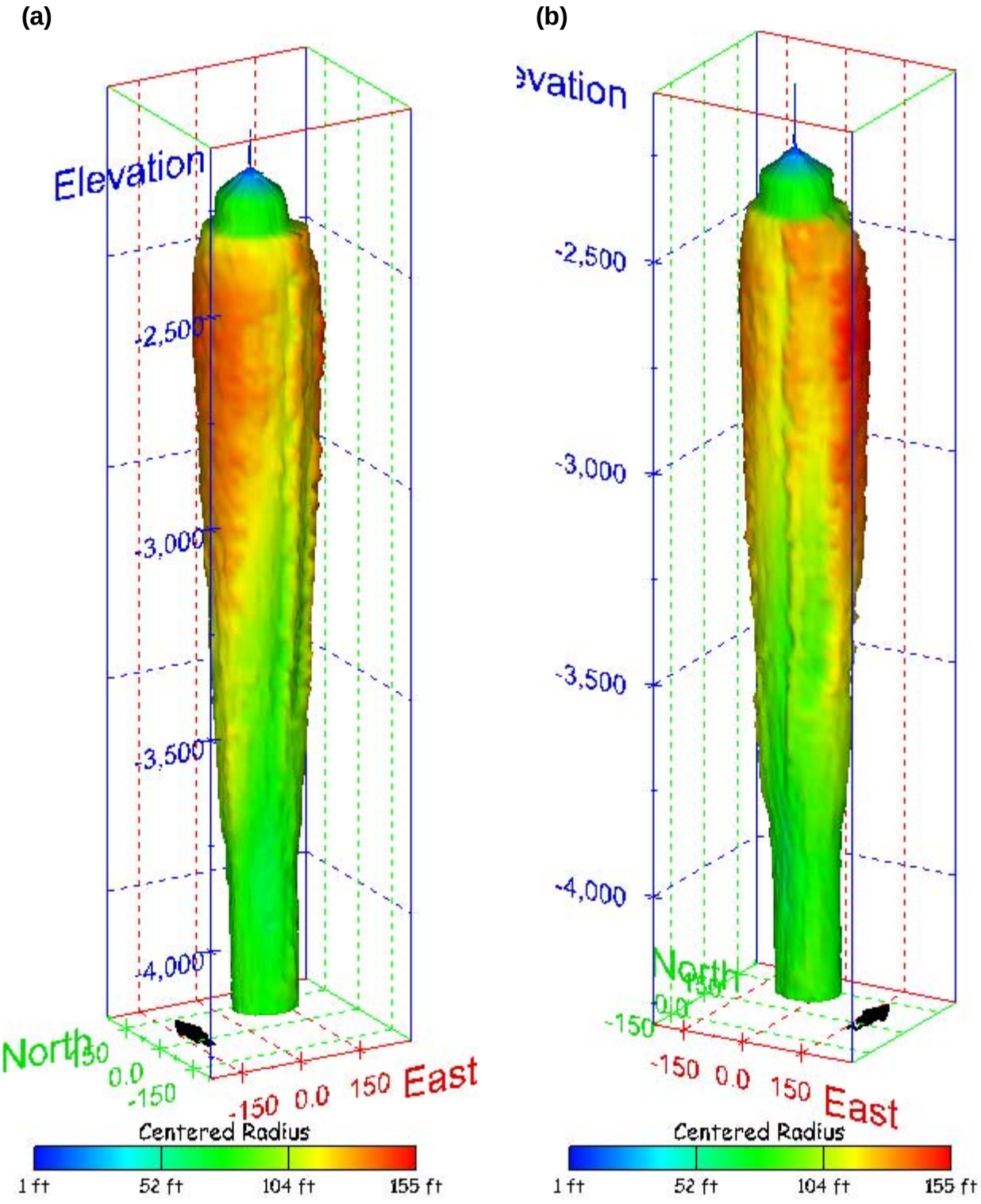

Figure 228. Sonar images of cavern BH-109, showing the geometry of the cavern colored by centered radius. View from (a) azimuth 210°, elevation 20°; (b) azimuth 150°, elevation 20°.

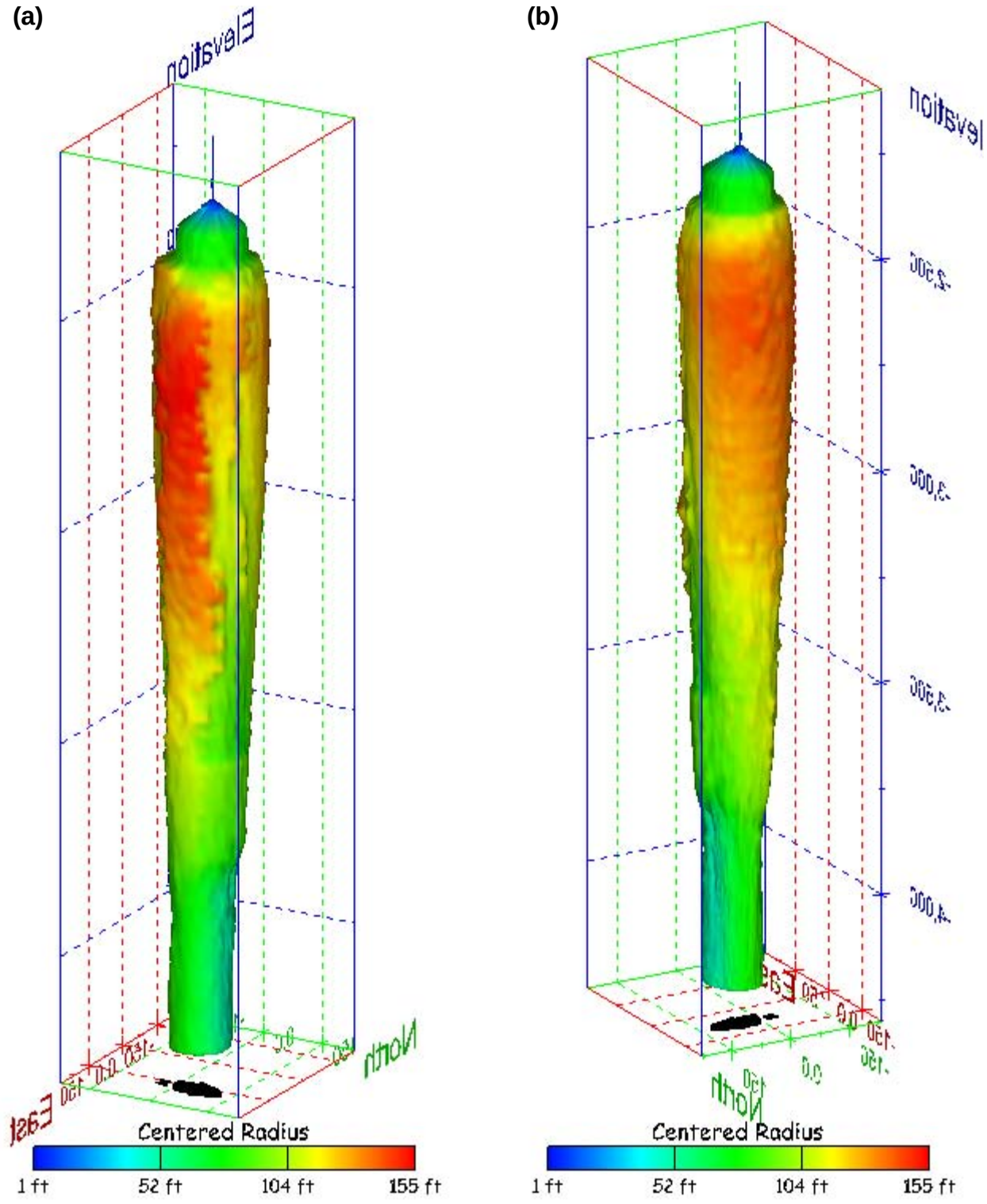

Figure 229. Sonar images of cavern BH-109, showing the geometry of the cavern colored by centered radius. View from (a) azimuth 60°, elevation 20°; (b) azimuth 300°, elevation 20°.

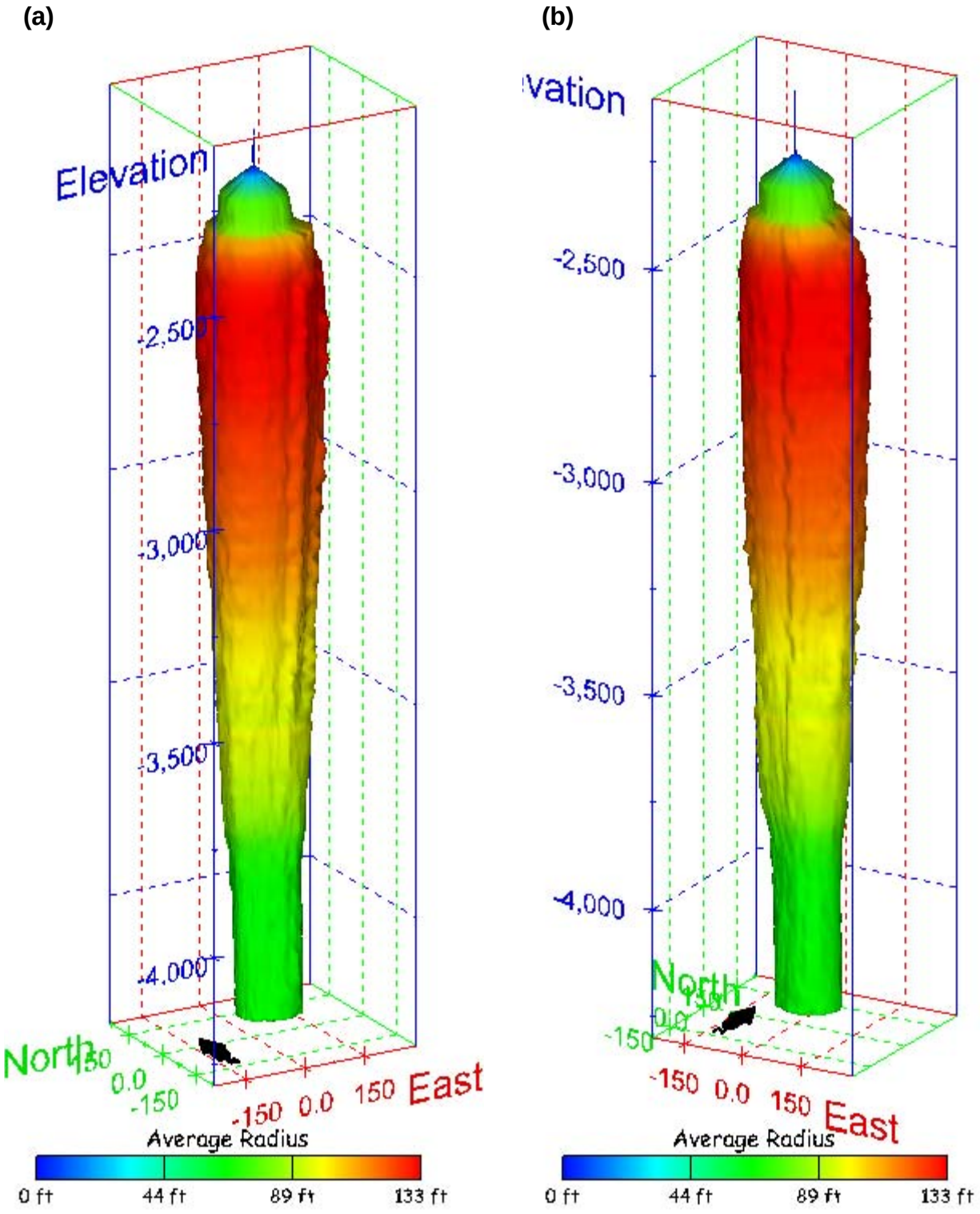

Figure 230. Sonar images of cavern BH-109, showing the geometry of the cavern colored by average radius. View from (a) azimuth 210°, elevation 20°; (b) azimuth 150°, elevation 20°.

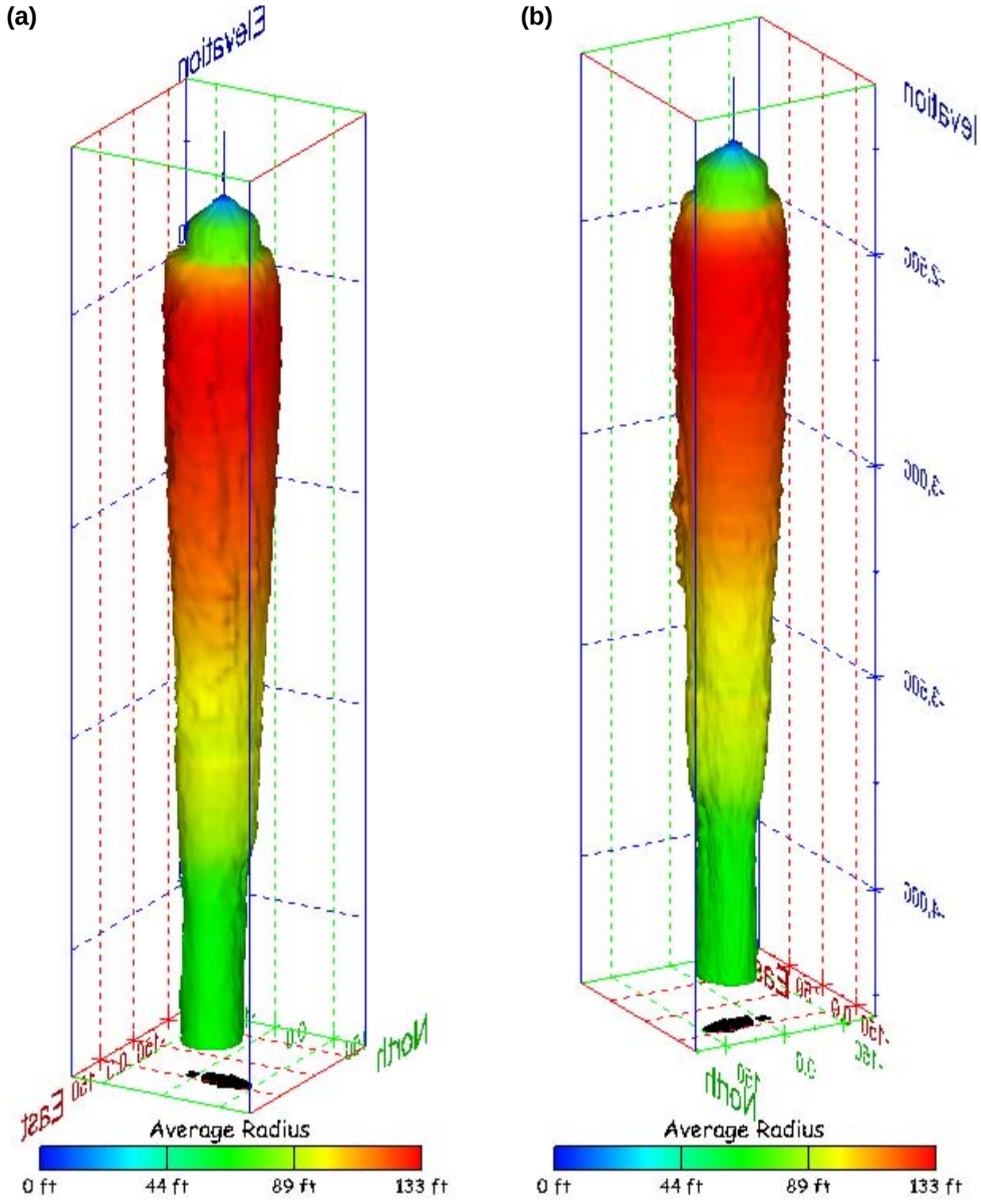

Figure 231. Sonar images of cavern BH-109, showing the geometry of the cavern colored by average radius. View from (a) azimuth 60°, elevation 20°; (b) azimuth 300°, elevation 20°.

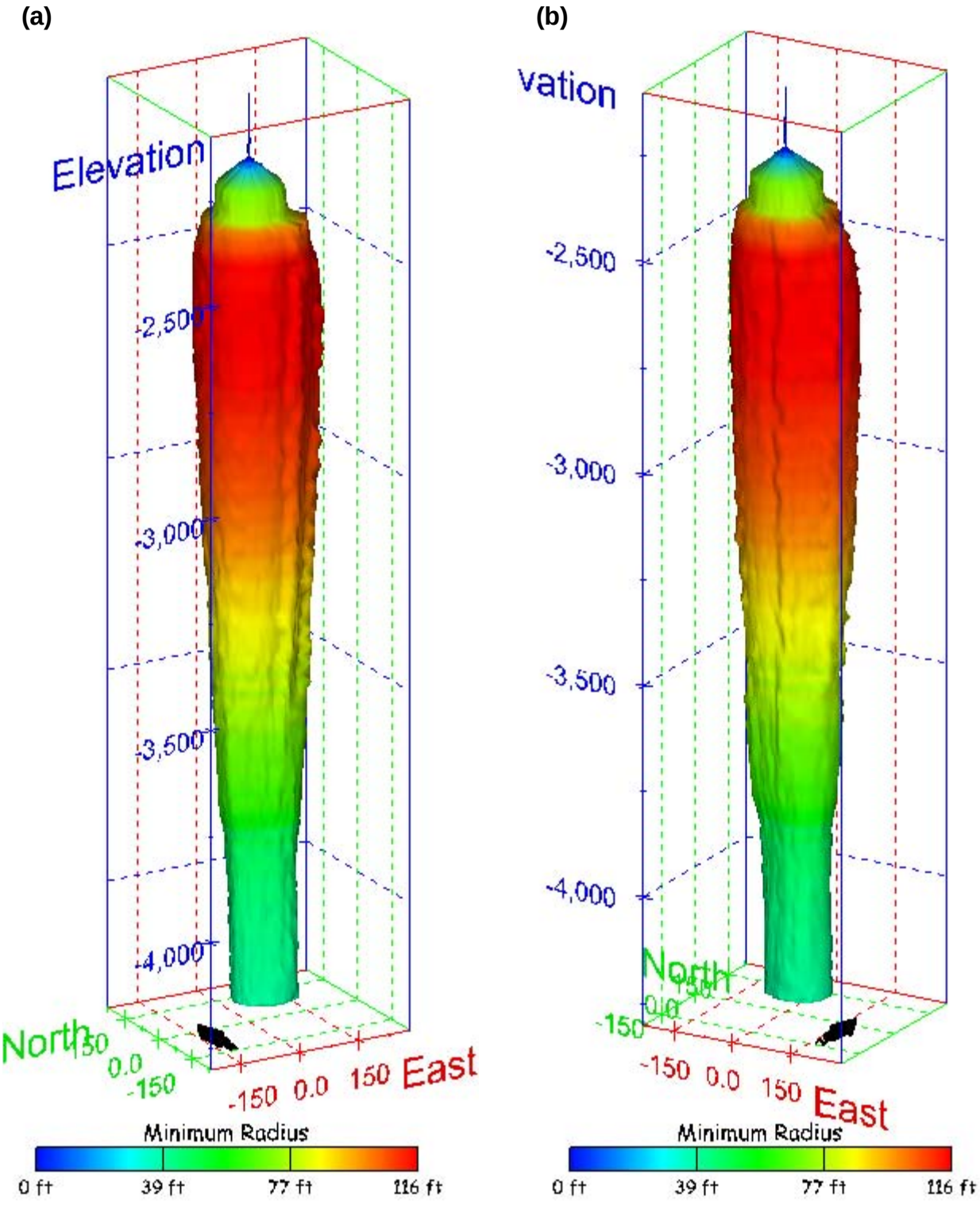

Figure 232. Sonar images of cavern BH-109, showing the geometry of the cavern colored by minimum radius. View from (a) azimuth 210°, elevation 20°; (b) azimuth 150°, elevation 20°.

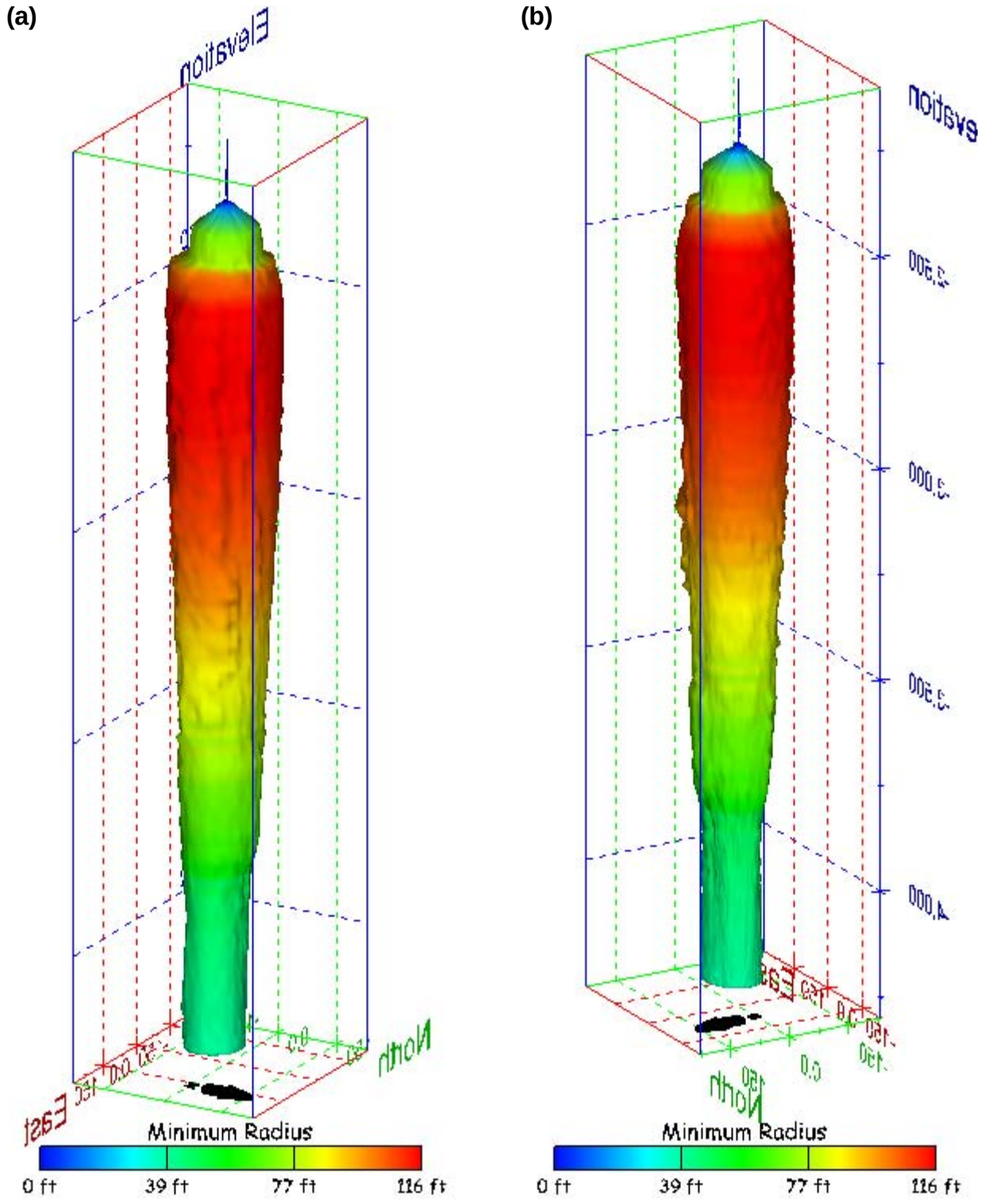

Figure 233. Sonar images of cavern BH-109, showing the geometry of the cavern colored by minimum radius. View from (a) azimuth 60°, elevation 20°; (b) azimuth 300°, elevation 20°.

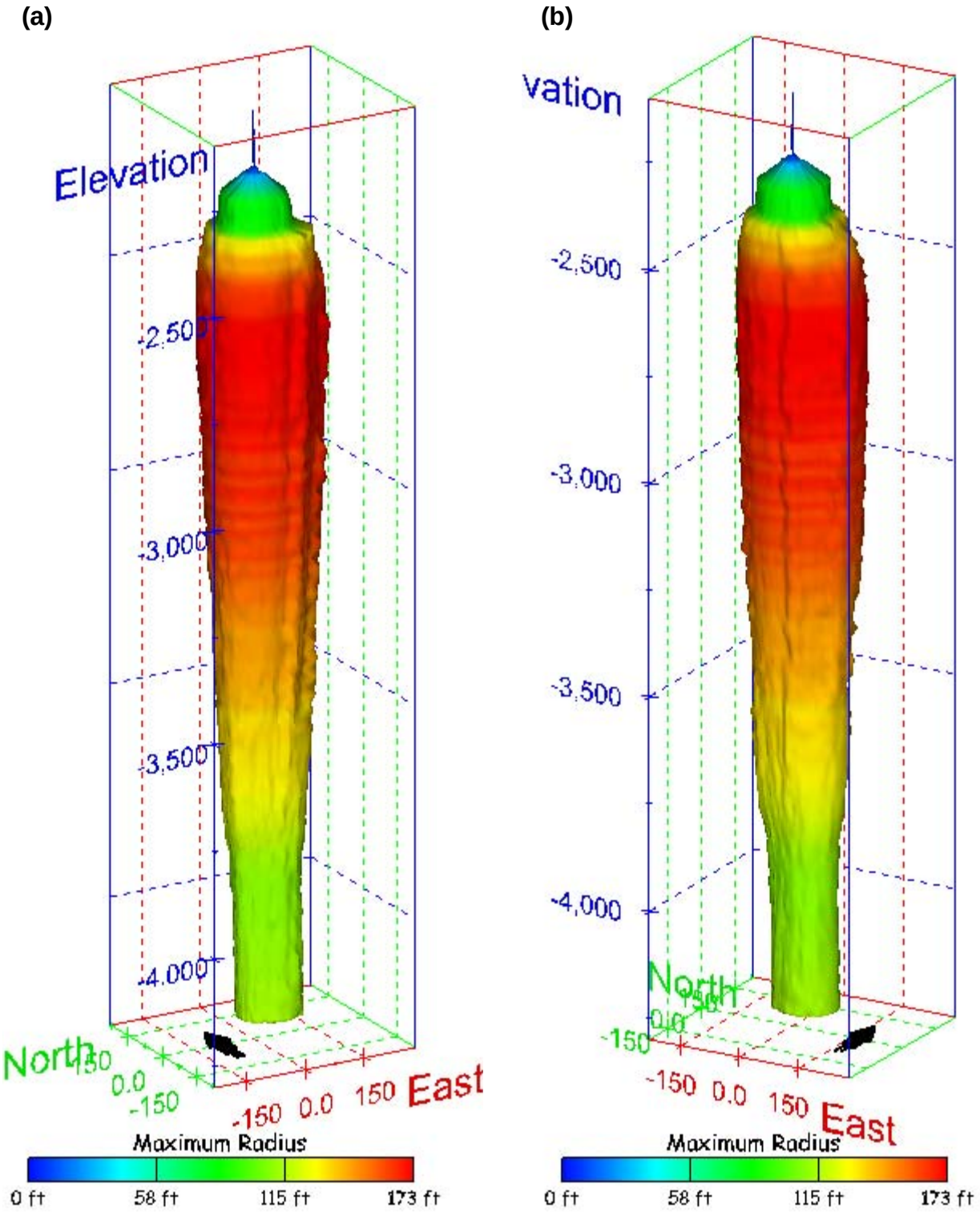

Figure 234. Sonar images of cavern BH-109, showing the geometry of the cavern colored by maximum radius. View from (a) azimuth 210°, elevation 20°; (b) azimuth 150°, elevation 20°.

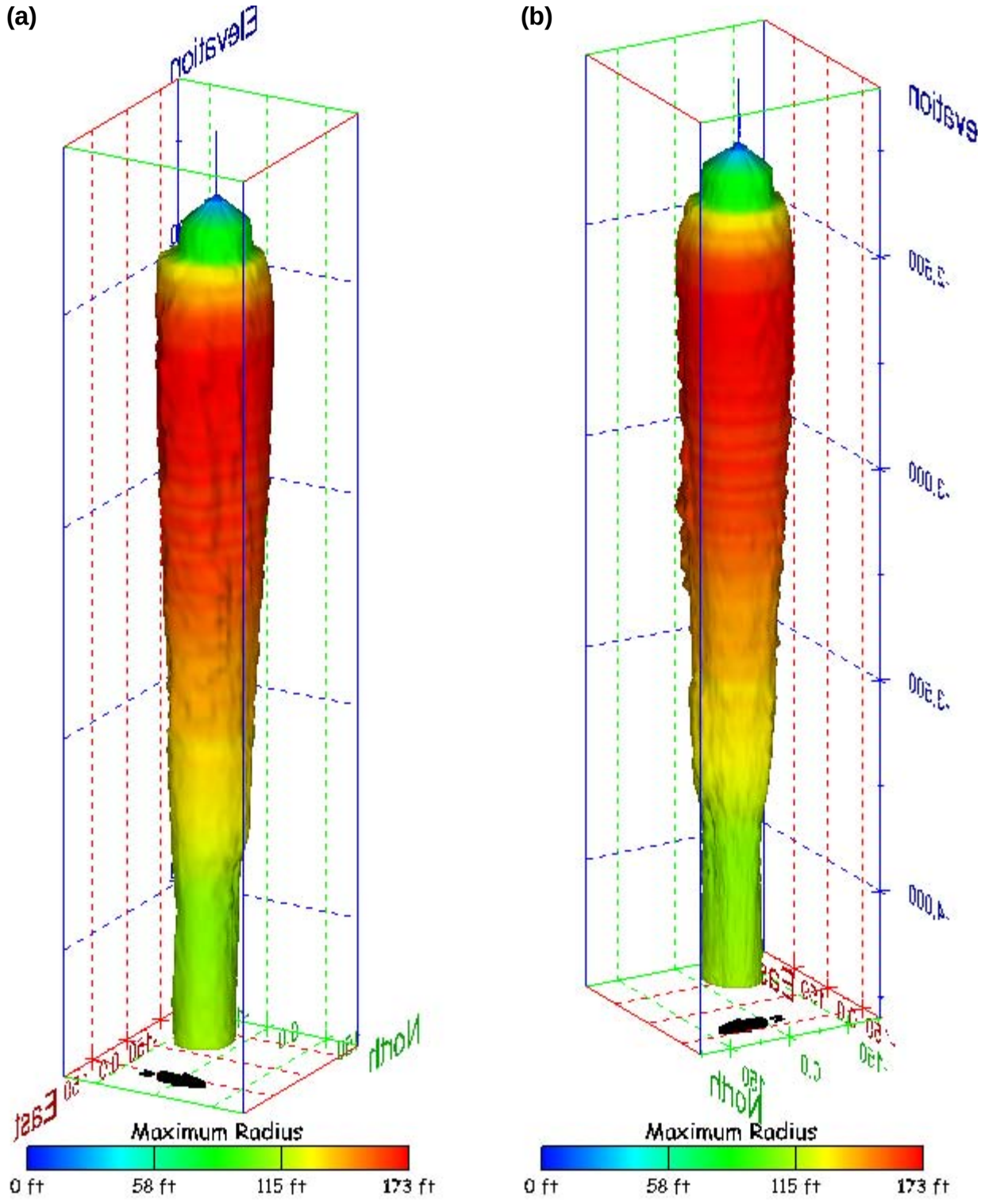

Figure 235. Sonar images of cavern BH-109, showing the geometry of the cavern colored by maximum radius. View from (a) azimuth 60°, elevation 20°; (b) azimuth 300°, elevation 20°.

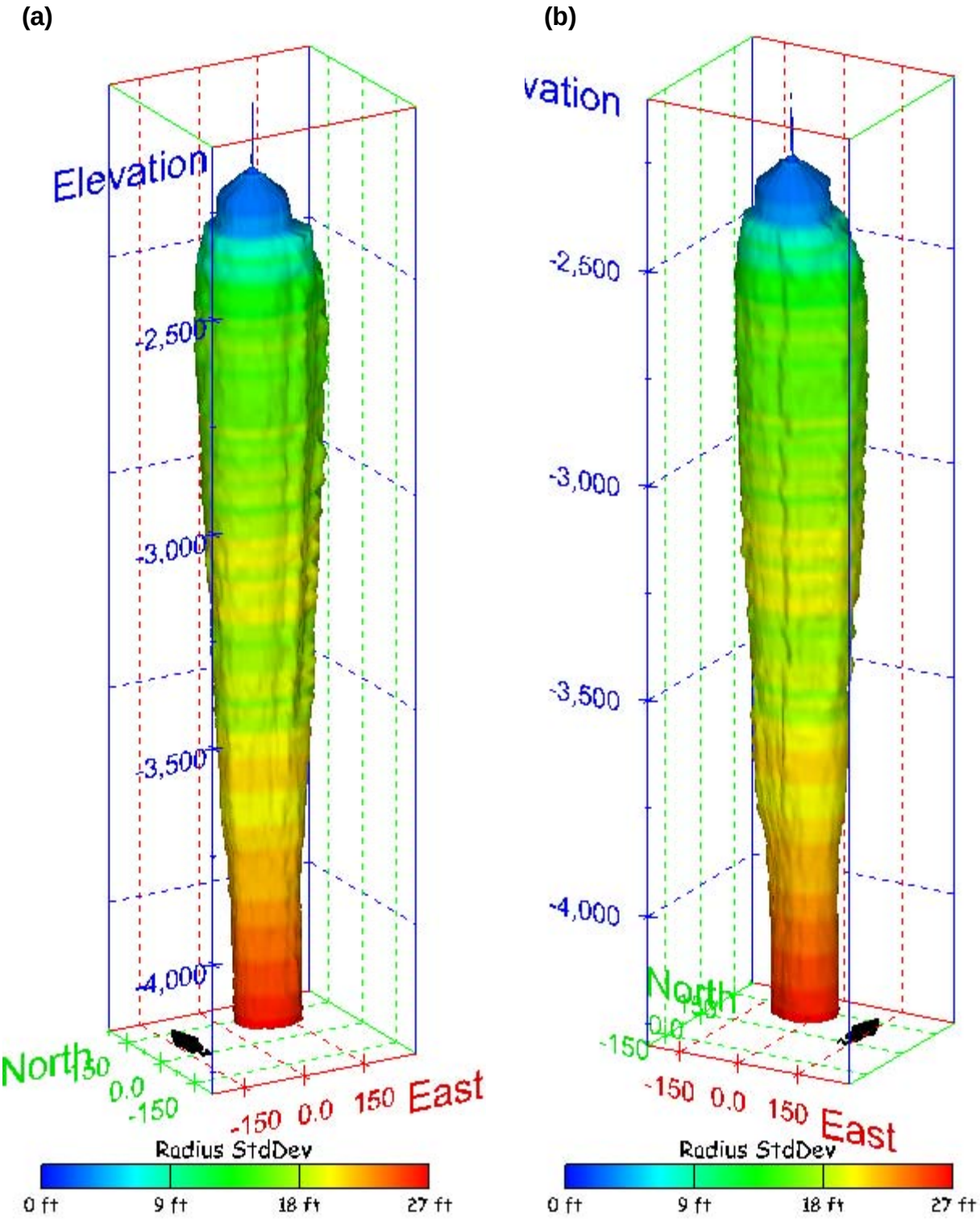

Figure 236. Sonar images of cavern BH-109, showing the geometry of the cavern colored by radius standard deviation. View from (a) azimuth 210°, elevation 20°; (b) azimuth 150°, elevation 20°.

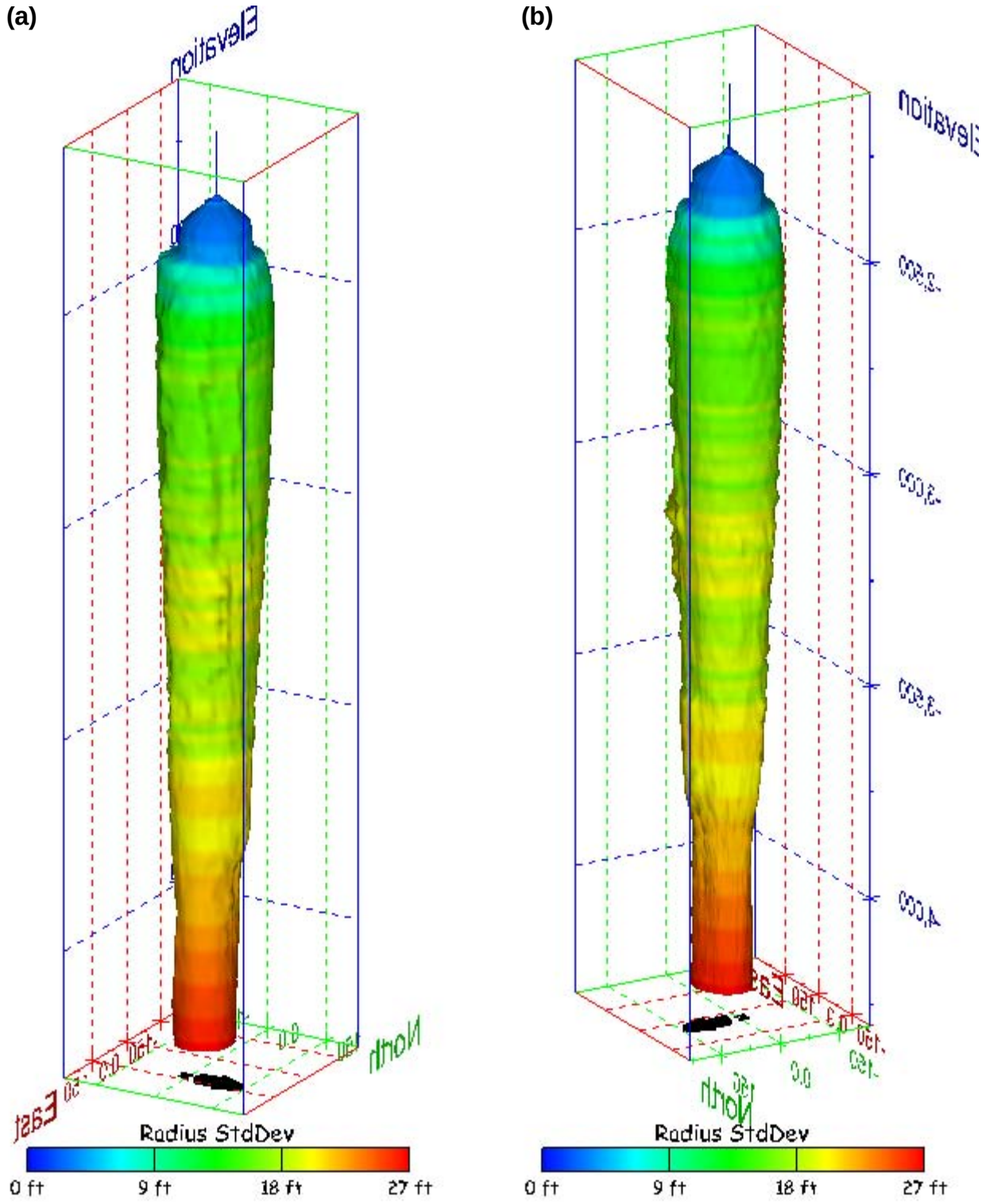

Figure 237. Sonar images of cavern BH-109, showing the geometry of the cavern colored by radius standard deviation. View from (a) azimuth 60°, elevation 20°; (b) azimuth 300°, elevation 20°.

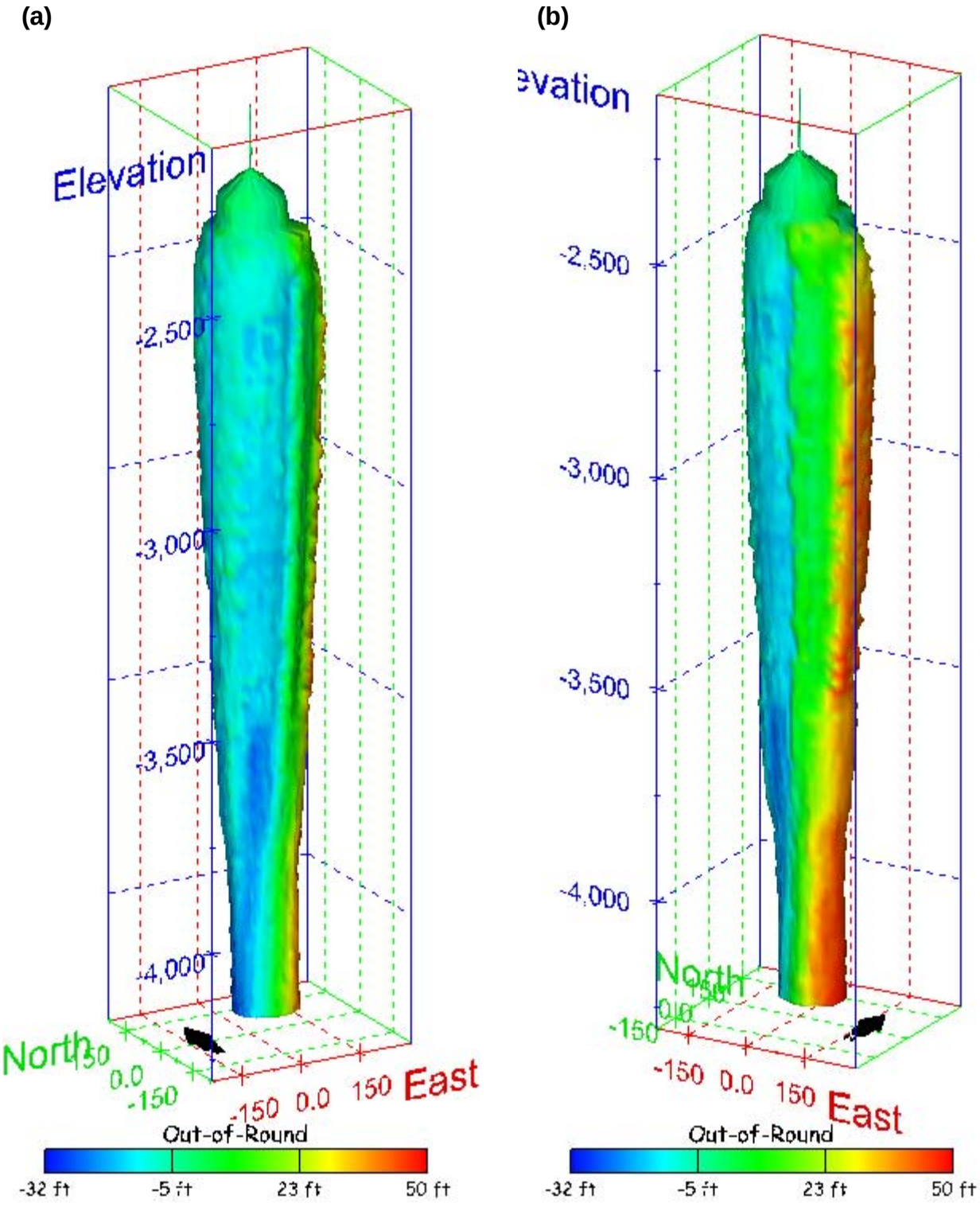

Figure 238. Sonar images of cavern BH-109, showing the geometry of the cavern colored by out-of-round distance. View from (a) azimuth 210°, elevation 20°; (b) azimuth 150°, elevation 20°.

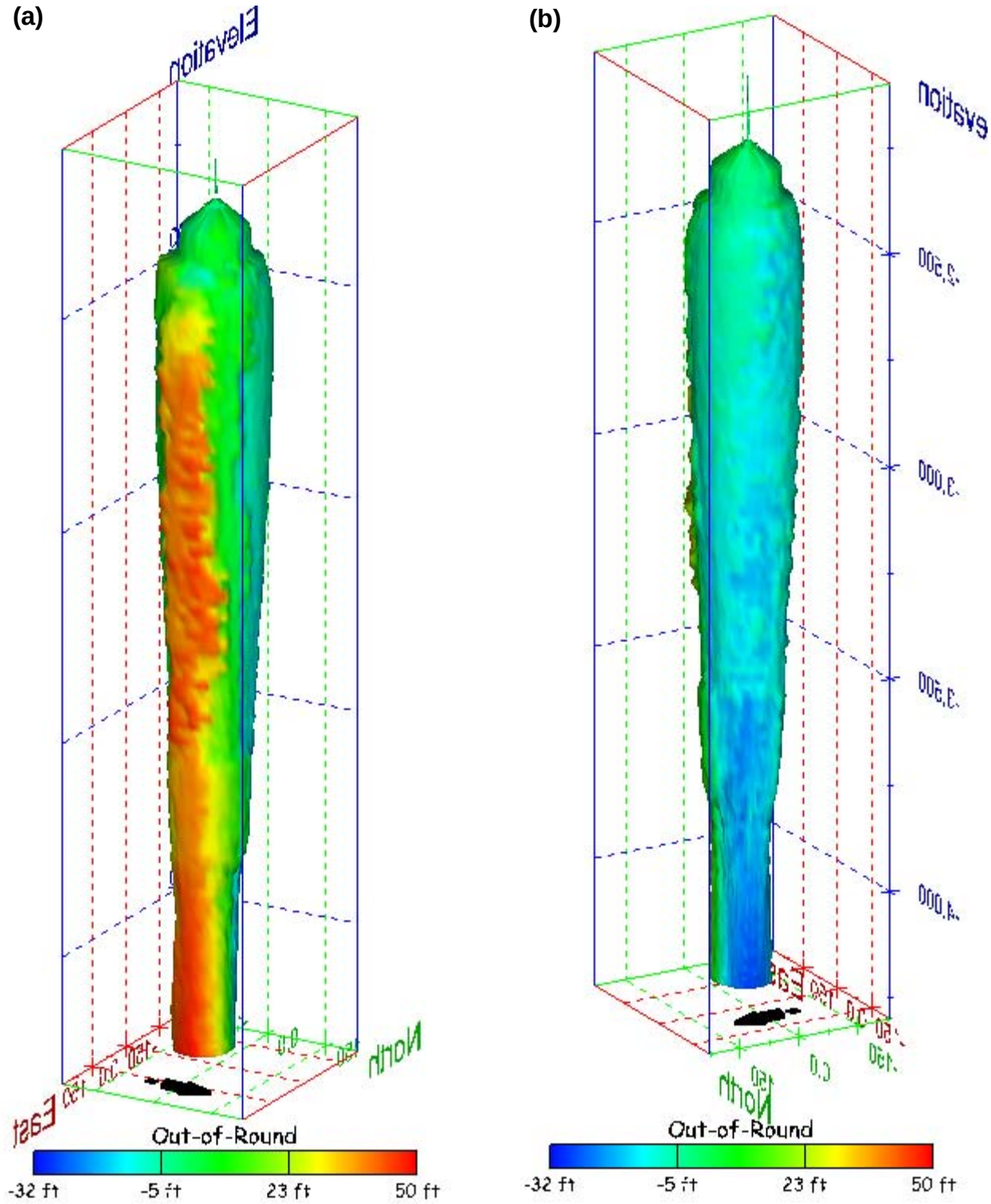

Figure 239. Sonar images of cavern BH-109, showing the geometry of the cavern colored by out-of-round distance. View from (a) azimuth 60°, elevation 20°; (b) azimuth 300°, elevation 20°.

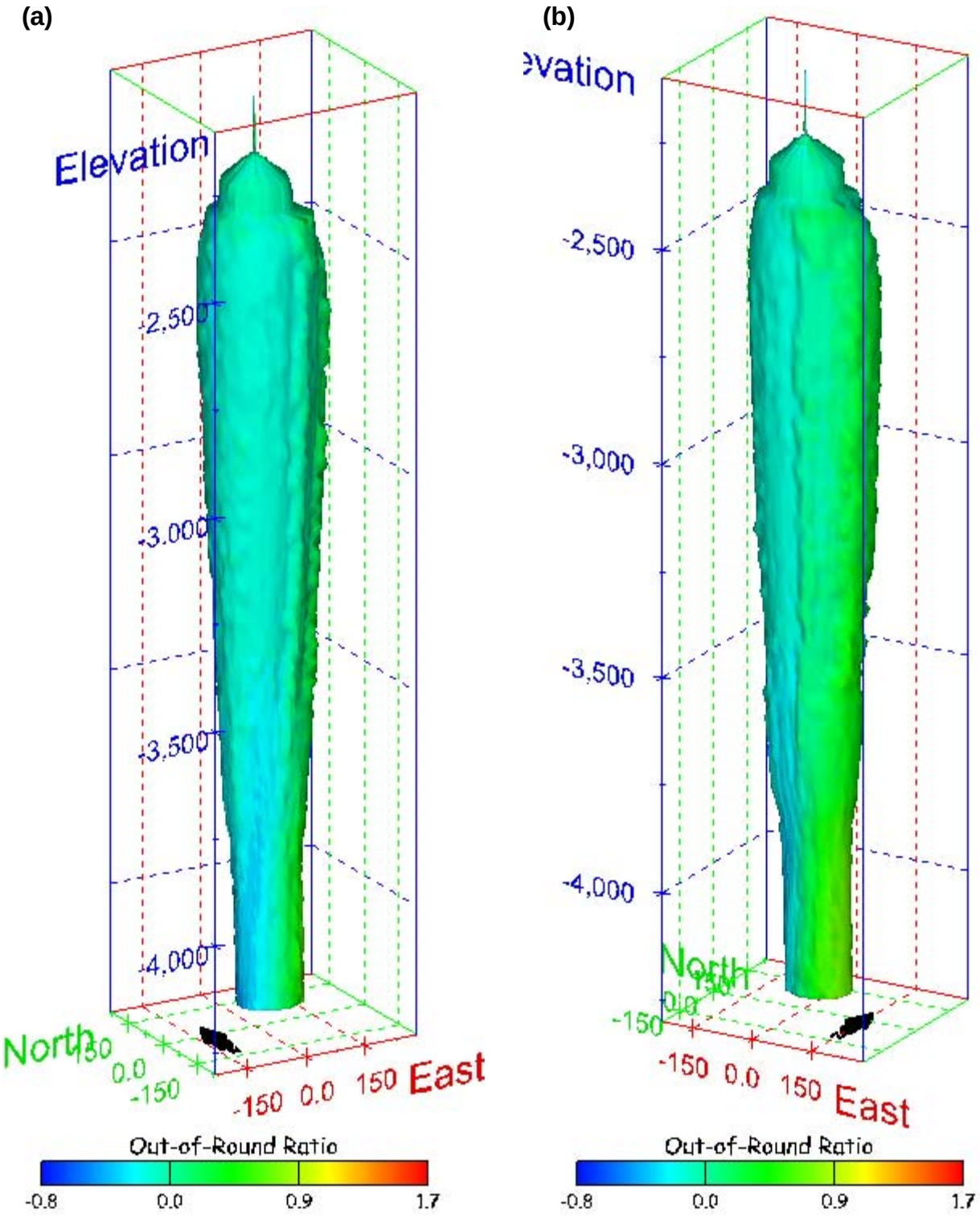

Figure 240. Sonar images of cavern BH-109, showing the geometry of the cavern colored by out-of-round ratio. View from (a) azimuth 210°, elevation 20°; (b) azimuth 150°, elevation 20°.

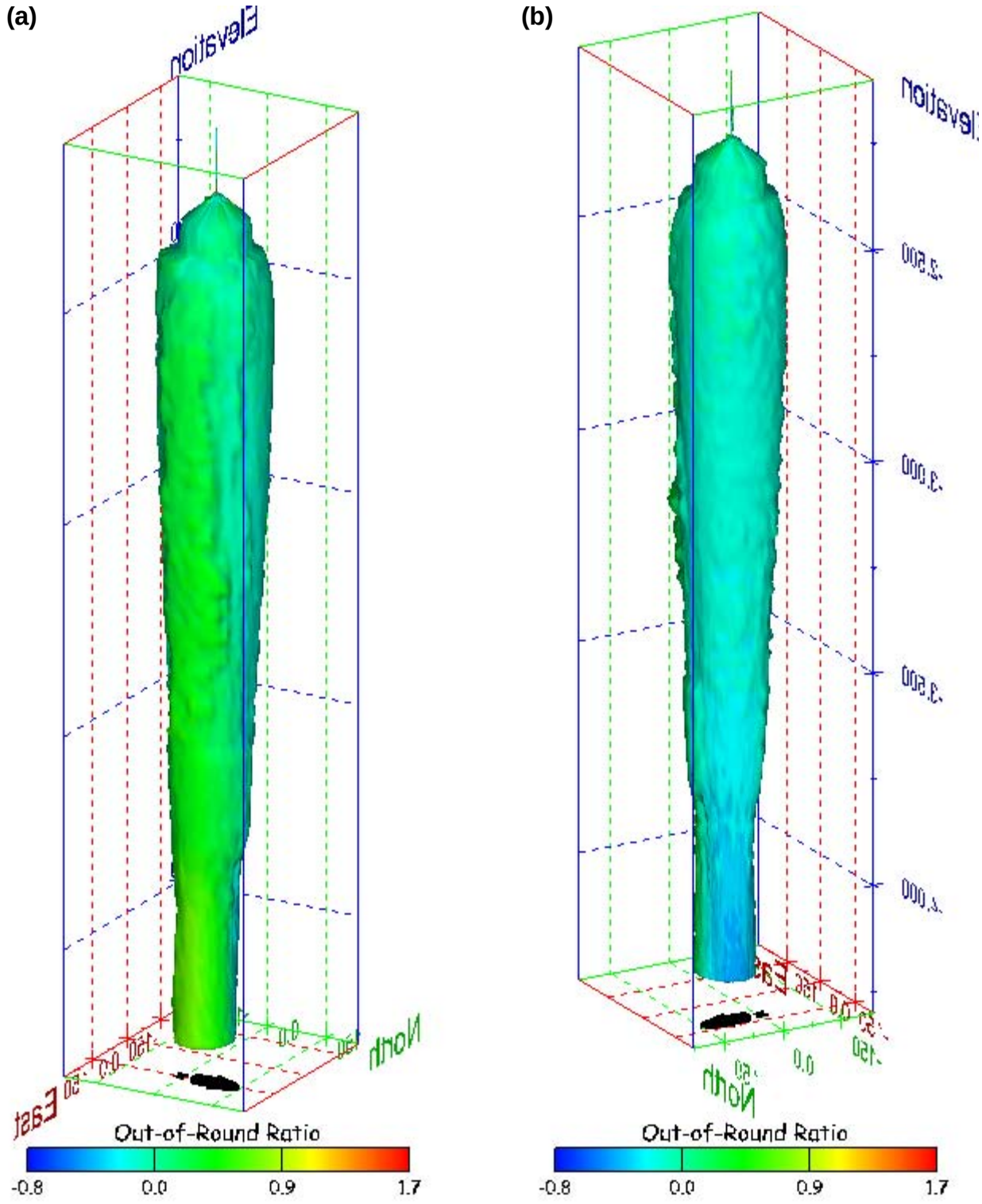

Figure 241. Sonar images of cavern BH-109, showing the geometry of the cavern colored by out-of-round ratio. View from (a) azimuth 60°, elevation 20°; (b) azimuth 300°, elevation 20°.

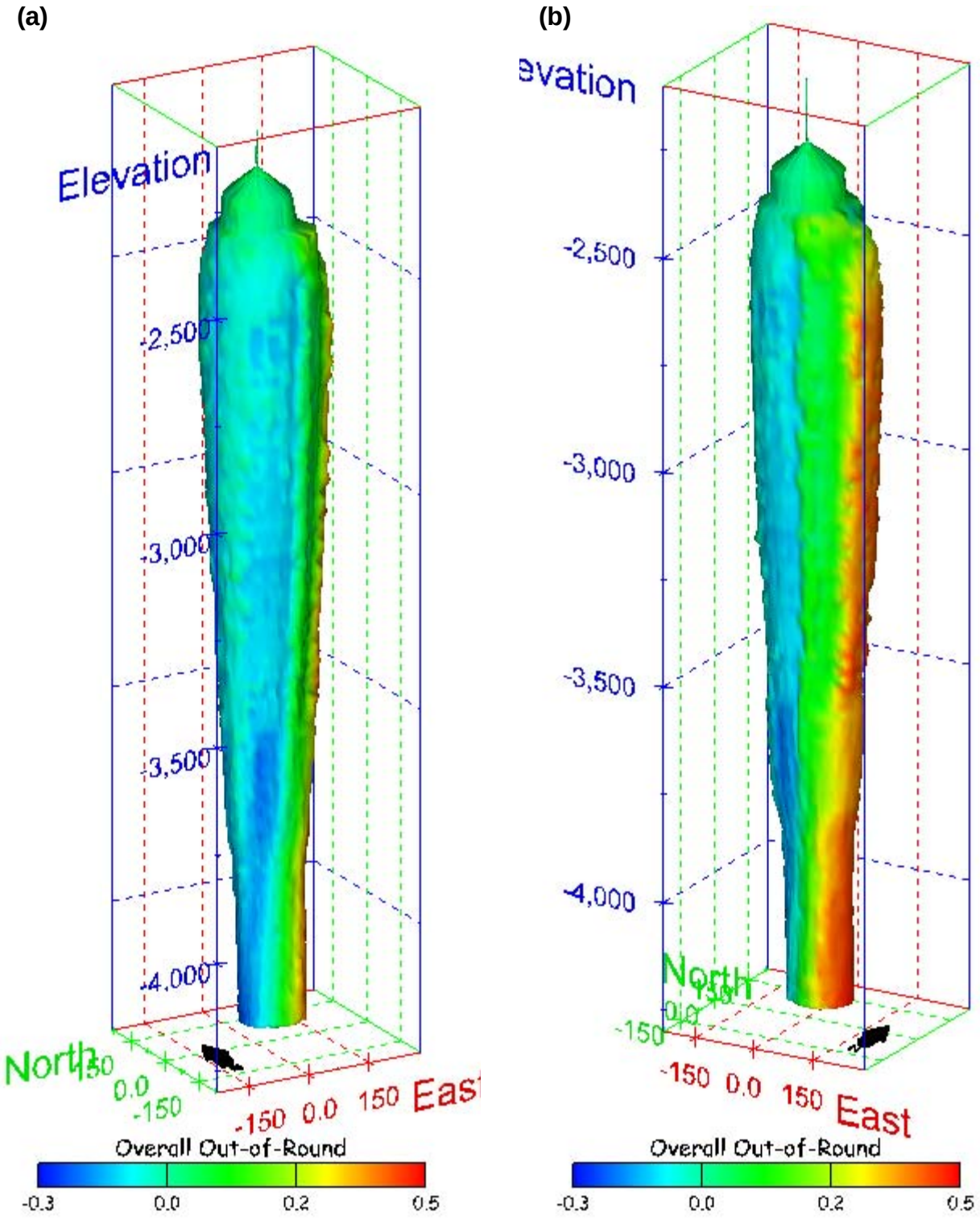

Figure 242. Sonar images of cavern BH-109, showing the geometry of the cavern colored by overall out-of-round ratio. View from (a) azimuth 210°, elevation 20°; (b) azimuth 150°, elevation 20°.

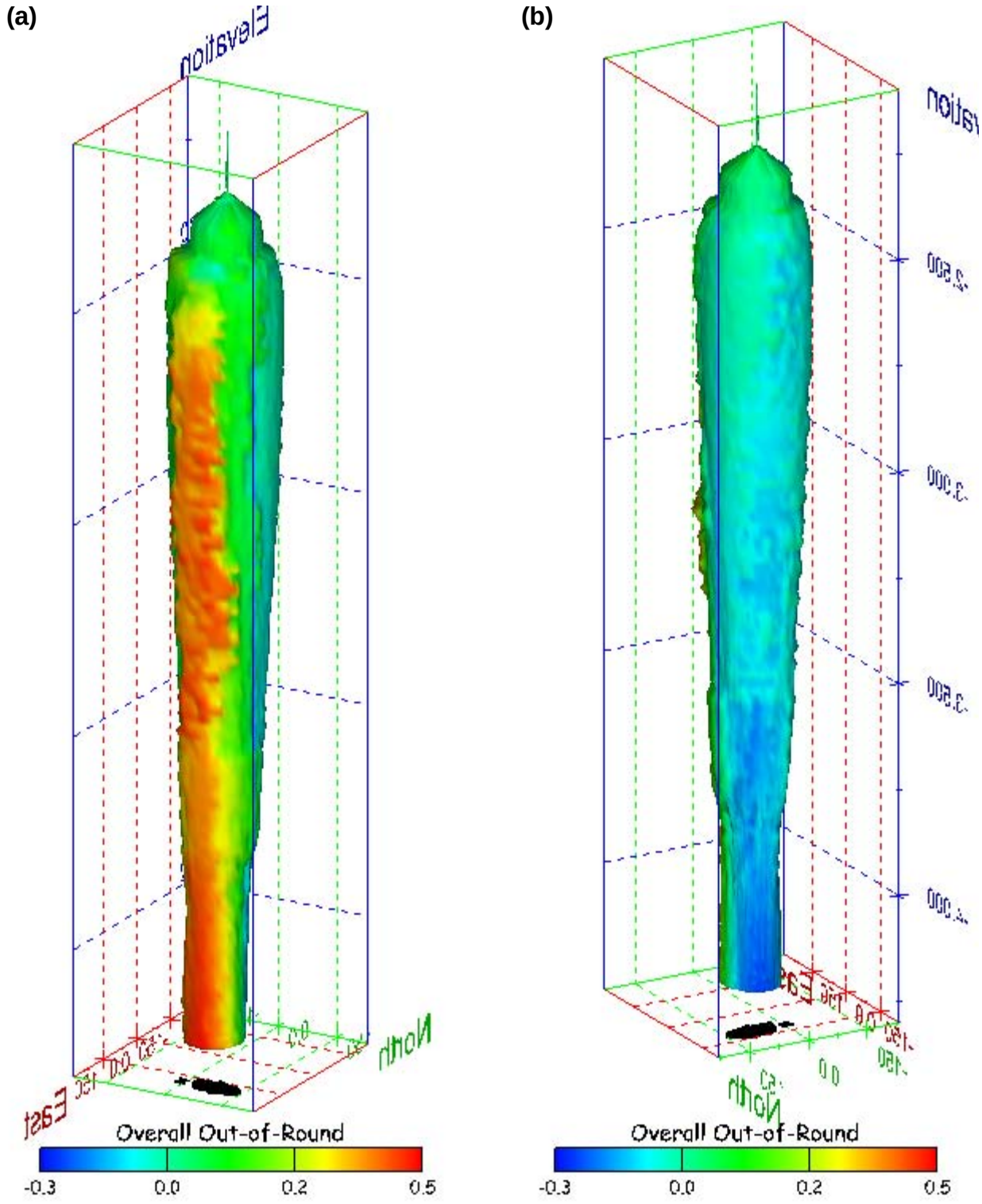

Figure 243. Sonar images of cavern BH-109, showing the geometry of the cavern colored by overall out-of-round ratio. View from (a) azimuth 60°, elevation 20°; (b) azimuth 300°, elevation 20°.

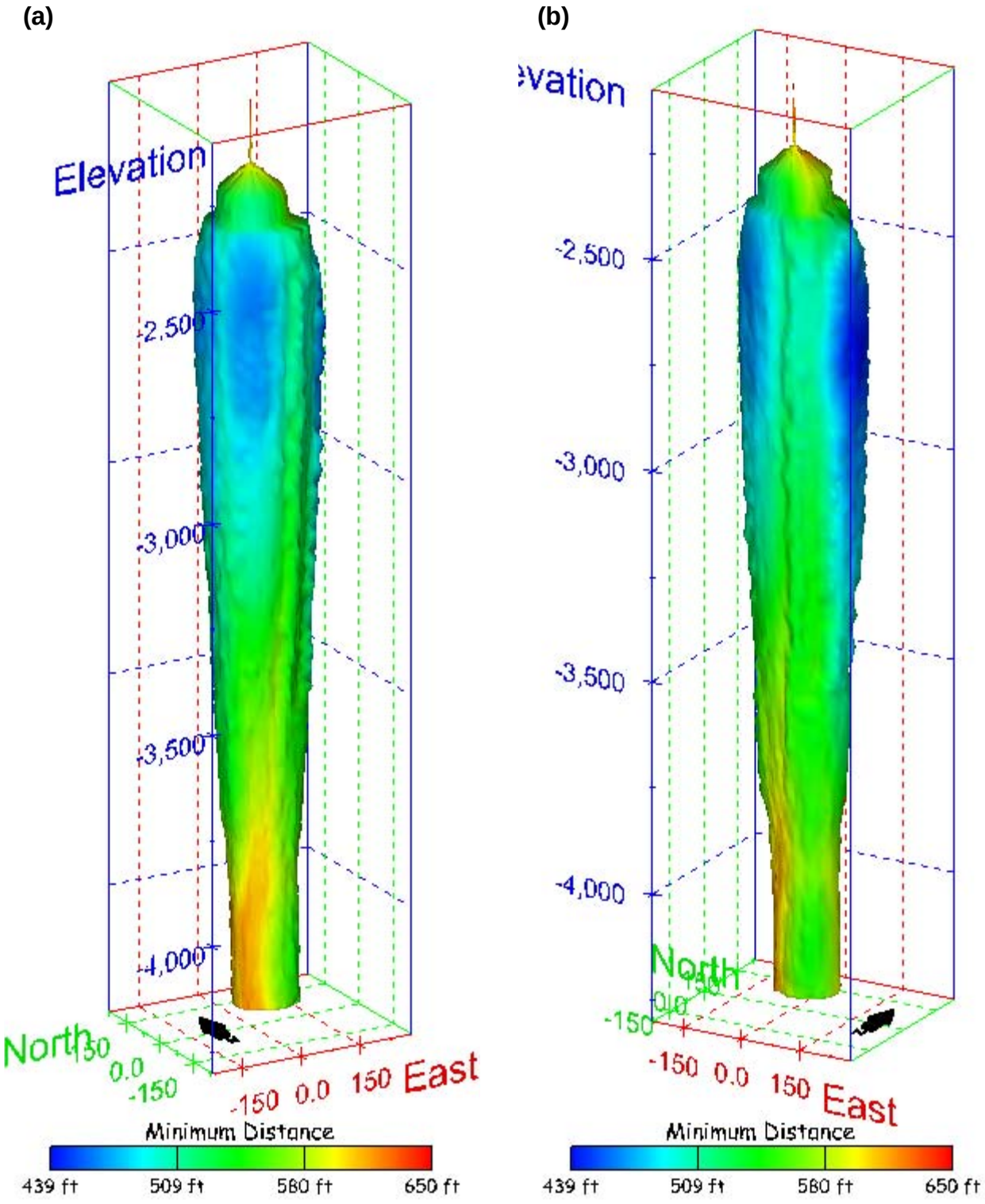

Figure 244. Sonar images of cavern BH-109, showing the geometry of the cavern colored by the minimum distance to the nearest neighboring cavern. View from (a) azimuth 210°, elevation 20°; (b) azimuth 150°, elevation 20°.

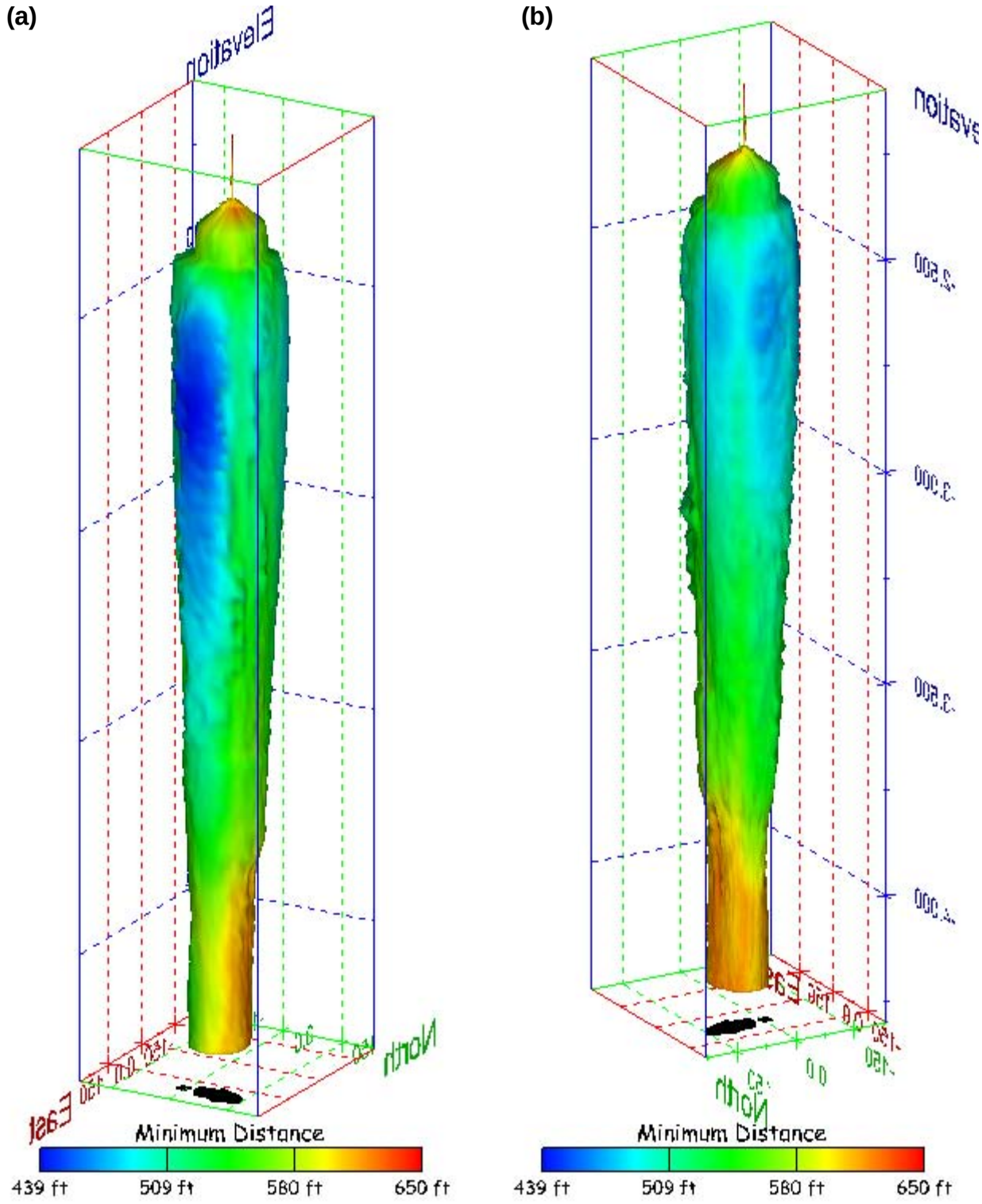

Figure 245. Sonar images of cavern BH-109, showing the geometry of the cavern colored by minimum distance to the nearest neighboring cavern. View from (a) azimuth 60°, elevation 20°; (b) azimuth 300°, elevation 20°.

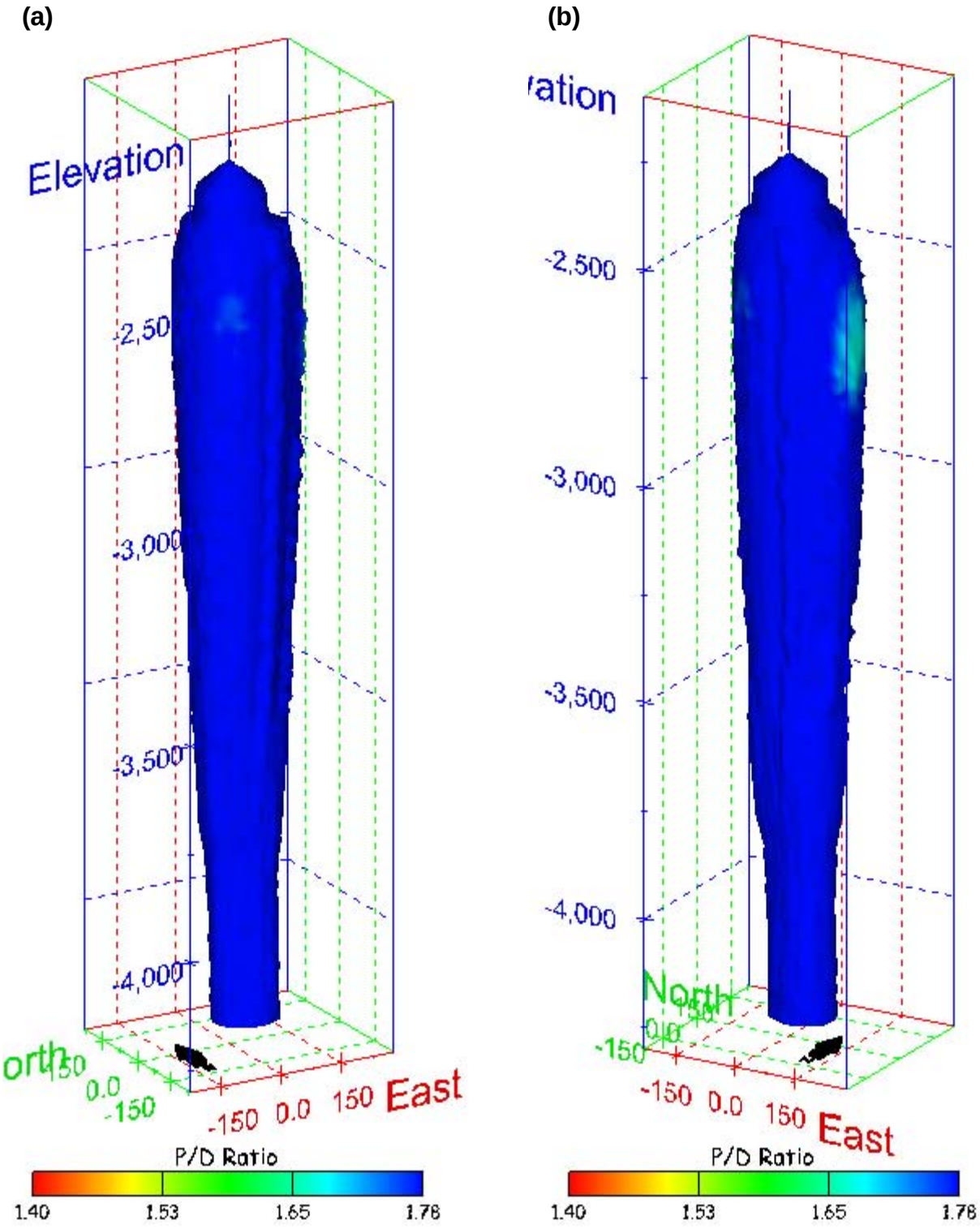

Figure 246. Sonar images of cavern BH-109, showing the geometry of the cavern colored by three-dimensional pillar-to-diameter ratio. View from (a) azimuth 210°, elevation 20°; (b) azimuth 150°, elevation 20°.

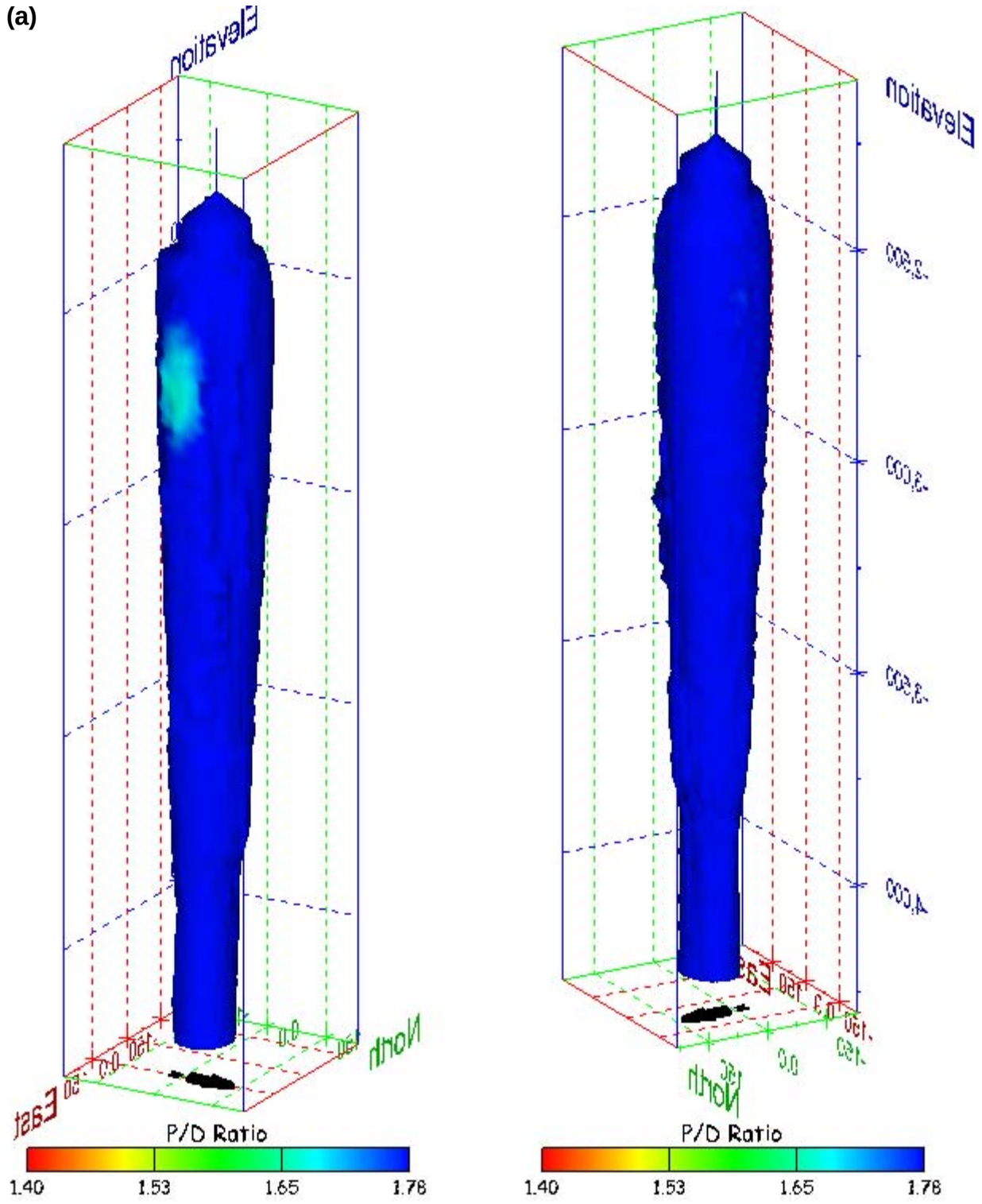

Figure 247. Sonar images of cavern BH-109, showing the geometry of the cavern colored by three-dimensional pillar-to-diameter ratio. View from (a) azimuth 60°, elevation 20°; (b) azimuth 300°, elevation 20°.

No Sonic Velocity Data Available for Socon Surveys

Figure 248. Sonar image of cavern BH-109, showing the geometry of the cavern colored by the reported velocity of sound on the survey date of March 2005. View from due south, elevation zero.

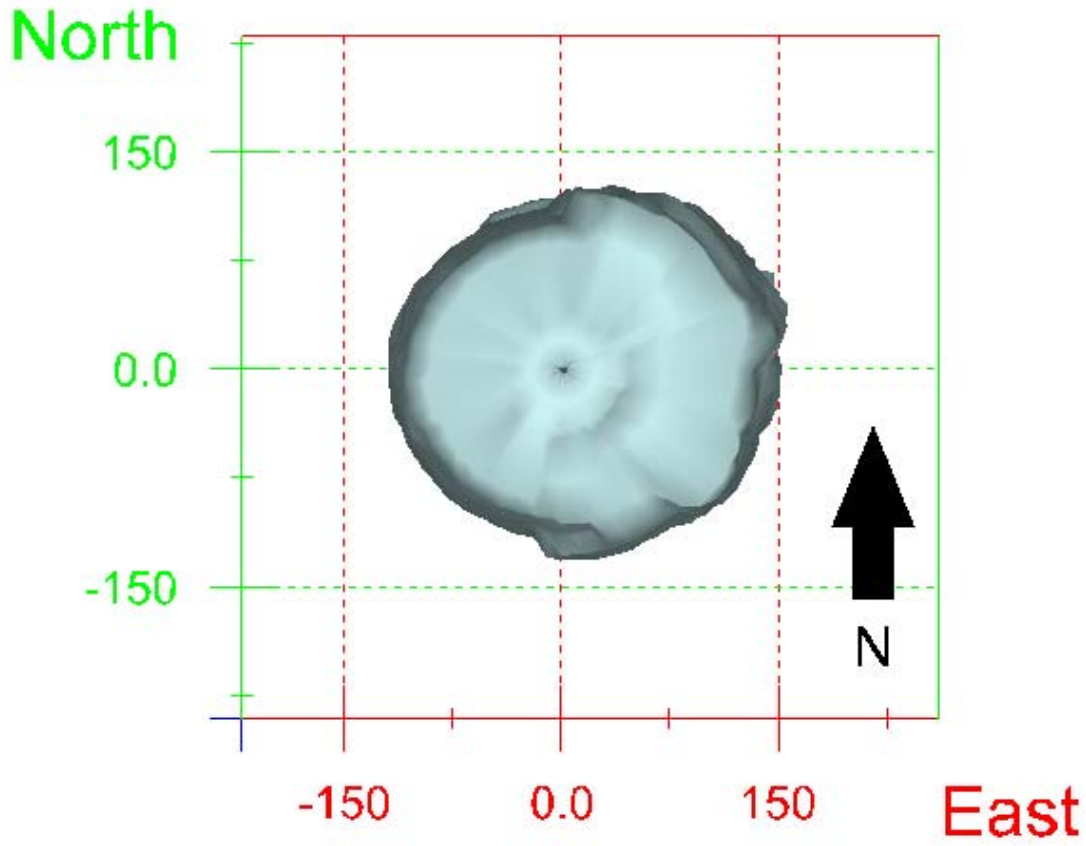

Figure 249. Map view sonar image of cavern BH-110, showing the basic geometry of the cavern. Grid squares represent 150 ft.

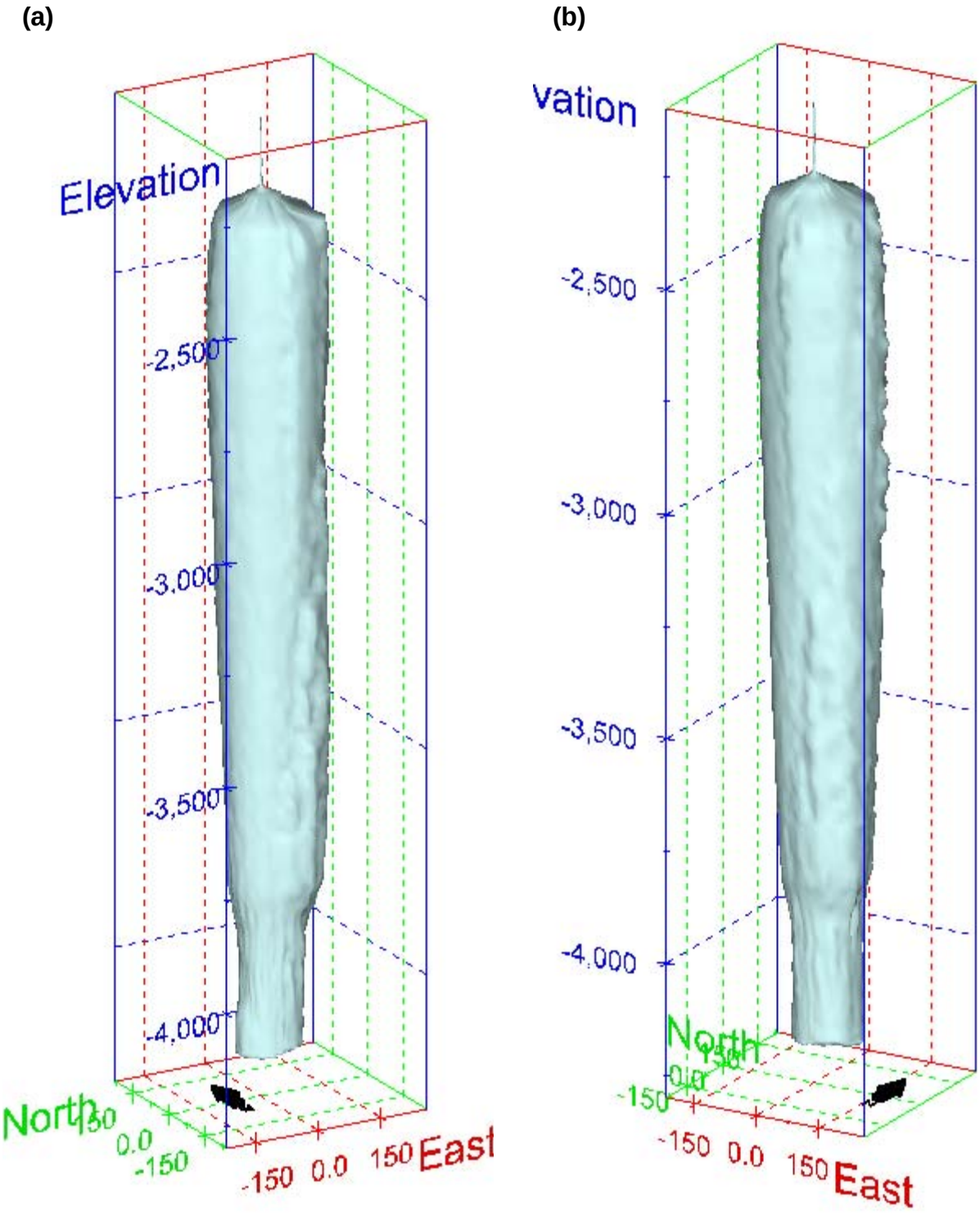

Figure 250. Sonar images of cavern BH-110, showing the basic geometric shape of the cavern. View from (a) azimuth 210°, elevation 20°; (b) azimuth 150°, elevation 20°.

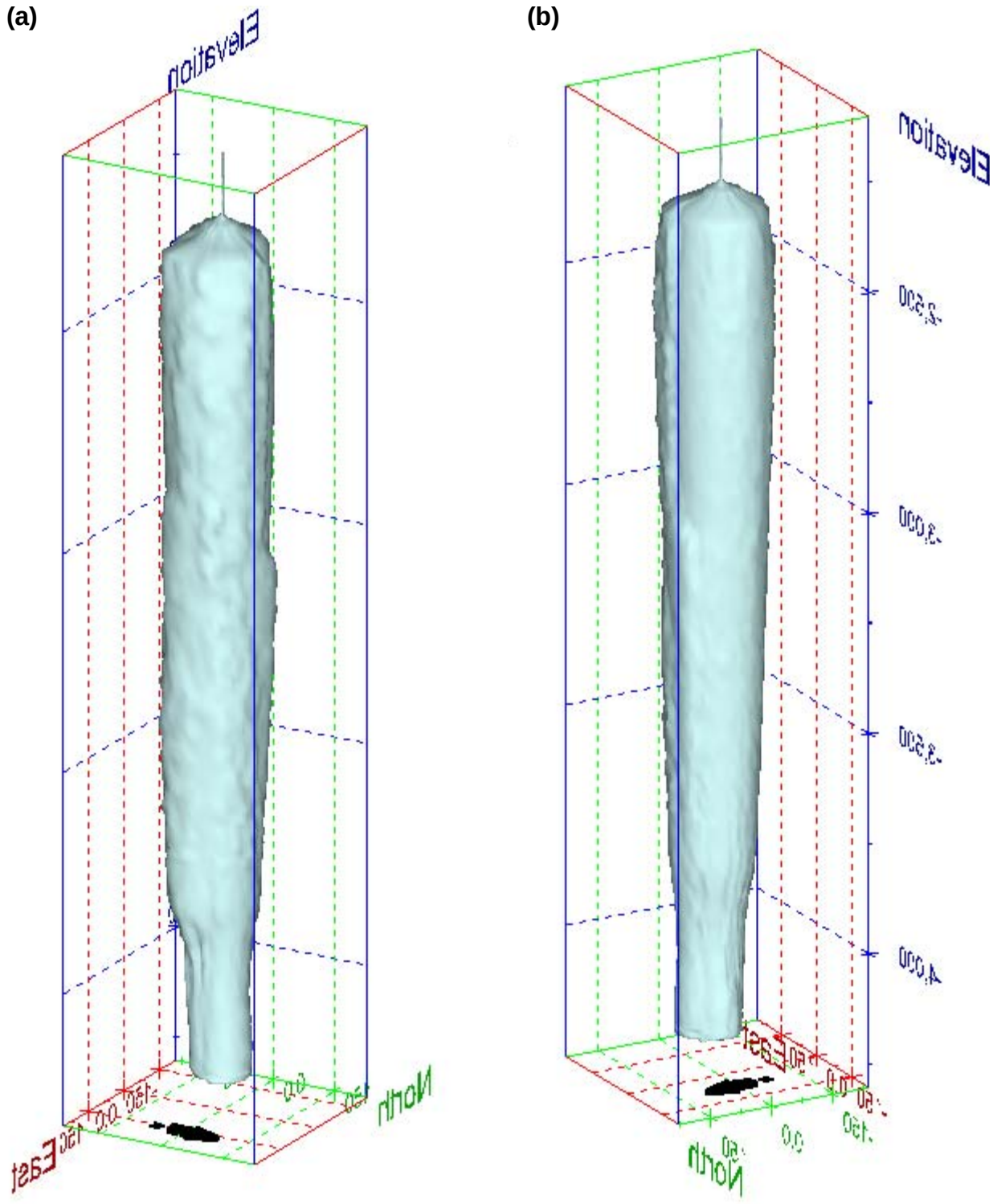

Figure 251. Sonar images of cavern BH-110, showing the basic geometric shape of the cavern. View from (a) azimuth 60°, elevation 20°; (b) azimuth 300°, elevation 20°.

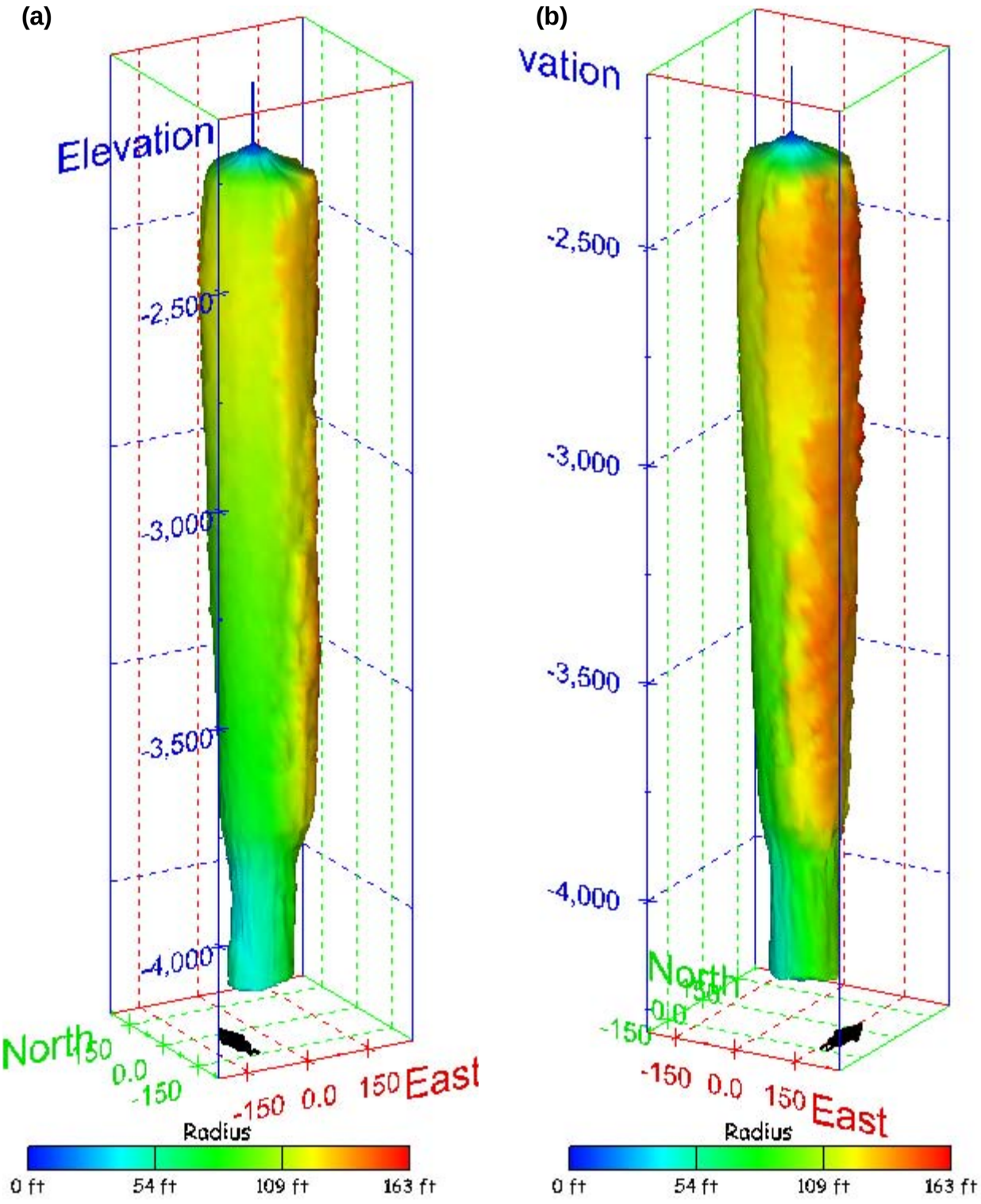

Figure 252. Sonar images of cavern BH-110, showing the geometry of the cavern colored by measured radius. View from (a) azimuth 210°, elevation 20°; (b) azimuth 150°, elevation 20°.

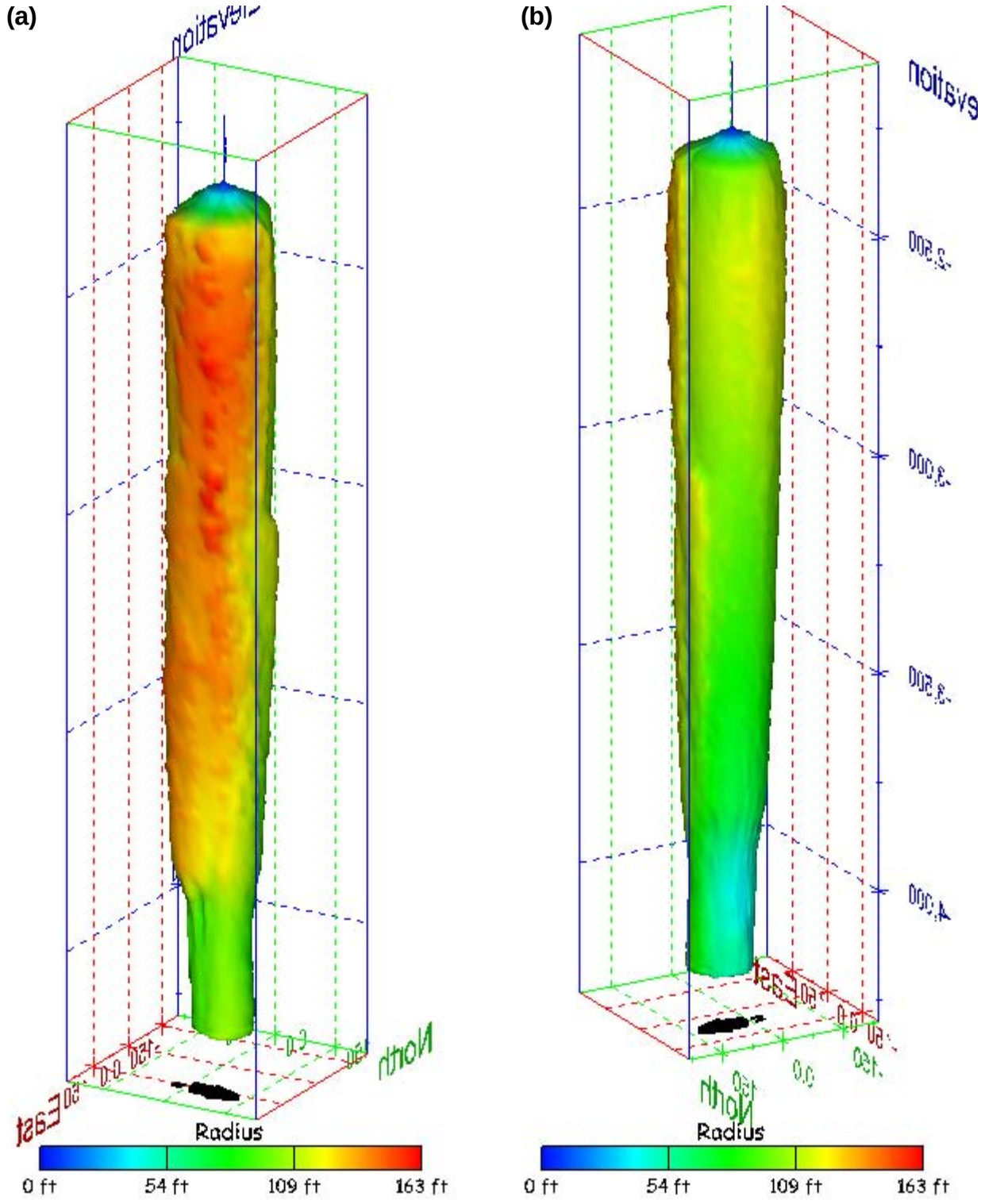

Figure 253. Sonar images of cavern BH-110, showing the geometry of the cavern colored by measured radius. View from (a) azimuth 60°, elevation 20°; (b) azimuth 300°, elevation 20°.

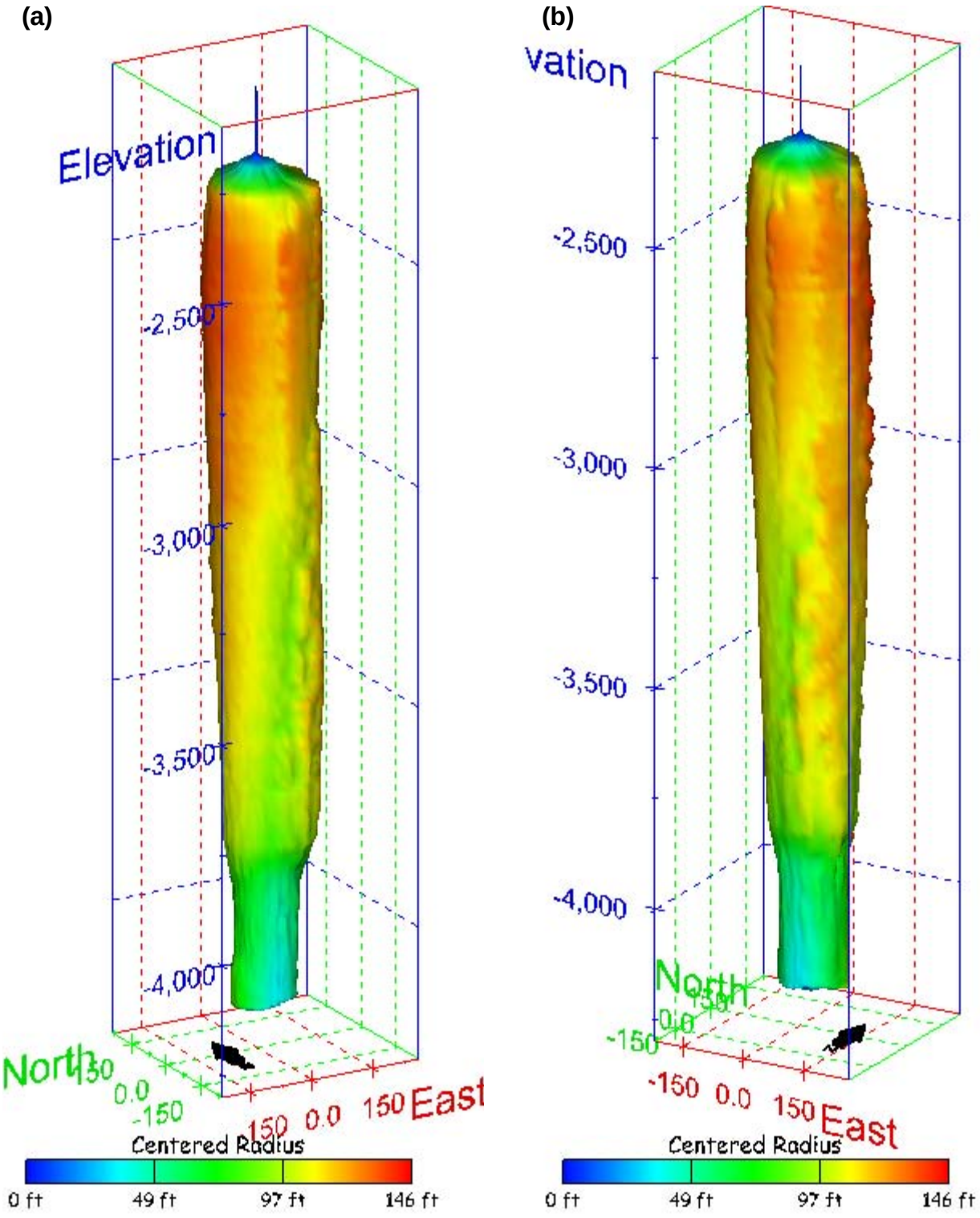

Figure 254. Sonar images of cavern BH-110, showing the geometry of the cavern colored by centered radius. View from (a) azimuth 210°, elevation 20°; (b) azimuth 150°, elevation 20°.

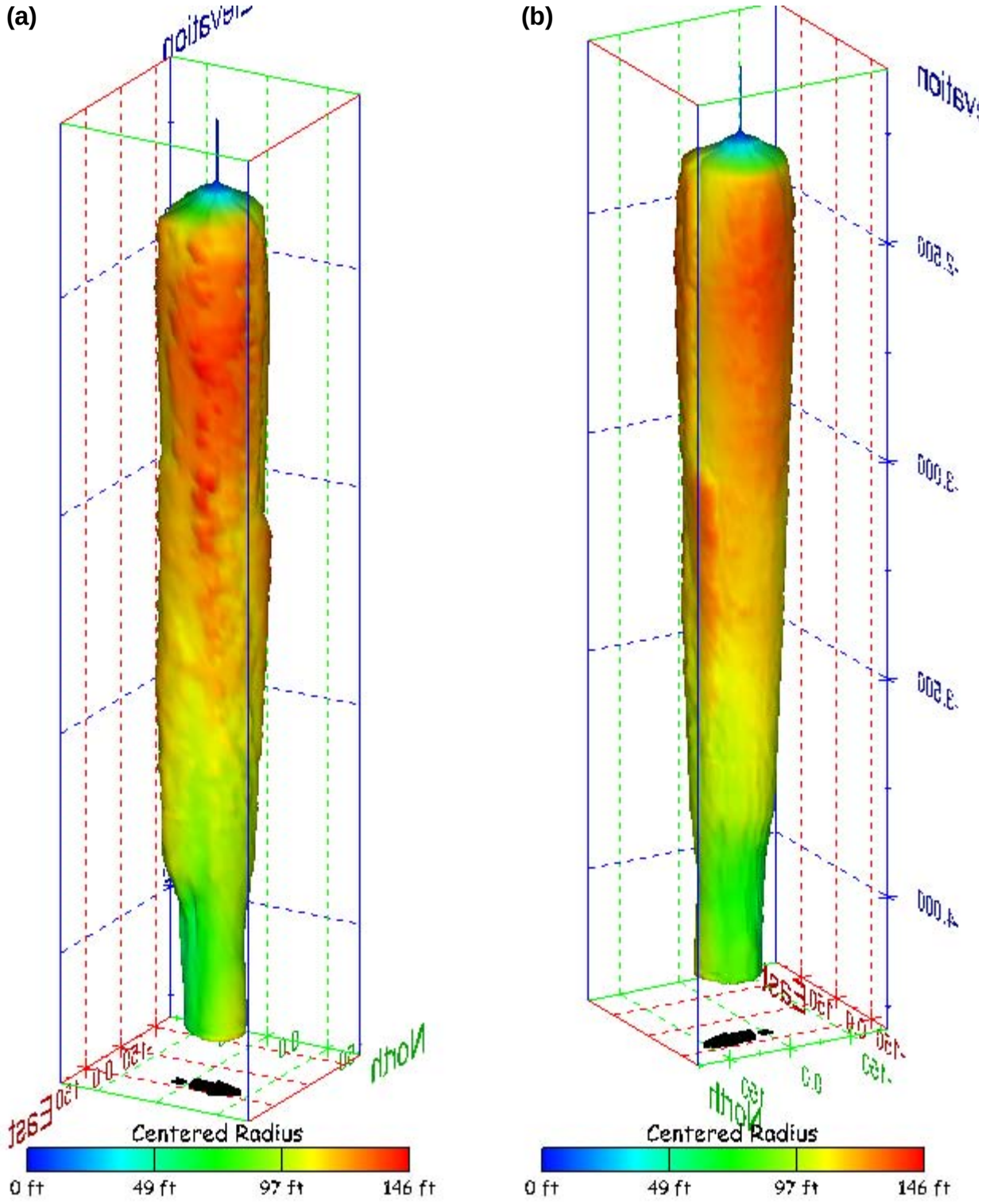

Figure 255. Sonar images of cavern BH-110, showing the geometry of the cavern colored by centered radius. View from (a) azimuth 60°, elevation 20°; (b) azimuth 300°, elevation 20°.

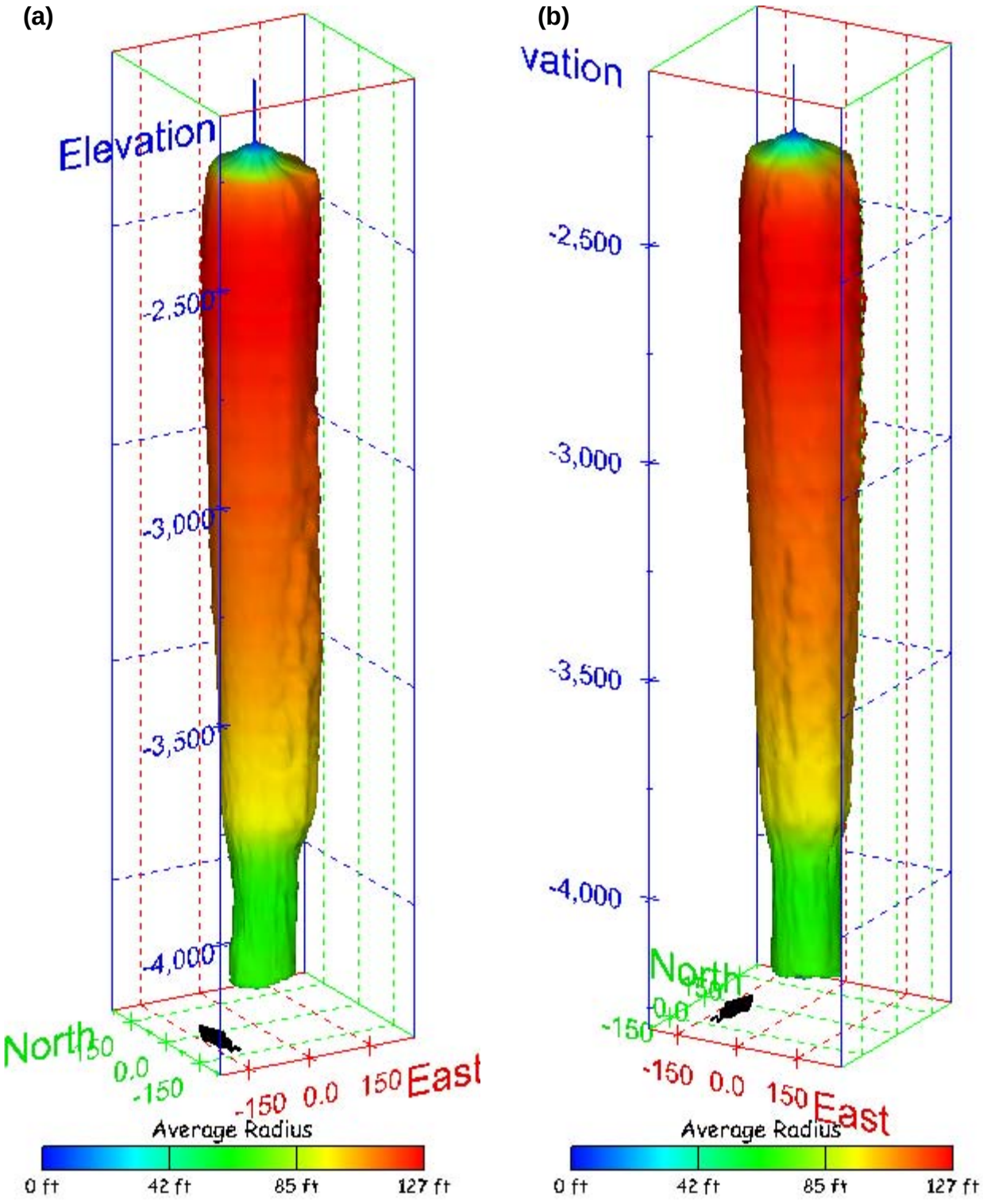

Figure 256. Sonar images of cavern BH-110, showing the geometry of the cavern colored by average radius. View from (a) azimuth 210°, elevation 20°; (b) azimuth 150°, elevation 20°.

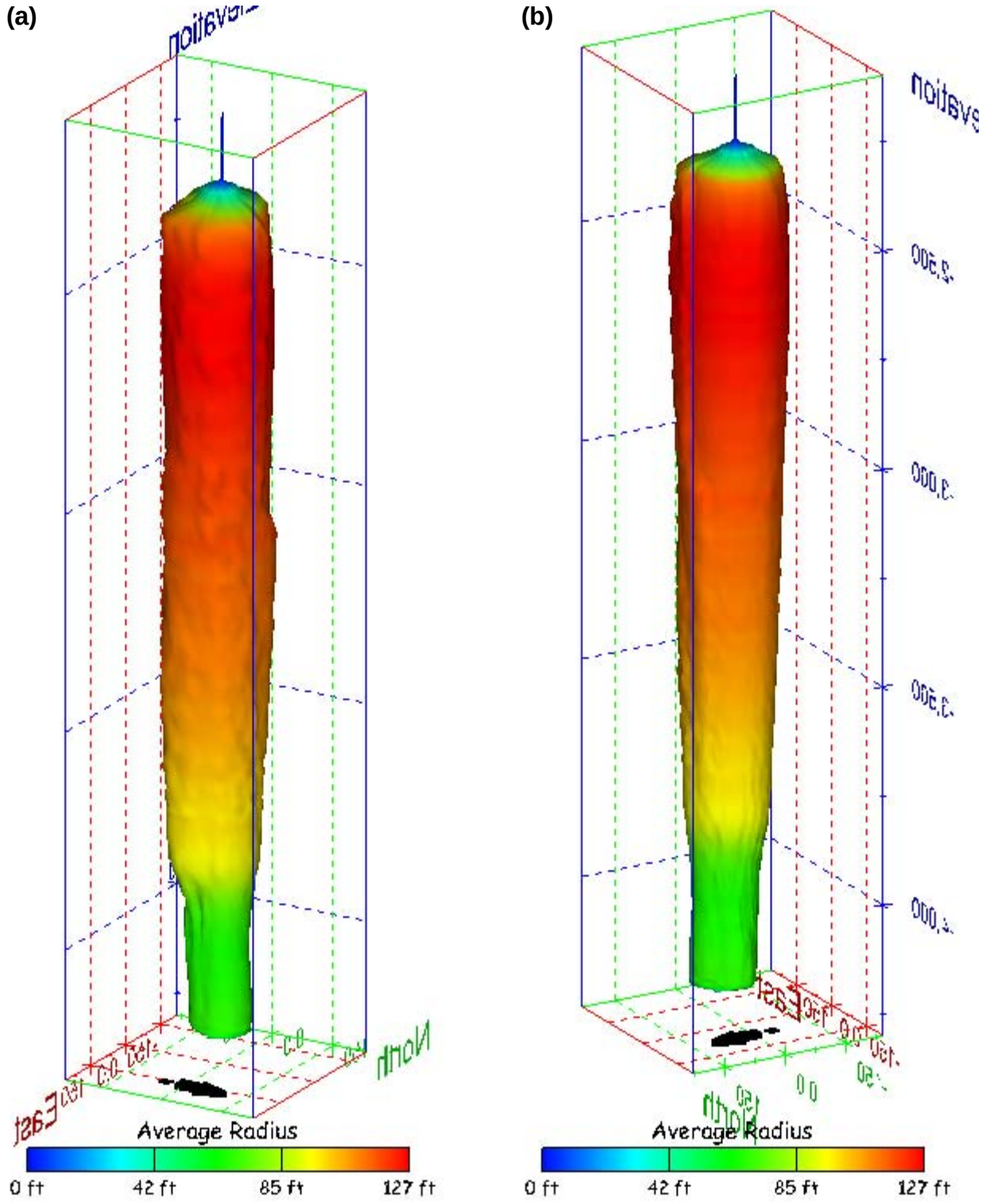

Figure 257. Sonar images of cavern BH-110, showing the geometry of the cavern colored by average radius. View from (a) azimuth 60°, elevation 20°; (b) azimuth 300°, elevation 20°.

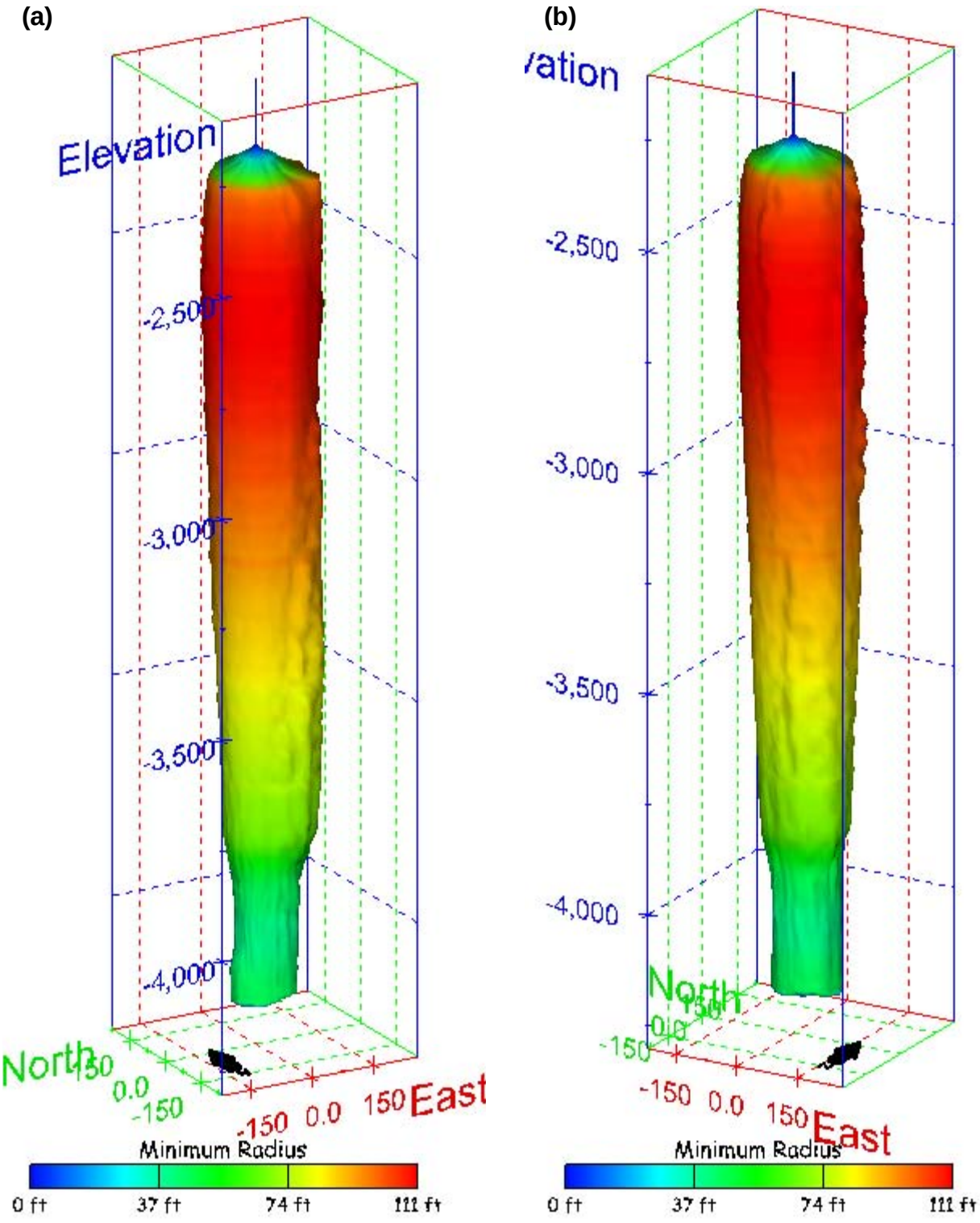

Figure 258. Sonar images of cavern BH-110, showing the geometry of the cavern colored by minimum radius. View from (a) azimuth 210°, elevation 20°; (b) azimuth 150°, elevation 20°.

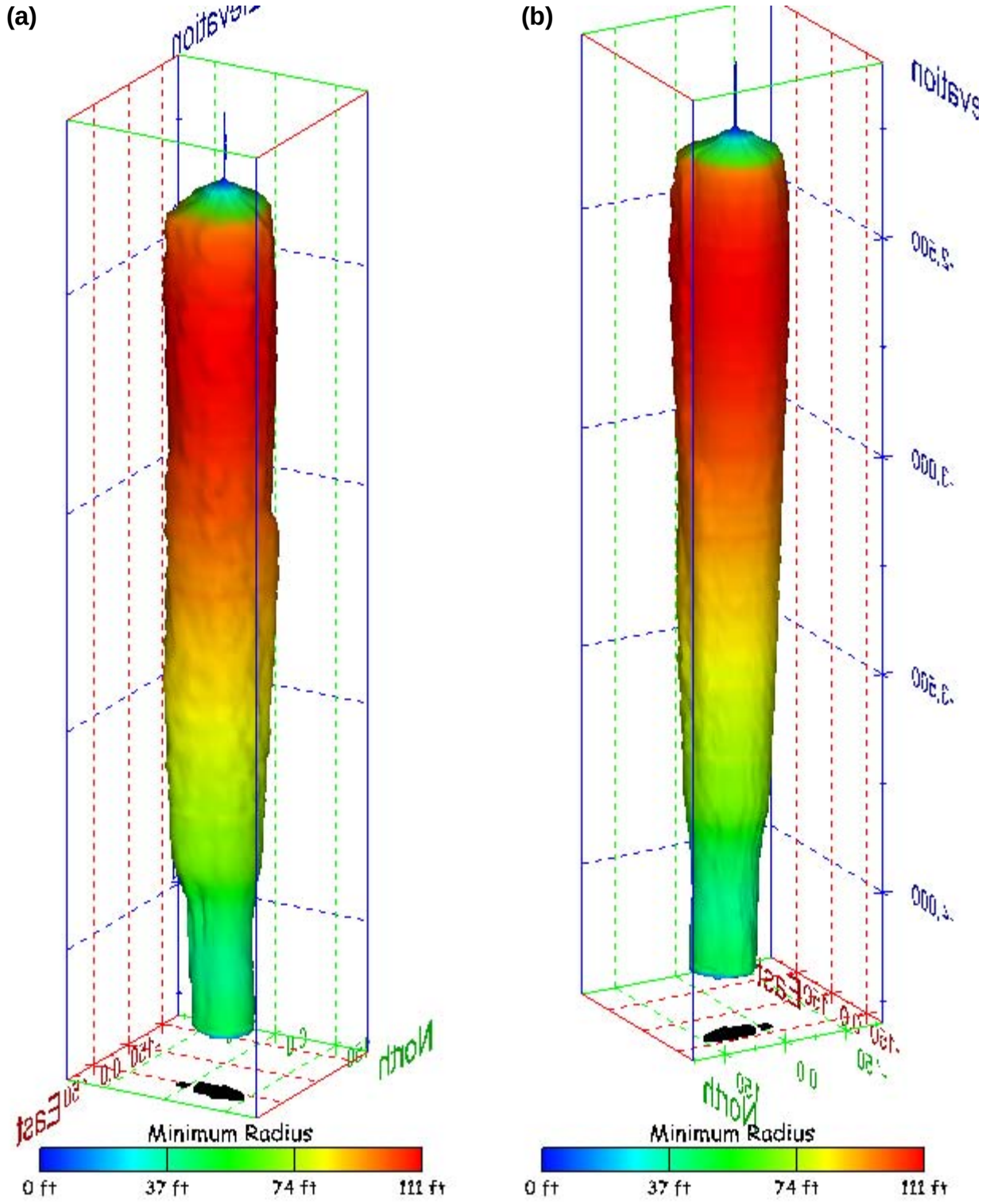

Figure 259. Sonar images of cavern BH-110, showing the geometry of the cavern colored by minimum radius. View from (a) azimuth 60°, elevation 20°; (b) azimuth 300°, elevation 20°.

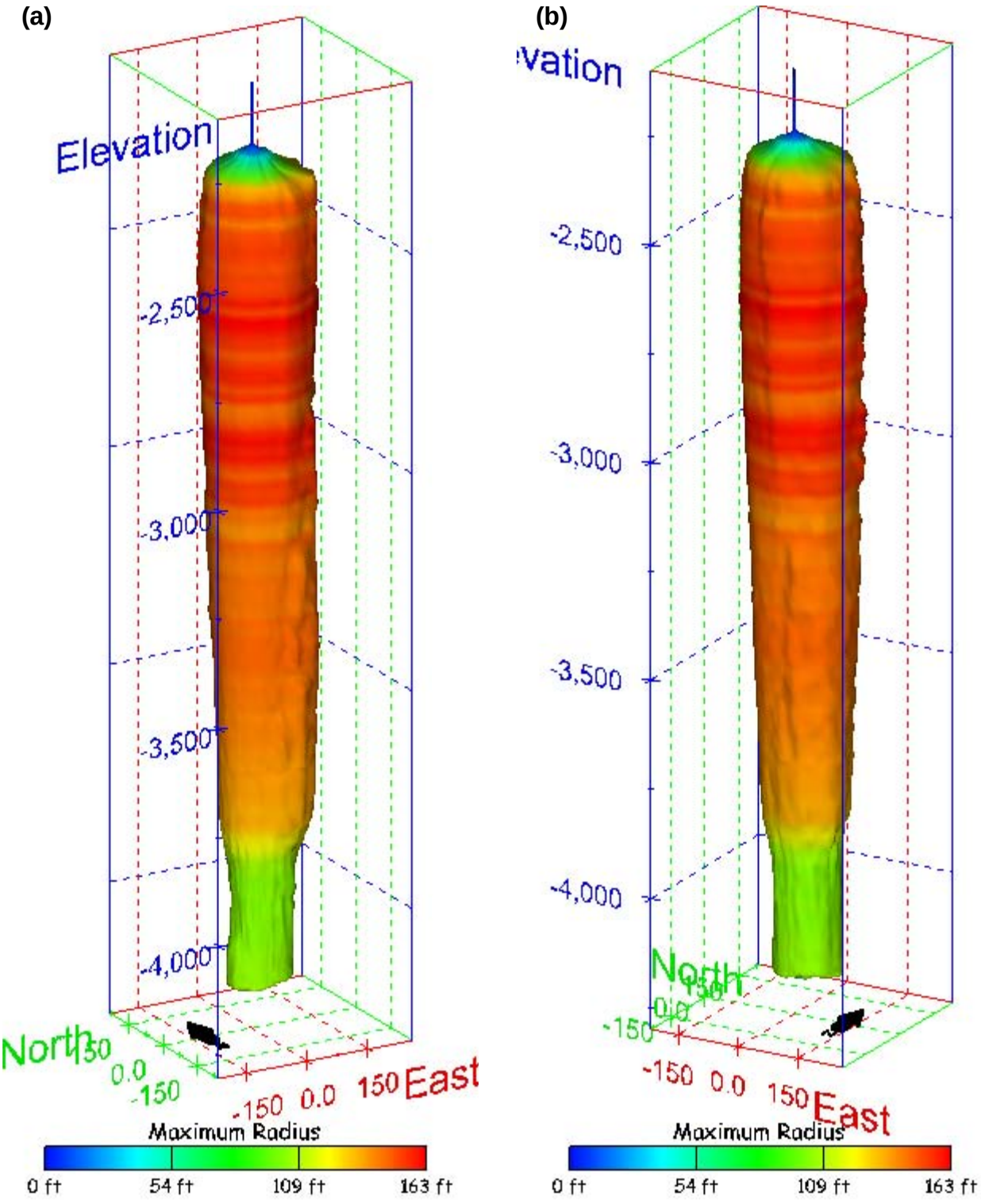

Figure 260. Sonar images of cavern BH-110, showing the geometry of the cavern colored by maximum radius. View from (a) azimuth 210°, elevation 20°; (b) azimuth 150°, elevation 20°.

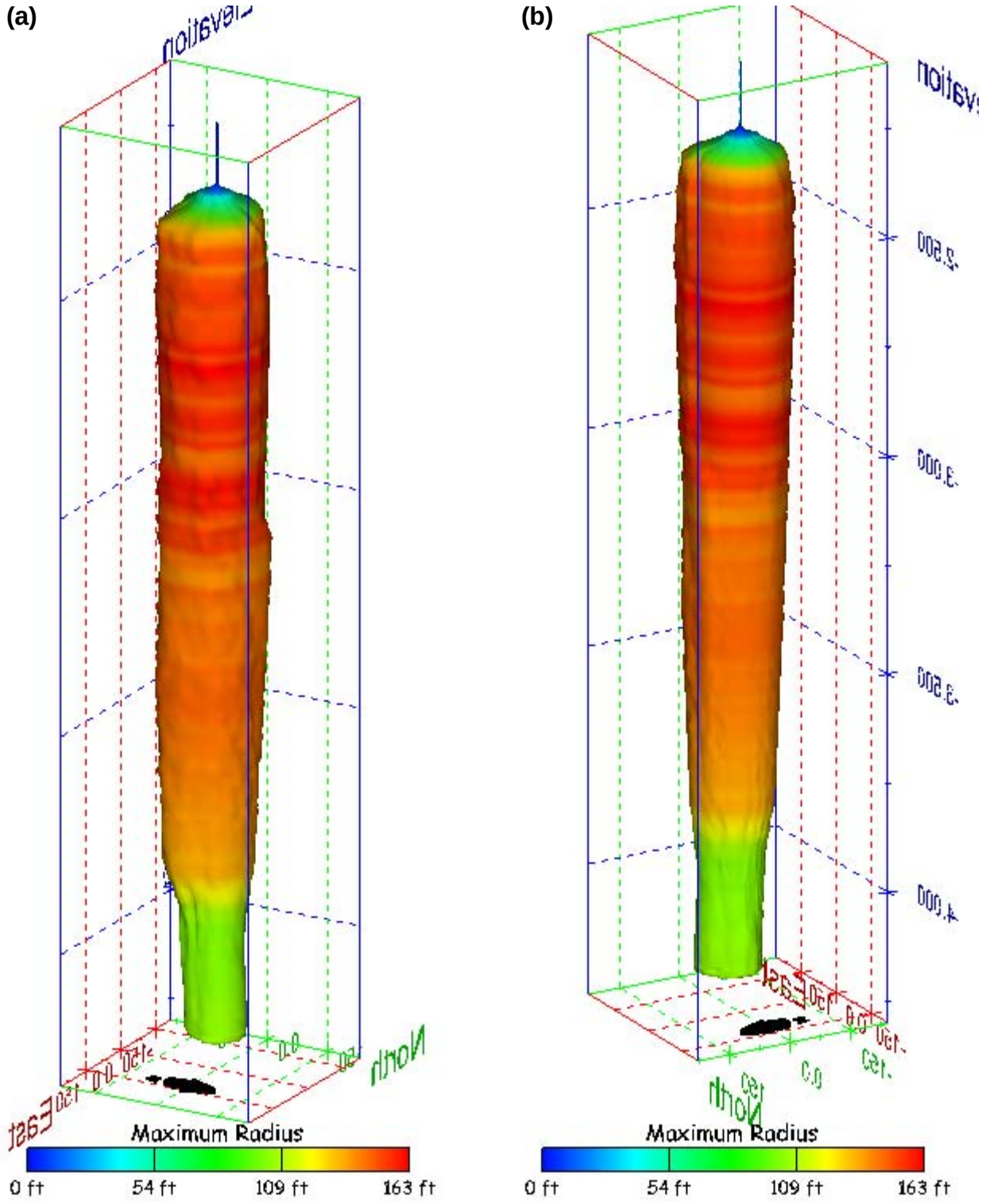

Figure 261. Sonar images of cavern BH-110, showing the geometry of the cavern colored by maximum radius. View from (a) azimuth 60°, elevation 20°; (b) azimuth 300°, elevation 20°.

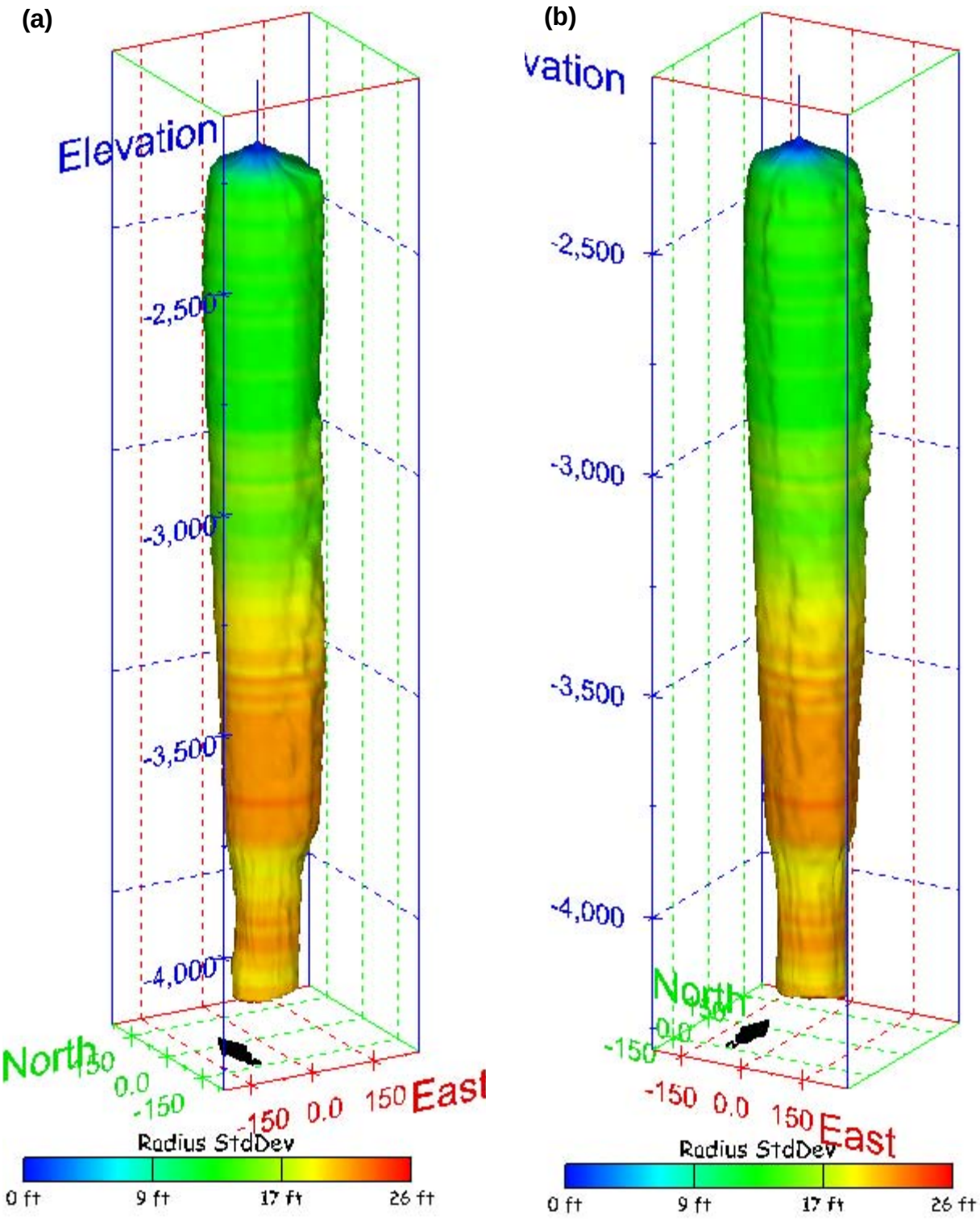

Figure 262. Sonar images of cavern BH-110, showing the geometry of the cavern colored by radius standard deviation. View from (a) azimuth 210°, elevation 20°; (b) azimuth 150°, elevation 20°.

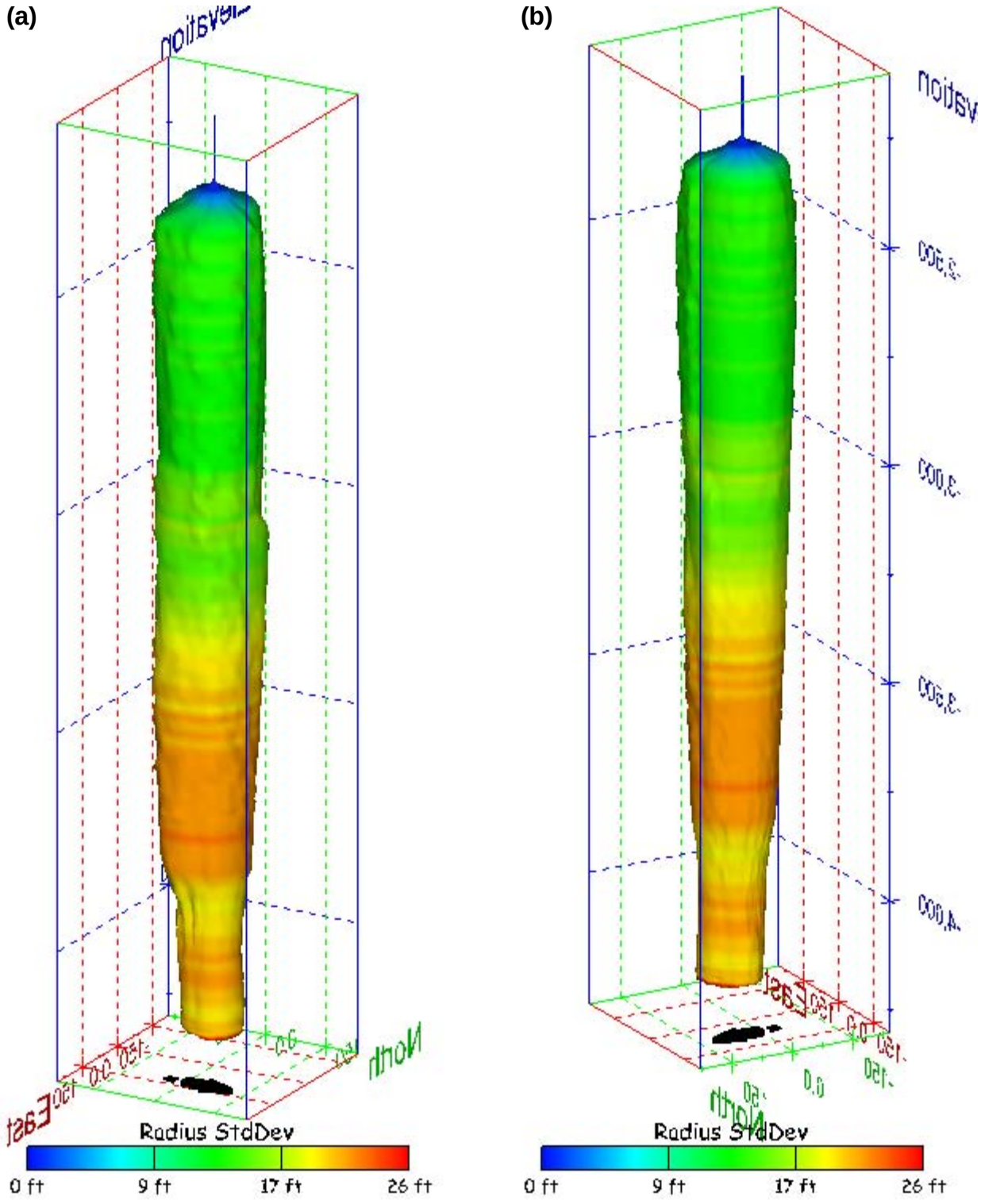

Figure 263. Sonar images of cavern BH-110, showing the geometry of the cavern colored by radius standard deviation. View from (a) azimuth 60°, elevation 20°; (b) azimuth 300°, elevation 20°.

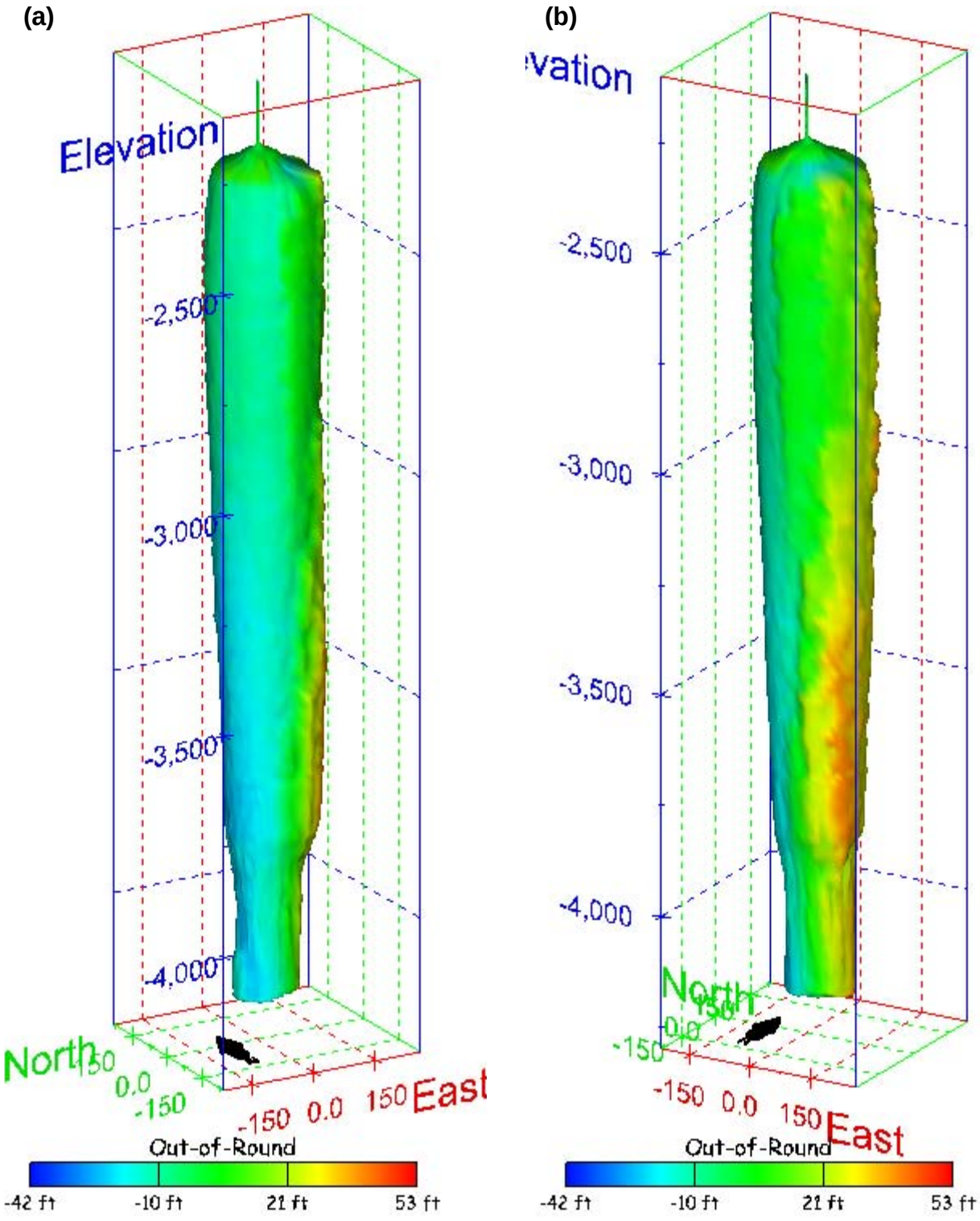

Figure 264. Sonar images of cavern BH-110, showing the geometry of the cavern colored by out-of-round distance. View from (a) azimuth 210°, elevation 20°; (b) azimuth 150°, elevation 20°.

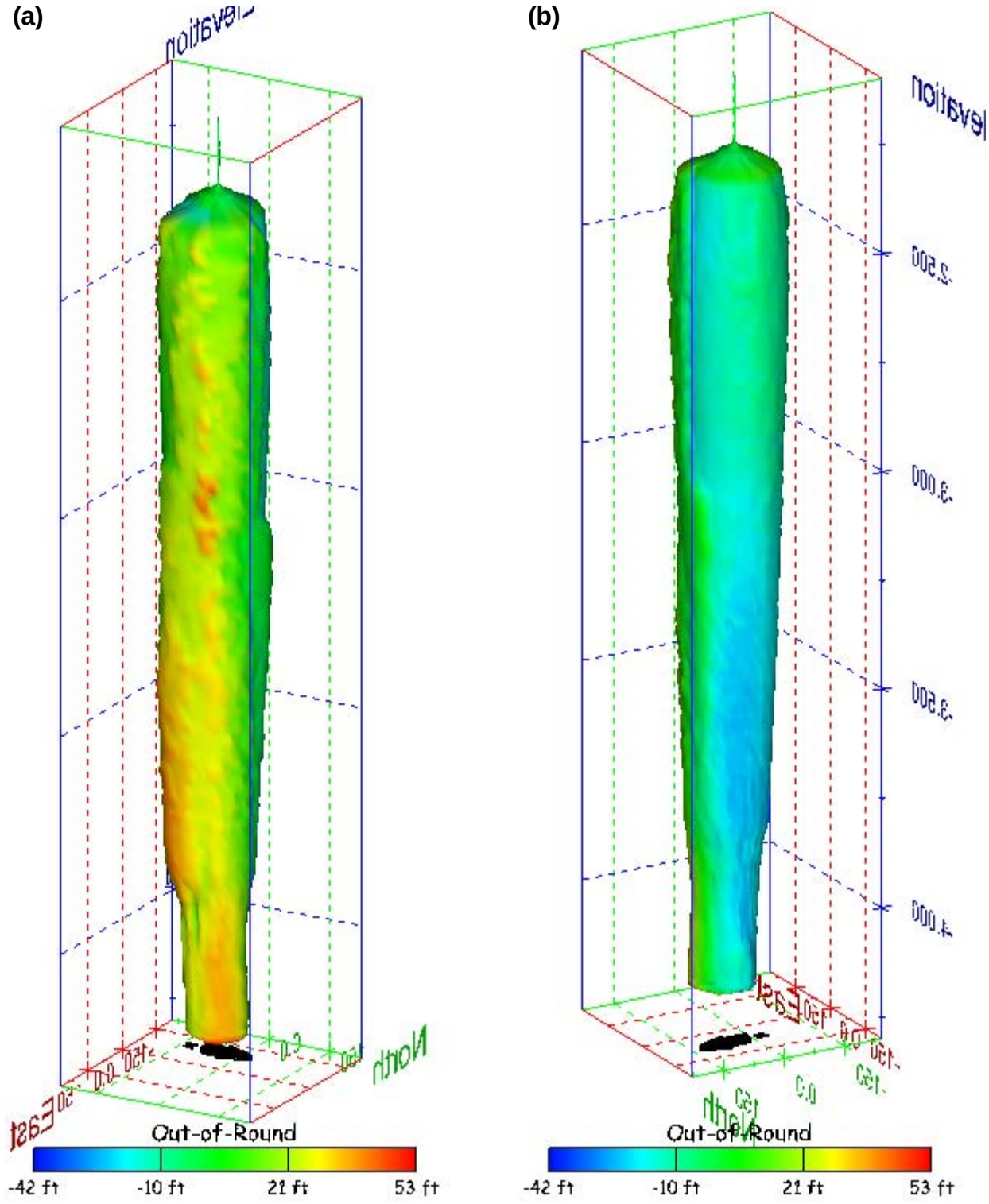

Figure 265. Sonar images of cavern BH-110, showing the geometry of the cavern colored by out-of-round distance. View from (a) azimuth 60°, elevation 20°; (b) azimuth 300°, elevation 20°.

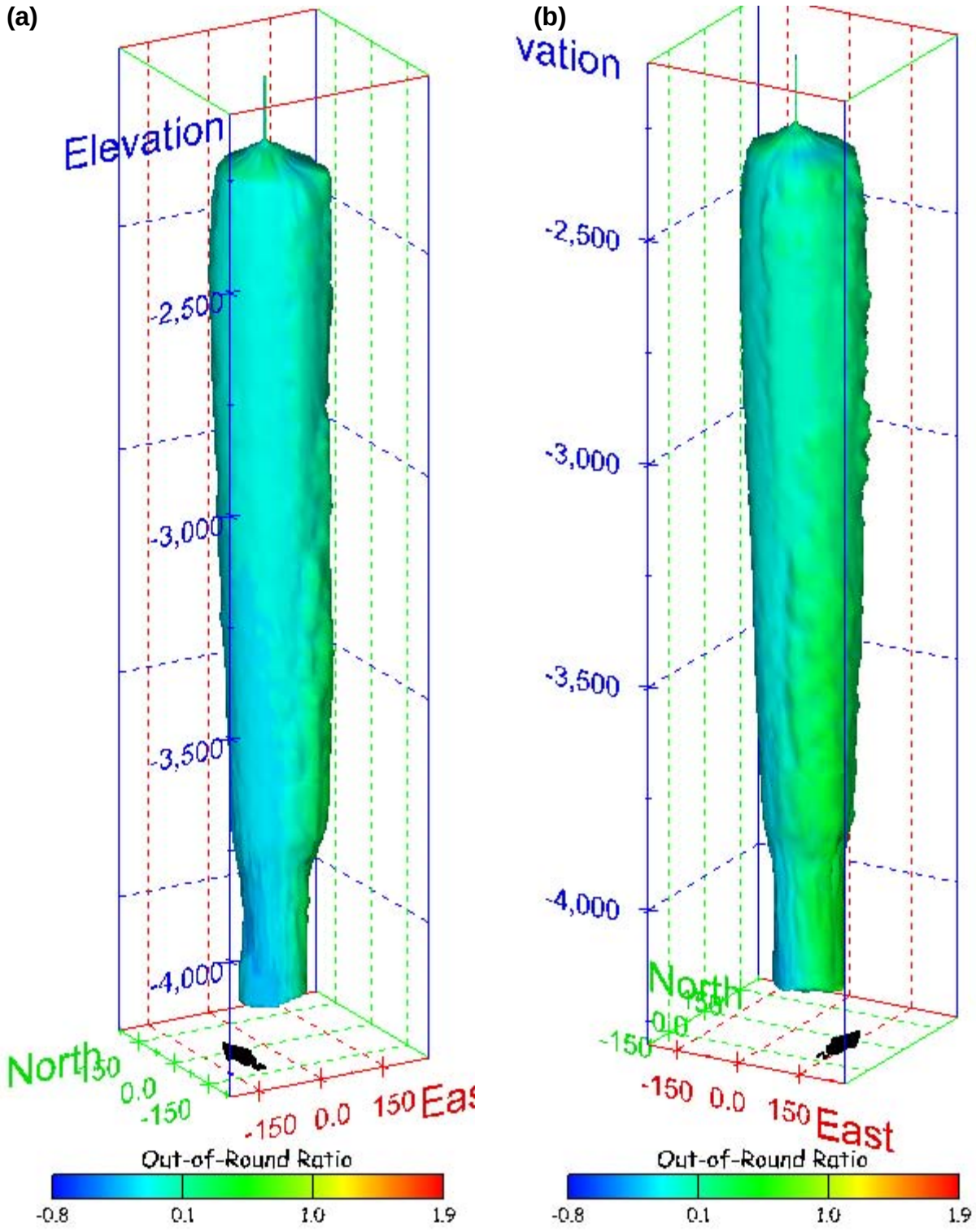

Figure 266. Sonar images of cavern BH-110, showing the geometry of the cavern colored by out-of-round ratio. View from (a) azimuth 210°, elevation 20°; (b) azimuth 150°, elevation 20°.

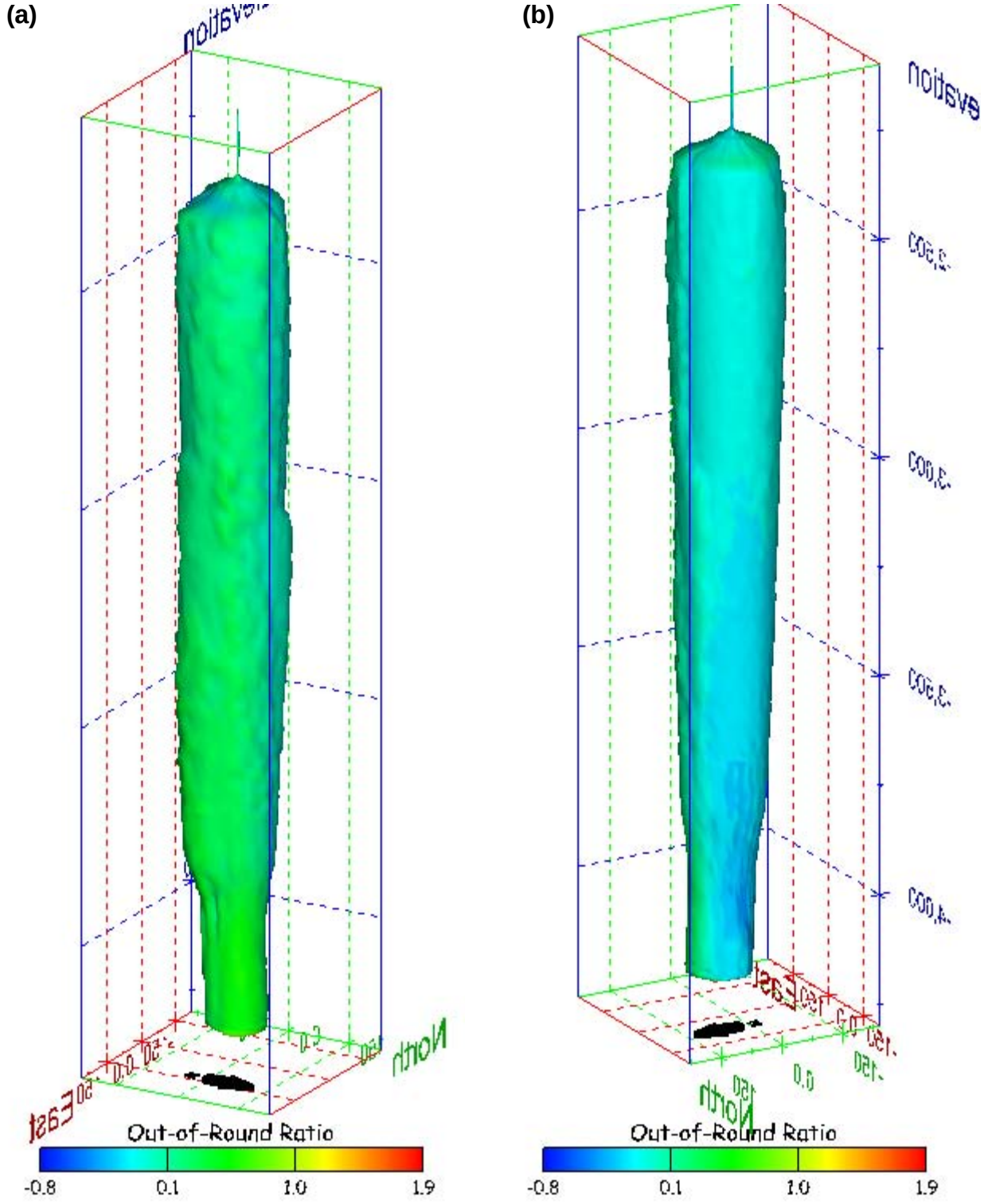

Figure 267. Sonar images of cavern BH-110, showing the geometry of the cavern colored by out-of-round ratio. View from (a) azimuth 60°, elevation 20°; (b) azimuth 300°, elevation 20°.

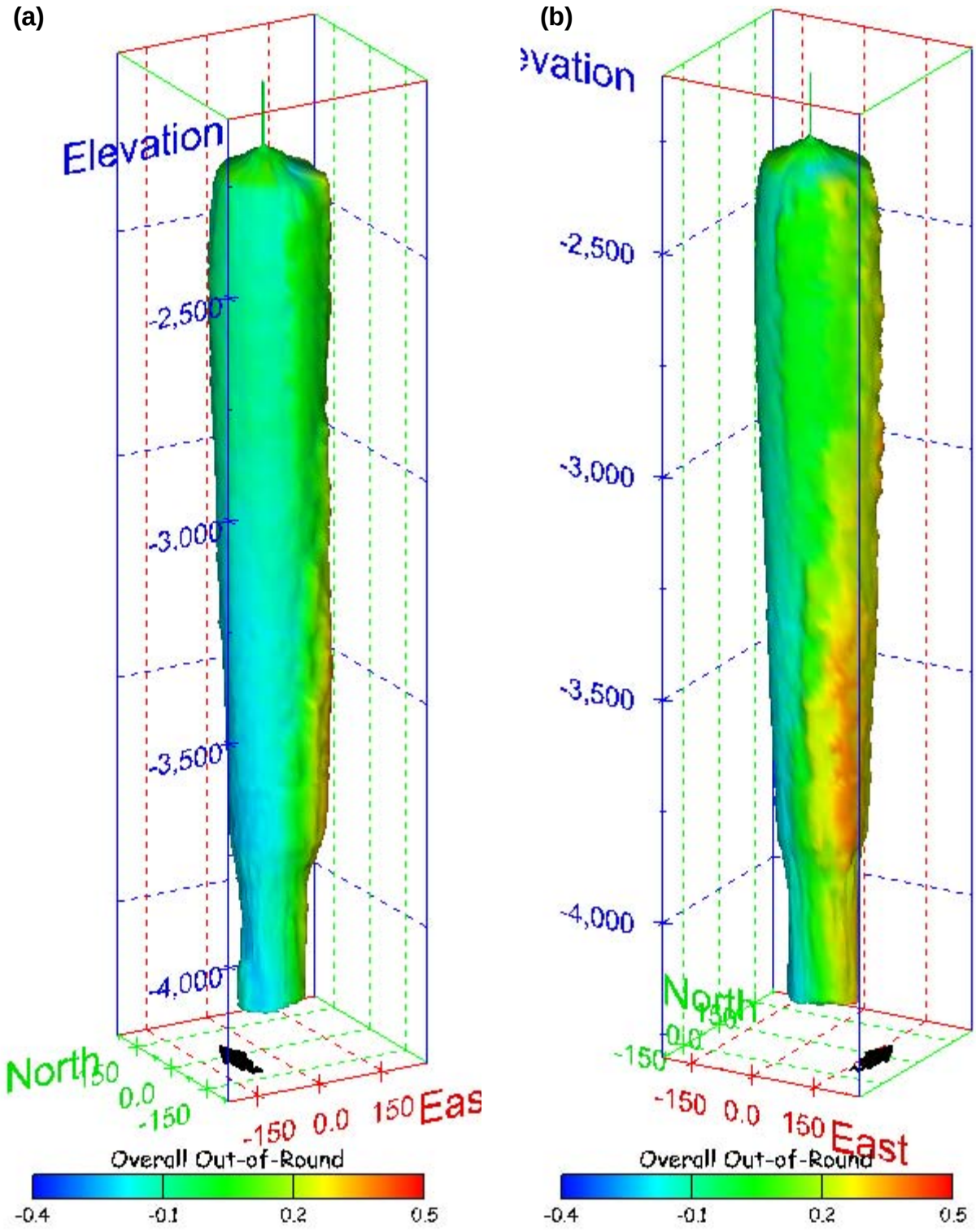

Figure 268. Sonar images of cavern BH-110, showing the geometry of the cavern colored by overall out-of-round ratio. View from (a) azimuth 210°, elevation 20°; (b) azimuth 150°, elevation 20°.

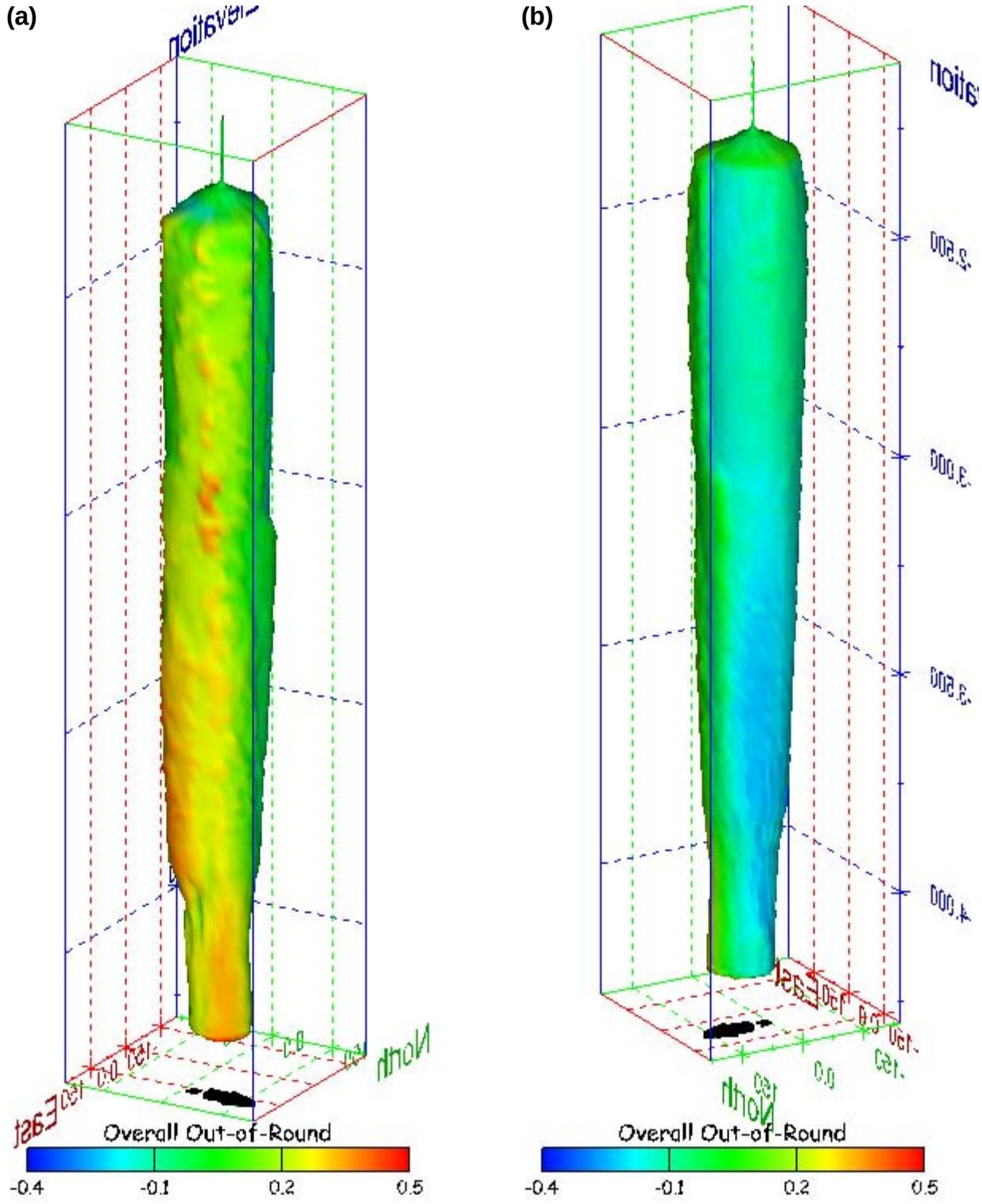

Figure 269. Sonar images of cavern BH-110, showing the geometry of the cavern colored by overall out-of-round ratio. View from (a) azimuth 60°, elevation 20°; (b) azimuth 300°, elevation 20°.

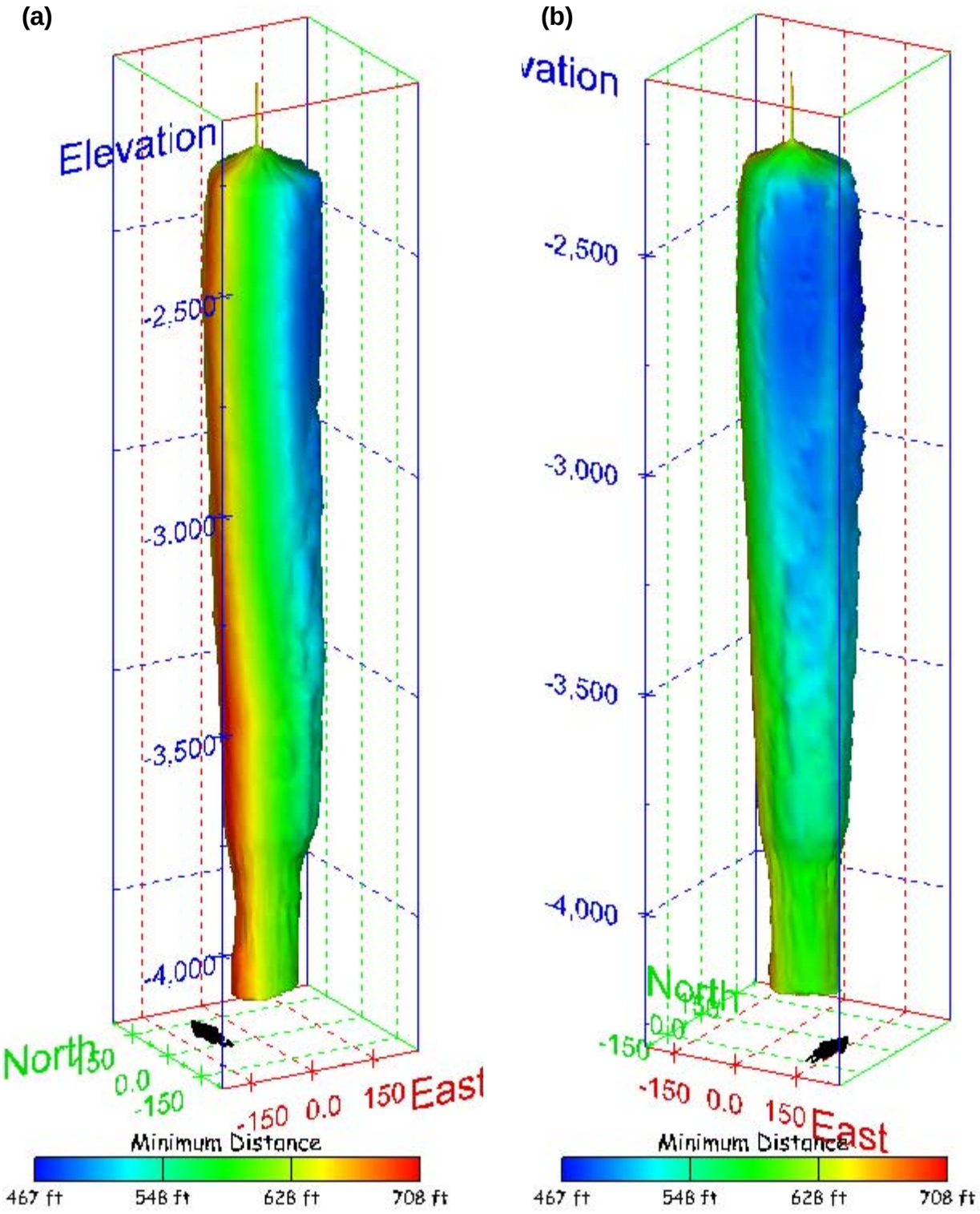

Figure 270. Sonar images of cavern BH-110, showing the geometry of the cavern colored by the minimum distance to the nearest neighboring cavern. View from (a) azimuth 210°, elevation 20°; (b) azimuth 150°, elevation 20°.

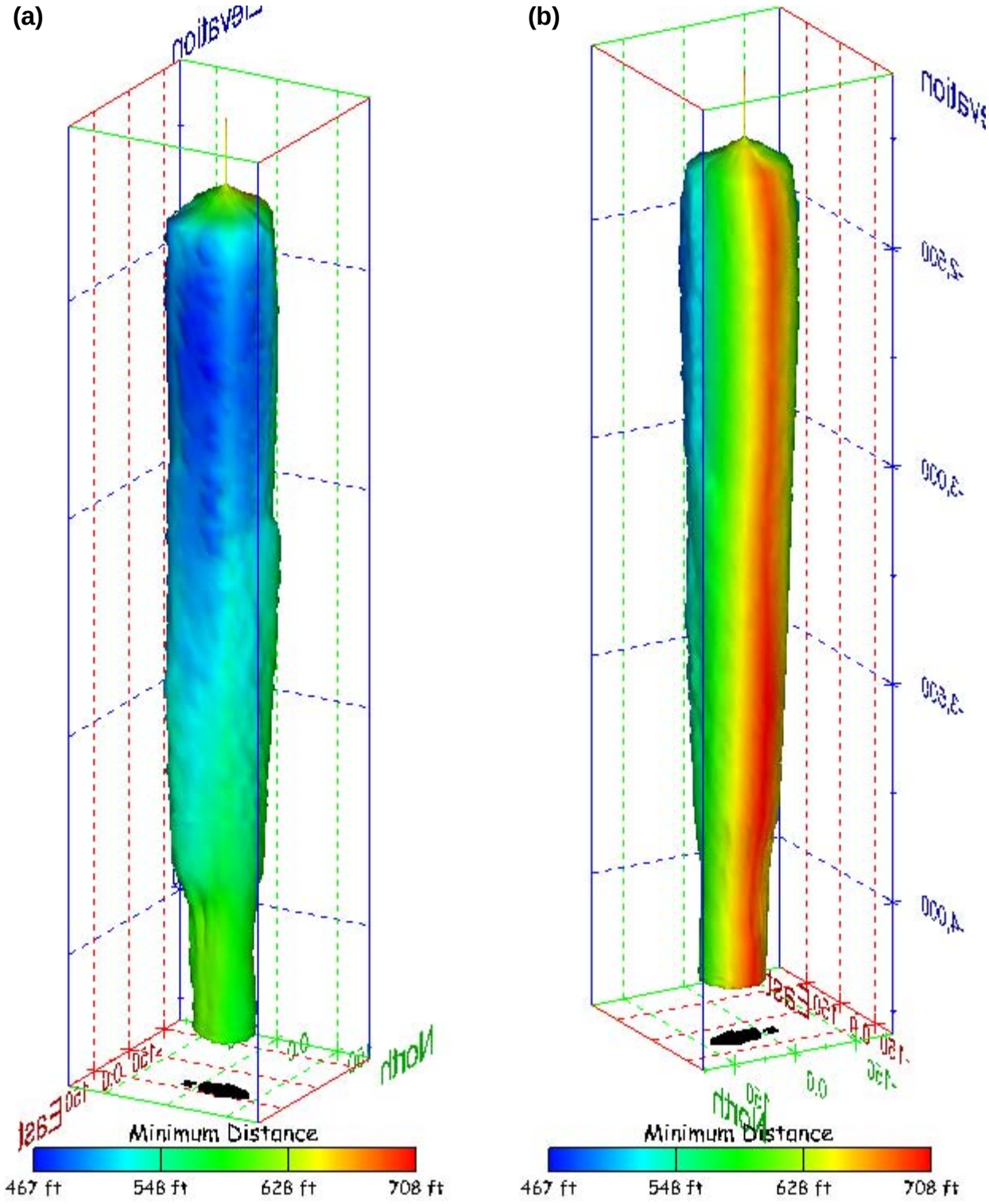

Figure 271. Sonar images of cavern BH-110, showing the geometry of the cavern colored by minimum distance to the nearest neighboring cavern. View from (a) azimuth 60°, elevation 20°; (b) azimuth 300°, elevation 20°.

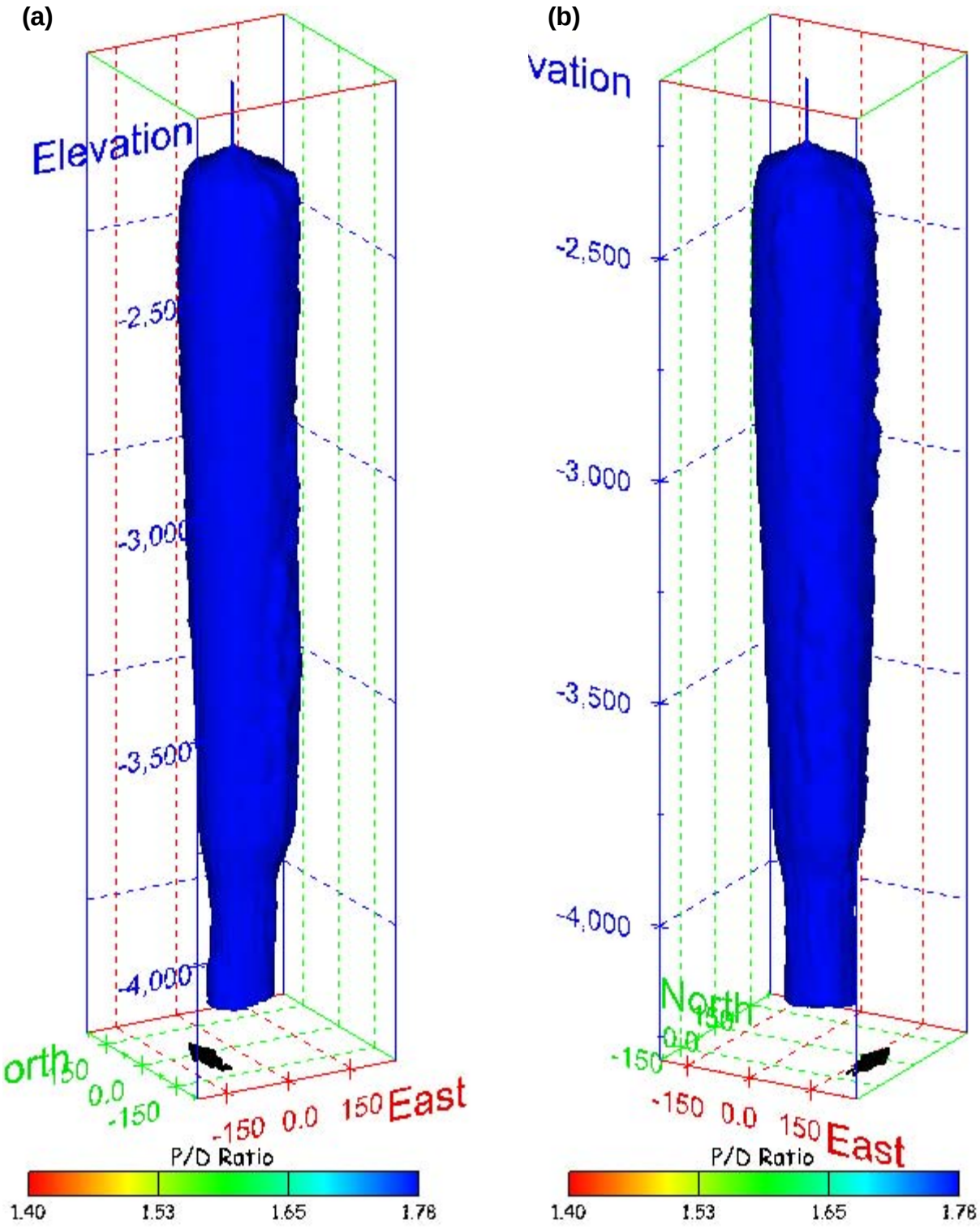

Figure 272. Sonar images of cavern BH-110, showing the geometry of the cavern colored by three-dimensional pillar-to-diameter ratio. View from (a) azimuth 210°, elevation 20°; (b) azimuth 150°, elevation 20°.

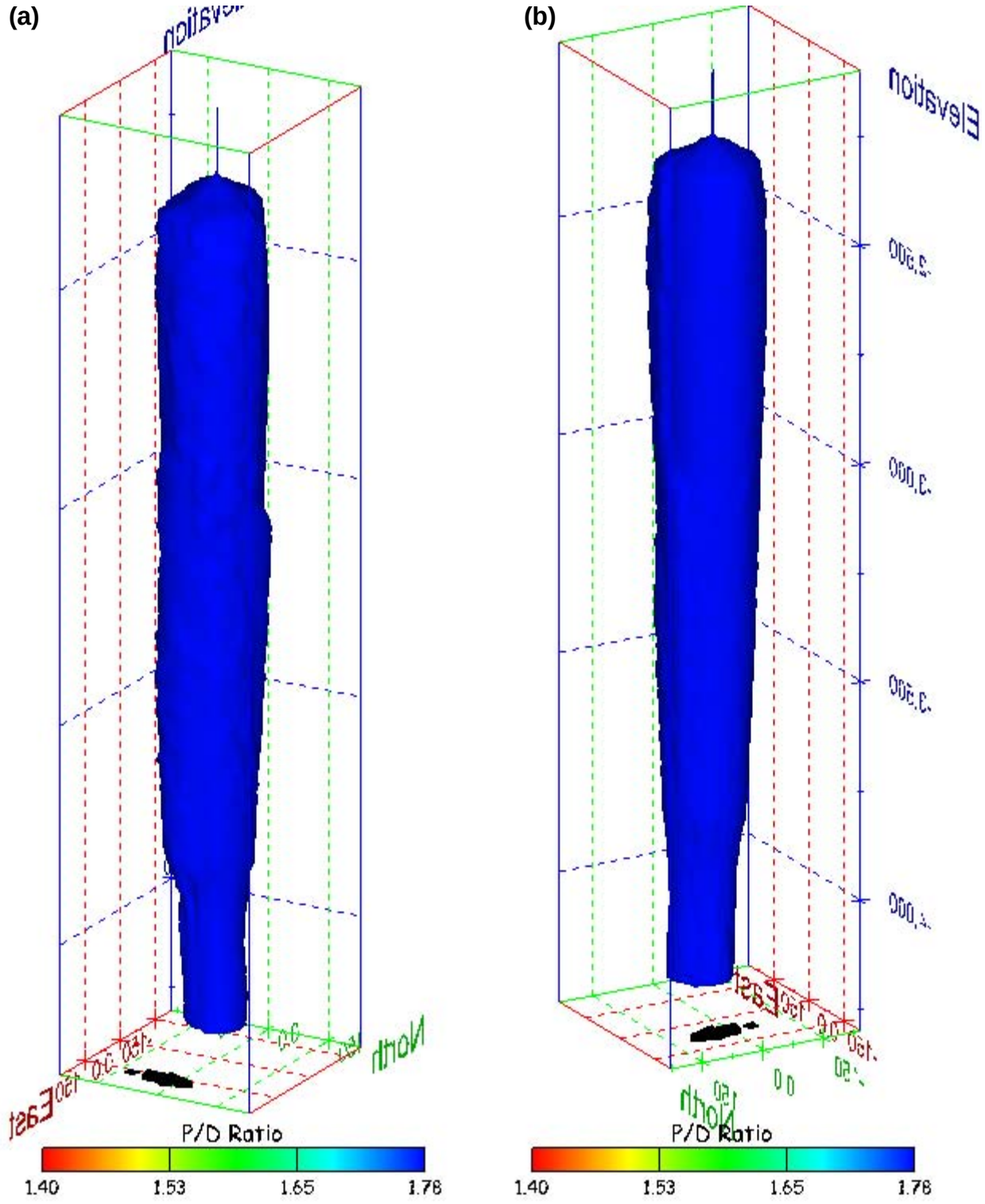

Figure 273. Sonar images of cavern BH-110, showing the geometry of the cavern colored by three-dimensional pillar-to-diameter ratio. View from (a) azimuth 60°, elevation 20°; (b) azimuth 300°, elevation 20°.

No Sonic Velocity Data Available for Socon Surveys

Figure 274. Sonar image of cavern BH-110, showing the geometry of the cavern colored by the reported velocity of sound on the survey date of March 2005. View from due south, elevation zero.

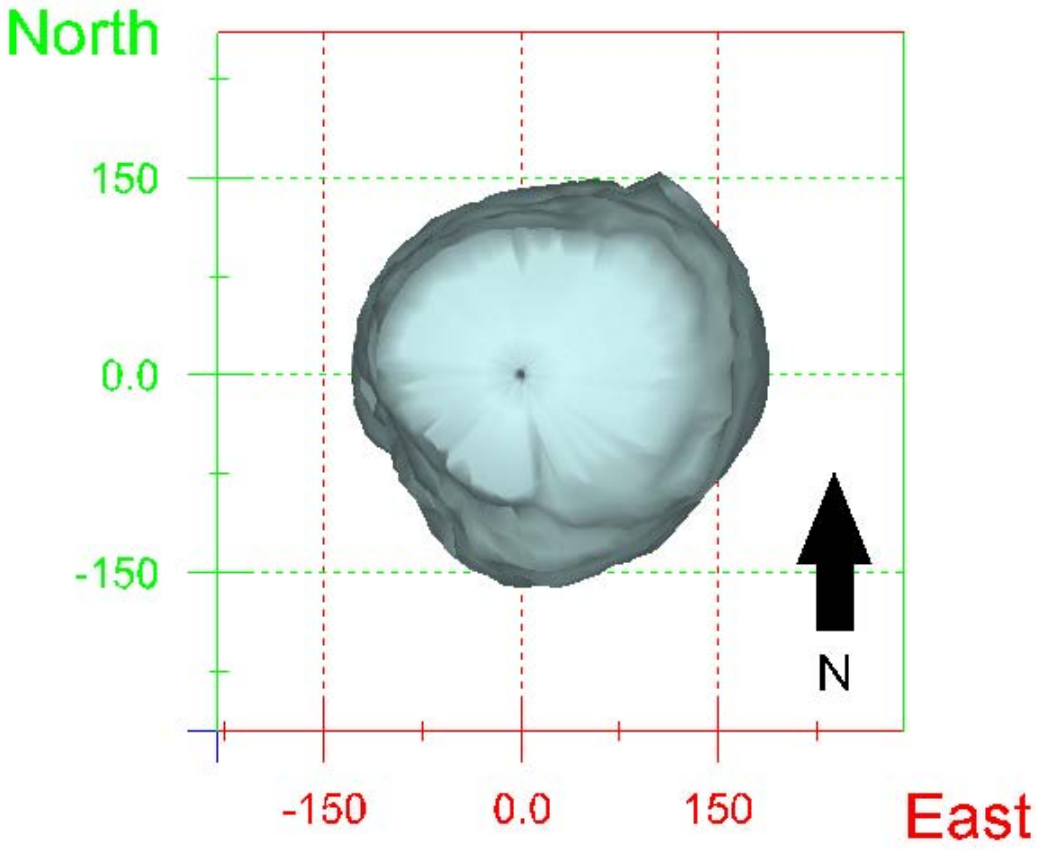

Map view sonar image of cavern BH-111, showing the basic geometry of the cavern. Grid squares represent 150 ft.

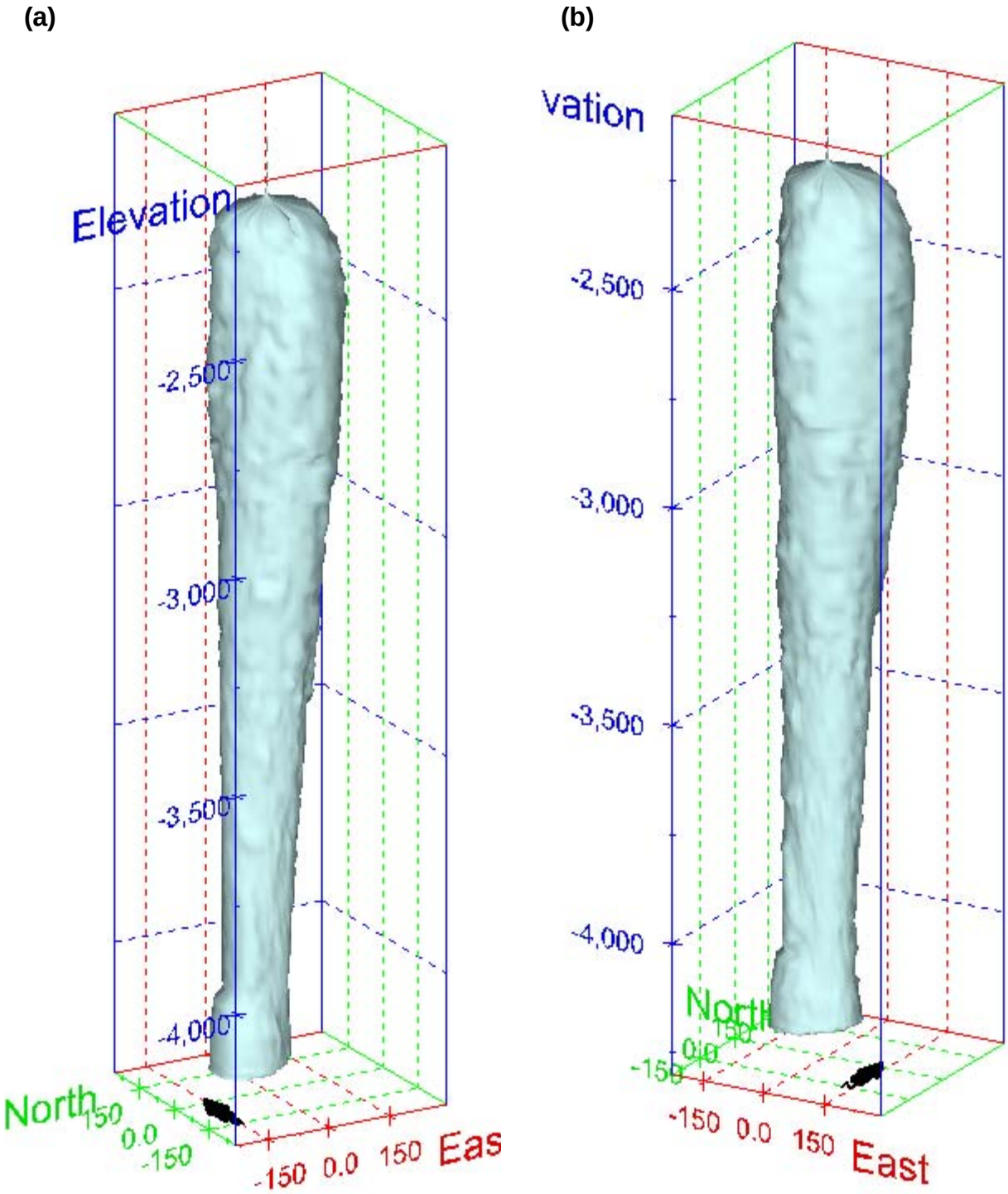

Figure 275. Sonar images of cavern BH-111, showing the basic geometric shape of the cavern. View from (a) azimuth 210°, elevation 20°; (b) azimuth 150°, elevation 20°.

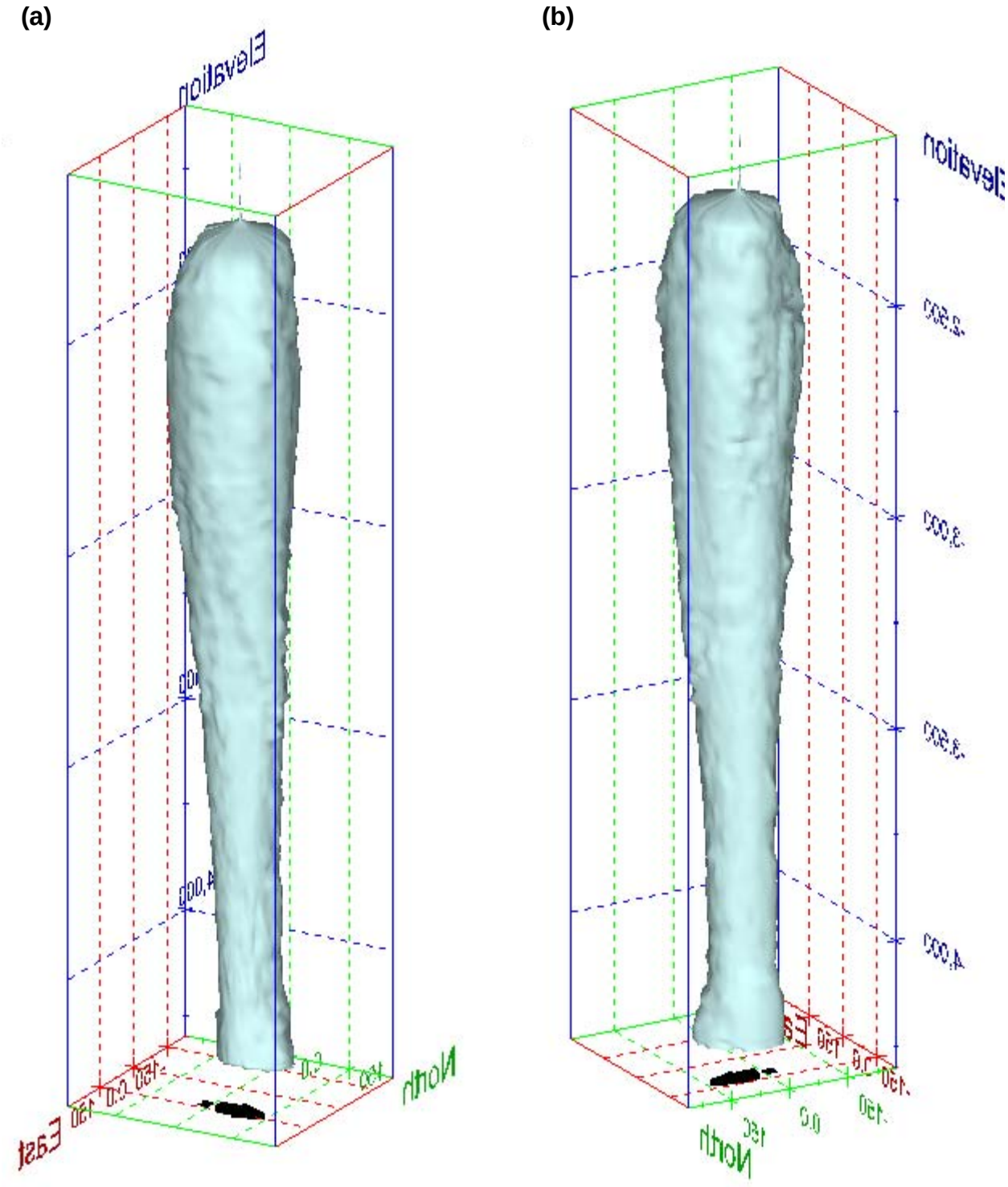

Figure 276. Sonar images of cavern BH-111, showing the basic geometric shape of the cavern. View from (a) azimuth 60°, elevation 20°; (b) azimuth 300°, elevation 20°.

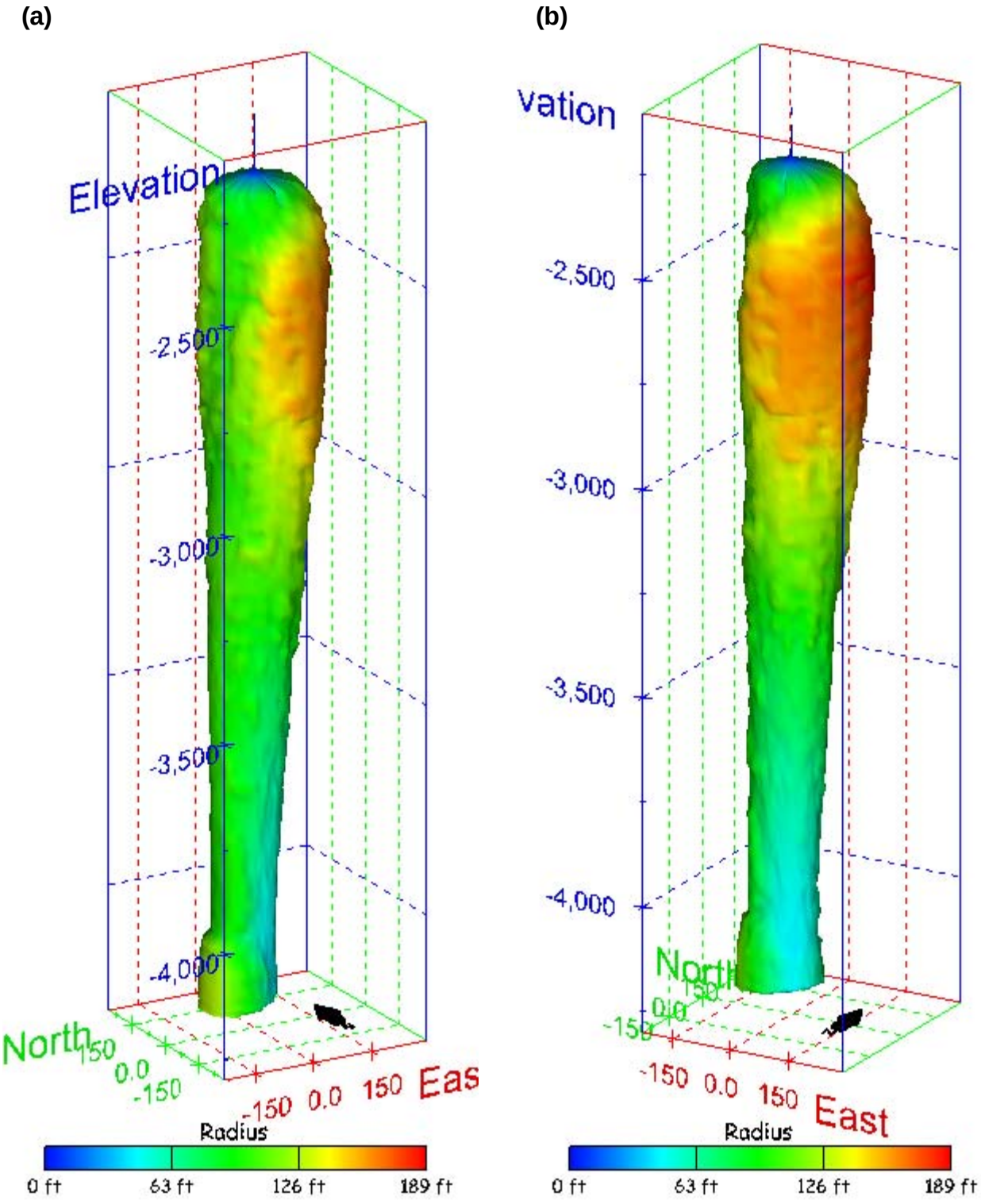

Figure 277. Sonar images of cavern BH-111, showing the geometry of the cavern colored by measured radius. View from (a) azimuth 210°, elevation 20°; (b) azimuth 150°, elevation 20°.

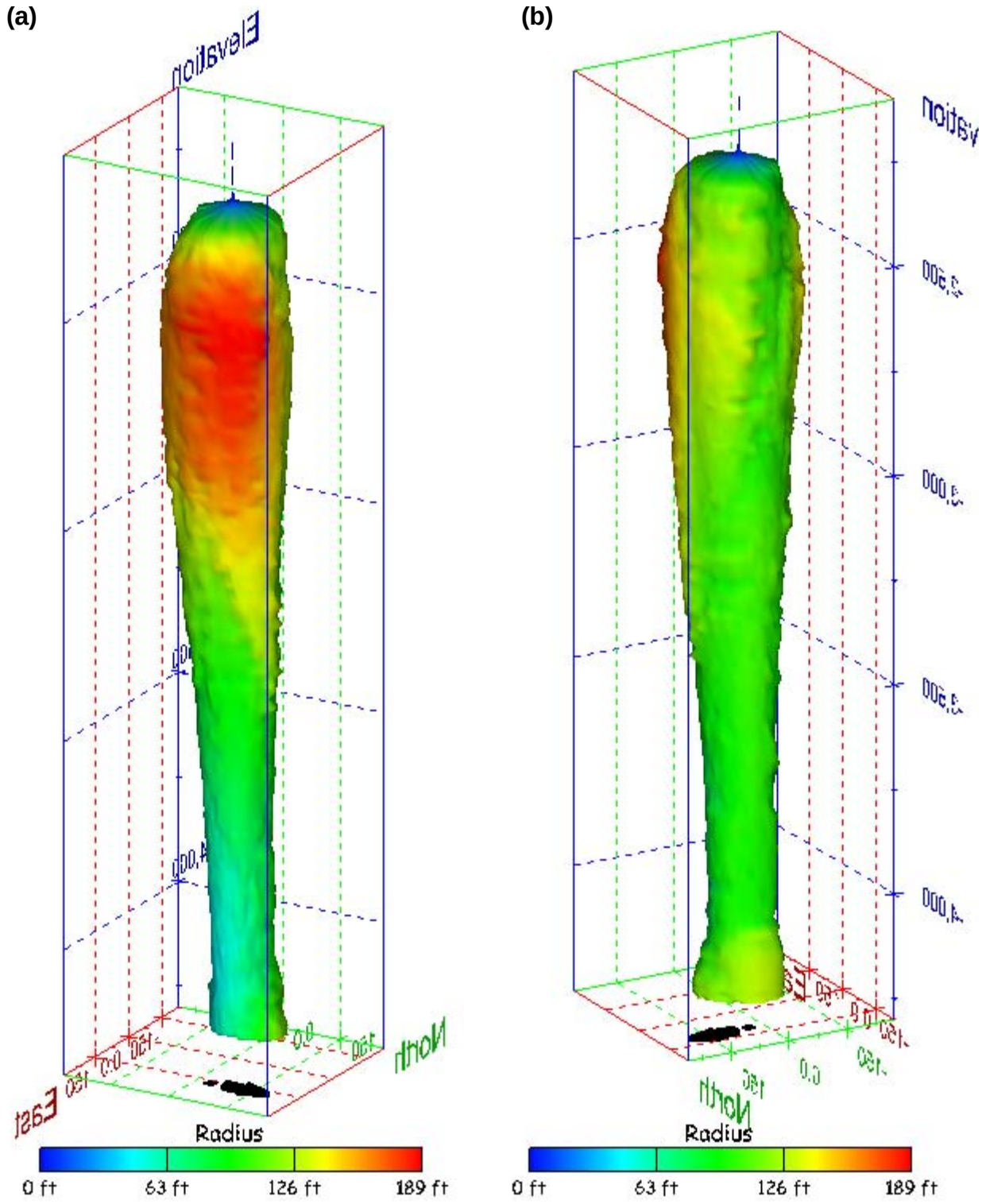

Figure 278. Sonar images of cavern BH-111, showing the geometry of the cavern colored by measured radius. View from (a) azimuth 60°, elevation 20°; (b) azimuth 300°, elevation 20°.

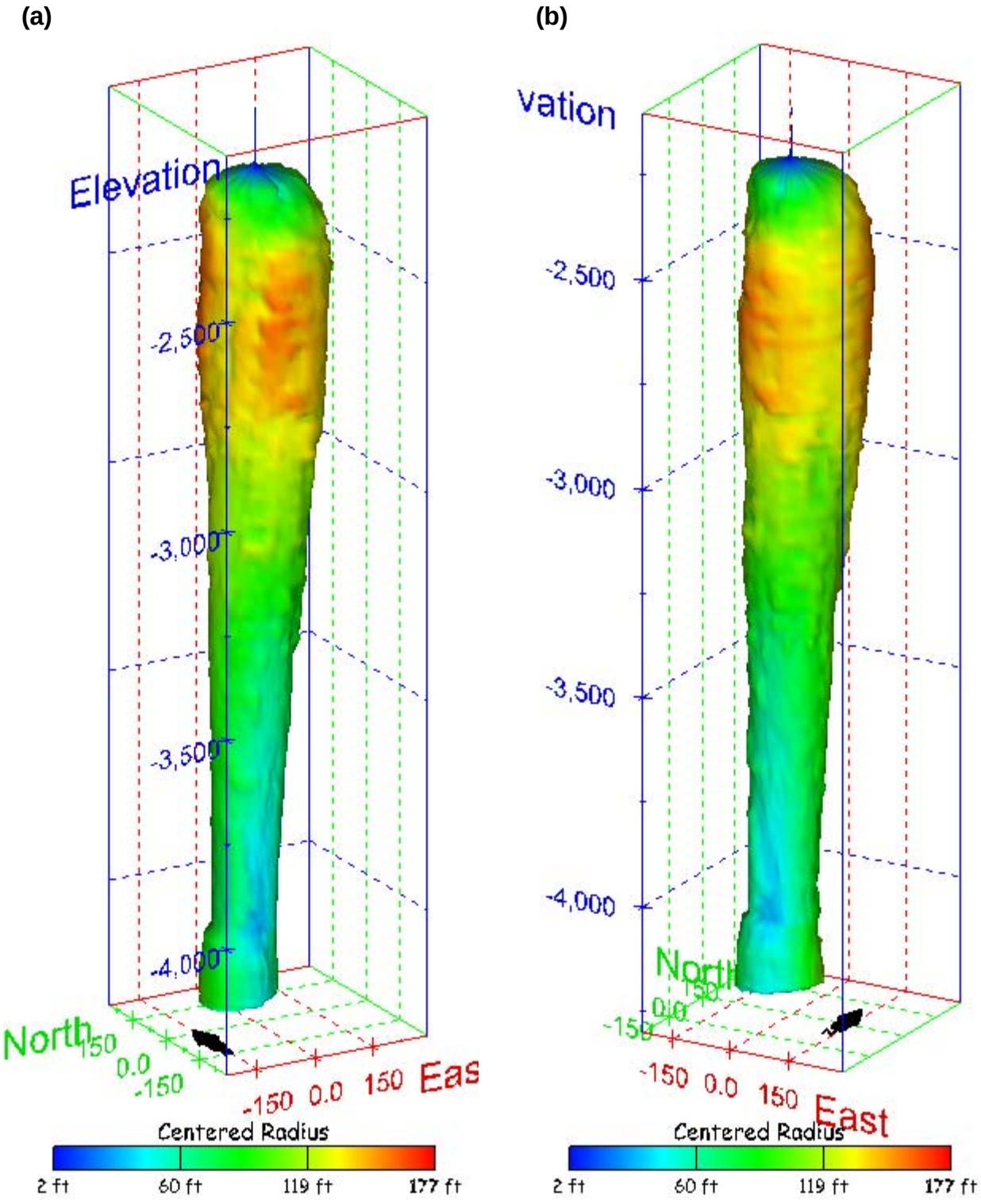

Figure 279. Sonar images of cavern BH-111, showing the geometry of the cavern colored by centered radius. View from (a) azimuth 210°, elevation 20°; (b) azimuth 150°, elevation 20°.

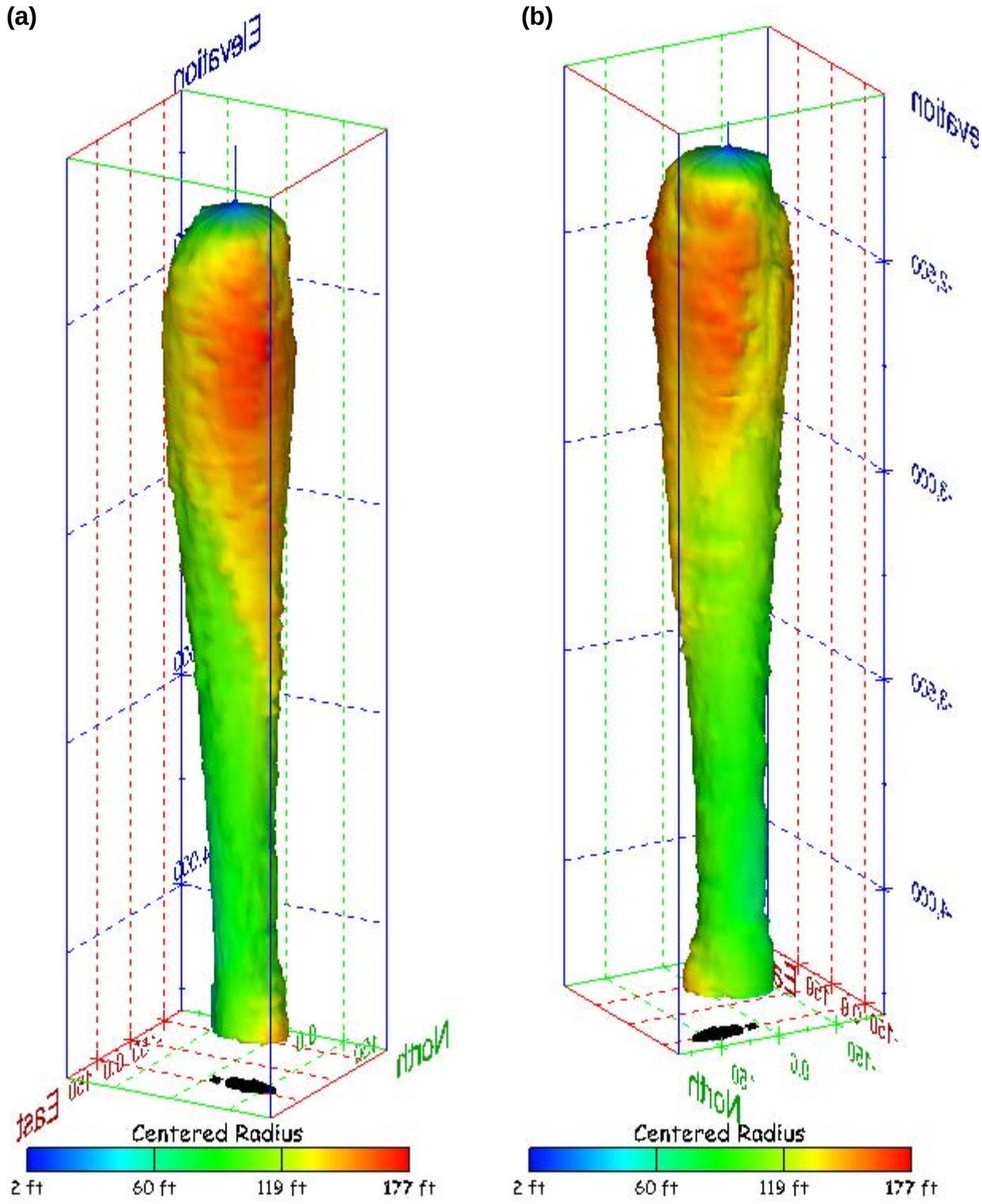

Figure 280. Sonar images of cavern BH-111, showing the geometry of the cavern colored by centered radius. View from (a) azimuth 60°, elevation 20°; (b) azimuth 300°, elevation 20°.

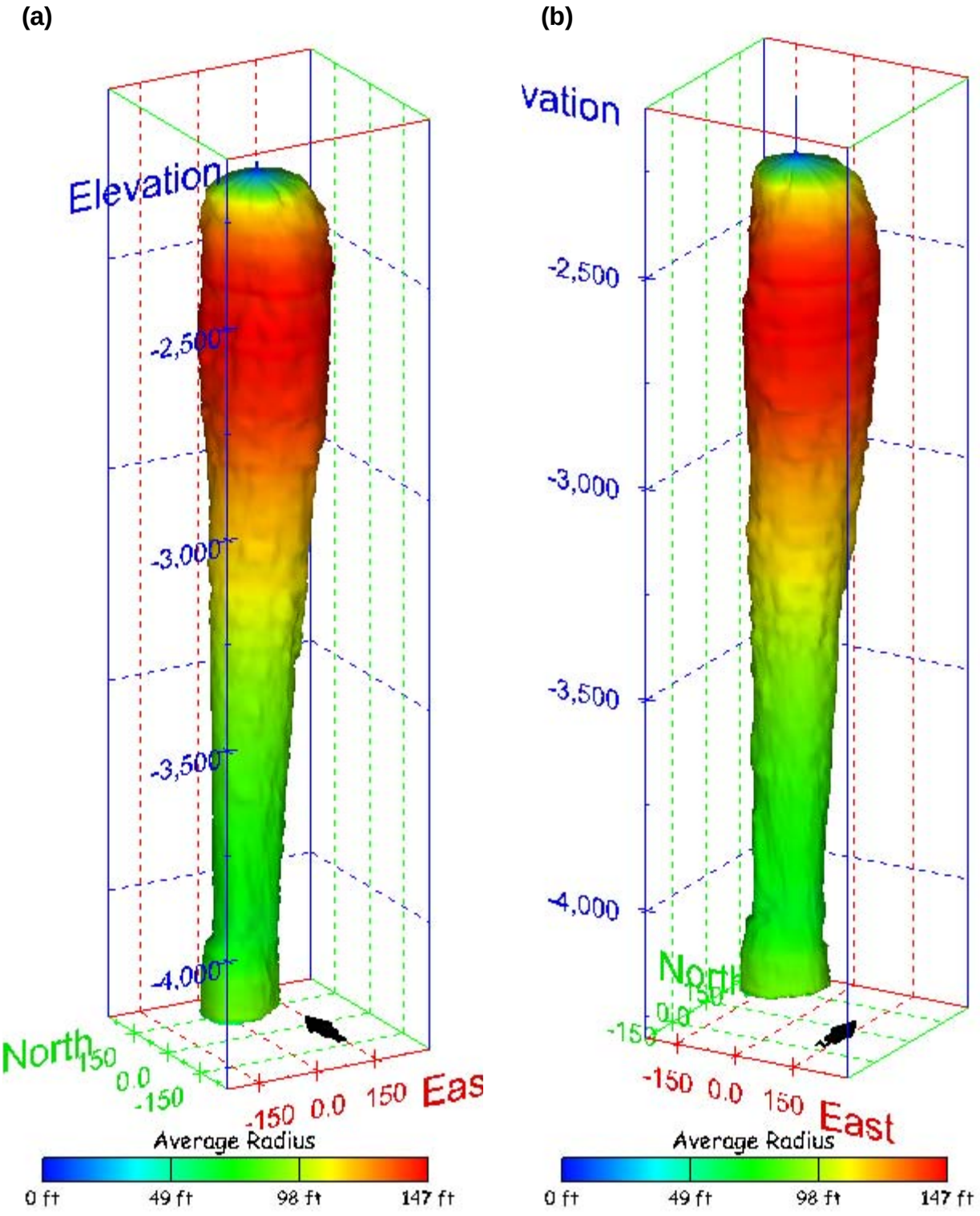

Figure 281. Sonar images of cavern BH-111, showing the geometry of the cavern colored by average radius. View from (a) azimuth 210°, elevation 20°; (b) azimuth 150°, elevation 20°.

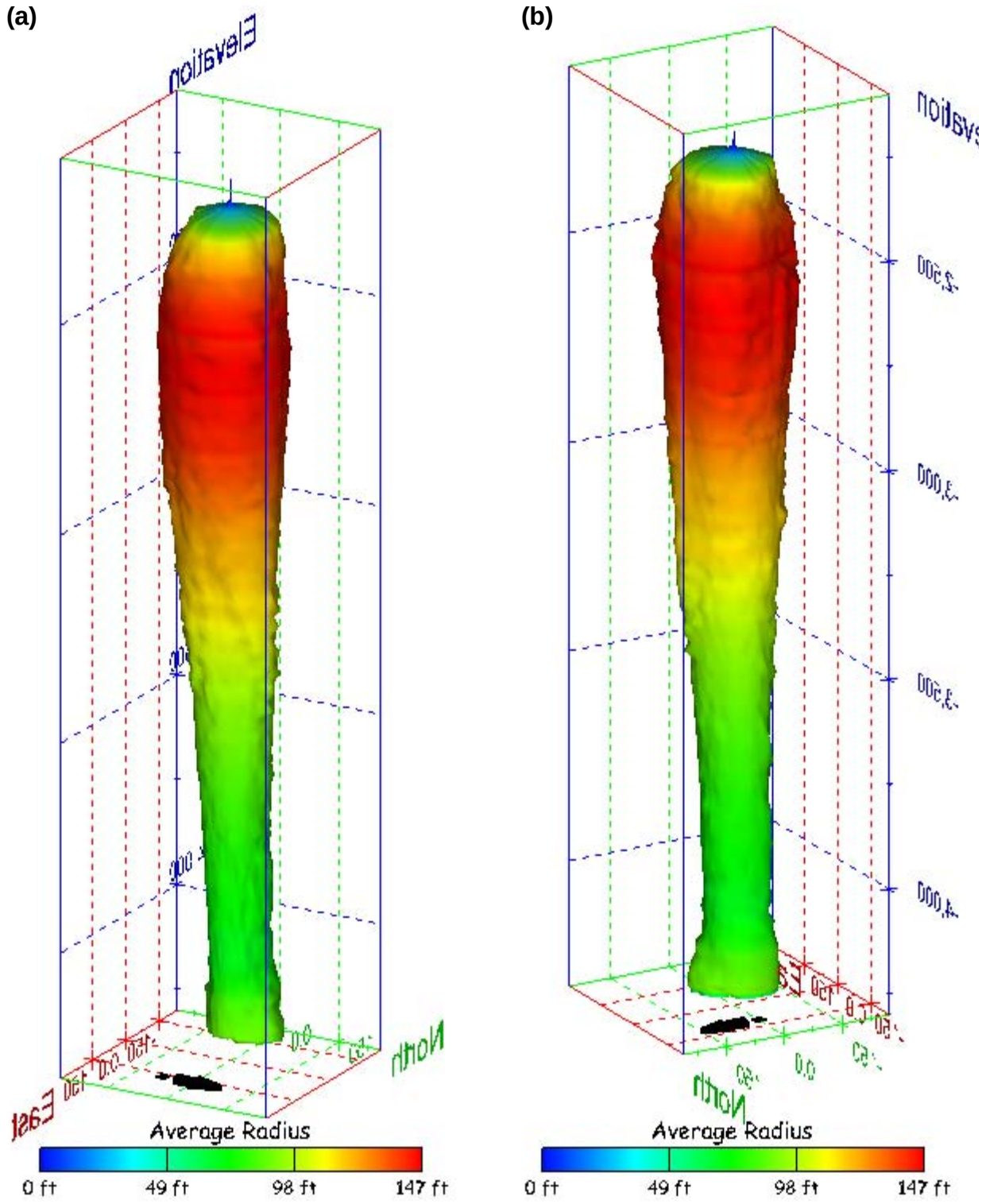

Figure 282. Sonar images of cavern BH-111, showing the geometry of the cavern colored by average radius. View from (a) azimuth 60°, elevation 20°; (b) azimuth 300°, elevation 20°.

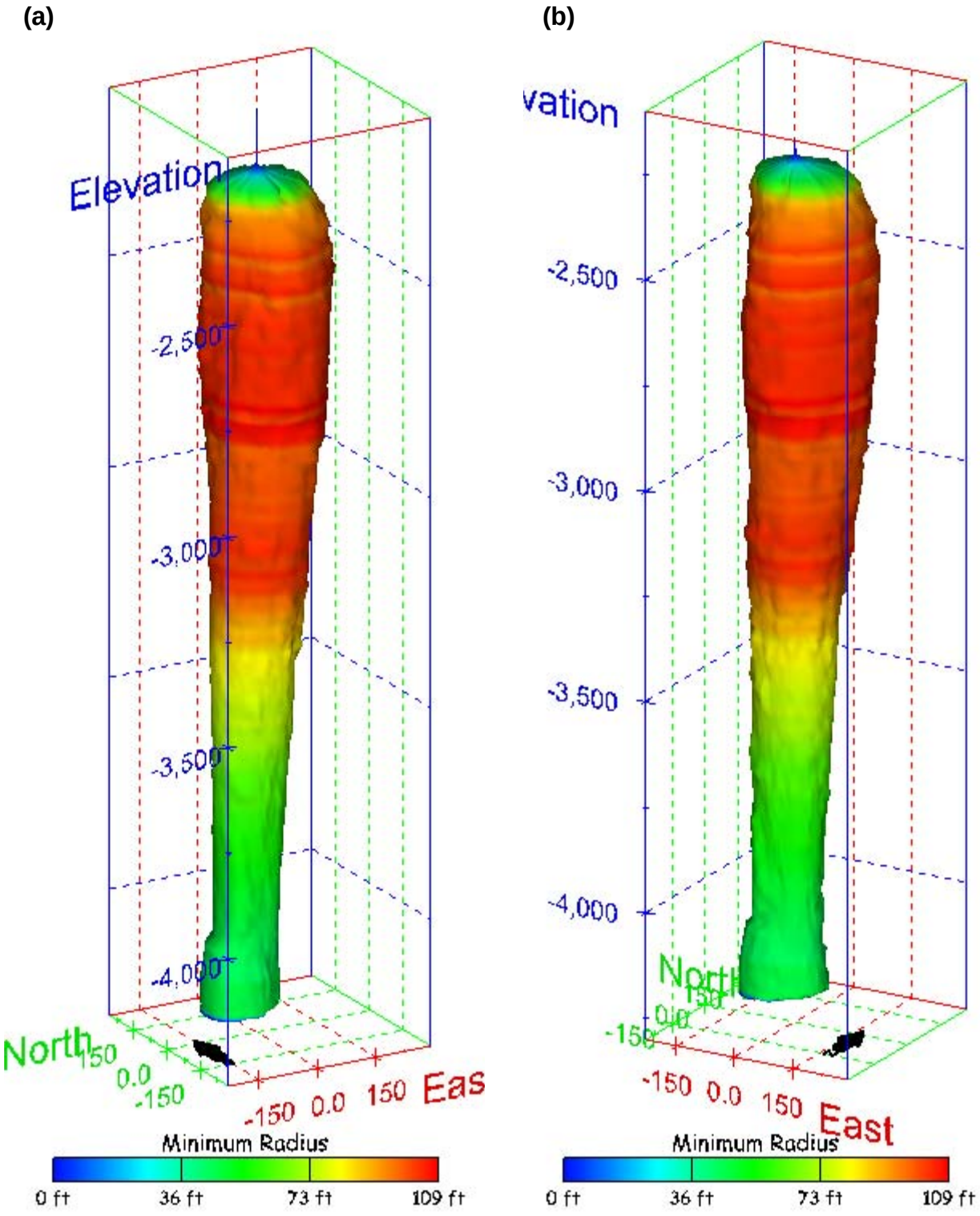

Figure 283. Sonar images of cavern BH-111, showing the geometry of the cavern colored by minimum radius. View from (a) azimuth 210°, elevation 20°; (b) azimuth 150°, elevation 20°.

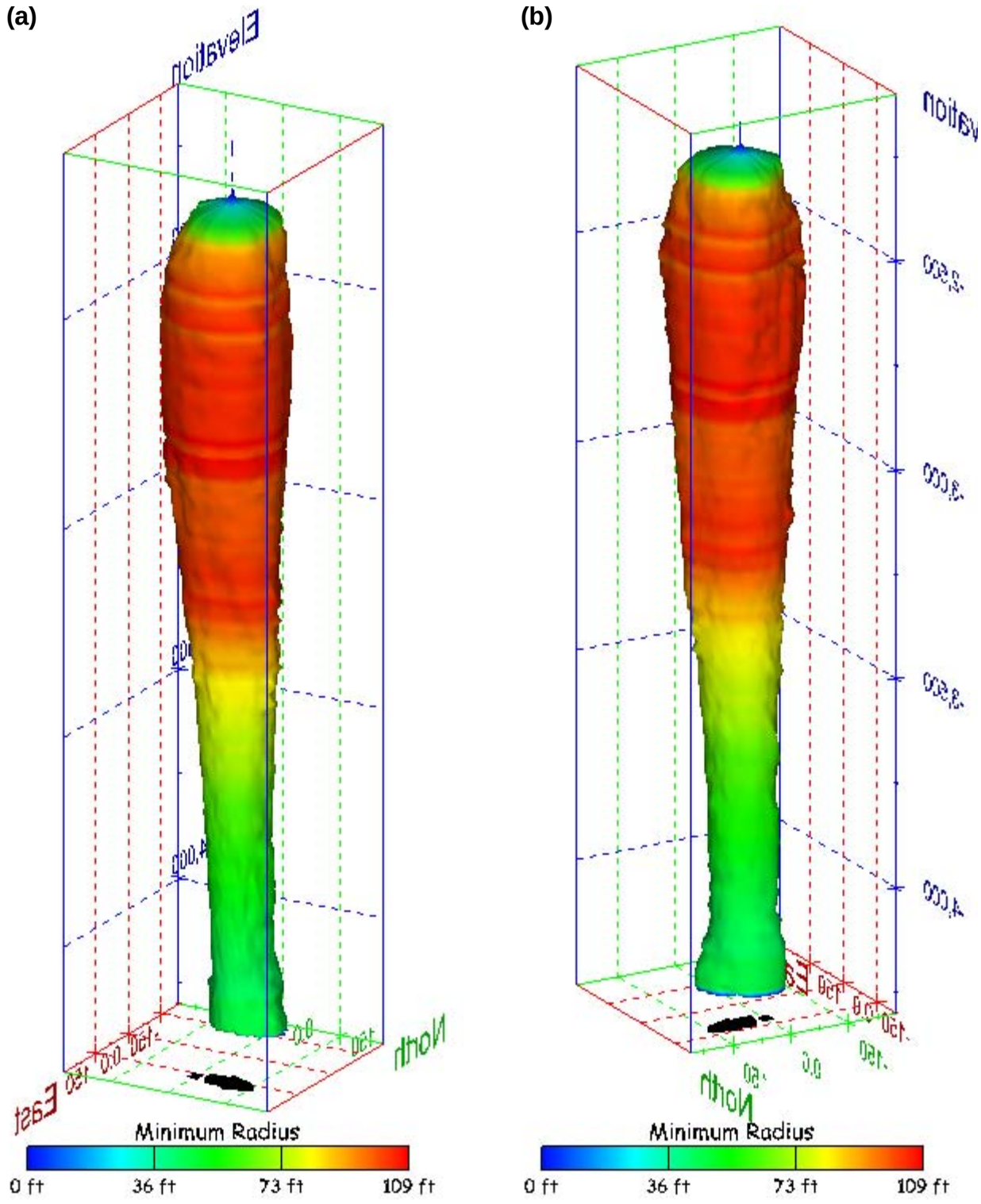

Figure 284. Sonar images of cavern BH-111, showing the geometry of the cavern colored by minimum radius. View from (a) azimuth 60°, elevation 20°; (b) azimuth 300°, elevation 20°.

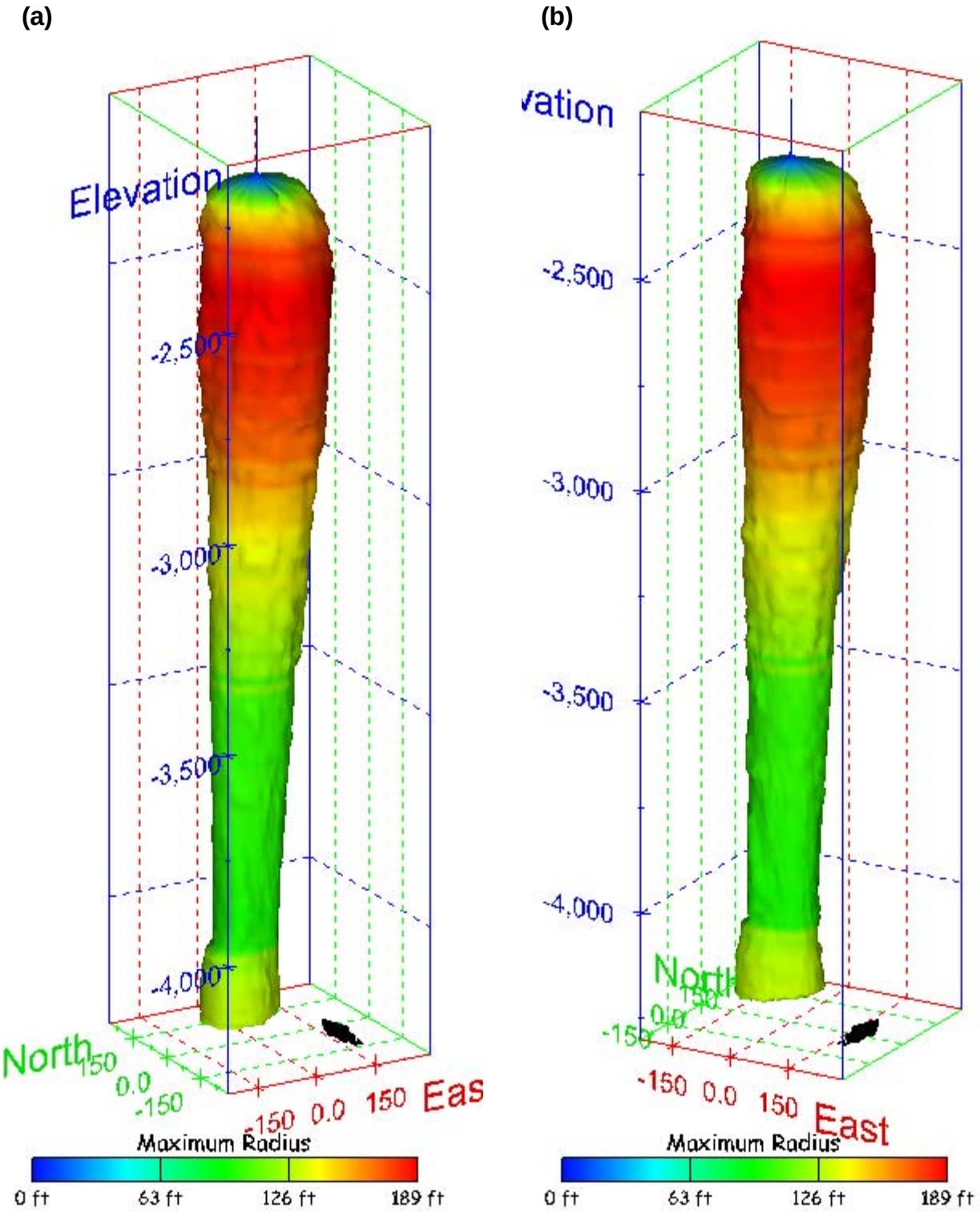

Figure 285. Sonar images of cavern BH-111, showing the geometry of the cavern colored by maximum radius. View from (a) azimuth 210°, elevation 20°; (b) azimuth 150°, elevation 20°.

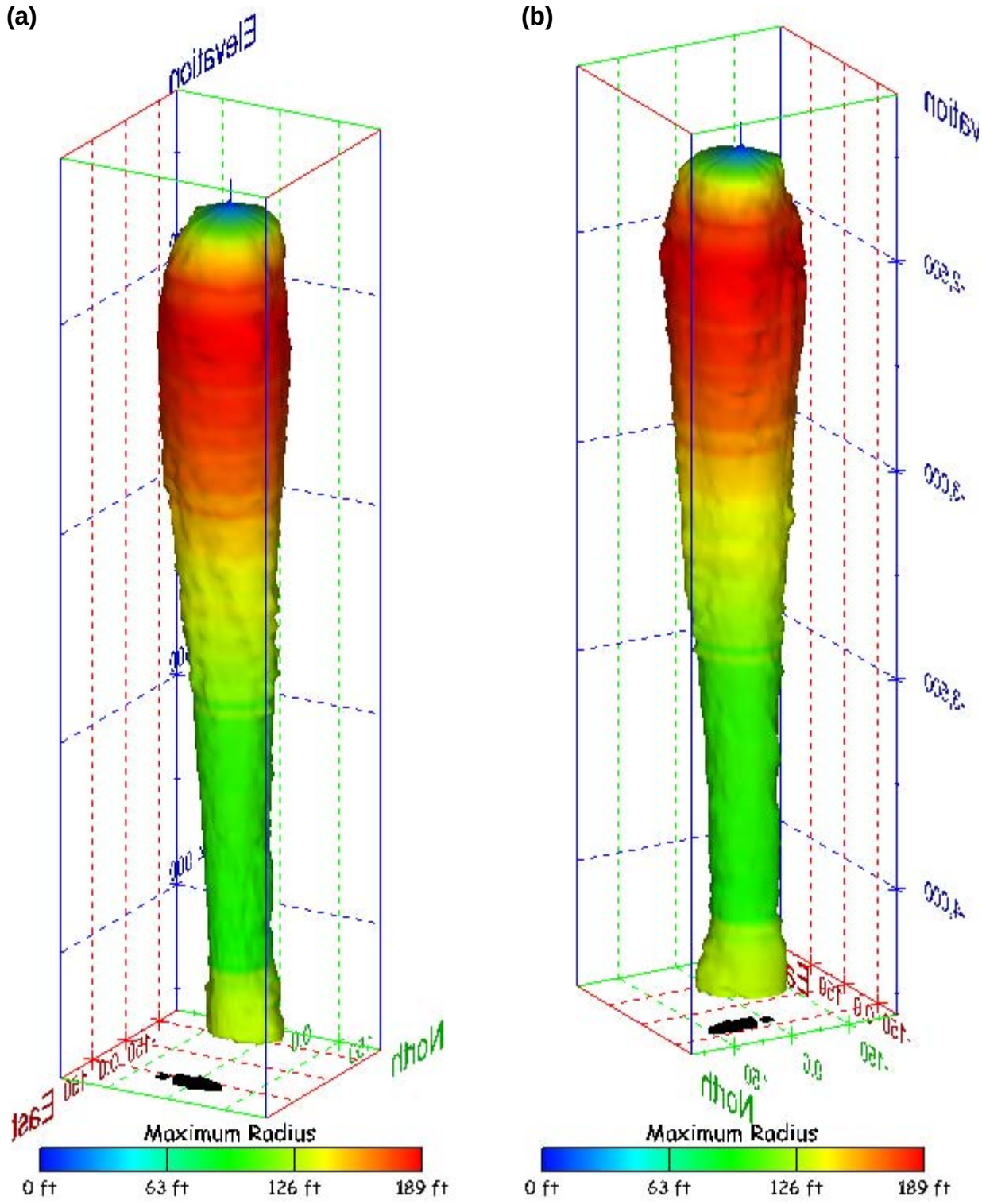

Figure 286. Sonar images of cavern BH-111, showing the geometry of the cavern colored by maximum radius. View from (a) azimuth 60°, elevation 20°; (b) azimuth 300°, elevation 20°.

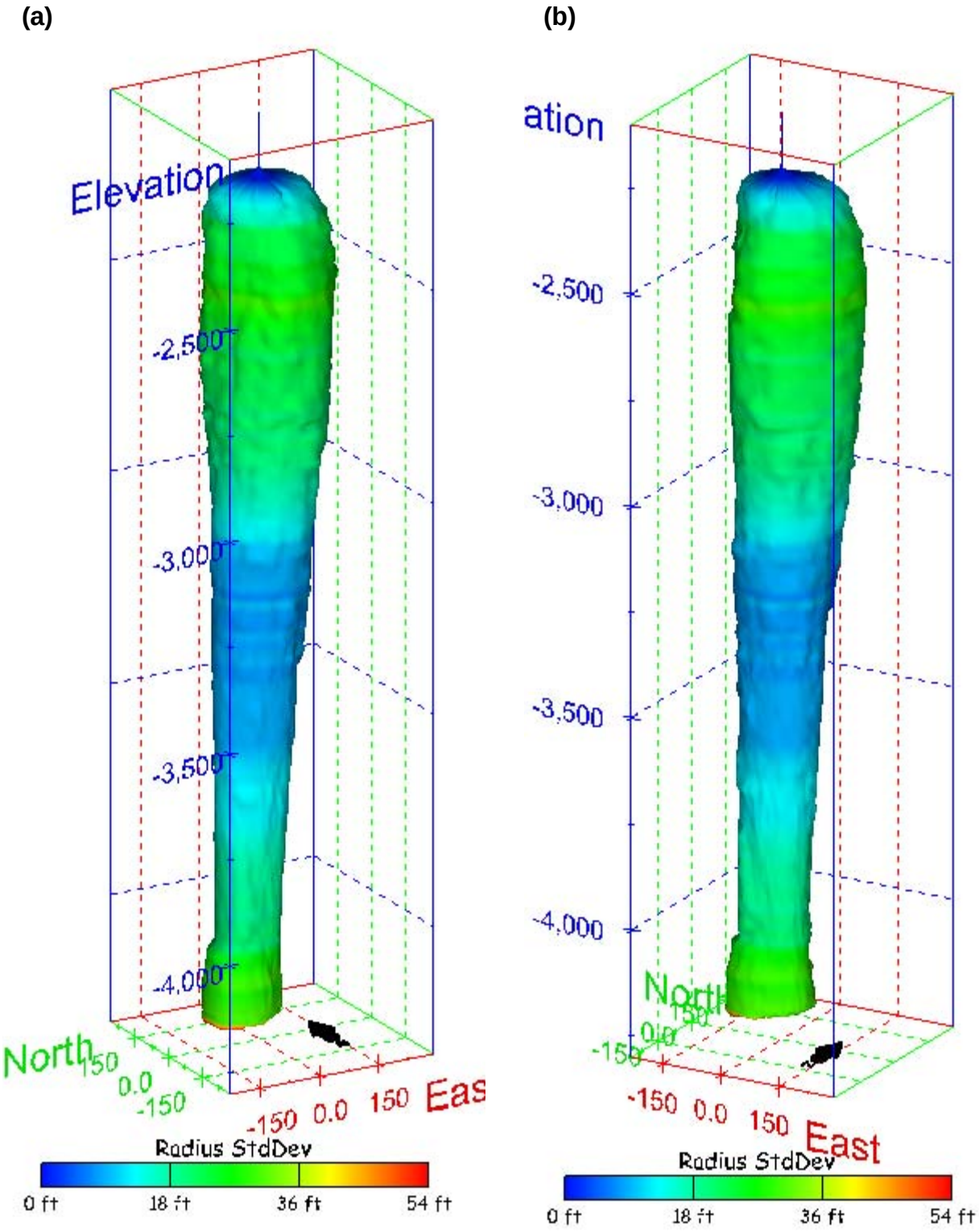

Figure 287. Sonar images of cavern BH-111, showing the geometry of the cavern colored by radius standard deviation. View from (a) azimuth 210°, elevation 20°; (b) azimuth 150°, elevation 20°.

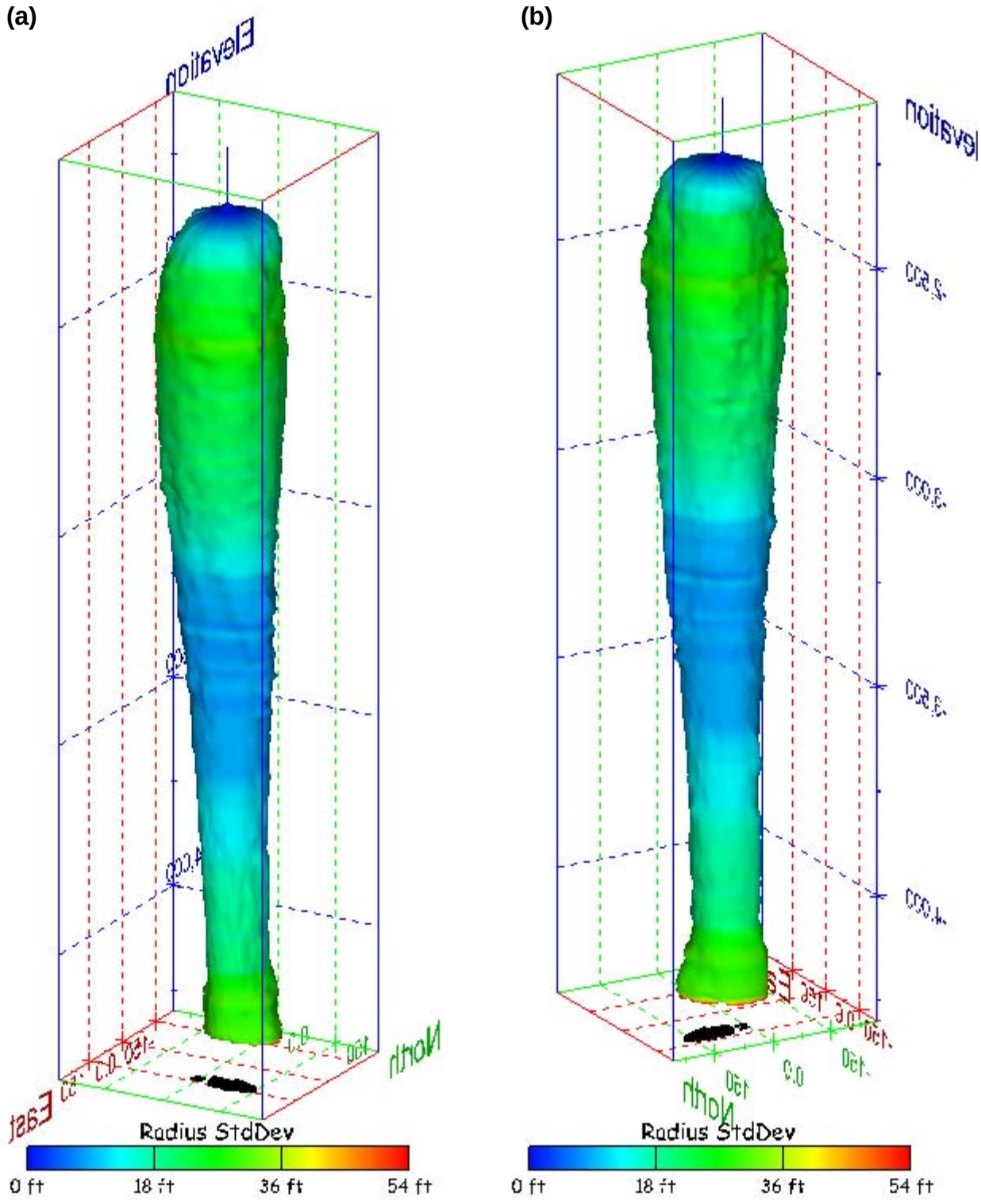

Figure 288. Sonar images of cavern BH-111, showing the geometry of the cavern colored by radius standard deviation. View from (a) azimuth 60°, elevation 20°; (b) azimuth 300°, elevation 20°.

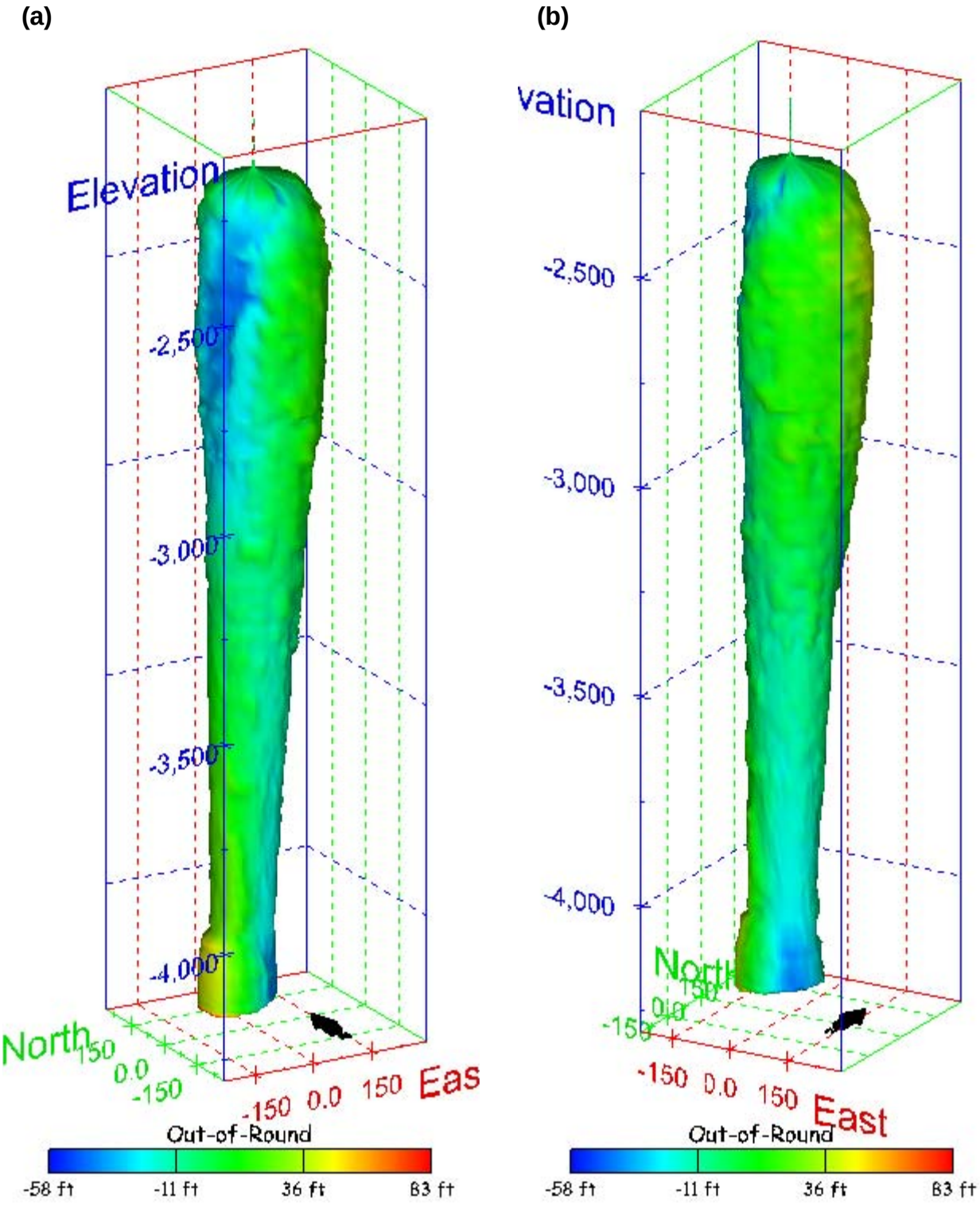

Figure 289. Sonar images of cavern BH-111, showing the geometry of the cavern colored by out-of-round distance. View from (a) azimuth 210°, elevation 20°; (b) azimuth 150°, elevation 20°.

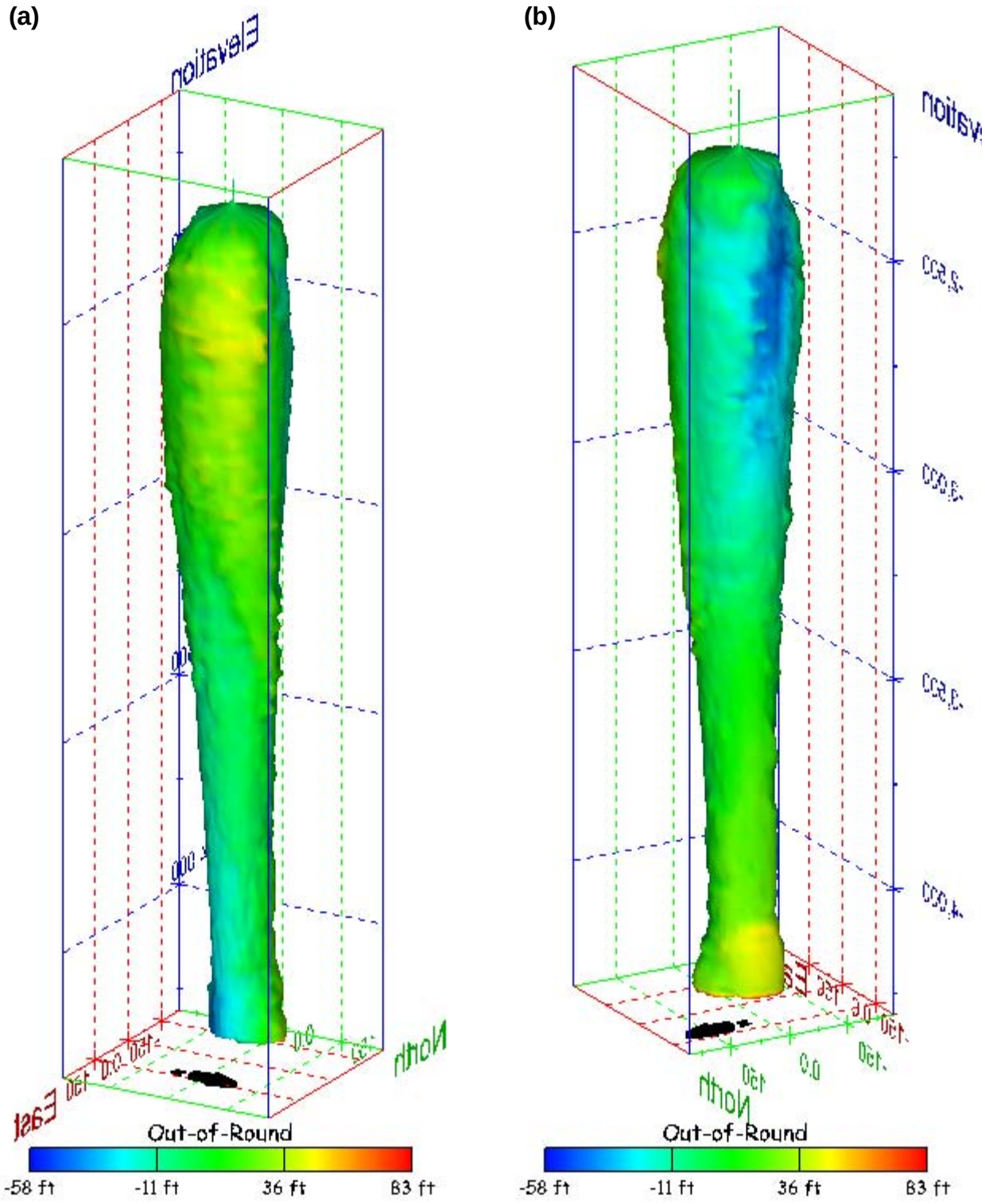

Figure 290. Sonar images of cavern BH-111, showing the geometry of the cavern colored by out-of-round distance. View from (a) azimuth 60°, elevation 20°; (b) azimuth 300°, elevation 20°.

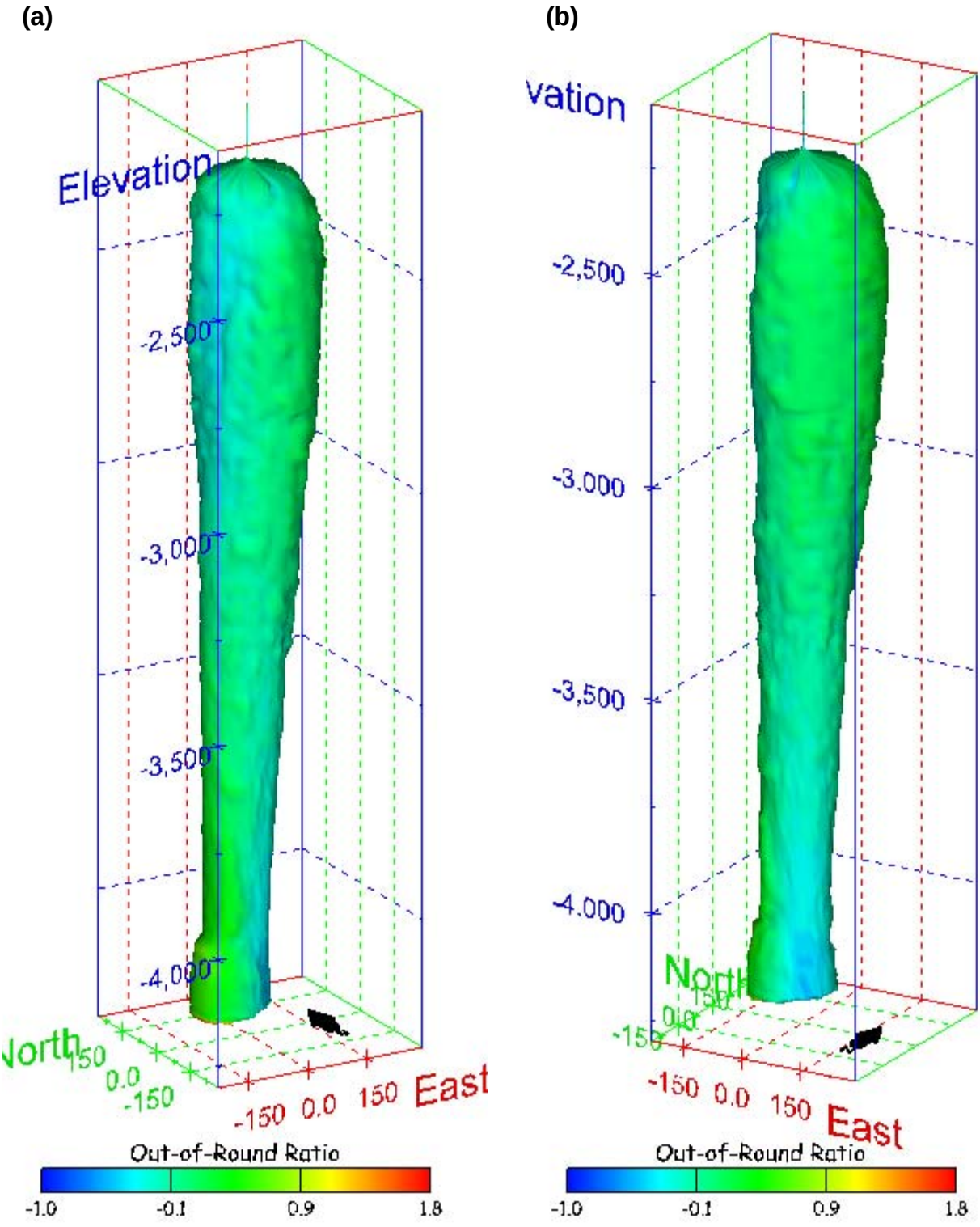

Figure 291. Sonar images of cavern BH-111, showing the geometry of the cavern colored by out-of-round ratio. View from (a) azimuth 210°, elevation 20°; (b) azimuth 150°, elevation 20°.

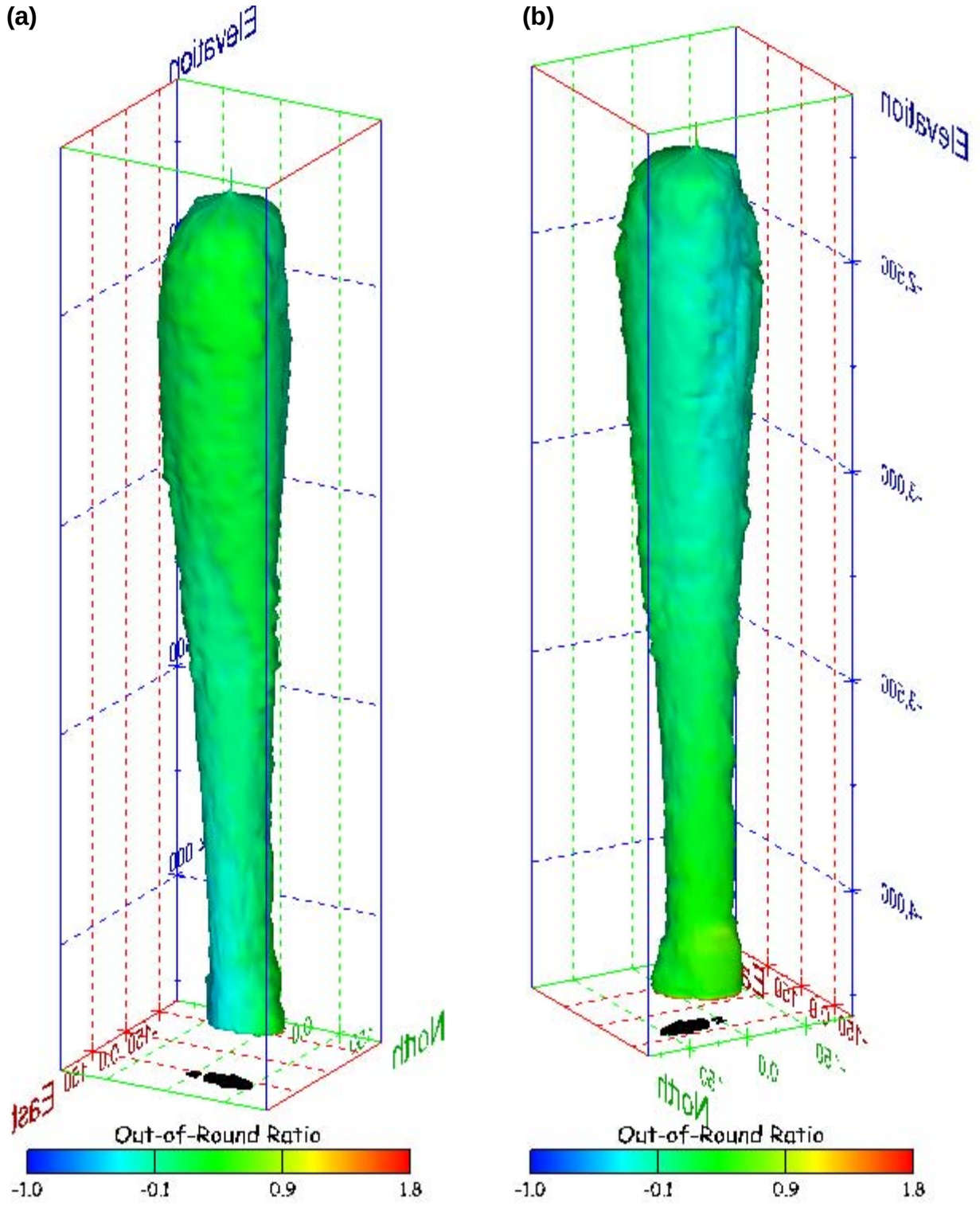

Figure 292. Sonar images of cavern BH-111, showing the geometry of the cavern colored by out-of-round ratio. View from (a) azimuth 60°, elevation 20°; (b) azimuth 300°, elevation 20°.

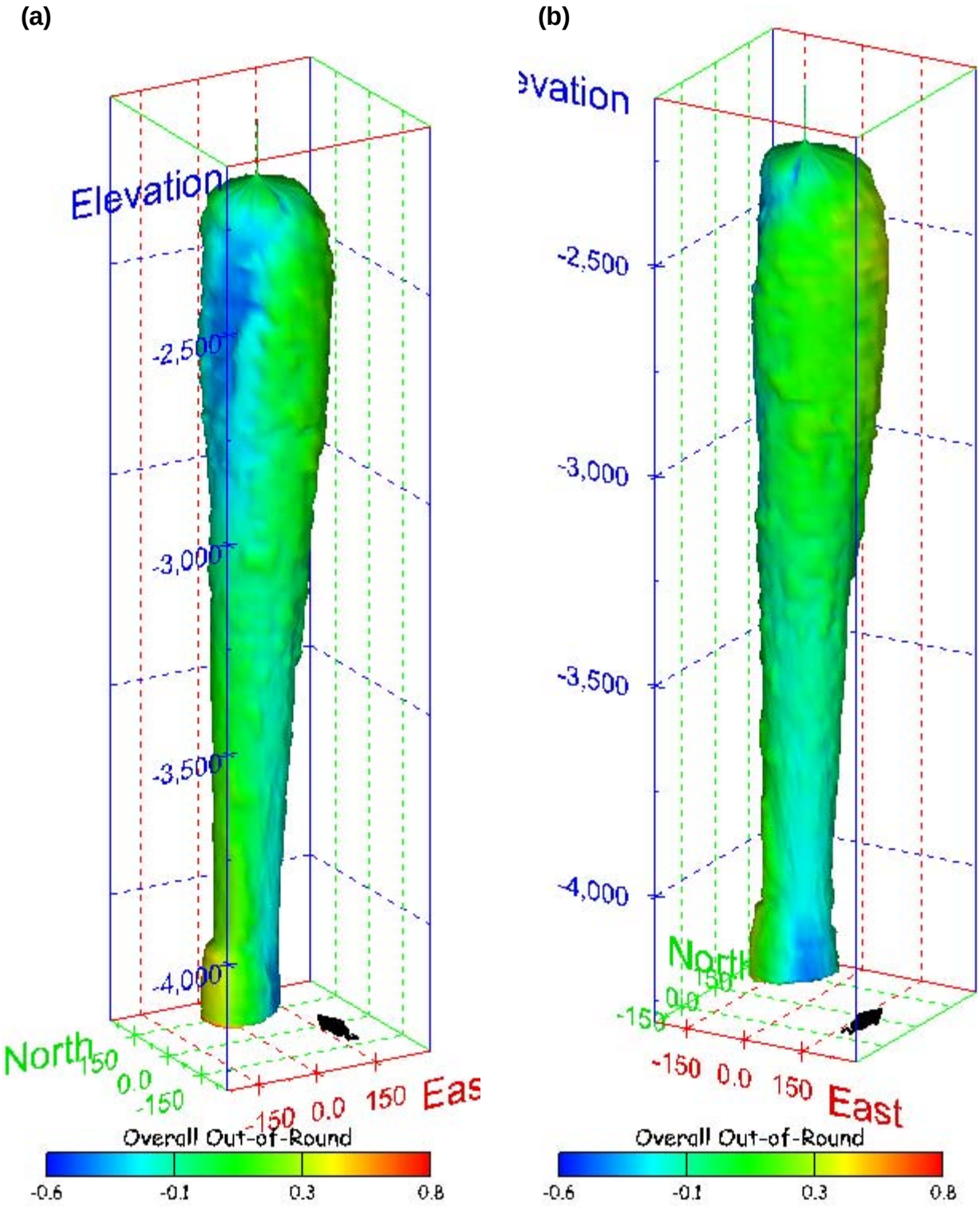

Figure 293. Sonar images of cavern BH-111, showing the geometry of the cavern colored by overall out-of-round ratio. View from (a) azimuth 210°, elevation 20°; (b) azimuth 150°, elevation 20°.

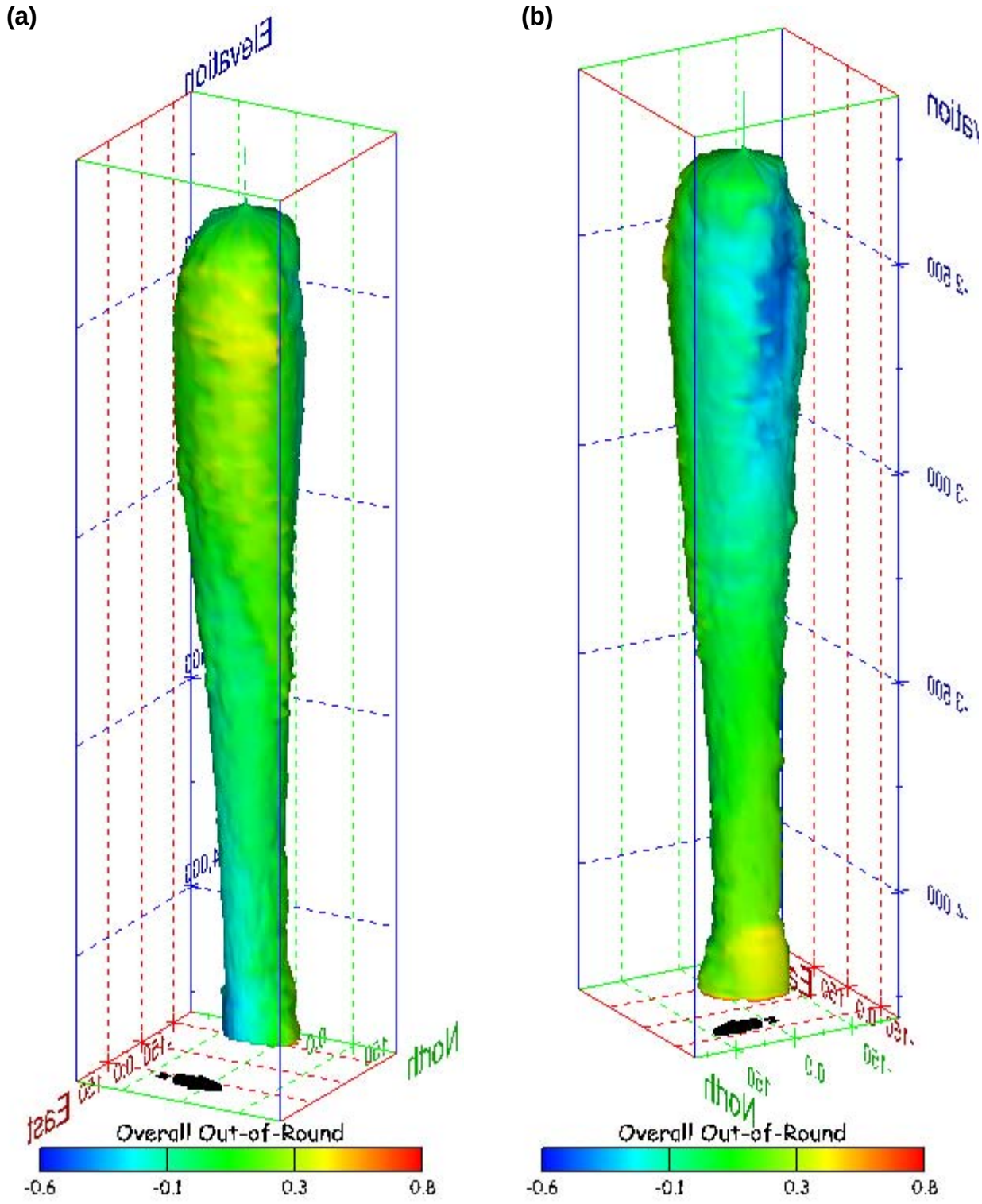

Figure 294. Sonar images of cavern BH-111, showing the geometry of the cavern colored by overall out-of-round ratio. View from (a) azimuth 60°, elevation 20°; (b) azimuth 300°, elevation 20°.

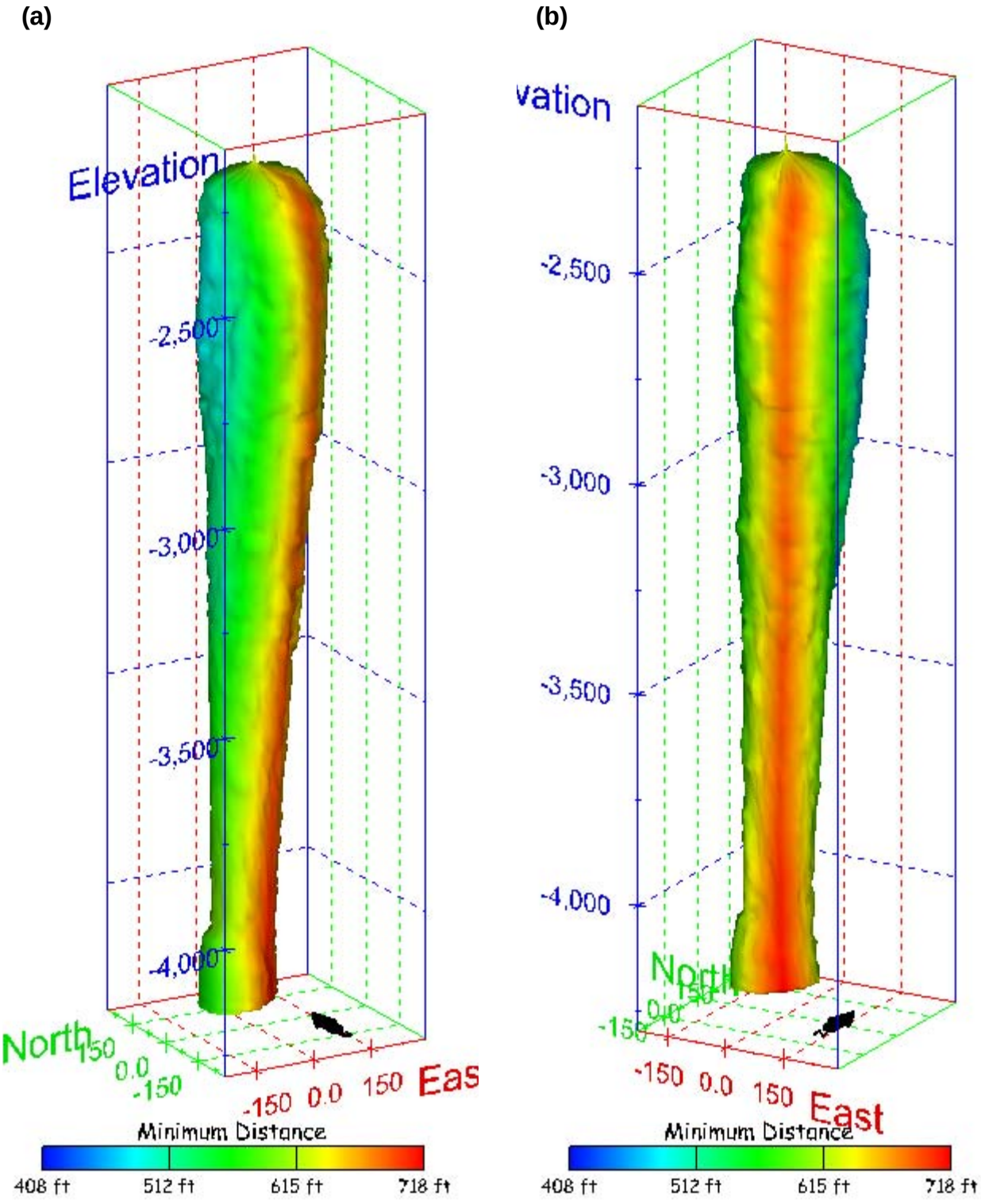

Figure 295. Sonar images of cavern BH-111, showing the geometry of the cavern colored by the minimum distance to the nearest neighboring cavern. View from (a) azimuth 210°, elevation 20°; (b) azimuth 150°, elevation 20°.

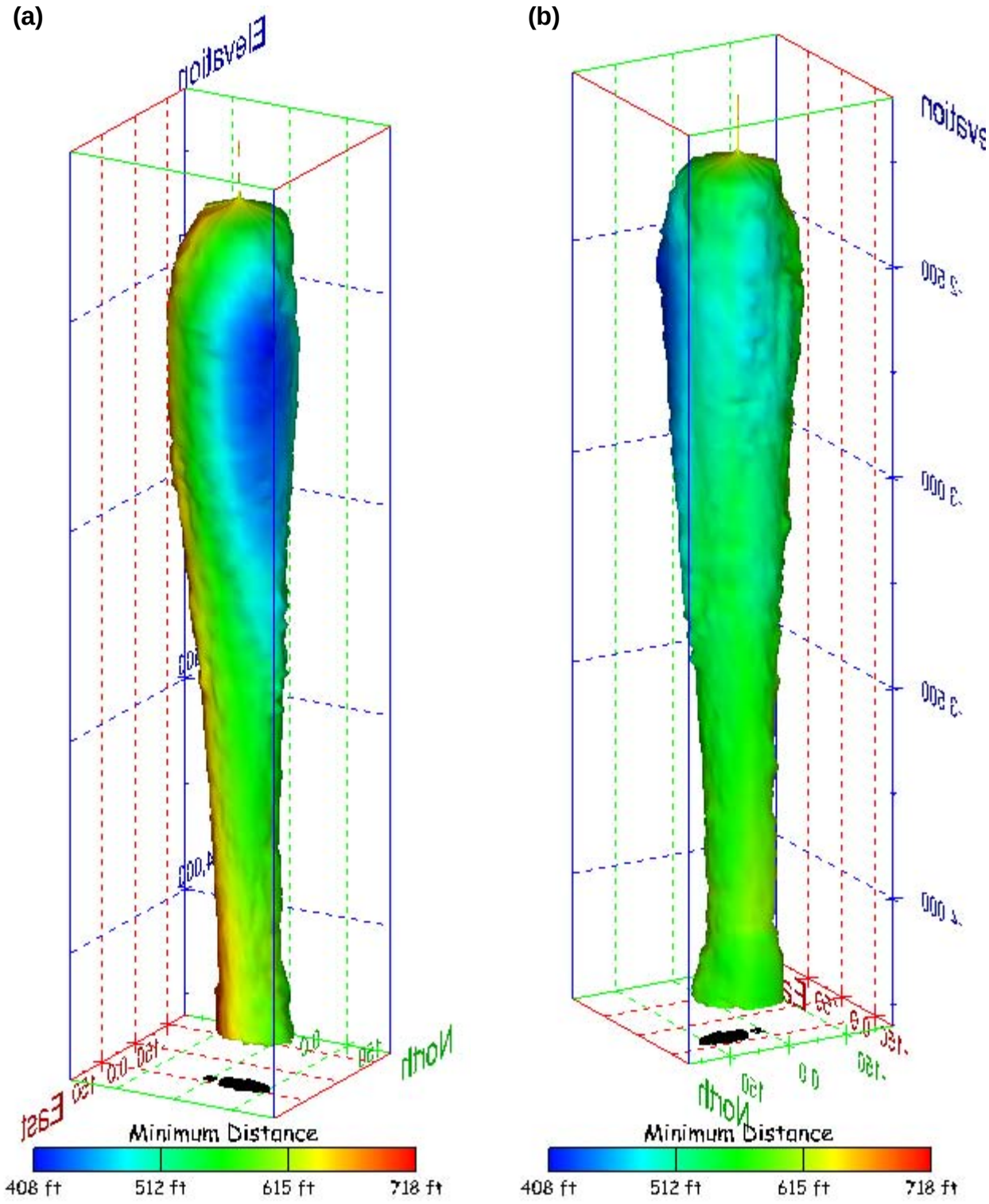

Figure 296. Sonar images of cavern BH-111, showing the geometry of the cavern colored by minimum distance to the nearest neighboring cavern. View from (a) azimuth 60°, elevation 20°; (b) azimuth 300°, elevation 20°.

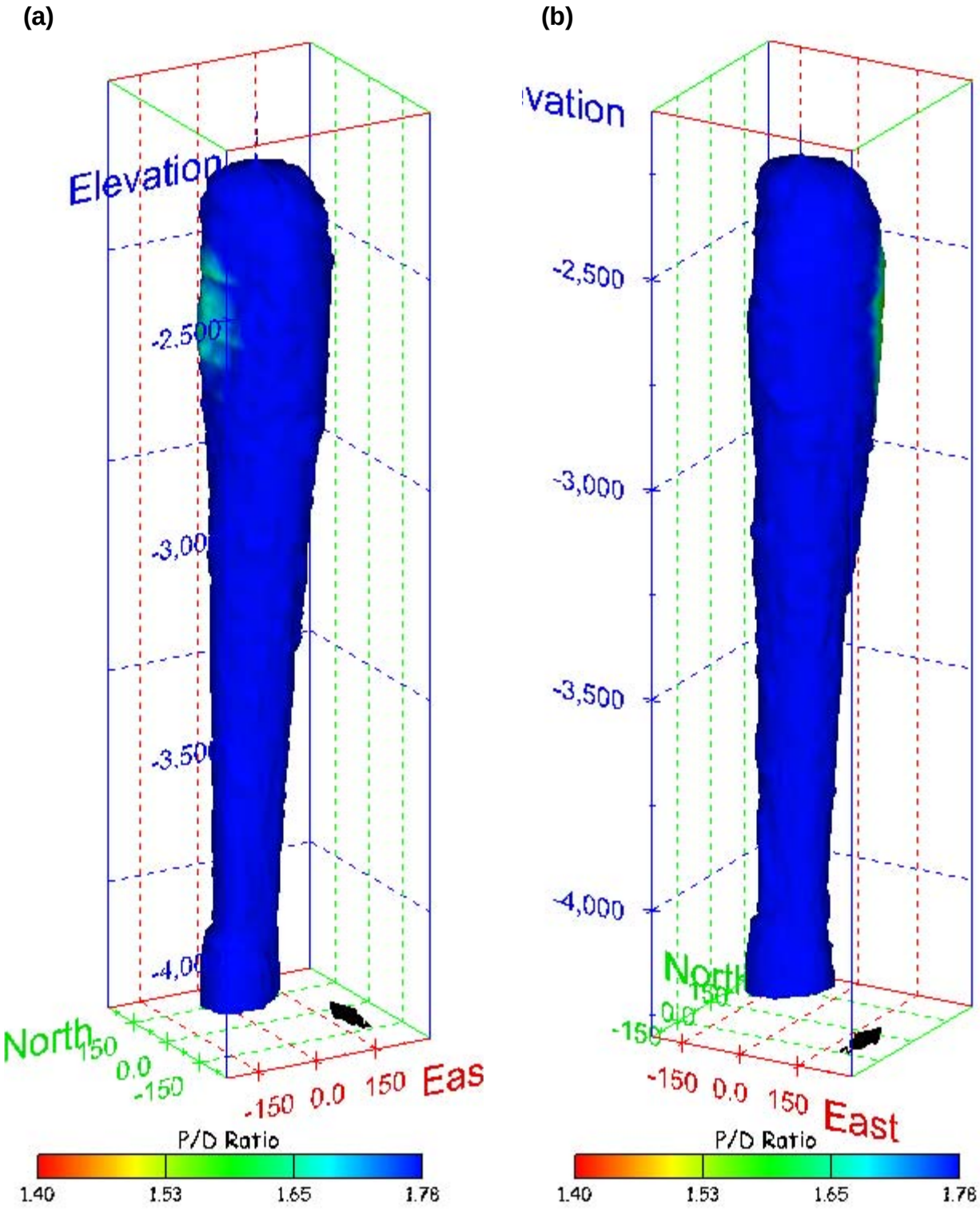

Figure 297. Sonar images of cavern BH-111, showing the geometry of the cavern colored by three-dimensional pillar-to-diameter ratio. View from (a) azimuth 210°, elevation 20°; (b) azimuth 150°, elevation 20°.

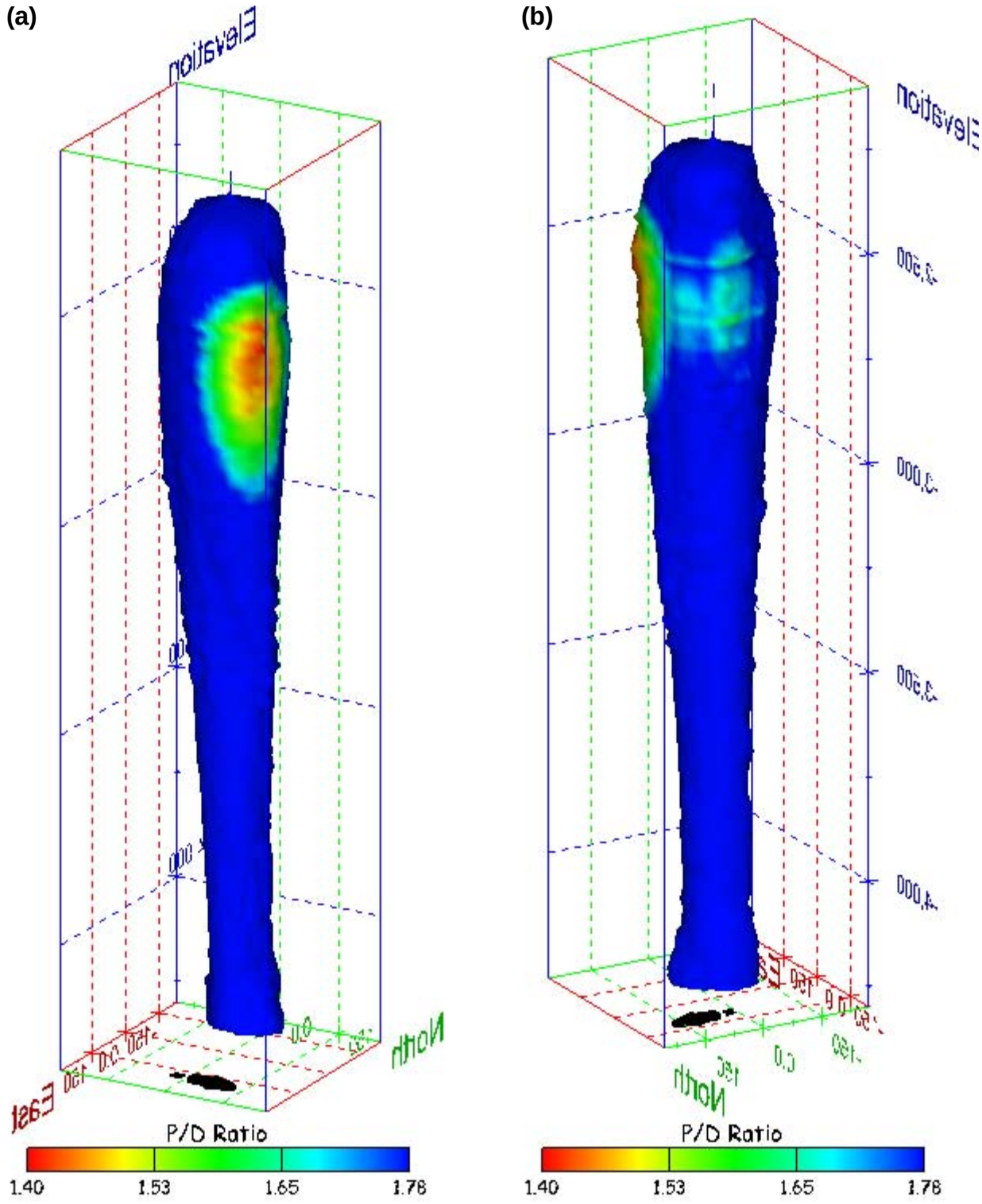

Figure 298. Sonar images of cavern BH-111, showing the geometry of the cavern colored by three-dimensional pillar-to-diameter ratio. View from (a) azimuth 60°, elevation 20°; (b) azimuth 300°, elevation 20°.

No Sonic Velocity Data Available for Socon Surveys

Figure 299. Sonar image of cavern BH-111, showing the geometry of the cavern colored by the reported velocity of sound on the survey date of March 2005. View from due south, elevation zero.

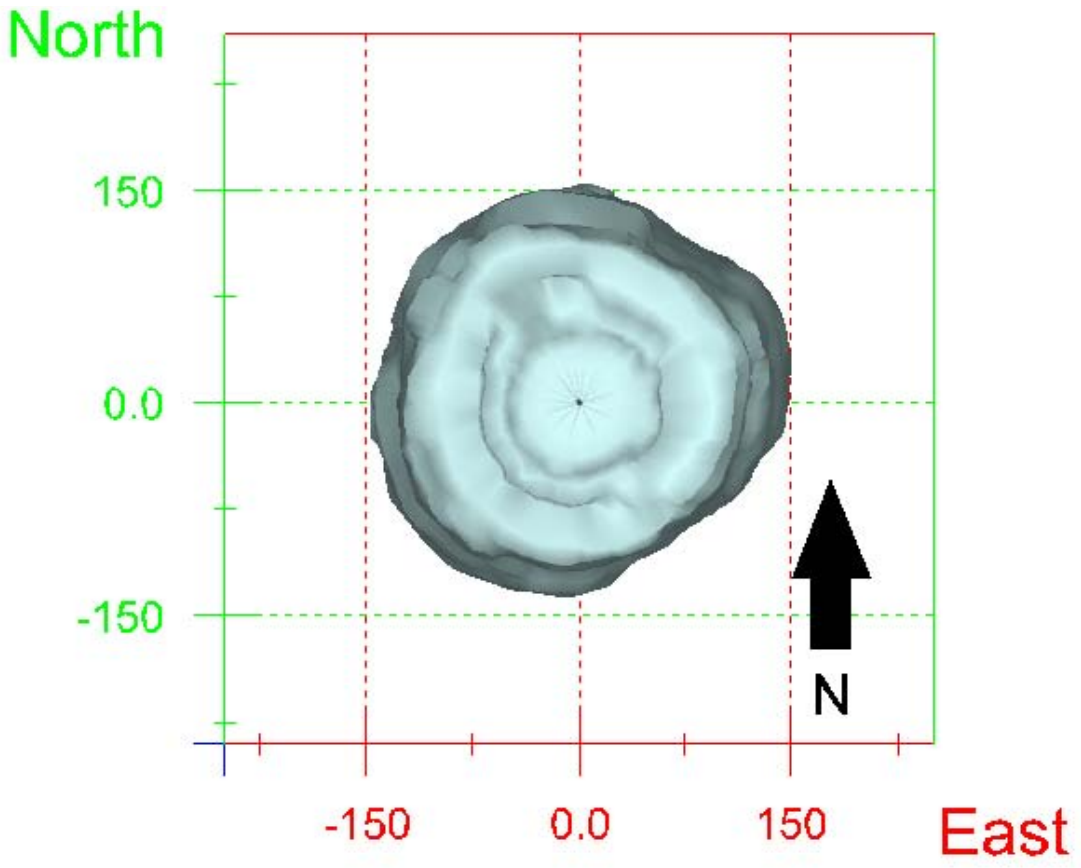

Figure 300. Map view sonar image of cavern BH-112, showing the basic geometry of the cavern. Grid squares represent 150 ft.

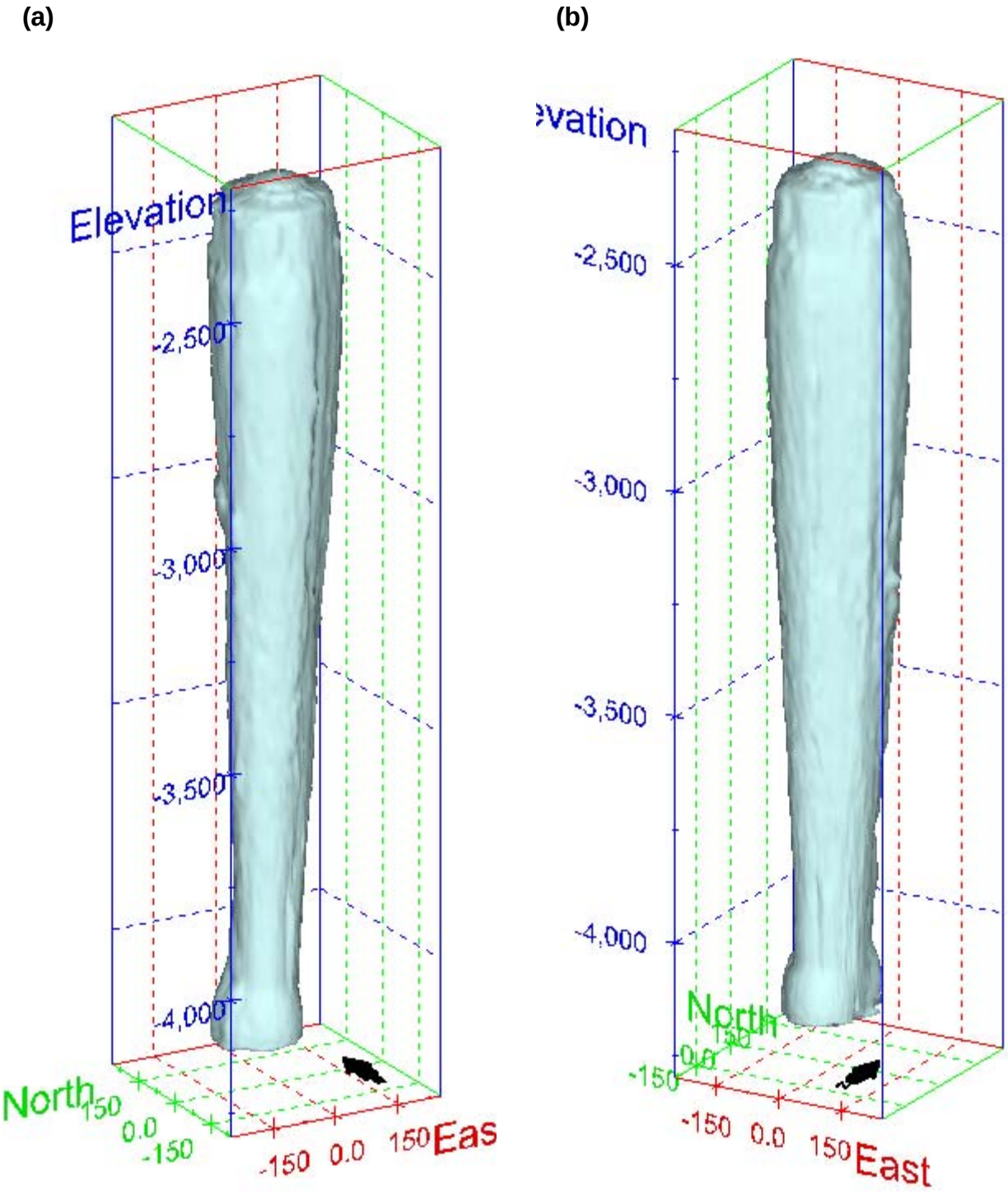

Figure 301. Sonar images of cavern BH-112, showing the basic geometric shape of the cavern. View from (a) azimuth 210°, elevation 20°; (b) azimuth 150°, elevation 20°.

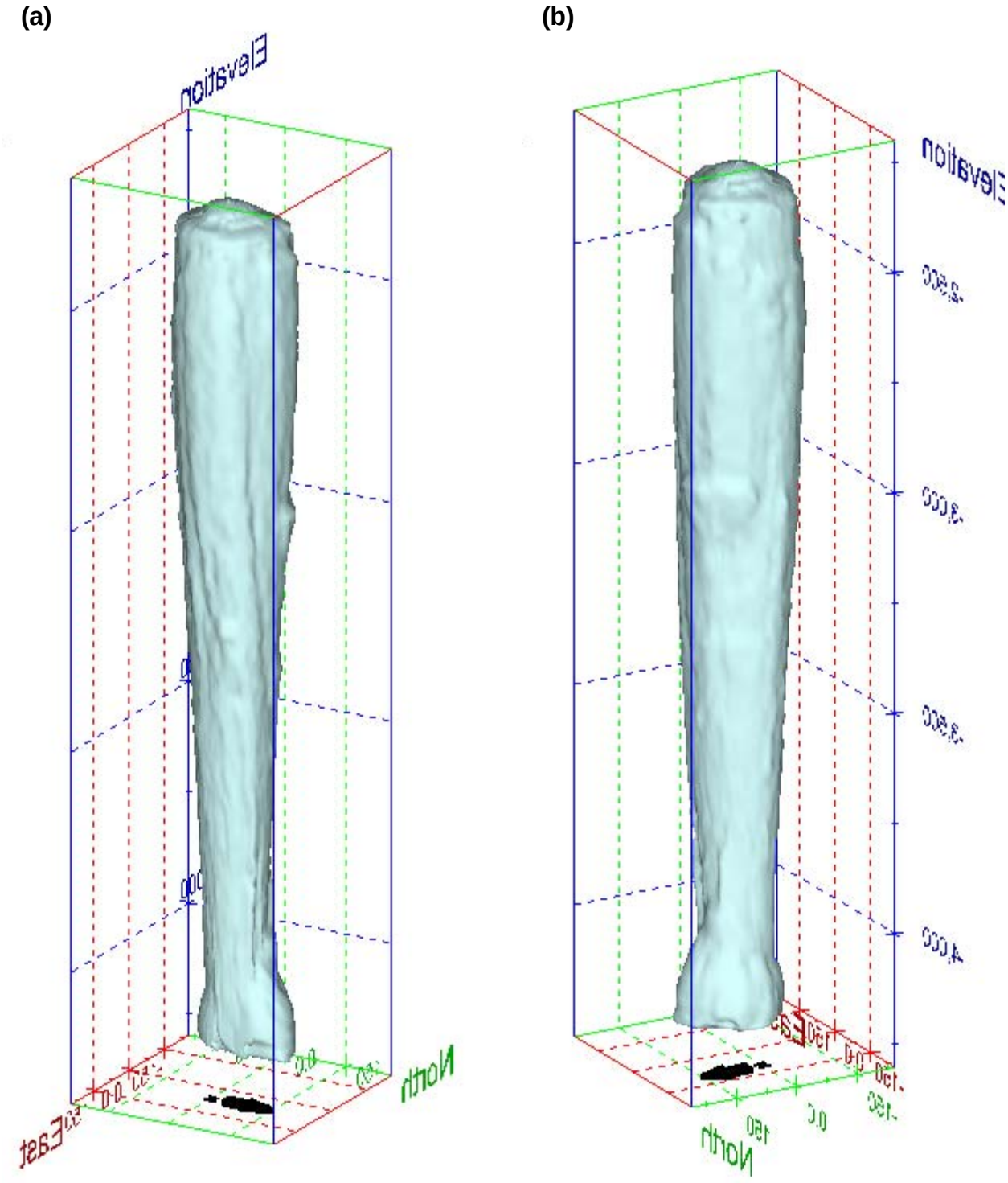

Figure 302. Sonar images of cavern BH-112, showing the basic geometric shape of the cavern. View from (a) azimuth 60°, elevation 20°; (b) azimuth 300°, elevation 20°.

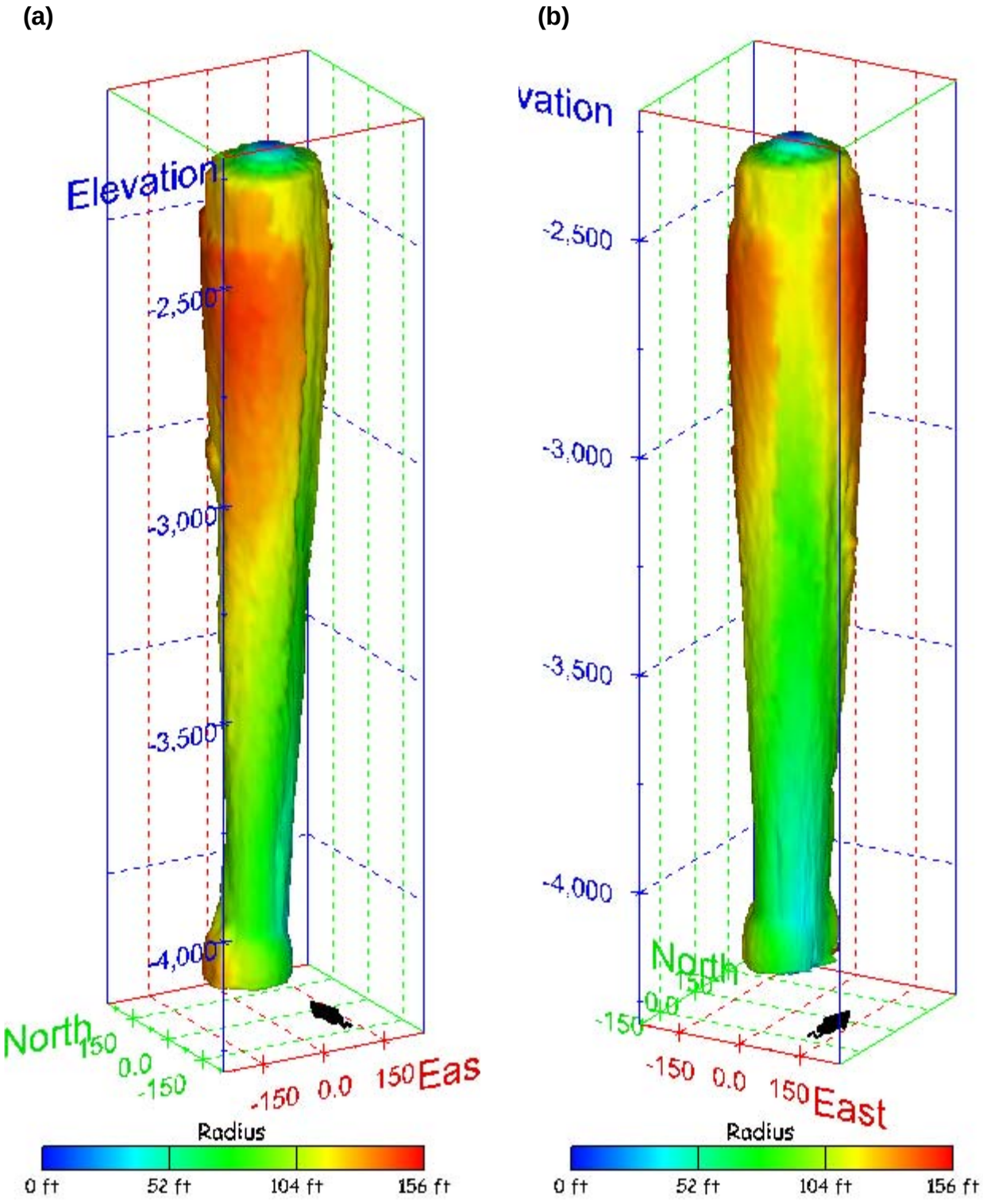

Figure 303. Sonar images of cavern BH-112, showing the geometry of the cavern colored by measured radius. View from (a) azimuth 210°, elevation 20°; (b) azimuth 150°, elevation 20°.

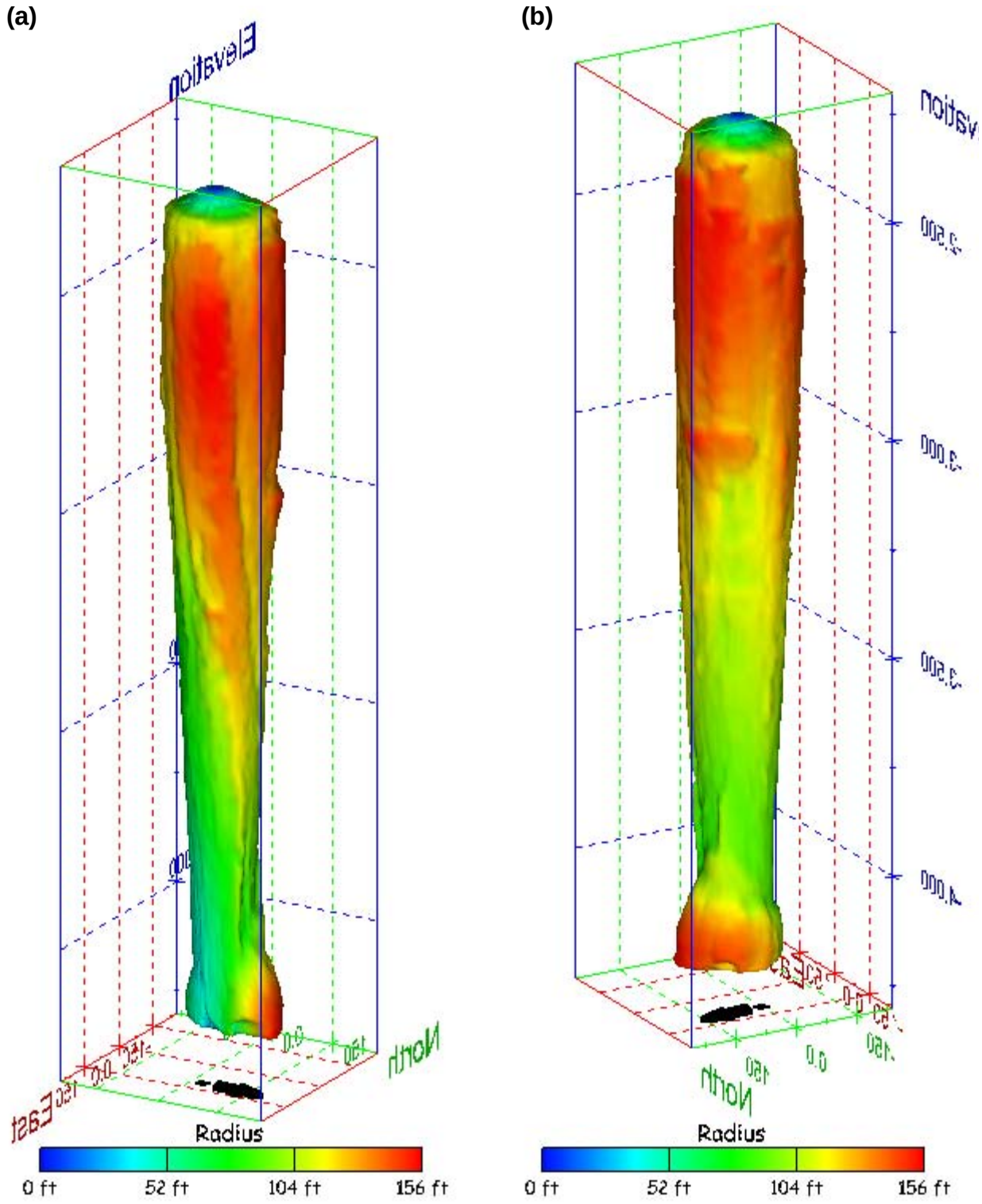

Figure 304. Sonar images of cavern BH-112, showing the geometry of the cavern colored by measured radius. View from (a) azimuth 60°, elevation 20°; (b) azimuth 300°, elevation 20°.

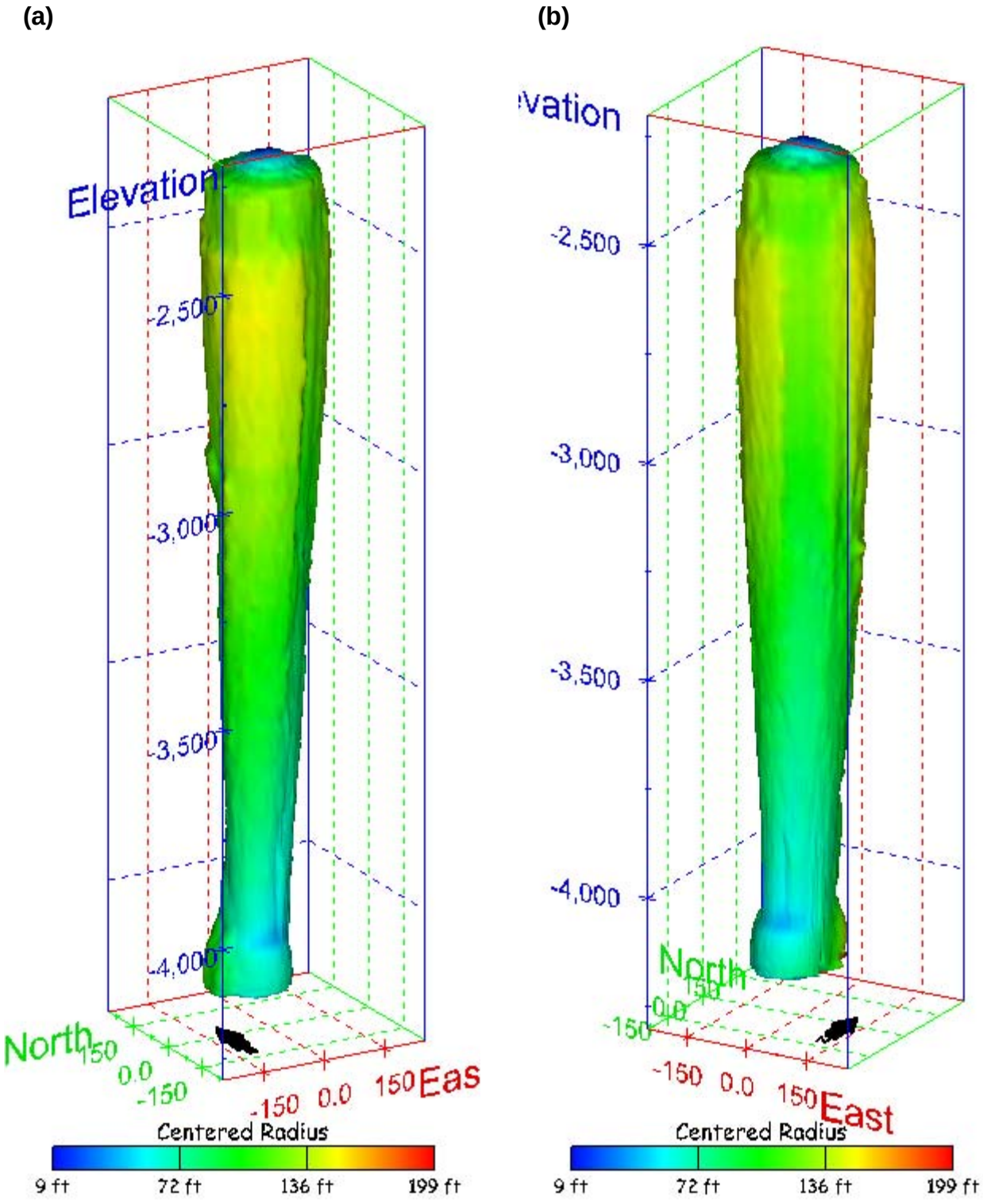

Figure 305. Sonar images of cavern BH-112, showing the geometry of the cavern colored by centered radius. View from (a) azimuth 210°, elevation 20°; (b) azimuth 150°, elevation 20°.

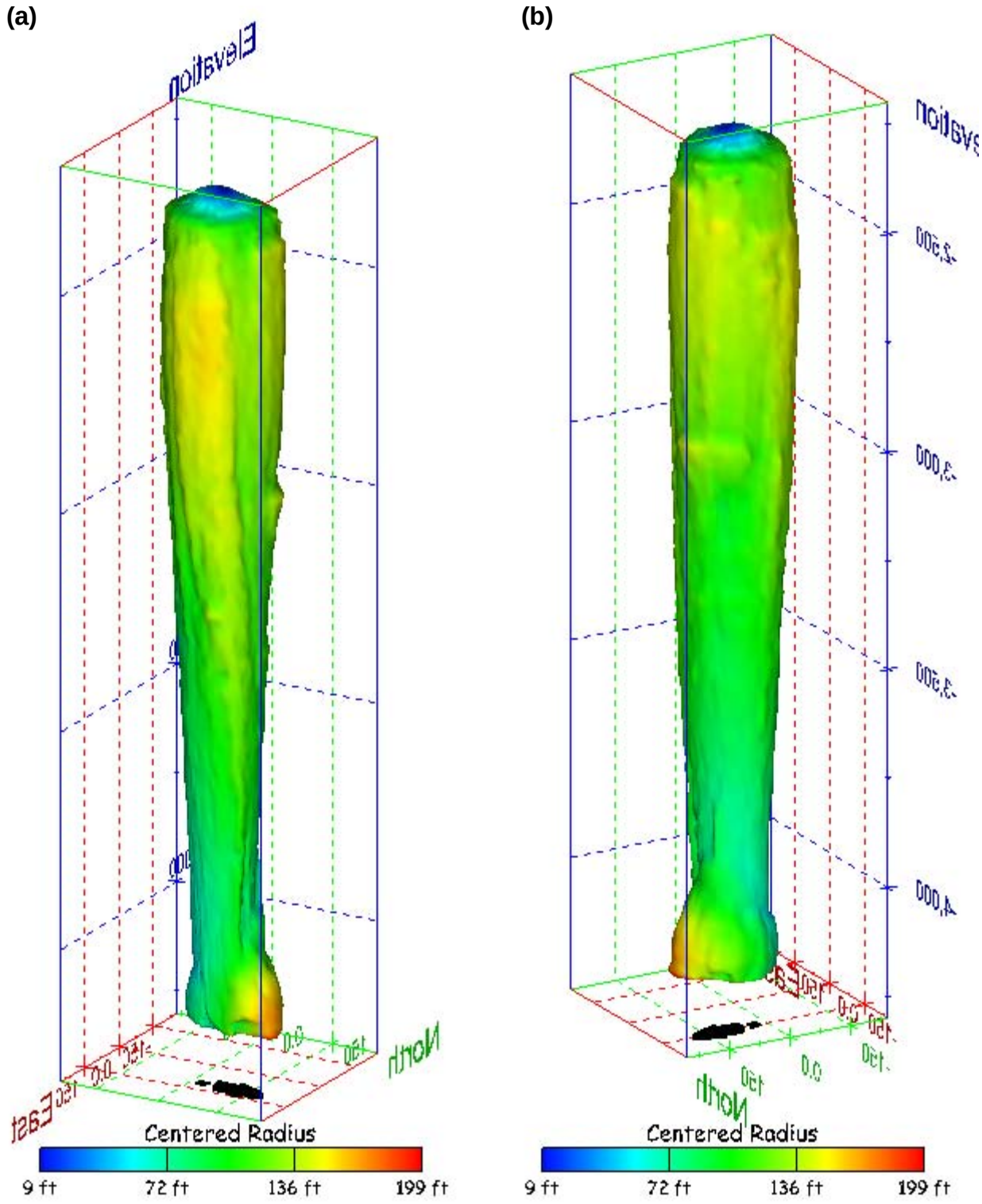

Figure 306. Sonar images of cavern BH-112, showing the geometry of the cavern colored by centered radius. View from (a) azimuth 60°, elevation 20°; (b) azimuth 300°, elevation 20°.

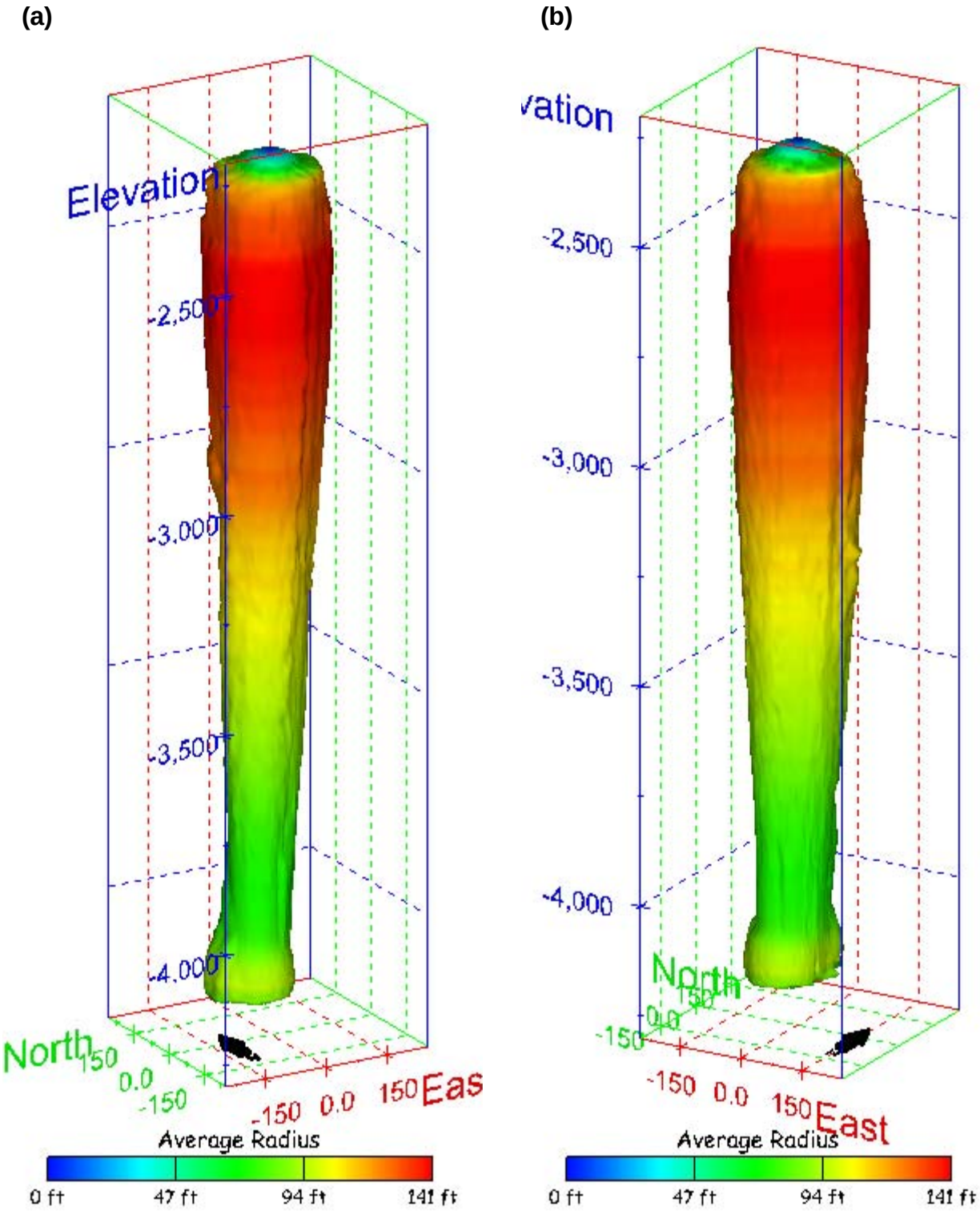

Figure 307. Sonar images of cavern BH-112, showing the geometry of the cavern colored by average radius. View from (a) azimuth 210°, elevation 20°; (b) azimuth 150°, elevation 20°.

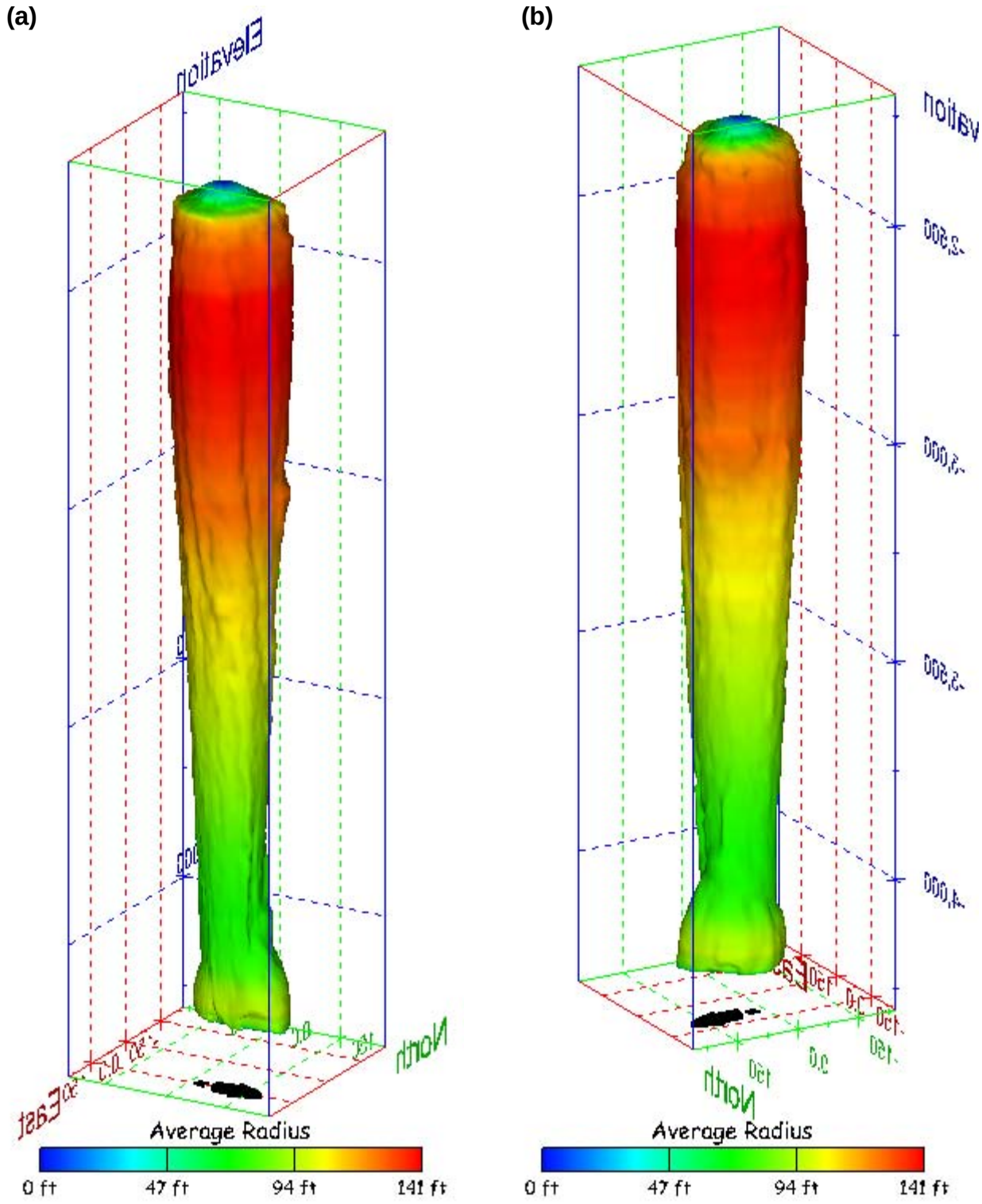

Figure 308. Sonar images of cavern BH-112, showing the geometry of the cavern colored by average radius. View from (a) azimuth 60°, elevation 20°; (b) azimuth 300°, elevation 20°.

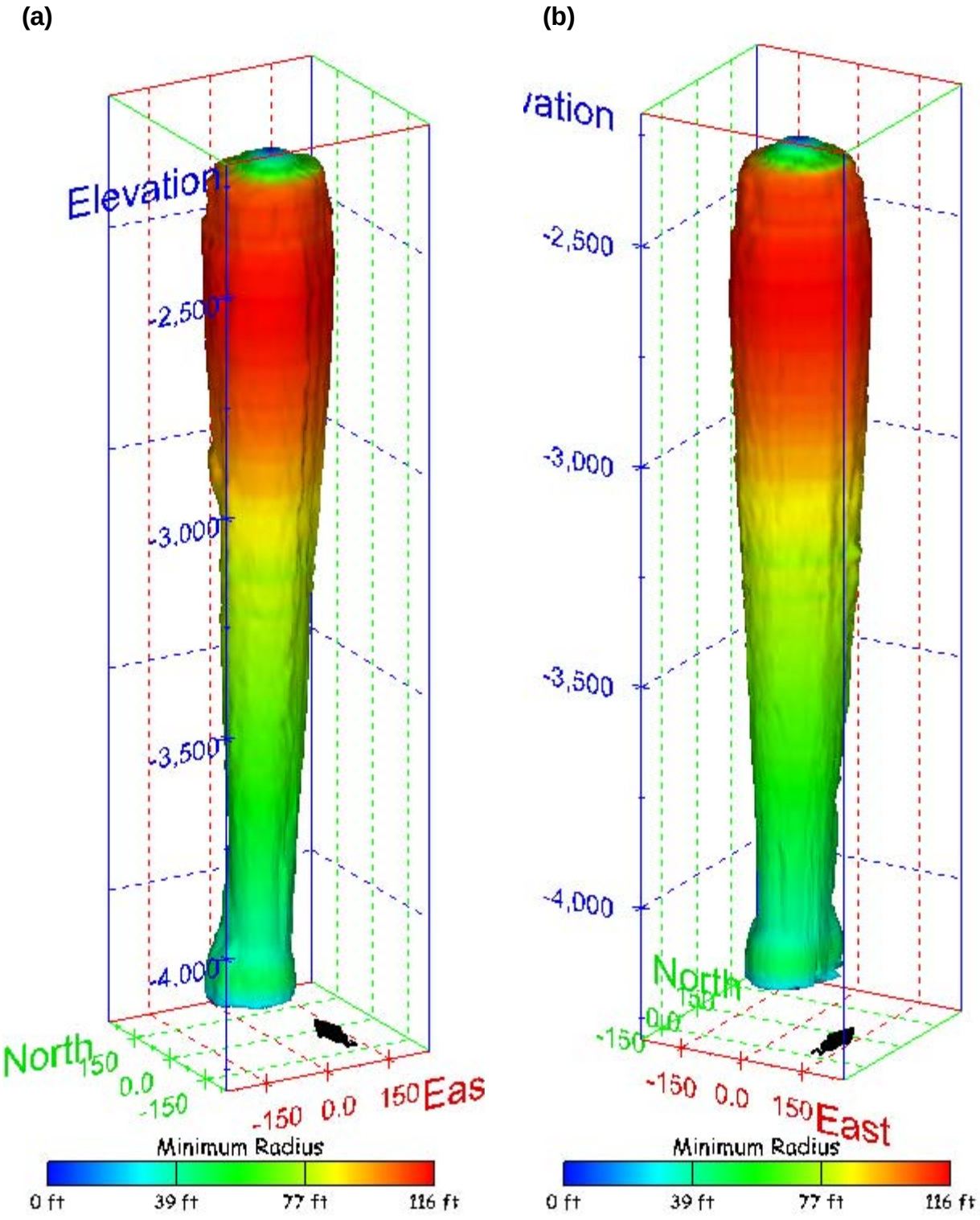

Figure 309. Sonar images of cavern BH-112, showing the geometry of the cavern colored by minimum radius. View from (a) azimuth 210°, elevation 20°; (b) azimuth 150°, elevation 20°.

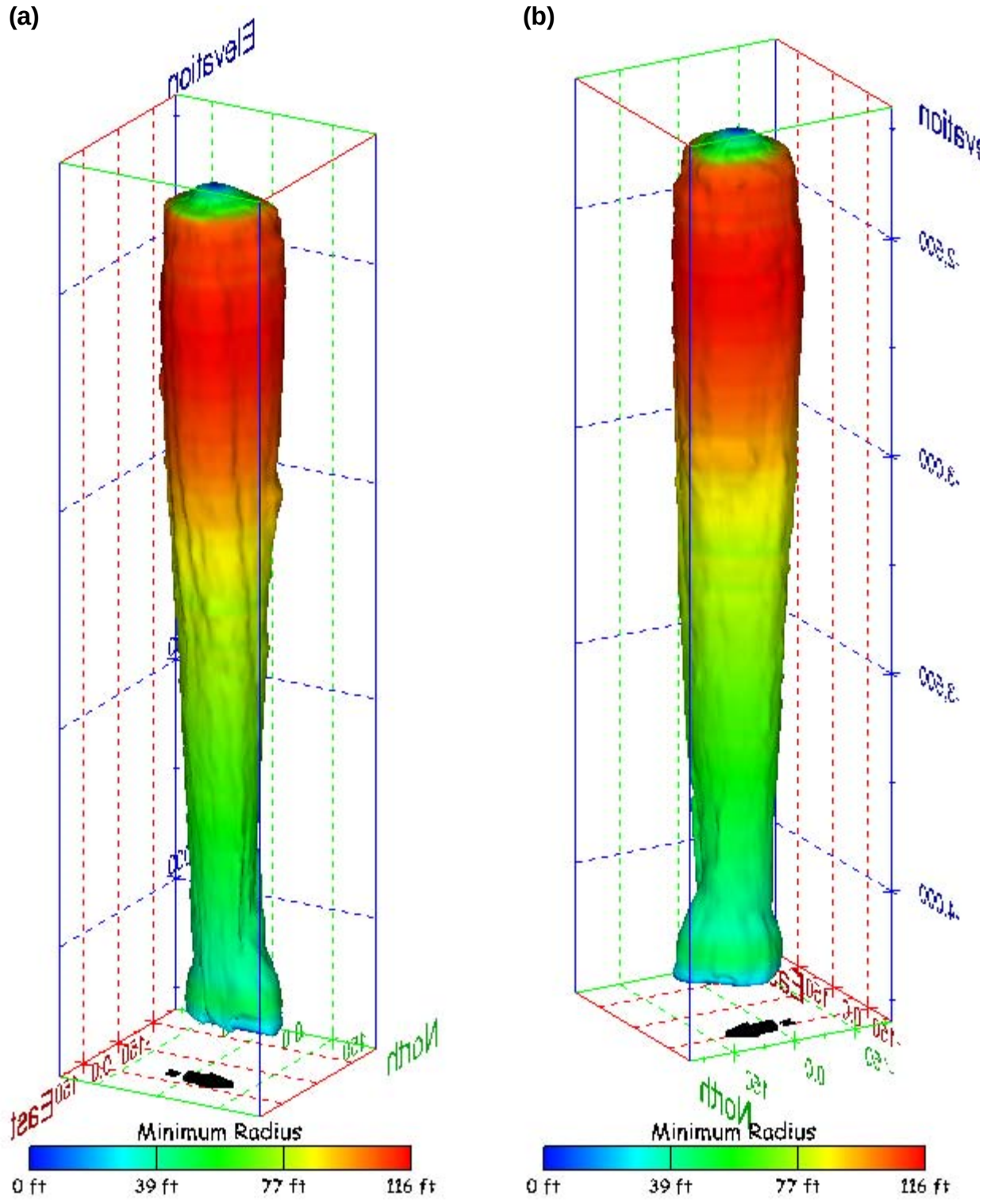

Figure 310. Sonar images of cavern BH-112, showing the geometry of the cavern colored by minimum radius. View from (a) azimuth 60°, elevation 20°; (b) azimuth 300°, elevation 20°.

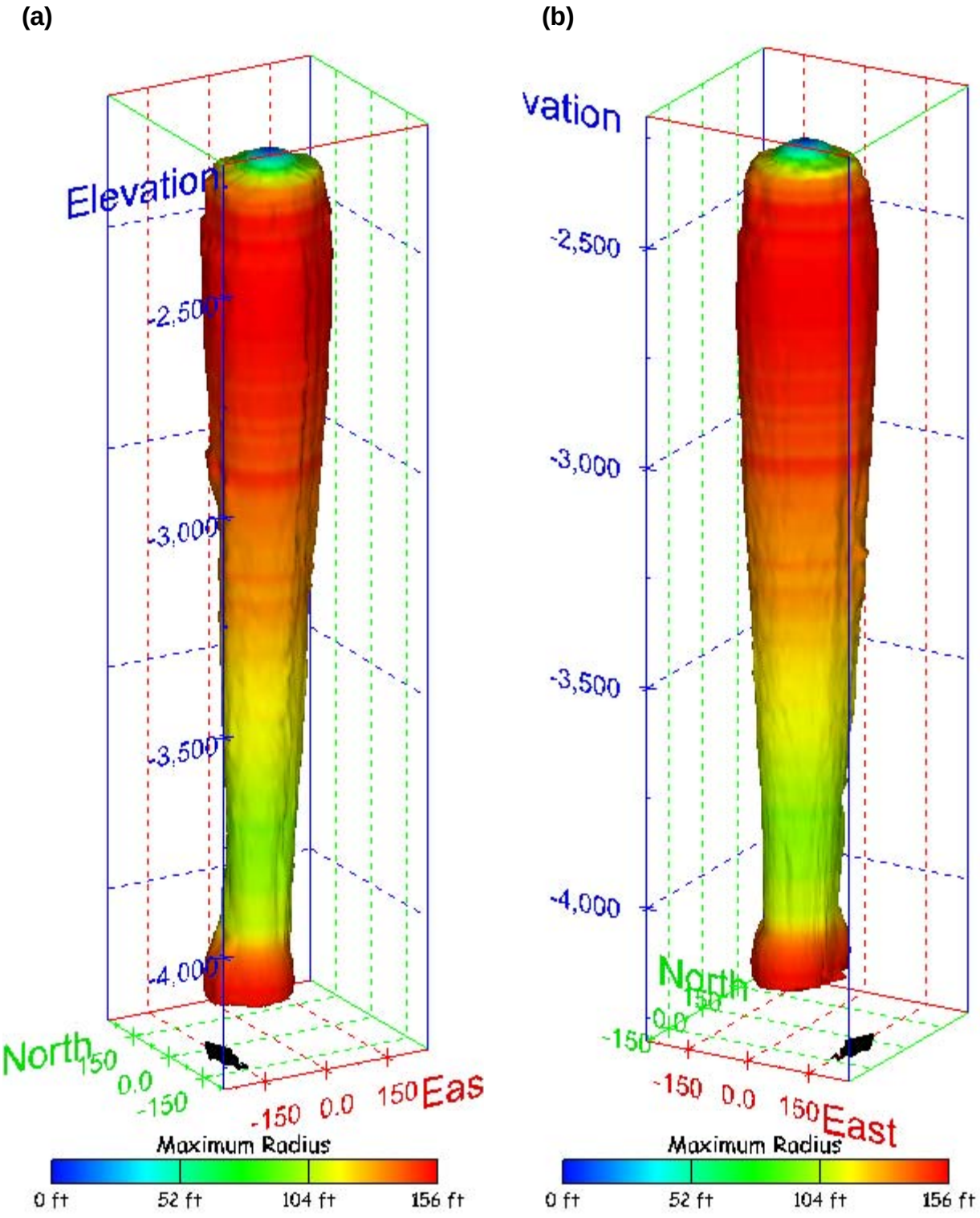

Figure 311. Sonar images of cavern BH-112, showing the geometry of the cavern colored by maximum radius. View from (a) azimuth 210°, elevation 20°; (b) azimuth 150°, elevation 20°.

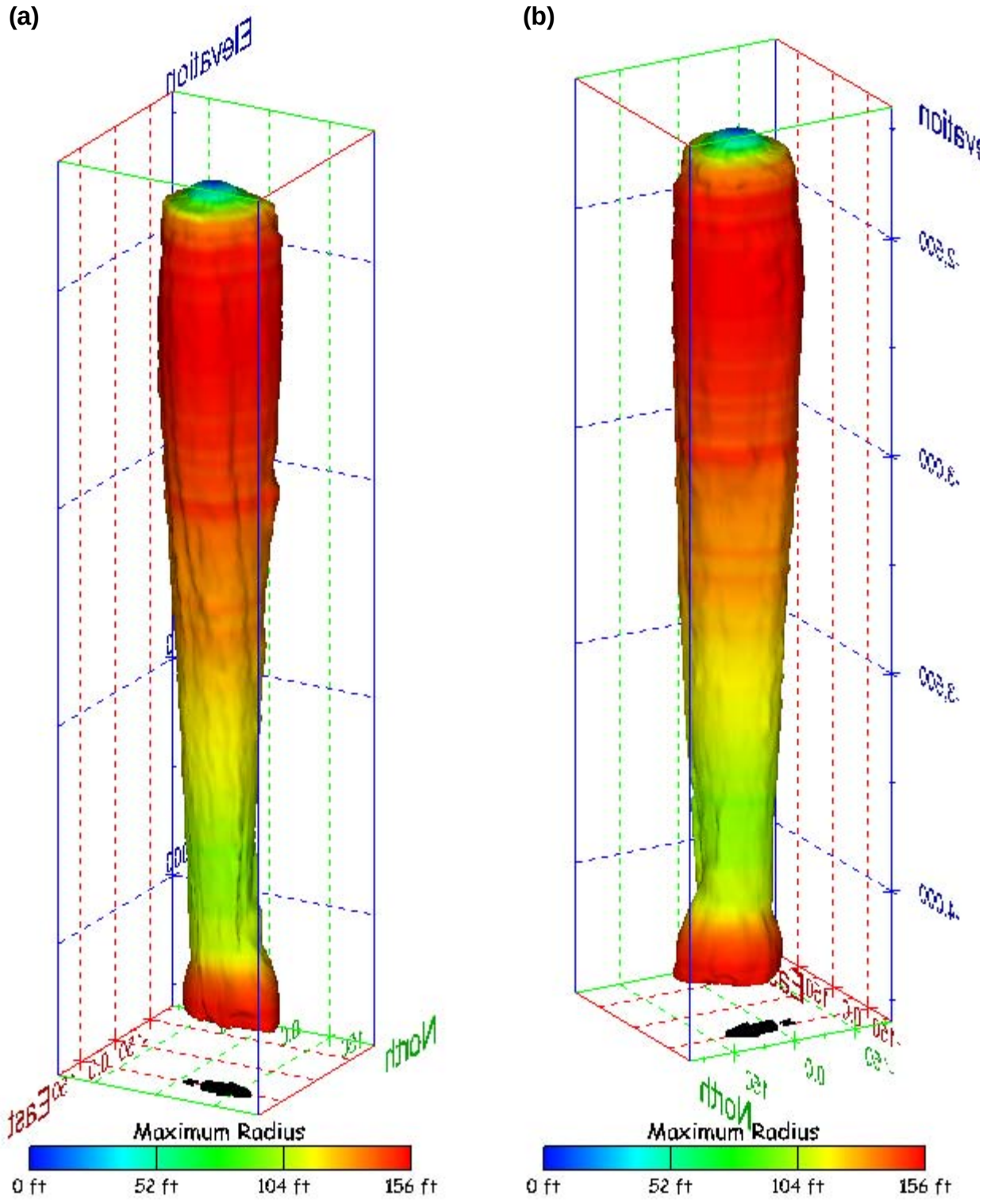

Figure 312. Sonar images of cavern BH-112, showing the geometry of the cavern colored by maximum radius. View from (a) azimuth 60°, elevation 20°; (b) azimuth 300°, elevation 20°.

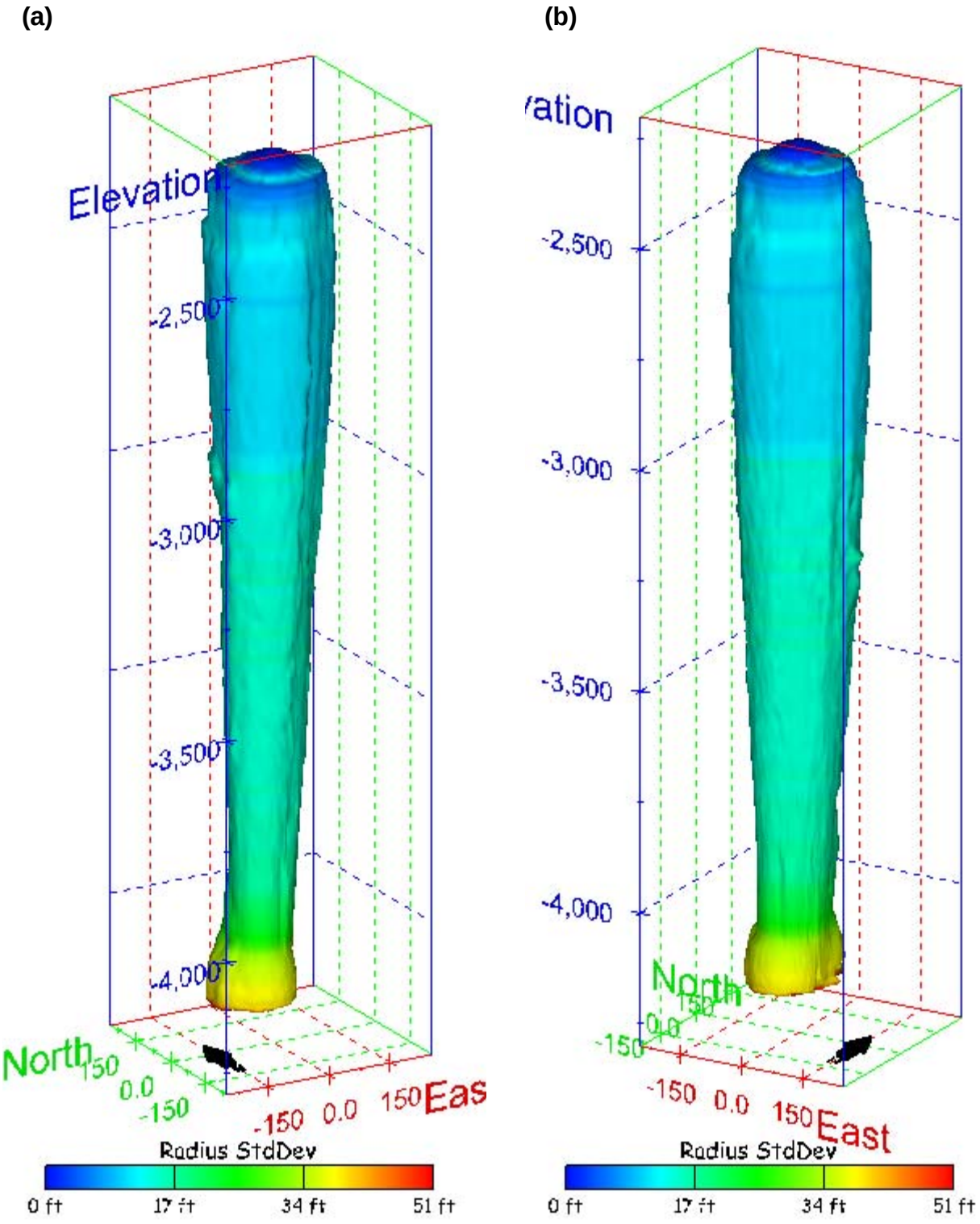

Figure 313. Sonar images of cavern BH-112, showing the geometry of the cavern colored by radius standard deviation. View from (a) azimuth 210°, elevation 20°; (b) azimuth 150°, elevation 20°.

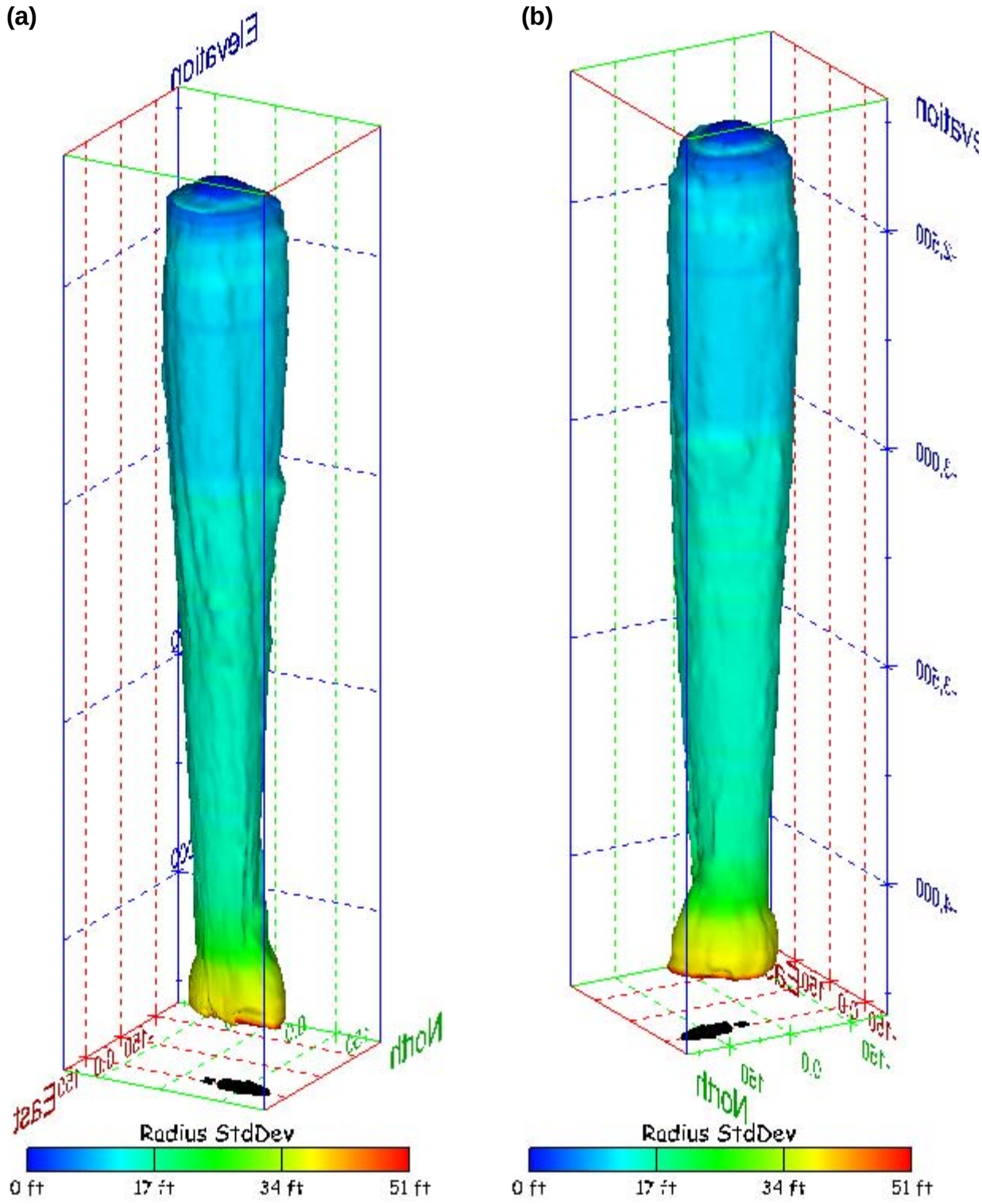

Figure 314. Sonar images of cavern BH-112, showing the geometry of the cavern colored by radius standard deviation. View from (a) azimuth 60°, elevation 20°; (b) azimuth 300°, elevation 20°.

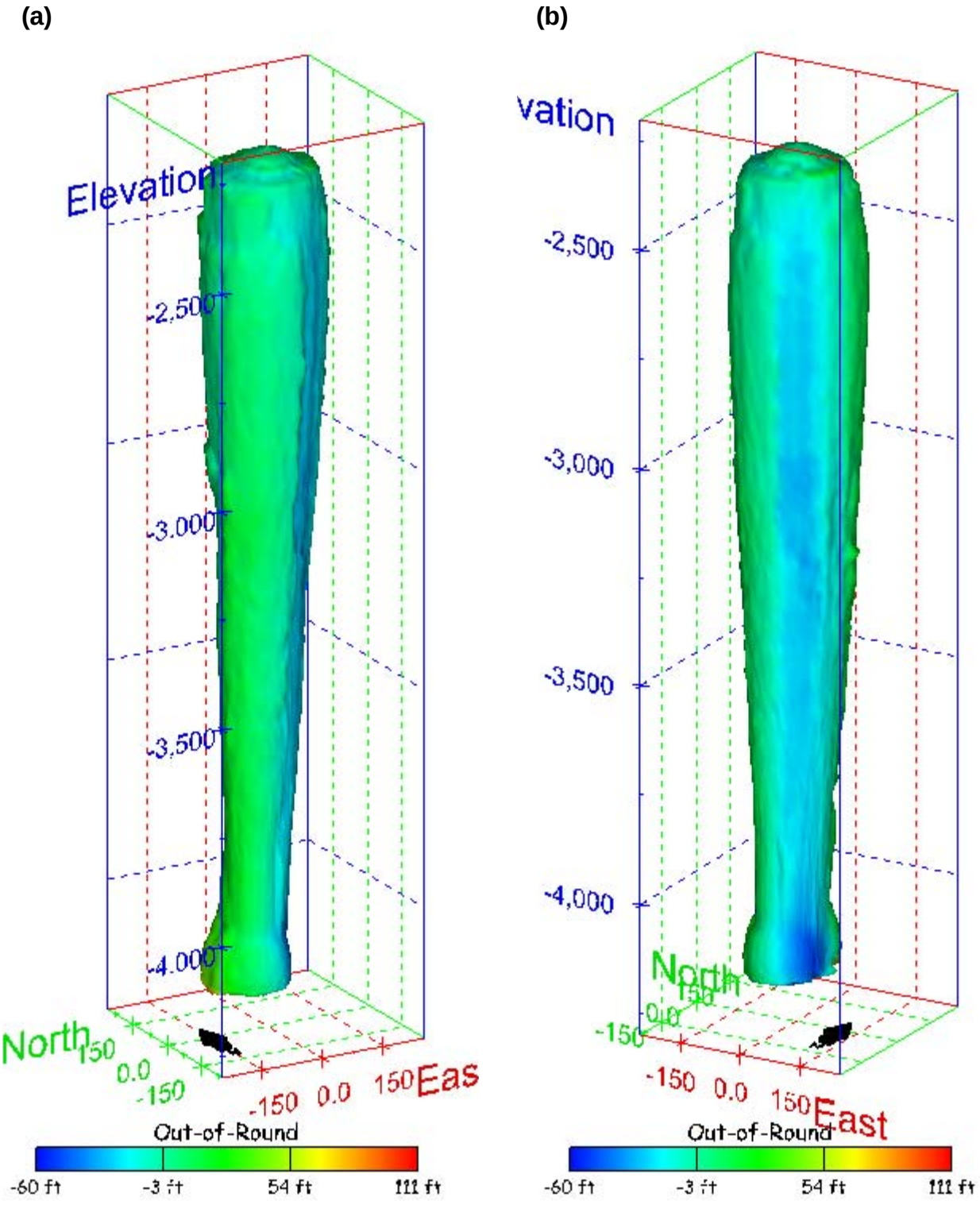

Figure 315. Sonar images of cavern BH-112, showing the geometry of the cavern colored by out-of-round distance. View from (a) azimuth 210°, elevation 20°; (b) azimuth 150°, elevation 20°.

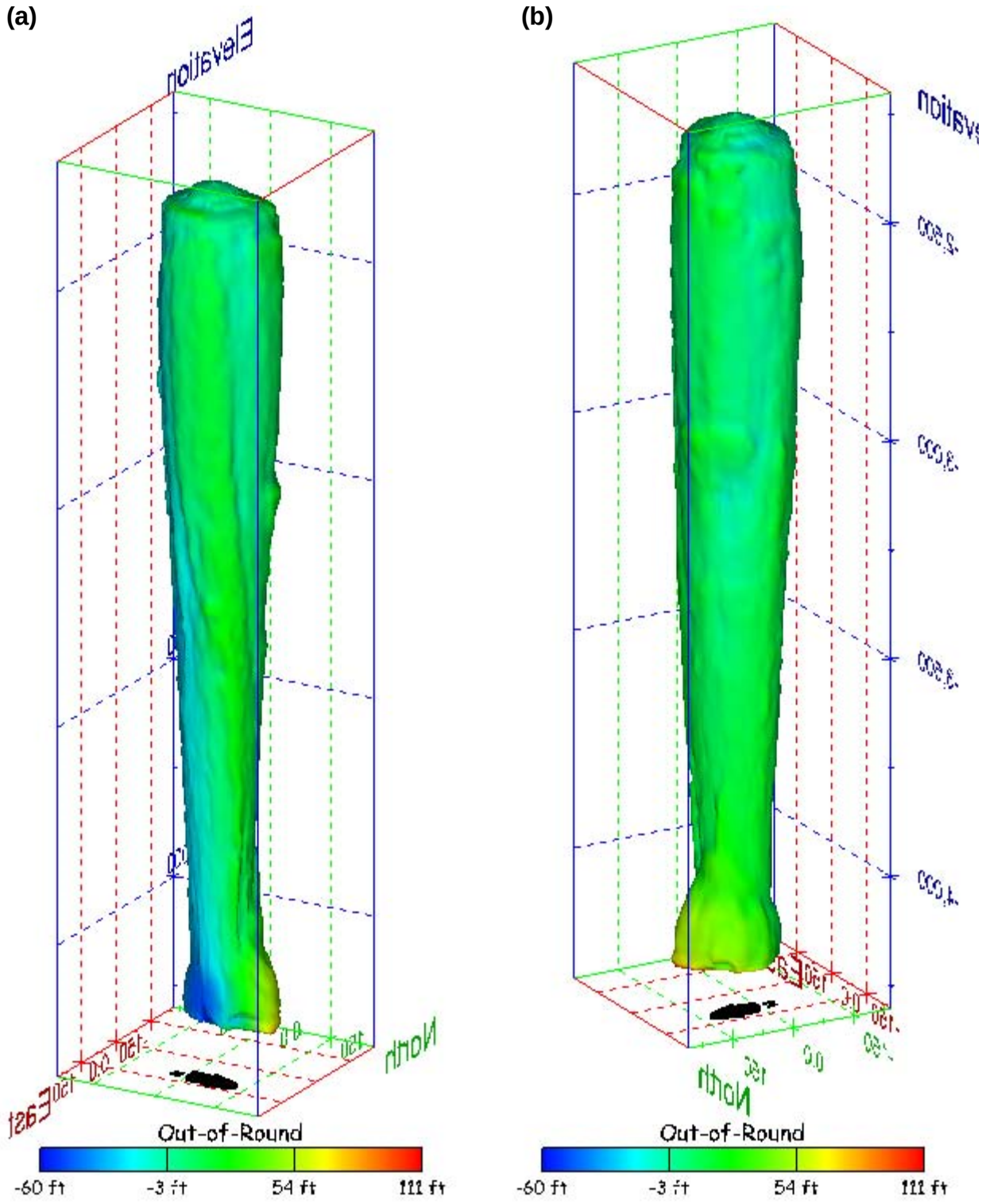

Figure 316. Sonar images of cavern BH-112, showing the geometry of the cavern colored by out-of-round distance. View from (a) azimuth 60°, elevation 20°; (b) azimuth 300°, elevation 20°.

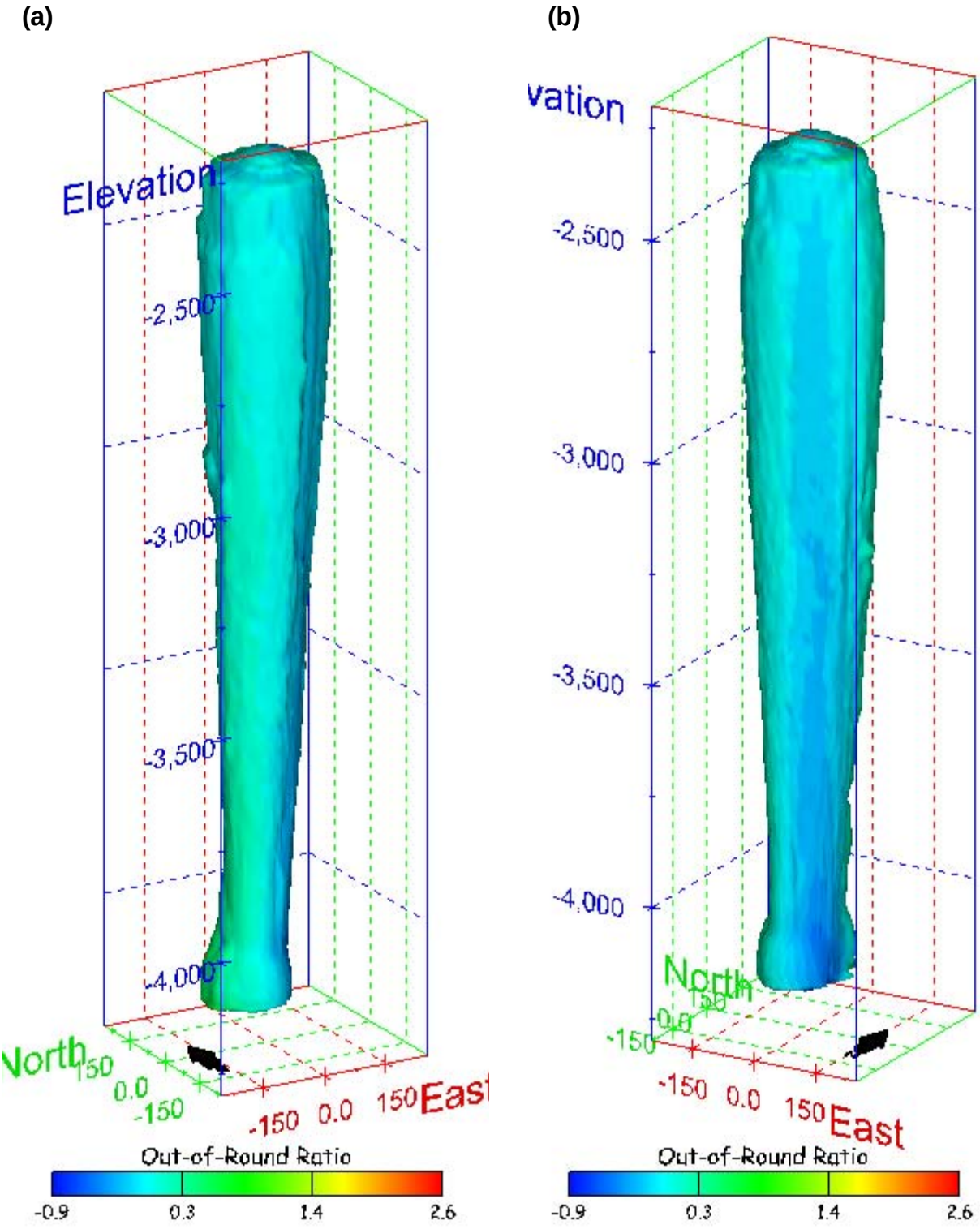

Figure 317. Sonar images of cavern BH-112, showing the geometry of the cavern colored by out-of-round ratio. View from (a) azimuth 210°, elevation 20°; (b) azimuth 150°, elevation 20°.

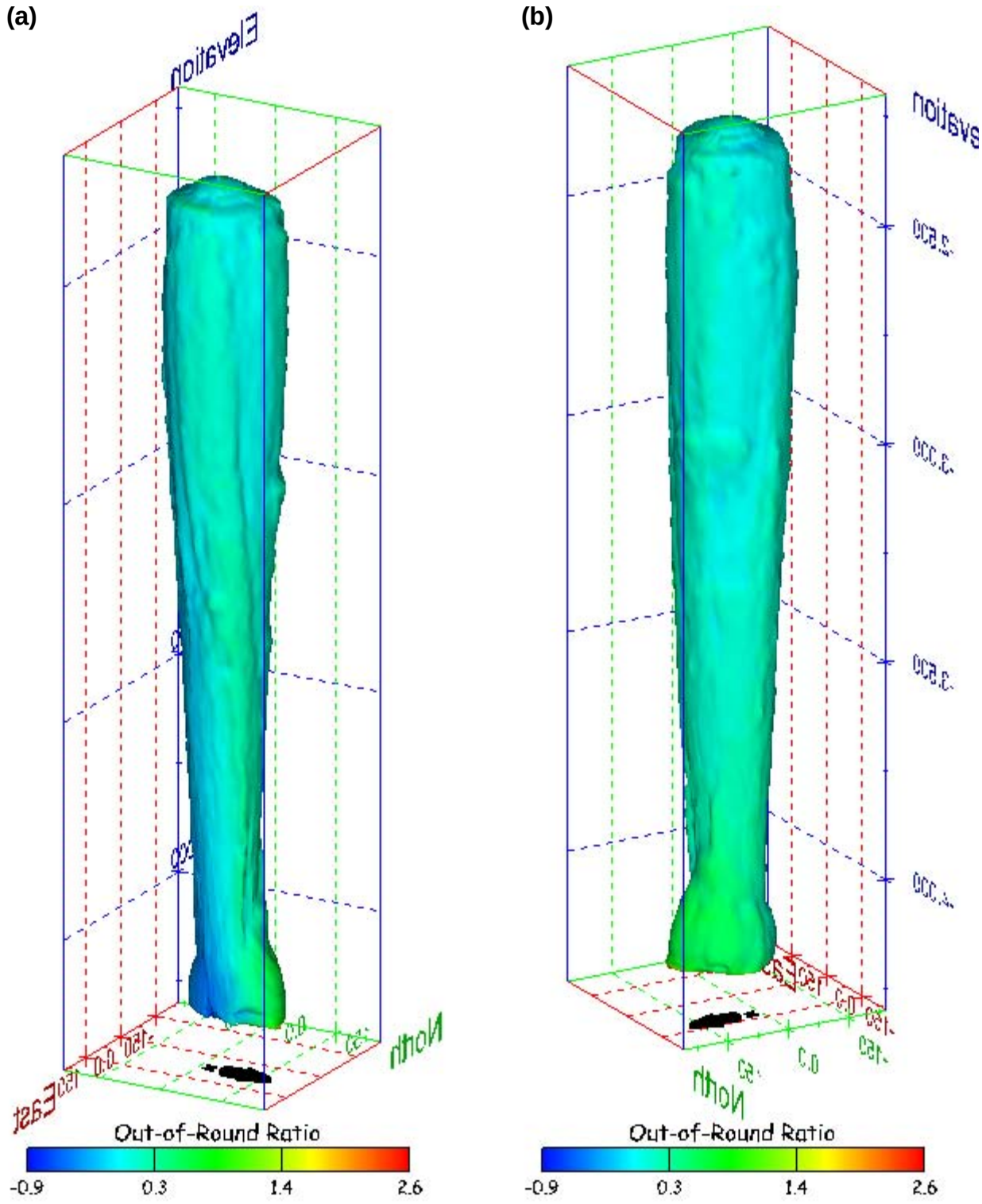

Figure 318. Sonar images of cavern BH-112, showing the geometry of the cavern colored by out-of-round ratio. View from (a) azimuth 60°, elevation 20°; (b) azimuth 300°, elevation 20°.

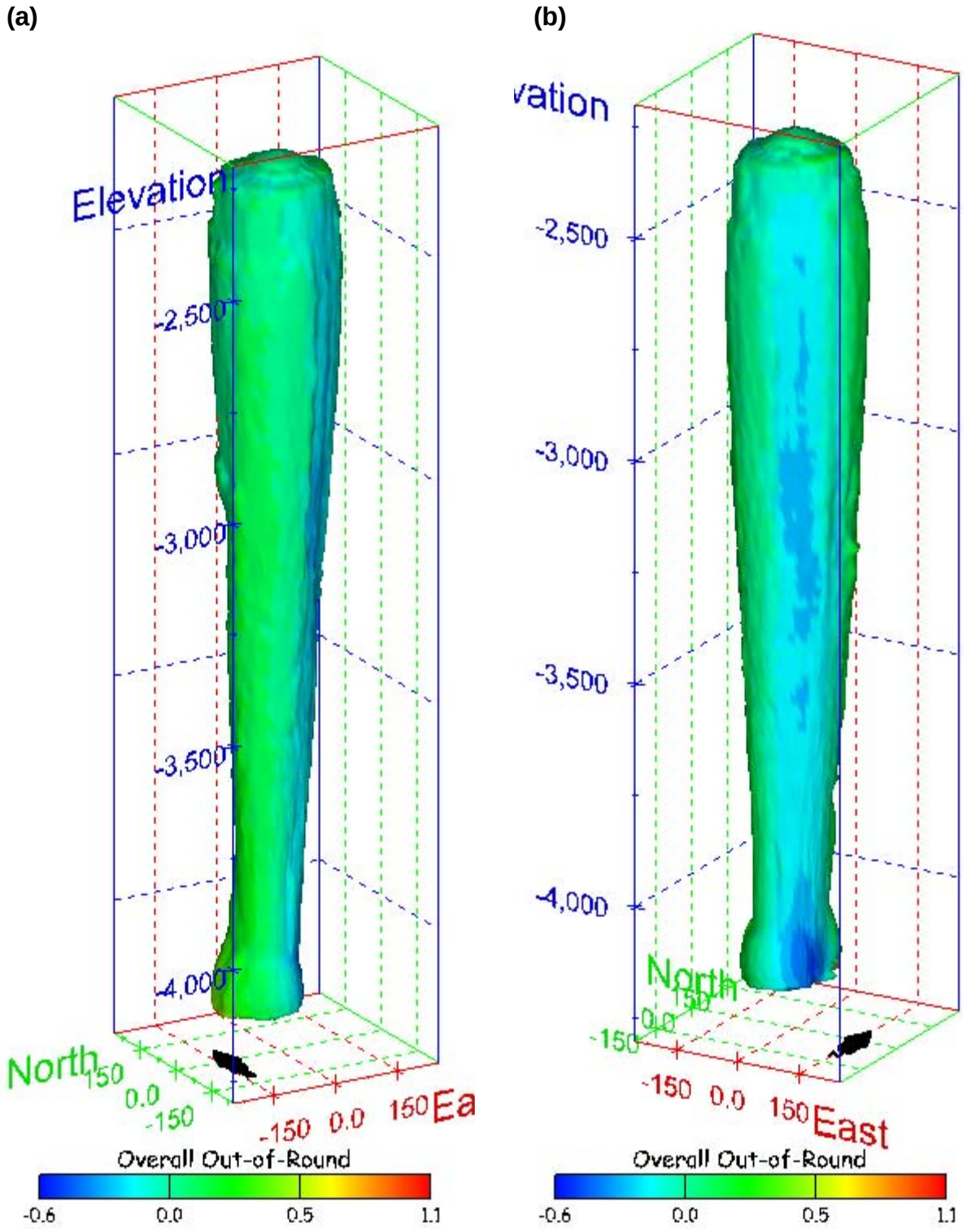

Figure 319. Sonar images of cavern BH-112, showing the geometry of the cavern colored by overall out-of-round ratio. View from (a) azimuth 210°, elevation 20°; (b) azimuth 150°, elevation 20°.

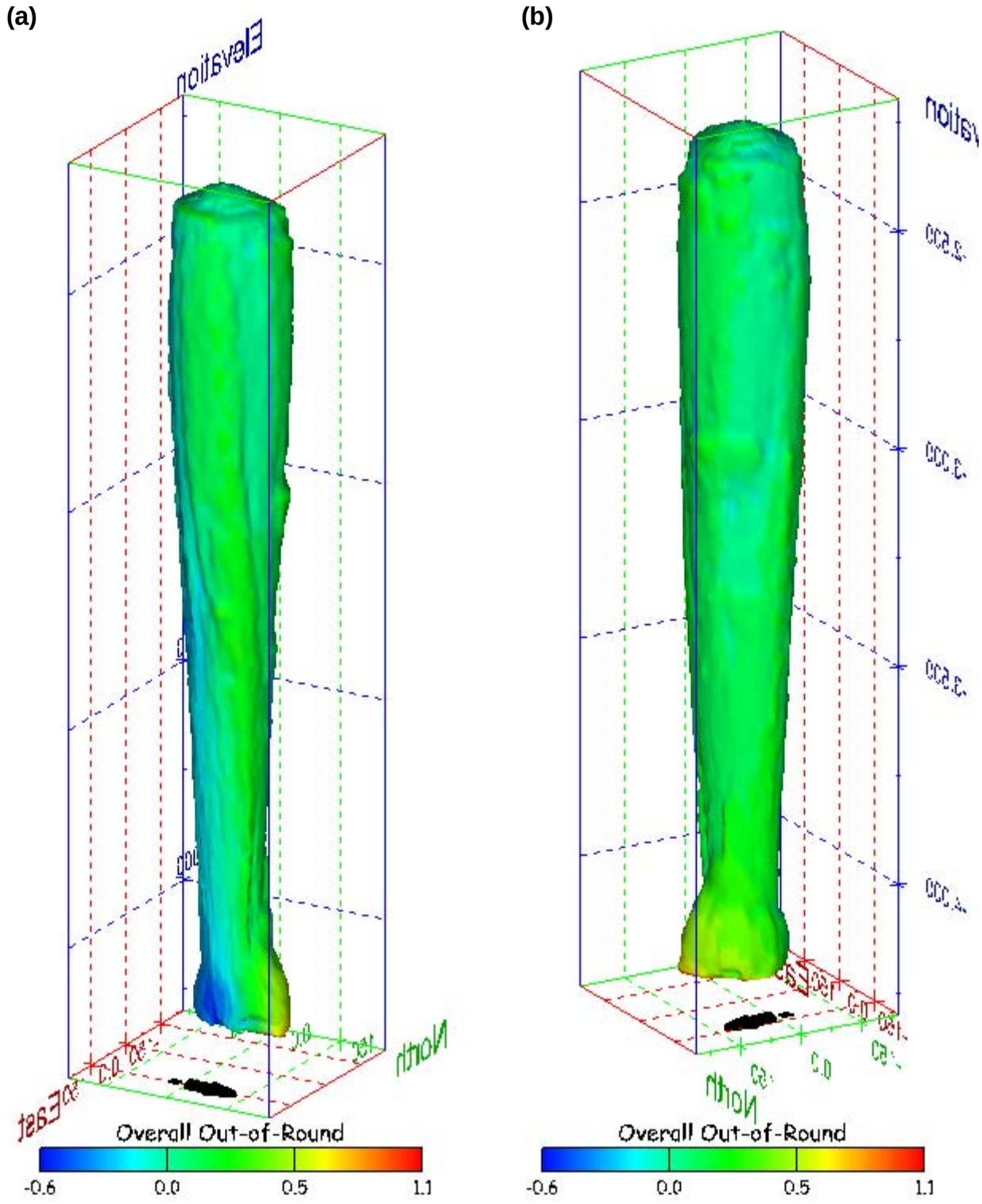

Figure 320. Sonar images of cavern BH-112, showing the geometry of the cavern colored by overall out-of-round ratio. View from (a) azimuth 60°, elevation 20°; (b) azimuth 300°, elevation 20°.

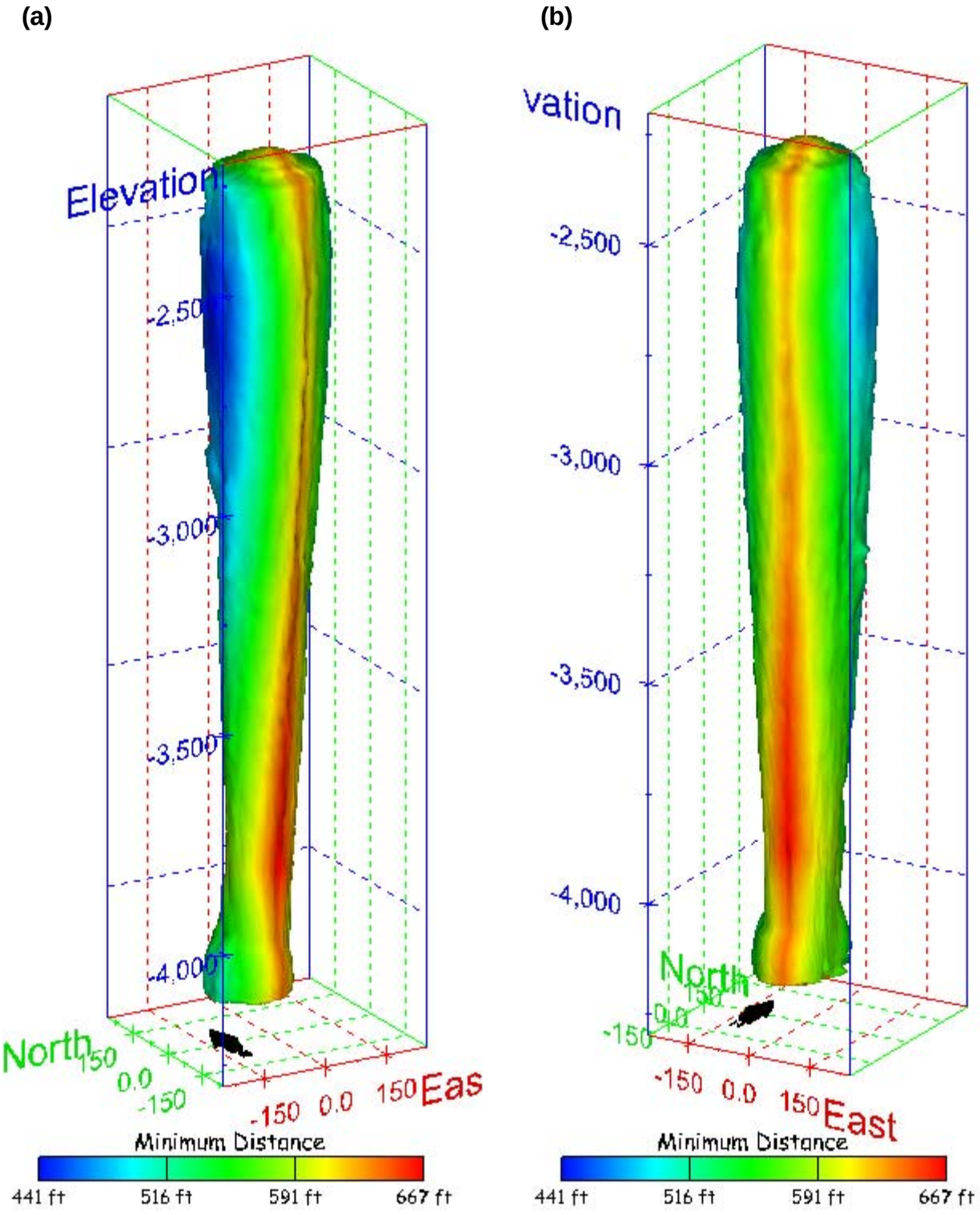

Figure 321. Sonar images of cavern BH-112, showing the geometry of the cavern colored by the minimum distance to the nearest neighboring cavern. View from (a) azimuth 210°, elevation 20°; (b) azimuth 150°, elevation 20°.

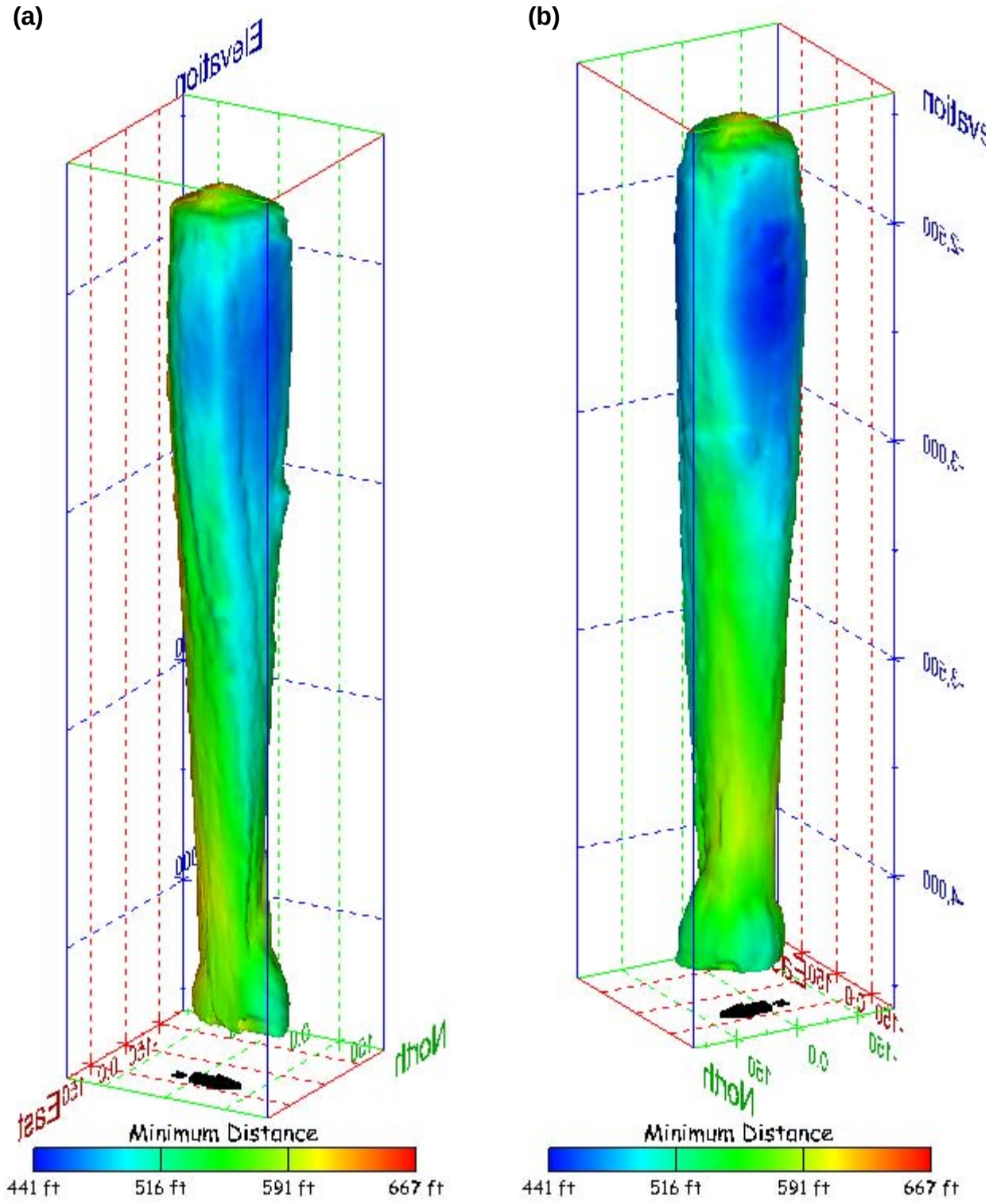

Figure 322. Sonar images of cavern BH-112, showing the geometry of the cavern colored by minimum distance to the nearest neighboring cavern. View from (a) azimuth 60°, elevation 20°; (b) azimuth 300°, elevation 20°.

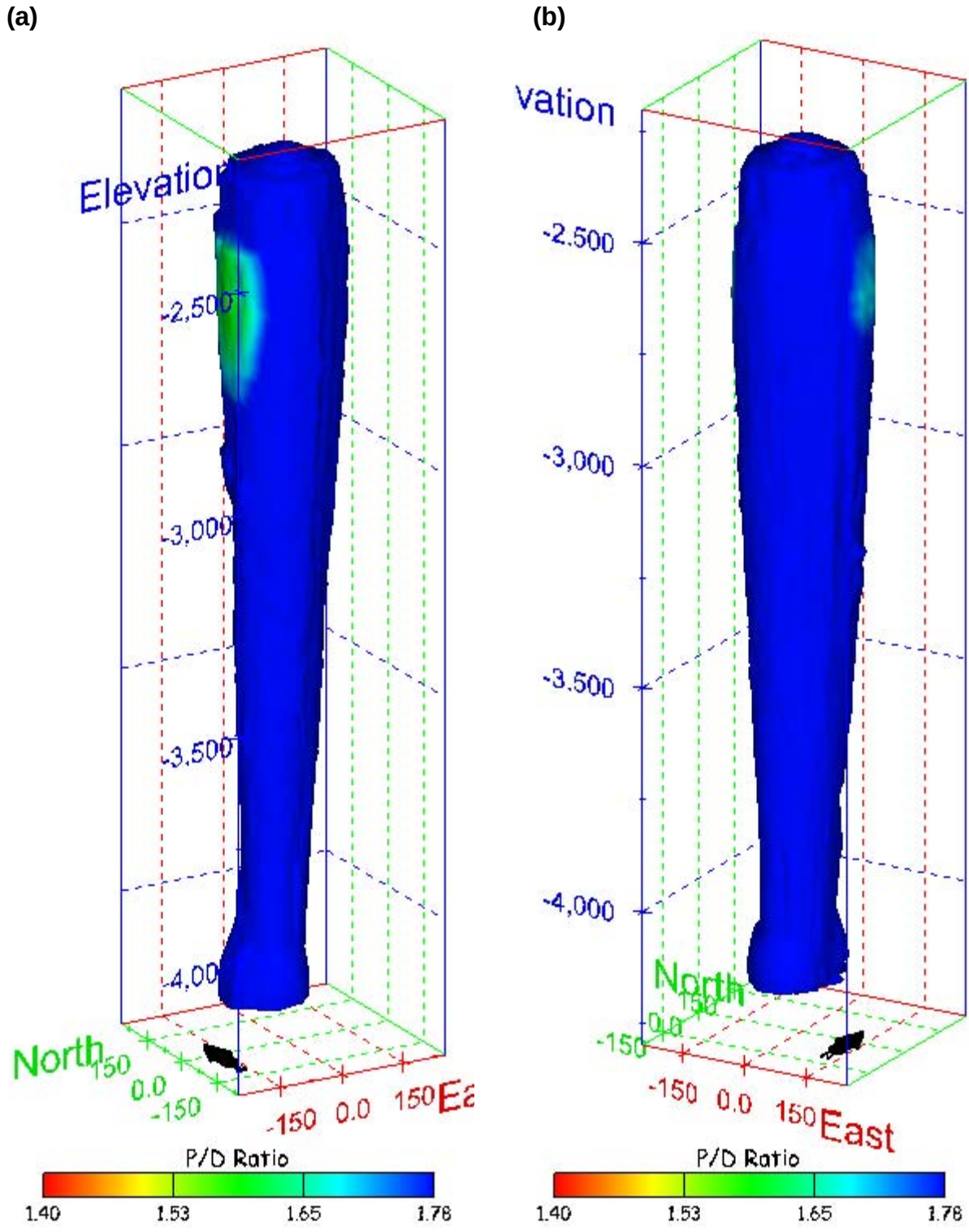

Figure 323. Sonar images of cavern BH-112, showing the geometry of the cavern colored by three-dimensional pillar-to-diameter ratio. View from (a) azimuth 210°, elevation 20°; (b) azimuth 150°, elevation 20°.

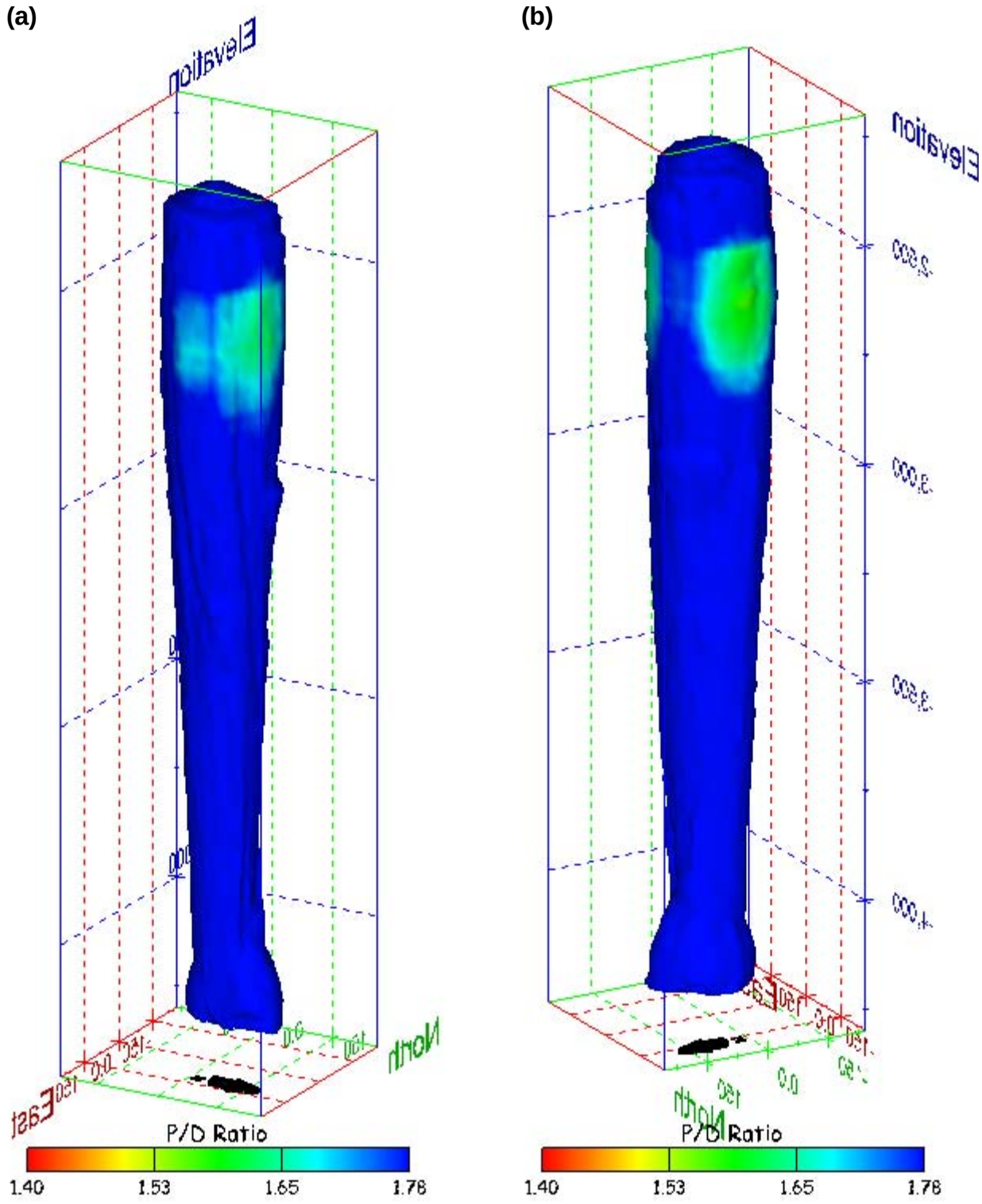

Figure 324. Sonar images of cavern BH-112, showing the geometry of the cavern colored by three-dimensional pillar-to-diameter ratio. View from (a) azimuth 60°, elevation 20°; (b) azimuth 300°, elevation 20°.

No Sonic Velocity Data Available for Socon Surveys

Figure 325. Sonar image of cavern BH-112, showing the geometry of the cavern colored by the reported velocity of sound on the survey date of April 2005. View from due south, elevation zero.

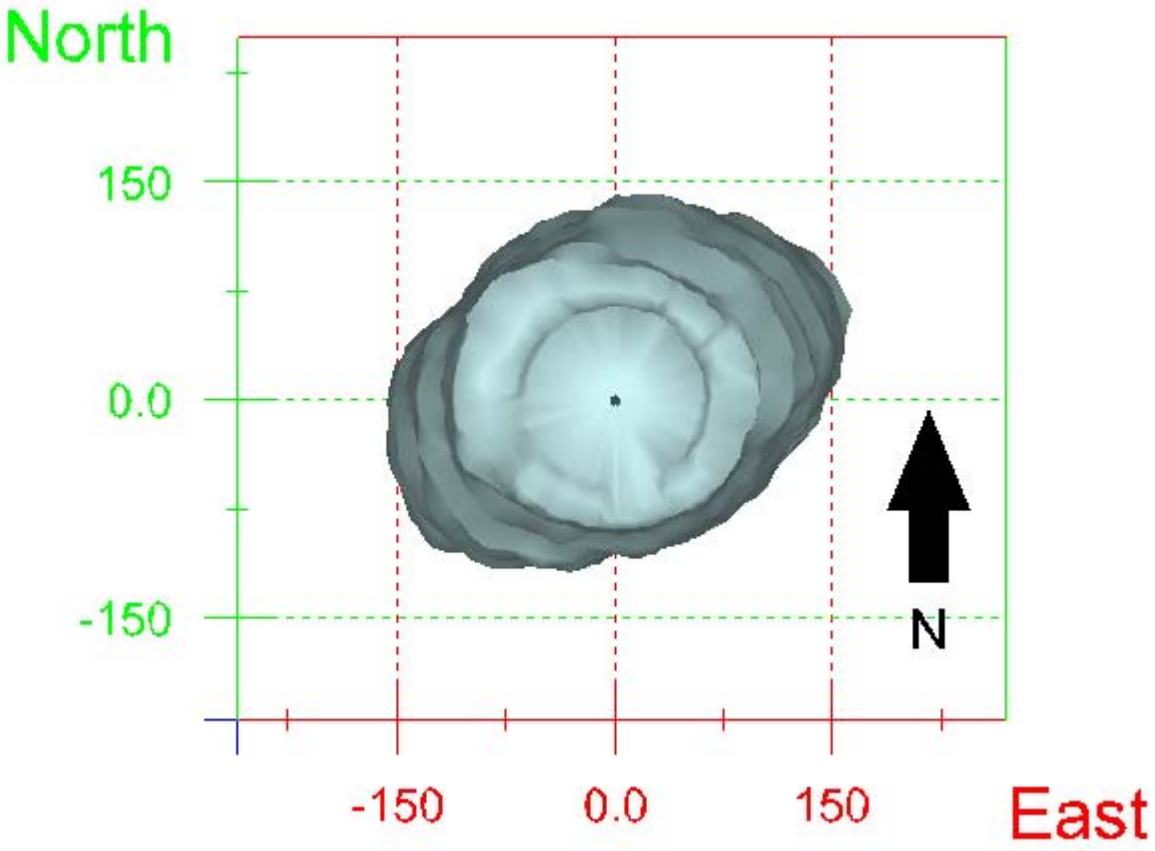

Figure 326. Map view sonar image of cavern BH-113, showing the basic geometry of the cavern. Grid squares represent 150 ft.

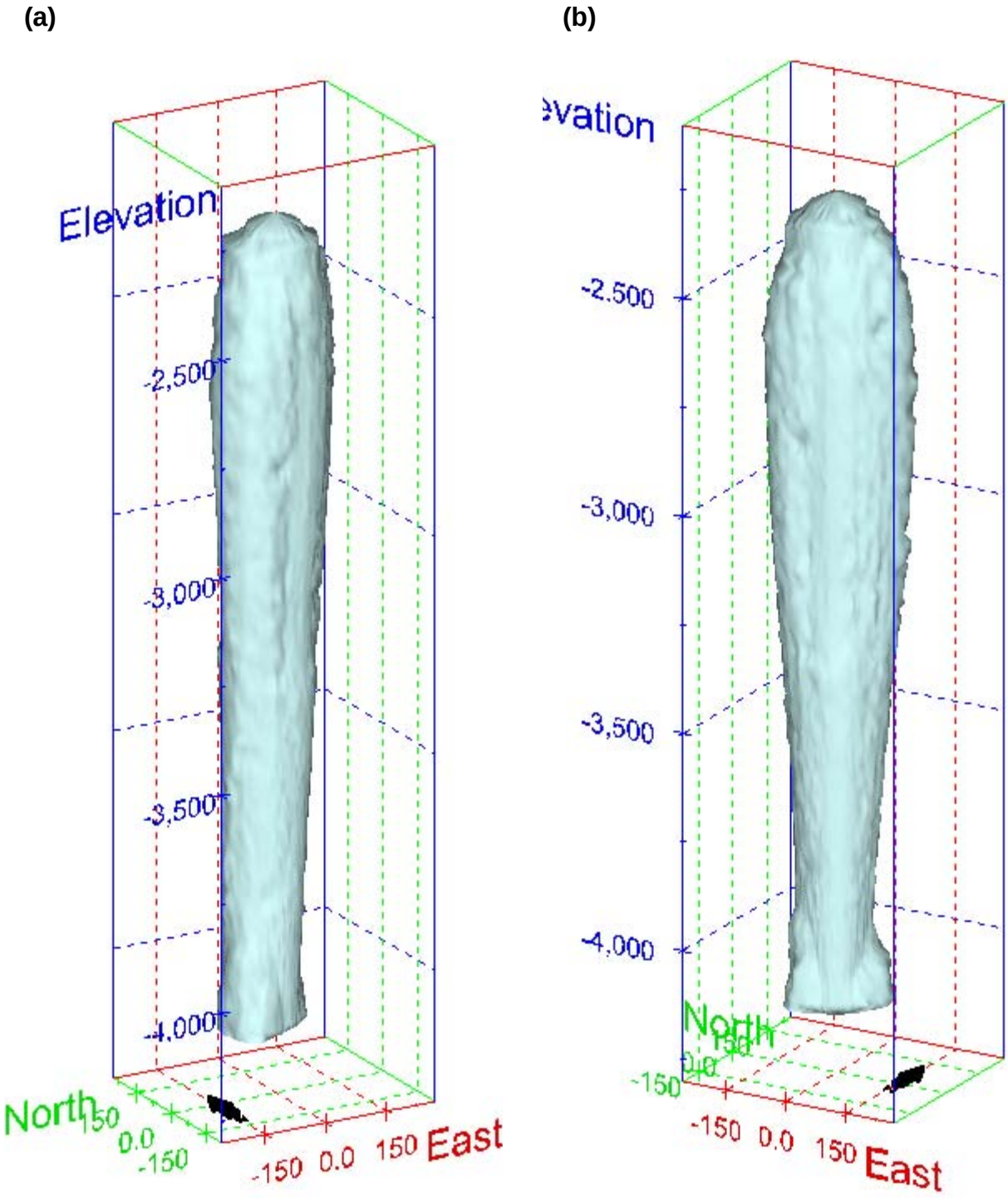

Figure 327. Sonar images of cavern BH-113, showing the basic geometric shape of the cavern. View from (a) azimuth 210°, elevation 20°; (b) azimuth 150°, elevation 20°.

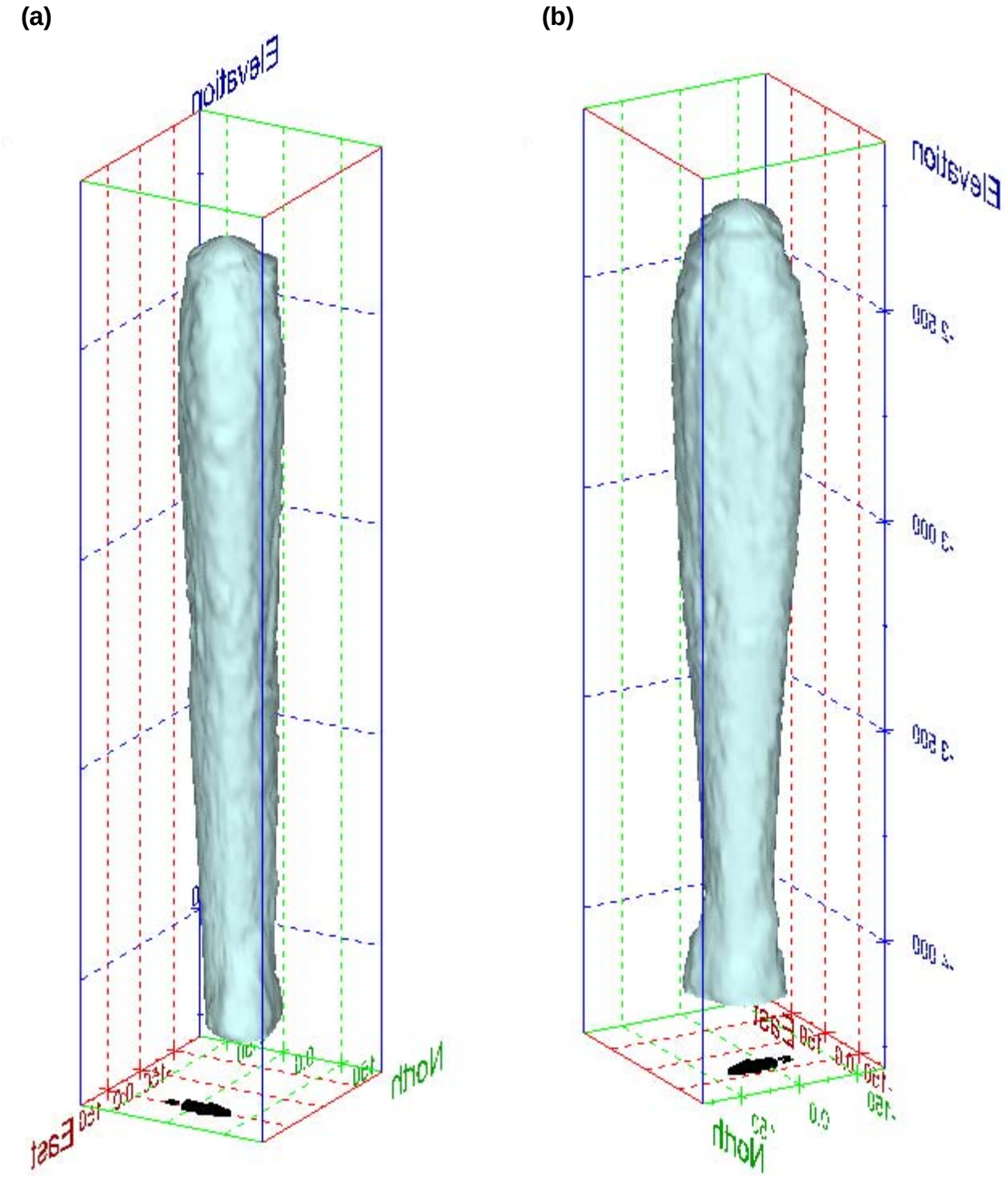

Figure 328. Sonar images of cavern BH-113, showing the basic geometric shape of the cavern. View from (a) azimuth 60°, elevation 20°; (b) azimuth 300°, elevation 20°.

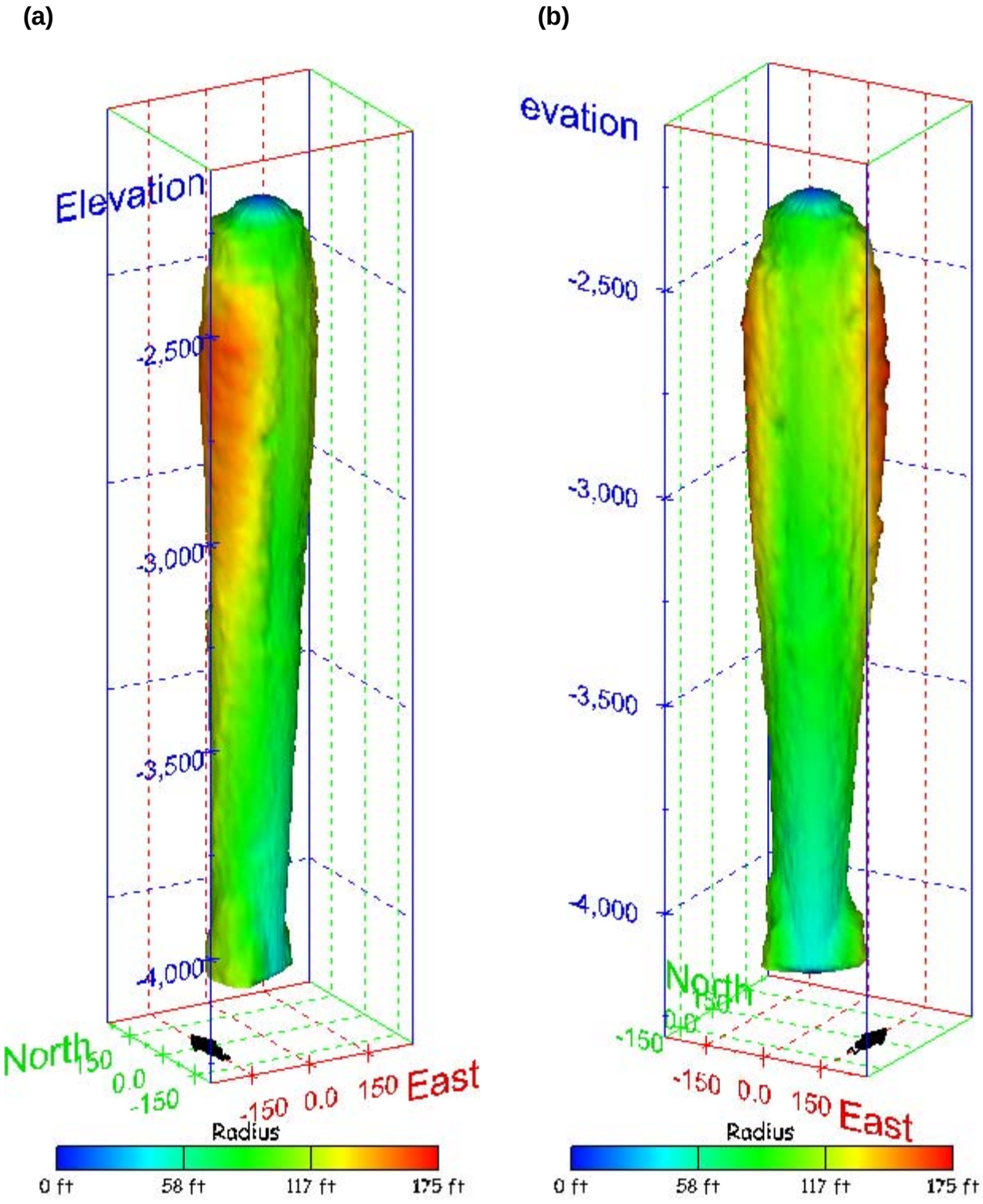

Figure 329. Sonar images of cavern BH-113, showing the geometry of the cavern colored by measured radius. View from (a) azimuth 210°, elevation 20°; (b) azimuth 150°, elevation 20°.

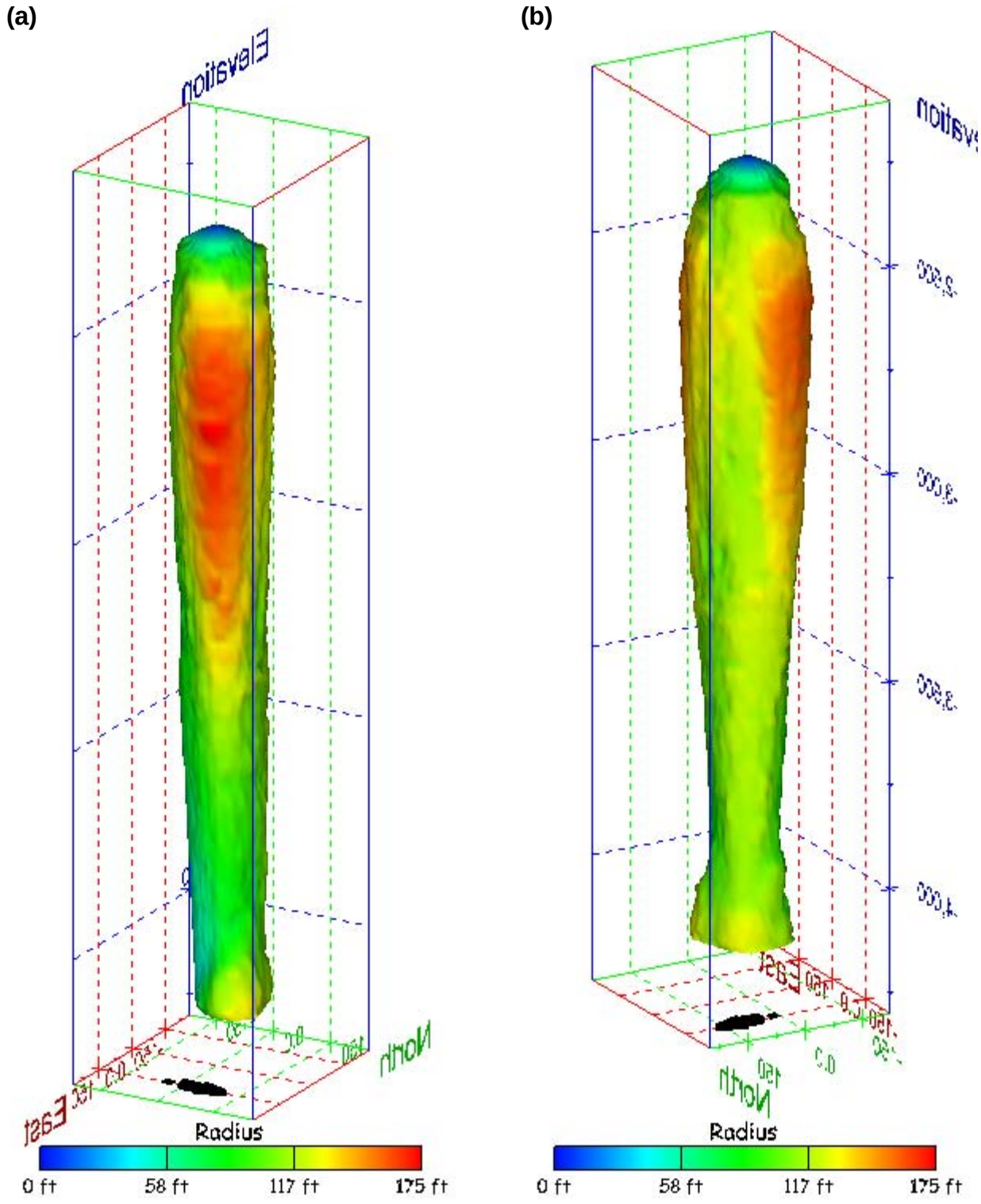

Figure 330. Sonar images of cavern BH-113, showing the geometry of the cavern colored by measured radius. View from (a) azimuth 60°, elevation 20°; (b) azimuth 300°, elevation 20°.

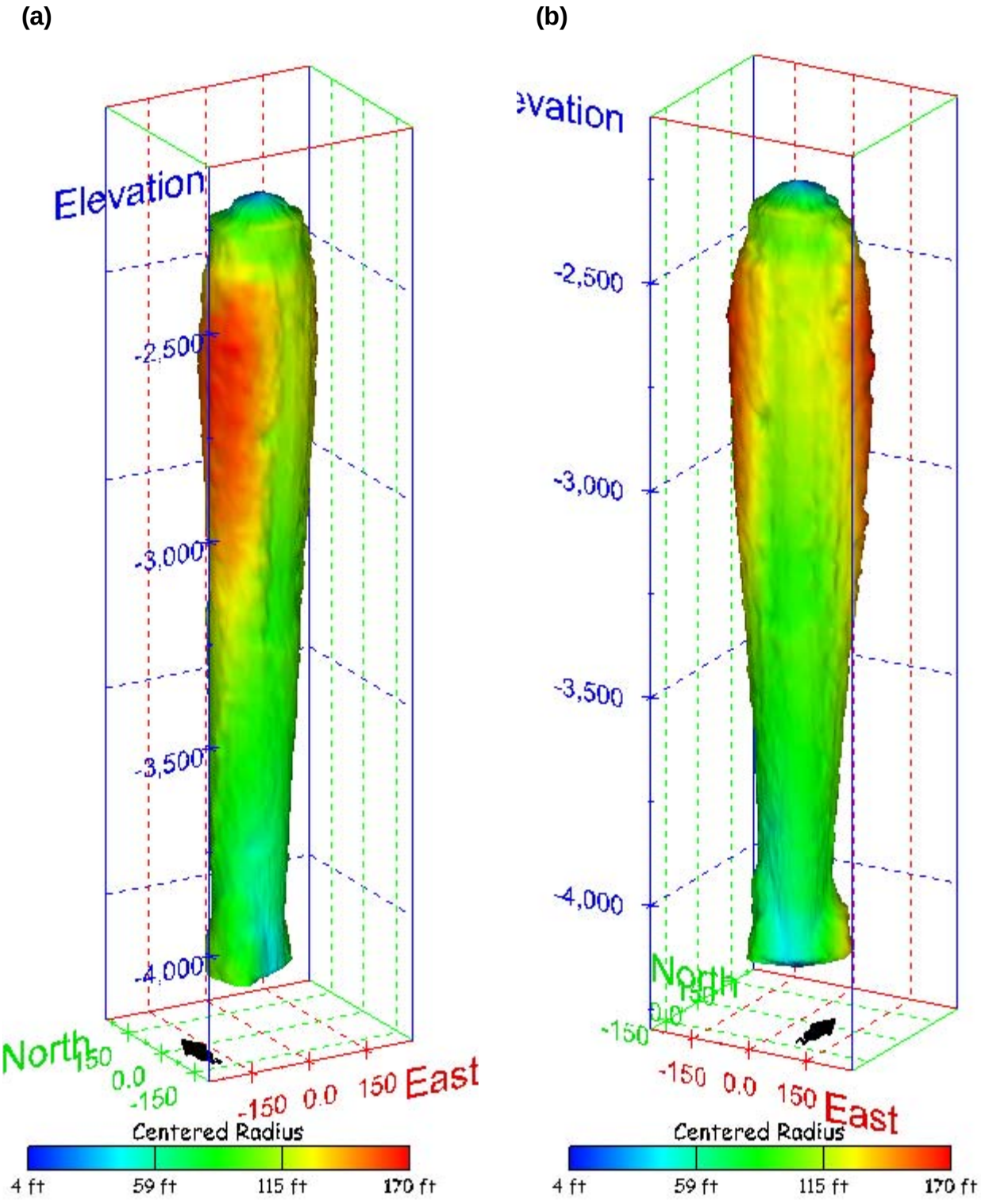

Figure 331. Sonar images of cavern BH-113, showing the geometry of the cavern colored by centered radius. View from (a) azimuth 210°, elevation 20°; (b) azimuth 150°, elevation 20°.

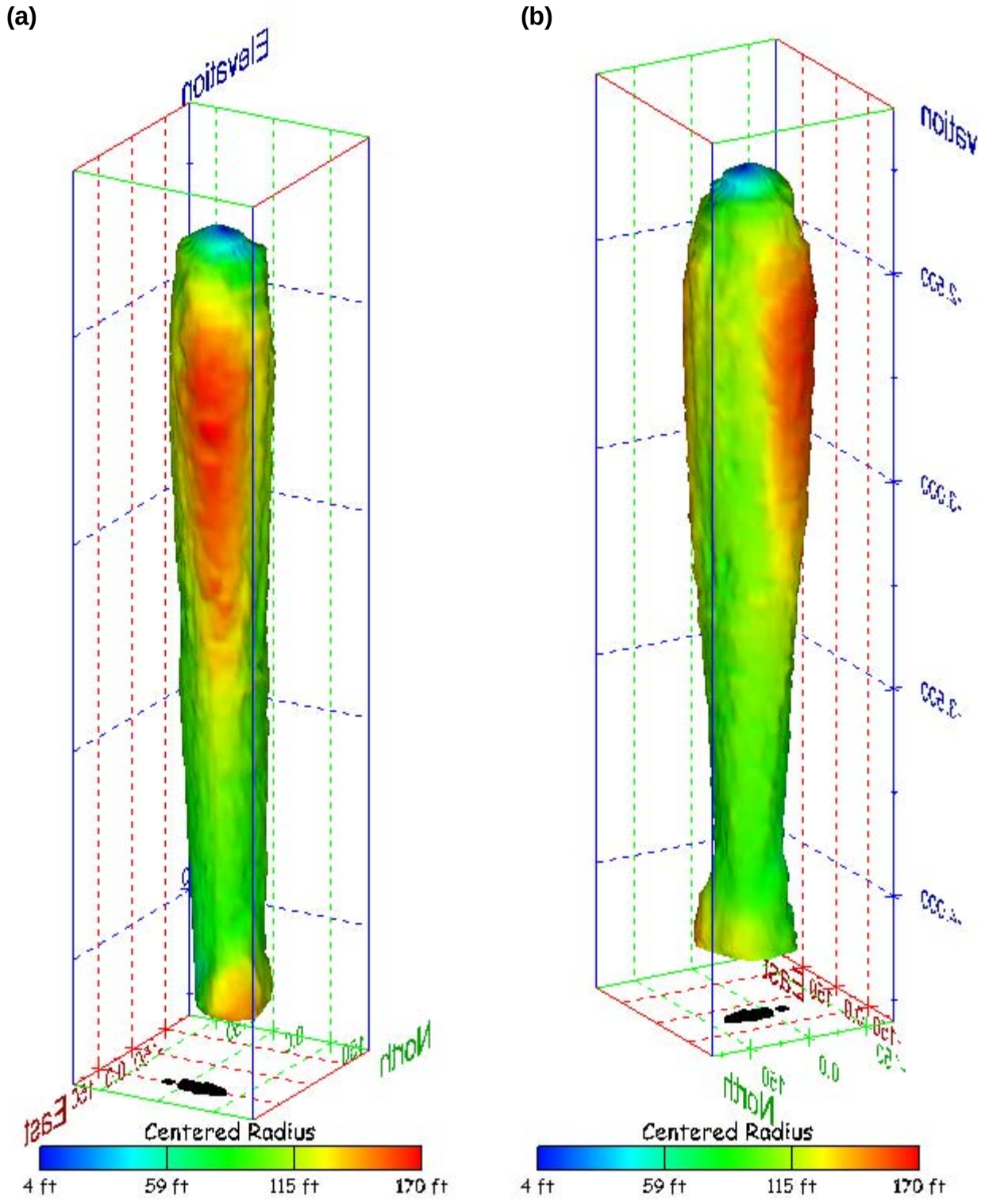

Figure 332. Sonar images of cavern BH-113, showing the geometry of the cavern colored by centered radius. View from (a) azimuth 60°, elevation 20°; (b) azimuth 300°, elevation 20°.

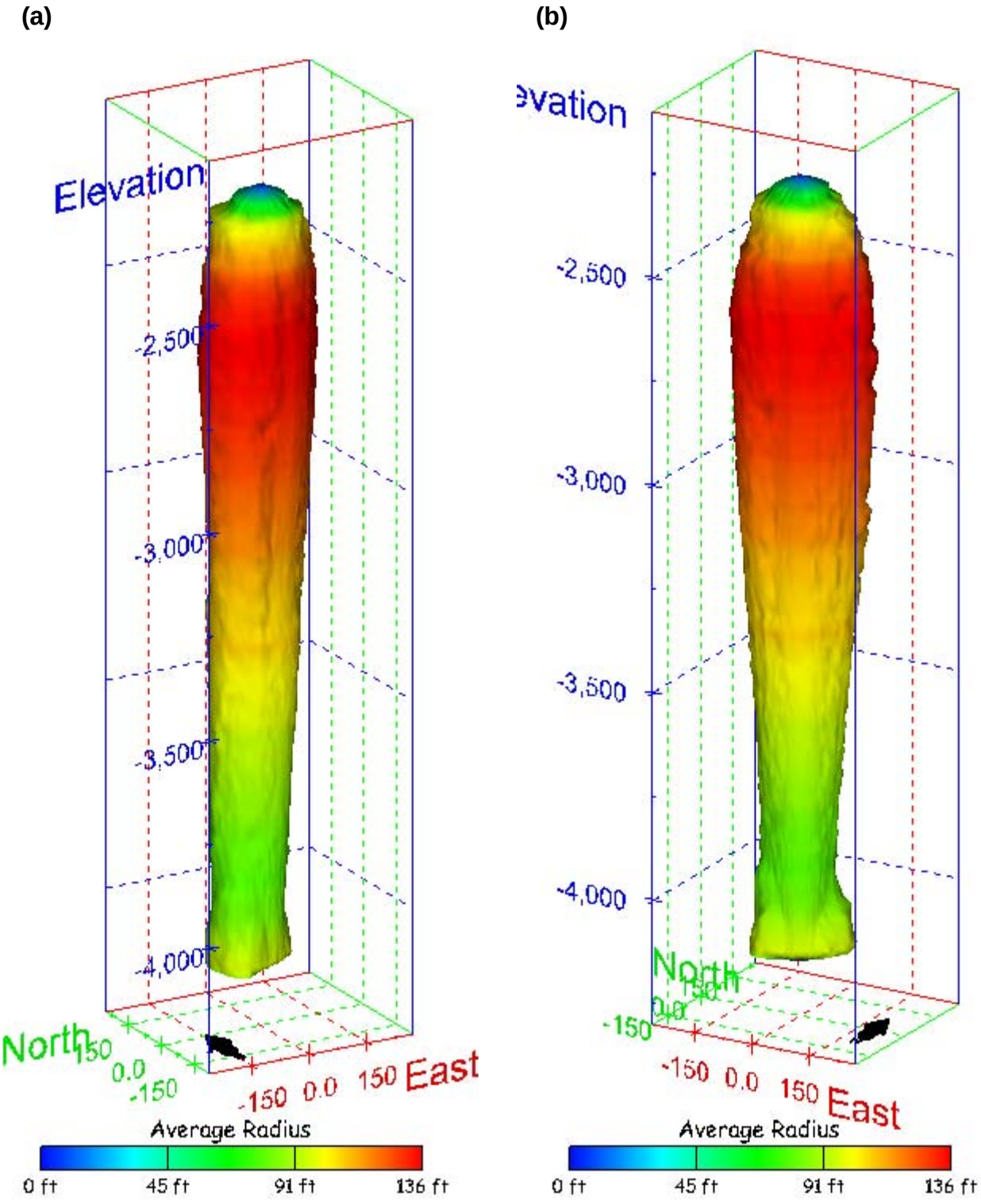

Figure 333. Sonar images of cavern BH-113, showing the geometry of the cavern colored by average radius. View from (a) azimuth 210°, elevation 20°; (b) azimuth 150°, elevation 20°.

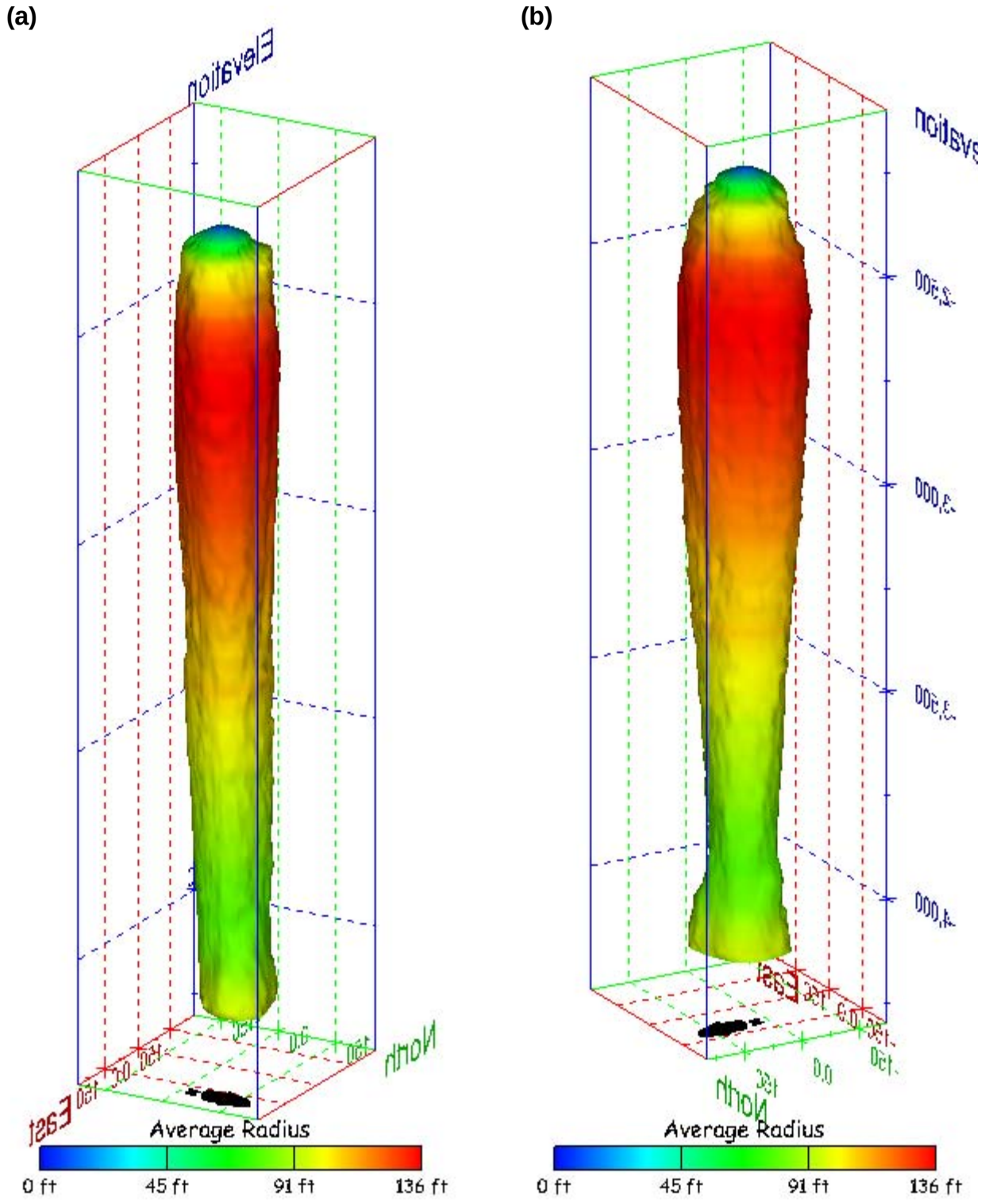

Figure 334. Sonar images of cavern BH-113, showing the geometry of the cavern colored by average radius. View from (a) azimuth 60°, elevation 20°; (b) azimuth 300°, elevation 20°.

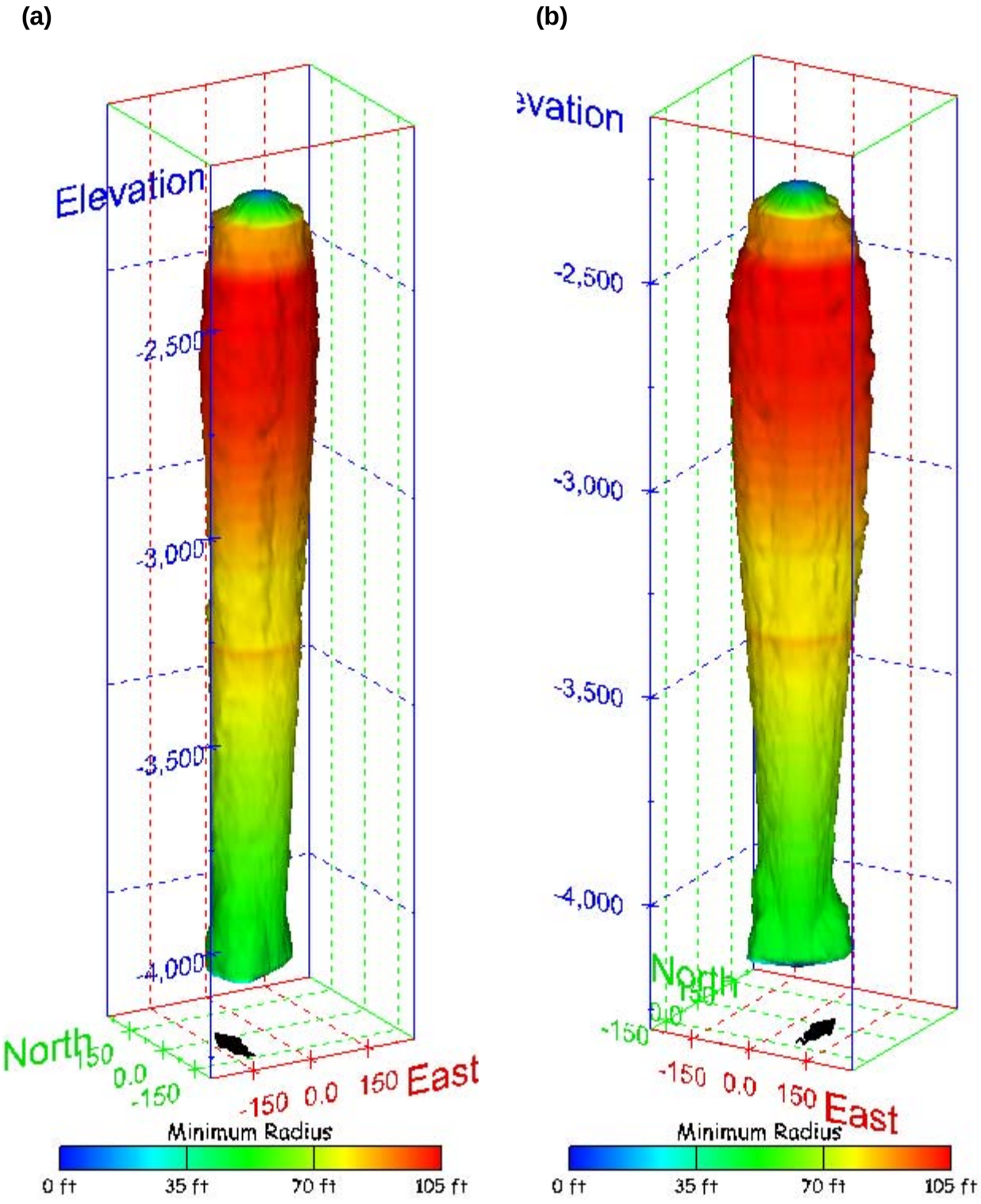

Figure 335. Sonar images of cavern BH-113, showing the geometry of the cavern colored by minimum radius. View from (a) azimuth 210°, elevation 20°; (b) azimuth 150°, elevation 20°.

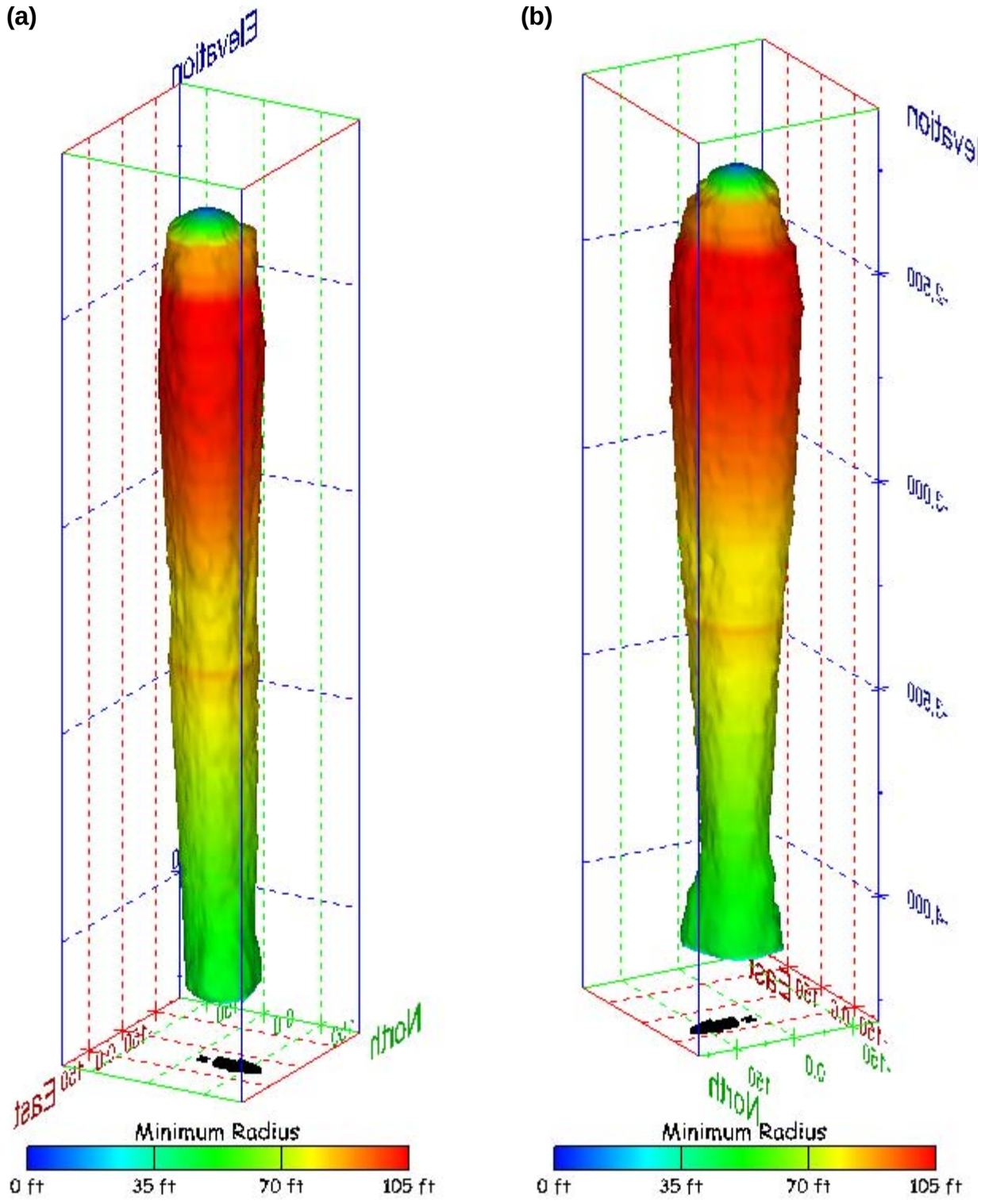

Figure 336. Sonar images of cavern BH-113, showing the geometry of the cavern colored by minimum radius. View from (a) azimuth 60°, elevation 20°; (b) azimuth 300°, elevation 20°.

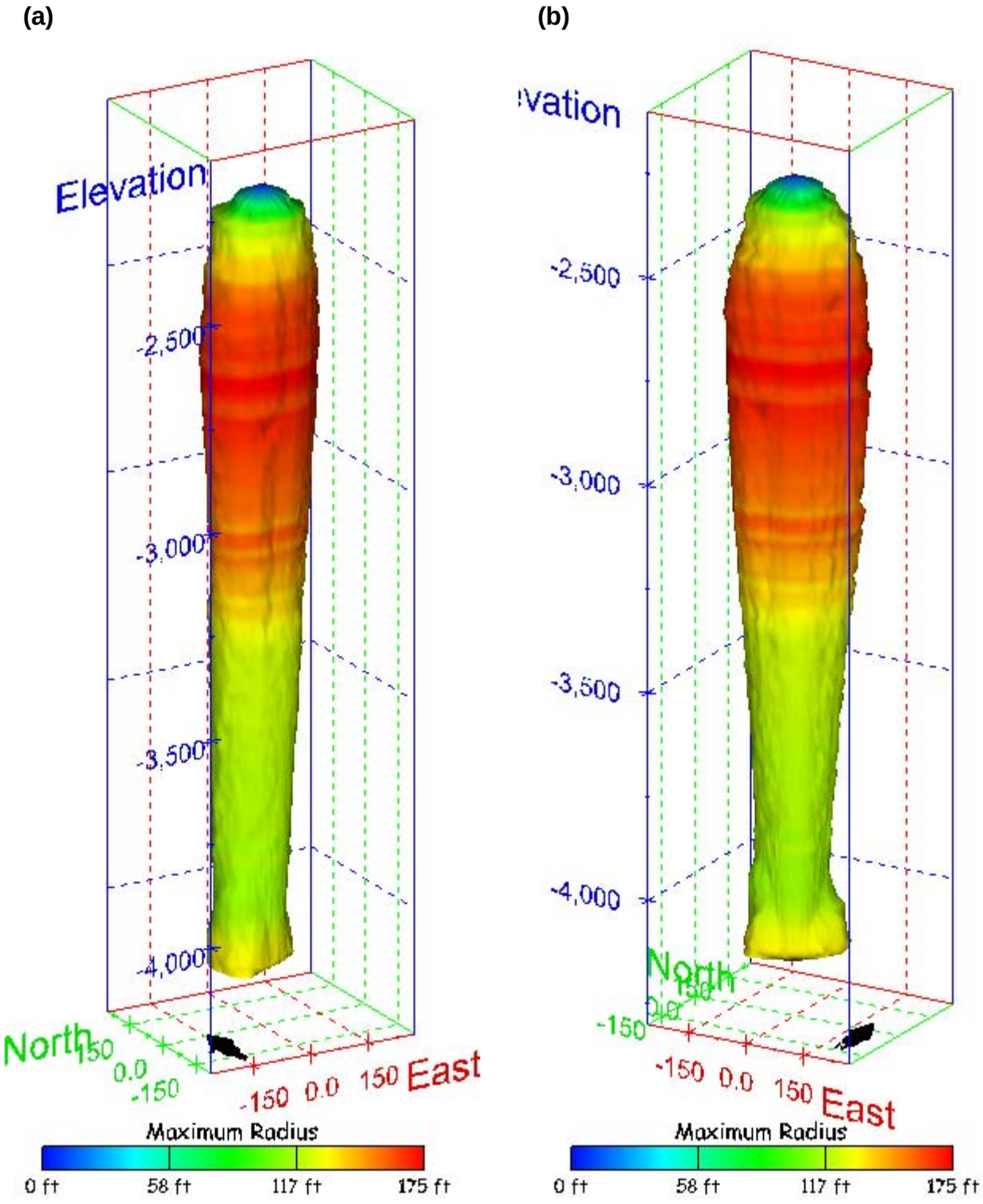

Figure 337. Sonar images of cavern BH-113, showing the geometry of the cavern colored by maximum radius. View from (a) azimuth 210°, elevation 20°; (b) azimuth 150°, elevation 20°.

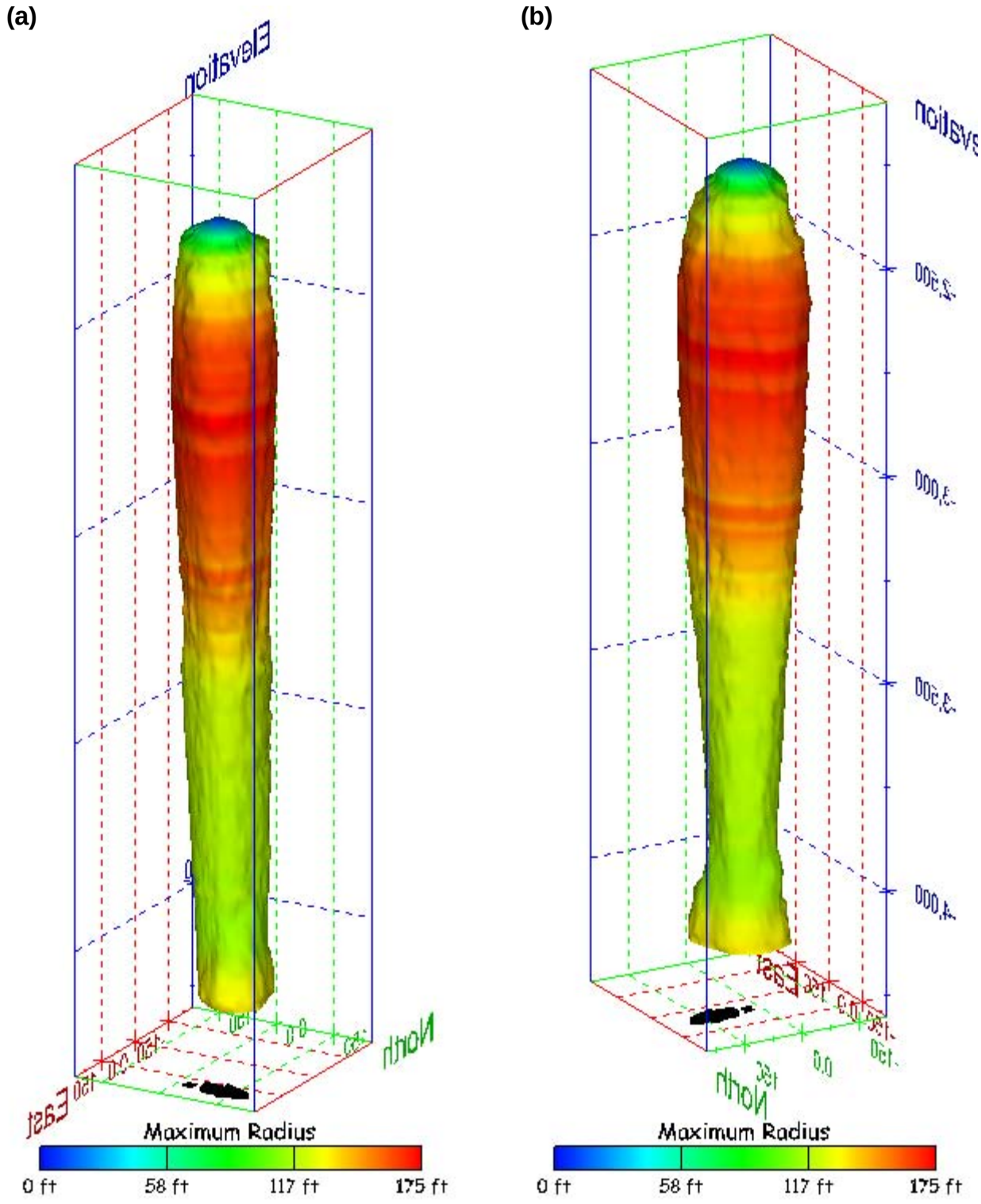

Figure 338. Sonar images of cavern BH-113, showing the geometry of the cavern colored by maximum radius. View from (a) azimuth 60°, elevation 20°; (b) azimuth 300°, elevation 20°.

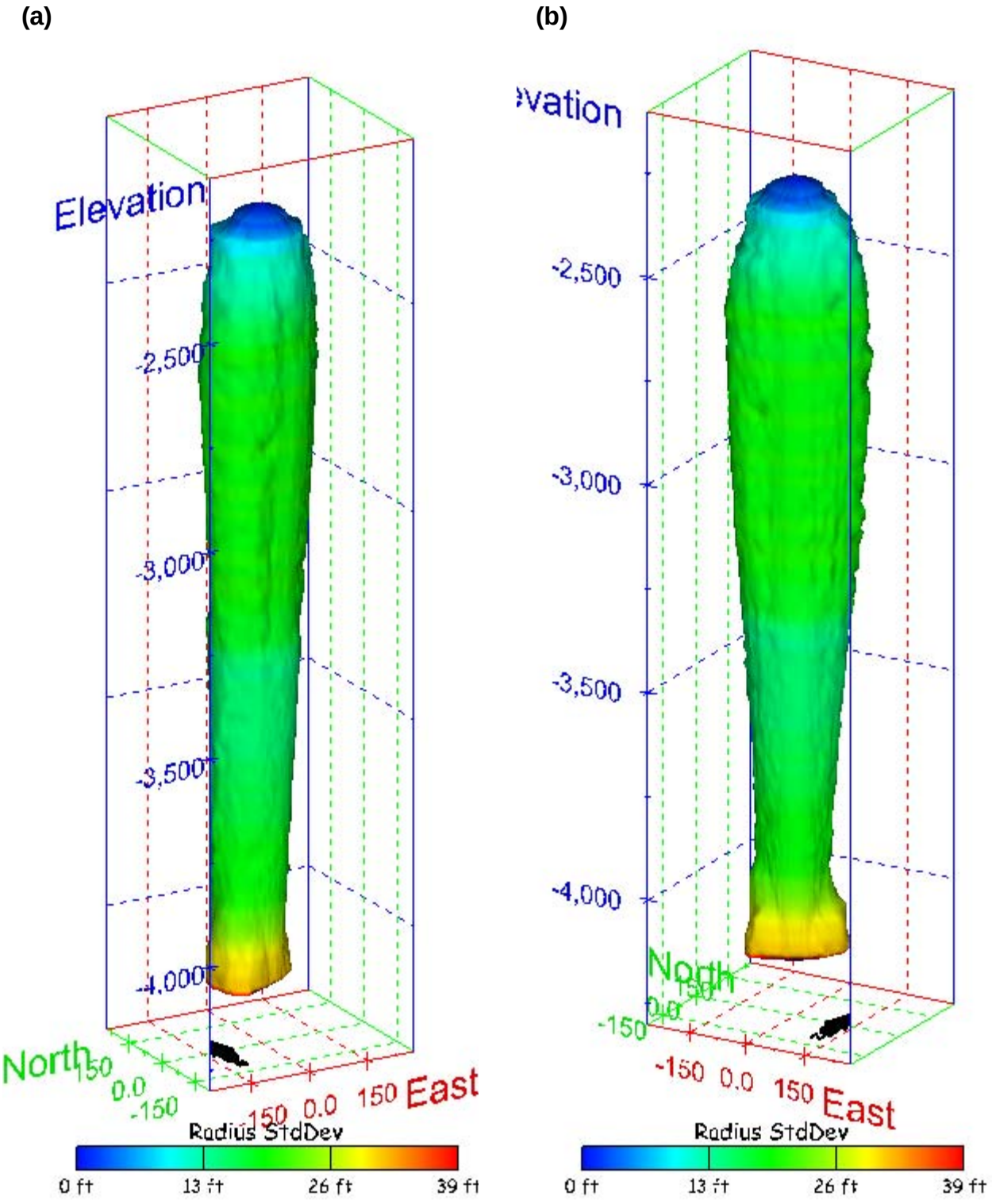

Figure 339. Sonar images of cavern BH-113, showing the geometry of the cavern colored by radius standard deviation. View from (a) azimuth 210°, elevation 20°; (b) azimuth 150°, elevation 20°.

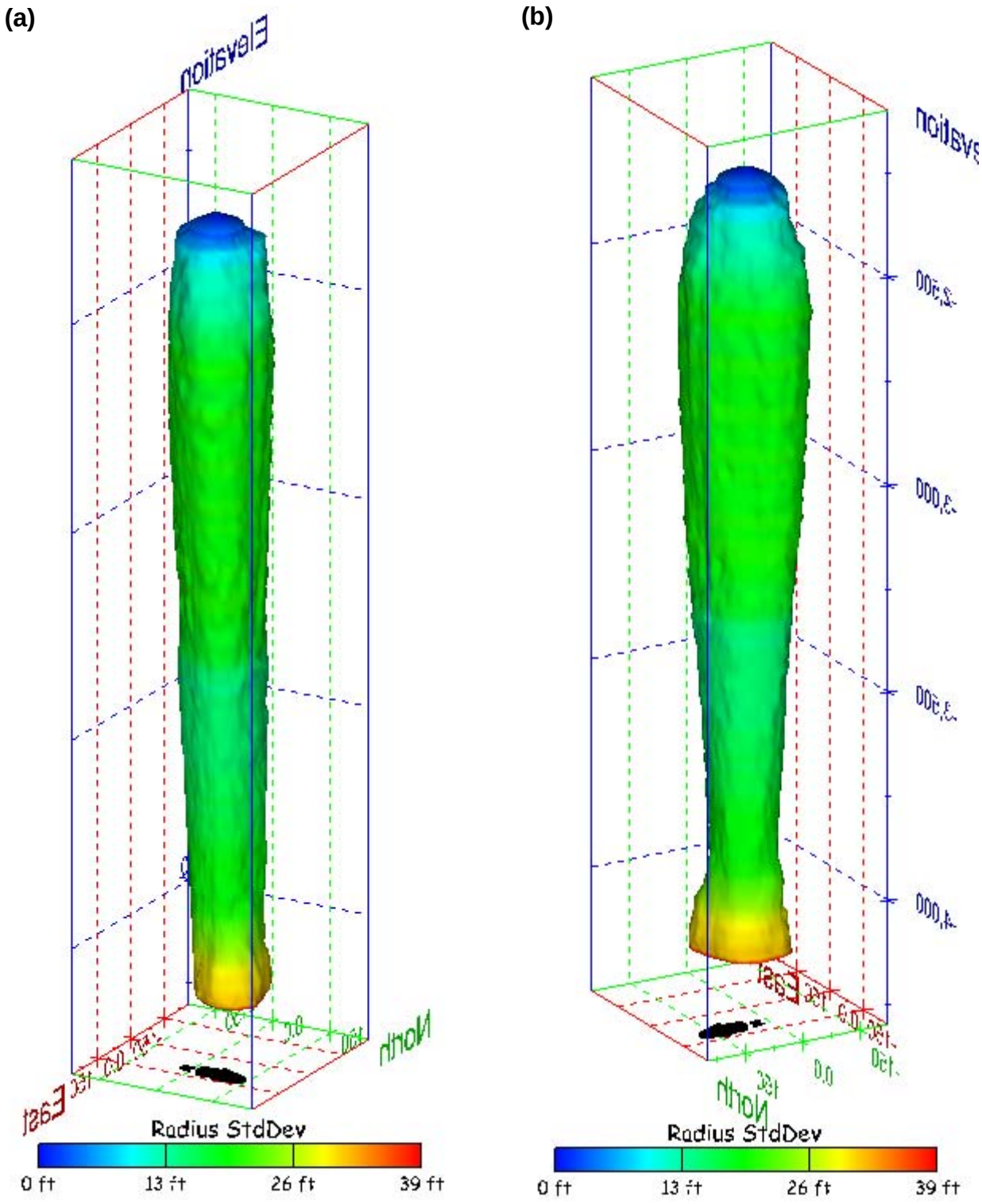

Figure 340. Sonar images of cavern BH-113, showing the geometry of the cavern colored by radius standard deviation. View from (a) azimuth 60°, elevation 20°; (b) azimuth 300°, elevation 20°.

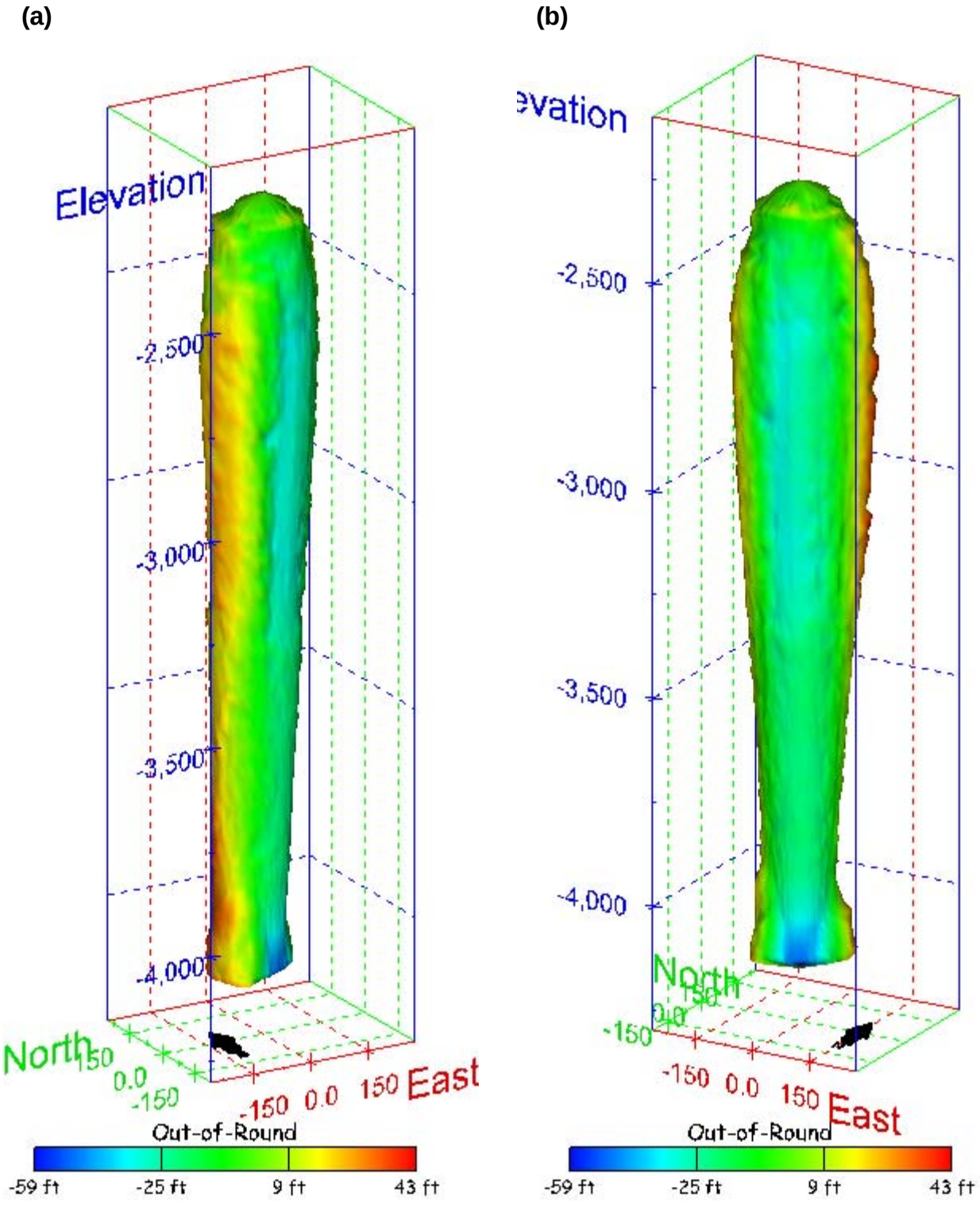

Figure 341. Sonar images of cavern BH-113, showing the geometry of the cavern colored by out-of-round distance. View from (a) azimuth 210°, elevation 20°; (b) azimuth 150°, elevation 20°.

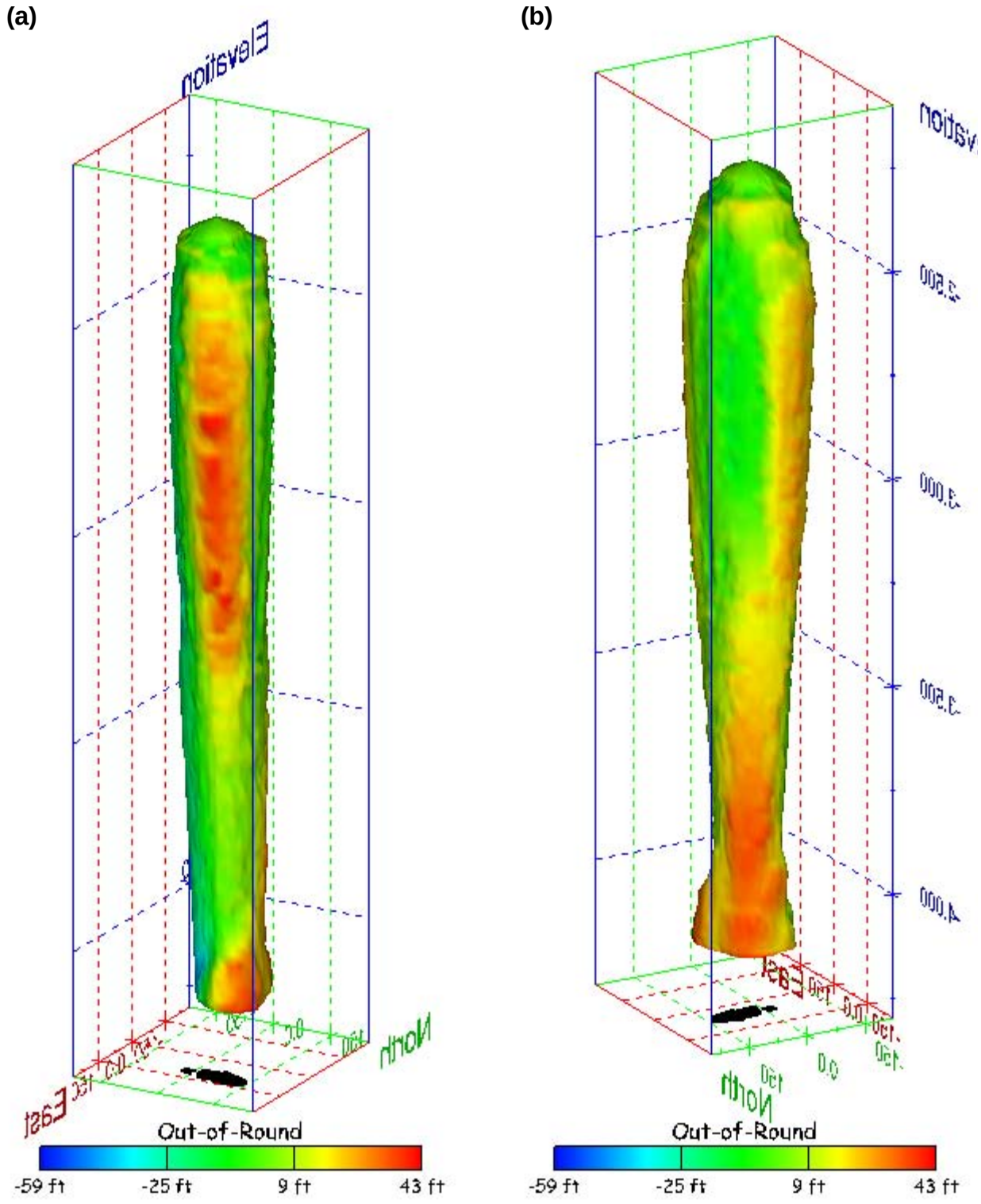

Figure 342. Sonar images of cavern BH-113, showing the geometry of the cavern colored by out-of-round distance. View from (a) azimuth 60°, elevation 20°; (b) azimuth 300°, elevation 20°.

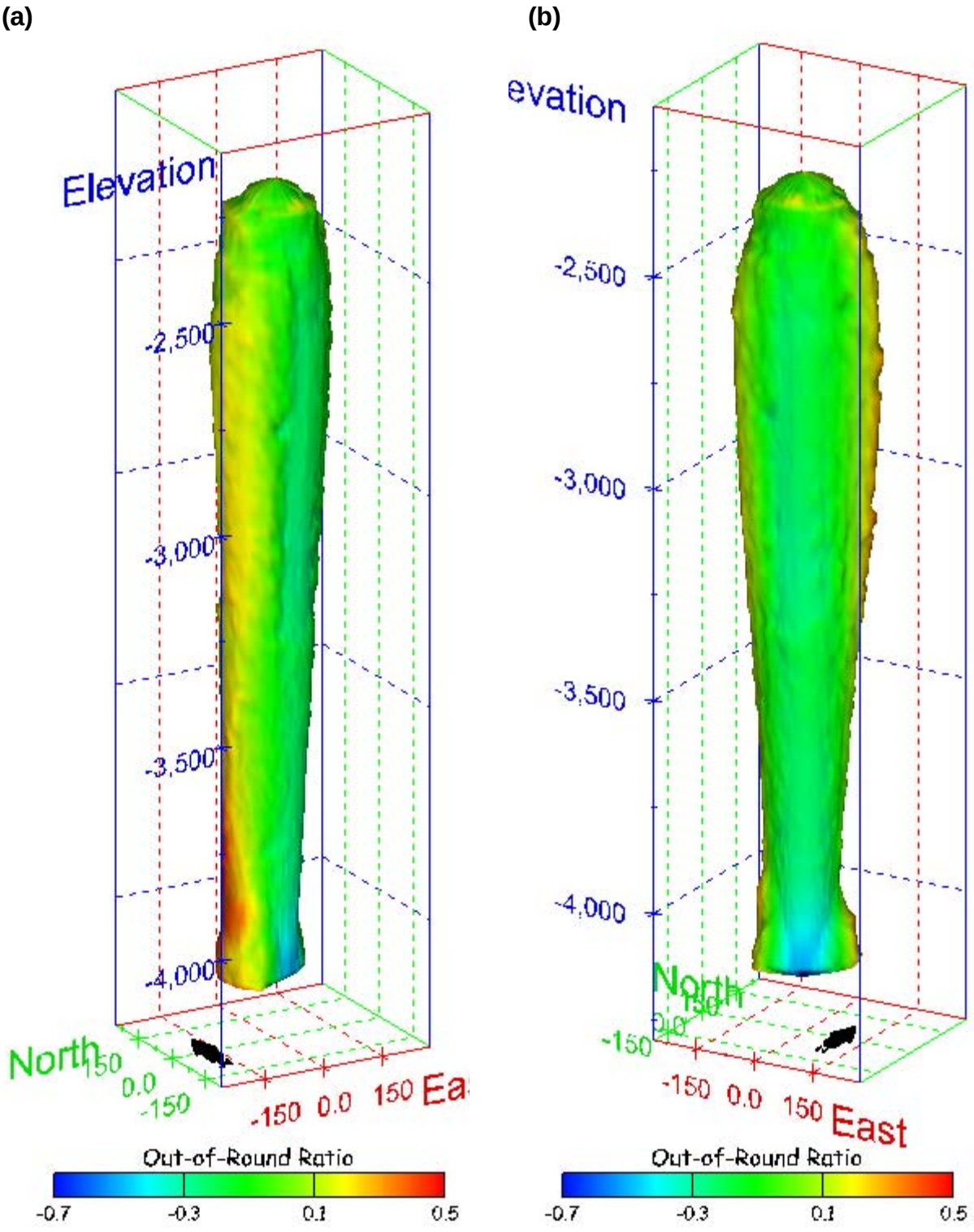

Figure 343. Sonar images of cavern BH-113, showing the geometry of the cavern colored by out-of-round ratio. View from (a) azimuth 210°, elevation 20°; (b) azimuth 150°, elevation 20°.

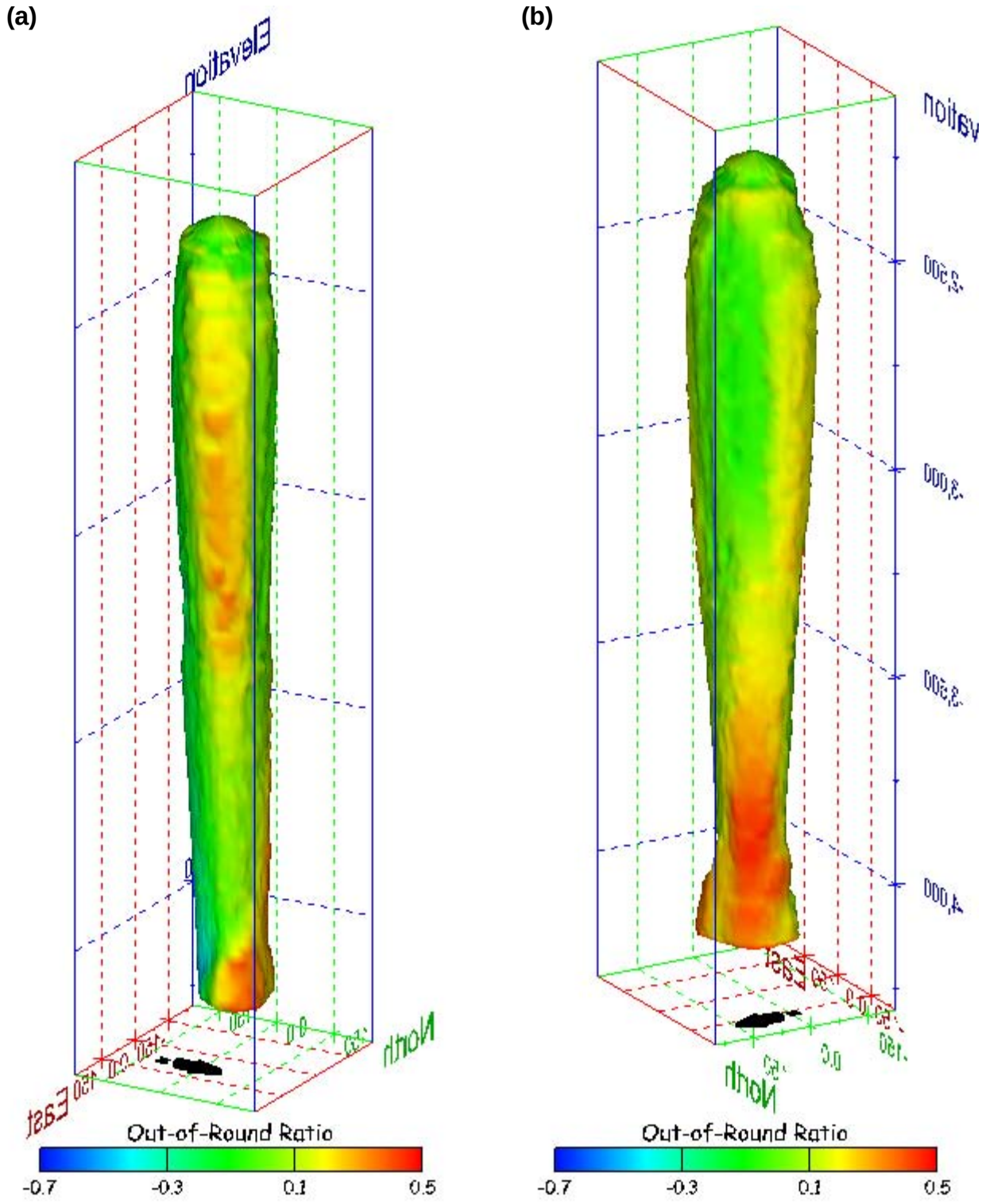

Figure 344. Sonar images of cavern BH-113, showing the geometry of the cavern colored by out-of-round ratio. View from (a) azimuth 60°, elevation 20°; (b) azimuth 300°, elevation 20°.

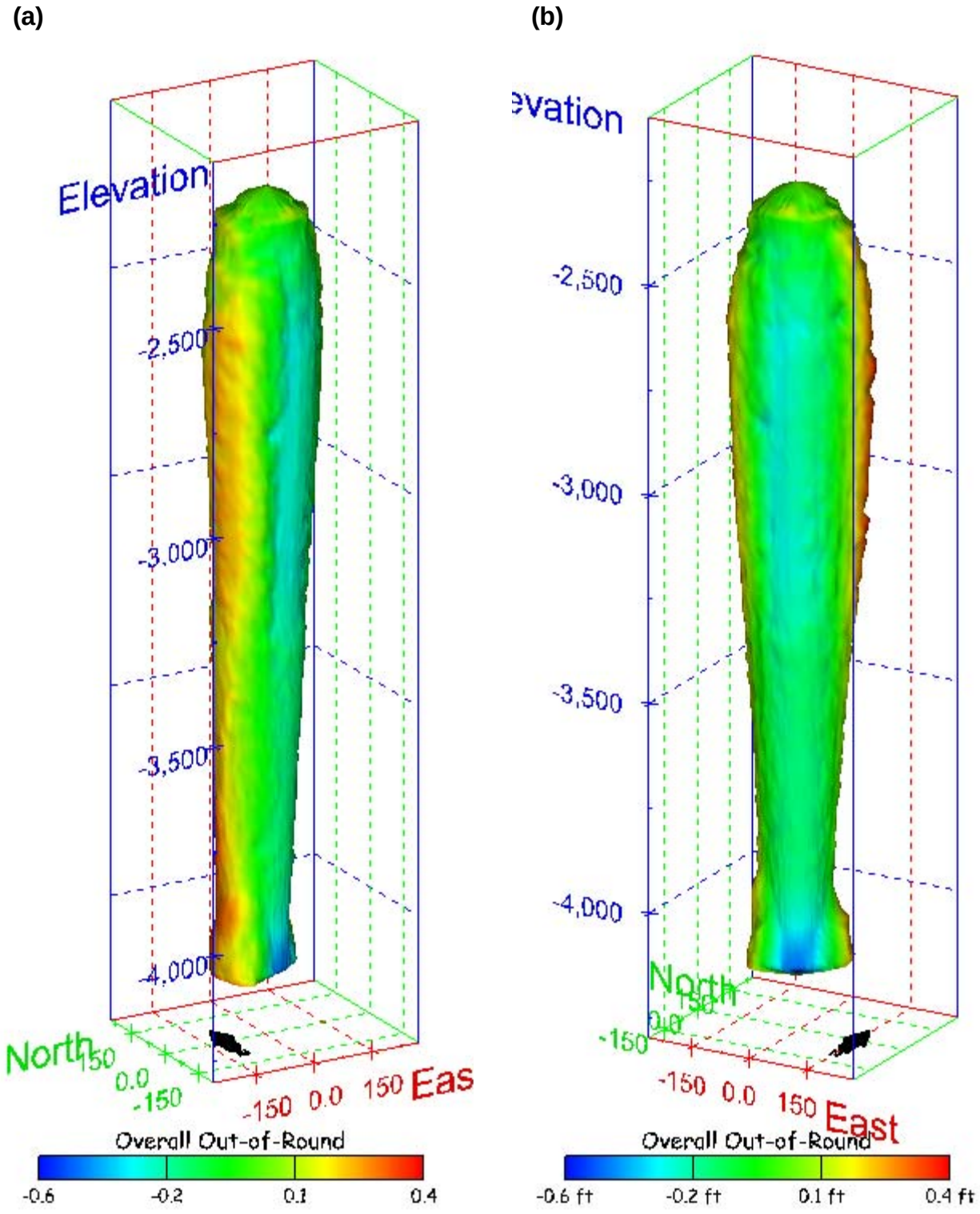

Figure 345. Sonar images of cavern BH-113, showing the geometry of the cavern colored by overall out-of-round ratio. View from (a) azimuth 210°, elevation 20°; (b) azimuth 150°, elevation 20°.

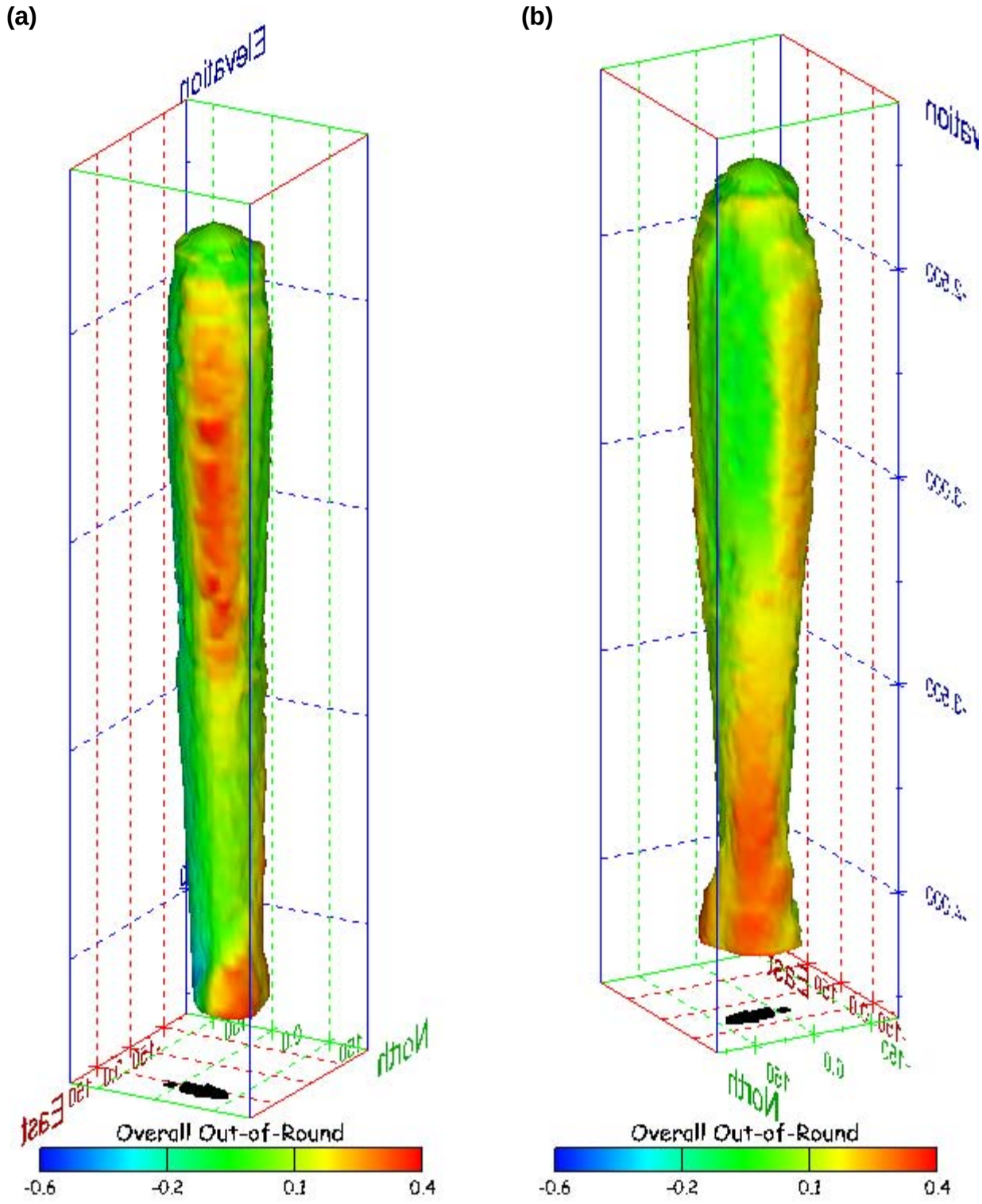

Figure 346. Sonar images of cavern BH-113, showing the geometry of the cavern colored by overall out-of-round ratio. View from (a) azimuth 60°, elevation 20°; (b) azimuth 300°, elevation 20°.

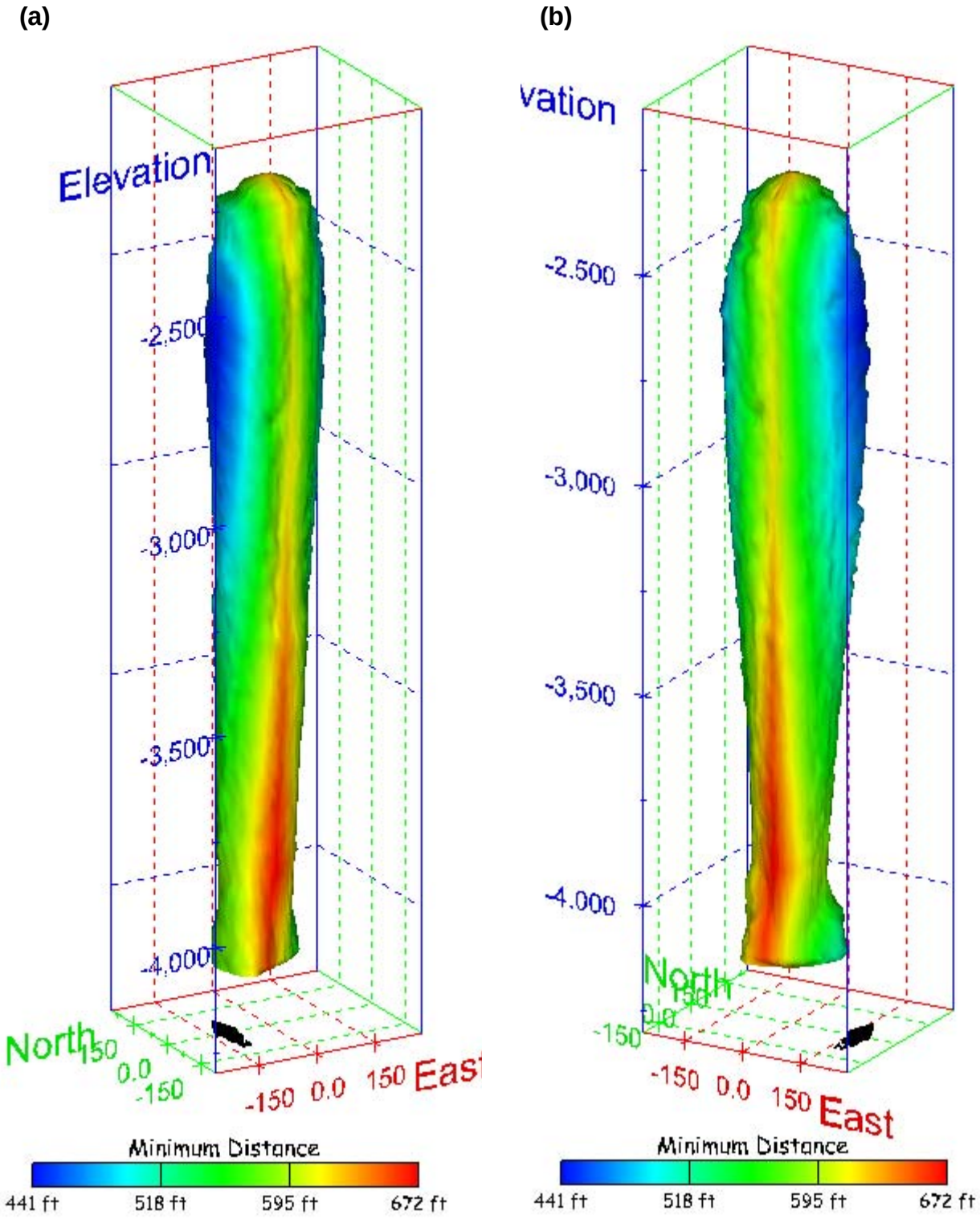

Figure 347. Sonar images of cavern BH-113, showing the geometry of the cavern colored by the minimum distance to the nearest neighboring cavern. View from (a) azimuth 210°, elevation 20°; (b) azimuth 150°, elevation 20°.

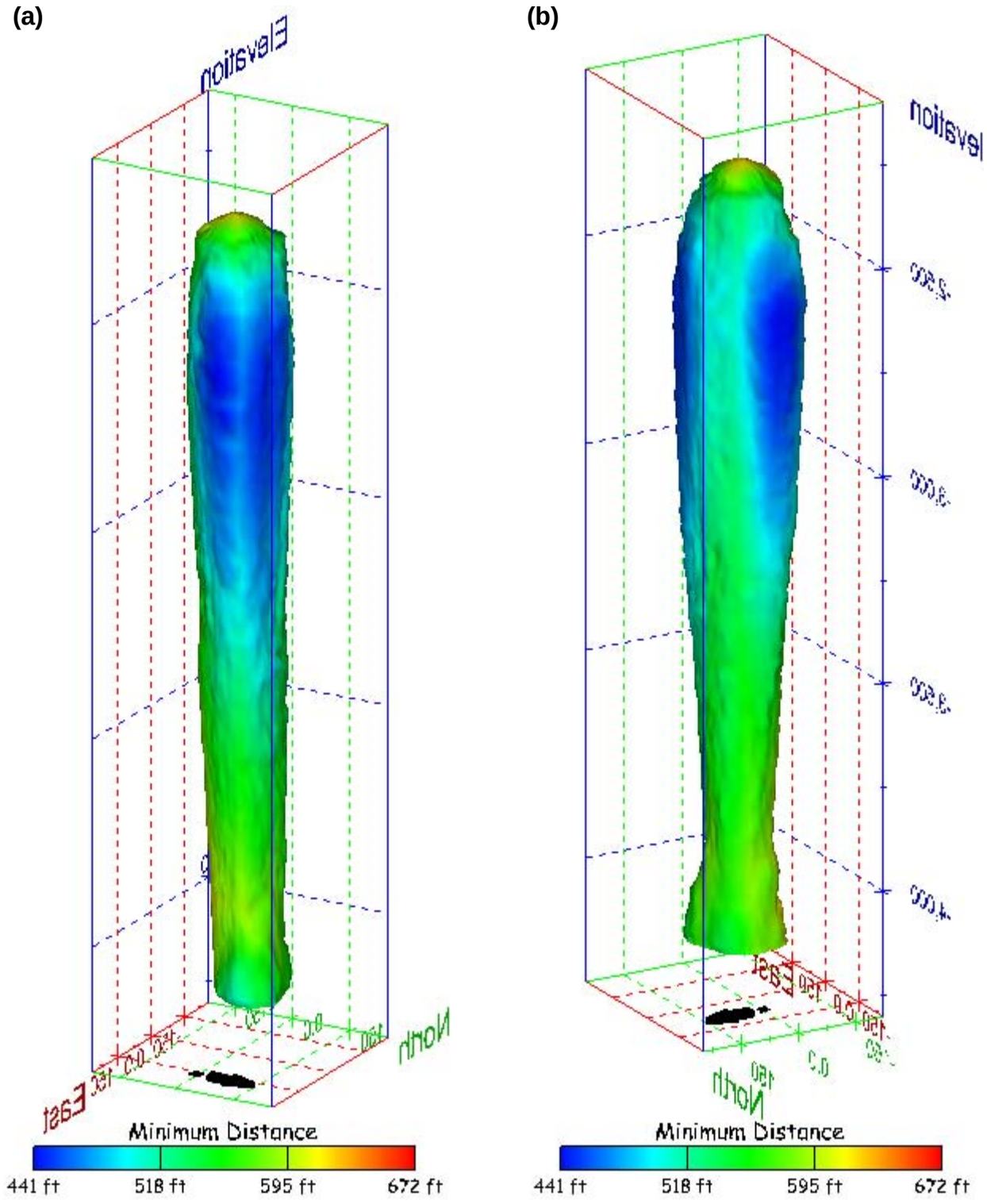

Figure 348. Sonar images of cavern BH-113, showing the geometry of the cavern colored by minimum distance to the nearest neighboring cavern. View from (a) azimuth 60°, elevation 20°; (b) azimuth 300°, elevation 20°.

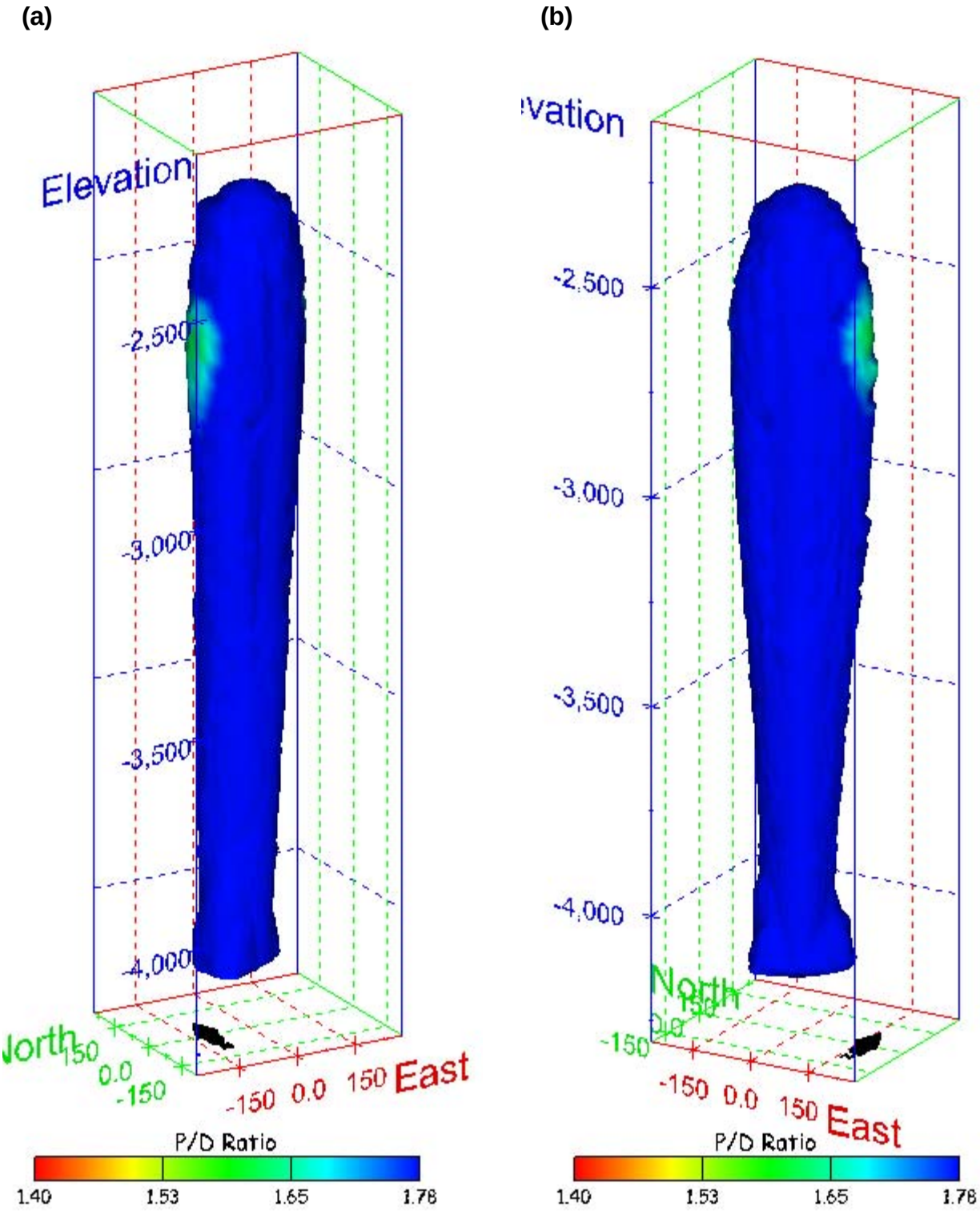

Figure 349. Sonar images of cavern BH-113, showing the geometry of the cavern colored by three-dimensional pillar-to-diameter ratio. View from (a) azimuth 210°, elevation 20°; (b) azimuth 150°, elevation 20°.

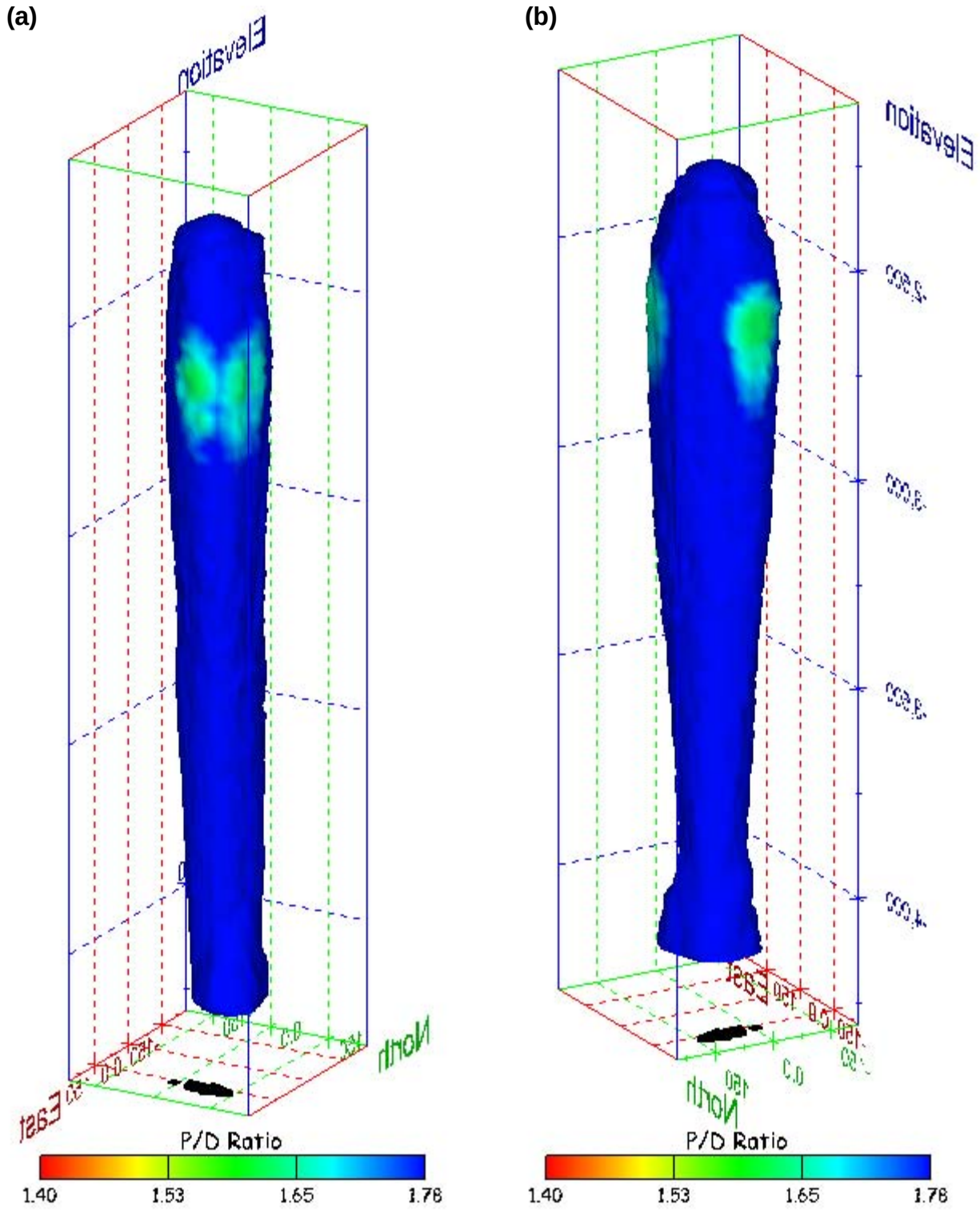

Figure 350. Sonar images of cavern BH-113, showing the geometry of the cavern colored by three-dimensional pillar-to-diameter ratio. View from (a) azimuth 60°, elevation 20°; (b) azimuth 300°, elevation 20°.

No Sonic Velocity Data Available for Socon Surveys

Figure 351. Sonar image of cavern BH-113, showing the geometry of the cavern colored by the reported velocity of sound on the survey date of February 2005. View from due south, elevation zero.

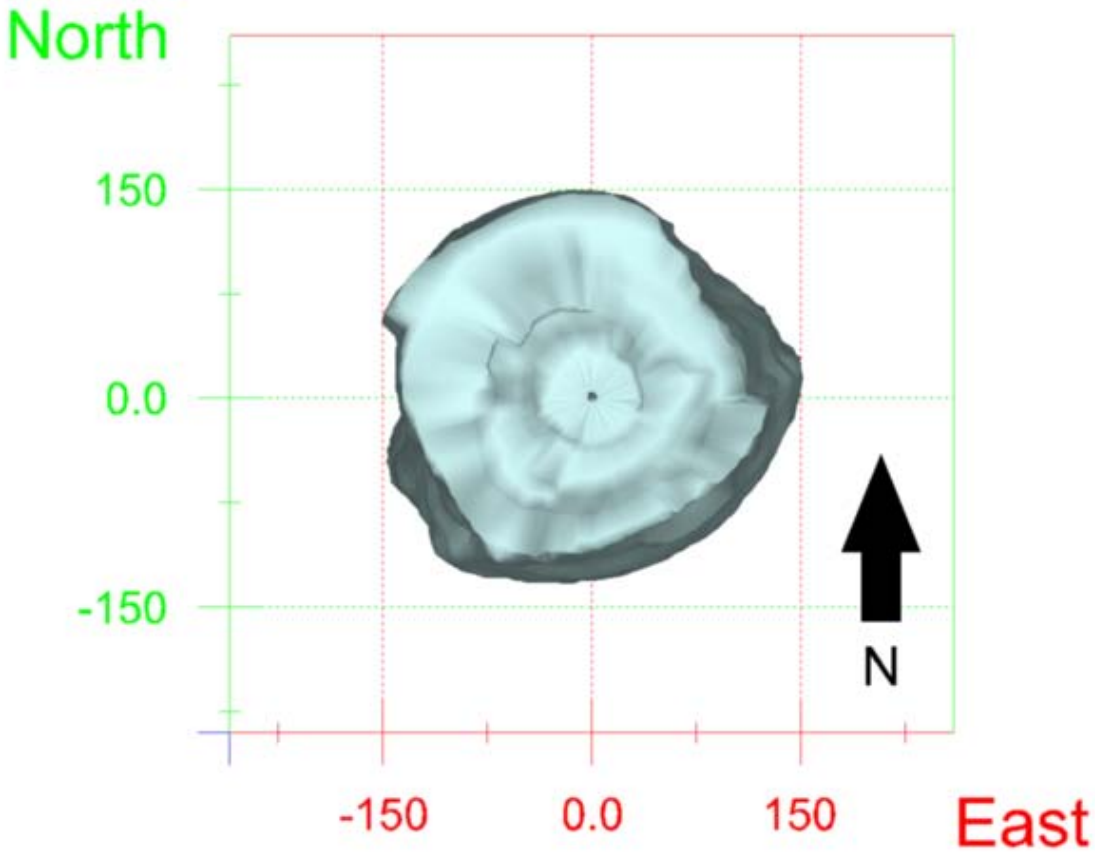

Figure 352. Map view sonar image of cavern BH-114, showing the basic geometry of the cavern. Grid squares represent 150 ft.

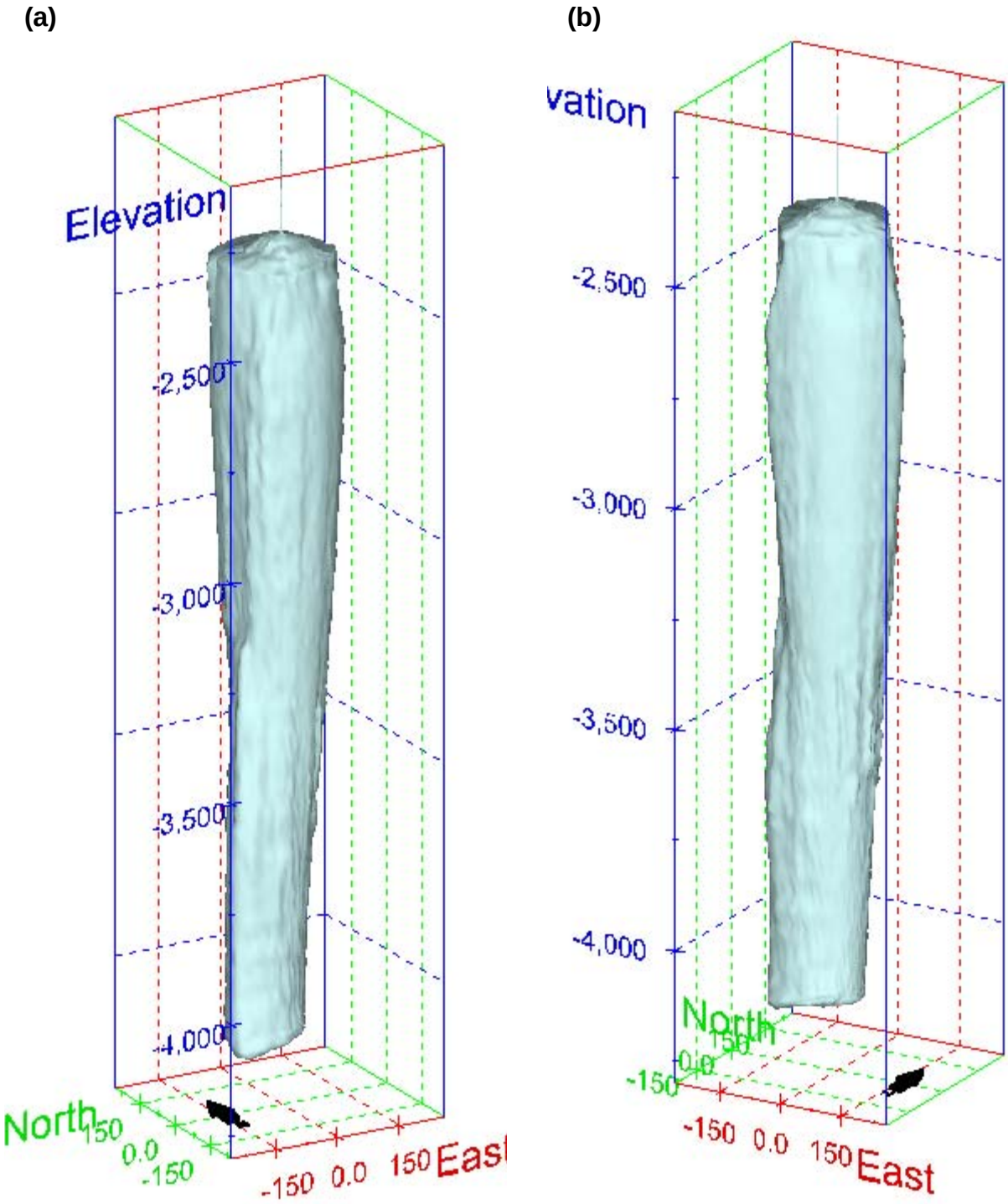

Figure 353. Sonar images of cavern BH-114, showing the basic geometric shape of the cavern. View from (a) azimuth 210°, elevation 20°; (b) azimuth 150°, elevation 20°.

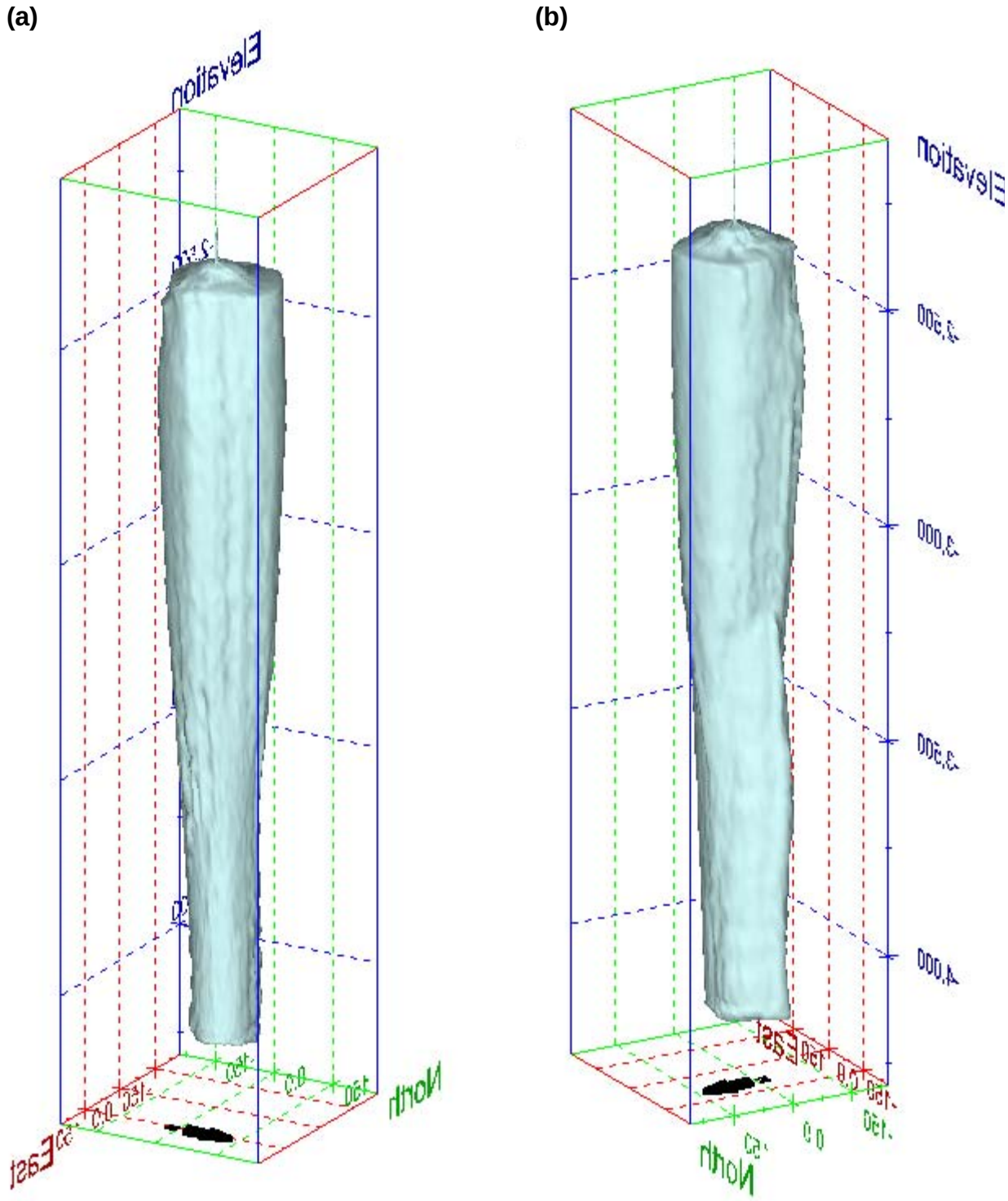

Figure 354. Sonar images of cavern BH-114, showing the basic geometric shape of the cavern. View from (a) azimuth 60°, elevation 20°; (b) azimuth 300°, elevation 20°.

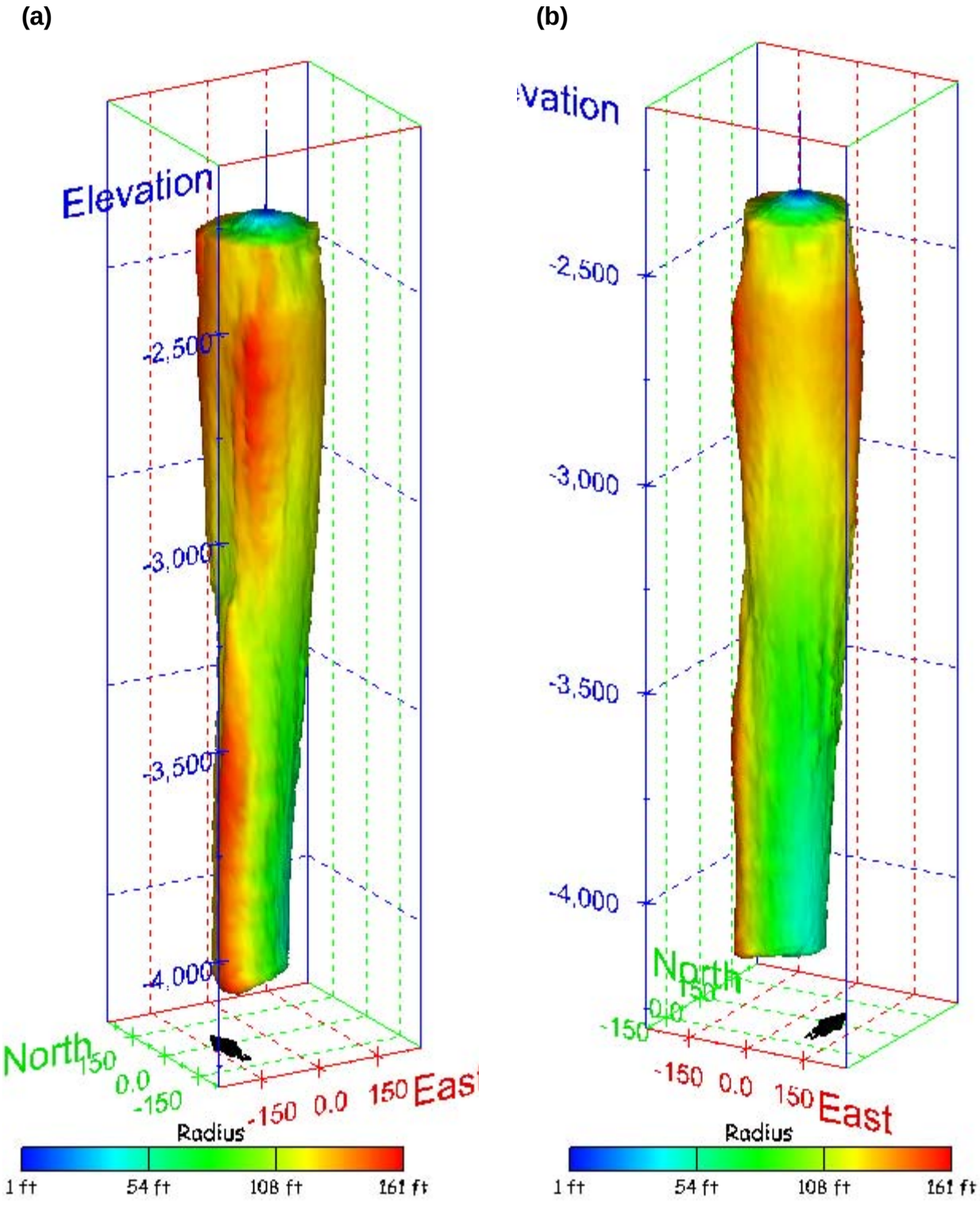

Figure 355. Sonar images of cavern BH-114, showing the geometry of the cavern colored by measured radius. View from (a) azimuth 210°, elevation 20°; (b) azimuth 150°, elevation 20°.

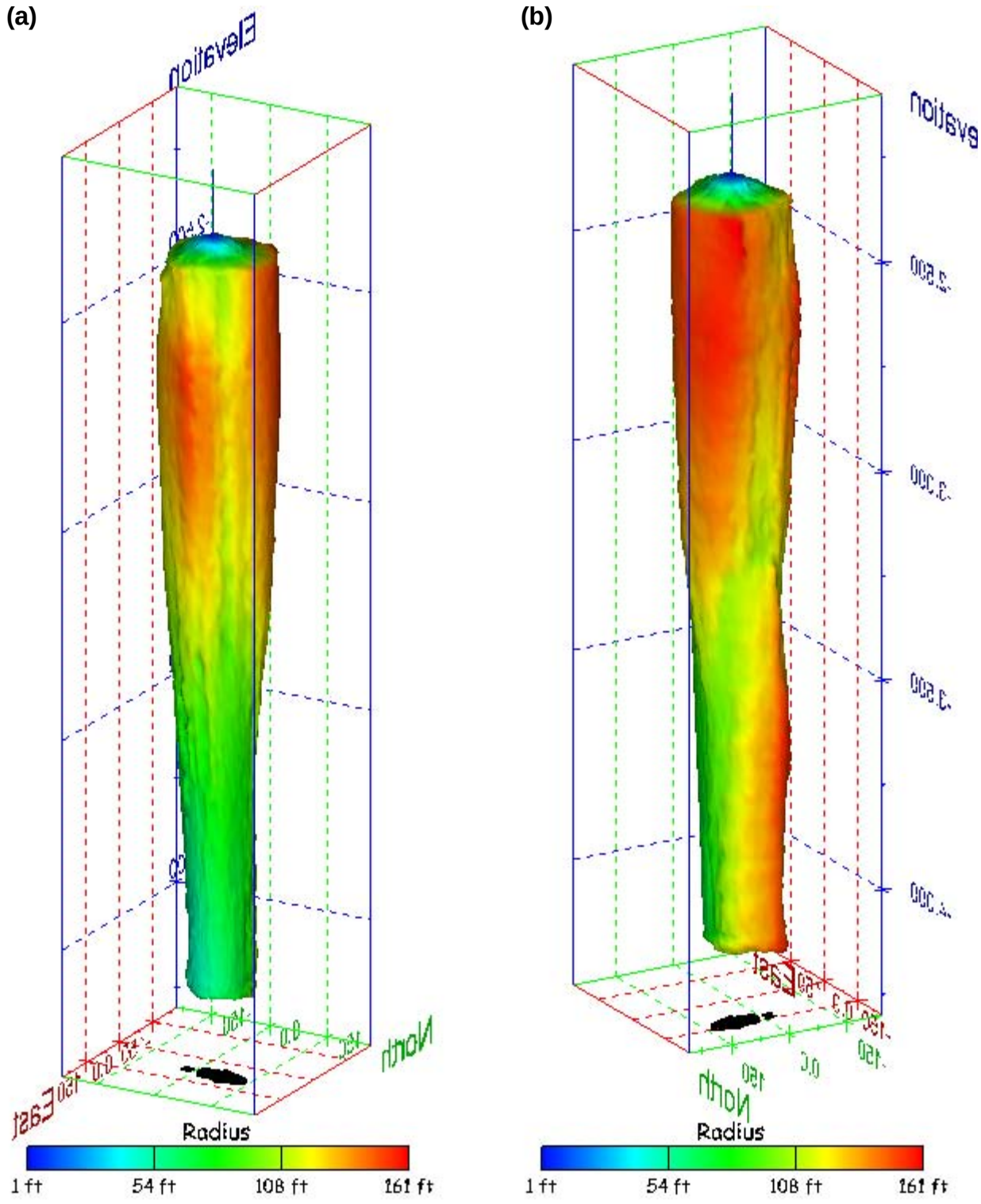

Figure 356. Sonar images of cavern BH-114, showing the geometry of the cavern colored by measured radius. View from (a) azimuth 60°, elevation 20°; (b) azimuth 300°, elevation 20°.

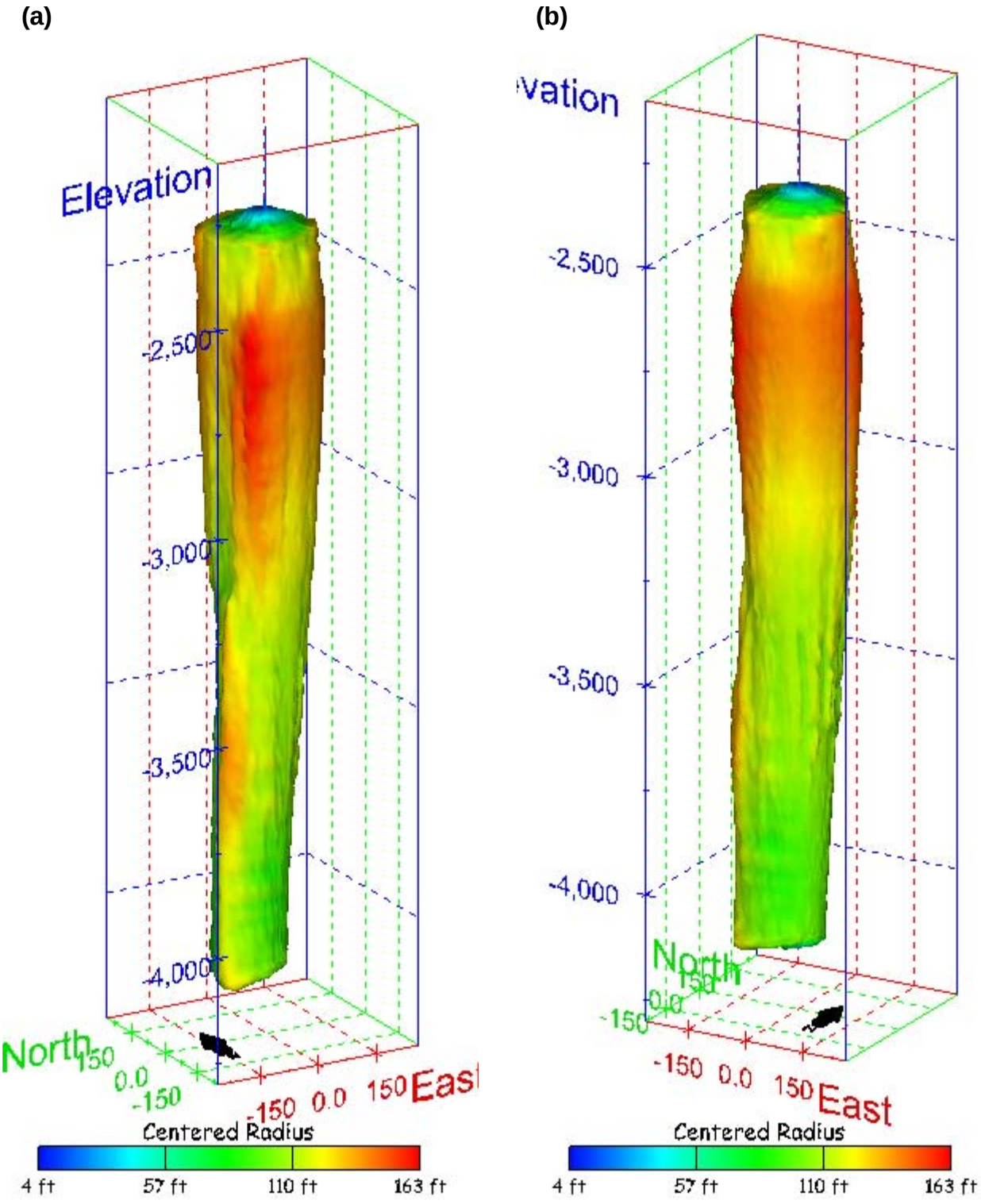

Figure 357. Sonar images of cavern BH-114, showing the geometry of the cavern colored by centered radius. View from (a) azimuth 210°, elevation 20°; (b) azimuth 150°, elevation 20°.

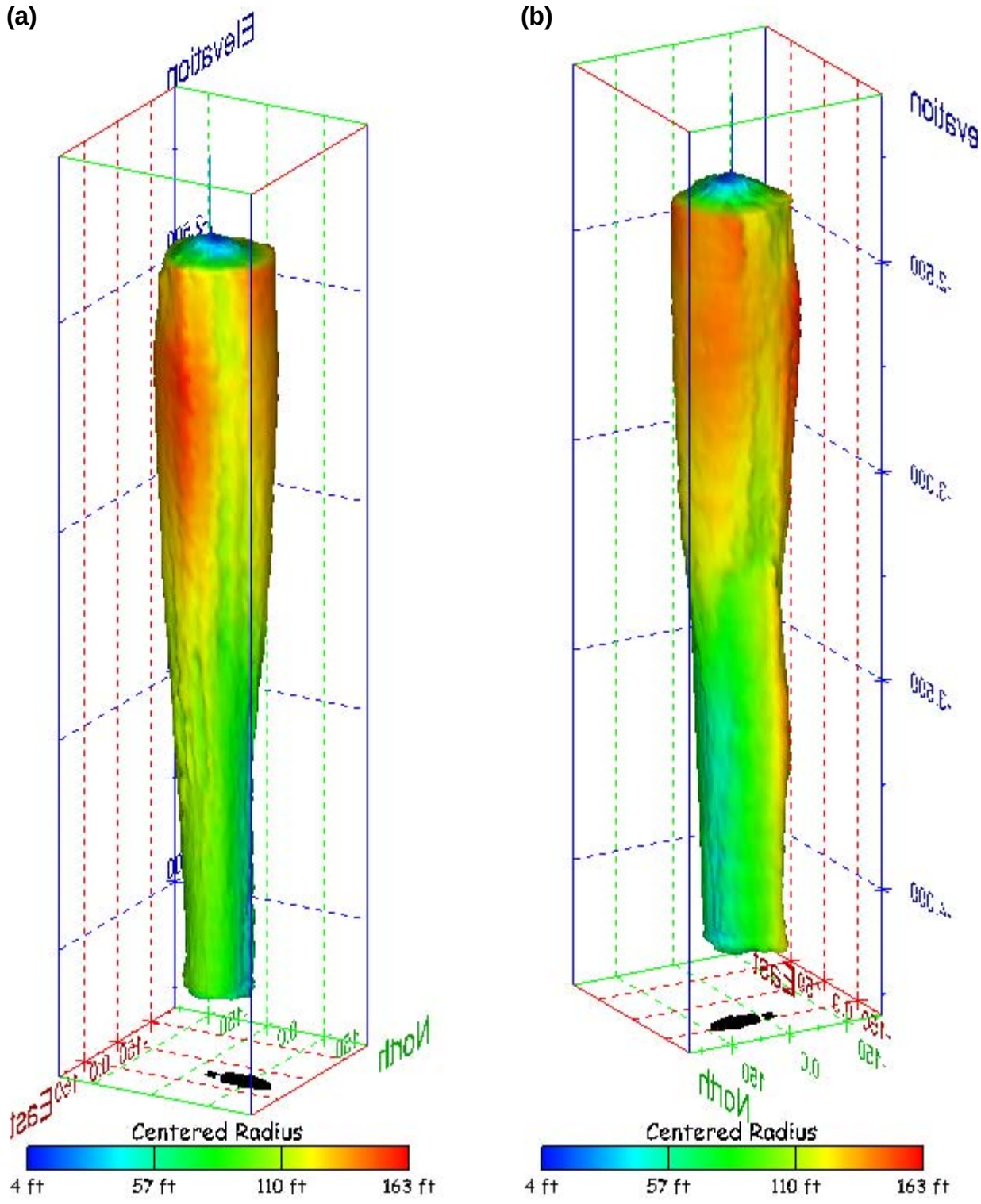

Figure 358. Sonar images of cavern BH-114, showing the geometry of the cavern colored by centered radius. View from (a) azimuth 60°, elevation 20°; (b) azimuth 300°, elevation 20°.

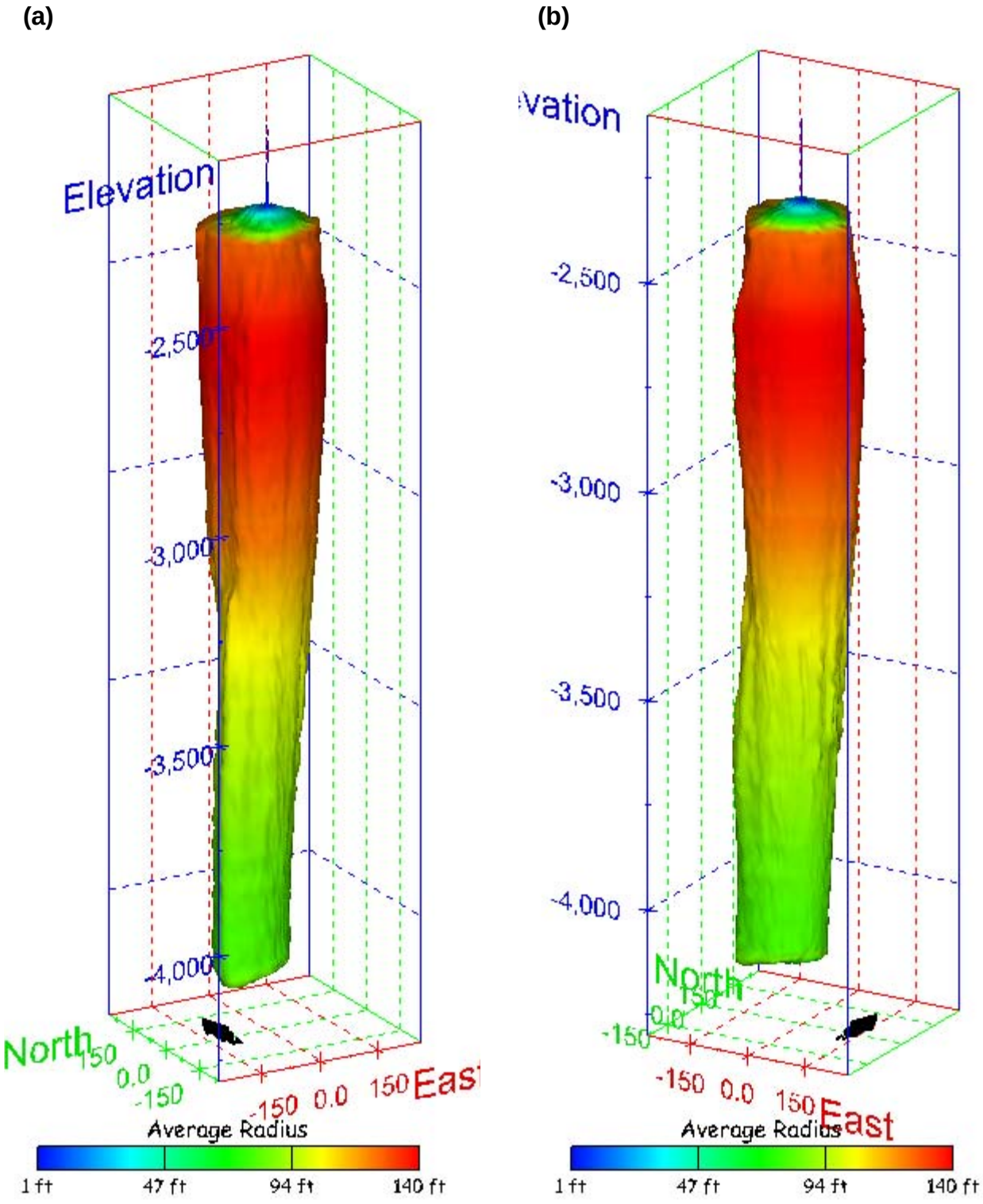

Figure 359. Sonar images of cavern BH-114, showing the geometry of the cavern colored by average radius. View from (a) azimuth 210°, elevation 20°; (b) azimuth 150°, elevation 20°.

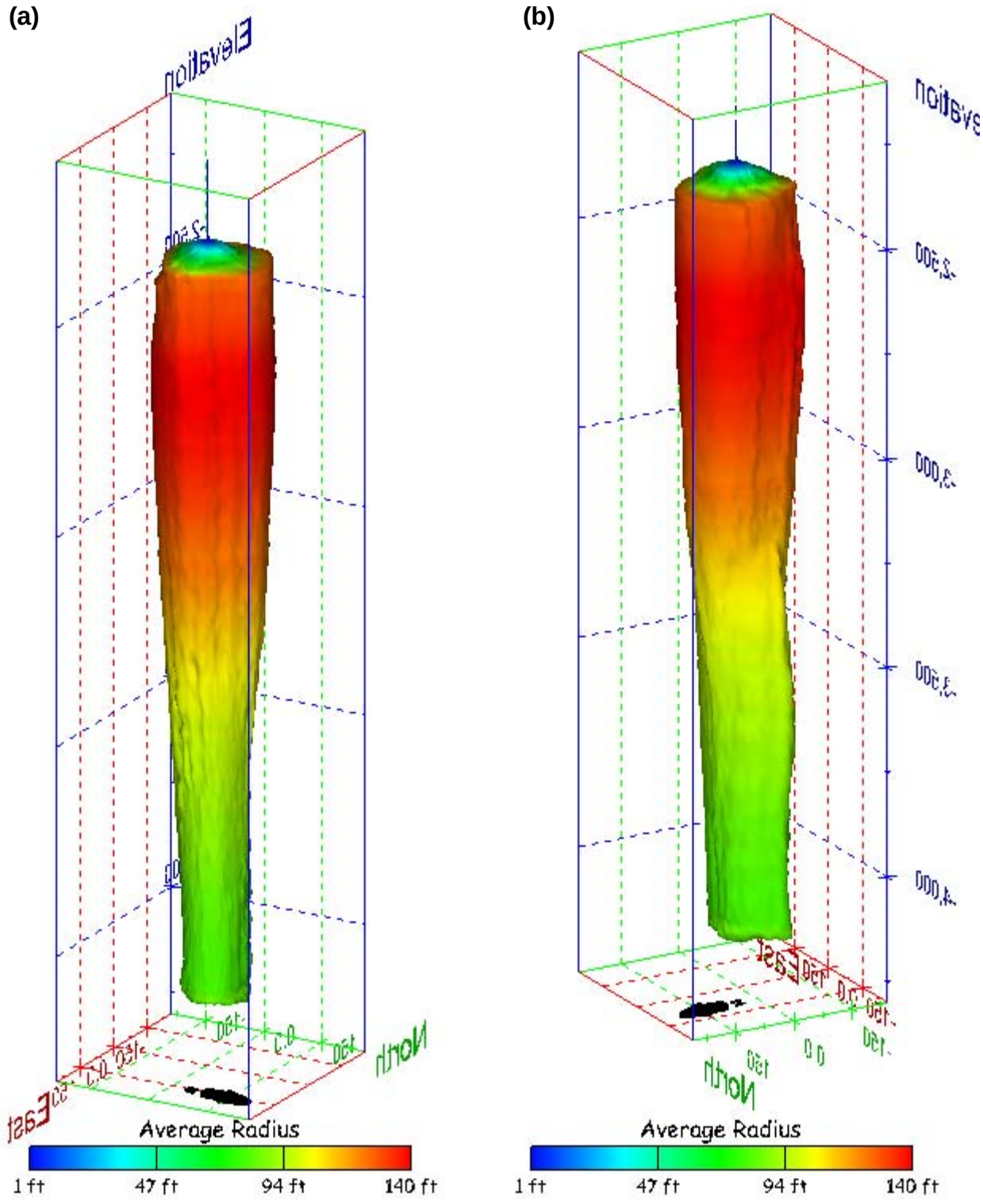

Figure 360. Sonar images of cavern BH-114, showing the geometry of the cavern colored by average radius. View from (a) azimuth 60°, elevation 20°; (b) azimuth 300°, elevation 20°.

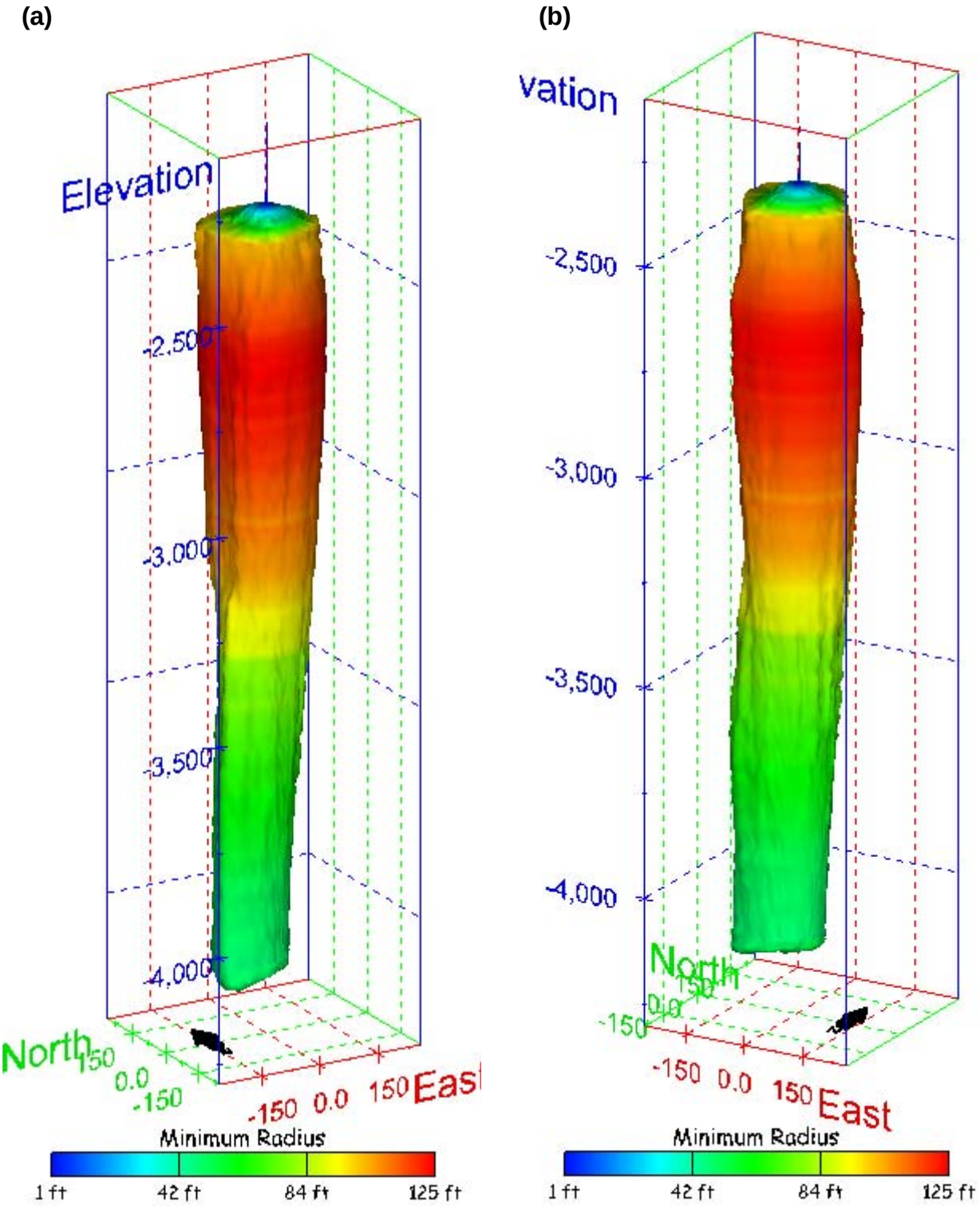

Figure 361. Sonar images of cavern BH-114, showing the geometry of the cavern colored by minimum radius. View from (a) azimuth 210°, elevation 20°; (b) azimuth 150°, elevation 20°.

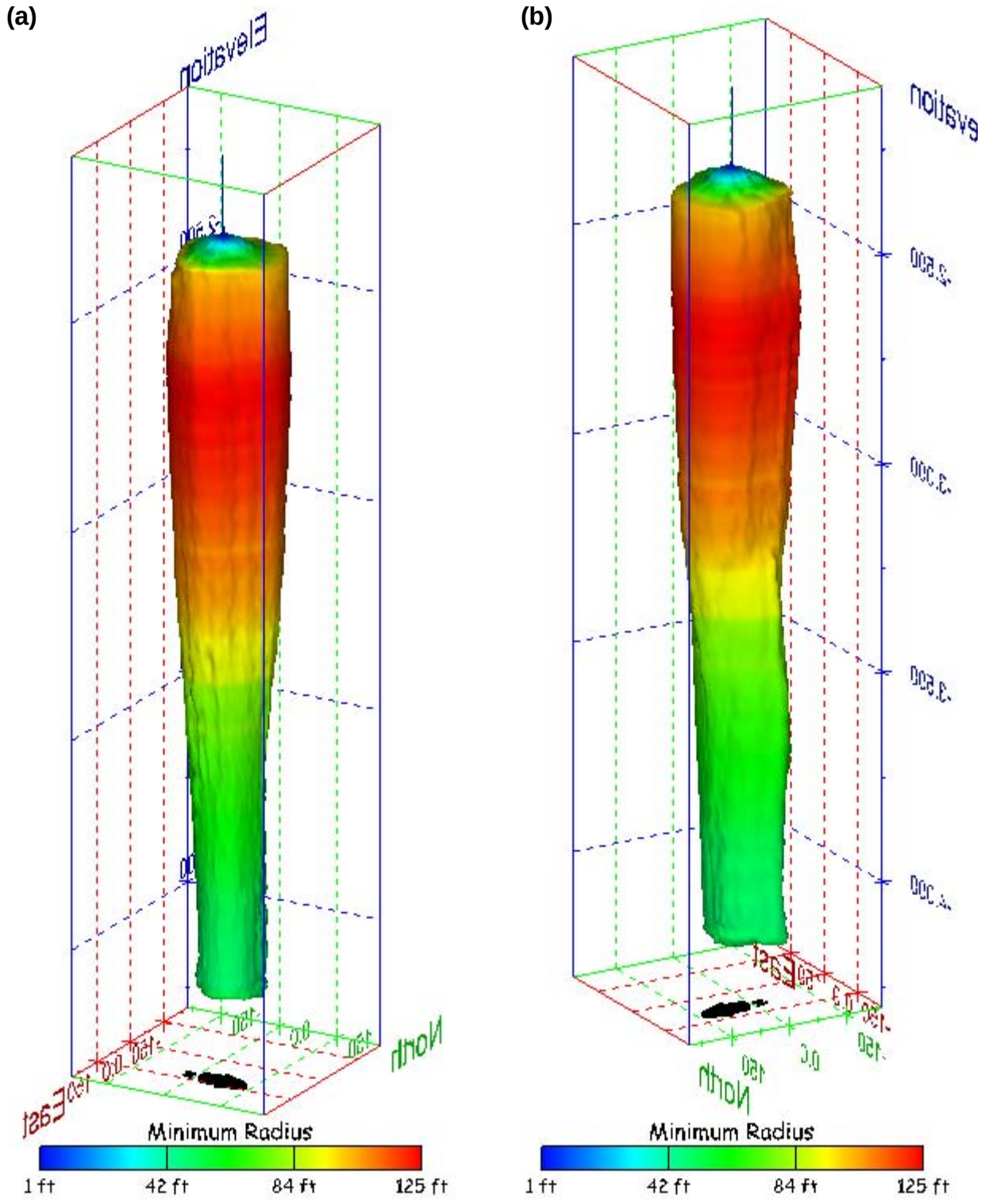

Figure 362. Sonar images of cavern BH-114, showing the geometry of the cavern colored by minimum radius. View from (a) azimuth 60°, elevation 20°; (b) azimuth 300°, elevation 20°.

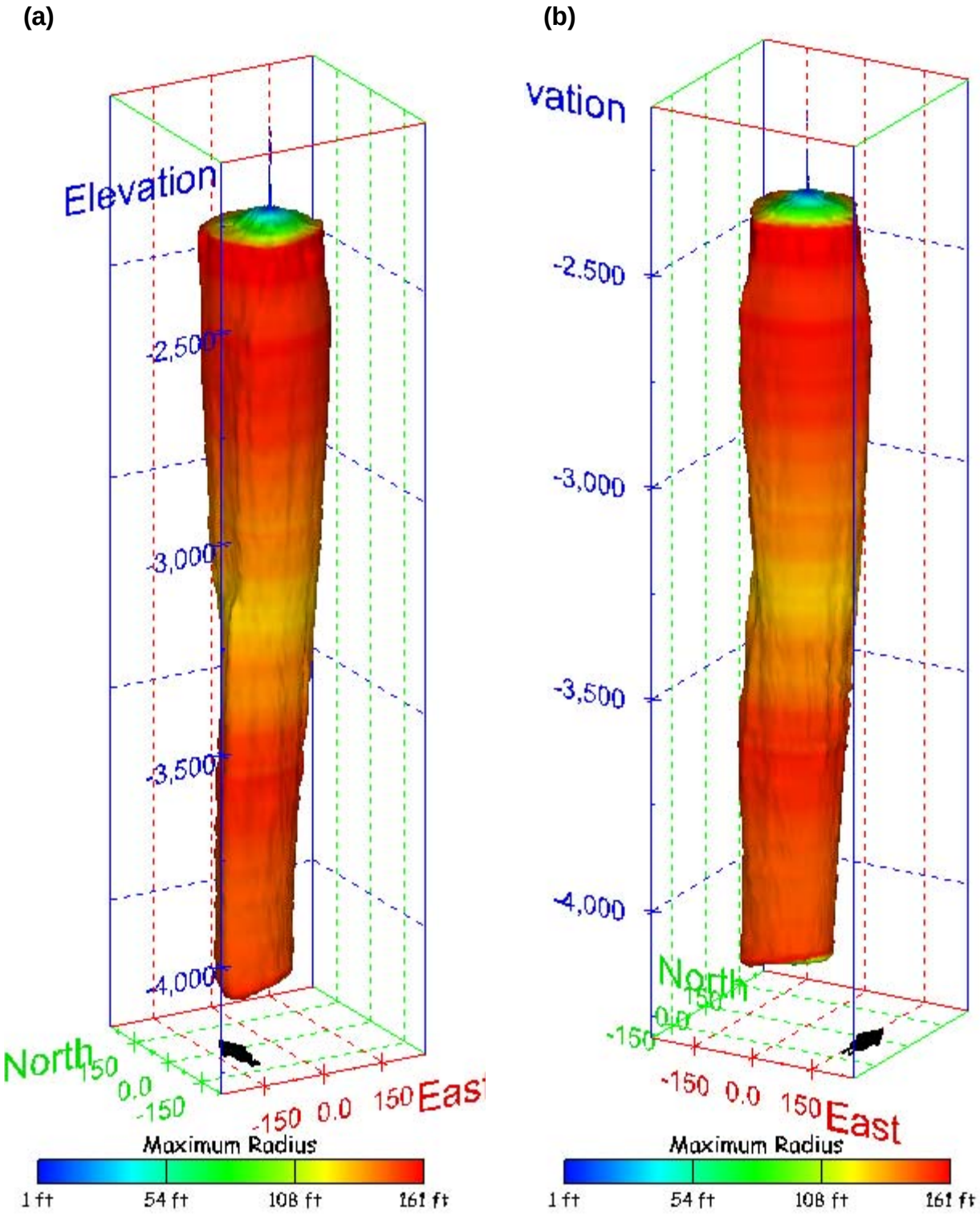

Figure 363. Sonar images of cavern BH-114, showing the geometry of the cavern colored by maximum radius. View from (a) azimuth 210°, elevation 20°; (b) azimuth 150°, elevation 20°.

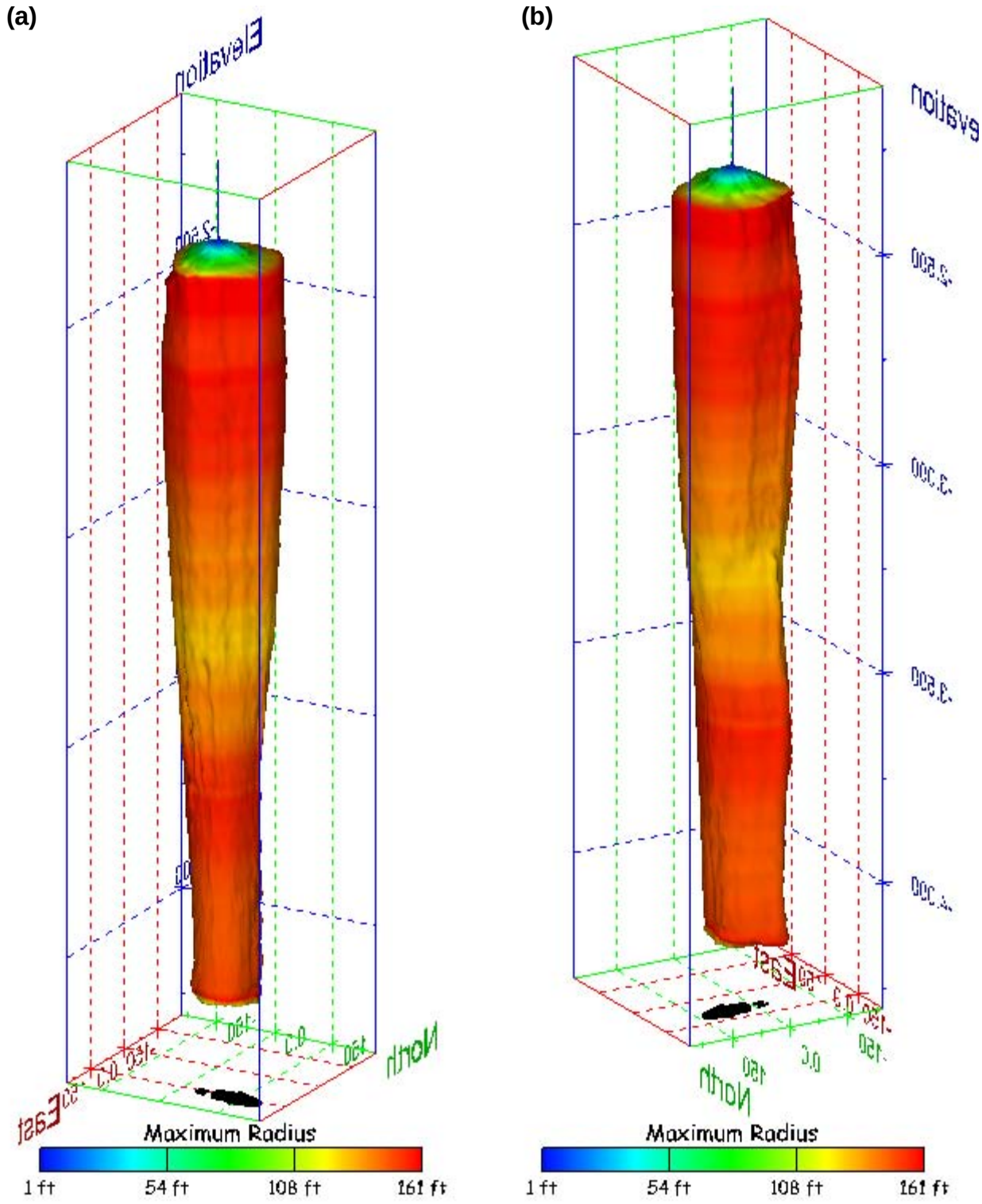

Figure 364. Sonar images of cavern BH-114, showing the geometry of the cavern colored by maximum radius. View from (a) azimuth 60°, elevation 20°; (b) azimuth 300°, elevation 20°.

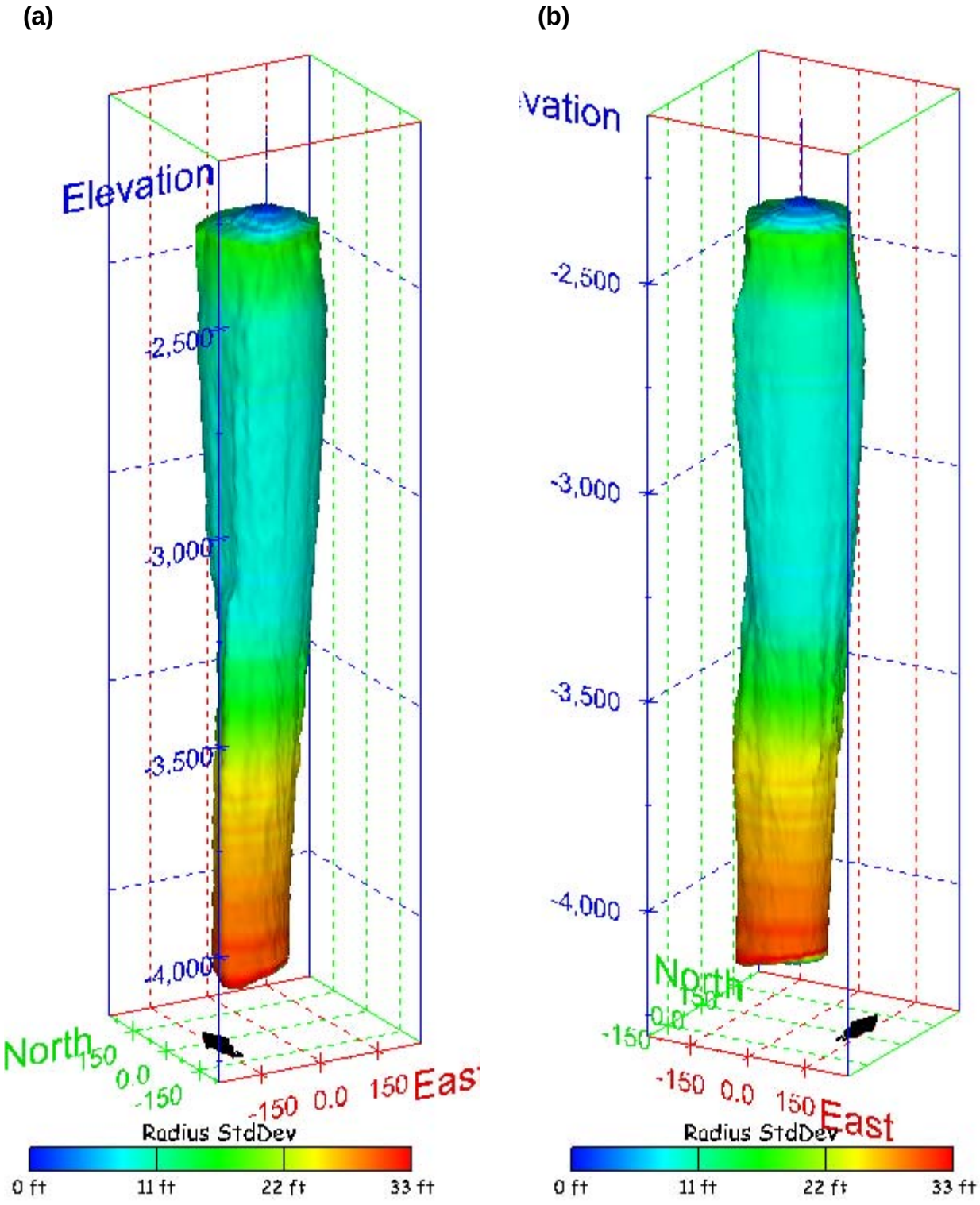

Figure 365. Sonar images of cavern BH-114, showing the geometry of the cavern colored by radius standard deviation. View from (a) azimuth 210°, elevation 20°; (b) azimuth 150°, elevation 20°.

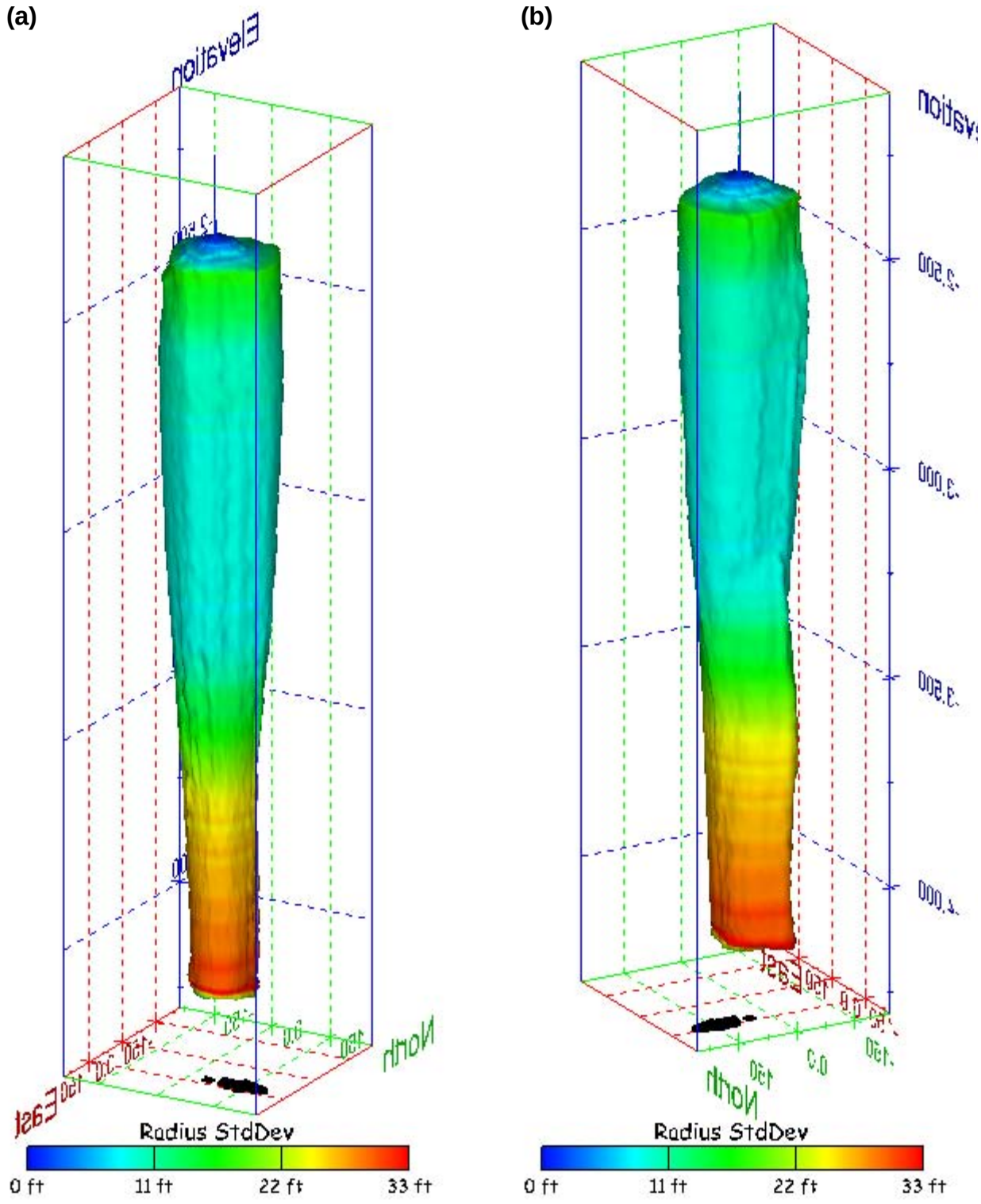

Figure 366. Sonar images of cavern BH-114, showing the geometry of the cavern colored by radius standard deviation. View from (a) azimuth 60°, elevation 20°; (b) azimuth 300°, elevation 20°.

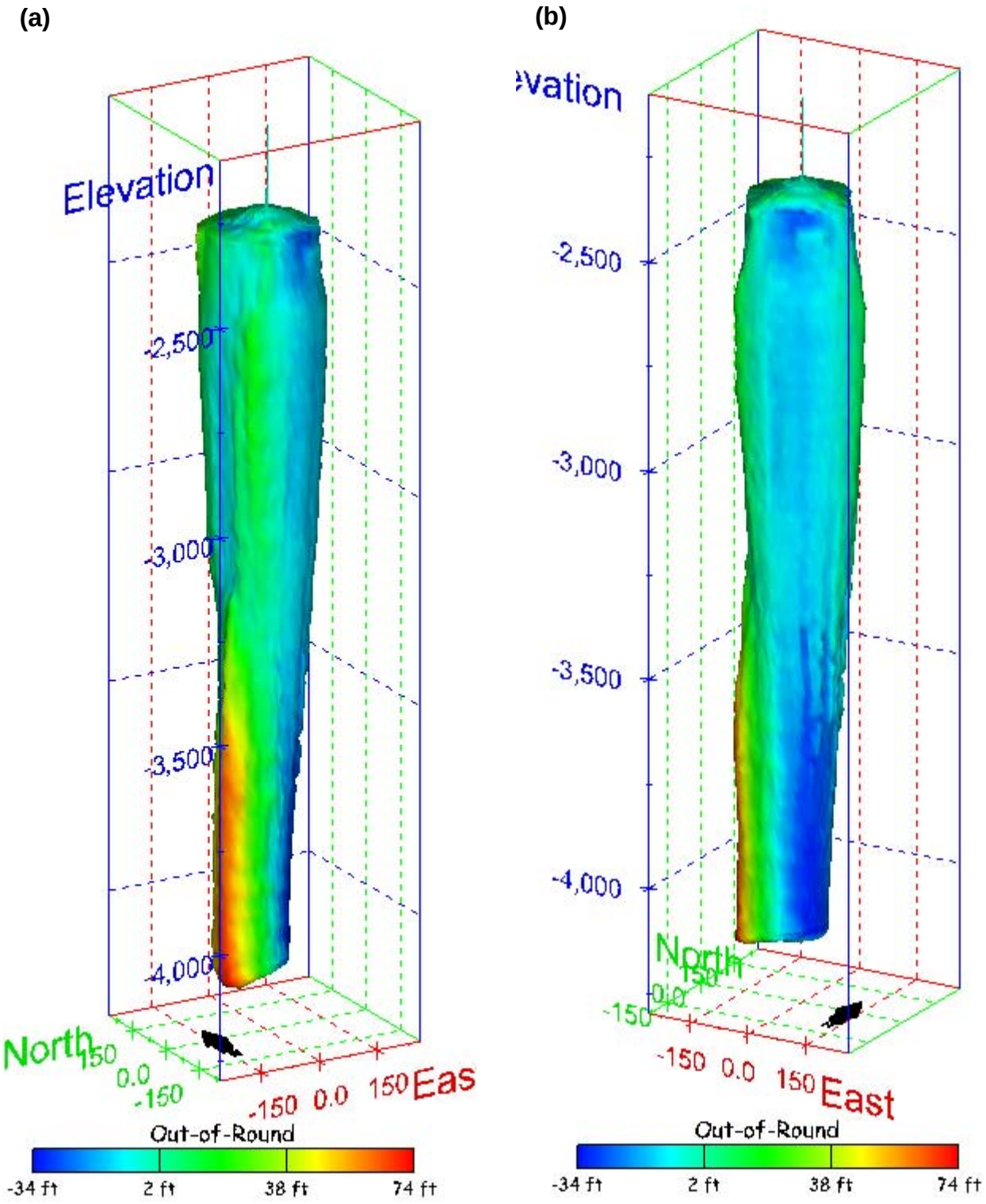

Figure 367. Sonar images of cavern BH-114, showing the geometry of the cavern colored by out-of-round distance. View from (a) azimuth 210°, elevation 20°; (b) azimuth 150°, elevation 20°.

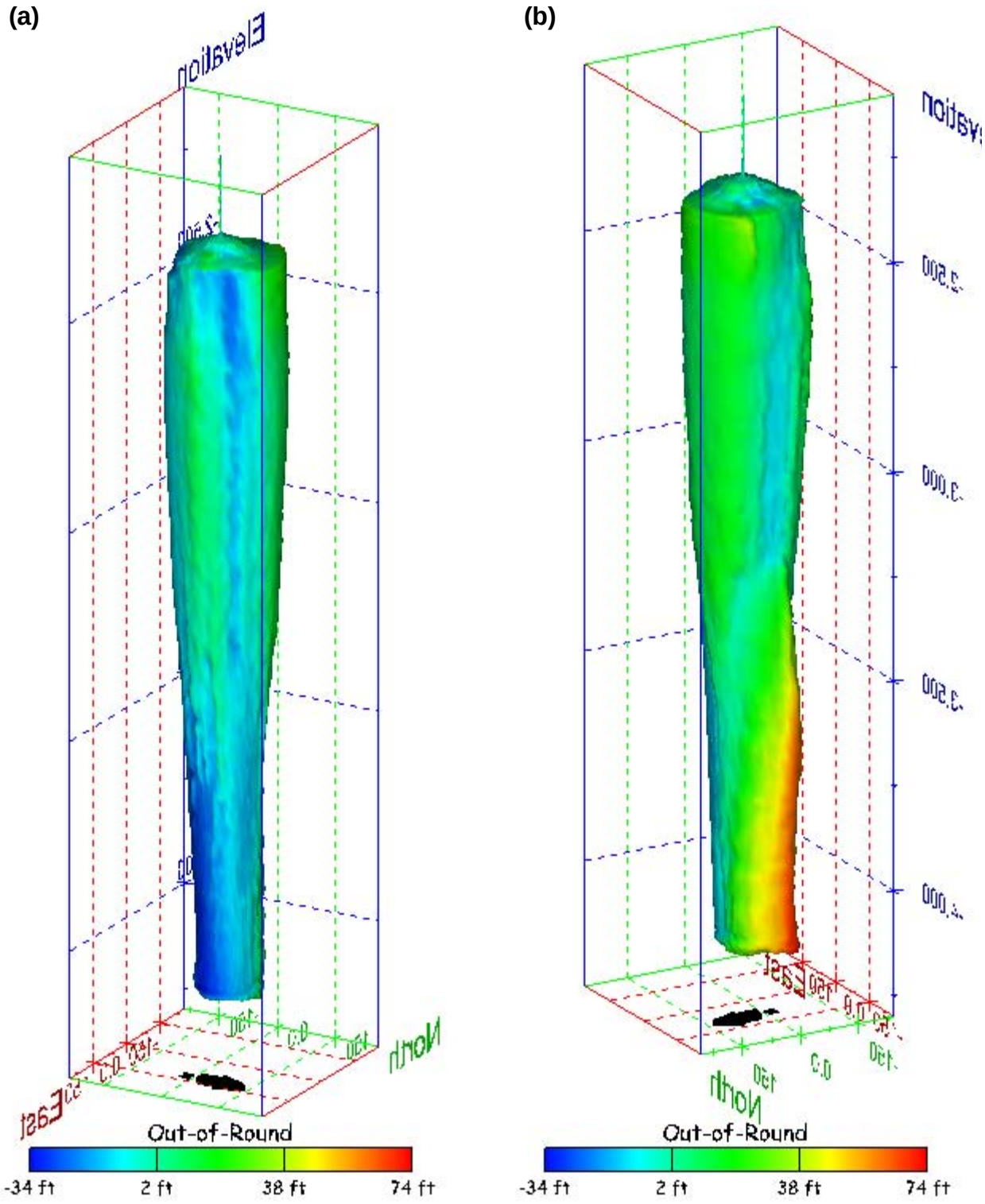

Figure 368. Sonar images of cavern BH-114, showing the geometry of the cavern colored by out-of-round distance. View from (a) azimuth 60°, elevation 20°; (b) azimuth 300°, elevation 20°.

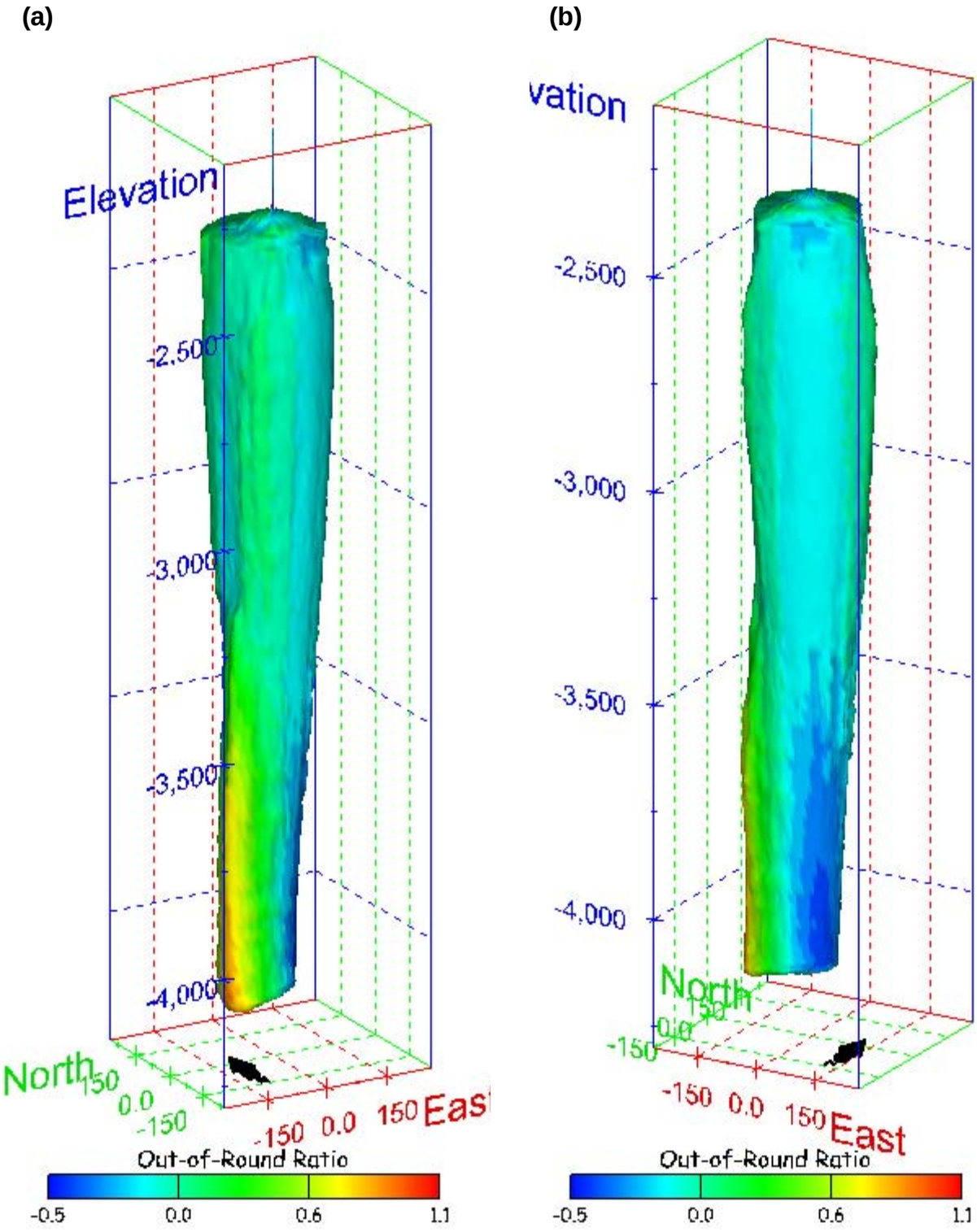

Figure 369. Sonar images of cavern BH-114, showing the geometry of the cavern colored by out-of-round ratio. View from (a) azimuth 210°, elevation 20°; (b) azimuth 150°, elevation 20°.

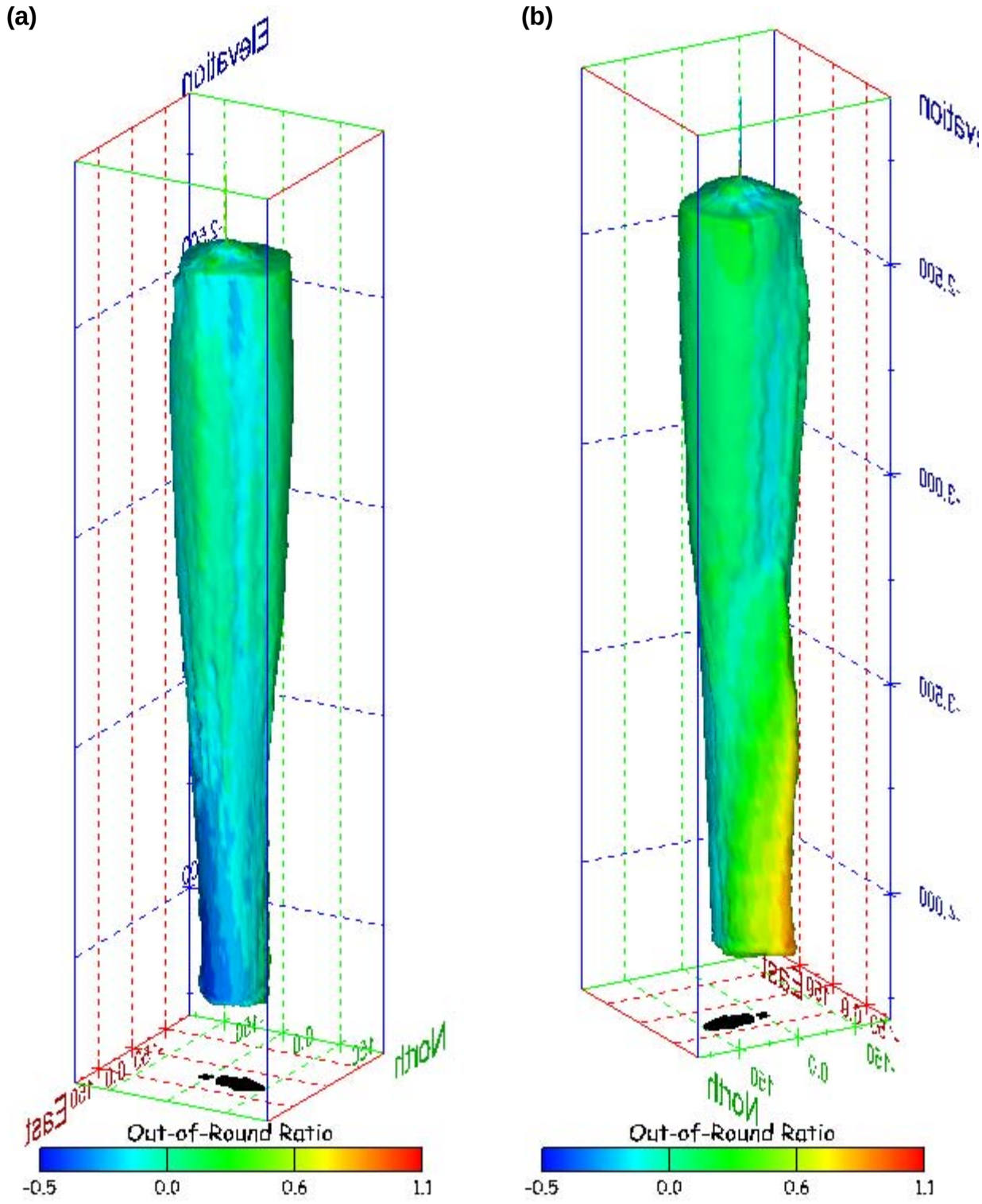

Figure 370. Sonar images of cavern BH-114, showing the geometry of the cavern colored by out-of-round ratio. View from (a) azimuth 60°, elevation 20°; (b) azimuth 300°, elevation 20°.

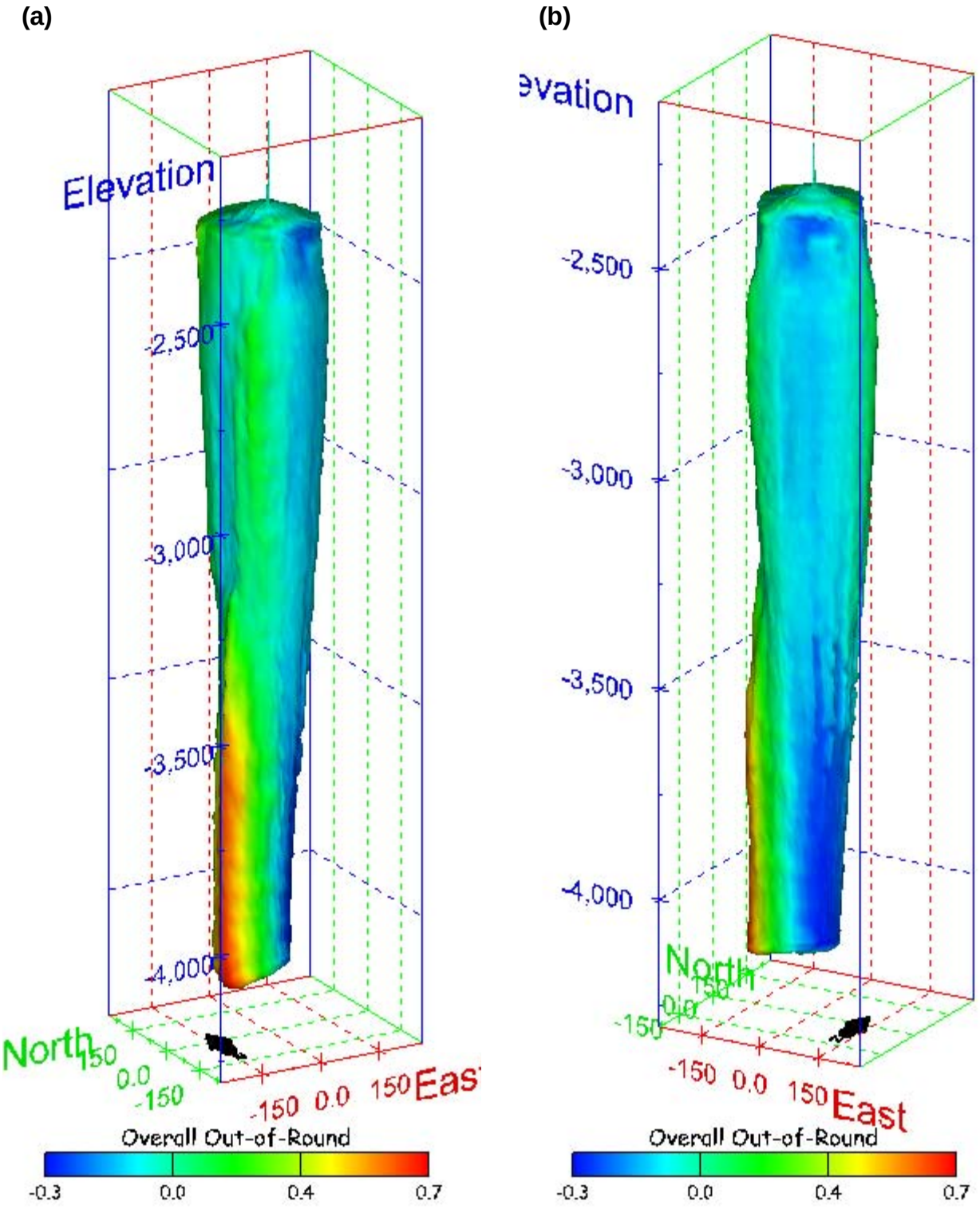

Figure 371. Sonar images of cavern BH-114, showing the geometry of the cavern colored by overall out-of-round ratio. View from (a) azimuth 210°, elevation 20°; (b) azimuth 150°, elevation 20°.

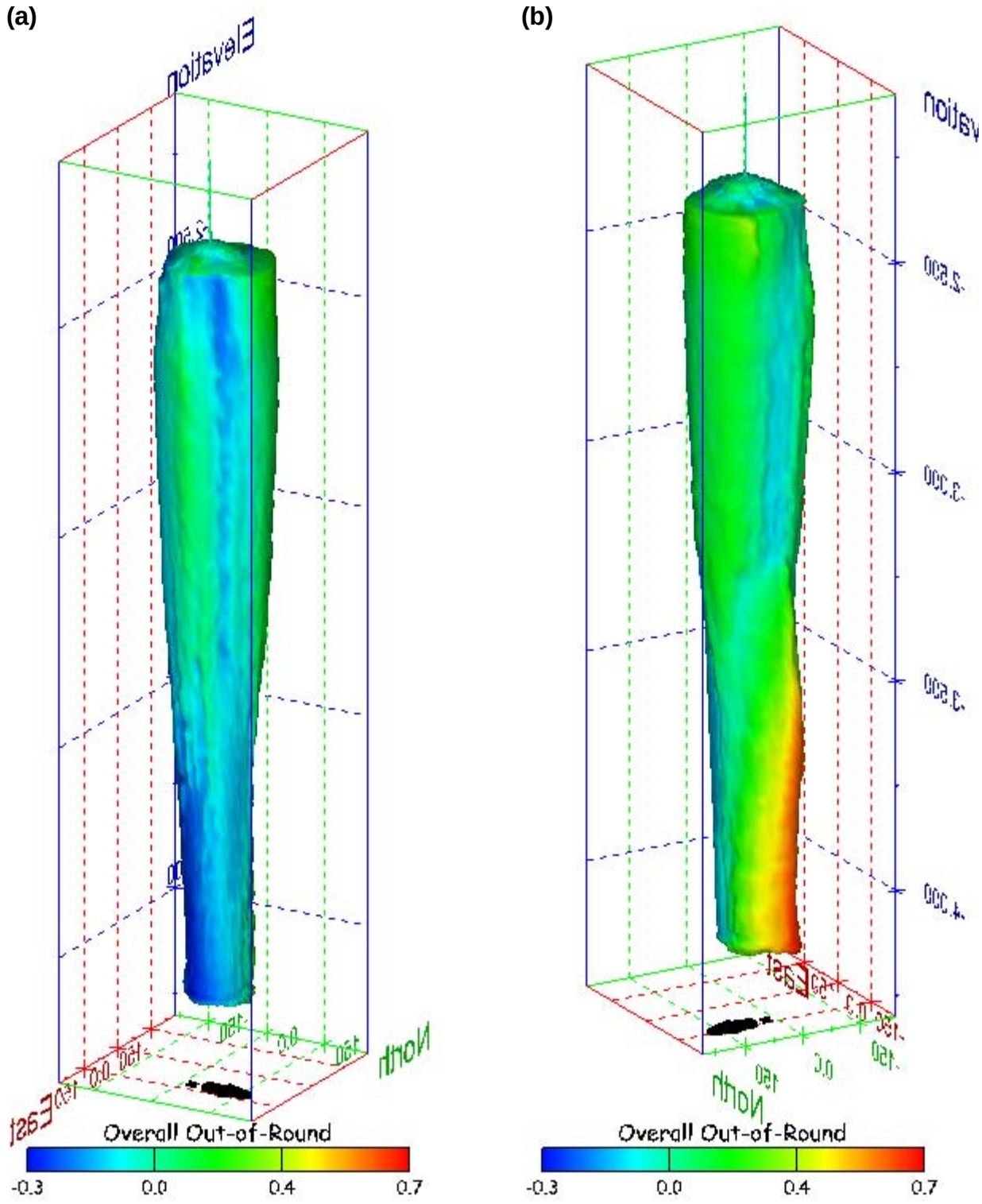

Figure 372. Sonar images of cavern BH-114, showing the geometry of the cavern colored by overall out-of-round ratio. View from (a) azimuth 60°, elevation 20°; (b) azimuth 300°, elevation 20°.

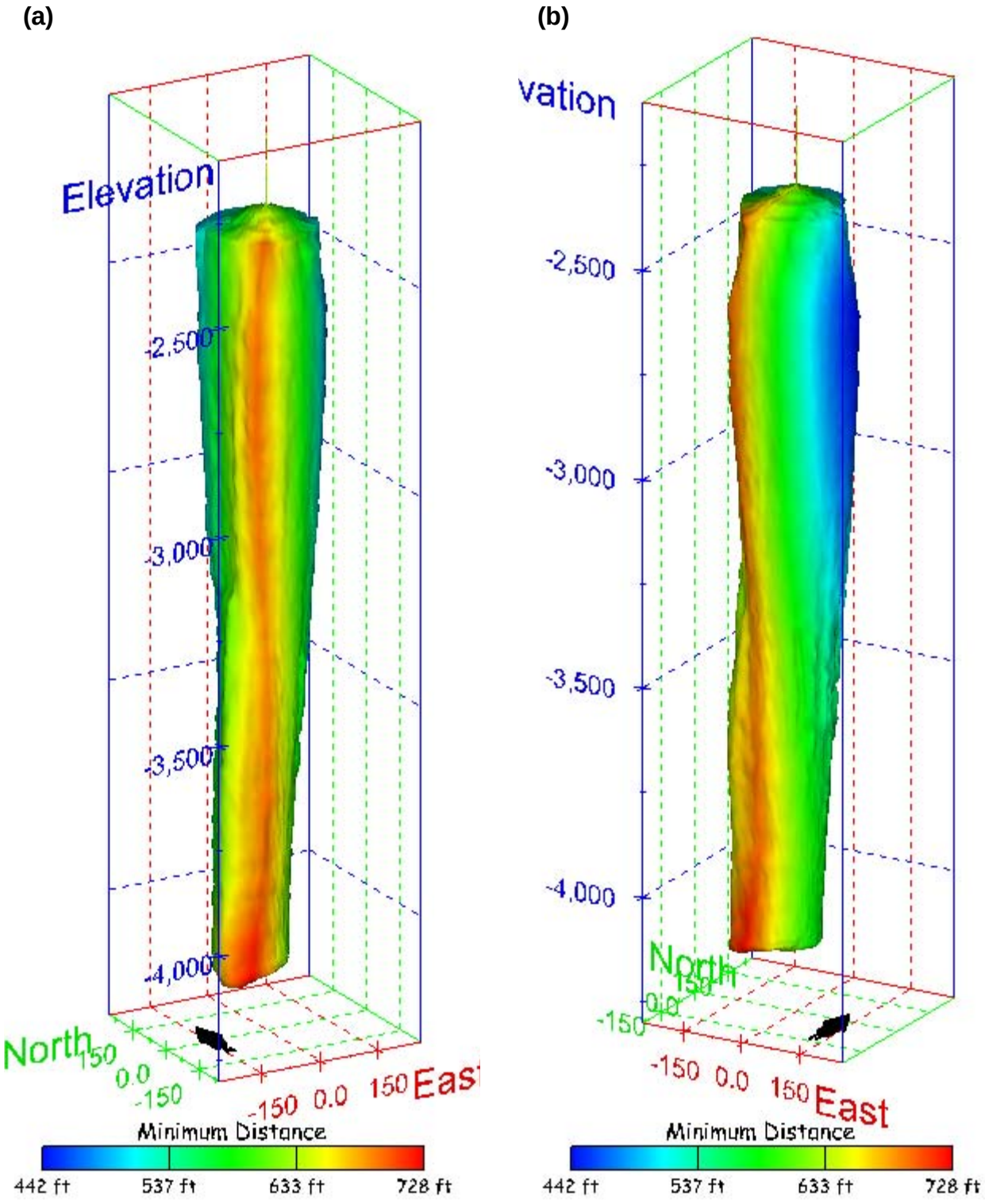

Figure 373. Sonar images of cavern BH-114, showing the geometry of the cavern colored by the minimum distance to the nearest neighboring cavern. View from (a) azimuth 210°, elevation 20°; (b) azimuth 150°, elevation 20°.

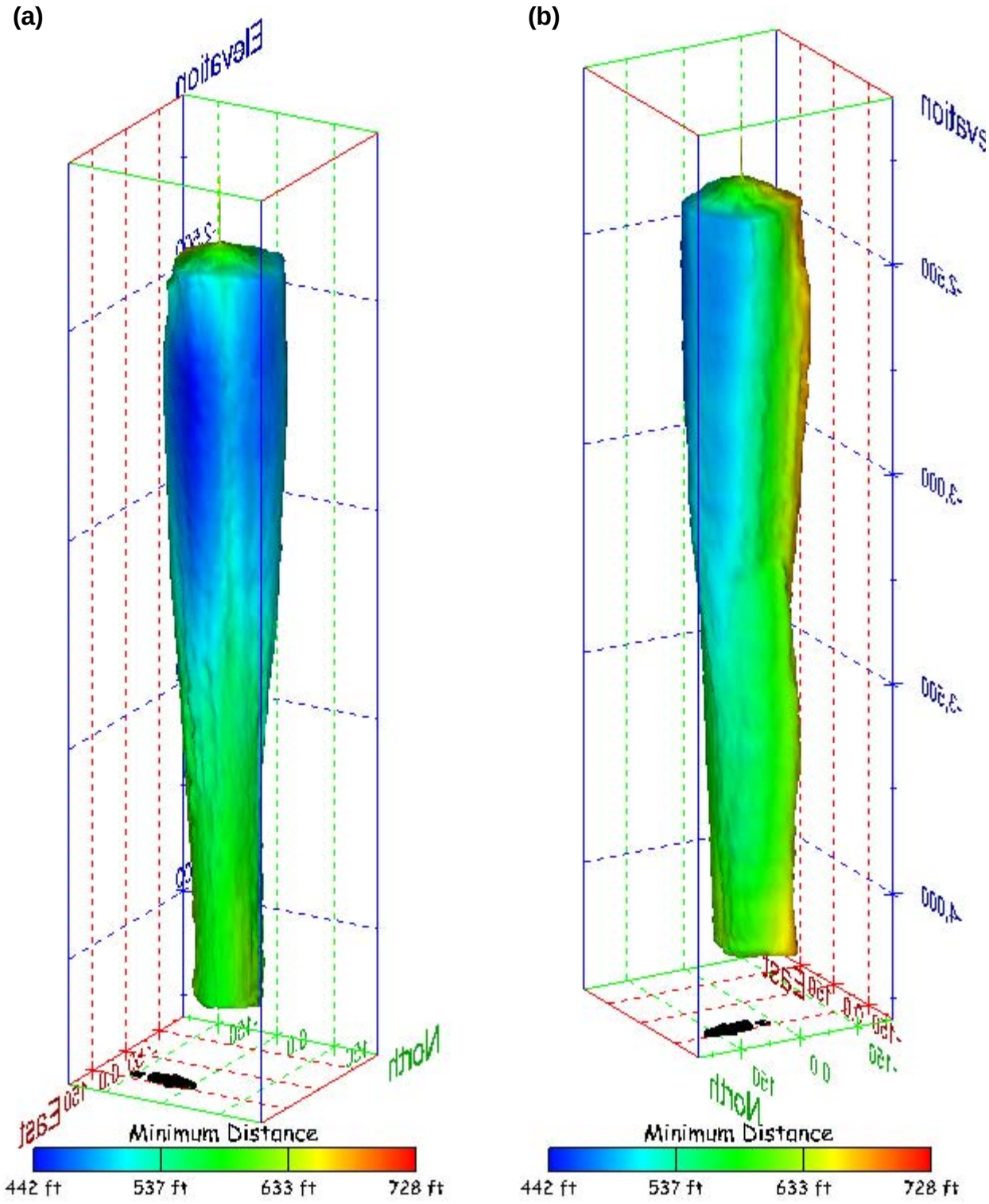

Figure 374. Sonar images of cavern BH-114, showing the geometry of the cavern colored by minimum distance to the nearest neighboring cavern. View from (a) azimuth 60°, elevation 20°; (b) azimuth 300°, elevation 20°.

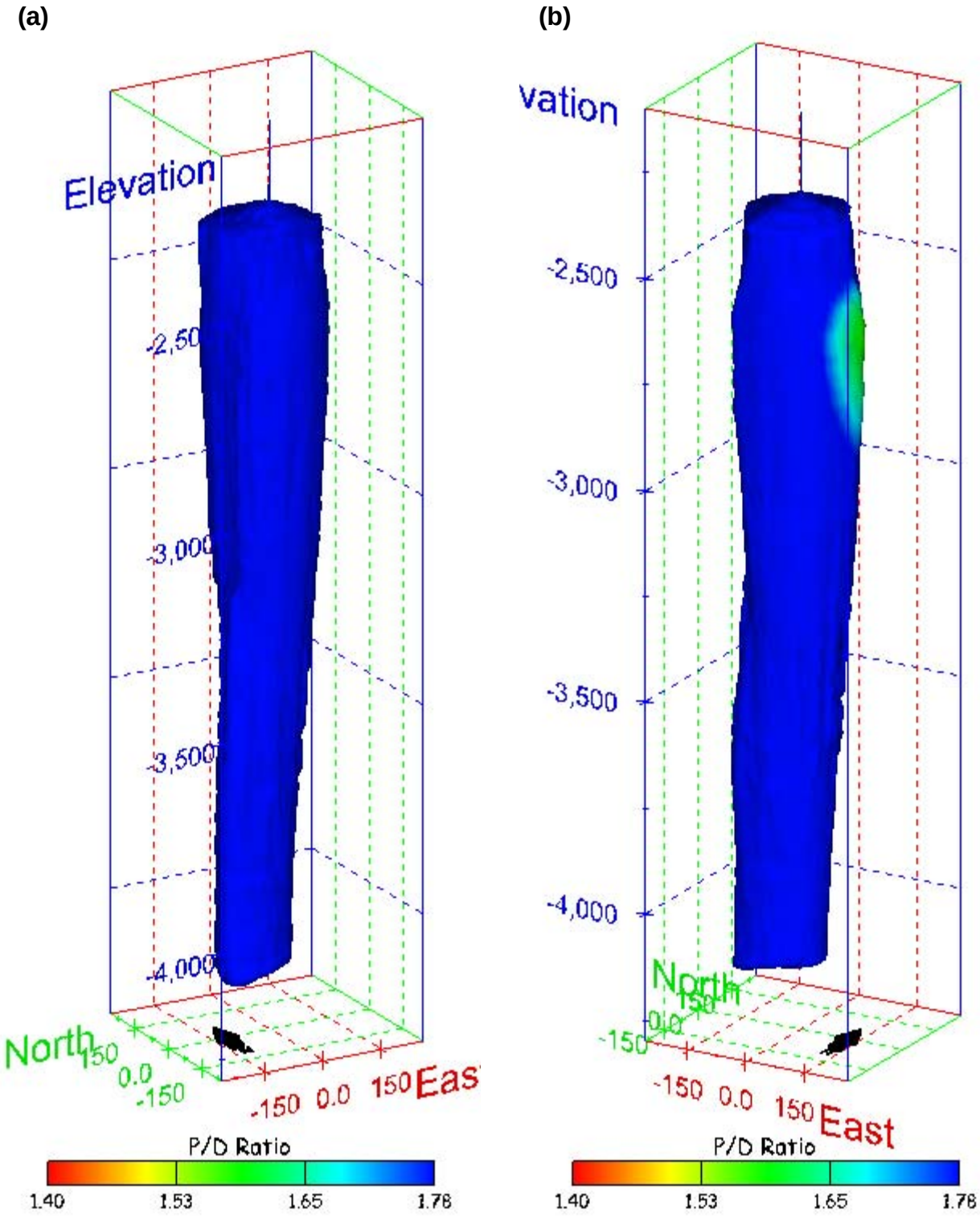

Figure 375. Sonar images of cavern BH-114, showing the geometry of the cavern colored by three-dimensional pillar-to-diameter ratio. View from (a) azimuth 210°, elevation 20°; (b) azimuth 150°, elevation 20°.

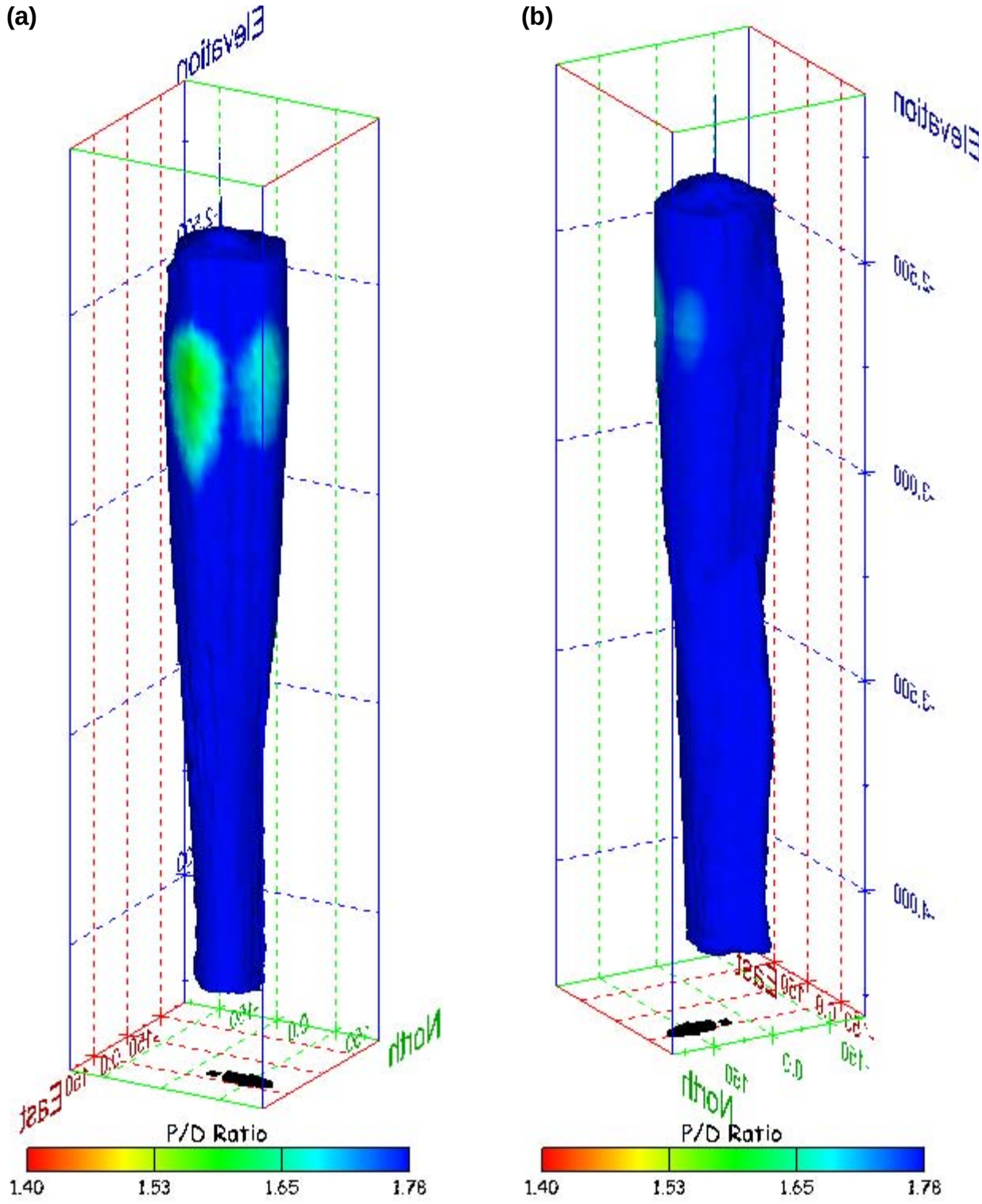

Figure 376. Sonar images of cavern BH-114, showing the geometry of the cavern colored by three-dimensional pillar-to-diameter ratio. View from (a) azimuth 60°, elevation 20°; (b) azimuth 300°, elevation 20°.

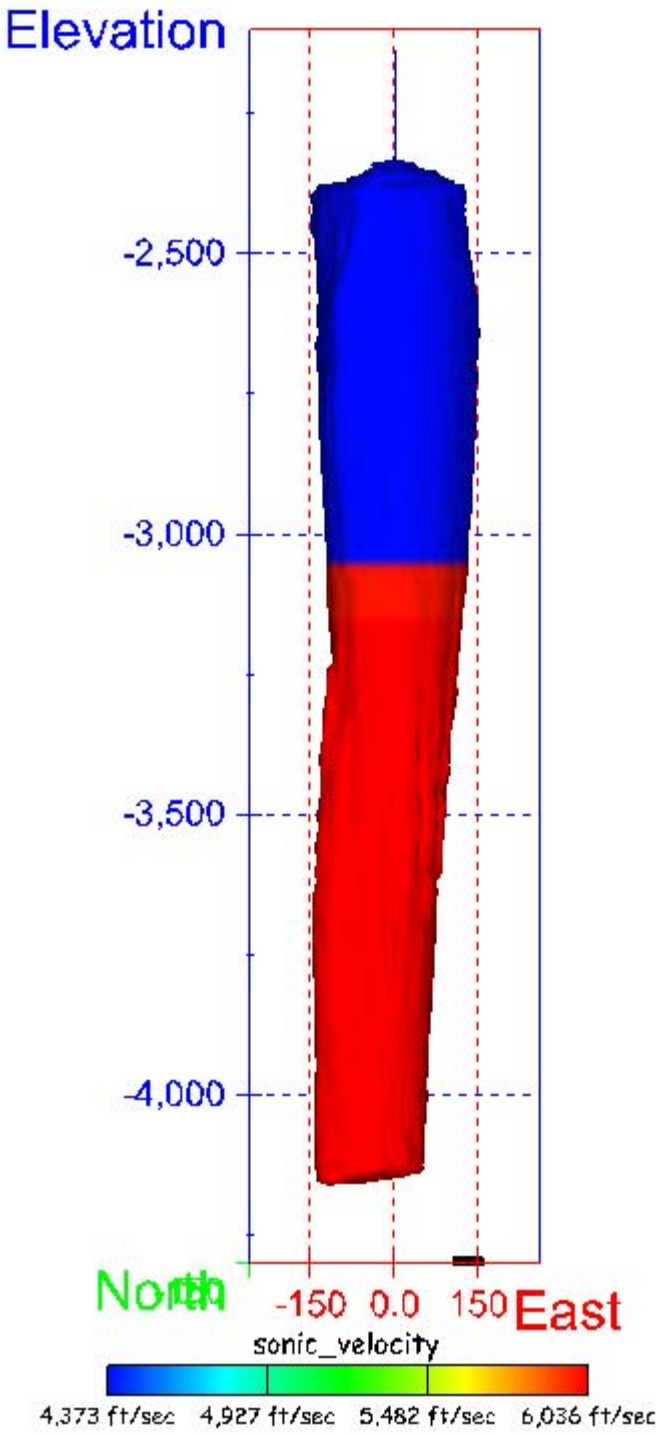

Figure 377. Sonar image of cavern BH-114, showing the geometry of the cavern colored by the reported velocity of sound on the survey date of October 2003. View from due south, elevation zero.

The Big Hill Cavern Field as a Whole

Figures 378 through 387 show the various caverns at the Big Hill SPR site in relationship to one another. Only data components that are particularly relevant to the cavern field, itself, are presented in this section. These include cavern elevation (figs. 378 and 379), overall average cavern radius (figs. 380 and 381), and the cavern out-of-round distances (figs. 382 and 383). Also included are the minimum distances to adjoining caverns (figs. 384 and 385), and the three-dimensional pillar-to-diameter ratio (figs 386 and 387).

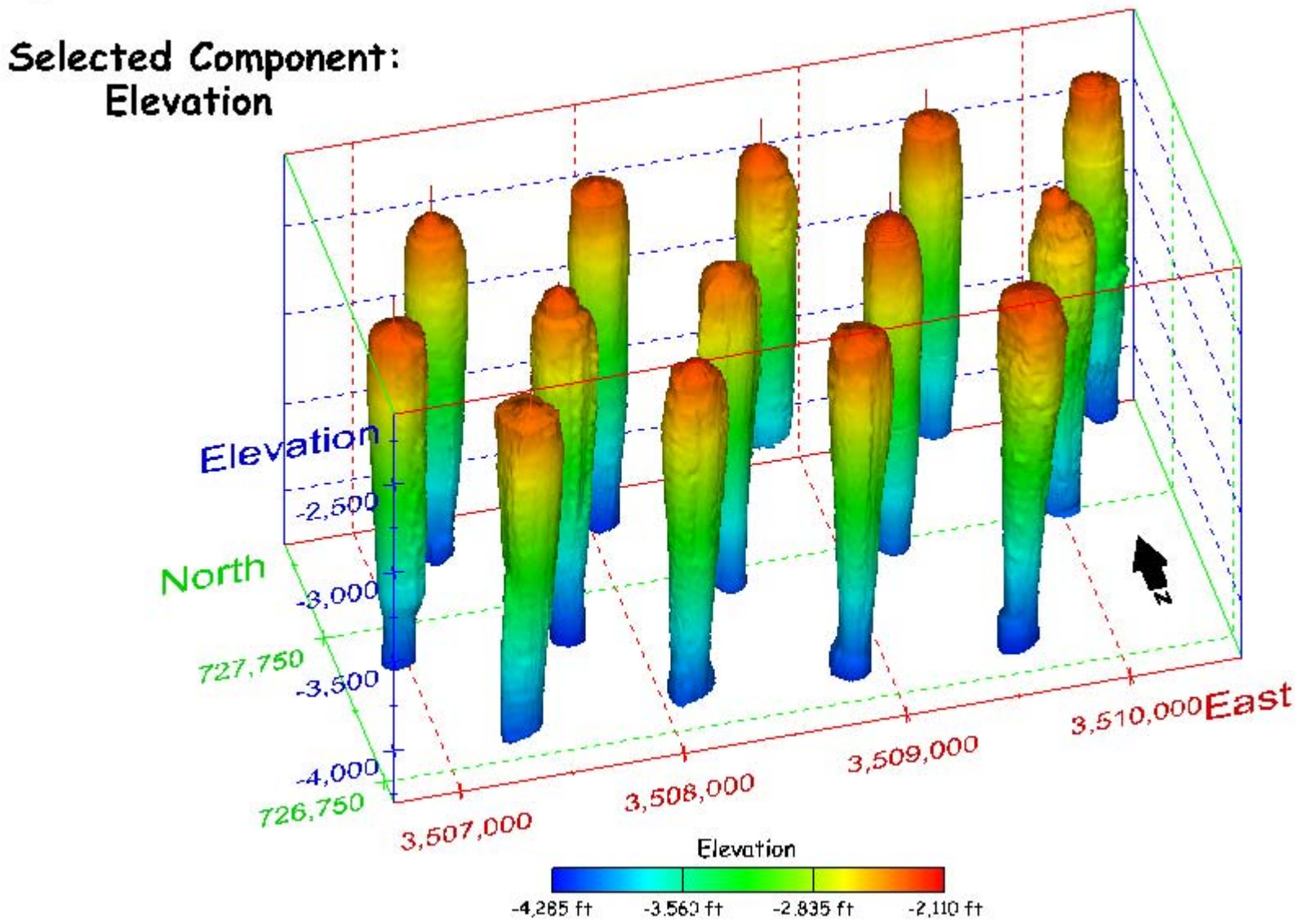

Figure 378. Perspective view of the entire cavern field at the Big Hill SPR site from the southwest. Component shown is elevation.

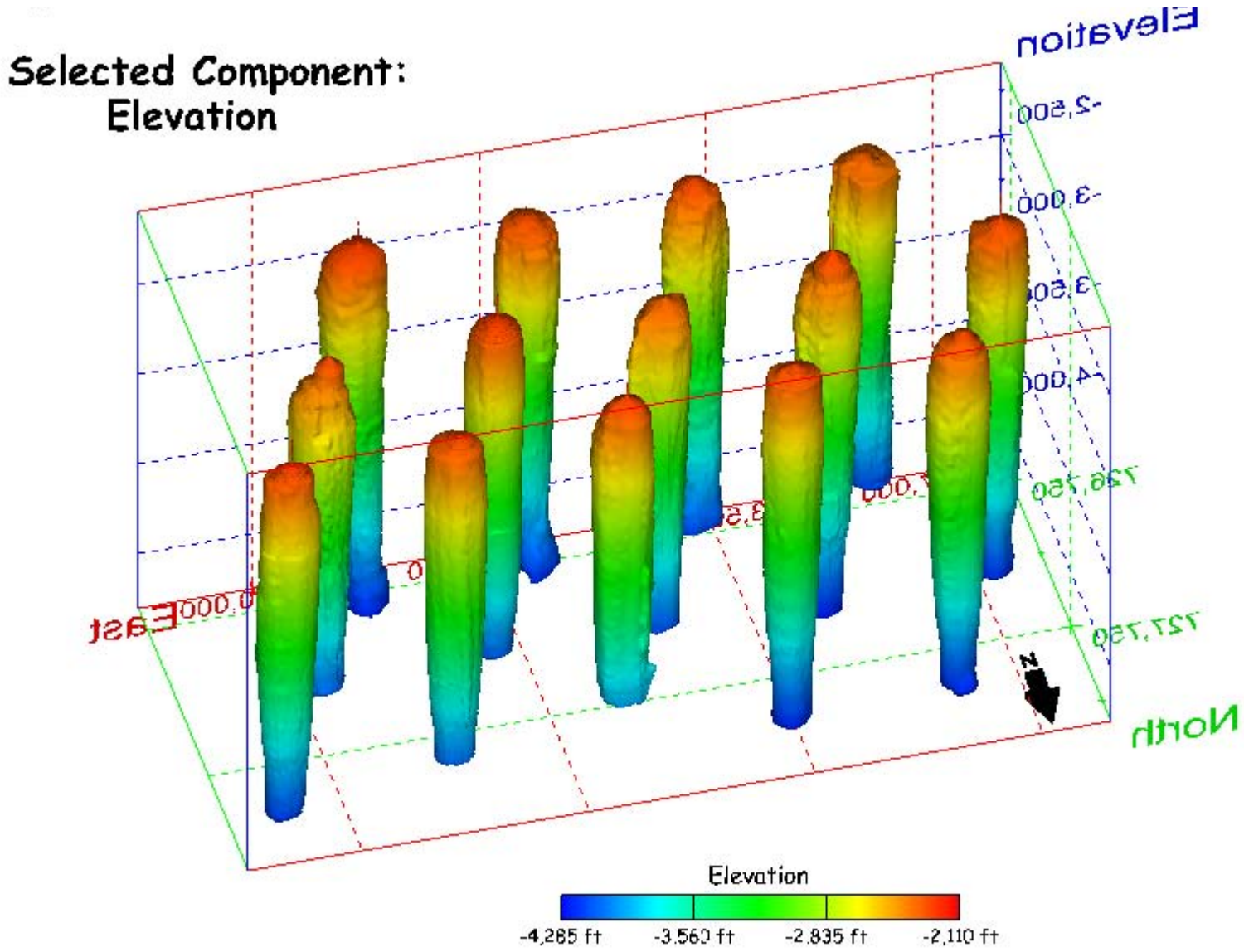

Figure 379. Perspective view of the entire cavern field at the Big Hill SPR site from the northeast. Component shown is elevation.

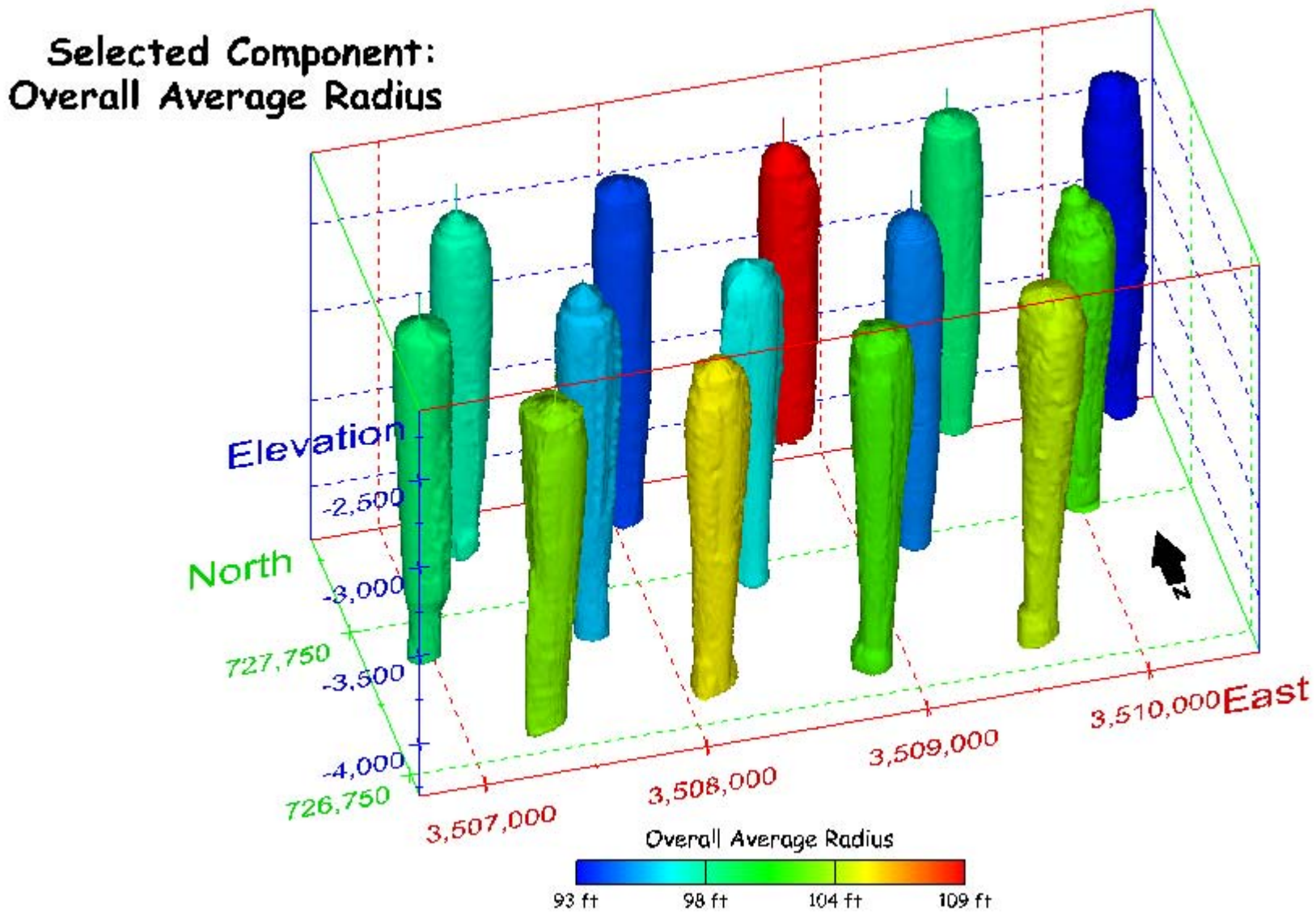

Figure 380. Perspective view of the entire cavern field at the Big Hill SPR site from the southwest. Component shown is overall average radius.

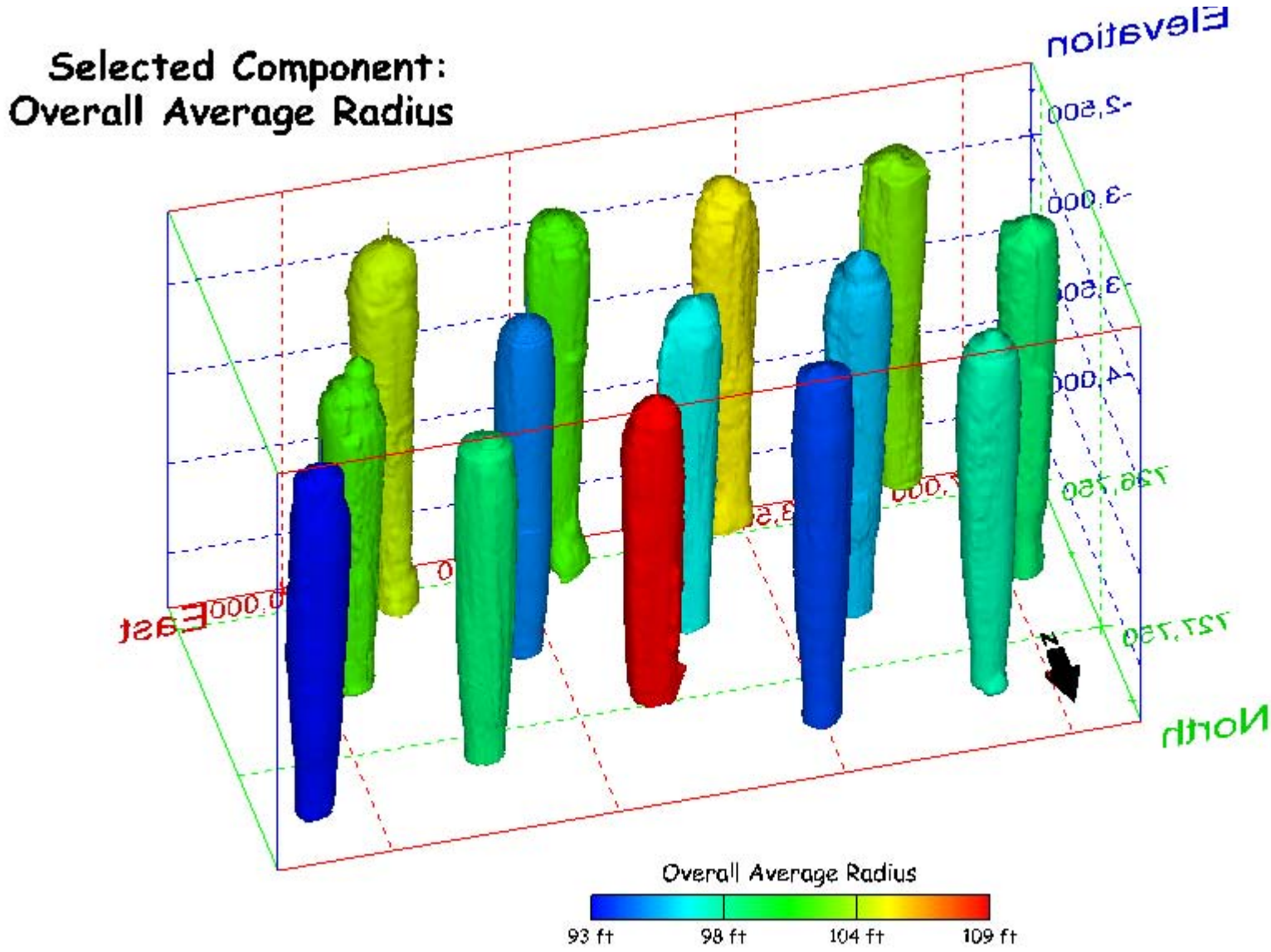

Figure 381. Perspective view of the entire cavern field at the Big Hill SPR site from the northeast. Component shown is overall average radius.

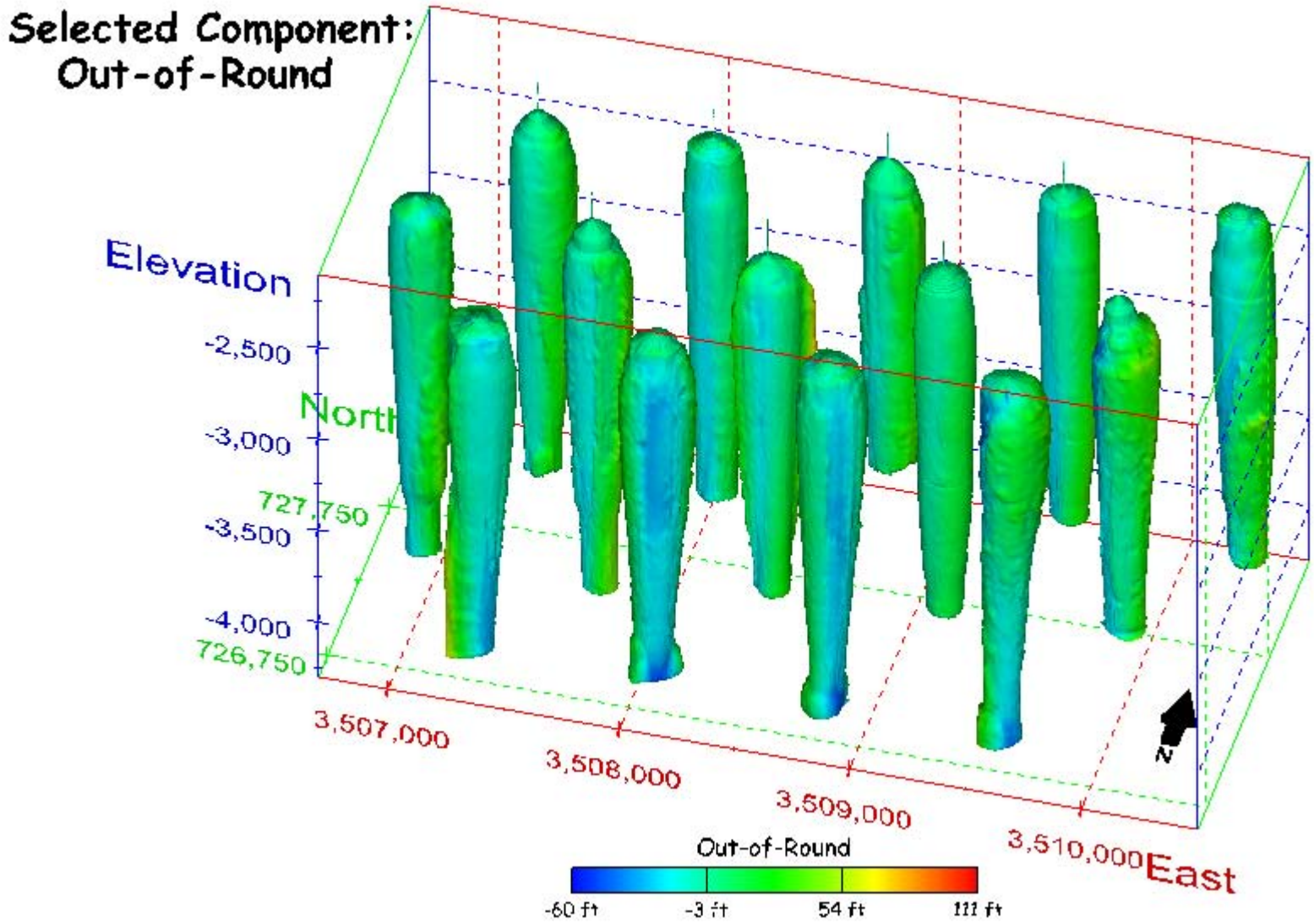

Figure 382. Perspective view of the entire cavern field at the Big Hill SPR site from the southwest. Component shown is the out-of-round distance.

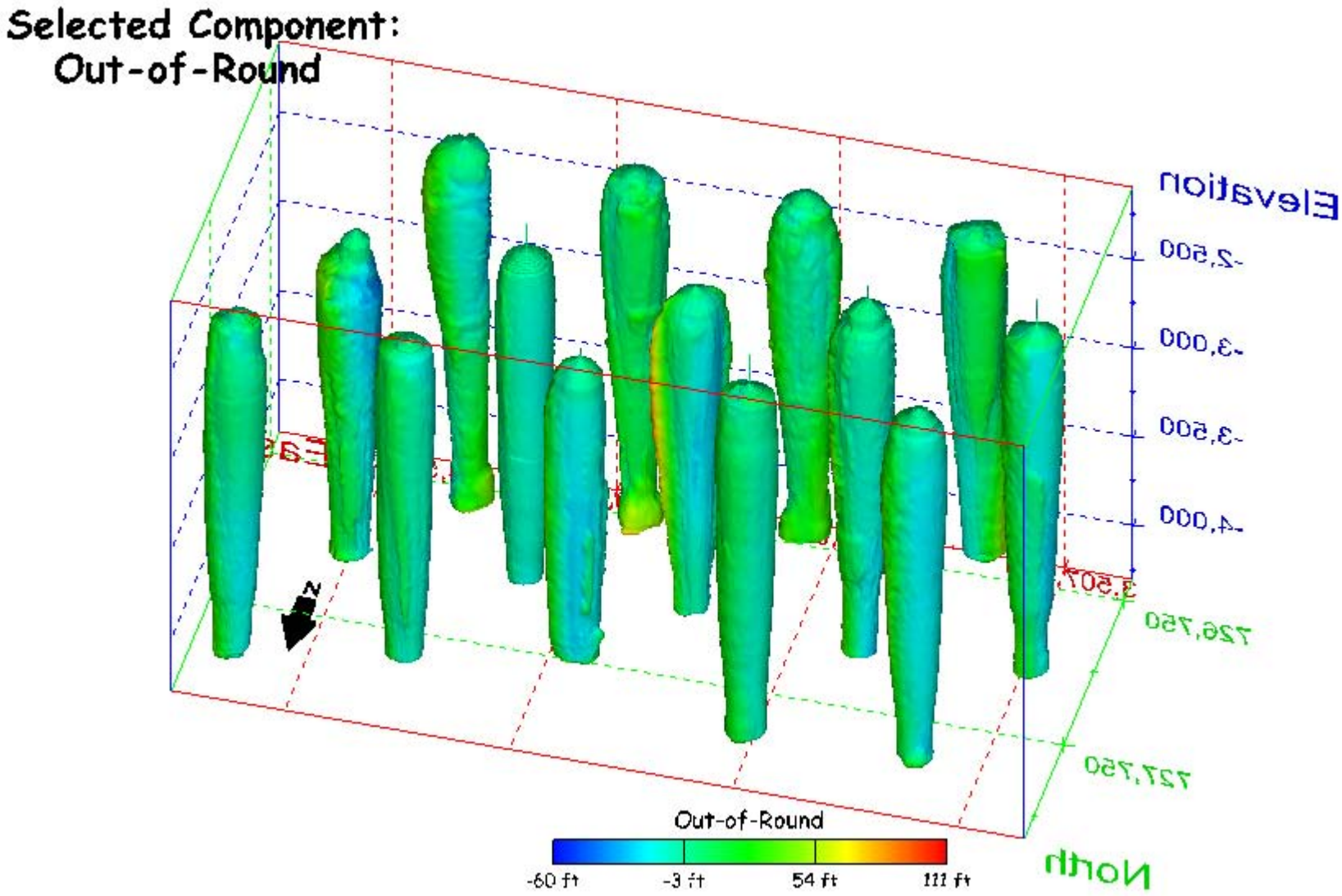

Figure 383. Perspective view of the entire cavern field at the Big Hill SPR site from the northeast. Component shown is the out-of-round distance.

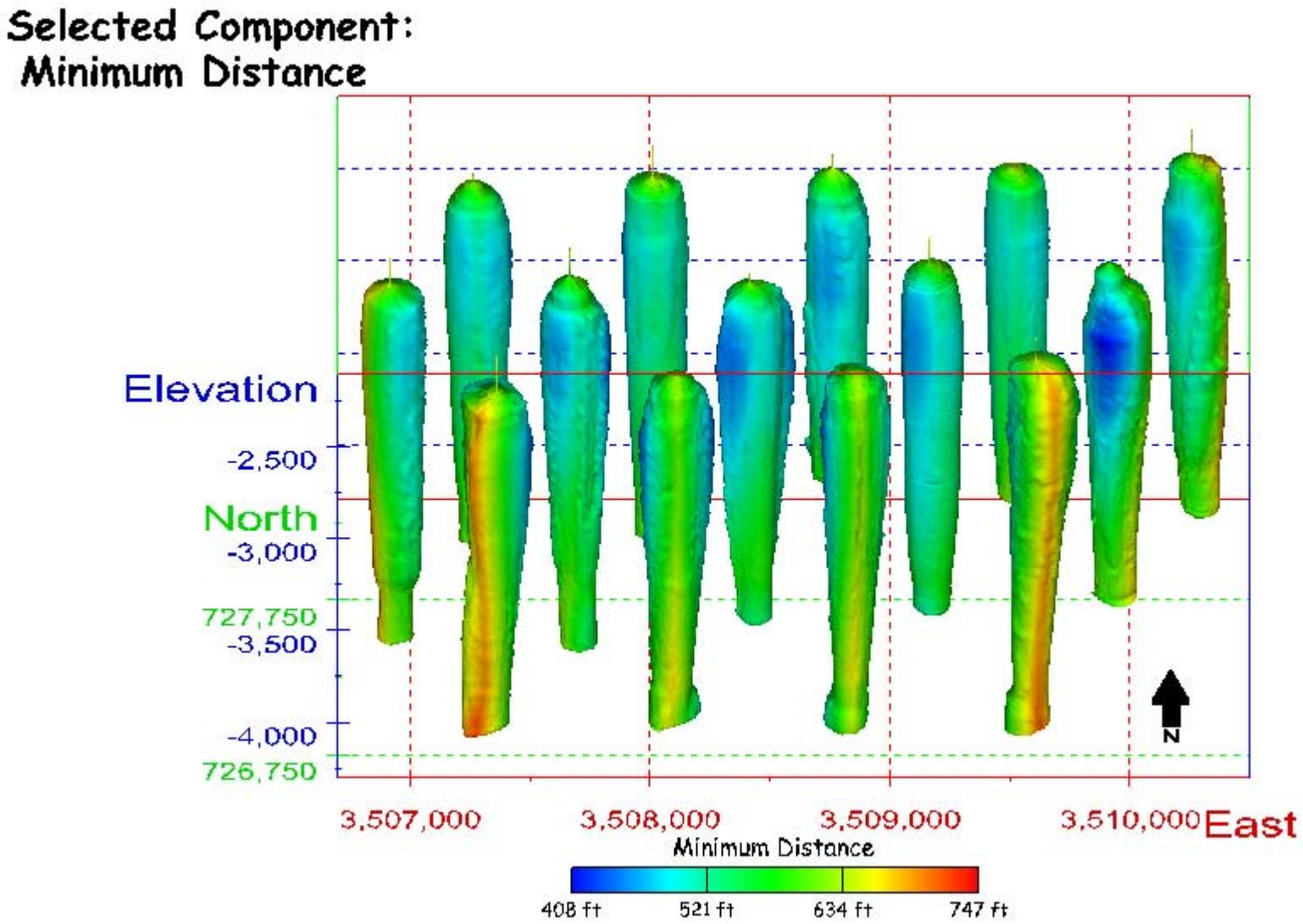

Figure 384. Perspective view of the entire cavern field at the Big Hill SPR site from the south. Component shown is the minimum distance to adjoining cavern(s).

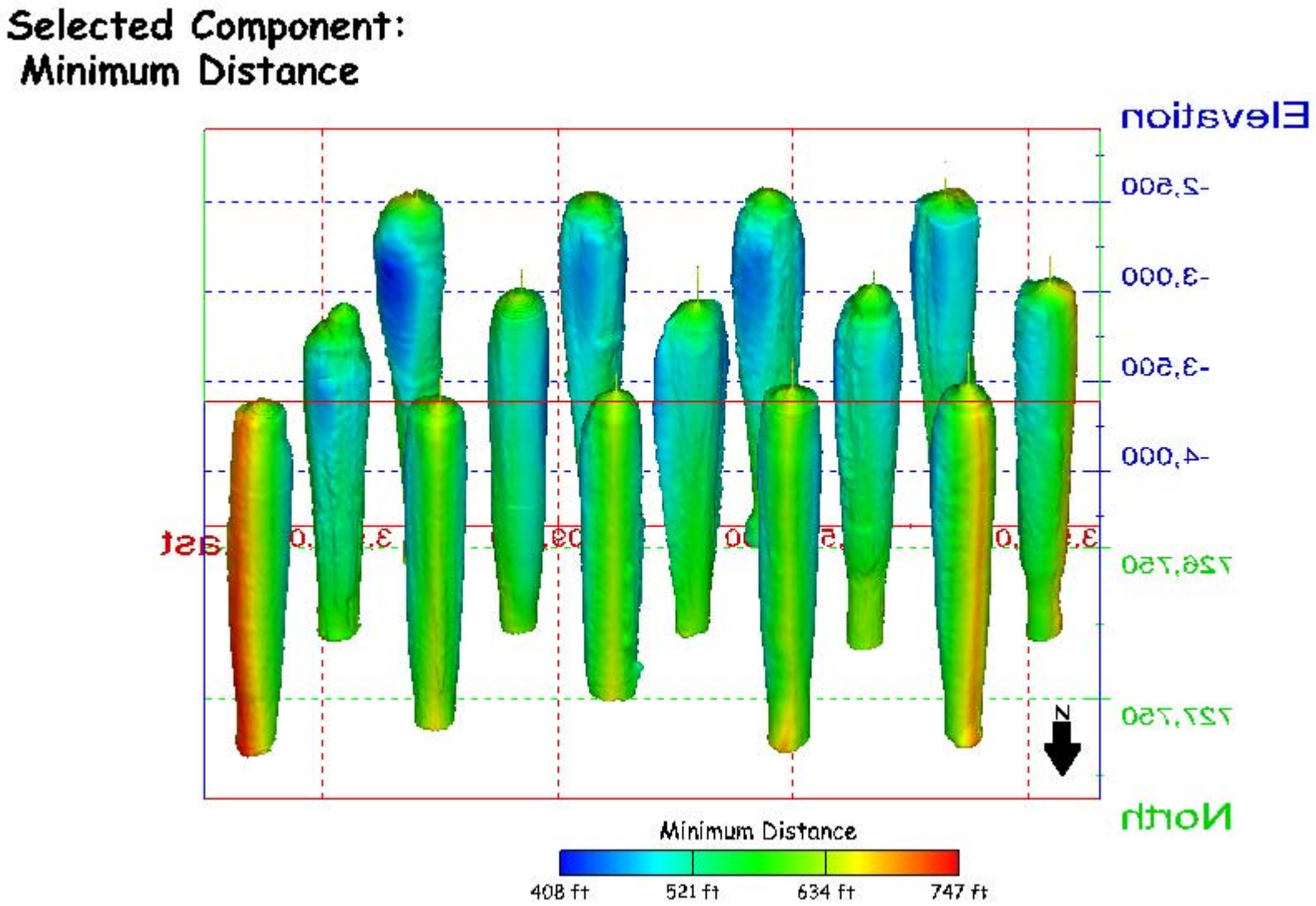

Figure 385. Perspective view of the entire cavern field at the Big Hill SPR site from the north. Component shown is the minimum distance to adjoining cavern(s).

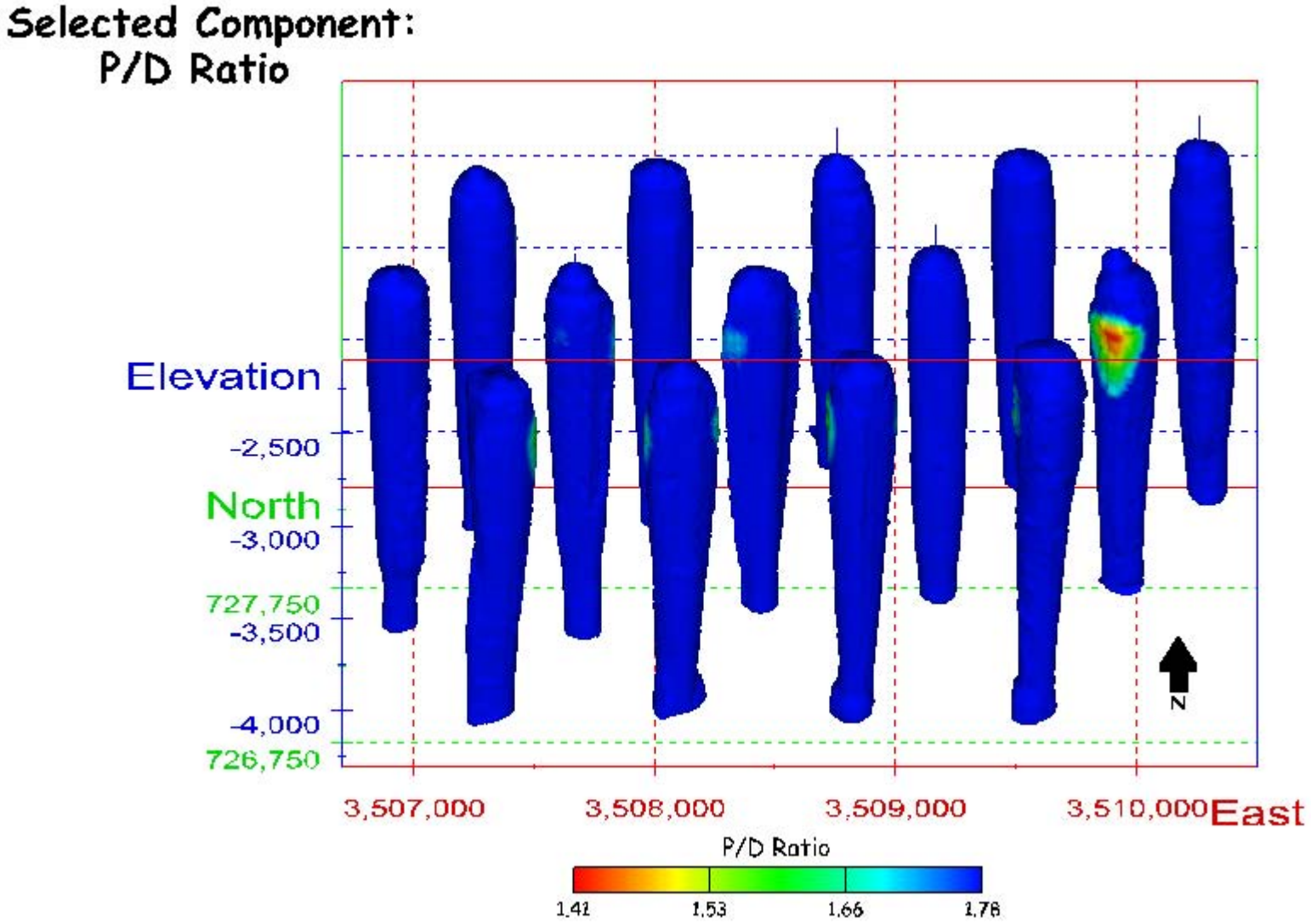

Figure 386. Perspective view of the entire cavern field at the Big Hill SPR site from the south. Component shown is the three-dimensional pillar-to-diameter ratio.

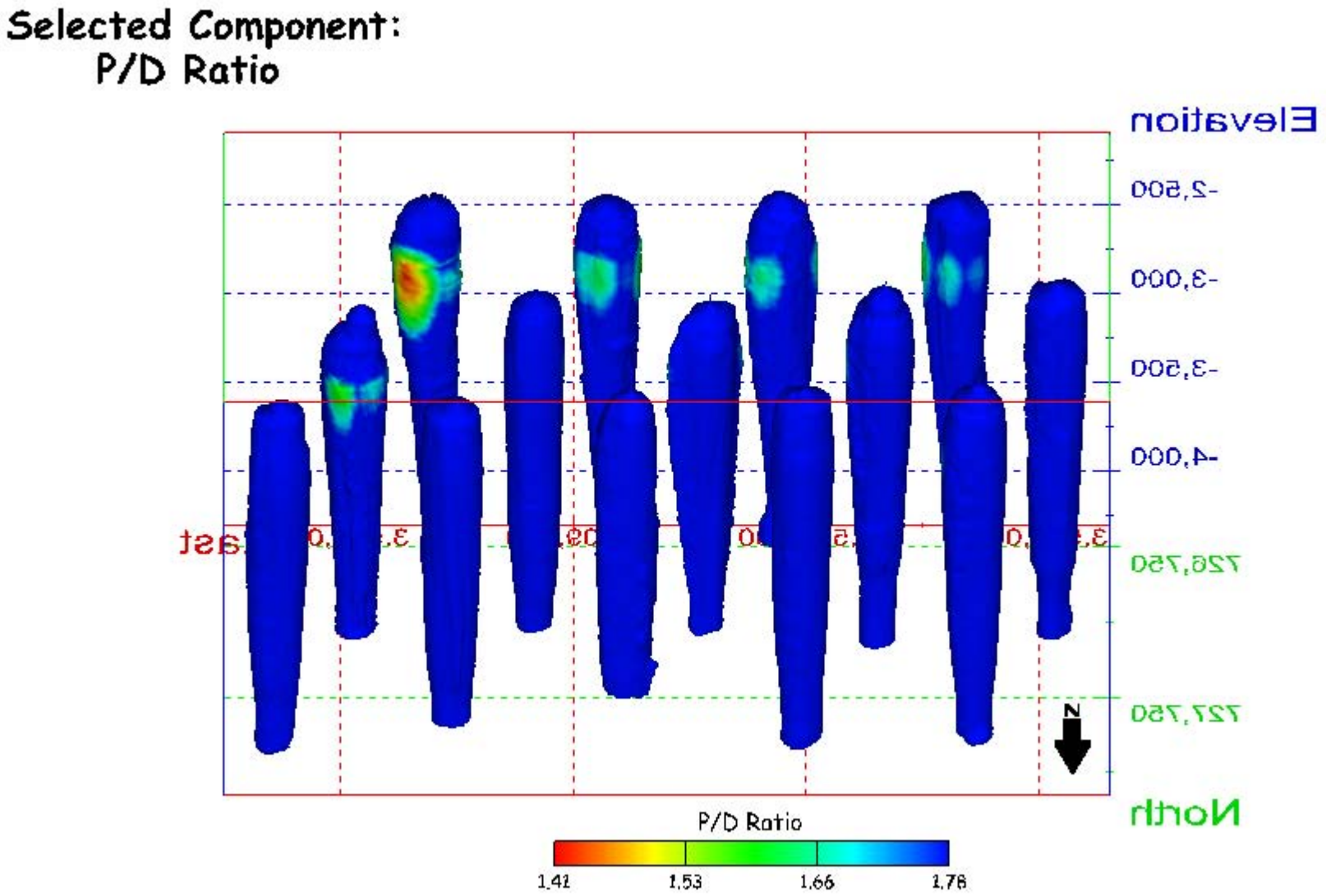

Figure 387. Perspective view of the entire cavern field at the Big Hill SPR site from the north. Component shown is the three-dimensional pillar-to-diameter ratio.

REFERENCES

Lord, A.S., and Stein, J.S. 2006. Three-dimensional pillar-to-diameter calculations for caverns at each of the four U.S. Strategic Petroleum Reserve sites. Fall 2006 Technical Meeting, Rapid City, S.Dak., October 1–4, 2006. Solution Mining Research Institute, Clarks Summit, Penna., p. 271–291.

Rudeen, D., and Lord, A.S., 2007. A Windows application for three-dimensional pillar-to-diameter calculations for the U.S. Strategic Petroleum Reserve. Milestone Report submitted to U.S. Department of Energy, Strategic Petroleum Reserve Project Office, New Orleans, La., March 21, 2007. Sandia National Laboratories, Albuquerque, N. Mex. 35 p.

APPENDIX: INSTALLATION AND USE OF 4DIM PLAYER SOFTWARE

This page intentionally left blank.

Introduction

This appendix describes a powerful means for examining a three-dimensional geologic model. the geological modeling software environment, collectively known as MVS (Mining Visualization System), developed by C Tech Development Corporation (www.ctech.com), includes a derivative model "type", known as *4DIM* files (for **4**-**D**imensional **I**nteractive **M**odel). 4DIM models are fully three-dimensional representations of selected model components, developed through the use of C Tech's modeling software.

The unique aspect of 4DIM models is that they are *user manipulable*. In contrast to a static still image or screen capture, the user may rotate, pan, and zoom in or out on any part of the model that is desired. The ability to rotate and change the viewing perspective of a three-dimensional model may be critical to understanding and conceptualizing detailed spatial relationships. Objects closer to the viewer behave in subtle, but importantly different, ways than objects located farther away. Such visual cues, obtained through on-screen interaction with a model, simply are not possible with any static view.

C Tech Development Corporation makes an "unlicensed" 4DIM viewer freely available over the internet. A "licensed" version is also available for purchase. Unlicensed, in this context, means that the player will not view *all* 4DIM files. A specially encoded 4DIM file is required in the "unlicensed" case. Only 4DIM models that have been created by the higher-end versions of C Tech software are capable of writing such model files. Functionally, a "license" is inserted, as binary code, into these files. 4DIM models generated by the lower-cost and more simplistic versions of C Tech's software do not generate these encoded files.

Sandia National Laboratories licenses MVS, the top-end modeling software from C Tech Development Corporation. Accordingly all 4DIM files generated using MVS are encoded with the necessary portable-license key for use with the unlicensed version of the player.

Software Installation Instructions

The 4DIM player software currently runs on personal computers under the Microsoft Windows® operating system. the unlicensed version of the player may be downloaded over the internet from `http://www.ctech.com`. As the website changes episodically, some internal navigation of the site may be required to located the downloadable version. A functioning version of the unlicensed 4DIM player is included on the CD-R in the back of this report. Administrator privileges are required to install the 4DIM player. However, these privileges are not required for routine running of the software.

To install the 4DIM player, located the file, `4DIM_setup.exe`, within the `install` subdirectory (folder) of the CD-R. Note that the `.exe` extension will not necessarily be visible if the Windows file manager option to "`Hide file extensions for known file types`" is checked. Double-click or otherwise open this file. the preferred installation location of a standard Windows PC is in a `c:\4DIM` directory (at the root level of the boot or system disk). This is the default location, and it may be changed as desired, so long as the caveat regarding not installing the software to a folder whose name contains a space, is observed. All defaults may simply be accepted during the installation process.

Software Operating Instructions

Once properly installed, the file extension "`.4d`" is associated by Windows with 4DIM model files and with the 4DIM player. Therefore, a 4DIM model may be viewed simply by navigating to the storage location of any .4d file and double-clicking on the relevant icon. The 4DM player may also be started via the `Windows Start │Programs` menu command structure, or by use of a desktop shortcut. In either

of these latter instances, in will be necessary to open a particular 4DIM model file using the player's `File | Open` menu command. The remaining menu buttons operate in a manner consistent with standard Windows programs.

Once a .4d file is opened in the viewer, the visible model may be manipulated as follows.

1. To rotate the model, left-click and drag somewhere on the visible model.
2. To pan (shift) the model on the screen, right-click and drag somewhere on the model.
3. To zoom in, left click which holding down the `Shift` key, and move the mouse pointer upward on the screen. To zoom out, left-click while holding down the `Shift` key and move the mouse pointer downward on the screen. Zooming in either direction is toward/from the center of the screen, so it may be necessary to pan the model (see above) to maintain the desired position on the screen.
4. To specify the view from a particular direction, open the `Az-El` (azimuth and elevation) menu option at the top of the 4DIM player screen. This operation will bring up a separate window that will allow specification of the azimuth *from* which to view the model, the elevation above (+) or below (–) the horizon from which to view the model, and the scale factor which controls the magnification (zoom level) of the image. Either the radio buttons or the slider or the indicated type-in boxes may be used to specify the view. Use of the "`RNC`" menu option may also be necessary when a file is first opened.
5. If the view becomes hopelessly confused, or if the model disappears completely from the view, there are two ways to re-center the default view: (a) Use the "`RNC`" menu button at the top of the 4DIM player screen, or click on the multicolored button in the upper left of the Az-El window.

More than one interactive "model" may be contained in a 4DIM file. If this is the case, the slider bar at the bottom of the main player window will indicate "`Current frame [xx of nn]`", where nn is the total number of individual model representations within the file. to step through the sequence of a multi-frame 4DIM file, simply click on the arrows at either end of the slider bar or left-click and drag on the slider itself.

Depending upon how a 4DIM file containing multiple model representations was constructed, the successive frames may constitute an animated sequence. To view such a sequence, use one or more of the eight arrow buttons at the bottom left of the main player window. It will most likely help to increase the "`Delay (seconds)`" setting on the bottom right of the main window from its default value of 0.0. This sets the time between successive images, and the value may be adjusted as desired to achieve an aesthetically pleasing progression of frames.

An important setting for 4DIM files generated by Sandia National Laboratories is the screen background. The default value is black. However, many sequences contained on the CD-R with this report are predicated upon a white background. Certain text and other objects *may not be visible* unless this setting is changed. To do so, issue the menu command "`Settings | View | Background | Set to white`".

DISTRIBUTION:

U.S. Department of Energy (via CD-R only)
Strategic Petroleum Reserve Project Management Office
900 Commerce Road East
New Orleans, LA 70123

U.S. Department of Energy (3)
Strategic Petroleum Reserve Program Office
1000 Independence Avenue, SW
Washington, DC 20585
ATTN: D. Johnson, FE-421

Sandia Internal:

MS 0735 J. Merson, 6310 (electronic copy)
MS 1104 Margie Tatro, 6200 (electronic copy)
MS 0706 D.J. Borns, 6312 (electronic copy)
MS 0706 B.L. Ehgartner, 6312 (electronic copy)
MS 0706 B.L. Levin, 6312 (electronic copy)
MS 0706 Anna S. Lord, 6312 (electronic copy)
MS 0706 David L. Lord, 6312 (electronic copy)
MS 0706 D.E. Munson, 6312 (electronic copy)
MS 0706 C.A. Rautman, 6312 (electronic copy)
MS 0706 A.R. Sattler, 6312 (electronic copy)
MS 0706 S. Wallace, 6312 for SPR library (5)
MS 9018 Central Tech. Files, 8944 (electronic copy)
MS 0899 Technical Library, 9536 (electronic copy)